



**12th
International
Corrosion
Congress**

AD-A273 667



①

PRECEEDINGS

S DTIC
ELECTE
DEC 09 1993
A

September 19-24, 1993

VOLUME 5B

Houston, Texas USA

93-29555



The information has been approved
for public release and sale; its
distribution is unlimited.

**CORROSION:
GENERAL ISSUES**

93 12 2 092

NACE
International

**Best
Available
Copy**

***CORROSION CONTROL FOR
LOW-COST RELIABILITY***



**12th
International
Corrosion
Congress**

PRECEEDINGS

VOLUME 5B

CORROSION: GENERAL ISSUES

The manuscripts in this volume have been printed from camera-ready copy and have been accepted without editing by NACE International.

Neither NACE International, its officers, directors, members thereof, nor instructors accept any responsibility for the use of the methods and materials discussed herein.

Any goods, products, and/or services mentioned are mentioned as items of information only. Such mention does not constitute an endorsement by NACE International.

The information is advisory only, and use of the materials and methods is solely at the risk of the user.

Printed in the USA. All rights reserved. This book, or parts thereof, may not be reproduced in any form without permission of the copyright owners.

Copyright, NACE International, 1993

ISBN: 1-877914-65-7

Published by

NACE International
P.O. Box 218340
Houston, TX 77218-8340

| | |
|--------------------|-------------------------------------|
| Accession For | |
| NTIS CRA&I | <input checked="" type="checkbox"/> |
| DTIC TAB | <input type="checkbox"/> |
| Unannounced | <input type="checkbox"/> |
| Justification | |
| By | Vol. 5B-9142 |
| Dist | SDC 400 |
| Availability Codes | |
| Dist | Avail. and/or Special |
| A-1 | 2 |

DTIC QUALITY INSPECTED 3

NACE
International

Degradation by Ripple-Load Effect: Impact on Life Prediction

P.S. Pao, R.A. Bayles, and D.A. Meyn
Naval Research Laboratory
Washington, D.C. 20375

G.R. Yoder
Office of Naval Research
Arlington, VA 22217

Abstract

If very small amplitude cyclic (or "ripple") loads perturb an otherwise constant load condition in an aggressive environment, life prediction based solely on the static stress-corrosion cracking threshold (K_{ISCC}) may prove nonconservative, as the ripple-load effect may produce fracture in a structural alloy at stress-intensity levels less than 50% of K_{ISCC} . By approaching ripple-load cracking as an extreme case of high stress-ratio (corrosion) fatigue, a threshold parameter (K_{IRLC}) is identified to ensure fail-safe life even in the presence of the ripple effect. From study of select materials in each of the primary structural alloy families - Fe, Ti, and Al, those materials which exhibit relatively high levels of K_{ISCC} appear to be more prone to degradation by the ripple effect. The occurrence of a ripple effect in a relatively benign environment is also explored for a titanium alloy in ambient air, which exhibits a sustained load cracking behavior that has been attributed to internal hydrogen content. Similarly, a significant ripple-load effect can be predicted, with a threshold level of K_{IRLC} less than 50% of the sustained load cracking threshold, K_{ISLC} .

Introduction

In many engineering applications, the primary function of a structural material is to carry loads reliably over a period of time. However, these loads are often borne in an aggressive environment where degradation in load-carrying capacity can occur over time by a variety of cracking phenomena, including stress-corrosion cracking (SCC). For a structural material which contains a crack or crack-like defect, the resistance to SCC is often evaluated in terms of the fracture mechanics parameter, K_{ISCC} , the threshold-stress-intensity factor below which crack extension will not occur. The measurement of K_{ISCC} and its application to the design of structures for a marine environment commonly presumes sustained or constant load conditions. Applications in the real world, however --- which span the gamut, e.g. from offshore platform structures to steam turbine blades --- rarely involve an absolutely constant load condition, but are far more apt to involve the superposition of relatively small amplitude cyclic load perturbations. Though such perturbations might at first glance seem virtually insignificant on the basis of their amplitude, mounting evidence indicates to the contrary, that the "ripple effect" - a term first used by Speidel¹, may be quite significant. For example, the work of Crooker et al.² demonstrated that the ripple-load effect could produce fracture in a steel at stress-intensity levels as much as 60% less than the K_{ISCC} threshold in aqueous sodium chloride solution, for a ripple-load amplitude equal to 10% of the maximum load. In fact, recent work with titanium and aluminum alloys similarly suggests that the presence of such ripple loads can significantly shorten structural life. Parkins^{3,4} has observed that small fluctuating loads may produce the initiation of SCC cracks at significantly lower stresses than those required to produce SCC under purely static

Key terms: ripple-load, stress-corrosion cracking, sustained-load cracking, threshold

loads. Thus, life prediction based solely on the static K_{ISCC} , without consideration of perturbing ripple loads, may be nonconservative.

Not all materials, however, appear susceptible to the ripple-load effect. For instance, though Crooker et al.² observed a 60% degradation in the case of an HY-130 steel, yet for identical loading conditions, they found absolutely no degradation in the case of a 4340 steel. Similar examination of sensitivities to the ripple-load effect has been made for materials in other families of structural alloys as well. To explain this seemingly enigmatic behavior, a predictive framework has been developed wherein ripple-load cracking is approached as an extreme case of very high stress-ratio fatigue crack growth. Critical conditions for ripple-load cracking are defined, and a new threshold parameter (K_{IRLC}) is identified which can ensure a fail-safe life under ripple conditions.

The extension of this predictive framework as it pertains to the influence of ripple loads on sustained load cracking (SLC) behavior in titanium alloys will also be examined. This case parallels that of SCC, except that the surrounding environment is air which is less aggressive. Some of the "dry" structures which could be potentially vulnerable to this type of ripple-load degradation include aircraft structures, gas turbine engine disks and blades, etc. where a large sustained load is usually accompanied by ripple loads. Inasmuch as subcritical time-dependent SLC failure can occur above a threshold level, K_{ISLC} , owing to the presence of internal hydrogen, the prediction of ripple-load degradation of the cracking threshold to levels significantly below K_{ISLC} will be explored as a function of hydrogen content in Ti-6Al-4V.

Experimental Procedures

Both SCC-resistant and susceptible alloys from the three major engineering alloy families were examined in this study, including 5Ni-Cr-Mo-V steel and AISI 4340 steel, beta-annealed (BA) and recrystallization-annealed (RA) Ti-6Al-4V alloy, and peakaged 7075-T651 and overaged 7075-T7351 aluminum alloys. To study the ripple-load effect in conjunction with SLC of titanium alloys in ambient air, the very same beta-annealed Ti-6Al-4V alloy was selected for examination at two levels of internal hydrogen content, viz. 60 and 1100 wppm. Specific chemical analysis, product form, and mechanical properties for these alloys are available from previous publications.⁵⁻⁷

To simulate a ripple-load condition and to measure threshold levels of stress-intensity range directly, precracked specimens were cyclically loaded at room temperature in a 3.5% NaCl solution with a stress ratio (minimum: maximum) of $R = 0.90$ (10% ripple loading), a haversine or a triangular waveform, and a cyclic frequency of either 0.1 or 5 Hz. SCC thresholds were determined in the 3.5% NaCl solution using either constant load cantilever bend bar tests or slow-strain rate tests with a loading rate of 10^{-4} MPa \sqrt{m} /s. Thresholds for SLC were similarly determined in an ambient air environment. Crack lengths were determined using a compliance related CMOD technique. Details of the experimental procedures have been published elsewhere.^{2,5-7}

Analysis of the Ripple-Load Effect

Ripple-load cracking can be approached as a case of corrosion-fatigue at very high stress ratio, with consideration of the relationship between the small amplitude stress-intensity range associated with ripple loading, ΔK , the threshold for corrosion fatigue, ΔK_{th} , the maximum stress intensity, K_{max} , and K_{ISCC} . In the context of a "ripple" or small amplitude cyclic load, the stress ratio is often presumed to be $R \geq 0.90$, although such a stipulation does not affect the generality of the treatment offered in this paper.

A structure stressed above K_{ISCC} and under a sustained load is expected to fail by a stress-corrosion cracking mechanism. In this study, our attention was focused on the regime below K_{ISCC} where propagation of existing cracks and failure are not expected under a constant load condition. Thus, with the presence of small ripples superimposed on a large sustained load, cf. Fig. 1a, the maximum stress intensity in the ripple-load cycle, K_{max}^{RL} , was equal to or less than K_{ISCC} . That is, the first condition for ripple-load cracking can be set as:

$$K_{max}^{RL} \leq K_{ISCC} \quad (1)$$

Next, from corrosion fatigue considerations, crack propagation is not going to take place during ripple loading unless ΔK^{RL} in the ripple cycle equals to or exceeds ΔK_{th} or:

$$\Delta K_{th} \leq \Delta K^{RL} \quad (2)$$

$$\text{or} \quad \frac{\Delta K_{th}}{1-R} \leq K_{max}^{RL} \quad (2a)$$

Thus, a new parameter, K_{IRLC} , the ripple-load cracking threshold below which ripple-load cracking does not occur, can be defined as:

$$K_{IRLC} = \frac{\Delta K_{th}}{1-R} \quad (3)$$

Combining (1), (2a) and (3), the conditions for a material to exhibit a ripple-load cracking are:

$$K_{IRLC} \leq K_{max}^{RL} \leq K_{ISCC} \quad (4)$$

Relation (4) is schematically illustrated in Fig. 1b. The ripple effect region, whose upper bound is the stress-corrosion cracking threshold, K_{ISCC} , and whose lower bound is the ripple-load cracking threshold, K_{IRLC} , defines a "window of susceptibility" in which the ripple-load effect would be anticipated. The wider the window the more susceptible the material is to ripple-load cracking. In the extreme case where K_{IRLC} approaches K_{ISCC} , the susceptibility window vanishes and no ripple-load effect is expected.

If one considers the difference between the threshold for ripple-load cracking, K_{IRLC} , and K_{ISCC} , then the maximum extent of ripple-load degradation can be defined as:

$$\% \text{ degradation} = (1 - K_{IRLC} / K_{ISCC}) \times 100 \quad (5)$$

Finally, the ripple-load cracking time-to-failure curve can be obtained from a simple piecewise numerical integration of the corrosion-fatigue crack growth rate curve³, for the particular structural geometry of concern. For the 5Ni-Cr-Mo-V steel, the time-to-failure curve was predicted from cantilever bend bar geometry, and for the other materials, from a compact tension geometry.

Results and Discussion

(A) Ripple Effect in Aggressive Environment

Figure 2 shows the effect of ripple loading on SCC-resistant 5Ni-Cr-Mo-V steel and SCC-prone, high strength AISI 4340 steel, respectively. The predicted ripple loading time-to-failure curve obtained through integration of corrosion-fatigue data for 5Ni-Cr-Mo-V steel⁸ is included in Fig. 2. As can be seen from Fig. 2, 5Ni-Cr-Mo-V steel, though resistant to SCC, is very susceptible to ripple-load cracking under a 10% ripple. The predicted ripple-load cracking threshold, K_{IRLC} , is only 31 MPa \sqrt{m} . This is much lower than the static K_{ISCC} of 110 MPa \sqrt{m} . This opens a large window for ripple-load cracking susceptibility, with a maximum potential degradation of 72%. The predicted time-to-failure curve under ripple loading agrees well with the direct experimental determination. Moreover, the prediction suggests a lower ripple-load threshold than that determined directly from 4000-hr tests. For AISI 4340 steel, the K_{IRLC} predicted from the ripple-load test is 33 MPa \sqrt{m} , which is identical to the measured level of K_{ISCC} . Using relation (4), the susceptibility window is nonexistent and, therefore, no ripple-load effect is expected on this SCC-prone steel. Ripple-load cracking data shown in Fig. 2b certainly support this prediction.

The predicted ripple-load cracking curves for two titanium alloys which exhibit different levels of SCC resistance are shown in Fig. 3. The SCC-resistant, beta-annealed Ti-6Al-4V has an SCC threshold of 60 MPa \sqrt{m} and the predicted K_{IRLC} is only about 28 MPa \sqrt{m} . Thus, a large susceptibility window, shown in Fig. 3a, representing a 53% ripple-load degradation, exists for this SCC-resistant titanium alloy. Experimental data illustrate a good agreement with the predicted time-to-failure curve. Figure 3b shows the ripple-load degradation of the recrystallization-annealed Ti-6Al-4V, which is less SCC resistant than the beta-annealed Ti-6Al-4V. The ripple-load cracking threshold was determined to be around 39 MPa \sqrt{m} , which is about 9% lower than the static K_{ISCC} .

The predicted ripple-load cracking curves for SCC-resistant and SCC-prone aluminum alloys are presented in Fig. 4. Figure 4a shows the ripple-load time-to-failure curve for overaged 7075-T7351, which exhibits excellent SCC resistance, even in the short-transverse (ST) orientation. Again, as in previous SCC-resistant ferrous and titanium alloys, the susceptibility window is large for overaged 7075-T7351. The predicted K_{IRLC} is 58% lower than K_{ISCC} . The ST-oriented, peakaged 7075-T651 is well known for its low SCC resistance and has accounted for the bulk of SCC failures in high strength aluminum alloys. Yet, like the SCC-susceptible AISI 4340 steel, this peakaged 7075 does not exhibit any ripple-load degradation (Fig. 4b). The K_{IRLC} and K_{ISCC} are identical in ST-oriented 7075-T651.

Analysis of Figs. 2-4 reveals that the materials which exhibit greater SCC resistance under static load conditions are far more susceptible to ripple-load degradation. For the specific materials and conditions examined in this work, the more SCC-resistant materials, from 5Ni-Cr-Mo-V steel to beta annealed Ti-6Al-4V to 7075-T7351 Al, are more prone to ripple-load degradation than the less SCC resistant materials, from high strength AISI 4340 steel to recrystallization annealed Ti-6Al-4V and 7075-T651 Al. The significance of this finding is obvious, at least phenomenologically, as a material selected for its superior SCC resistance may fail if ripple-load conditions exist.

A few words are also in order regarding the ripple-load time-to-failure curves. It is significant to note that the predicted curves not only agree well with the experimental data but also permit the saving of the much greater time and expense associated with the direct experimental determination of such time-to-failure curves. For instance, as shown in Fig. 2a, a test duration up to 30,000 hours (~ 3.5 yr) would be required to establish experimentally the ripple-load time-to-failure curve for 5Ni-Cr-Mo-V steel.

Ripple-load cracking characteristics can be affected by mechanical and environmental parameters, however, many of which are not adequately understood. The size of the ripple can significantly influence the ripple-load cracking phenomenon⁵. Extremely small ripple loads (less than 2.5% of the sustained load) were found to have no damaging effect on 5Ni-Cr-Mo-V steel. Temperature and ripple-load frequency, which are known to affect corrosion-fatigue crack growth kinetics, should influence ripple-load cracking.

(B) Ripple Effect in a Benign Environment

To investigate the influence of ripple loads on the SLC behavior of titanium alloys in ambient air, the analysis presented above in Eqs. (1) - (4) and illustrated in Fig. 1 is modified by simply replacing the parameter K_{ISCC} with the K_{ISLC} stress-intensity threshold measured for an air environment, and interpreting ΔK_{th} as the fatigue crack propagation threshold measured in ambient air for an alloy of a particular internal hydrogen content. For the Widmanstätten BA Ti-6Al-4V alloy studied, fatigue crack propagation data are shown in Fig. 5a for hydrogen contents of 60 and 1100 wppm. The lower threshold ΔK_{th} observed in the case of the 1100 wppm H alloy may be attributable to a mechanism involving hydrogen assisted plasticity⁹. For the 60 wppm H material, the K_{ISLC} threshold in air is measured to be about 58 MPa \sqrt{m} , as indicated in Fig. 5b. Thus, for this 60 wppm H material, with a ripple-load threshold, K_{IRLC} , of 28 MPa \sqrt{m} predicted via Eq. 3, a degradation as much as 52% below K_{ISLC} could be anticipated, as displayed in Fig. 5c. For the 1100 wppm H material, the lower ΔK_{th} translates to a lower K_{IRLC} threshold of 21 MPa \sqrt{m} . The K_{ISLC} threshold and the extent of ripple-load degradation for this high hydrogen-containing material is currently under study. It is thought that such ripple-load cracking could potentially impact the performance of "dry" structures such as airframe components as well as gas turbine engine disks and blades.

Conclusions

- In an aggressive environment, if a structural material subjected to a constant load condition is perturbed by very small amplitude cyclic (or "ripple") loads, any life prediction based on K_{ISCC} may be nonconservative, as the ripple-load effect may produce fracture at stress-intensity levels substantially less than the static K_{ISCC} threshold.
- To assure a fail-safe life from the ripple effect, a threshold parameter (K_{IRLC}) below which fracture will not occur can be identified by approaching ripple-load cracking as an extreme case of high stress-ratio corrosion fatigue.
- For certain materials from each of the primary structural alloy families, ripple-load thresholds (K_{IRLC}) in aqueous sodium chloride solution are predicted to be at levels some 50% of the K_{ISCC} threshold, or less; materials which exhibit greater cracking resistance under static load conditions seem to exhibit greater ripple-load degradation.

- In a relatively benign environment, such as ambient air in the case of a titanium alloy, a significant ripple-load effect, which appears to be influenced by internal hydrogen content, is similarly predicted relative to the sustained load cracking threshold (K_{ISLC}).

Acknowledgments

This work was funded by the Office of Naval Research, Corrosion Science Program, and monitored by Dr. A. J. Sedriks, Program Manager.

References

1. M.O. Speidel, Corrosion Fatigue of Steam Turbine Blade Materials, (New York, NY: Pergamon, 1983), p. 1.
2. T.W. Crooker, J.A. Hauser II and R.A. Bayles, Environmental Degradation of Engineering Materials, (University Park, PA: Pennsylvania State University Press, 1987), p. 521.
3. R.N. Parkins, B.S. Greenwell, Metal Science, Aug./Sept. 1977: p. 405.
4. R.N. Parkins, P.M. Singh, Corrosion, 46 6 (1990): p.485.
5. P.S. Pao, R.A. Bayles and G.R. Yoder, Trans. ASME, J. Eng. Matls Tech., Series H, 113 (1991): p. 125.
6. G.R. Yoder, P.S. Pao, and R.A. Bayles, Scripta Met., 24 (1990): p. 2285.
7. P.S. Pao, S.J. Gill, R.A. Bayles, and G.R. Yoder, Scripta Met., 25 (1991): p. 2085.
8. O. Vosikovsky, J. Testing and Evaluation, 6 (1978): p. 175.
9. C.D. Beachem, Met. Trans., 3 (1972): p. 437.

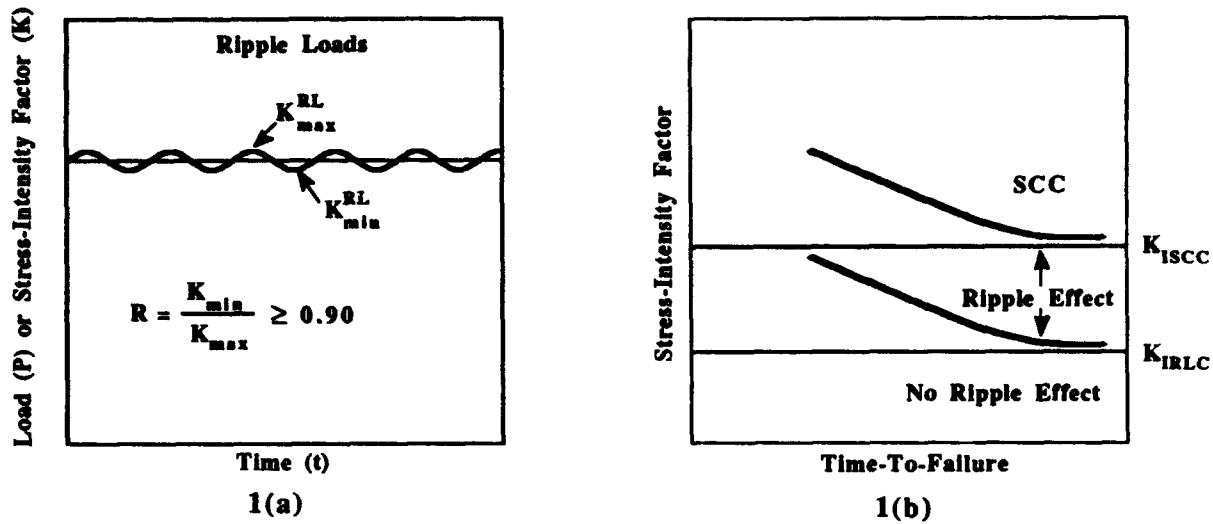


Fig. 1 Schematics on analysis of ripple-load effect. (a) "Ripple" load superposed on much larger sustained load. (b) Susceptibility to ripple-load effect.

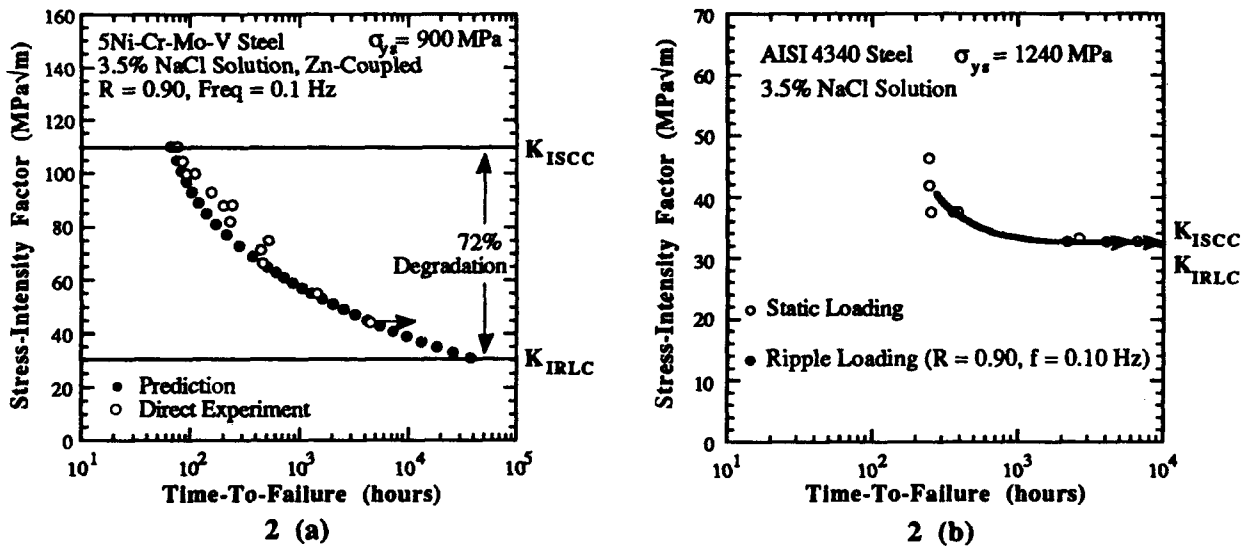
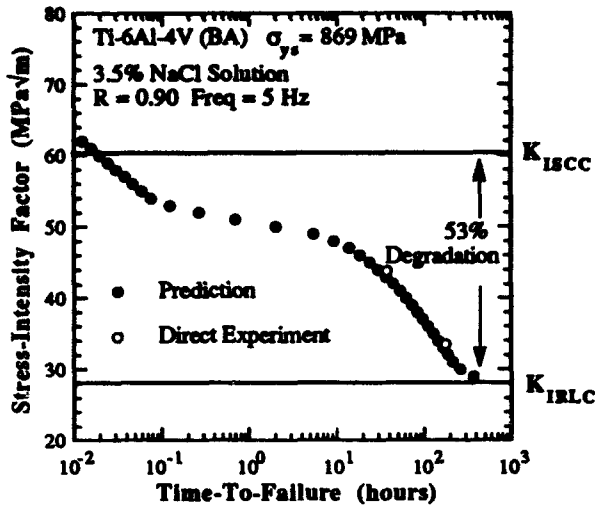
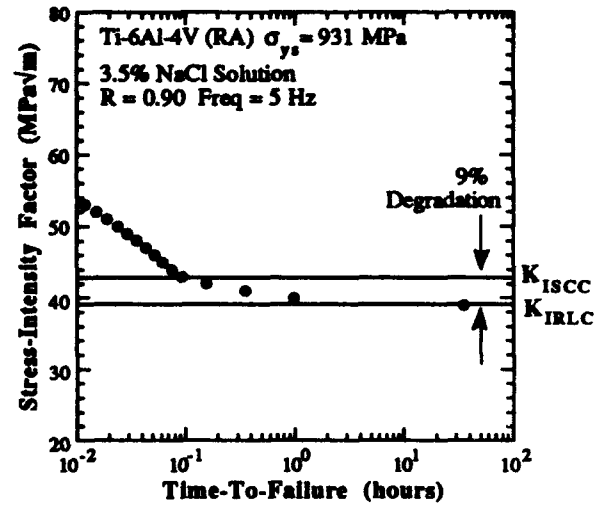


Fig. 2 (a) Ripple-load degradation in 5Ni-Cr-Mo-V steel. (b) Ripple-load cracking and stress-corrosion cracking in AISI 4340 steel.

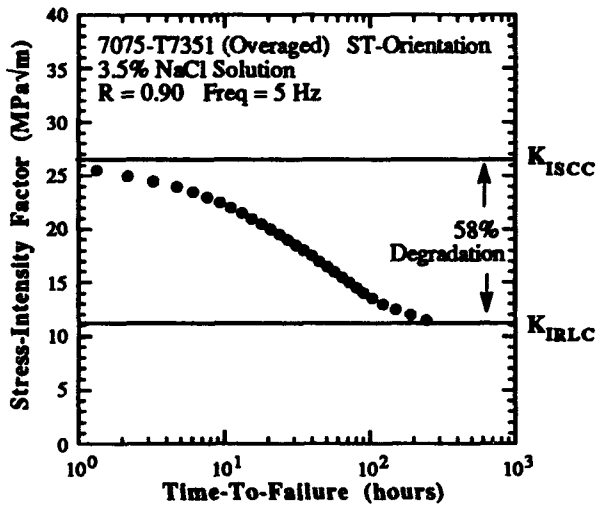


3 (a)

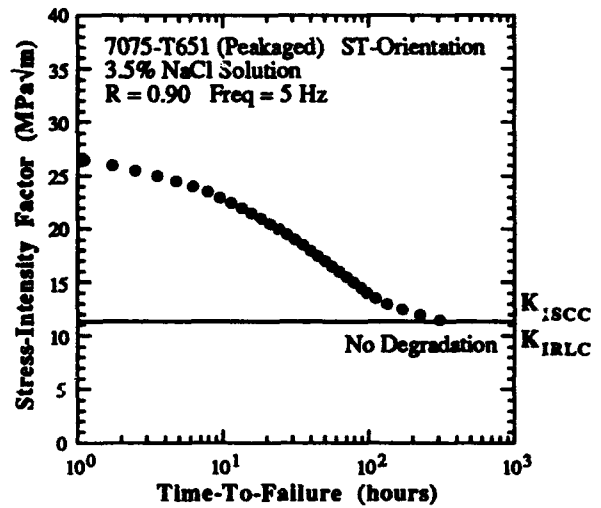


3 (b)

Fig. 3 Ripple-load degradation in (a) beta-annealed Ti-4Al-4V and (b) recrystallization-annealed Ti-6Al-4V.



4 (a)



4 (b)

Fig. 4 (a) Ripple-load degradation in ST-oriented, overaged 7075-T7351. (b) Ripple-load effect in ST-oriented, peakaged 7075-T651.

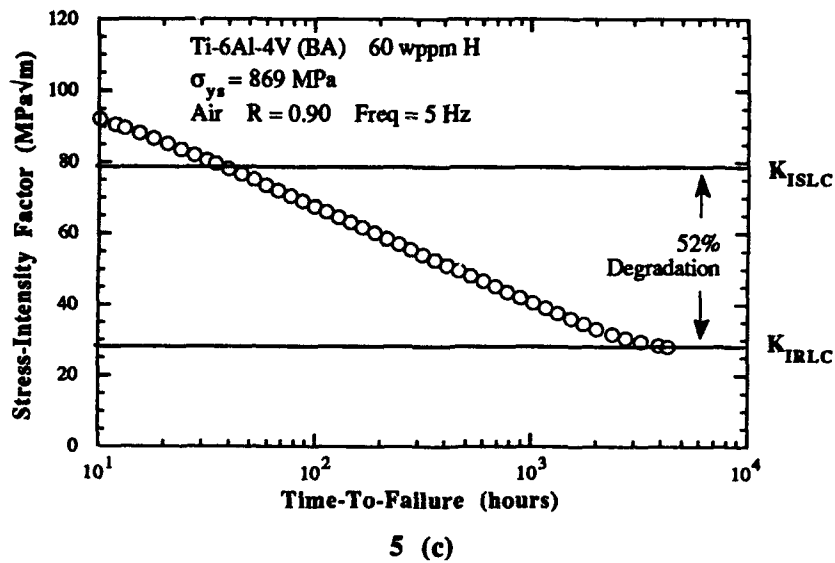
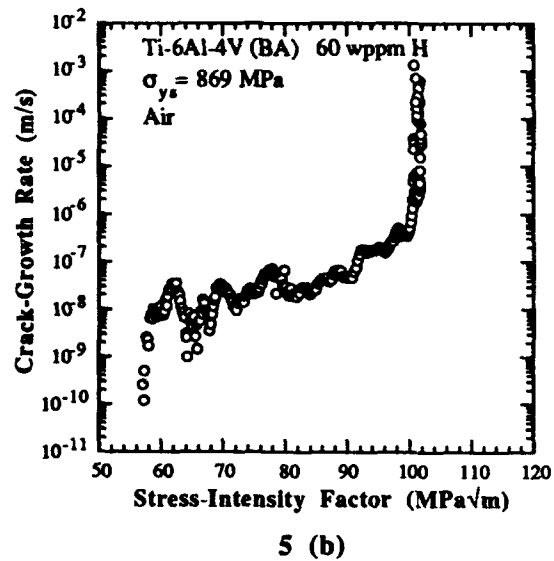
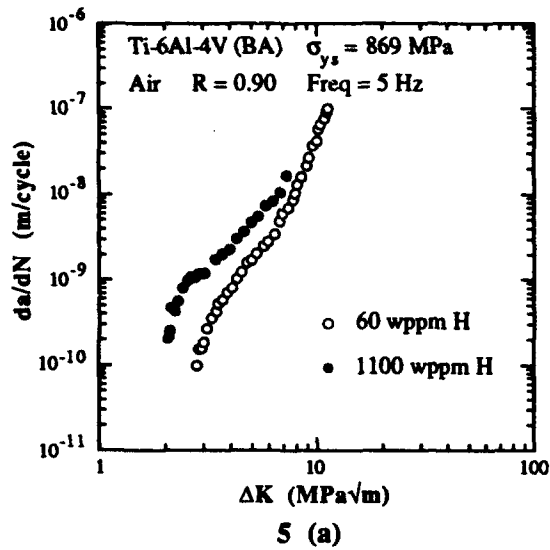


Fig. 5 (a) Fatigue crack growth rate of beta-annealed Ti-6Al-4V in air @ $R=0.90$.
 (b) Crack growth rate of beta-annealed Ti-6Al-4V (60 wppm H) in air under slow strain rate condition. (c) Ripple-load degradation in air in beta-annealed Ti-6Al-4V (60 wppm H).

**Some Through-Life Risk/Reliability Considerations
For Components Subject To Corrosion - A Safety Assessor's View**

R Crombie

AEA Technology - Safety and Reliability
SRD
Wigshaw Lane
Culcheth
Warrington
Cheshire
WA3 4NE
UK

Abstract

Surveys and assessments of pressure vessel and piping failure statistics can provide useful information on failure modes and frequencies. However, design codes and standards do not always rigorously address all those failure modes which failure statistics and operating experience show to be important, and this is shown to be true for corrosion - related degradation mechanisms.

This paper, written from the viewpoint of the independent Safety Assessor, considers the findings of recent pressure vessel failure surveys with particular reference to the influence of corrosion - related processes on component integrity. The paper indicates the extent to which the through-life reliability of components subject to corrosion continues to depend to a significant degree on judgement based upon experience. Attention is focused on pitting and stress corrosion cracking and the paper discusses the roles of in-service inspection and corrosion monitoring in ensuring component integrity and high reliability. Some implications arising as a result of recent developments in these fields are considered.

Key terms: risk, reliability, integrity, corrosion, environmentally assisted cracking.

Introduction

Prediction of the lifetime for safe and reliable operation has become a topic of major importance to those involved in the design and operation of large and complex high cost plant. The topic is not only of interest for predicting the remanent life of comparatively young plant, but is also particularly relevant in the case of ageing plant which has given safe and reliable operation, and for which the owners/operators can envisage a case for plant life extension beyond the original design life. For many types of component or plant, for which the consequences of failure may be severe, the complete life cycle from design, through manufacture, construction, operation and decommissioning is likely to be subject to strict national regulatory and licensing criteria. Formal safety justifications will invariably be required to cover the complete life cycle of such items, and these will almost certainly require modification with increasing time in service. Against this background demand for maximised service life and increasingly more stringent design, regulatory and licensing criteria, there is a parallel need to minimise construction, operation and maintenance costs whilst maintaining, and indeed improving safety and reliability of operation. Very often decisions concerning these apparently conflicting requirements have to be based upon the same sources of available information, and on the same design/assessment criteria and analytical techniques/methodologies. The various tools and techniques usually available for this purpose include data obtained from structural failure surveys, application of appropriate design codes and standards, structural analysis and integrity assessment methodologies, repair, replacement and inspection.

The technical issues which affect the reliability of a component or vessel subject to corrosion and the risks associated with its operation are invariably the same as those which need to be addressed in life prediction studies or in the preparation of through-life safety justifications. A previous paper¹, written from the viewpoint of the independent Safety Assessor, discussed the two alternative routes to a safety

justification, namely the deterministic and the probabilistic approaches, and highlighted some of the difficulties encountered in sustaining a truly deterministic approach. That earlier paper considered the extent to which design codes generally address the more common failure modes as indicated by vessel failure statistics, and discussed the manner in which corrosion-related processes may be addressed in life prediction studies or safety cases in the light of current knowledge and understanding.

This present paper develops and expands upon the theme of that earlier paper¹, and highlights the extent to which the integrity and reliability of components subject to corrosion continues to rely to a significant degree on judgement based upon experience. Some examples are given. A section then focuses on pitting and stress corrosion cracking (SCC) and considers the roles of both in-service inspection and corrosion monitoring in minimising risk of failure. Some current developments in these areas are summarised and possible implications discussed.

Life Prediction And Safety Assessment Routes

The two methodologies available for the production of a safety case are the deterministic and the probabilistic approaches. The relative merits of these two routes and the difficulties frequently encountered in sustaining a deterministic safety justification are discussed in more detail elsewhere¹. These difficulties are exacerbated in the case of older plant for which component-specific data are more difficult, if not impossible, to obtain and for which no recognised design code or standard may have existed at the time of manufacture. A degree of judgement must therefore invariably be introduced into the analysis. Despite these limitations the deterministic approach remains the route favoured by safety authorities. On the other hand, at the present time the probabilistic approach is generally regarded by the Safety Assessor as a valuable support to, but not a substitute for, a deterministic analysis. The value of the approach lies in its ability to identify the parameters of primary importance in the overall safety case, such as the critical regions of the component or vessel and the operational or material factors having the greatest influence on the analysis.

Failure Statistics, Failure Modes And Design Codes

A number of pressure vessel and piping surveys have been reported in recent years²⁻⁵. Certain shortcomings in defining failure categories and in data reporting procedures have created difficulties in cross-comparing the results of different surveys, either to establish trends or to increase the database⁶. Nonetheless such statistics do provide useful information on failure frequencies and, especially, on the various failure modes to which components may be liable in service. The results of the third United Kingdom survey² of pressure vessel failure statistics have been widely quoted in most subsequent surveys and form a useful basis for discussion. Smith and Warwick² reviewed statistics for 20,000 "Class 1" pressure vessels for the period 1962 - 78 and covered more than 300,000 vessel years operation. The survey recorded 229 failures with cracking as the most common cause, being associated with 216 of these cases. Pre-existing fabrication faults were the most common origin of cracking, accounting for about 30% of the cases, and in about 14% of the cracking failures corrosion was judged to be the major factor affecting crack propagation. The results of that survey are summarised in Tables 1-3.

The most recent UK survey³ covering the period 1983-88, involves 360,000 vessels and encompasses about 1.8×10^6 vessel years operation. The scope of this survey was extended beyond so-called "Class 1" vessels to include all unfired pressure components, thus providing more general figures for pressure vessel reliability and the more frequent causes and modes of failure for a wider population. Davenport³ reports a total of 92 failures, 60 of which involved cracking with fatigue as the most common cause. Corrosion was identified as the principal cause of failure in 23 of the 92 cases (ie 25%). An observation of interest as regards component reliability is that about 75% of all fatigue failures occurred after at least 10 years service, whereas about 65% of corrosion failures occurred at between 5 and 10 years.

The two UK surveys^{2,3} both demonstrate the most common cause of pressure vessel failure to be associated with the existence and growth of cracks. The Smith and Warwick data (Tables 1-3) indicate that in most cases cracking was associated with fabrication-induced defects; fatigue cracking was second in importance and corrosion assisted crack growth accounted for 14%. Cause of failure was not ascertained for 28% of the reported failures and it is therefore possible that the true figures for the other causes may be higher than suggested by Table 2. Davenport's survey³ ranked corrosion assisted crack growth as the second most common principal cause of failure after fatigue.

Table 4, due to Harrop⁷, on the other hand, presents an indication of the extent to which design codes currently address various failure modes. The relative degree of coverage can be considered as typical of that associated with nuclear vessels and non-nuclear, unfired pressure vessels. It is evident that corrosion-related processes are not addressed in any depth despite their significance in terms of failure mode as demonstrated by vessel failure statistics.

Corrosion Considerations and Component Reliability

The cost of corrosion to developed countries has been estimated⁸ to be about 4% of gross national product with up to about 25% of this cost being preventable by the application of existing knowledge. A recent analysis⁹ of over 400 incidents causing environmental harm has indicated that about one hundred of these fall into a category defined as "mechanical failure", which includes failure modes such as fatigue, valve failure and corrosion; five of these are attributable to corrosion¹⁰. These various surveys^{8,9} indicate the potential for corrosion related processes, both in terms of cost to industry and in terms of resulting hazard to the environment. Failure statistics confirm the importance of corrosion-related processes as a contributor to pressure vessel failures. Even so, however, failure frequencies associated with corrosion are low, forming a subset of the overall data from a given survey. For example, Davenport's³ data indicate overall failure frequencies of about 7.8×10^{-6} and 4.3×10^{-5} per vessel year respectively for catastrophic and non-catastrophic failures; the corresponding frequencies for failures associated with corrosion will be lower than these values by a factor of about 3-4. Corrosion-related processes are materials-environmental interactions which can be significantly affected by other factors, such as stress or temperature. It could thus be argued that the low failure frequencies associated with corrosion represent the degree to which adverse combinations of materials, environment and other influencing factors are actually avoided in the design and operation of such vessels.

The corrosion-related mechanisms of potential importance as regards integrity and reliability are general corrosion, pitting and environmentally assisted cracking (EAC). The two forms of EAC are corrosion fatigue and stress corrosion cracking (SCC). Vessel failure statistics indicate that pressure vessel failure due to general corrosion, and not involving crack growth, is a comparatively rare event. Pitting in itself may not hazard overall integrity, but is an insidious form of localised attack which could lead to premature failure due to leakage. However, conditions conducive to pitting could also be conducive to the initiation of EAC which does pose a potential threat to vessel integrity. The failure statistics discussed in the previous section indicate that between 14% and 25% of recorded failures are attributable to a corrosion influence on crack growth. Significant achievements have been made in the understanding of corrosion fatigue in both austenitic stainless steels and low alloy reactor pressure vessel steels. These achievements have largely been realised through the collaborative efforts of the former International Cyclic Crack Growth Rate Group (ICCGR), now recently renamed the International Co-operative Group on Environmentally Assisted Cracking (ICGEAC), and by the contributions of individual members of the Group. Fatigue crack growth expressions are now available for these materials in both air and in a light water reactor environment. However, despite much effort and progress in the understanding of SCC, again principally through the work of the ICGEAC, a quantitative predictive model for this form of EAC is not yet available.

The previous section has shown that, in general, the coverage of corrosion processes by pressure vessel design codes and standards, in relation to structural integrity, is fairly superficial (see Table 4). Regarding the ASME Boiler and Pressure Vessel Code, for example, Bernstein¹¹ points out that protection against corrosion-related failure modes is considered the responsibility of the designer, and the code provides no specific guidance since environmental conditions can be so variable. BS 5500¹²

for unfired, fusion welded pressure vessels places responsibility on the purchaser and manufacturer to "give consideration to the likely effect which corrosion will have upon the useful life of the vessel". Guidance on stress corrosion cracking is to the effect that where this may occur "consideration should be given to the materials used and the residual stress in the vessel". Pitting is scarcely, if ever, mentioned.

It follows from above that, with the possible exception of corrosion fatigue, the absence from design codes and standards of specific guidelines or directives for addressing corrosion-related mechanisms not only places responsibility upon the designer and/or user of the component, but creates a situation where decisions have to be based upon knowledge, judgement or experience, or a combination of all three. Lessons learned from past experience (failure surveys?) can be of vital importance as a basis of decision making for new plant. In the field of corrosion, organisations such as NACE and symposia such as this provide effective means for disseminating the fruits of knowledge gained through practical experience. Siebert, in publications of this Association^{13,14}, has given numerous examples of design/manufacturing decisions which have been made where previous service experience was available. A selection of the cases quoted by Siebert is given in Table 5. More recently Bonora¹⁵ has reported the premature failure of longitudinally welded carbon-manganese steel pipe for potable water supply. Although other factors were found to exert an influence, the principal cause of failure was ascribed to the use of welding consumables which produced a longitudinal weld deposit anodic to the base material. The pipework was approximately six years old and Bonora reported that the principal of low first cost prevailed; the true price was now being paid.

Other typical examples concern ships propellers and small heat exchangers¹⁶. In the first of these severe wastage was observed on a manganese bronze propeller. The problem was identified as dezincification and was attributed to an undesirable microstructure in combination with a very low tin content. Propellers of identical design on a number of similar ships were found to be similarly affected and for the same reasons. The second example concerned a number of small heat exchangers, again operating in a marine environment. The general design consisted of aluminium brass tubes expanded into a naval brass tube plate. The heaters were originally fitted with cast iron headers which were lined internally to prevent wastage due to dissimilar metal attack. Early local failure of the lining led to rapid perforation of some headers. The operators decided to replace the cast iron by a "better" material, and gun metal was selected. This transferred the problem to the tube plates and tubes, severe wastage of which was sustained by the modified units after about one year. The gun metal headers remained in good condition! The suggested solution was to refit unlined cast iron headers and to implement a policy of planned inspection and replacement.

The feature common to all of the above examples is that most, if not all, could have been avoided by the application of knowledge which not only existed, but was readily available. However, the most classic example of all has to be the case quoted by Siebert¹³ of a minesweeper built during World War II. The ship was constructed from stainless steel to exploit the non-magnetic properties of that material, and the vessel was of welded construction. Siebert¹³ reports that the ship failed by chloride SCC during its shakedown cruise. Regrettably, Siebert gave no reference for his source document. Where is it now? What other lessons are to be found within its covers and at what cost will these lessons be relearned? What other examples of failures which should never have happened will be reported at this Congress?

Looking Ahead

The third UK survey² recorded 229 failures from a population of 20,000 Class 1 vessels covering about 310,000 vessel years operation during the period 1962 - 78. The fourth survey³ has yielded 92 recorded failures from a wider range of pressure vessels, covering 360,000 vessels and 1.8 million vessel years during the period 1983 - 88. Although these two surveys are not comparing like with like, the data do nevertheless suggest that lessons are being learned from past experience. The reduction in the number of failures between these two surveys is likely to be associated with improvements in both manufacturing methods and non-destructive examination techniques coupled with better standards covering both materials and design.

Estimates⁸ of the cost of corrosion to developed countries serve to highlight the potential for corrosion-related failures. Against this, the probability of failure of fairly high integrity pressure vessels due to corrosion-related mechanisms is quite low. Since the treatment of corrosion-related degradation mechanisms by most design codes is at best superficial, consideration of such mechanisms during the design phase, and indeed throughout the service life of the component, has to be based to a large degree upon knowledge, judgement or experience, or a combination of all of these. Whilst various surveys estimate⁸ that up to 25% of the cost of corrosion could be prevented by the application of existing knowledge, recorded case histories tend to support the view that lessons are hard learned as regards corrosion. With regard to the theme of this Congress experience tends to demonstrate that the lowest first-cost option is invariably the worst choice in relation to long-term operational reliability, especially as regards time-dependent degradation mechanisms; on the other hand, the high technology, high cost option is not always the best. Elliott¹⁷ claims that only about half of the agreed information on failures reaches designers, whilst contractors may only receive about 10%. There therefore continues to be tremendous scope for improvement in the gathering, recording and communication of relevant information. However, in terms of failure modes these account for a significant proportion of the recorded failures.

Of the various corrosion mechanisms affecting structural integrity and component reliability general corrosion appears of least concern. Pressure vessel failure due to general corrosion, and which is not associated with crack growth, is a comparatively rare event, and there are a number of mitigating factors which might offset any reduction in pressure boundary thickness resulting from general corrosion¹. Although pitting in itself may not hazard component integrity, leakage of the vessel will obviously affect both reliability and availability. More especially, however, conditions favourable for the initiation of pitting may also be conducive to the initiation of EAC, either through corrosion fatigue or as SCC, with the pits forming preferential sites for EAC initiation^{18,19}. Initiation of EAC does pose a potential threat to component integrity. No validated, quantitative predictive methodology for pitting is yet available. With regard to the corrosion fatigue of austenitic stainless steels and low alloy ferritic steels exposed to a light water reactor environment, the principal factors affecting corrosion fatigue crack growth rates are now quite well understood; the general quality of published data and level of mechanistic understanding is now such that reasonable calculations of corrosion fatigue crack growth can be performed for life prediction or safety justification purposes, and for defining inspection intervals. A good foundation thus exists upon which to base test programmes for studying corrosion fatigue crack growth in other materials exposed to other environments. The notable success achieved by the ICGEAC for RPV materials demonstrates the value of collaboration at both national and international level in addressing and resolving problems of common interest.

Despite considerable recent achievements in understanding the factors affecting SCC behaviour of austenitic stainless steels and low alloy steels in an aqueous environment, a quantitative predictive model for SCC is, as is the case for pitting, not yet available. Of these various corrosion mechanisms pitting and SCC are, therefore, arguably the most difficult to address with respect to component integrity and reliability.

Recognising the shortcomings of vessel design codes as regards corrosion-related mechanisms, and pending the development and validation of quantitative predictive methodologies for pitting and SCC, it seems reasonable to suppose that, for the foreseeable future, demonstration of component integrity and reliability will depend upon more pragmatic approaches. Such approaches are likely to involve judgement, corrosion monitoring and surveillance, and appropriate programmes of in-service inspection. These are discussed below.

Judgement-Based Decisions Which Depend Upon Experience

Observations of plant/component behaviour provide the experience which forms the basis of judgement. Predictive models and methodologies must in turn reflect plant observations. Plateau stress corrosion crack growth rates for low alloy steels published in the open literature^{20,21} cannot support a viable inspection interval and these rates would, if sustained, lead to failure in very short timescales. Such data would imply a high frequency of pressure vessel failures due to stress corrosion cracking; this is not supported by available failure statistics^{2,3}. Similar observations apply in the case

of gas transmission pipelines where field experience does not reflect the implications which could be drawn from the high SCC growth rates measured in the laboratory testing of pre-cracked specimens^{22,23}. Such observations from operating experience strongly suggest that high SCC growth rates are not continuously sustained, and support the concept of an incubation period and/or period of "time at risk". Although based primarily on pipeline steels, further development of the model proposed by Parkins^{22,23} would appear to hold promise, particularly for the life prediction/safety assessment of ageing vessels. For these the application of SCC growth rates derived from pre-cracked specimens would be unlikely to sustain a satisfactory safety justification. Likewise, studies aimed at clarifying the factors affecting time at risk would appear of value as well as of relevance to model development.

Corrosion Monitoring and Surveillance

It is generally accepted that three criteria must be simultaneously satisfied for SCC to occur, ie the co-existence of a susceptible microstructure, a source of tensile stress and an aggressive environment. For most welded vessels and components, and especially for older plant, the first two of these criteria are likely to be satisfied to some degree and cannot be controlled. In general it is only possible to exercise control over the environment.

Dawson²⁴ has recently reviewed a number of the techniques available for corrosion monitoring and surveillance purposes. The key role of electrochemical potential (ECP) in relation to both pitting and SCC is now well established, as is the importance of oxygen in raising ECP in an aqueous environment²⁵. It is equally known that the propensity of steel to both pitting and SCC can be markedly influenced by the type and distribution of manganese sulphide non-metallic inclusions^{25,26,27,28}. The concept of "active" and "inactive" inclusions is not new, and the presence of "active" non-metallic inclusions in ferritic steels has been correlated with an increased propensity to pitting in an aqueous environment²⁸. There is no evidence to suggest that dissolution of soluble "active" inclusions will be prevented by maintaining a low ECP through control of water chemistry. This therefore raises the possibility of pit initiation under conditions of low ECP. Since local environmental conditions within a pit may differ substantially from bulk water chemistry, will maintenance of a low ECP via control of bulk chemistry be able to inhibit further pitting and initiation of SCC? The more "active" behaviour observed in laboratory tests has been associated with sub-micron size inclusions²⁸; on the other hand, in terms of their influence on environmentally assisted cracking large manganese sulphide inclusions generally enhance crack growth rates, whereas materials containing small spherical inclusions are less susceptible²⁹. There would thus appear to be scope for further work to attempt to clarify the role of inclusions, particularly during the early stages of pit development and initiation of SCC. In addition to a quantitative, predictive model for "living with SCC", there seems need for a similar methodology for "living with pitting".

In-Service Inspection

In-service inspection programmes must consider the items to be inspected and the inspection interval. As regards item selection, two categories can be identified depending upon the purpose of the inspection. The first category covers those items which have to be inspected on a technical needs basis, as identified either by, say, fatigue crack growth and fracture analysis, or on the basis of known operational problems. The second category covers those components which are subject to in-service inspection to validate the design intent and to verify the absence of unexpected or unanticipated failure mechanisms. The large number of components of this second category which can exist in complex plant creates difficulties both in the selection of items for inspection and in defining a suitable inspection interval; for many years selection of such items has been based on judgement. Whilst this approach has withstood the test of time, with arguable success, the overall benefits of inspections carried out on this basis, in terms of plant reliability and risks associated with operation are difficult, if not impossible, to quantify. In more recent times great interest has been shown in the use a risk-based approach for the selection of items in this second category. Further details of this approach are presented elsewhere^{30,31,32}. In essence the approach subdivides a plant or component into a number of sub-items and attempts to rank these in decreasing order of risk resulting from failure of the sub-item. Item selection for inspection purposes is then focused on those which make the greatest

contributions to overall risk. The measure of risk associated with each item is the product of its probability of failure and a parameter defining the consequence of failure. This approach is still at a comparatively early stage of development and there are a number of identifiable difficulties and disadvantages. Firstly, there must exist an overall risk criterion against which the output of the approach can be assessed, and below this there has to be an identifiable consequence of failure of the item or component. Secondly, application of the approach demands an input of component failure or item failure probability. This information can only come from failure statistics or from mathematical models. The latter can only at present deal with systematic defects, such as fatigue crack growth, and cannot at present address SCC. Moreover, such models are difficult to validate. Confidence in their use can only be built up by a feed-back loop of plant inspection information, and this will take time. For many engineering components and structures, on the other hand, the failures database is at present too restricted in terms of operating time to give anything other than a qualitative indication of failure frequency. A potential limitation is, therefore, that some failure probabilities thus obtained may be assigned a quantitative significance which is difficult to justify. Nevertheless, if applied in a qualitative manner for ranking purposes, the risk-based approach often possesses certain attractions. By offering a means of ranking based upon contribution to risk, the element of judgement can be reduced and available resources directed to those items or components where inspection will demonstrate the greatest benefits in terms of reduced risk. There is current interest in the approach for a number of applications including nuclear and non-nuclear power plant and for civil engineering, marine and aircraft structures³⁰.

The question of inspection interval remains. In the absence of quantitative predictive models for pitting and SCC, definition of inspection intervals for components or items of either inspection category must for the present remain largely judgement based. This will continue to depend upon the operational experience feed-back information loop, supplemented by progress in understanding of the mechanisms as provided by the results of continuing research and development programmes. The former again underlines the importance attached to the gathering and dissemination of information, and the latter leads on to the issue of quality assurance in research activities. This is a topic for debate in its own right which hopefully will be addressed elsewhere during the course of this Congress.

Concluding Remarks

This paper has sought to highlight the value of information obtainable from component failure statistics. Corrosion-related degradation mechanisms are not particularly well addressed in pressure vessel design codes and standards, despite the fact that such mechanisms account for a significant proportion of pressure vessel failures. In the absence of specific guidelines or directives, decisions affecting integrity and reliability must be based upon knowledge, judgement or experience, or a combination of these. The high potential for corrosion-related failures, and the savings believed achievable through the application of existing knowledge, place importance on the collection and dissemination of information to assist the decision making process. Feed-back of operational experience, as illustrated by examples in the text, demonstrates there is scope for improvement in this area.

Pitting and SCC are perceived to be the more important corrosion-assisted mechanisms as regards integrity and reliability. Predictive models for these are not yet available. Plateau stress corrosion crack growth rates available from the open literature cannot support a viable inspection interval and would, if sustained, lead to failure in short timescales. Such data would imply a high frequency of SCC type failure of pressure vessels which is not borne out by vessel failure statistics.

Pending the development of predictive models for pitting and SCC, which must be capable of reconciliation with plant observations, the paper suggests that, for the foreseeable future, demonstration of integrity and reliability will continue to depend upon a more pragmatic approach. Once again judgement, along with control of environment and in-service inspection will all play key roles. The paper highlights the importance of continuing research to improve understanding of the various combinations of factors which can lead to a vulnerable situation. For safety justification or life prediction purposes the Safety Assessor seeks assurance that such conditions have been and will

be avoided. Finally, an outline is given of some current developments in the fields of chemistry control and in-service inspection, and the paper highlights some possible implications associated with the application of these approaches.

A number of the topics addressed in this paper will hopefully form the subjects of other presentations to this Congress.

Acknowledgements

The author gratefully acknowledges debate with colleagues within SRD on component integrity and reliability issues. However, the views expressed in this paper are his own and do not necessarily represent the views of AEA Technology - Safety and Reliability.

References

1. R Crombie, D W Phillips, "Reliability Considerations For Pressure Vessels Subject To Corrosion". 3rd NACE International Region Management Committee Symposium on "Life Prediction of Corrodible Structures", Cambridge UK, 23-26 September 1991. (NACE; Houston Texas, 1991).
2. T A Smith, R G Warwick, "A Survey Of Defects In Pressure Vessels In The UK For The Period 1962-78 And Its Relevance To Nuclear primary Circuits", United Kingdom Atomic Energy Report, SRD-R-203, December 1981.
3. T J Davenport, "A Further Survey Of Pressure Vessel Failures In The UK". Paper presented at "Reliability 91", London, 10-12 June 1991. (SRD/Institute of Quality Assurance, UK, 1991).
4. S H Bush, Transactions of the ASME, Journal of Pressure Vessel Technology, 110, August 1988, p225.
5. D W Phillips, "Structural Reliability Of Pressurised Metal Components", presented at the Institute Of Mechanical Engineers Seminar on "General Lessons From Simulated Failures And Practical Experience", London, 1 May 1990.
6. L P Harrop, International Journal of Pressure Vessels and Piping, 38 (1989), p189.
7. L P Harrop, "Reliability of Pressure Vessels - Experience And Methods of Analysis". Technical Presentation No 6, Proceedings of 18th Annual Meeting of the Systems Reliability Service Associate members, 27-28 October 1988. UK Atomic Energy Authority.
8. J T N Atkinson, H Van Droffelaar, "Corrosion And Its Control - An Introduction To The Subject", (Houston, Texas: National Association Of Corrosion Engineers, 1982), p107.
9. M Zahid, "EnvIDAS - A Database Of Incidents Causing Environmental Harm", Safety and Reliability Digest, Winter 1992, p7 (SRD, AEA Technology, Wigshaw Lane, Culcheth, Cheshire WA34NE, UK).
10. M Zahid, private communication.
11. M D Bernstein, Transactions of the ASME, Journal of Pressure Vessel Technology, 110, November (1988), p430.

12. BS 5500: 1988, British Standard Specification For Unfired Fusion Welded Pressure Vessels. British Standards Institution.
13. O W Siebert, *Materials Performance*, 17, No 4, April (1978): p33.
14. O W Siebert, *Materials Performance*, 22, No 10, October (1983): p9.
15. P L Bonora, "Corrosion Of Welded Steel Pipes For Potable Water Supply", presented at the Institute of Materials/Society Of Chemical Industry Meeting on "Corrosion And Related Aspects Of Materials for Potable Water Supplies", 8 -9 December 1992; London, UK.
16. R Crombie, unpublished work.
17. P Elliott, *Materials Performance*, 28, No 7, July (1989): p70.
18. P McIntyre, "Crack Initiation At Corrosion Pits - Review Of Power Industry Experience", presented at Institute of Metals Seminar on "Corrosion Pitting And Its Practical Implications", 14 March 1989, London.
19. R F Smith, "Pitting-Related Experience In The Chemical Industry", presented at Ref 18.
20. R M Magdowski, M O Speidel, *Metallurgical Transactions A*, 19A, Jun (1988): p.1583.
21. M O Speidel, R M Magdowski, *International Journal of Pressure Vessels and Piping*, 34 (1988): p119.
22. R N Parkins, *Corrosion Science*, 29, 8 (1989): p1019.
23. R N Parkins, see reference 1, Paper No 52.
24. J L Dawson, see reference 1, Paper No 35.
25. "International Co-operative Group On Cyclic Crack Growth (ICCG) Tenth Anniversary Report", *International Journal of Pressure Vessels and Piping - Special Issue*, 40, 5 (1989).
26. H Hänninen, W Cullen, M Kemppainen, *Corrosion*, 46, 7 (1990): p563.
27. J Kumiya, H Anzai, I Masaoka, *Corrosion*, 48, 5 (1992): p419.
28. G Wranglen, *Corrosion Science*, 14, (1974): p331.
29. H Hänninen, I Aho-Mantila, K Törrönen, *International Journal of Pressure Vessels and Piping*, 30, (1987): p253.
30. American Society of Mechanical Engineers, "Risk-Based Inspection - Development of Guidelines", Vol 1 General Document: CRTD - Vol 20-1. ASME 1991.
31. O J V Chapman, R B Lloyd, *Nuclear Energy*, 31, No 5, Oct (1992): p363.
32. P Carr "A Probabilistic Strategy For Subsea Inspection Of Steel Structures", SPE European Petroleum Conference, London 1986.

Table 1

Distribution of Pressure Vessel Failures by Cause - From third UK Survey²

| Cause of Failure | No of Cases | % |
|---|-------------|-----|
| Crack Propagation | 216 | 94 |
| Defects Existing Prior to Commissioning | 5 | 2 |
| Corrosion | 1 | |
| Mal-operation | 3 | 4 |
| Creep | 3 | |
| Not ascertained | 1 | |
| | 229 | 100 |

Table 2

Distribution of Causes by Failure Due to Cracking - From Third UK Survey²

| Cause | No of Cases | % |
|--|-------------|-----|
| Fatigue | 52 | 24 |
| Corrosion | 30 | 14 |
| Defects Existing Prior to Service | 63 | 29 |
| Not Ascertained | 61 | 28 |
| Miscellaneous (Creep, Mal-operation etc) | 10 | 5 |
| | 216 | 100 |

Table 3

Method by which Failure Detected - From Third UK Survey²

| Cause | No of Cases | % |
|-----------------------------|-------------|-----|
| Visual Inspection | 88 | 38 |
| Non-Destructive Examination | 49 | 21 |
| Leakage | 76 | 33 |
| Hydro Test | 3 | 2 |
| Catastrophic (In-service) | 13 | 6 |
| | 229 | 100 |

Table 4
Modes of Failure and How Design Codes Deal With Them - From Harrop⁷

| MODE OF FAILURE | CONSIDERED IN DESIGN CODES |
|---|--|
| 1 Bursting due to plastic rupture of shell wall or ductile tearing at a discontinuity | Very well-historically the first mode of failure dealt with by design codes |
| 2 Fatigue | Quite well. Usually based on S-N data. But eg ASME VIII Div 1 rarely requires a fatigue assessment |
| 3 Brittle fracture | To some extent. Usually by requiring material to pass some sort of impact test |
| 4 Corrosion fatigue or stress corrosion | Hardly at all |
| 5 Creep rupture | For special applications |
| 6 Ductile fracture | Not at all |

Table 5
Some Examples From Practice - From Seibert^{12,14}

- A salt crystalliser tank made of wood was replaced after 20 years service by a carbon steel tank lined with thin A1S1 304 stainless steel sheet. Rapid failure of the replacement occurred due to SCC at spot and seam welds in the stainless steel.
- A 20 year old rubber-lined hydrofluoric acid tank was replaced by a fibre reinforced plastic vessel having a lining whose integrity was critical to the overall vessel integrity. The vessel failed catastrophically within one year. The replacement was a rubber-lined steel vessel.
- A lead-lined wooden tank installed in the 1860's after a century of service as a sulphuric acid/zinc chloride mix tank. A replacement in kind was not acceptable.
- A submarine design specified Monel launching tubes for aluminium torpedoes, creating a very active dissimilar metal battery with the aluminium as the anode.
- A plumbing system was made from low carbon steel pipe coupled to copper pipe via a ceramic insulating joint to avoid bimetallic contact. Metal brackets attached the pipework to the wall which was made of sheet metal, thus shorting-out the insulating joint.

Management of Corrosion in the Power Industry

Harvey J. Flitt
Queensland Electricity Commission
55 Paringa Road Murarrie
Queensland 4172 Australia

Abstract

This paper gives an overview of the technological management of corrosion in the power industry. The impact of corrosion on power generation economics is significantly large that correct management of it is a necessity.

Of major importance is that continuing cooperation occurs between scientists, engineers and plant operators to master ways of achieving high availability with low maintenance in the control and prevention of corrosion. The North American Association of Engineers (NACE) have now recognised the importance of combining corrosion science with engineering in solving materials degradation problems (Materials Performance July Viewpoint 1991).

In most cases the prediction of corrosion behaviour is difficult as plant corrosion failures are multi-dimensional problems which are complicated by mechanistic changes, e.g. from passivity to active corrosion or pitting. An incorrect assessment could lead to premature failures or conservative action with associated additional cost.

Introduction

The realisation that corrosion is a process (dynamic) and not a property (static) is fundamental to the management of corrosion. Corrosion control methods are numerous and have different costs and long term consequences. Hence the effective and efficient control of corrosion requires a strategic planning approach¹ which encapsulates for the methodology the following,

- (1) thorough analysis and assessment,
- (2) the ability to change or modify to ensure the long term survival of materials, and
- (3) a certainty of performance with cost effectiveness.

Strategic planning² is therefore ideally suited to address the long term effects of plant corrosion damage. The emphasis is being proactive rather than reactive to corrosion problems.

Economics

Economics and materials reliability are a contrariety. A indication of this linkage is that the electricity production costs of a power plant and component failure modes versus operating time, generally follow a broad U-shaped or bathtub curve. Conversely the cash flow and availability arising from a plant is the inverse of the bath tub curve. Corrosion control technology and expenditure must be balanced to achieve a cost effective solution and a low risk of component failure³.

Costs associated with corrosion control are not always evident and directly accountable. In general the replacement costs incurred by a corroded part may not be trivial when the indirect costs are considered⁴.

Dillon⁵ has outlined the methods for economic evaluation of corrosion control measures both before and after implementation. It is considered that economic evaluation for corrosion control can be applied effectively to decisions involving items or projects of different costs and different lifetimes.

Edeleanu and Hines⁶ have suggested that at the design stage of a plant corrosion costs arise from uncertainty and there must be available means to avoid this uncertainty. Their conclusion was the collective use of various corrosion management subfunctions which will be discussed individually below.

Corrosion Control

Definition

The suggested definition of corrosion control is the regulation of the corrosion reaction so that the physical and mechanical properties of the metal are preserved during the anticipated life of the plant.

The enormous scope of corrosion control methods requires both decision making and problem solving. Thus the term control, used universally in a corrosion context is considered to be synonymous

with management.

Corrosion control can be effectual at the design, operation, and maintenance stages during the lifetime of a plant. Figure 1 is a schematic of these periods and their relationship to the principal parameters responsible for corrosion, i.e. environment, material and thermo-mechanical stress⁷.

Methods

The practical methods of corrosion control⁸ are given in Table 1. A single or a combination of methods can be used. On pipelines for example both cathodic protection and coatings are used as the corrosion control method.

Assessment

To assess plant corrosion control a structured approach is initially required. The concept by Sommm et al.⁴ for (1) local (2) component and (3) systems approaches is considered the most applicable.

Approach (3) with the knowledge derived from approaches (1) and (2) can be considered the basis of mastering power plant corrosion and achieving high plant availability.

A "local approach" investigates corrosion mechanisms at a fundamental level to understand the electrochemical and chemical environments which will initiate localised corrosion.

These investigations are undertaken in a laboratory with attempted simulation of the plant conditions. An example of the local approach for corrosion control of condenser tubing has been given by Flitt and Spero⁹.

The "component approach" is the investigation of specific plant components which encounter corrosion due to operational and environment conditions¹⁰.

The "systems approach" considers the plant as a series of discrete entities each made up of various individual components. A combination of the local and component outcomes are required initially to establish the systems approach.

In the power industry "water chemistry" is an example of a systems approach. Maintaining the environment of the water/steam cycle controls the corrosion of a series of components in unison, which individually may suffer specific localised attack.

Figure 2 is a simplistic schematic of the water/steam cycle indicating the major components which define the system and their relative location. Corrosion management is mechanistically obtained by the maintenance of stable self inhibiting magnetite by the management of cycle water chemistry.

Figure 3 depicts a block diagram of the nine components comprising the water/steam system totally bounded by a systems

box. Each component has specific localised corrosion mechanistic attributes. The localised approach for condensers has been expanded in the right hand side of Figure 3 to indicate the probable mechanisms that can be responsible for corrosion damage.

The assessment of a corrosion control methodology will follow four distinct phases during the lifetime of the plant and use the approaches discussed above. The four phases which are given in Figure 4 and are listed below.

- (1) Plant and Process Design
- (2) Equipment Fabrication
- (3) Construction
- (4) Operation

Corrosion Management Subfunctions

In the actual practise of corrosion control there are management subfunctions that all have an important role. These subfunctions are listed adjacent the phases of corrosion control in Figure 4. Each subfunction, discussed further below, can be a contributor to or have direct involvement on the four plant lifetime phases.

Hence as discussed in the introduction a strategic management approach to corrosion control, by integrating the subfunctions, gives the required holistic perspective and avoids any fragmentation of effort.

Corrosion Maintenance

Associated periodically with the operation phase is maintenance which can be either, preventive or corrective.

Maintenance is usually based on factors such as wear and lubrication problems of rotating machinery and not specifically corrosion. The usual practise is to shut down the plant and disassemble components which allows at the same time inspection and monitoring of corrosion damage.

Corrosion maintenance procedures are established from the correct interpretation of data and information gained from on and off-line corrosion inspection and monitoring.

Corrosion Reliability

Reliability of engineering materials (or the probability of failure) is a relative new practice that has evolved from the application of reliability engineering to materials science. The two approaches used are phenomenological and mechanistic¹¹.

The phenomenological approach is the recording of events, for example pit depths in heat exchanger tubing and evaluation of the data in terms of statistical models¹⁰.

The mechanistic approach has an analytical emphasis and is linked to methods of design, lifetime prediction, and failure analysis. Turpin et al.¹² have demonstrated the value of statistical approaches for assessment of high impact industrial corrosion

problems.

Component corrosion reliability (adapted from systems reliability) is a dynamic characteristic which results from statistical interference in space and time, between a component being able to perform, and the required operational durability. The corrosion process is modelled with stochastic methods¹³.

The interference hence occurs between probability distributions for an operational characteristic of the corrosion process (pit depth, stress intensity or, crack length) and the operational limits (component thickness or strength)¹⁴.

Failure Analysis

Failure analysis is the technique for gathering and evaluating facts to establish the cause of premature corrosion failure of a plant component or part. This may not directly solve problems.

Hence the common view is that failure analysis is only a corrective technique. This opinion is not mindful that valuable information and knowledge can be generated which assists corrosion management in regard to failure prevention or reliability.

Corrosion failure analysis uses metallography to assess the corroded metal microstructure and define the form of corrosion damage. Fractography which is a function of metallography is required to investigate cracking failures (stress corrosion cracking, corrosion fatigue) and high temperature corrosion.

A review of failure analysis by Siebert¹⁵ has indicated that effective implementation can only occur if hands-on and application experience of the industry are present. The output of university based or commercial testing

Corrosion Monitoring

Corrosion monitoring can be defined as the systematic measurement of the corrosion or degradation of an equipment item with the objective of assisting the understanding of the corrosion process and/or obtaining information for use in controlling corrosion and its consequences¹⁶.

The intent from this definition is to create a feed-back loop consisting of change, observation, and diagnosis. Figure 5 represents this relationship with the association of corrosion control methodology, processes and monitoring. The corrosion process must have a cause and effect.

A corrosion monitoring method is any plant based technique that provides an assessment of equipment condition or an evaluation of the corrosivity of the environment. Table 2 gives a listing of the commonly used corrosion monitoring techniques.

Corrosion monitoring is undertaken for the following reasons.

- (1) Corrodent characteristics changes

- (2) Materials corrosivity changes
- (3) Unanticipated operational conditions develop
- (4) Unknown corrosion processes may occur
- (5) Verification of control methods

Britton and Tofield¹⁷ have conducted two industry surveys in the UK to ascertain the effectiveness of corrosion monitoring. Their findings indicated that more awareness was present of the benefits of corrosion monitoring and that programs should be incorporated at the plant design stage. Cost was considered to be the major factor when considering on-line corrosion monitoring. The reliability of equipment, and the cost of installation and cabling, are factors limiting the usage of on-line monitoring.

Additional information on corrosion monitoring can be found in the books edited by Moran and Labine¹⁸ and Wanklyn¹⁹.

Information Technology

The deficiency of effective communication of materials degradation causes and resultant effects, within an organisation, can have serious consequences. Corrosion control can only be effective and timely if information is acquired, processed, and communicated efficiently. Hence information technology is an important role to play in the management of corrosion.

Computer usage for corrosion control and monitoring has been reviewed by Haroun et al.²⁰. The authors have considered the computer can be used successfully for corrosion, rate evaluation, monitoring, and process modelling. The most efficient method for the storage and retrieval of information is a computer corrosion database system.

Corrosion information suitable for databases can be developed from theoretical studies, laboratory standard tests, and plant experience. It is important to understand that standard tests are only acceptance tests to determine if a metal has the required corrosion resistance within the compositional specification²¹.

Source material can be provided from the open literature, and individuals. Standards are an important information source for corrosion control as they are needed to assure that materials meet mechanical, physical and chemical properties required. They are prepared as specifications, test methods, recommended practices, and codes.

Corrosion Knowledge

Corrosion knowledge is required by an individual to solve plant problems. Problem solving is made possible by using experience and an understanding of corrosion. Experience is a collection of data, observations, and rules needed to problem solve. Understanding for this situation is the theoretical basis of corrosion knowledge.

Expert systems are now being considered as serious practical tools for providing corrosion problem solving knowledge. An

example is ESCARTA²² developed by EPRI as an expert trouble-shooter for boiler tube failures.

Hines and Basden²³ have given an introduction to introducing expert systems and mathematical modelling to provide corrosion control problem solving. The authors have concluded that these approaches are complementary rather than completitive.

Conclusions

For the management of corrosion to be effective it must be strategically planned to return maximum efficiency and costs savings. Corrosion technology management is hence a combination of analysis, judgement, experience, and synthesis. These actions are incorporated in the integrated use of the seven corrosion management subfunctions.

Importantly the strategic approach to corrosion will ensure the long term survival of plant. The participants involved with corrosion control must have a holistic perspective as all practices are linked together to achieve long term plant availability.

Acknowledgment

This paper is published with the permission of the Queensland Electricity Commission.

References

1. L. W. Steele, Managing Technology, McGraw-Hill Company, 1989.
2. J. R. Gardner, R. Rachlin, H. W. A. Sweeny, Eds, Handbook of Strategic Planning, John Wiley & Sons New York 1986.
3. J. Douglas, EPRI Journal, 7/8 (1987): p. 20.
4. E. Somm, W. Schlachter, A. Schwarzenbach, "Power Generating Equipment" (Corrosion In Power Generating Equipment, Eds M.O. Speidel and A. Atrens, Plenum Press New York 1984).
5. C. P. Dillon, Materials Protection, 4 5 (1965): p39
6. C. Edeleanu, J. G. Hines, Materials Performance, 29 12 (1990): p. 68.
7. A. Sonnenmoser, J. A. von Planta. R. Svoboda, "Design Criteria for Corrosive Environments and Implications for Maintenance" (Corrosion In Power Generating Equipment, Eds M.O. Speidel and A. Atrens, Plenum Press New York 1984).
8. D. Fyfe, "Corrosion Control in Chemical and Petrochemical Plant" (Corrosion Control Ed L.L. Shreir, Volume 2, Newnes-Butterworths, London, 1976)
9. H. J. Flitt, C. Spero, "Corrosion Rate Measurement of Copper Alloy - Power Station Condenser Tubing", Paper 40

CASS 90, (Australian Corrosion Association Inc. Conference 30, Auckland, New Zealand, 19-23 November 1990).

10. H. J. Flitt, C. Spero, "Waterside Pitting of Condenser Tubing - A Review of Investigation Methods" Paper 4 Session 5, Corrosion In Industry, (Australian Corrosion Association In Conference 28, Perth Western Australia, 21-25 November 1988).
11. A. L. Smith Ed, Reliability of Engineering Materials, Butterworths, London, 1984.
12. M. P. Turpin, I. Young, J. Abbott, A. Kamath 2 (1984): p. 14.
13. J. W. Proven, E. S. Rodriguez, Corrosion 45 3 (1989): p. 178.
14. E. S. Rodriguez, J. W. Proven, Corrosion 45 3 (1989): p. 178.
15. O. W. Seibert, Failure Analysis, Process Industries Corrosion Theory and Practise, 1986 NACE, Houston, Texas.
16. J. L. Dawson, M. E. D. Turner, Metals and Materials, 4 4 (1988): p. 218.
17. C. F. Britton, B. C. Tolfield. Materials Performance 27 4 (1988): p. 41.
18. C. G. Moran, P. Labine, Eds, Corrosion Monitoring in Industrial Plants Using Nondestructive Testing and Electrochemical Methods, ASTM STP 808,(1986).
19. J. Wanklyn, Ed, Corrosion Monitoring In the Oil, Petrochemical and Process Industries, Oyez Scientific and Technical Services Ltd, London UK. (1982).
20. M. R. Haroun, R. Erbar, R. Heidersbach, Materials Performance, 27 11 (1988): p. 23.
21. M. E. D. Turner, Materials Performance, 28 3 (1989): p. 77.
22. J. Douglas, EPRI Journal 4/5 (1987): p. 24.
23. J. G. Hines, A. Basden, British Corrosion Journal, 21 (1986): p. 151.

Table 1: Corrosion Control Methods and Examples

| METHODS | EXAMPLES |
|--|---|
| Materials Selection Steels Non-metallics | C/Mn Cr, stainless, Ni, Cr. alloys plastics, GRP, ceramics |
| Coatings applications Organic Metallic | paints and polymers galvanized, clad steel and plating |
| Environmental change Inhibitors dehumidification | cooling waters and process streams packaging and mothballing |
| Electrical methods cathodic protection anodic protection | pipelines, pumps vessel internals |
| Design details Metal Compatibility Vibration/stress | galvanic effects fatigue and SCC |

Table 2: Corrosion Monitoring Methods

| Methods | Comments |
|---|--|
| Electrochemical | |
| Corrosion Potential Polarization Resistance Impedance Developmental Current/Potential Noise | Continuous real time On line corrosion rate Developmental Continuous real time |
| Non-Electrochemical | |
| Chemical Analysis Weight loss coupons Electrical resistance Hydrogen diffusion Microbiological Thin layer Activation | On line or laboratory Field tests Corrosion rate On line test Laboratory testing Corrosion rate |
| Non Destructive Testing | |
| Visual Inspection Radiography Ultrasonics Eddy current Magnetic Particle Dye Penetrant | Preventive maintenance Non destructive testing Crack detection Pitting detection Flow detection Crack detection |
| Condition Monitoring | |
| Wear debris analysis Vibration analysis Fouling monitoring | Lubricant corrosion Stress corrosion Biological corrosion |

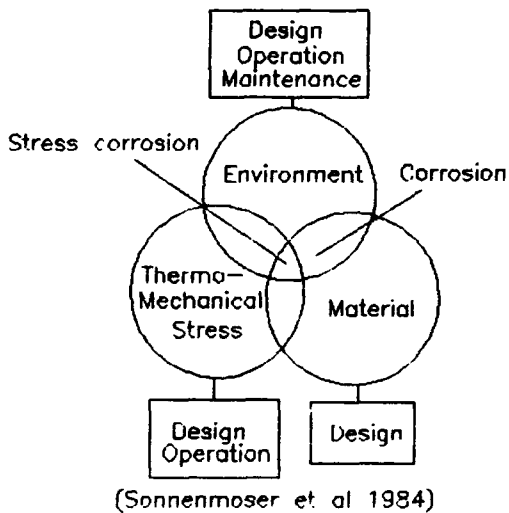


Figure 1: Factors Influencing Plant Corrosion

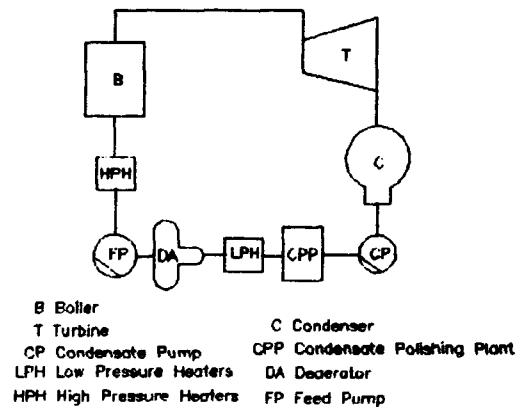


Figure 2: Systems Approach Water/Steam Cycle

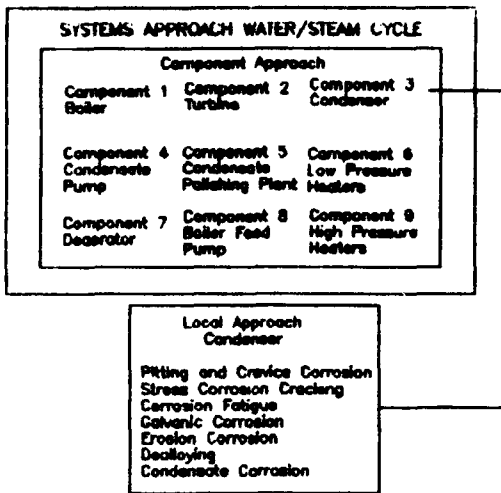


Figure 3: Block Diagram Water Steam Cycle

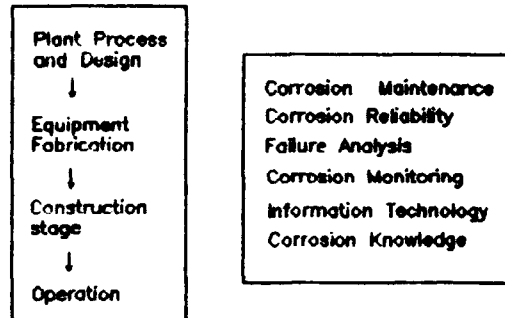


Figure 4: Plant History and Management Subfunctions

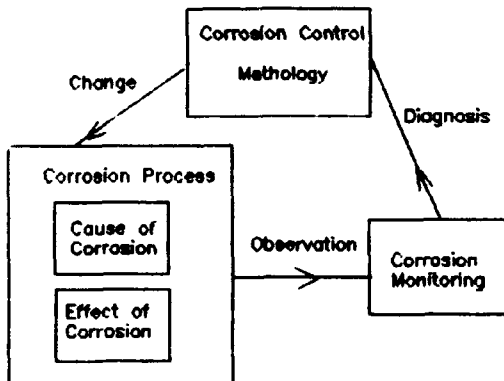


Figure 5: Corrosion Monitoring Feedback

Prediction of Corrosion Rate and Probability on Underground Pipes

Yukio Katano
Pipe Engineering Dept., KUBOTA Corporation
2-47, Shikitsuhigashi 1-chome
Naniwa-ku, Osaka Japan 556-91

Toshihiro Kubo
Pipe Research Dept., KUBOTA Corporation
2-26, Ohama Amagasaki
Hyogo, Japan 660

Youichi Igawa
Pipe Research Dept., KUBOTA Corporation
2-26, Ohama Amagasaki
Hyogo, Japan 660

Abstract

Predictions have been made on external corrosion for water pipes in soils containing peat. The corrosion rate of underground pipe was explained by the corrosiveness of soils. In many results of the field investigations that were carried out on the underground pipes, the corrosion pit was found in few samples. In these cases, it is important to draw out information from the samples of non-corroded. These samples can be used for analyzing the probability of corrosion occurrence (Pr) by dealing the dependent variable as a binary data. Pr is expressed as a logistic regression model with the environmental factors (X) and the installation period (t): $Pr = t^n \exp(\sum B_j X_j) / (1 + t^n \exp(\sum B_j X_j))$ ($j=1, \dots, q$), with B estimated by the maximum likelihood method. In this study, Pr was related to soil type and t; the existence of peat and the longer installation time increase Pr.

The pitting depth (Y) is expressed as the following multiplicative regression model: $Y = \eta \exp(e)$ ($e \sim N(0, \sigma^2)$), $\eta = t^n \exp(\sum B_j X_j)$ ($j=1, \dots, q$), with n and B estimated by the least squares method. The higher corrosive conditions were effected by the neutral pH, the higher content of sulfur and the higher content of soluble organic matter in soil. These conditions are enough for increasing the activity of the sulfate-reducing bacteria (SRB). On the other hand, several kinds of soil exist in this field. Therefore the fundamentals of differential aeration cells are adequate to react. The results of this analysis support the assumption that the parts in contact with peat become the macro-anode and SRB affect the reaction.

Key terms: soil corrosion, peat, regression analysis, cast iron pipe, corrosion probability

Introduction

Pipelines are playing an important part in maintaining urban functions. The effected range of the accident on pipelines is greater as a city life becomes more upgrade. Now, the great loss results from troubles of pipeline such as a leakage. Corrosion is a cause of these leakages. Therefore the development of techniques for predicting corrosion damage is desired as much as that of protections.

A corrosion rate is under the control of the properties and condition of soils, except for those cases due to the stray current corrosion and long line currents. In this case, the rate is predicted by making a relation between corrosion and corrosiveness of soil clear.

The statistical methods were used to predict a corrosion rate. As the result, two kinds of models that represent the probability of corrosion occurrence and the growth rate of the pitting depth are proposed to predict the corrosion rate with accuracy. The probability can be evaluated from information of non-corroded samples that are not used in predicting the growth rate.

In this paper, a case study about corrosion in peat is reported and the usefulness of the methods of prediction is discussed. Also the corrosion mechanism is considered.

Prediction Method

Investigation of Pipe Condition

The investigation of actual pipe conditions was carried out as follows. The depth of corrosion was measured within about 1m length of the pipe at the exposed sites. Soil samples were brought to the laboratory to be analyzed. The items to be investigated and their definitions are shown in Table 1.

Prediction Model

Corrosion samples were not always found on pipes. In this investigation, corrosion was observed on 40% of samples. Usually the analysis is carried out only on corroded data. Non-corroded samples are not used to determine a relation between the corrosion and the environment. On the other hand, to predict the corrosion with accuracy, it is better that all samples, including non-corroded one, are used. Therefore the pitting depth (Y) was treated as a binary data ($Y>0, Y=0$) and the probability of corrosion occurrence was predicted.¹

The probability (Pr) is given by the logistic regression model in the following equation(1) with $Pr(Y_i>0)=Pr_i$, $Pr(Y_i=0)=1-Pr_i$:

$$\log(\text{Pr}_i / (1 - \text{Pr}_i)) = \sum_{j=0}^q B_j X_{ij} + B_{q+1} \log t_i \quad (1)$$

($i=1, 2, \dots, n$: the number of samples)

in which

X: the explanatory variables ($X_{i0}=1$),
 q: the number of environmental items,
 t: the exposure period.

Equation(1), substituted $B_{q+1}=n$, is rewritten as

$$\text{Pr} = t^n \exp\left(\sum_{j=0}^q B_j X_j\right) / \left(1 + t^n \exp\left(\sum_{j=0}^q B_j X_j\right)\right) \quad (2)$$

The corrosion rate is seemed to be controlled by the condition of soil around pipes. The pitting depth (Y) is expressed as a power of time (t): $Y = kt^n \exp(e)$ (e: the error term), with k and n as constants.² The parameter, k, is related to environmental factors by the following expression of eq.(3):

$$Y = \eta \exp(e), \quad \eta = t^n \exp\left(\sum_{j=0}^q B_j X_j\right) \quad (3)$$

in which
 $e \sim N(0, \sigma^2)$

The parameters, B_j , were determined by the method of least squares.

Results and Discussion

Statistic of the Data

The inspection was carried out on buried cast-iron pipes in soils containing peat. The number of inspected points was 119. Corrosion was found on 48 points. The statistic of the data is shown in Table 2.

Probability of Corrosion Occurrence

The data was divided into two groups, $Y=0$ and $Y>0$. The category data of soil type was put into a dummy variable as shown in Table 3.

The regression model of eq.(1) was used. The parameters, B_j , were

estimated by the maximum likelihood method. The solution was obtained by the Newton-Raphson method.

The predictor variables were selected on the bases of the statistical test, put into eq.(4):

$$\hat{Pr} = t^{2.92} \exp(-3.64 - 1.13X_1 + 3.81X_2) / (1 + t^{2.92} \exp(-3.64 - 1.13X_1 + 3.81X_2)) \quad (4)$$

in which

X_1 : H_2O_2 pH,
 X_2 : Peat. ($X_2=1$ or 0)

The level of significance about these parameters was over 1%. The likelihood ratio test and the χ^2 test were done as shown in Table 4 to check the goodness of fit of this model. It was found that the logistic regression model, eq.(1), was able to explain the probability of corrosion occurrence.

The scatter diagrams of probability (\hat{Pr}) vs. the corrosion rate (Y/t) for each soil were shown in Fig. 1, indicating the following trends:

- 1) There is high probability of corrosion in peat soil with a wide range of corrosion rate.
- 2) Both the probability and the corrosion rate of sand are low compared with those of peat.
- 3) The properties of volcanic-gravel are similar to those of sand.

Prediction of Corrosion Rate^{3,4}

Correlation. The correlation coefficient, r , is a measure of the linear relationship between variables; a linear relation is applied if $|r|$ is close to one. The correlation, r , was calculated from 48 samples of corroded as shown in Table 5. It was found that no variables were related to the corrosion rate by confirming r and scatter diagrams. In environmental factors, EVAP was closely correlated with SO_4 , Cl and ACID. It was suggested that soluble salts in soils, which are mostly peat, contain sulfate and/or chloride.

Environmental Factor Classification. The principal component analysis was applied to make features of variables clear and to classify the variables, for the factors of predictor would be selected reasonably.

The factor loadings that are correlation coefficients between variables and principal components were plotted for the 1st-2nd principal component coordinates as shown in Fig. 2. It was considered that the variables encircled by a line have similar characteristics. As a result, two groups were found in this case.

The factors in the 1st-group that are closely related to the 1st principal component (Z1) were SO₄, ACID, EVAP, REST, pH and so on. Z1 was interpreted as indicating the concentration of salt. In the 2nd-group, the factors that are related to the 2nd principal component (Z2) were ALKA, Cl, WATR and SULF. Though the interpretation of Z2 is not clear, it seems that the soil type is reflected in Z2, since the soil type is closely related to WATR and SULF.

The eigenvectors and eigenvalues of the correlation matrix were shown in Table 6. After all, 61% of the variation of this sample were explained by Z1 and Z2; that is, the concentration of salt and the soil type.

Corrosion Rate. The distribution of the pitting depth, Y, was checked. The normal probability plotting of residuals was shown in Fig. 3. The regression model of eq.(3) could be used to predict Y. The predictor variables in the model of eq.(3) were chosen in consideration of the result of the principal component analysis. The result of the regression analysis was shown in eq.(5) and Table 7:

$$\hat{\eta} = t^N \exp(B_0 + B_1 X_1 + B_2 X_2 + B_3 X_3 + B_4 X_4) \quad (5)$$

in which

- X₁: pH,
- X₂: SULF,
- X₃: KMnO₄,
- X₄: ALKA.

The multiple correlation coefficient R=0.546 was over 1% level of significance, though not so high that of the regression coefficient was. The scatter diagram of the predicted value ($\log \hat{\eta}$) vs. the standardized residual (e_s) was shown in Fig. 4. The plots are scattered randomly, so there is no bias in the estimation.

It was confirmed whether the multicollinearity was found among these variables by use of the eigenvalues of the correlation matrix. Some eigenvalues are nearly zero if there is the problem of multicollinearity. As shown in Table 8, this problem was not found among these variables.

The regression coefficients in eq.(5) imply that the corrosion rate is increased in the following conditions:

- 1) The pH is neutral.
- 2) The concentration of sulfur is higher.
- 3) The consumption of KMnO₄ is more.
- 4) The alkalinity is lower.

Considering the microbiological activity, it is found that the corrosive places estimated by eq.(5) give good conditions to sulfate-reducing bacteria (SRB) as shown in Fig. 5 schematically. The anaerobic corrosion of pipe occurs in some soils-mixture

environments. The peat-adhering area, where the above factors promote conditions conducive to proliferation of SRB, becomes macro-anodic part.

Concluding Remarks

Statistical methods have been applied to corrosion of cast-iron pipes in soil containing peat to devise two prediction equations related to environmental factors and service period. The results are:

1. If it is assumed that k in $Y(\text{pitting depth})=kt^n$ represents the environmental corrosivity, the corrosion probability (Pr) and Y are well predicted by the following models respectively: the logistic regression model;

$$Pr = t^n \exp(\sum B_j X_j) / (1 + t^n \exp(\sum B_j X_j))$$

the multiplicative regression model;

$$Y = \eta \exp(e), \quad \eta = t^n \exp(\sum B_j X_j)$$

2. The probabilities of corrosion occurrence are a higher level on pipes in peat. The aggressive condition of peat soils are made, when pH is neutral and there are the higher content of sulfur and the higher consumption of $KMnO_4$.

3. The results of this statistical analysis support the assumption that peat adhering to the pipe is a necessary condition to react as anode and the anaerobic corrosion is accelerated with the increase of the microbiological activity in this area.

Acknowledgment

Dr. T. Isogai of Osaka University is thanked for advice with the statistical analysis.

References

1. D. R. Cox, The Analysis of Binary Data, (Chapman and Hall, 1970)
2. H. H. Uhlig, Corrosion and Corrosion Control, (John Wiley & Sons, Inc., 1967), P.154
3. S. Chatterjee and B. Price, Regression Analysis by Example, (John Wiley & Sons, Inc., 1977)
4. Y. Tanaka, K. Wakimoto, Methods of Multivariate Statistical Analysis, (Gendai-Sugaku-Sha, 1983)(in Japanese)

Table 1 Definitions of variables

| No. | Variable | Unit | Symbol | Definition |
|-----|---|------------|----------------------------------|--|
| 1 | Pitting depth | mm | Y | Maximum depth of corrosion pit. |
| 2 | Installation period | year | t | Period from installation until investigation. |
| 3 | Soil resistivity | Ω m | REST | Minimum soil resistivity. |
| 4 | pH | | pH | pH of water extracted from dry soil. (ratio 1:2.5) |
| 5 | Redox potential | V | Eh | Redox potential of soil. |
| 6 | Water content | % | WATR | Water content ratio of soil sample. |
| 7 | Sulfur content | % | SULF | Sulfur content of dry soil. |
| 8 | Soil pH after oxidation | | H ₂ O ₂ pH | pH of soil as oxidized with H ₂ O ₂ . |
| 9 | Sulfate ion | mg/l | SO ₄ | Concentration of SO ₄ ²⁻ contained in soil water. |
| 10 | Chlorine ion | mg/l | Cl | Concentration of Cl ⁻ contained in soil water. |
| 11 | The consumption of potassium permanganate | mg/l | KMnO ₄ | The amount of consumption in KMnO ₄ -titration of soil water. |
| 12 | Evaporation residue | mg/l | EVAP | Concentration of soluble salt in soil water. |
| 13 | Acidity | mg/l | ACID | Acidity of soil water. |
| 14 | Alkalinity | mg/l | ALKA | Alkalinity of soil water. |

Table 2 Statistic of the data (n=119)

| No. | Variable | Minimum | Maximum | Mean | Standard deviation |
|-----|----------------------------------|---------|---------|--------|--------------------|
| 1 | Y (mm) | 0.0 | 3.6 | 0.66 | 0.92 |
| 2 | t (year) | 1 | 28 | 14.1 | 5.3 |
| 3 | REST (Ω m) | 6.2 | 292.0 | 67.53 | 58.62 |
| 4 | pH | 4.1 | 7.9 | 6.17 | 0.77 |
| 5 | Eh (V) | 0.26 | 0.68 | 0.485 | 0.080 |
| 6 | WATR (%) | 4 | 598 | 77.5 | 97.0 |
| 7 | SULF (%) | 0.01 | 1.23 | 0.118 | 0.186 |
| 8 | H ₂ O ₂ pH | 1 | 7 | 4.9 | 1.1 |
| 9 | SO ₄ (mg/l) | 41 | 2869 | 378.2 | 372.2 |
| 10 | Cl (mg/l) | 4 | 679 | 75.0 | 82.5 |
| 11 | KMnO ₄ (mg/l) | 64 | 6694 | 996.5 | 919.7 |
| 12 | EVAP (mg/l) | 337 | 6397 | 1887.4 | 1146.9 |
| 13 | ACID (mg/l) | 10 | 530 | 78.9 | 86.0 |
| 14 | ALKA (mg/l) | 0 | 1469 | 115.2 | 179.7 |

Table 3 Dummy variable of soils

| Soil | X2 |
|--------|----|
| Peat | 1 |
| Others | 0 |

Table 4 Test of logistic regression model eq.(5)

| Method | Test statistic | Degrees of freedom | Significance |
|------------------|----------------|--------------------|--------------|
| Pearson | 97.3 | 115 | 0.882 |
| Likelihood ratio | 72.3 | 115 | 0.999 |

Table 5 Correlation coefficient r (n=48)

| | 1 | 2 | 3 | 4 | 5 | 6 |
|----------|--------|--------|--------|--------|--------|--------|
| | Y/t | REST | pH | Eh | WATR | SULF |
| 1 Y/t | 1.000 | -0.098 | 0.104 | -0.001 | 0.078 | 0.092 |
| 2 REST | -0.098 | 1.000 | 0.290 | 0.390 | -0.427 | -0.439 |
| 3 pH | 0.104 | 0.290 | 1.000 | 0.523 | -0.179 | -0.417 |
| 4 Eh | -0.001 | 0.390 | 0.523 | 1.000 | -0.057 | -0.368 |
| 5 WATR | 0.078 | -0.427 | -0.179 | -0.057 | 1.000 | 0.504 |
| 6 SULF | 0.092 | -0.439 | -0.417 | -0.368 | 0.504 | 1.000 |
| 7 H2O2pH | -0.111 | 0.384 | 0.510 | 0.417 | -0.086 | -0.301 |
| 8 SO4 | -0.064 | -0.351 | -0.333 | -0.401 | -0.289 | 0.424 |
| 9 Cl | -0.049 | 0.049 | 0.237 | 0.057 | -0.444 | -0.107 |
| 10 KMnO4 | 0.091 | -0.249 | -0.063 | -0.173 | -0.285 | -0.103 |
| 11 EVAP | -0.099 | -0.265 | -0.203 | -0.330 | -0.488 | 0.148 |
| 12 ACID | 0.026 | -0.278 | -0.556 | -0.461 | -0.264 | 0.273 |
| 13 ALKA | -0.133 | 0.253 | 0.520 | 0.164 | -0.395 | -0.255 |

| | 7 | 8 | 9 | 10 | 11 | 12 |
|----------|--------|---------|---------|--------|---------|---------|
| | H2O2pH | SO4 | Cl | KMnO4 | EVAP | ACID |
| 1 Y/t | -0.111 | -0.064 | -0.049 | 0.091 | -0.099 | 0.026 |
| 2 REST | 0.384 | -0.351 | 0.049 | -0.249 | -0.265 | -0.278 |
| 3 pH | 0.510 | -0.333 | 0.237 | -0.063 | -0.203 | -0.556 |
| 4 Eh | 0.417 | -0.401 | 0.057 | -0.173 | -0.330 | -0.461 |
| 5 WATR | -0.086 | -0.289 | -0.444 | -0.285 | -0.488 | -0.264 |
| 6 SULF | -0.301 | 0.424 | -0.107 | -0.103 | 0.148 | 0.273 |
| 7 H2O2pH | 1.000 | -0.334 | 0.136 | -0.283 | -0.229 | -0.450 |
| 8 SO4 | -0.334 | 1.000 | 0.350 | 0.315 | 0.875** | 0.657 * |
| 9 Cl | 0.136 | 0.350 | 1.000 | 0.392 | 0.630 * | 0.223 |
| 10 KMnO4 | -0.283 | 0.315 | 0.392 | 1.000 | 0.580 | 0.544 |
| 11 EVAP | -0.229 | 0.875** | 0.630 * | 0.580 | 1.000 | 0.689 * |
| 12 ACID | -0.450 | 0.657 * | 0.223 | 0.544 | 0.689 * | 1.000 |
| 13 ALKA | 0.127 | 0.073 | 0.626 * | 0.401 | 0.340 | 0.003 |

| | 13 |
|----------|---------|
| | ALKA |
| 1 Y/t | -0.133 |
| 2 REST | 0.253 |
| 3 pH | 0.520 |
| 4 Eh | 0.164 |
| 5 WATR | -0.395 |
| 6 SULF | -0.255 |
| 7 H2O2pH | 0.127 |
| 8 SO4 | 0.073 |
| 9 Cl | 0.626 * |
| 10 KMnO4 | 0.401 |
| 11 EVAP | 0.340 |
| 12 ACID | 0.003 |
| 13 ALKA | 1.000 |

Table 6 The eigenvector and eigenvalue

| | z1 | z2 | z3 | z4 | z5 |
|------------------------------------|--------|--------|--------|--------|--------|
| 1 REST | -0.254 | 0.240 | -0.456 | 0.269 | -0.452 |
| 2 pH | -0.280 | 0.316 | 0.368 | -0.069 | -0.004 |
| 3 Eh | -0.309 | 0.185 | 0.111 | 0.006 | 0.394 |
| 4 WATR | -0.090 | -0.422 | 0.473 | -0.152 | -0.049 |
| 5 SURF | 0.217 | -0.311 | 0.409 | 0.349 | -0.309 |
| 6 H ₂ O ₂ pH | -0.288 | 0.188 | 0.157 | 0.431 | 0.420 |
| 7 SO ₄ | 0.414 | 0.073 | 0.071 | 0.392 | 0.106 |
| 8 Cl | 0.160 | 0.415 | 0.287 | 0.152 | -0.058 |
| 9 KMnO ₄ | 0.282 | 0.236 | 0.045 | -0.590 | 0.197 |
| 10 EVAP | 0.411 | 0.257 | 0.059 | 0.187 | 0.161 |
| 11 ACID | 0.421 | 0.028 | -0.232 | -0.018 | 0.107 |
| 12 ALKA | 0.021 | 0.445 | 0.285 | -0.180 | -0.524 |
| Eigenvalue | 4.146 | 3.186 | 1.157 | 0.948 | 0.609 |
| Contribution rate | 0.345 | 0.266 | 0.096 | 0.079 | 0.051 |
| Cumulus | 0.345 | 0.611 | 0.707 | 0.786 | 0.837 |

Table 7 Regression analysis eq.(6)

| Predictor | B _j | Student's t |
|---|----------------|-------------|
| Constant | -2.340 | -3.181 |
| B ₁ :pH | 0.273 | 3.167 |
| B ₂ :SULF (%) | 0.432 | 1.807 |
| B ₃ :KMnO ₄ (g/l) | 0.128 | 1.150 |
| B ₄ :ALKA (g/l) | -2.462 | -1.930 |
| n:log t (yr) | 0.378 | 1.556 |

Multiple correlation coefficient R=0.546 (n=48)

Table 8 The eigenvector and eigenvalue

| | z1 | z2 | z3 | z4 | z5 |
|---------------------|--------|--------|--------|--------|--------|
| 1 pH | 0.592 | 0.228 | -0.122 | 0.437 | 0.625 |
| 2 SULF | -0.405 | 0.127 | 0.783 | 0.405 | 0.207 |
| 3 KMnO ₄ | 0.156 | -0.773 | 0.272 | -0.346 | 0.429 |
| 4 ALKA | 0.559 | -0.281 | 0.312 | 0.359 | -0.618 |
| 5 log t | 0.385 | 0.505 | 0.448 | -0.629 | -0.021 |
| Eigenvalue | 2.039 | 1.294 | 0.906 | 0.471 | 0.290 |
| Contribution rate | 0.408 | 0.259 | 0.181 | 0.094 | 0.058 |
| Cumulus | 0.408 | 0.667 | 0.848 | 0.942 | 1.000 |

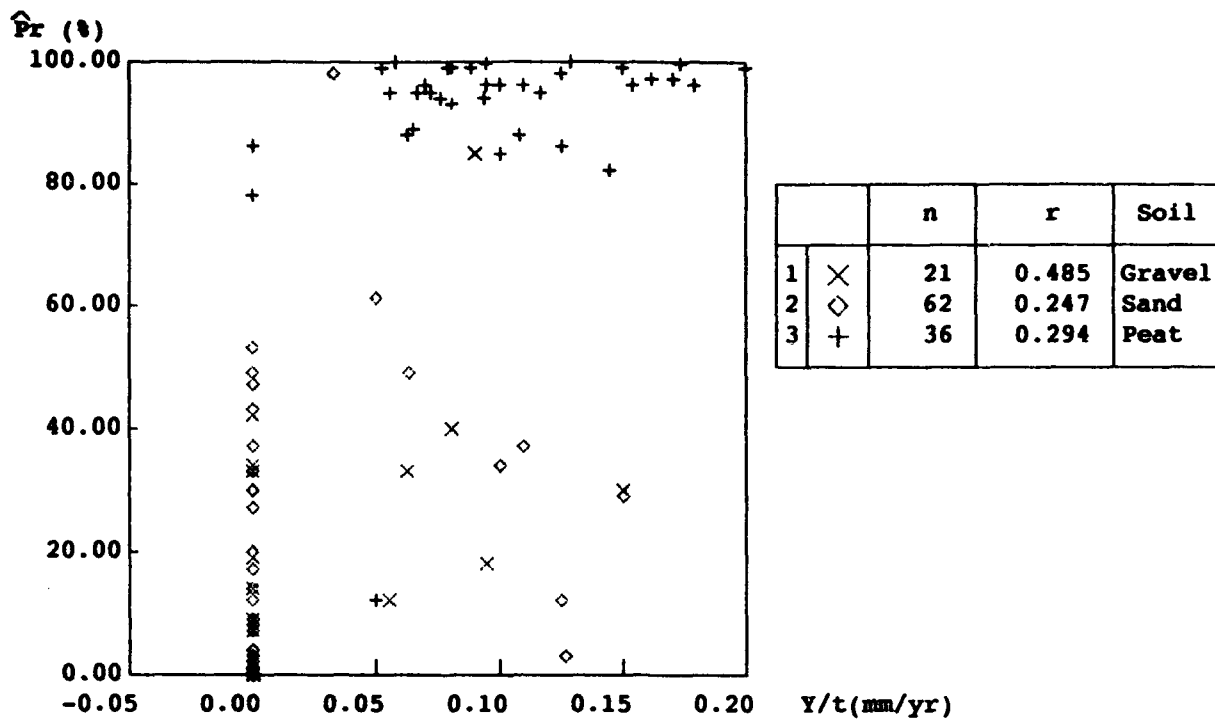


Fig. 1 The corrosion probability \hat{P}_r vs. the corrosion rate Y/t

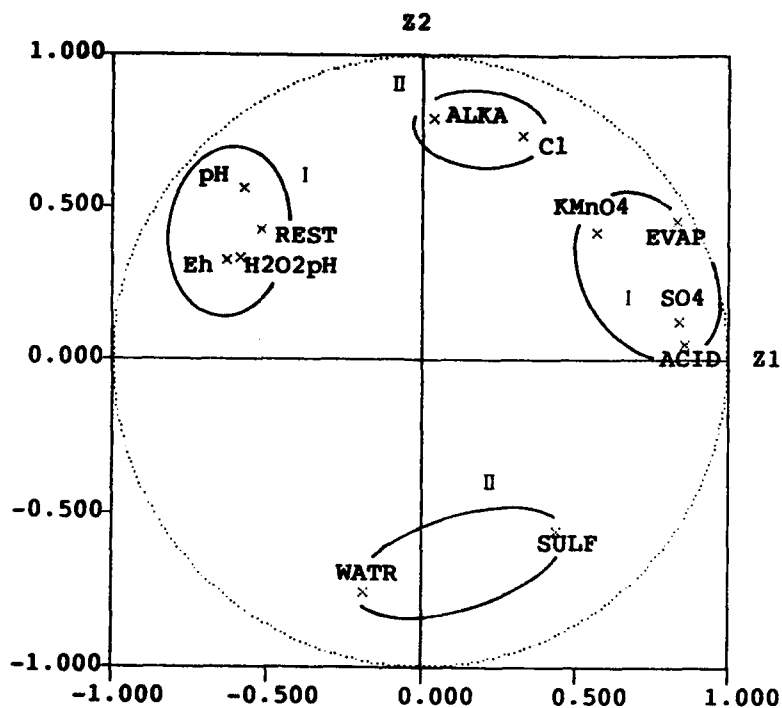


Fig. 2 The factor loadings on the 1st-2nd principal components coordinates.

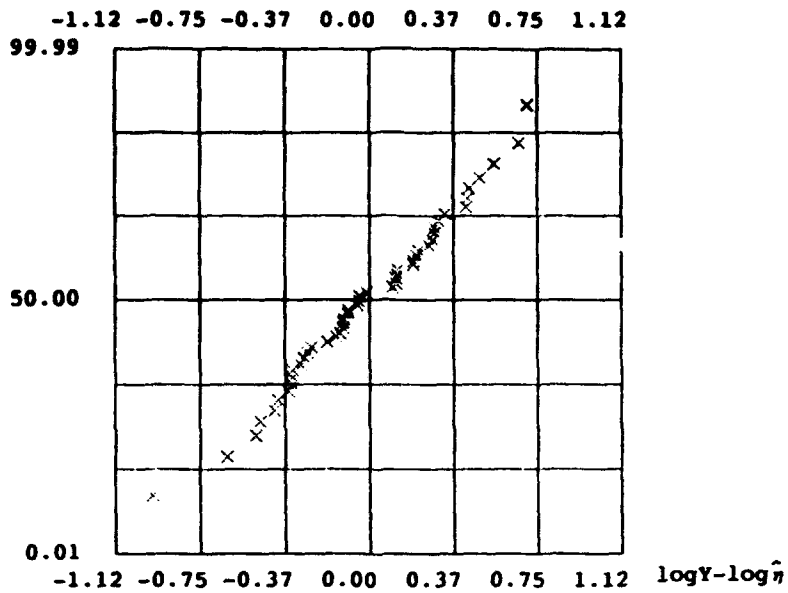


Fig. 3 The normal probability plotting of residuals.

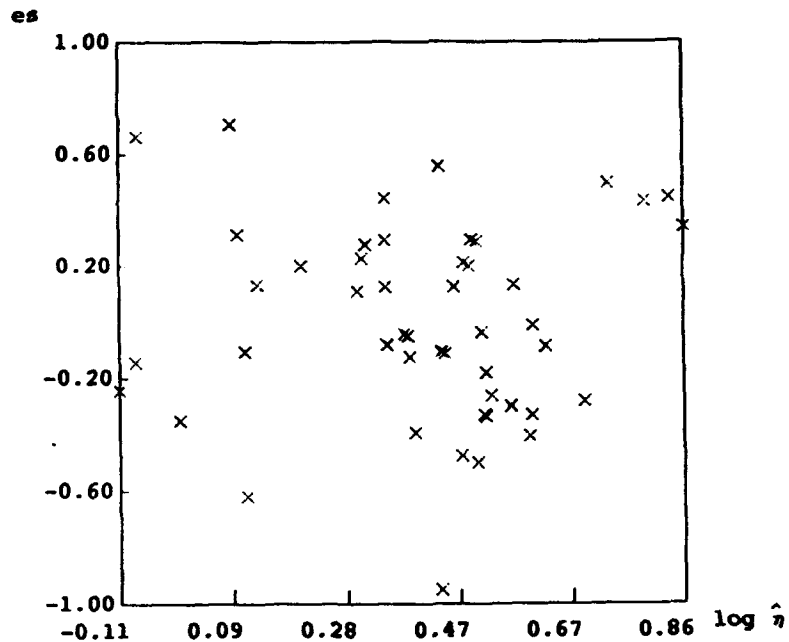


Fig. 4 The predicted depth $\log \hat{\eta}$ vs. the standardized residual e_s

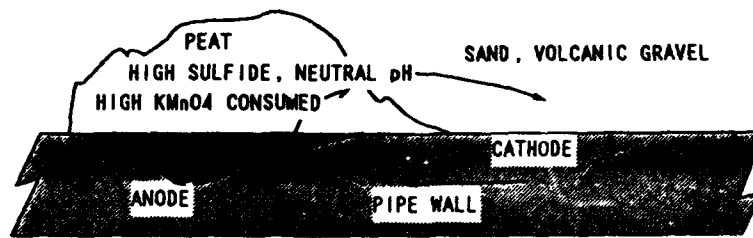


Fig. 5 The conditions increasing the activity of corrosion in the peat.

A Dominant Flaw Probability Model for Corrosion and Corrosion Fatigue

D. Gary Harlow
Department of Mechanical Engineering and Mechanics
LEHIGH UNIVERSITY
19 Memorial Drive West
Bethlehem, PA 18015 USA

Robert P. Wei
Department of Mechanical Engineering and Mechanics
LEHIGH UNIVERSITY
19 Memorial Drive West
Bethlehem, PA 18015 USA

Abstract

An approach and a methodology for developing a mechanistically based probability model for life prediction are described. A single flaw probability model for localized corrosion and corrosion fatigue crack growth in steels in aqueous environments is used to demonstrate its construction and to evaluate the approach. Statistically tight estimates of the life, for conditions that are beyond the range used in typical supporting data, can be produced with this approach. The probability considerations are included in the initial stages and are integrated throughout the modeling process. The contribution and significance of each fundamental variable in the mechanistically based model for the failure process is described. It is to be noted that the model is somewhat empirical. Assumptions are made which simplify certain aspects of the damage mechanism. Also the assumed parameters for the model are only reasonable estimations of the physical values; they are not the result of carefully executed experiments.

Introduction

Localized corrosion (e.g., pitting in steel), and corrosion fatigue crack initiation and growth are recognized as degradation mechanisms that affect the durability and integrity of structures. A quantitative methodology for life prediction is needed to help define suitable inspection intervals, to mandate repairs, and to assess the durability and integrity of new and aging components and structures. Current life prediction methodologies are largely statistically based, and reflect, at most, a limited number of loading and environmental variables. Their accuracy is acceptable only for characterizing response within the range of supporting experimental data. To be effective, however, the methodology must provide statistically accurate estimates of response for conditions not included within the available experimental observations and must reflect the influences of key *external* and *internal* variables. The *external variables* include applied stress, environmental chemistry, and temperature, and the *internal variables* include chemistry within a pit or at the crack tip, material properties, initial defect size, etc. As such, in contradistinction to many current methods, this methodology requires mechanistic understanding and quantification of the damage processes.

In this paper a mechanistically based probability approach to life prediction for pitting corrosion and corrosion fatigue crack growth in steel is described. The differences between the statistical and mechanistic approaches to life prediction are addressed, and the need for adopting a mechanistically based approach is demonstrated. The approach and the process for developing this type of model is described, and it is illustrated through a model for pitting and corrosion fatigue crack growth in steels. Because, in reality, mechanistic models for pitting and corrosion fatigue crack growth are not available, simplified models that capture the essential chemical and physical features of these processes are assumed. Damage accumulation is modeled in terms of the growth of a single hemispherical pit, which transitions at a critical size and then grows as a corrosion fatigue crack. Pitting is considered as a constant volumetric-dissolution rate process that depends on temperature. Corrosion fatigue crack

Key terms: life prediction; probability modeling; corrosion; corrosion fatigue; fracture mechanics; steel

growth is assumed to follow a simple power-law relationship in terms of the cyclic stress intensity range ΔK , with transition from pitting to crack growth defined by the fatigue threshold ΔK_{th} . Taking the pitting corrosion rate and corrosion fatigue crack growth rate coefficients, initial pit size, and ΔK_{th} as the key random variables, the mechanistically based approach is used to estimate the influence of applied stress and temperature on corrosion and corrosion fatigue life. The sensitivity to each of the key random variables is also examined.

It is recognized that the probability considerations are part of the initial stages of the model construction, and they are integrated throughout the process. In fact, the probability considerations and analysis must be an integral part of the process. It cannot be an ex post facto addition to a mechanistic study. Along with being able to make predictions well beyond the range of available data, the model is able to account for the contributions of each key random variable and to provide an assessment of the significance of each. It is also recognized that pitting of steel is much more complex, and involves continuous nucleation, growth and coalescence at multiple sites. The illustration described herein, therefore, should not be construed as being representative of actual behavior. Nevertheless, it does provide an estimate based on a single flaw model, and it serves to demonstrate the effectiveness of this approach. The direction and importance for adopting this approach in the development of life prediction methodology and directions for future research are considered.

Mechanistically based probability approach and process for model development

The essential advantage of this approach is the use of a mechanistically based damage accumulation model to capture the functional dependence on all of the key (random) variables. This is a vastly different approach than the typical statistically based approach which relies on the use of parametric models of experimental data.

It is granted that constructing a mechanistic model for which probabilistic analyses can be made is difficult, nevertheless, is essential for making meaningful predictions. The probabilistic component of the model must be included from the outset. It cannot be an ad hoc add-on after the mechanism is understood because accurate parameter identification and characterization is an integral part of both the experimental design and the modeling. The essential elements of the modeling process and their interrelationships are outlined in Table 1 and are shown schematically in Figure 1. The initial step is to identify the mechanisms and all of the critical variables which contribute to the failure process. These variables can be separated into two categories: external variables, which describe such things as loading and environmental conditions; and internal variables, which include the structure and properties of the material and its response to the external conditions. The design of experiments is highly dependent on the choice of the variables used in the model because those variables, and their interrelationships, must be identified in order to analytically evaluate the proposed probability model. In other words, the effect of a variable must be known before it can be incorporated meaningfully into the model. Thus, one essential aspect of the design of experiments is the verification and refinement of the mechanistic model. The development of the mechanistic model is crucial. All of the physical, chemical, and material processes which critically determine the degradation process must be identified, if tight estimates are to be achieved. Another aspect of the design of experiments is the estimation of a joint probability density function (*jpdf*) for the internal and external variables. Such issues as the degree of scatter and the statistical interdependence of the variables must be addressed. Finally, the mechanistic model and the *jpdf* are merged to produce a probability model which can estimate long-term reliability. One of the strengths of this approach is that it is iterative in that as more data or insight become available the modeling process can be repeated to include the additional information. This feature is especially key to modeling long-term processes for which data become available through several years of service.

Pitting corrosion and corrosion fatigue in aqueous environments

To demonstrate the integration of mechanistic understanding with probabilistic modeling, a simplified model for pitting corrosion and corrosion fatigue is developed. Damage is assumed to be initiated by pitting corrosion, from which a corrosion fatigue crack can nucleate and grow. The model is illustrated schematically in Figure 2. Randomness associated with material properties and their sensitivity to the environment are explicitly represented in the model. Because detailed mechanistic models for pitting corrosion and corrosion fatigue are yet to be developed, an empirically based model is used as the basis for this example.

The key variable of interest in probability modeling is the time-to-failure t_f of the component or the structure. The goal is to find the cumulative distribution function (cdf) for t_f . It is the cdf which accounts for scatter in a variable and which allows for identification, estimation, and prediction of the reliability. For pitting corrosion and corrosion fatigue, t_f can be considered as follows:

$$t_f = t_{tr} + t_{cg} \quad (1)$$

where t_{tr} is the time for a nucleated pit to grow and transition into a crack and t_{cg} is the time for a crack to grow to a prescribed critical length, given by a failure criterion. To find explicit expressions for t_{tr} and t_{cg} , the following model is employed.

Pitting corrosion model

In keeping with [1, 2], it is assumed that a growing pit remains hemispherical in shape and grows at a constant volumetric rate dV/dt given by

$$\frac{dV}{dt} = 2\pi a^2 \frac{da}{dt} = \frac{MI_{p_0}}{nF\rho} \exp\left[-\frac{\Delta H}{RT}\right], \quad (2)$$

where a is the pit radius, M is the molecular weight of the material, n is the valence, $F = 96514$ coul/mol is Faraday's constant, ρ is density, ΔH is the activation energy, $R = 8.314$ Joule/mol-K is the universal gas constant, T is the absolute temperature, and I_{p_0} is the pitting current coefficient. Thus, t_{tr} is found after a simple integration to be as follows:

$$t_{tr} = \frac{2\pi nF\rho}{3MI_{p_0}} (a_{tr}^3 - a_0^3) \exp\left[\frac{\Delta H}{RT}\right], \quad (3)$$

where a_{tr} is the pit radius at which a crack is initiated and a_0 is the initial pit radius.

The transition pit radius a_{tr} can be expressed in terms of the threshold driving force ΔK_{th} via the crack growth mechanism [1, 2]. For the sake of simplicity and computational expediency, assume that

$$\Delta K = \frac{2.2}{\pi} \Delta\sigma \sqrt{\pi a}, \quad (4)$$

where $\Delta\sigma$ is the far field stress range, and the factor of $2.2/\pi$ is for a semi-circular flaw in an infinite plate. Thus,

$$a_{tr} = \pi \left(\frac{\Delta K_{th}}{2.2\Delta\sigma} \right)^2. \quad (5)$$

The expression for t_{tr} is found by substituting (5) into (3).

Corrosion fatigue model

A model for corrosion fatigue crack growth has been proposed on the basis of a superposition model [3 - 5]. In the model the rate of corrosion fatigue crack growth, $(da/dN)_c$, is identified microstructurally with two parallel mechanisms for crack growth; namely, *pure* (mechanical) fatigue and *pure* corrosion fatigue:

$$\left(\frac{da}{dN}\right)_c = \left(\frac{da}{dN}\right)_r (1-\theta) + \left(\frac{da}{dN}\right)_c \theta. \quad (6)$$

In (6), $(da/dN)_r$ is the rate of fatigue crack growth in an inert (reference) environment, and it is identified with *pure* (mechanical) fatigue; $(da/dN)_c$ represents the cycle-dependent contribution which requires synergistic interactions of fatigue and environmental attack, and it is identified with *pure* corrosion fatigue; and the fraction of the crack that is under going *pure* corrosion fatigue is identified with a non-dimensional measure of the extent of surface reaction (or surface coverage θ) during each fatigue loading cycle. It should be noted that the rates themselves may be composed of contributions from several concurrent micromechanisms. Herein, the model is focused on transport or surface reaction controlled processes. For steels, crack growth follows the surface reaction controlled model [5, 6].

For the sake of illustration, a generic application is considered, where the loading - unloading duty cycle is 4 and 20 cycles per day. These frequencies ν are so small or the time duration is so long that θ is essentially unity. Thus, the simplified model, which is used henceforth, assumes that θ is identically one, and (6) simply reduces to the corrosion fatigue growth rate $(da/dN)_c$.

For demonstrating the proposed probabilistic approach, the basic power law form for the corrosion fatigue growth rate $(da/dN)_c$ is assumed to be the mechanistically based model. Thus,

$$\left(\frac{da}{dN}\right)_c = C_c (\Delta K)^{n_c}. \quad (7)$$

In this model n_c represents the mechanistic dependence, specifically the functional dependence of the crack growth rate on the driving force ΔK , and it is taken to be deterministic. The coefficient C_c reflects material properties, and the contributions of microstructural and environmental parameters are included in its variability. As above, ΔK is given by (4).

Substituting (4) into (7) yields a simple differential equation in that the variables a and N can be separated, and an explicit solution can be found. Assuming that $N = \nu t$, and since (7) governs the time of crack growth t_{cg} , then

$$t_{cg} = \begin{cases} \frac{\pi \ln(a_f/a_r)}{\nu C_c (2.2\Delta\sigma)^2}, & n_c = 2 \\ \frac{2(\sqrt{\pi})^{n_c} \left[(\sqrt{a_r})^{2-n_c} - (\sqrt{a_f})^{2-n_c} \right]}{\nu (n_c - 2) C_c (2.2\Delta\sigma)^{n_c}}, & n_c > 2. \end{cases} \quad (8)$$

The resulting model is not intended to be the most accurate or general, but it is used here to demonstrate several important modeling concepts.

Selection of deterministic and random variables

With reference to Table 1 or Figure 1, observe that $\Delta\sigma$, ΔK , ν , and T , for example, are external variables, whereas C_c , ΔK_{th} , a_o , and a_f are examples of internal variables. It is to be noted that none of the rvs are stochastic processes, i.e., the rvs are chosen to be mechanistically and statistically independent of time. The parameter C_c reflects variability in material properties, more specifically, it is characteristic of the resistance of the material to fatigue crack growth and of environmental sensitivity. The initial pit size a_o represents material and manufacturing quality. The fatigue threshold ΔK_{th} is also a function of the material variability. The final rv I_{Po} reflects the scatter associated with the electrochemical reaction for pit growth.

Deterministic variables

Table 2 contains the values for the deterministic variables which are used in the numerical computations. It is to be noted that some of these variables could be considered to be random; however, they are assumed to be deterministic for this example. Most of the values in the table are self explanatory; however, a few comments are in order. The values for the frequency ν are selected to represent a long duty cycle ($\nu = 4\text{cyc/day}$) and a short duty cycle ($\nu = 20\text{cyc/day}$) flights. The temperature values are selected to cover a reasonable range of operating temperatures. Finally, the applied stresses $\Delta\sigma$ are typical of the design stress range for steels used in many applications.

The characterization of a_f is more difficult because it is associated with the failure condition, the experimental termination criterion, or the replacement or repair condition of a component. Certainly, there are ways in which to define a_f so that it is not deterministic, and indeed, these may be more suited to reality. For simplicity, a_f is assumed to be deterministic here. Such an assumption, for example, corresponds to the specification of an inspection limit for a_f .

Random variables

For this model, randomness is assumed to be introduced through the following four variables: the pitting current coefficient I_{Po} , the initial pit size a_o , the corrosion fatigue crack growth coefficient C_c , and the fatigue crack growth threshold ΔK_{th} . In order to select an appropriate *cdf* for each random variable (rv), extensive experimental and statistical testing is needed within the context of the theoretical probability foundations on which the *cdfs* are constructed.

Because the *cdfs* are not known, the Weibull *cdf* is chosen, for the illustration, for all of the rvs . The Weibull *cdf* is sufficiently robust to provide an adequate estimate the statistical character of the rvs [7, 8]. The three parameter Weibull *cdf* is given by:

$$F(x) = 1 - \exp\left\{-\left[\frac{(x-\gamma)}{\beta}\right]^\alpha\right\}, \quad x \geq \gamma \quad (9)$$

where α is the shape parameter, γ is the location parameter or minimum value, and β is the scale parameter. The parameters in the Weibull *cdf* are related to physical quantities in the following way: α is characteristic of the scatter in the rv , $(\beta + \gamma)$ is approximately the mean value, and γ is the minimum value of the rv . It should be noted, however, that the choice of the Weibull *cdf* is not an essential feature of the model development, and in fact, any properly defined *cdf* can be used for the probability development.

While the approximations for the rvs are intended to be typical, at least qualitatively, they are not necessarily quantitatively accurate. Table 3 contains the assumed values for the Weibull parameters for each rv . The main

purpose of this illustration is to demonstrate the probabilistic approach, and the technique is sufficiently general to allow for any changes which are more realistic physically. As far as the mathematical modeling is concerned, the numerical values given for any of the parameters are inconsequential, but they are very important from the standpoint of the physical model. It is precisely at this point where accurate experimental and statistical modeling are required.

Computation of the cdfs

The computation of the *cdf* $F_f(t)$ for the life t_f is, in principle, straightforward since the time-to-failure is a sum of two *rvs*; see (1). However, t_{tr} and t_{cg} are functions of the underlying *rvs*, and the *cdf* for t_f is found by an application of the standard change-of-variables theorem for multidimensional *rvs*. The simplest form of the result can be found in most standard probability texts; e.g. see [9]. However, a more advanced treatment containing engineering applications is given in [10].

The first step in the analysis is to find an explicit expression for the life t_f . Substituting equations (3, 5, and 8) into (1), when $n_c = 2$, yields

$$t_f = \frac{\pi \ln \left[\frac{a_f (2.2\Delta\sigma)^2}{\pi (\Delta K_{th})^2} \right]}{vC_c (2.2\Delta\sigma)^2} + \frac{2\pi n F \rho \exp \left[\frac{\Delta H}{RT} \right]}{3MI_p} \left\{ \pi^3 \left(\frac{\Delta K_{th}}{2.2\Delta\sigma} \right)^6 - a_o^3 \right\}. \quad (10)$$

The computation of the *cdf* for t_f is rather tedious, in fact, the only possible solution requires the numerical evaluation of a multidimensional integral which is nontrivial. Nevertheless, the numerical analysis is sufficiently well behaved that standard procedures are applicable, and the numerical accuracy is within the model precision. For another application, with more details, which is very similar to this problem see [11].

Results and discussion

Deterministic parameters such as frequency, far-field stress range, or temperature are often used to accelerate testing. These are, therefore, the key external variables in time extrapolation. With the model at hand the influence of each of these variables can be considered collectively or in turn. Similarly, the statistical contribution of each of the *rvs* can be assessed. These analytical sensitivity studies are useful in constructing an experimental design of experiment and in refining a mechanistic model for the failure process.

The influence of the applied stress range $\Delta\sigma$ on the predicted distribution $F(t)$ for the time-to-failure t_f is shown in Figure 3, for a frequency of 20cyc/day. The *cdfs* are more spread as $\Delta\sigma$ decreases which indicates that the variability is increasing. The variability principally reflects the variations in all of the random variables. Another observation, which is consonant with experimental results, is that $F(t)$ is stochastically ordered in that, for fixed t , $F(t)$ strictly decreases as $\Delta\sigma$ decreases. In other words, for fixed $F(t)$, the random life t_f decreases as the applied stress range increases. The consequence of changing the applied stress is manifest. It is demonstrated by observing that the mean life, from smaller to larger values, differs by a factor of about 10 over the given range. Figure 4 is identical to Figure 3 except that the frequency has been lowered to 4cyc/day. There is less scatter for each *cdf* in this case. The range of the mean failure times is more narrow, differing by a factor of about 4. Also, notice that the mean times-to-failure are larger.

Figure 5 is the *cdf* for the time-to-transition, i.e. pitting corrosion, of equation (3). Notice that the amount of scatter is the same for each *cdf*. In fact, a significant portion of the total life is expended in pit growth. This phenomenon is clearly shown on Figure 6, where the *cdfs* for the time-to-transition and the times-to-failure for the

two different frequencies are shown. Notice that the mean time-to-transition is about 25% and 8% of the mean times-to-failure when the frequencies are 20 and 4cyc/day, respectively.

The influences of temperature and frequency are contained in Figures 7 and 8. The temperature varies from 273 to 313K for two frequencies, 4 and 20cyc/day. The predicted lives reflect the influence of temperature which only affects the time-to-transition in equation (3). The mean time-to-transition is the largest fraction of the mean time-to-failure for the smaller temperatures, and the fraction decreases as the temperature increases. It is also manifest that the *cdfs* are stochastically ordered similarly, i.e., the life decreases as the temperature decreases. At 4 and 20cyc/day, the difference in mean lives is about a factor of 1.2 and 2, respectively.

Since ΔK_{th} is such a critical ν in both the time-to-transition t_{tr} and the time-to-failure t_f , its effect is displayed in Figures 9 and 10. The mean for ΔK_{th} varies from 3.0 to 4.0MPa \sqrt{m} . As the mean increases, the scatter increases. The difference in mean life varies by about a factor of 1.5, and again, a majority of the total life is due to the pit growth.

Some observations

In order to insure that the single flaw model is physically consistent, the rate of flaw growth for the pitting corrosion must be considerably less than the corrosion fatigue growth for times beyond the time-to-transition. Figures 11 and 12 show the mean flaw radius versus time for the two mechanisms of growth. The key observation is that the pit must be sufficiently large for the transition to crack growth to be instantaneous. This requirement is directly responsible for the moderately long times-to-transition. Thus, the single flaw model for steels is not as accurate as desired. Furthermore, it has been observed that there is substantial interaction between corrosion pits during nucleation and growth [12]. Therefore, the proper model for pitting corrosion and crack growth must include a nearest neighbor interaction and effect. This will be the thrust of a future effort.

The next most critical aspect of the approach is the identification of all of the variables, deterministic and random. Certainly, this will include an extensive design of experiments, but it may also include derivations for distribution functions from the first principles of probability theory, or even some simple assumptions. The latter is primarily the case needed to accurately model pit interactions. Also associated with this aspect of the modeling is the need for improved mechanistic descriptions for the pitting and fatigue processes. Greater accuracy in modeling directly results in greater accuracy in reliability estimations.

Summary

A probabilistic approach for the prediction of service lives of engineered components and structures, designed for operation in deleterious (or corrosive) environments, has been described. Such an approach is needed for making stochastically tight estimates (or predictions) of service life at times or loading conditions that are well beyond the range containing typical supporting data. The methodology and utility of the approach has been illustrated in terms of pitting corrosion and corrosion fatigue crack growth for steels in aqueous environments. The model is for a single flaw, and the flaw growth is governed by a model for electrochemical reaction controlled pit and corrosion fatigue crack growth, employing, for simplicity, a power-law (Paris-Erdogan) relationship for corrosion fatigue.

The probabilistic contributions from the material properties on the times-to-failure were assessed as functions of applied stress, loading frequency and temperature. The results are qualitatively consistent, but they are not quantitatively accurate because assumed parameters were used. Even so, this example illustrates that the modeling approach is well-suited for making predictions beyond the range of laboratory observations, and it facilitates parametric analysis which is not possible with most statistical approaches. The example also clearly indicates that the mechanistic understanding of corrosion fatigue crack growth is incomplete and the distribution functions for the key variables have not been characterized adequately. It is precisely at this point where additional research to further develop the necessary information and understanding is needed in formulating a complete, rational methodology for service life prediction.

It has been shown that probability considerations and analysis must be an integral part of the modeling process. It cannot be an ex post facto addition to a mechanistic study. Thus, the effectiveness of the approach depends explicitly upon the quality of the mechanistic understanding of the underlying failure process and upon the appropriate conjunction with probabilistic modeling to describe the influences of fundamental random variables (*rvs*). One of the most critical aspects of the process is the selection of the internal and external variables, which describe the degradation process, each of which may be random or deterministic.

References

1. Y. Kondo, *Corrosion* **45** (1989): p. 7.
2. Y. Kondo and R.P. Wei, Approach on Quantitative Evaluation of Corrosion Fatigue Crack Initiation Condition, *Proc. EVALMAT* (1989): p. 135.
3. R.P. Wei and M. Gao, *Scripta Metall.*, **17** (1983): p. 959.
4. R.P. Wei, Environmentally Assisted Fatigue Crack Growth, *Advances in Fatigue Science and Technology*, (Branco, M. and Guerra-Rosa, L., eds., Kluwer Academic Publishers, 1989): p. 221.
5. J.P. Thomas and R.P. Wei, *Mats. Sci. and Engr.* **A159** (1992): p. 205.
6. J.P. Thomas and R.P. Wei, *Mats. Sci. and Engr.* **A159** (1992): p. 223.
7. R.E. Barlow and F. Proschan, *Statistical Theory of Reliability and Life Testing*, 2nd edition, (To Begin With, Silver Spring, MD, 1981).
8. K.C. Kapur and L.R. Lamberson, *Reliability in Engineering Design*, (John Wiley, New York, 1977).
9. I.F. Blake, *An Introduction to Applied Probability*, (John Wiley, New York, 1979).
10. D.G. Harlow and T.J. Delph, *Math. and Comp. in Simulation*, **33** (1991): p. 243.
11. D.G. Harlow and R.P. Wei, A Mechanistically Based Approach to Probability Modeling for Corrosion Fatigue Crack Growth, *Engr. Fracture Mech.* to appear.
12. *Localized Corrosion*, (R.W. Staehle, B.F. Brown, J. Kruger, and A. Agrawal, eds., NACE - 3, 1974).

Table 1. The process

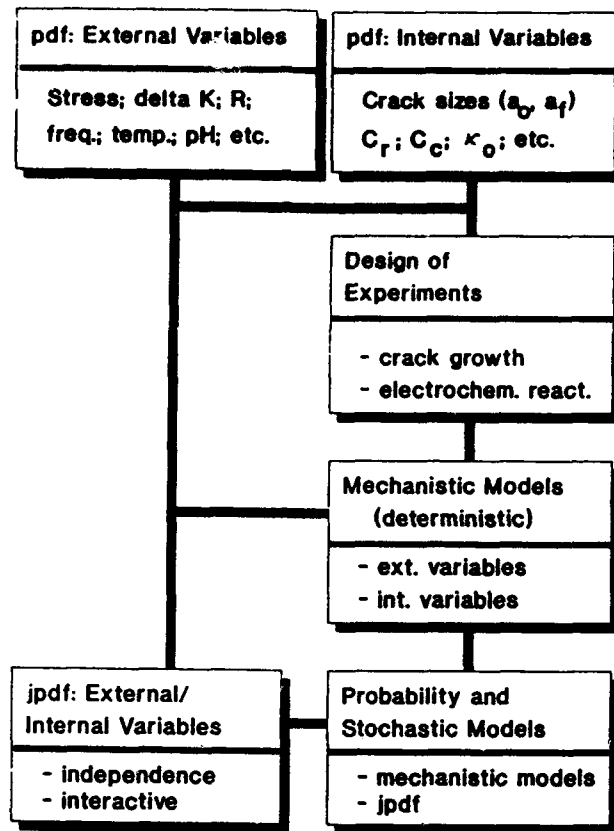
- Identification of damage mechanisms
- Identification and characterization of key (random) variables
 - * Variables - external and internal
 - * Probability density functions
 - * Independent and dependent
- Mechanistic model of damage process
 - * Functionale dependent on the key (random) variables
 - * Validation and range of applicability
- Joint probability density function (*jpdf*)
- Mechanistically based probability model for life prediction
 - * Integration of the *jpdf* with the mechanistic model
 - * Validation (beyond the supporting data)
 - * Revise and refine

Table 2. Deterministic parameters used in the model for steel

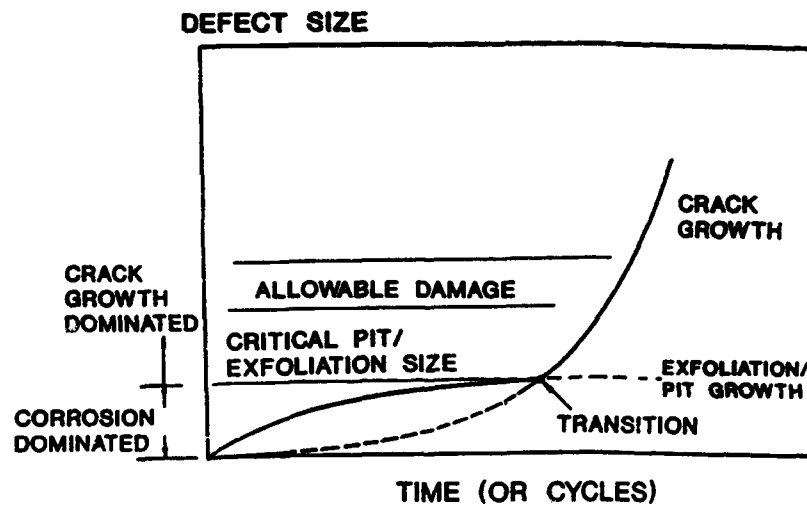
| parameter | steel |
|---|---------------------|
| density ρ (gm/m ³) | 7.8×10 ⁶ |
| molecular weight M | 56 |
| valence n | 3 |
| activation energy ΔH (kJoule/mol) | 35 |
| crack growth exponent n_c | 2 |
| final crack size a_f (mm) | 3 |
| temperature T (K) | 273, 293, 313 |
| applied stress $\Delta\sigma$ (MPa) | 400, 600, 800 |
| frequency ν (cyc/day) | 4, 20 |

Table 3. Weibull parameters used in the model for steel

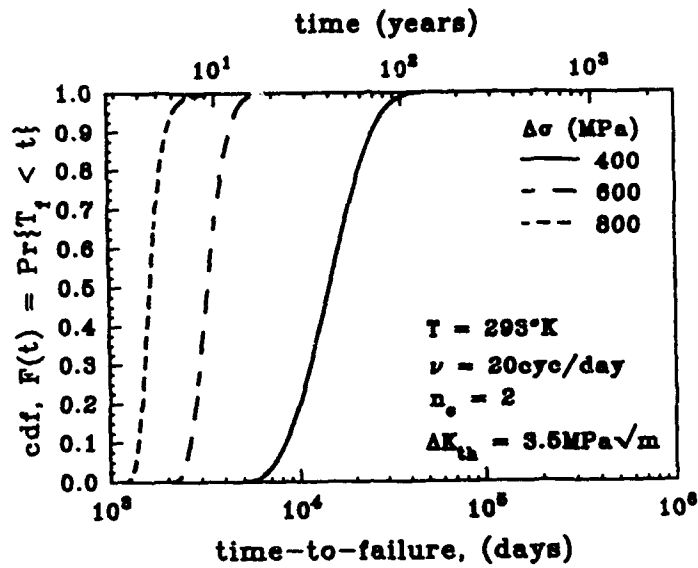
| random variable | α | β | γ | μ |
|--|----------|-------------------------|-------------------------|-------------------------|
| initial pit radius a_o (m) | 12 | 5.0×10 ⁻⁷ | 1.5×10 ⁻⁶ | 1.98×10 ⁻⁶ |
| fatigue coefficient C_c (m/cyc)(MPa√m) ⁻² | 8 | 2.0×10 ⁻¹⁰ | 0 | 1.77×10 ⁻¹⁰ |
| pitting current constant I_{p_o} (coul/sec) | 1 | 1.2175×10 ⁻⁵ | 1.2175×10 ⁻⁵ | 2.4350×10 ⁻⁵ |
| threshold driving force ΔK_{th} (MPa√m) | 10 | 2.102 | 1.0 | 3.0 |
| | 10 | 2.628 | 1.0 | 3.5 |
| | 10 | 3.153 | 1.0 | 4.0 |



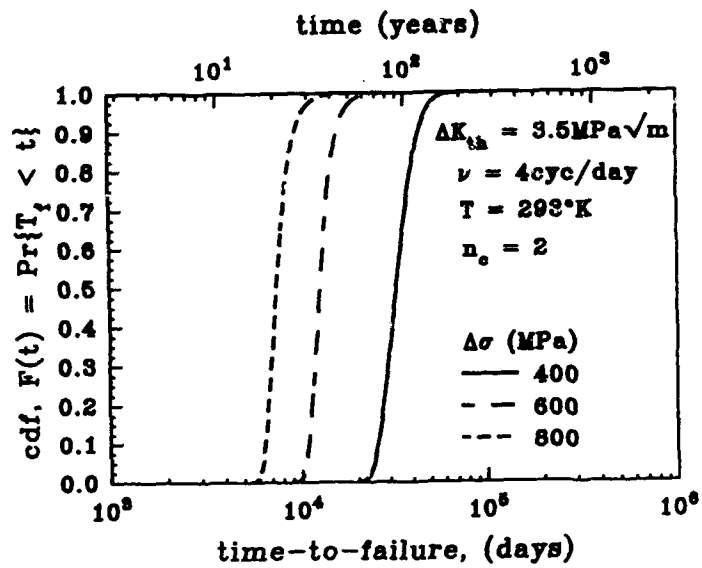
1. Key elements for the formulation of a mechanistically based probability model for life prediction.



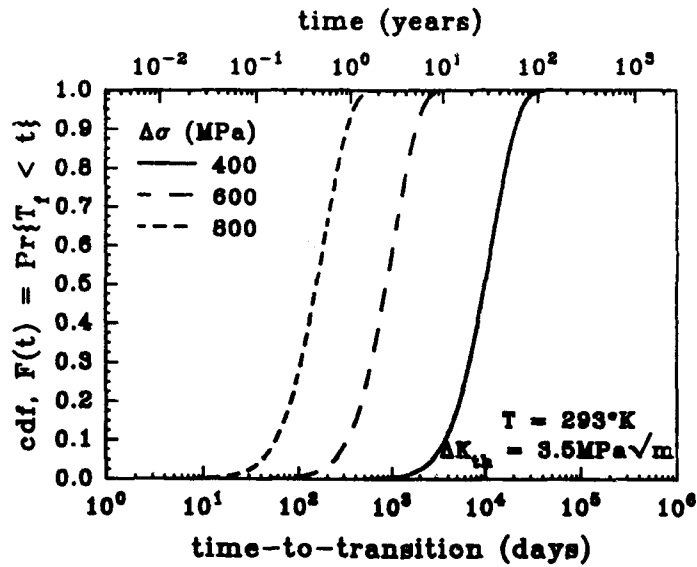
2. Schematic representation of pitting corrosion and corrosion fatigue.



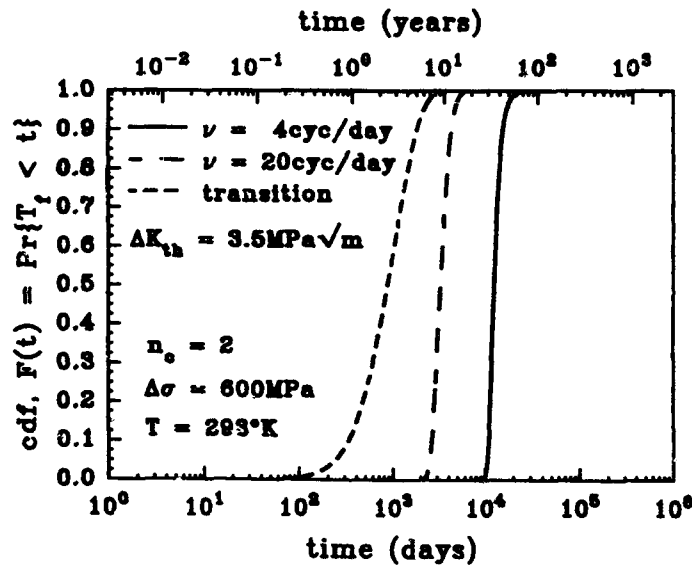
3. Influence of applied stress on the *cdf* for the time-to-failure at 293K and 20cyc/day.



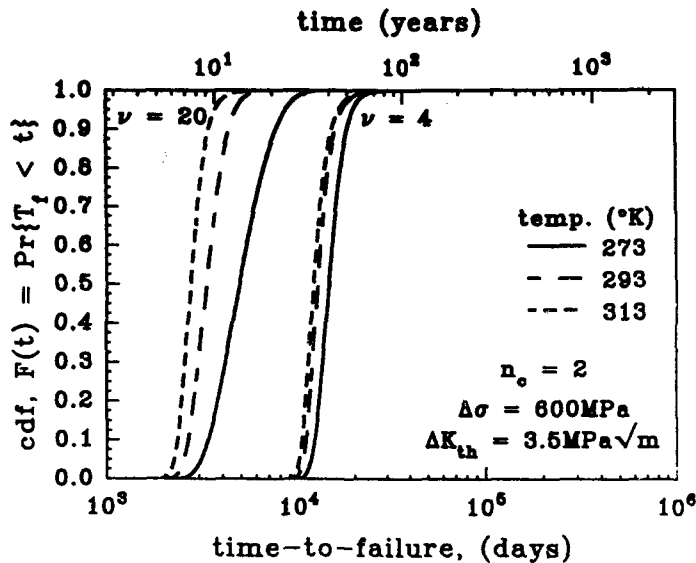
4. Influence of applied stress on the *cdf* for the time-to-failure at 293K and 4cyc/day.



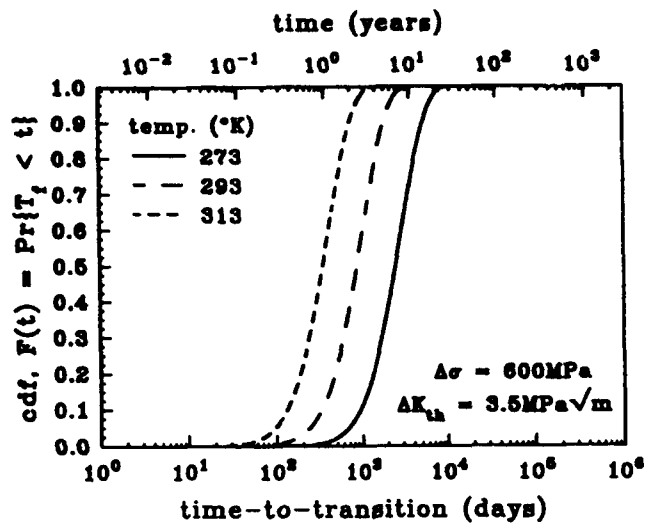
5. Influence of applied stress on the *cdf* for the time-to-transition at 293K.



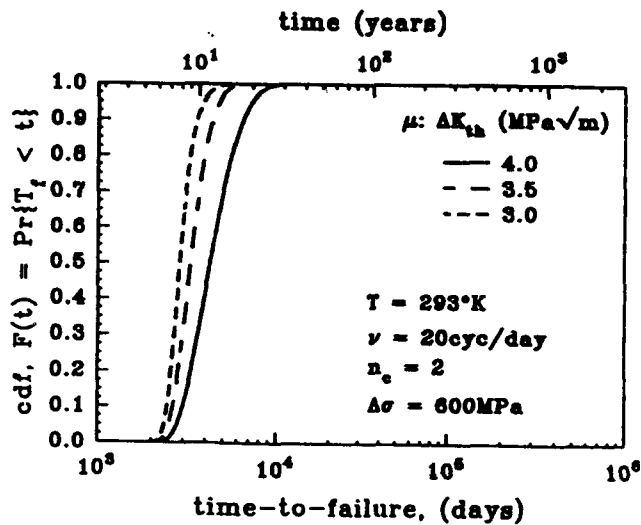
6. Relative contribution of the time-to-transition and the time-of-crack growth on the *cdf* for the time-to-failure at 293K and 600MPa.



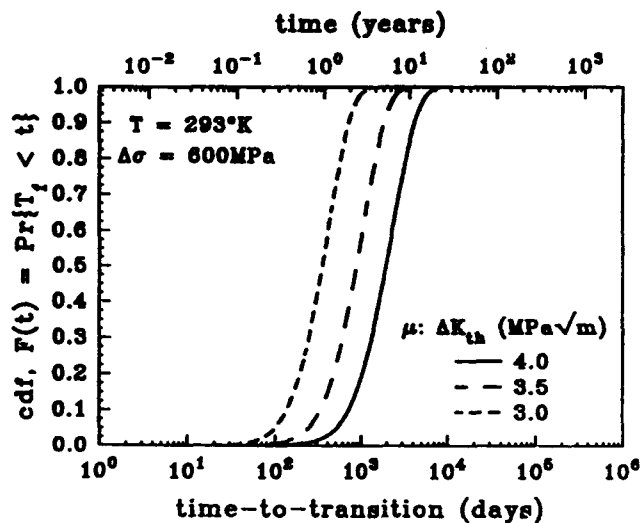
7. Influence of temperature on the *cdf* for the time-to-failure at 4 and 20cyc/day and 600MPa.



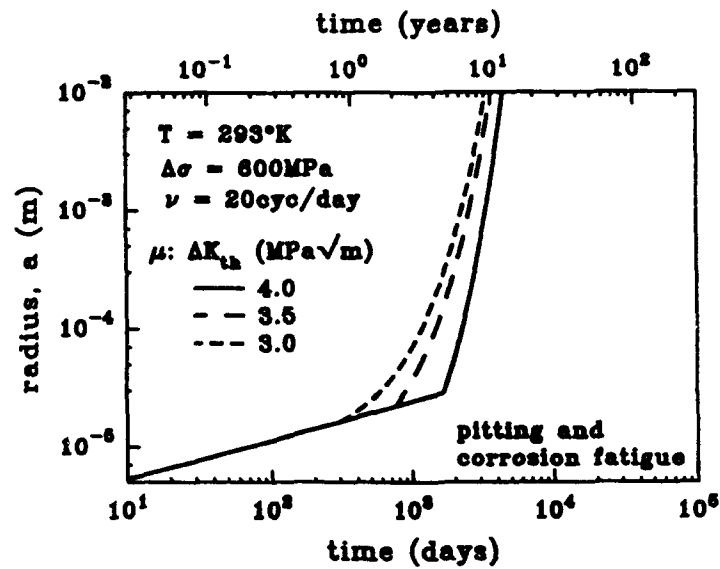
8. Influence of temperature on the *cdf* for the time-to-transition at 600MPa.



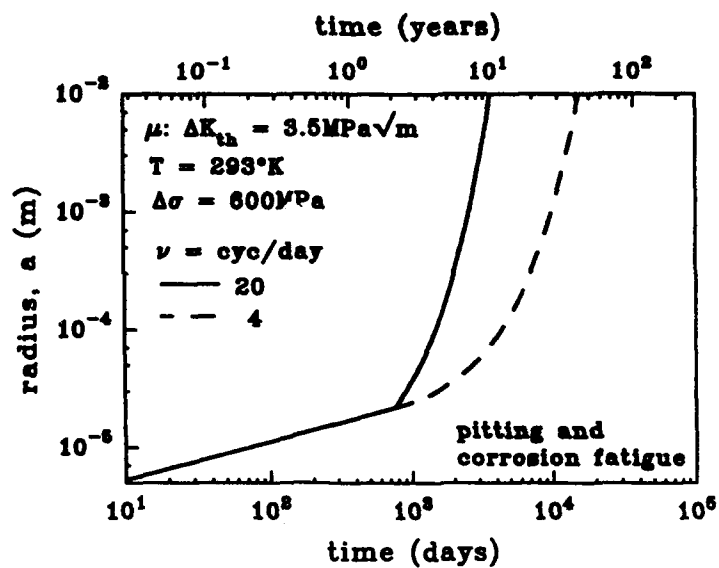
9. Influence of the mean threshold driving force on the *cdf* for the time-to-failure at 20cyc/day, 293K, and 600MPa.



10. Influence of the mean threshold driving force on the *cdf* for the time-to-transition at 293K, and 600MPa.



11. Influence of the mean threshold driving force on the flaw growth during pitting corrosion and corrosion fatigue at 20cyc/day, 293K, and 600MPa.



12. Influence of frequency on the flaw growth during pitting corrosion and corrosion fatigue at 293K, and 600MPa.

The Effects of Complexing Agents on the Corrosion of Copper-Nickel Alloys in Sulfide Polluted Seawater under Impingement Attack

Dr. Mahmoud R. Reda
Chemical Engineering Department
College of Engineering and Petroleum
Kuwait University
P. O. Box 5969-Safat
Kuwait

Dr. Jamal N. Alhajji
Mechanical Engineering Department
College of Engineering and Petroleum
Kuwait University
P. O. Box 5969-Safat
Kuwait

Abstract

Five copper-nickel alloys with nickel content ranging from 0 w/o to 100 w/o were electrochemically investigated in sulfide polluted seawater (0 to 100 ppm S⁼). The purpose of this research is to investigate the effect of both the nickel content and the sulfide ion concentration under a simulated impingement condition. In addition, three different complexing agents were investigated. It is found that fuchsin or EDTA can have a beneficial effect in reducing the corrosion rate.

Introduction

Nickel alloys and particularly copper nickel alloys are commonly used in seawater applications. A great deal of research has concentrated on studying the performance of these alloys in this environment (e.g. 1-5). The corrosion performance of these alloys has been shown to be very suitable in marine service. Although these alloys have been shown to be highly suitable in unpolluted seawater, enhanced corrosion in this environment has been shown to be associated with sulfide contamination (6-8). These alloys were also shown to be susceptible to impingement attack even in unpolluted seawater (1 and 3). As indicated by Evans (3) even with the best materials (e.g. pure nickel) there is still risk to corrosion to condenser tubes if the water used contains hydrogen sulfide or *cystine*



a substance derived from seaweed. It was concluded (3) that this trouble has not been entirely overcome. In this investigation it is attempted to investigate the corrosion

behavior of nickel alloy (0 to 100 w/o) under impingement attack in sulfide polluted seawater (0 to 100 ppm S^{2-}). In addition the effects of addition of various organic and inorganic complexing agents was undertaken in order to investigate a possible mode of inhibition.

EXPERIMENTAL METHODOLOGY

Test Specimens

Nickel containing alloys including copper-nickel specimens were supplied in the form of sheets. The copper-nickel alloys were 90/10 and 70/30 Cu/Ni (C70600 and C71500). In addition pure copper and pure nickel were investigated. An additional alloy was investigated which contains Cu/Ni in the ratio of 30/70. The chemical analysis of the alloys investigated are shown in Table 1. They were prepared by punching out of 5/8 inch disks for corrosion measurement and evaluation. This was followed by a grinding process of the surface of each specimen according to ASTM standards.

Testing Conditions

Experiments of corrosion measurement were conducted utilizing standard seawater. This was prepared with distilled water and standard seawater salt. Standard seawater salt (Marinemix + Bio-Elements from Wiegandt GMBH & Co. F. R. Germany) was used to reduce the variability effects resulting from conducting measurements using natural seawater. Experiments were also conducted in sulfide polluted seawater. The sulfide was introduced using research grade sodium sulfide (Na_2S). The level of sulfide in the seawater was checked by the iodimetric method of analysis. Various experiments were performed as shown in Table 2. The specification of organic and inorganic complexing agents (analytical grades) used in this study are shown in Table 3.

Testing Equipment and Procedure

Electrochemical corrosion measurements were made at 20 °C for all the previously mentioned conditions, using a computer controlled Potentiostat / Galvanostat (EG&G). A modified electrochemical corrosion testing cell was used where a combination of a circulating pump and a jet nozzle (diameter = 0.001 m) was set up to simulate jet impingement attack as was shown in Figure 1. The stream velocity was measured at the tip of the nozzle and was found to be 6.1 m/s. The separating distance between the tip of the nozzle and the working electrode was fixed at 3 mm. Preliminary corrosion measurements were always performed after four hours. Also, repeated linear-polarization measurements were performed on all the specimens after four hours of exposure to the environment and the values of polarization resistance (R_p) were determined. Cyclic voltammograms sweep were also performed to check the susceptibility to localized attack. The electrochemical tests were run with a saturated Calomel Reference Electrode (SCE). The stability of the SCE was checked following each experiment against a fresh SCE to ensure the reliability of the experiments. The scan rate of the experiments was 0.166 mV/sec. The experiments were conducted repeatedly under the same environmental conditions in order to obtain reproducible results. In unpolluted seawater, reproducibility was good. In polluted seawater, reproducibility of the Tafel slopes were poor, which is consistent with reported results in the literature (4).

RESULTS AND DISCUSSION

Influence of Sulfide Concentration

Figure 2 shows the reciprocal of the polarization resistance of nickel-copper alloys in sulfide polluted seawater. It is clear that sulfide is very deleterious to the alloys with low nickel content. The sulfide is most deleterious for pure copper and least influential for pure nickel alloys. It can be seen that as the sulfide concentration is increased, there is a gradual increase in the electrochemically determined corrosion rate. This is particularly true for alloys with lower nickel content. Thus for 30Cu:70Ni and pure nickel the deleterious effect of sulfide is not influenced by sulfide concentration. This more clearly shown in Figure 3. Reasonable protection against sulfide attack is achieved beyond 30% nickel. This is in agreement with the results which are shown in reference (9) for these alloys in unpolluted seawater.

Mechanism of Corrosion in the presence of Sulfide

In Figure 4 the anodic Tafel slopes for the effects of variations in sulfide concentrations and nickel content of the alloys are shown. It can be concluded that β_a for the copper-nickel alloys ranges between 60 to 100 mV per decade consistent with reported values for electrochemical reactions (9). This trend breaks for alloys with low nickel content in highly polluted seawater (e.g. 100 ppm S^{2-}). This can be due to the formation of dense sulfide corrosion product which even under jet impingement condition still persists at the surface which is associated with alloys with high copper content. In this case there is a shift in the corrosion potential to a very high active corrosion potential as shown in Figure 5 (i.e. -900 mV). Figure 5 shows that in unpolluted seawater, increasing the nickel content results in a shift in the corrosion potential in the noble direction, indicating the formation of a more passive layer with increasing nickel content. This is also true when sulfide is present. It should be noted that generally increasing the sulfide concentration will render these alloys more active for alloys with high nickel content. However, for alloys with low nickel content and for low sulfide concentration there is a tendency for the alloys exhibit a shift in the noble direction. This supports the idea that the mechanism of corrosion reaction is coupled to the amount of nickel present (2). This effect particularly important on the cathodic reaction. This is clearly shown in Figure 6, where the cathodic Tafel slopes for alloys with lower nickel content differs from those with high nickel content (e.g. greater than 30%).

Table 4 gives the slope of the reciprocal of the polarization resistance with the sulfide concentration. At high sulfide concentration, the corrosion rate is practically independent on the sulfide concentration. This is also true for low sulfide concentrations for alloys containing high nickel content. However, the alloys become highly sensitive to sulfide concentration at lower sulfide concentrations and as the nickel content is decreased. From Table 5, it can be seen that at low sulfide concentration (<10 ppm) the alloys with lower nickel content become more active with increasing sulfide concentration. While, at high sulfide concentration (>10 ppm) these alloys tend toward nobility with increasing sulfide. At high sulfide concentration (>10 ppm), the alloys are tending toward nobility at a decreasing rate with increasing nickel content.

Effects of Complexing Agents

Figures 7 to 10 show the influence of various complexing agents on the corrosion rate. Figure 7 and 8, show that the effect of addition of 5 ppm fuchsin and 200 ppm EDTA respectively. It is clear that both of these organic complexing agents are effective in reducing the corrosion rate. It was also possible to achieve a corrosion rate lower than even unpolluted seawater as in the case of pure copper. While ferric ions (100 ppm) alone, as shown in Figure 9, or in combination with 200 ppm EDTA, as shown in Figure 10, increases the corrosion rate over the whole range of nickel content (i.e. 0.0 to 100 w/o). Thus ferric ions can be classified as a stimulator for the corrosion reaction.

Effects of Complexing Agents on localized Corrosion

The extent of localized attack was evaluated using potentiodynamic scanning or cyclic voltammograms (10) in the presence of various complexing agents in 2 ppm sulfide polluted seawater. It is shown in Table 6 that, in the presence of fuchsin or EDTA, alloys with high nickel content are susceptible to localized attack. While at low nickel content (i.e. 0.0 to 30 w/o), localized attack is limited. Although ferric ions alone or in combination with EDTA are stimulator for corrosion reaction where they increase the corrosion rate by an order of magnitude as shown in Figures 9 and 10, the susceptibility to localized attack was low.

Mechanism of Corrosion in the presence of Complexing Agents

In Table 7 shows the anodic Tafel slopes for unpolluted and sulfide polluted seawater containing various complexing agents. It is seen that β_a for unpolluted seawater is around 59 mV/decade independent of the nickel content. In the presence of 2 ppm sulfide polluted seawater the Tafel slopes shift to around 100 mV/decade. This indicates that in the presence of sulfide the rate determining step of the anodic reaction changes from two electrons charge transfer to one electron charge transfer reaction. However in sulfide polluted seawater the addition of fuchsin will change the rate determining step of the anodic reaction to one electron transfer reaction. However, the addition of EDTA or ferric or a combination of the two, the corrosion mechanism of the anodic reaction is not significantly affected. In support of this mechanism are the corrosion potential values shown in Table 8 which indicate that in unpolluted seawater and in polluted seawater containing fuchsin, the corrosion potential gradually shift in the noble direction with increasing nickel content. This is the situation where the corrosion reaction is under cathodic control. It can be concluded from Table 9 that in sulfide polluted seawater with or without additives the cathodic partial reactions are under diffusion control since the cathodic Tafel slopes approaches infinite value for most of the cases investigated.

Conclusions

The following conclusions can be drawn on the corrosion of nickel alloys in sulfide polluted seawater under jet impingement conditions :

- Sulfide is shown to be very corrosive toward nickel alloys with low nickel content.
- The effect of sulfide toward nickel alloys is strongly influenced by both the sulfide concentration and the nickel content.
- The effect of nickel in improving the corrosion resistance in sulfide polluted seawater is related to the effect of nickel on the cathodic part of the corrosion reaction.
- It is shown that complexing agents such as fuchsin and EDTA can greatly improve the corrosion resistance these alloys under these conditions. However, at high nickel content these complexing agents might lead to enhanced susceptibility toward localized attack.
- Ferric ions addition alone or in combination with EDTA can enhance the electrochemically determined corrosion rate under these conditions. However, in the presence of ferric ions, the susceptibility to localized attack was unlikely.

Acknowledgment

This work was financially supported by Kuwait University Research Unit under Contract No. EM-067 . This support is gratefully acknowledged.

References

- (1) J. T. Adrian Roberts, *Structural Materials in Nuclear Power Systems*, (Plenum Press Publishing Corporation., New York, NY., 1980), pp. 388-391.
- (2) J. O'M Bockaris, B. T. Rubin, A. Despic and B. Lovrecek, *Electrochimica Acta*, 17 (1972): p. 973.
- (3) U. R. Evans, *An Introduction to Metallic Corrosion*, 3rd Edition (Edward Arnold Publishers Limited, Scotland, 1981), p. 129.
- (4) S. de Sanchez and D. Schiffrin, *Corros. Sci.*, 22 (1982): p. 585.
- (5) W. Stewart and F. LaQue, *Corrosion*, 8 (1952): p. 2259.
- (6) J. N. Alhajji and M. R. Reda, *Corrosion Science Jour.*, 34 (1992): p. 163.
- (7) M. R. Reda and J. N. Alhajji, *Kuwait University Journal (Science)*, In Press. (1993)
- (8) J. N. Alhajji and M. R. Reda, Presented at the First Asian Corrosion Conference, Singapore; National Association of Corrosion Engineers: Houston, TX, (1992).

- (9) H. H. Uhlig and R. W. Revie, Corrosion and Corrosion Control, Third Edition, (John Wiley and Sons, New York, NY, 1991) p. 82.
- (10) K. R. Trethewey and J. Chamberlain, Corrosion, (Longman Group UK Limited, London, UK, 1988), p. 146.

TABLE 1
The Chemical Analysis of the Alloys Investigated.

| Alloy | Composition | | | |
|-----------------|-------------|------|------|------|
| | %Cu | %Ni | %Fe | %Mn |
| Cu | 99.9 | - | - | - |
| CDA 706 | 88 | 10 | 1.4 | 0.4 |
| CDA 715 | 69 | 30 | 0.6 | 0.5 |
| VDM 30/70 | 32.1 | 64.7 | 1.97 | 0.72 |
| VDM NICKEL 99.6 | 0.01 | 99.7 | 0.03 | 0.10 |

TABLE 2
The Environmental Test Matrix for the Two Alloys under Investigation.

| TESTING CONDITIONS | Pure Copper | 90/10 Cu/Ni | 70/30 Cu/Ni | 30/70 Cu/Ni | Pure Nickel |
|--|-------------|-------------|-------------|-------------|-------------|
| UNPOLLUTED SEAWATER | √ | √ | √ | √ | √ |
| POLLUTED SEAWATER | | | | | |
| 2 PPM S ⁼ | √ | √ | √ | √ | √ |
| 10 PPM S ⁼ | √ | √ | √ | √ | √ |
| 100 PPM S ⁼ | √ | √ | √ | √ | √ |
| 2 PPM S ⁼ POLLUTED SEAWATER | | | | | |
| 5 PPM FUCHSIN | √ | √ | √ | √ | √ |
| 200 PPM EDTA | √ | √ | √ | √ | √ |
| 100 PPM FERRIC | √ | √ | √ | √ | √ |
| 200 PPM EDTA + 100 PPM FERRIC | √ | √ | √ | √ | √ |

TABLE 3
The Organic Complexing Agent Used in the Present Investigation.

| Abbreviation | Chemical Name | Chemical Formula | Molecular Weight |
|--------------|--|--|------------------|
| EDTA | Ethylene Diamine Tetra-acetic Acid-diasodium salt | $[\text{CH}_2\text{-N}(\text{CH}_2\text{-COOH})\text{-CH}_2\text{-COONa}]_2 \cdot 2\text{H}_2\text{O}$ | 372.24 |
| Fuchsin | Fuchsine basic; Magenta; Rosaniline Methanol,(4-amino-3-methylphenyl)-bis(4-amino-phenyl) | $\text{C}_{20}\text{H}_{21}\text{N}_3\text{O}$ | 282.66 |
| Ferric Ions | Iron (III) Chloride Hexahydrate | $\text{FeCl}_3 \cdot 6\text{H}_2\text{O}$ | 270.1 |

TABLE 4
The slope of the reciprocal of the polarization resistance with sulfide concentration.

| Nickel Content | $\frac{d(1/R_p)}{d[S^{=}]}$ $\text{k}\Omega^{-1} \text{cm}^{-2} \text{ppm}^{-1}$ | |
|----------------|--|----------------------------|
| | low sulfide concentration | high sulfide concentration |
| w/o | | |
| 0.0 | 0.30 | ~ 0.0 |
| 10.0 | 0.14 | ~ 0.0 |
| 30.0 | 0.10 | ~ 0.0 |
| 70.0 | 0.02 | ~ 0.0 |
| 100.0 | 0.02 | ~ 0.0 |

TABLE 5
The slope of the corrosion potential with sulfide concentration.

| Nickel Content w/o | $-\frac{d(E_{corr})}{d[S^{2-}]}$ mV ppm ⁻¹ | |
|-----------------------|---|---|
| | low sulfide concentration (<10 ppm) | high sulfide concentration (>10 ppm) |
| 0.0 | ~ 0.0 | ~ +7.0 |
| 10.0 | ~ -7.0 | ~ +4.0 |
| 30.0 | ~ -3.0 | ~ +3.0 |
| 70.0 | ~ +11.0 | ~ +2.0 |
| 100.0 | ~ +13.0 | ~ +1.5 |

TABLE 6
The extent of localized attack for 2 ppm sulfide polluted seawater in the presence of various extraneous ions by cyclic voltammograms examination.

| Type | Nickel Content (%) | | | | |
|---------------|--------------------|----------|----------|--------|--------|
| | 0 | 10 | 30 | 70 | 100 |
| None | none | moderate | moderate | severe | severe |
| Fuchsin | none | slight | moderate | severe | severe |
| EDTA | none | none | moderate | severe | severe |
| Ferric Ions | none | none | none | none | none |
| Ferric + EDTA | none | none | none | none | none |

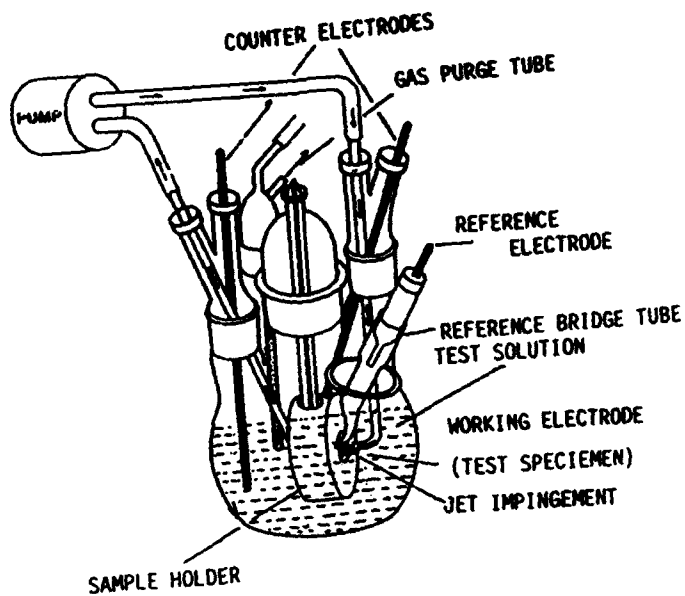


FIGURE 1
The electrochemical cell utilized in the experimental method.

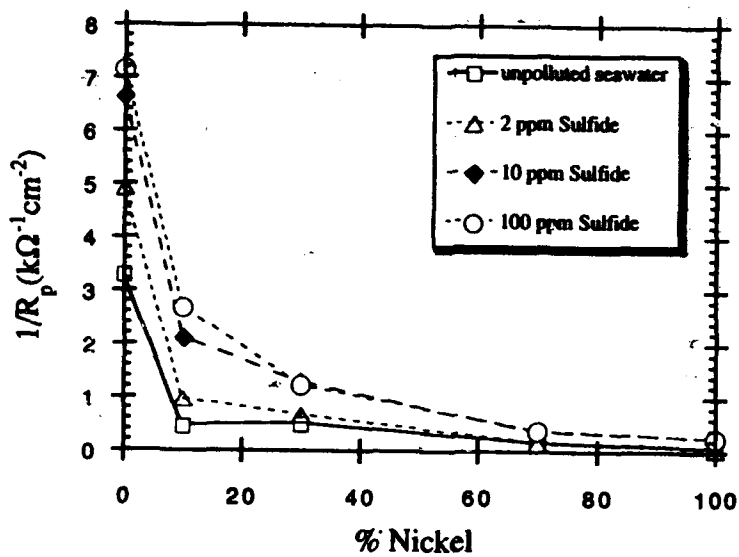


FIGURE 2
The tendency to corrode ($1/R_p$) in sulfide polluted seawater under impingement attack as a function of nickel content.

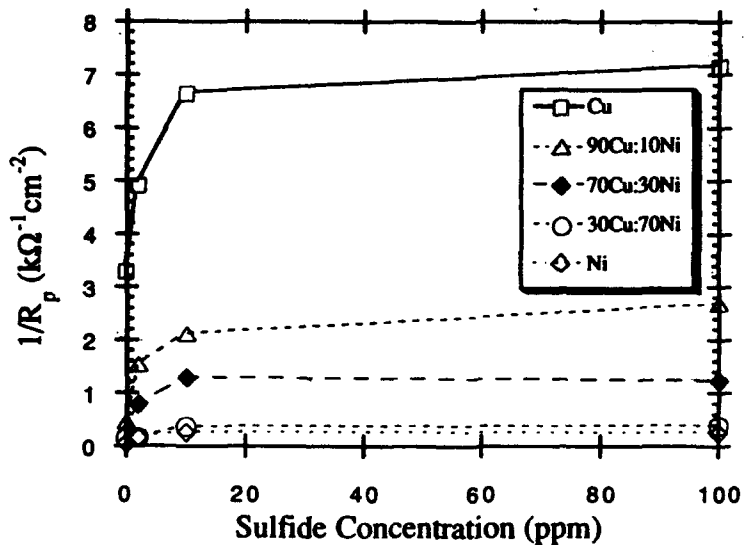


FIGURE 3
The tendency to corrode ($1/R_p$) in sulfide polluted seawater under impingement attack as a function of sulfide concentration.

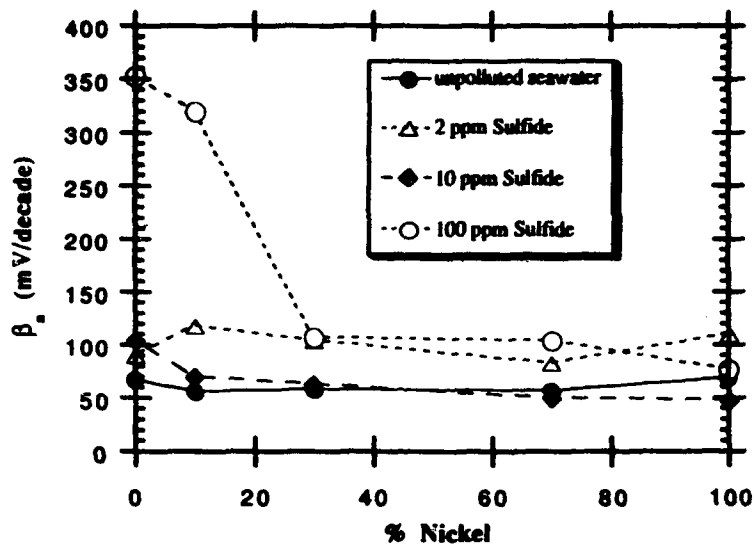


FIGURE 4
The anodic Tafel slope of the nickel alloys in sulfide polluted seawater under impingement attack as a function of nickel content.

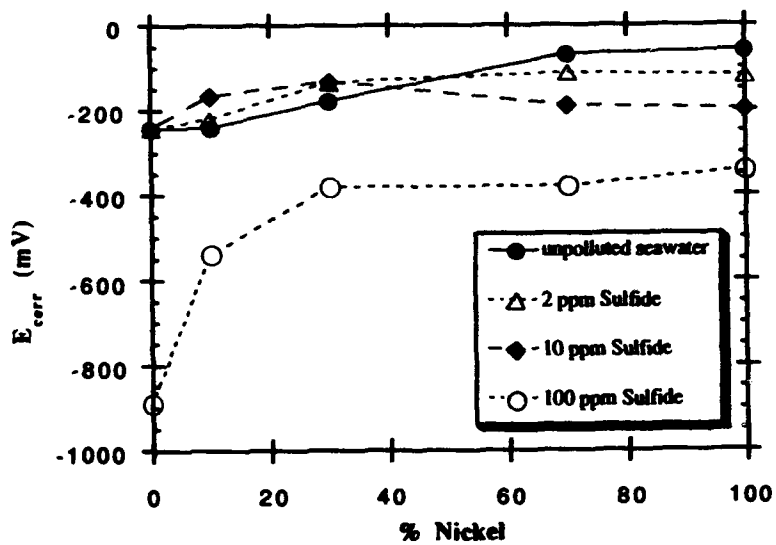


FIGURE 5
The corrosion potential of the nickel alloys in sulfide polluted seawater under impingement attack as a function of nickel content.

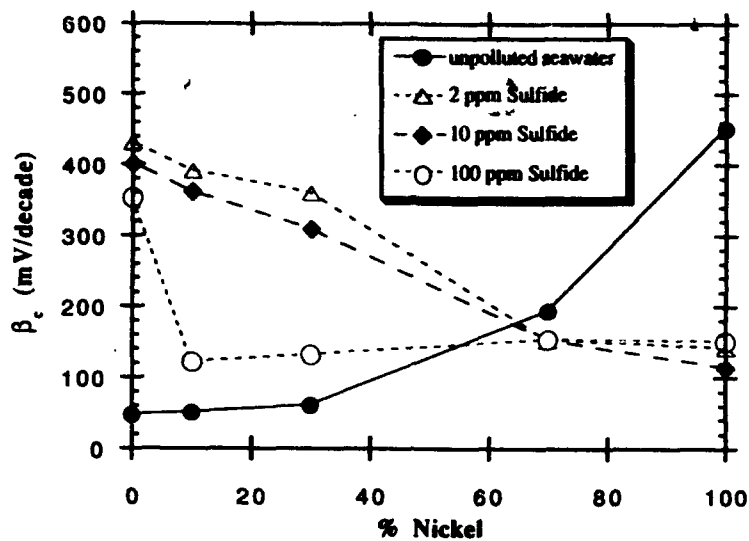


FIGURE 6
The cathodic Tafel slope of the nickel alloys in sulfide polluted seawater under impingement attack as a function of nickel content.

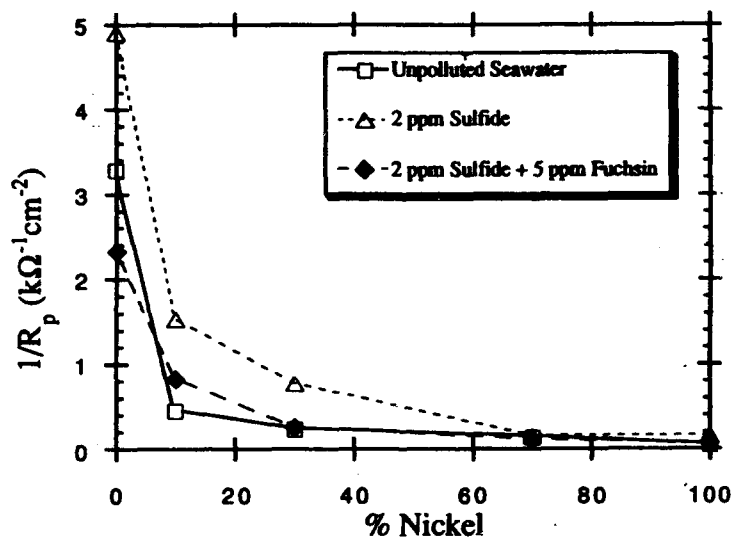


FIGURE 7
The effect of fuchsin addition on the tendency to corrode ($1/R_p$) in sulfide polluted seawater under impingement attack as a function of nickel content.

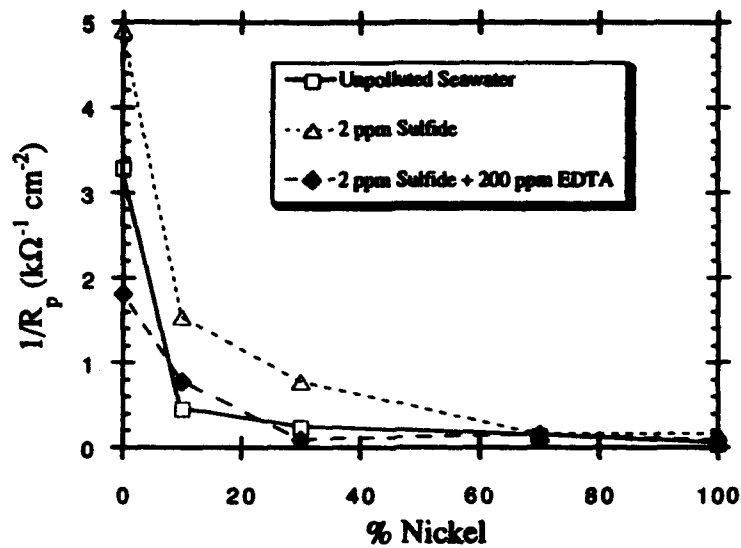


FIGURE 8
The effect of EDTA addition on the tendency to corrode ($1/R_p$) in sulfide polluted seawater under impingement attack as a function of nickel content.

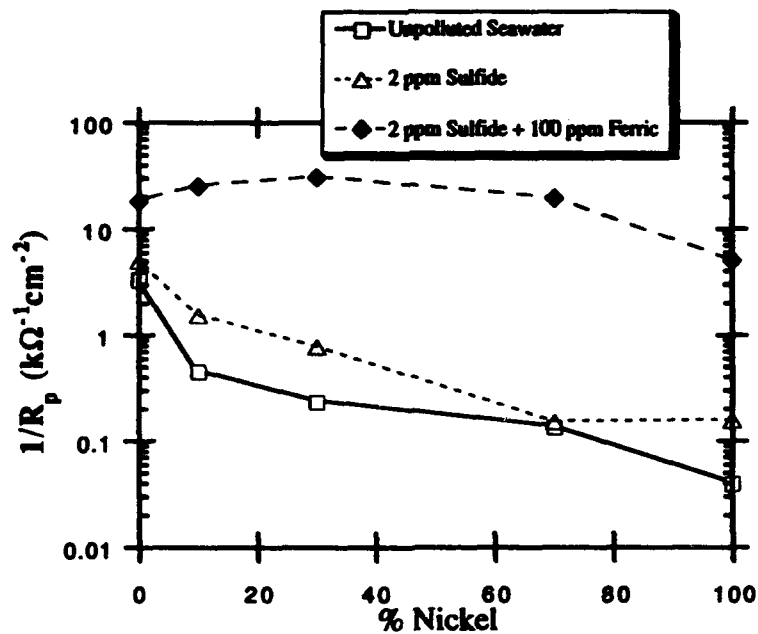


FIGURE 9
The effect of ferric ions addition on the tendency to corrode ($1/R_p$) in sulfide polluted seawater under impingement attack as a function of nickel content.

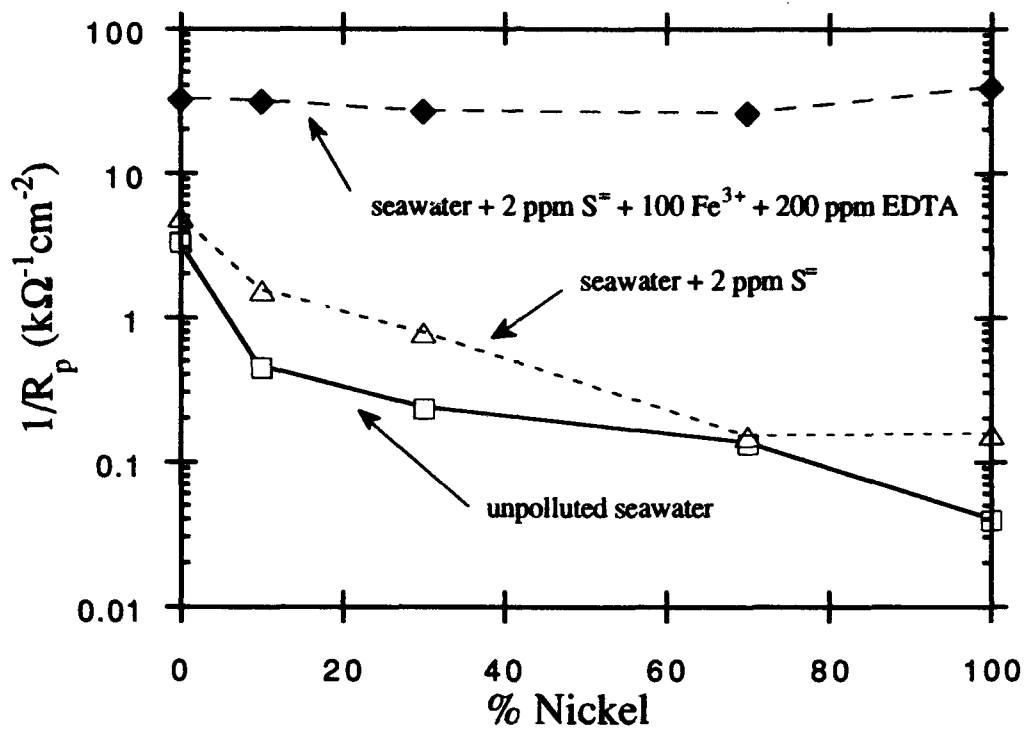


FIGURE 10
 The effect of the addition of a combination of ferric ions and EDTA on the tendency to corrode ($1/R_p$) in sulfide polluted seawater under impingement attack as a function of nickel content.

A Study of Flow-Dependent Corrosion of Nodular Cast Iron in Arabian Gulf Seawater

A. H. Al-Hashem, H. M. Shalaby
Kuwait Institute for Scientific Research,
P.O. Box 24885, 13109 Safat,
Kuwait

V. K. Gouda
National Research Center
Corrosion Laboratory
Tahrir St., P.O. Box 12311
Dokki, Cairo, Egypt

Abstract

This paper presents an investigation of the erosion-corrosion and cavitation-corrosion behaviour of nodular cast iron in seawater. The investigation stemmed from a failure analysis of cast iron globe valves which were used in flowing seawater cooling systems of a petroleum refinery. Under stagnant conditions, the corrosion rate was very low and thin scales were formed, while there was a sharp increase in the corrosion rate and thick scales were formed under flow conditions. Removal of the scales revealed that corrosion was more intensive around graphite nodules. The cavitation corrosion rate was found to be 38 times higher than that under erosion-corrosion conditions and the cavitation damage initiated at the ferrite phase in addition to the graphite nodules. The mechanical factor was found to override the electrochemical factor during cavitation. The application of cathodic protection was found, however, to decrease the mass loss rate by about 50%. In the absence of applied protection methods, nodular cast iron was found not to be suitable as a valve material for refinery service in the Arabian Gulf seawater.

Key terms: erosion-corrosion, cavitation-corrosion, nodular cast iron, seawater

Introduction

Cast irons remain to be the most important and versatile materials for the manufacturing of valves although in some industries they are slowly being supplemented by more expensive alloys. There is no economic alternative to the extremely attractive cost/life ratio of the cast irons despite some limitations in brittleness, ductility, and pressure performance. Cast iron globe valves are used worldwide for flow regulations of seawater. One of the major needs of designers is knowledge of the operating limitations imposed by flow-dependent corrosion phenomena. As higher rates of flow are introduced, specific types of corrosion often appear, namely, corrosion due to mass transfer, erosion-corrosion, and cavitation-corrosion¹⁻³. These

types of corrosion are described according to their appearances and causes which are brought about by the flow mechanics of the system.

This article presents the results of a study conducted to compare the erosion-corrosion and cavitation-corrosion behaviour of nodular cast iron in Arabian Gulf seawater. The study stemmed from a failure analysis which was carried out on globe valves of sizes 3-, 4-, and 6-in. (7.62, 10.16, and 15.24 cm, respectively) used in the return lines of seawater heat exchangers of a petroleum refinery in Kuwait⁴. Several of these valves failed within just six months of service, although the expected service life was three to five years. It was suspected that the operating seawater flow velocity exceeded the design value and consequently led to the early failures. Therefore, it was deemed desirable to compare the corrosion behaviour under stagnant, erosion and cavitation conditions.

Experimental

Erosion-corrosion tests were conducted using an apparatus similar to that used by Molgaard⁵. The apparatus consisted of a wheel that rotated in a tank containing an arrangement of baffles to inhibit the movement of seawater in the direction of rotation of the wheel. The wheel and baffles were made of perspex and the shaft was made of stainless steel. The test specimens of nodular cast iron were mounted on the wheels using nylon screws to avoid galvanic corrosion. Arabian Gulf seawater was used in testing. It was slowly refreshed every 48 h in an external tank connected to the testing tank.

The test specimens were machined from the base of a failed valve. They were rectangular in shape, measuring 3 cm in length, 2.3 cm in width, and 0.65 cm in thickness. An average area of 12.5 cm² of each specimen was exposed to the seawater. The tests were carried out at rotational speeds of 300, 650 and 1000 rpm (2.5, 5.4, and 8.3 m/s, respectively) at room temperature. The mass loss was determined by calculating the difference in weight before and after cleaning in Clark's solution for two specimens taken out of the apparatus at each interval of time. The mass of the scales as well as the corrosion rate in stagnant seawater were also determined.

Cavitation tests were carried out at a frequency of 20 kHz and an amplitude of 25 μm , using an ultrasonically induced cavitation facility. The test specimens were also cut from a failed valve. They had a diameter of 1.59 cm and a thickness of about 0.27 cm. They were either attached or unattached to the apparatus horn. When they were not attached to the horn, they were mounted on a special holder which was placed at a distance of 0.125 cm from the horn. Before testing, all specimens were mechanically polished with silicon carbide papers up to 1200 grit. They were subsequently cleaned, degreased, and then weighed before and after testing. For morphological studies, some specimens were etched in 3% nital etchant solution before testing.

Some cavitation tests were conducted under cathodic protection to eliminate the effect of electrochemical dissolution. In these tests, the specimens were polarized potentiostatically at -

50 mV with respect to the free corrosion potential value. Linear polarization resistance technique was also used to determine the electrochemical corrosion rate. Saturated calomel reference and graphite counter electrodes were used in these experiments.

After testing, detailed morphological examinations were made on the specimens using optical microscopy and scanning electron microscopy (SEM).

Results

Erosion-corrosion Tests

Figure 1 shows the rate of mass loss of nodular cast iron as a function of time and seawater flow velocity. The rate of mass loss sharply increases with time until a peak is reached after about 3 d of testing, which is then followed by a gradual decrease until almost a steady state is attained after about 21 d of exposure. The rate of mass loss at the peak increases with the increase in the seawater flow velocity. The rate of mass loss at the steady state is almost the same at flow velocities of 5.4 and 8.3 m/s, and is slightly higher than that at 2.5 m/s. Under stagnant condition, the mass loss was low and the rate amounted to 0.14 mg/cm²/d.

In stagnant seawater, a loosely adherent corrosion product layer was formed on the surface of the material. The layer was smooth and mostly dark grey in colour. In flowing seawater, a fairly uniform and thin reddish-brown scale was initially formed. The scale was similar to that observed during testing in stagnant seawater but was considerably more adherent to the surface. After a few days of testing, small portions of the scale became swollen and then started to flake off. Parallel markings representing seawater flow pattern developed in the scales after 7 d of exposure. After 14 d of exposure, the scales became relatively thick, and in some areas the swollen blisters flaked off showing either bare metal or a surface covered with a thin scale layer (Figure 2). When the testing time was increased up to 25 d, the overall appearance of the scales remained the same. However, a second scale layer was observed filling the flaked blisters. Table 1 shows the mass of the adhered scales at the different flow velocities. In general, the increase of exposure time leads to an increase in the mass of the scale until about 17 d of exposure, after which a further increase of exposure time significantly increases the mass of the scale.

Microscopic examination of the metal surface after removal of the scale, which was formed during 7 d of exposure to the flowing seawater, revealed that the corrosion attack had a localized nature and was more intensified around the graphite nodules below the swollen blisters (Figure 3). The appearance of the metal after removal of the scale was almost the same at the different velocities. The localized attack was found to spread laterally after 15 d. At this stage, the surface became rough. The spreading of this attack was noticed to be associated with loosening and removal of neighboring graphite nodules. After 25 d of exposure, the same morphological features were found. However, the corrosion around the graphite nodules spread over the surface and increased in depth.

Cavitation-Corrosion Tests

The mass loss as a function of time of the nodular cast iron specimens, whether attached or unattached to the horn of the cavitation apparatus was followed for about 400 min. of testing in seawater. Figure 4 shows that the mass loss rate initially increases rapidly until it reaches a maximum value after about 1 min, decreases sharply up to about 4-6 min., and then decreases more slowly until reaching a steady state after 12-20 min. of cavitation. The mass loss values were higher for the attached specimens than for the unattached specimens.

Other mass loss experiments were conducted on unattached specimens, wherein protection, by impressed cathodic current, was applied during cavitation testing. The results indicated that at the steady state the rate of mass loss under cathodic protection (cavitation erosion rate) amounted to $0.026 \text{ mg/cm}^2/\text{min.}$ as compared to $0.052 \text{ mg/cm}^2/\text{min.}$ under free corrosion conditions (cavitation corrosion rate).

The polarization resistance of cast iron exposed to cavitation or quiescent conditions in seawater was determined as a function of time. The electrochemical corrosion rates were computed and the results are given in Figure 5. It is clear that the corrosion rate under quiescent conditions was almost constant throughout the test and was considerably lower than that of the cavitated specimens whether attached or unattached.

During the first minute of cavitation testing, the surface was bright, and damage could not be identified visually. After cavitation for 2-10 min., the specimens showed erosion markings in the form of radial rays pointing towards the specimen periphery (Fig. 6a). After exposure for longer periods, cavitation took the form of deep craters and cavities over the entire surface of the specimen (Fig 6b). For attached specimens, the damage was observed after shorter exposure times than for unattached specimens.

SEM examinations were carried out on the attached specimens to determine the micromorphology of the cavitation damage. After 1 min. of cavitation, localized areas suffered from surface damage: some graphite nodules were fragmented and others were completely removed, leaving circular craters of cavities; the surrounding matrix remained smooth and unattacked (Figure 7a). After 5 min., microcavities (erosion pits) appeared in the matrix of the attacked areas together with other cavities caused by the loss of graphitic nodules. The erosion pits were randomly scattered in the matrix and were unrelated to the graphite. Their diameter was about $2 \mu\text{m}$ compared with the $30\text{-}80 \mu\text{m}$ diameter of the cavities. After 10 min., the areas of localized attack became more pronounced, with increasing numbers of cavities, micropits, and surface deformations (undulations). After 30 min., further mechanical damage to the surface appeared; the attacked areas became larger, more distorted and engulfed the microcavities. Longer cavitation testing (5.5 h) led to non-uniform surface erosion and showed ductile removal of material from the matrix (Figure 7b) and cracks (Figure 7c) that passed through areas of the matrix where a cluster of graphite nodules had been removed.

The above characteristics of the cavitation damage were similar for the attached and unattached specimens as well as for cavitated specimens under cathodic protection. However, the time needed to reach a certain stage of damage was longer in the case of unattached specimens or under cathodic protection.

Specimens cavitated for 5.5-6 h were cross-sectioned and optically examined. For the attached and unattached specimens, the cross-sections showed some differences in roughness profiles. The attached specimens had fewer but deeper craters than the unattached ones. Examination of the attached specimens showed cracks 3-21 μ m long that propagated into the matrix (Figure 8a). These cracks originated at the bottom of non-uniform deep craters, 0.05-0.2 mm in depth and 0.2-0.5 mm in width. Other subsurface cracks which did not originate from the eroded surface were also found in the matrix (Figure 8b). All crack forms that were observed in the attached specimens were also found in the unattached specimens.

Discussion

Effect of Flow on Corrosion Morphology

In general, erosion-corrosion or cavitation-corrosion damage increases in corrosive liquids such as seawater due to the combined action of the electrochemical corrosion and the fluid mechanical component⁶. Arabian Gulf seawater seems to be more aggressive than other water bodies⁷. It contains higher salt, different pollutants such as sulfide, ammonia, and organic materials, as well as suspended matters such as sand and silt. Other factors include the hot climate and wide variations in seasonal temperatures.

The failure investigation⁴ revealed that the 4- and 6-in. valves (10.16 and 15.24 cm, respectively) suffered from both general and localized corrosion enhanced by the flowing seawater. The presence of voluminous corrosion products in these two valves indicated that the flow conditions inside these two valves were not severe and falls within the domain of corrosion due to enhanced mass flow. This conclusion is supported by the present erosion-corrosion work where thick scales were formed during testing in seawater. Corrosion blisters and cracked blisters were also observed on the scales. It is worth noting that under stagnant seawater condition the scales were very thin and no blisters were observed. The cracking of the blisters in flowing seawater exposed the underlying metal to further corrosion which was more intensive around the graphite nodules. Lotz, et al.,⁸ observed that bulky surface layers were formed in chloride solutions at velocities up to 10 m/s, while at higher flow velocities the surface layer was thin and more adherent.

The 3-in. (7.62 cm) valve, on the other hand, was shown⁴ to have been exposed to a high turbulent flow, enhanced may be by its small size and globe design. This was evident in the presence of cavities and cracks within the material. The present laboratory cavitation work reproduced the same morphological features which were observed in the 3-in. valve. The damage in laboratory testing appeared as fragmentation of graphitic nodules and complete removal of some nodules, leaving surface cavities. As cavitation time increased, erosion pits

appeared randomly on the ferrite matrix. Thus, cavitation damage in cast iron not only initiated at graphite nodules as mentioned by Okada and co-workers^{9,10}, but also in the ferrite matrix. The cavities in the ferrite matrix appeared to be due to ductile tearing caused by the sudden collapse of the liquid bubbles. It is worth noting that surface cracks also initiated at the eroded surface and propagated into the matrix. These cracks were similar to those previously observed in the failed 3-in. valve.

Effect of Flow on Rate of Mass Loss

The results of the laboratory work indicate that the mass loss rate curves during erosion-corrosion and cavitation-corrosion show three zones: the accumulation zone, in which the mass loss rate increases to a maximum; the attenuation zone in which the mass loss rate decreases; and the final steady state zone. Many investigators¹¹ believe that the mass loss rate in the steady state regime is the most important, since it depends on the characteristics of the material itself and, thus, is usually taken for comparison and correlation purposes, the other zones depend on specimen surface condition, geometry, test conditions and temperature.

Under erosion-corrosion conditions, the steady state corrosion rate was about 18 times that obtained under stagnant conditions. The decrease in the mass loss following the peak can be attributed to the increase in the thickness of the scales in addition to the scales becoming more compact after long exposure to the seawater^{4,8}. Thus, at a certain stage, the corrosion product layer serves as a barrier and retards further corrosion. Under these conditions, phase-boundary reactions, pore diffusion in the scale layer⁸, as well as the mechanical destruction of the scale are all participating in controlling the corrosion process. In other words, the rate of damage is predominantly electrochemically controlled.

At the steady state, the mass loss rate during cavitation-corrosion of attached specimens was found to be 38 times that during erosion-corrosion. The results of the cavitation study also indicate that the mass loss rates for the attached specimens are 25% higher than those for unattached specimens. These results can be explained on the basis that material removal as a result of cavitation (mechanical and electrochemical action) is much higher than that due to enhanced mass flow such as during erosion-corrosion and that the attached specimen is exposed to an extra mechanical factor¹².

The results obtained under cathodic protection may throw some light on the separation of the electrochemical corrosion and the mechanical deterioration of the material due to cavitation. The lowest possible cathodic potential was applied so that hydrogen evolution was limited. In this situation, the possibility of a reduction in the bubble collapse pressure due to the cushioning effect of hydrogen is diminished¹³. Table 2 shows the mass loss rates obtained under different conditions of testing. It is clear that the mass loss rate of a cavitated specimen under cathodic protection (W_c) is about 50% lower than that in the free corrosion condition (W_f). The difference between these two values ($W_f - W_c = W$) should be equivalent to the electrochemical corrosion rate (W_e) of the alloy. However, as shown in Table 2, W_e amounted to less than 0.001% of W . In other words, W cannot be related only to electrochemical corrosion. Consequently, the only available explanation is that the

electrochemical factor must have enhanced the mechanical damage and thus led to much higher mass loss than the sum of W_c and W_e .

A comparison of the electrochemical corrosion rate obtained under quiescent condition (W_q) with that under cavitation condition (W_c) reveals that the rate increases by about six times due to cavitation. This is expected as the kinetics of the electrode process are enhanced by cavitation, which can be ascribed to the role played by several factors, e. g. turbulent flow under cavitation, diffusional processes, and breakup of the adsorbed layers¹⁴. It is interesting to observe that the cavitation corrosion rate was about 75000 times higher than the electrochemical corrosion rate under cavitation conditions. In other words, the greatest portion of damage is due to mechanical breakdown of the material surface and subsequent particle separation and ejection from the metal. This indicates that the mechanical factor overrode the electrochemical factor in the acceleration of material loss.

The above results reveal that nodular cast iron is not performing satisfactorily in Arabian Gulf seawater whether the flow velocity is low or high. This is particularly true in the absence of cathodic protection. Work on alternative valve materials⁷ revealed that high chromium cast steel was immune to corrosion and/or erosion damage. Moreover, accelerated tests showed that the service life of Ni-resist cast iron is eight times that of nodular cast iron⁷.

Conclusions

1. In seawater under flowing or cavitation conditions, the corrosion rate of nodular -cast iron was greatly enhanced reaching peak values which were followed by a gradual decrease till steady states were reached. At the steady states, the cavitation-corrosion rate was about 38 times that under erosion-corrosion conditions which was about 18 times that under stagnant conditions.
2. At moderate to low flow velocity, corrosion of nodular cast iron initiated around graphite nodules, leading to loosening and removal of the graphite. However, under cavitation condition. the initiation of damage was not only at the graphite nodules, but also in the ferrite matrix.
3. The mechanical factor was found to override the electrochemical factor during cavitation damage. The application of cathodic protection was found, however, to decrease the mass loss rate by about 50%.
4. In the absence of cathodic protection, nodular cast iron was found not to perform satisfactorily in Arabian Gulf seawater whether the flow velocity was low or high.

Acknowledgement

The authors of this paper would like to acknowledge the support given by the Kuwait Foundation for the Advancement of Sciences, Kuwait National Petroleum Company,

Petrochemical Industries Company, and Abu Dhabi National Oil Company (Project No. 86-08-02).

References

1. U. Lotz, E. Heitz, *Werkst. Korros.*, 34 (1983), p. 454.
2. E. Heitz, G. Kreysa, and C. Loss, *J. Appl. Electrochem.*, 9 (1979), p. 243.
3. F. Franz, E. Heitz, G. Herbsleb, and W. Schwenk, *Werkst. Korros.*, 24 (1973), p. 38.
4. V. K. Gouda, H. M. Shalaby and W. T. Riad, *Materials Performance*, 28 8 (1989), p. 53.
5. J. Molgaard, *Proc. of the 5th International Congress on Metallic Corrosion, Tokyo, May 1972*, p. 792.
6. A. Karimi, J. L. Martin, *Int. Met Reviews*, 31 (1988), p. 1.
7. H. M. Shalaby, S. Attari, W. T. Riad and V. K. Gouda, *Corrosion*, 48 3 (1992), p. 206.
8. U. Lotz, M. Schollmaier and E. Heltz, *Werkst. Korros.*, 36 (1985), p. 183.
9. T. Okada, *J. Ship Res.*, 25 4 (1981), p. 711.
10. T. Okada, Y. Iwai and A. Yamamoto, *Wear*, 84 (1983), p. 297.
11. C. M. Preese: *Treatise on materials science and technology, Cavitation-erosion* Orlando, FL, Academic Press, 16 (1979), p. 249.
12. V. K. Gouda, A. H. Al-Hashem, A. M. Abdullah and W. T. Riad, *Br. Corros. J.*, 26 2 (1991), p. 109.
13. M. S. Plesset, *J. Basic Eng. (Trans. ASME)*, 82 (1960), p. 808.
14. A. I. Nekoz, G. A. Preis and N. A. Sologub: *Sov. J. Frict. Wear*, 2 4 (1981), p. 596.

Table 1. Mean Mass of Adhered Scale in mg/cm² at Different Flow Velocities

| Duration (days) | 2.5 | 5.4 (m/s) | 8.3 |
|--------------------|-------|--------------|-------|
| 3 | -- | 19.71 | 18.89 |
| 7 | 10.89 | 28.90 | 33.70 |
| 10 | 20.91 | 35.09 | 37.80 |
| 14 | 23.95 | 39.10 | 31.25 |
| 17 | 25.07 | 42.39 | 30.77 |
| 21 | 31.82 | 50.08 | 37.55 |
| 25 | 49.13 | 54.78 | 37.00 |

Table 2. Rates of electrochemical corrosion, cavitation-corrosion, and cavitation-erosion under various test conditions for nodular cast iron in seawater

| Test condition | Mass loss rate, μg/cm ² /min. |
|--|---|
| 1. Cavitation under free corrosion condition, mass loss (cavitation-corrosion W_f) | 52.0 |
| 2. Cavitation under cathodic protection, mass loss (cavitation-erosion W_c) | 26.0 |
| 3. Cavitation under free corrosion condition, polarization resistance (electrochemical corrosion W_e) | 0.00035 |
| 4. Quiescent under free corrosion condition, polarization resistance (electrochemical corrosion W_q) | 0.000056 |

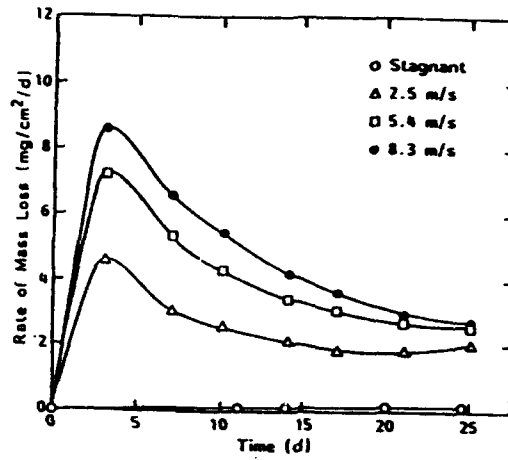


Figure 1. Rate of mass loss of nodular cast iron as a function of time in stagnant and flowing seawater.

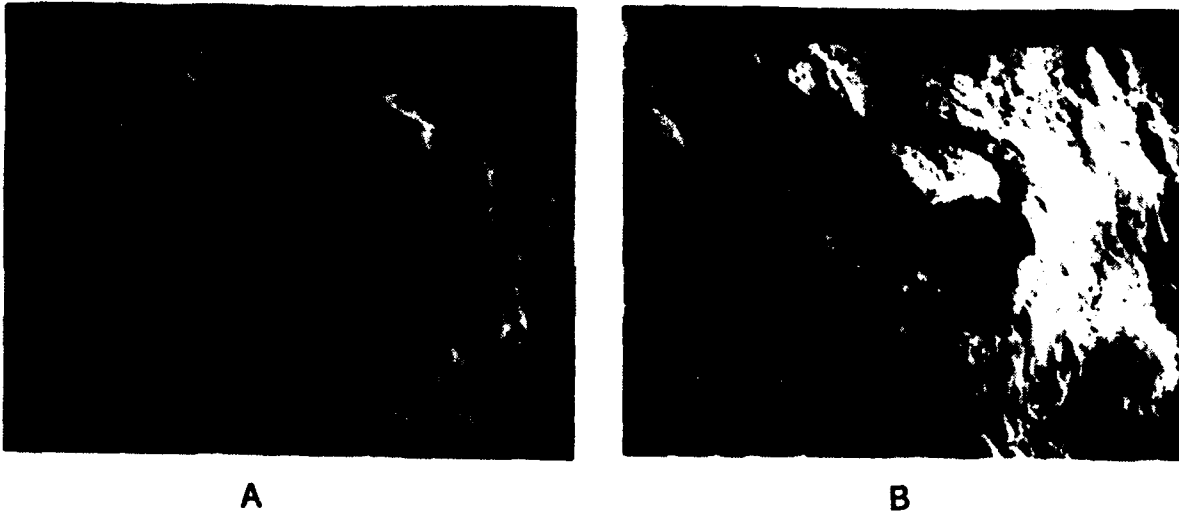


Figure 2. SEM micrographs showing: (a) a swollen blister, and (b) a cracked blister in nodular cast iron tested in seawater flowing at 5.4 m/s for 14 d.

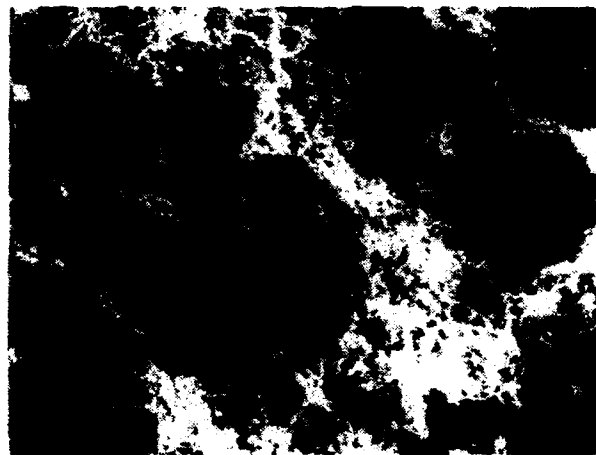


Figure 3. SEM micrograph showing corrosion around graphite nodules, magnification 200X.

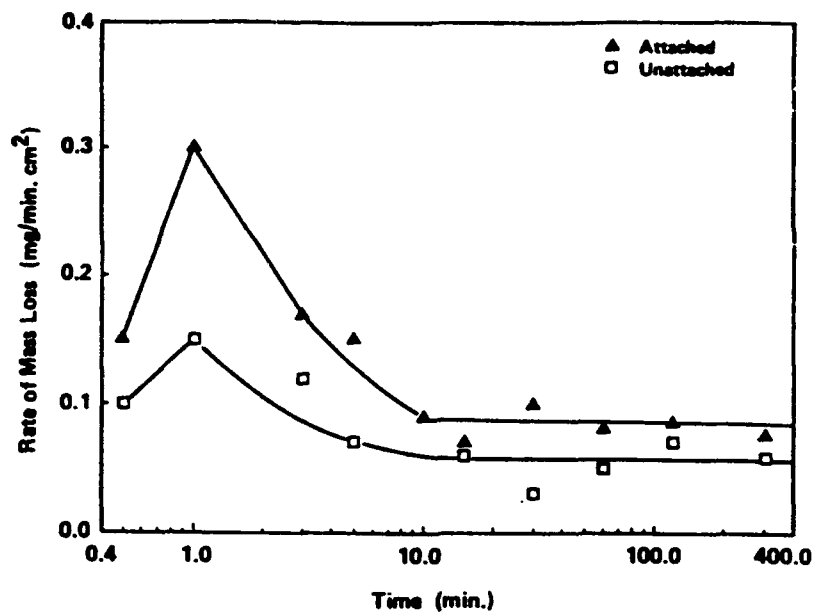


Figure 4. Mass loss rates of cavitated cast iron in seawater as a function of time for attached and unattached specimens.

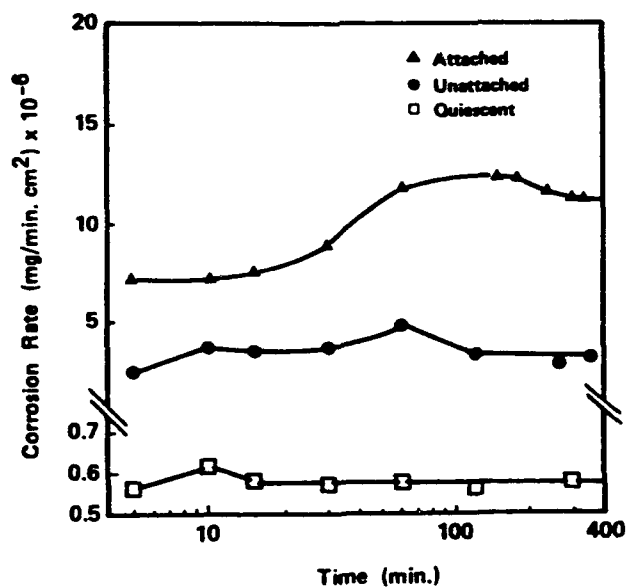
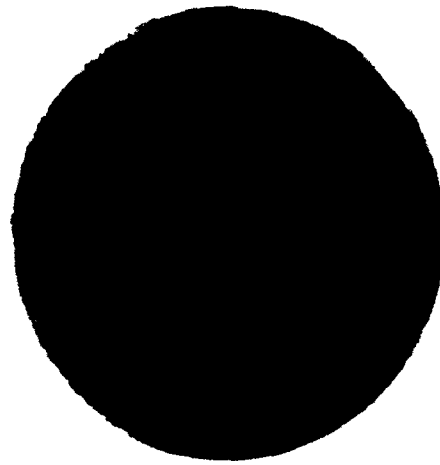


Figure 5. Electrochemical corrosion rate vs time for cast iron in seawater calculated from polarization resistance measurements.



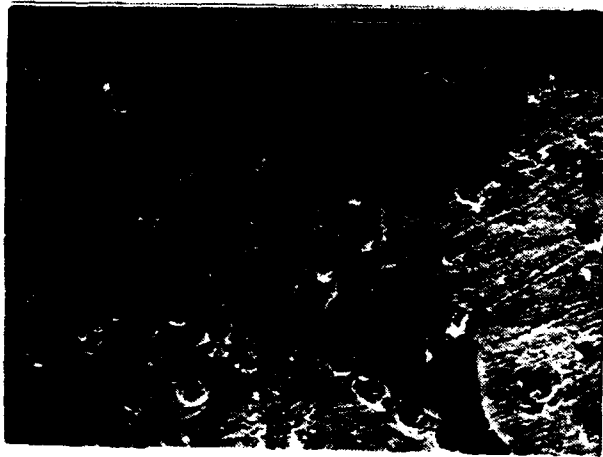
A



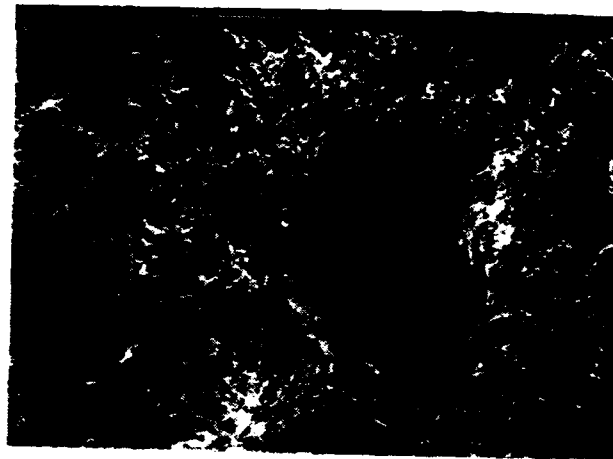
B

Figure 6. Photographs showing surface appearance of cast iron after cavitation testing.
(a) after 30 min; and
(b) after 5.5 h.

A



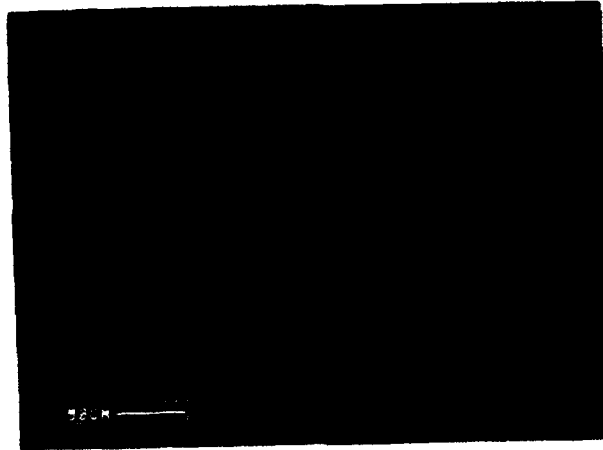
B



C

Figure 7. SEM micrographs of attached cast iron after cavitation testing in seawater.
(a) after 1 min, fragmented nodules and cavities;
(b) after 5.5 h, ductile removal of material from the ferrite matrix; and
(c) after 5.5 h, cracks in the cast iron

A



B

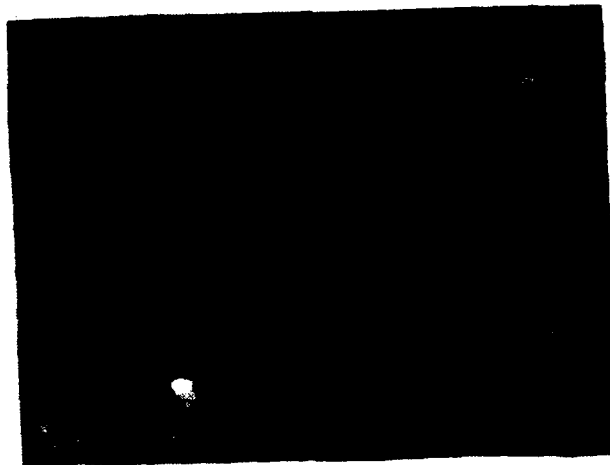


Figure 8. Optical micrographs of cross-section of attached specimens after cavitation testing in seawater.
(a) cracks originating from bottom of craters; and
(b) subsurface cracks.

Effect of sulfide ions on the corrosion behaviour of aluminium alloy (H₂O) in synthetic sea water.

M. VALLIAPPAN

Central Electrochemical Research Institute
Karaikudi - 623 006
India.

M. NATESAN

Central Electrochemical Research Institute
Karaikudi - 623 006
India.

G. VENKATACHARI

Central Electrochemical Research Institute
Karaikudi - 623 006
India.

K. BALAKRISHNAN

Central Electrochemical Research Institute
Karaikudi - 623 006
India.

Abstract

Aluminium alloys are extensively used in seawater because of the formation of protective oxide layer on the surface. This oxide layer formation can be affected by the presence of pollutants like sulfides in sea water. The effect of sulfide ions on the corrosion behaviour of aluminium alloy (H₂O) in synthetic seawater has been studied by polarisation method. A marked shift of open circuit potential in the cathodic direction with increase of the sulfide concentration ≥ 50 ppm has been found. At these concentrations, a well defined passive range is observed due to the formation of sulphur film. Due to this, the pitting tendency of H₂O aluminium is decreased in the presence of high sulfide concentration which is confirmed from the pitting and repassivation potentials.

Key terms : Pitting, Aluminium alloy, Sulfide, Synthetic seawater

Introduction

In recent years aluminium alloys find applications in offshore structures for oil production¹. Among the aluminium alloys, Al-Mg-Si alloys are found to be the most suitable alloy for sea water applications due to its more corrosion resistant properties. Corrosion of aluminium alloys in seawater is mainly of pitting type with the rate of pitting of 3 to 6 microns per year initially and 0.8 to 1.5 microns per year over the period of ten years². The corrosion behaviour of aluminium alloys in seawater has been reviewed by Fink, et.al.,³. The pitting corrosion of aluminium alloys is minimised by the addition of suitable inhibitors⁴ like chromates, nitrates etc., Besides the

addition of the inhibitors, addition of sulfide ions⁵ has been shown to improve the pitting resistance of aluminium alloys in seawater. In this paper, the corrosion behaviour of H2O aluminium alloys in synthetic seawater in the presence of sulfide ion is reported.

Experimental

Aluminium alloy (H2O) with stem exposing an area of 2 sq.cm was used. The stem was masked with araldite. The electrodes were polished with cloth emery wheel and degreased with trichloroethylene. Potentiodynamic polarisation studies were carried out in a three electrode cell at a sweep rate of 1 mV/Sec using potentiostat (PAR 173, USA), Universal programmer (PAR 175, USA) and X-Y recorder. The potential of the electrode was measured with respect to saturated calomel electrode and a platinum electrode was used as an auxiliary electrode. Synthetic seawater and sulfide solutions were prepared using ANALAR chemicals in distilled water. All the experiments were carried out at $28 \pm 1^\circ\text{C}$.

Results and Discussion

The effect of sulfide ions, in the concentration range of 0 to 100 ppm, on the corrosion and pitting tendency of H2O aluminium alloy in synthetic sea water has been studied by potentiodynamic polarisation method. Figs 1.a and 1.b show the polarisation behaviour of H2O aluminium alloy in synthetic seawater containing sulfide ions. Table 1 summarises the corrosion parameters like open circuit potential, corrosion current, pitting and repassivation potential. The corrosion rate has been found to be increased markedly even in the presence of 10 ppm of sulfide ion. On further increase in sulfide ion concentration the corrosion rate increases and reaches a steady value at 50 ppm of sulfide ion concentration.

The open circuit potential remains unaffected upto 10 ppm of sulfide ions. At higher concentrations of sulfide ions, the open circuit potential has shifted to more cathodic values indicating a decrease of cathodic reaction. Moreover, for sulfide concentration greater than 50 ppm, a well defined passivation behaviour has been observed. It has been found that the pitting potential is $\geq -650\text{mV}$ and the repassivation potential is around -750 mV for sulfide concentrations greater than 50 ppm. The magnitude of the pitting and repassivation potential is more than $+ 300\text{ mV}$ from the opencircuit potential. On visual inspection of aluminium electrode after polarisation experiments in synthetic seawater containing 50 ppm and more sulphide concentration formation of sulphur film has been observed. This is due to the oxidation of sulfide ion. Huang⁶ et al have reported that during anodic oxidation of sulfide on gold, multilayers of elemental sulphur film is formed.

Conclusion

The presence of sulfide ions in synthetic seawater increases the corrosion rate of H₂O aluminium alloy. However the pitting tendency is very much reduced in the presence of higher concentrations of sulfide ions due to the formation of sulphur film.

Acknowledgement

The authors thank the Director, Central Electrochemical Research Institute, Karaikudi for his permission to publish this paper.

References

1. H.Sigurðsson, Proc. 11th ICC, AIM (1990), p.2.591
2. E.H.Hollipworth and H.Y.Hunicker in corrosion and corrosion protection hand book, Ed. P.A Schwitzer, Marcel Dekker Inc. (1983) p.140.
3. F.W.Fink and W.K. Boyd, DIMC report 245, Bayer and Company Inc., OHIO (1970).
4. A.H.Roebuck in corrosion inhibitors, Ed.C.C.Nathan, NACE (1973) p.240
5. A.Bjorgum, H.Sigurðsson and K.Nisaniciogul Proc. 11th ICC, AIM, (1990) p.5.421
6. L.H.Huang, J.M.Bandreay, S.M.Wilhelum, S.D.Kapusta and N.Hackerman, Proc. Inter. Symp. Surfaces, inhibition and passivation, The Electrochem.Soc., (1986), p.498.

TABLE I
CORROSION PARAMETERS FOR H₂O ALUMINIUM ALLOY IN SYTHETIC SEAWATER CONTAINING SULFIDE

| S.No. | Sulfide ppm | OCP mV vs SCE | E _{pit} mV vs SCE | E _{repassivation} mV vs SCE | i _{corr2} uA/cm ² |
|-------|-------------|---------------|----------------------------|--------------------------------------|---------------------------------------|
| 1. | 0 | -730 | -720 | --- | 0.1 |
| 2. | 10 | -730 | -715 | --- | 0.65 |
| 3. | 25 | -880 | -710 | -720 | 1.00 |
| 4. | 50 | -1150 | -650 | -750 | 0.75 |
| 5. | 75 | -1180 | -630 | -750 | 0.60 |
| 6. | 100 | -1250 | -600 | -750 | 0.60 |

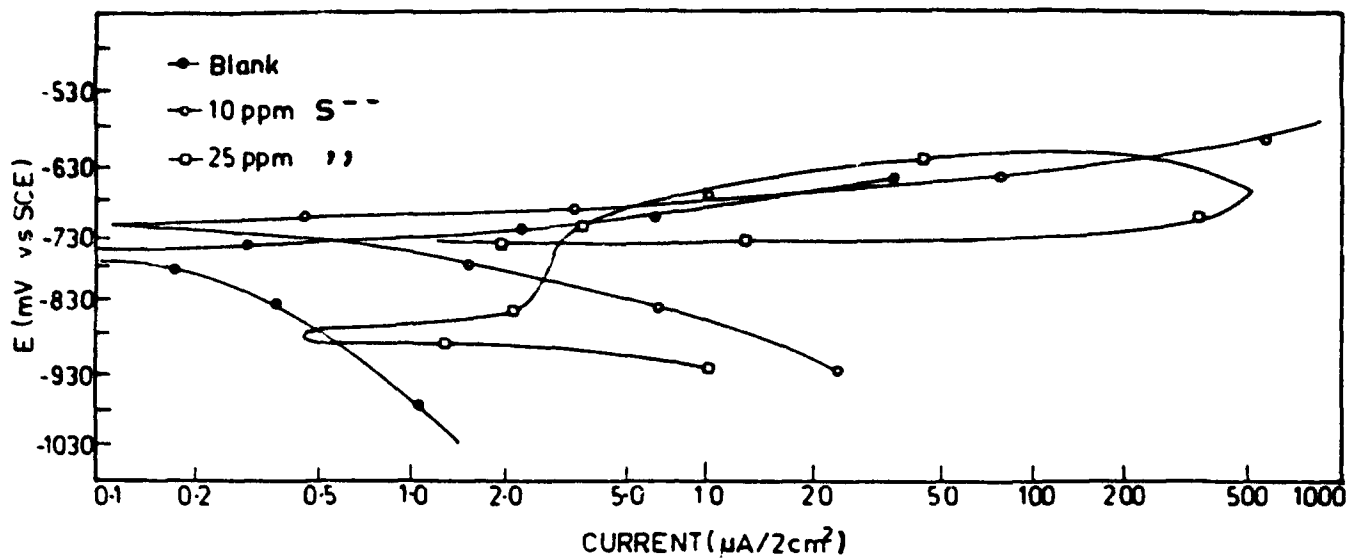


Fig.I(a) : Polarisation behaviour of H₂O Al in synthetic seawater containing sulfide.

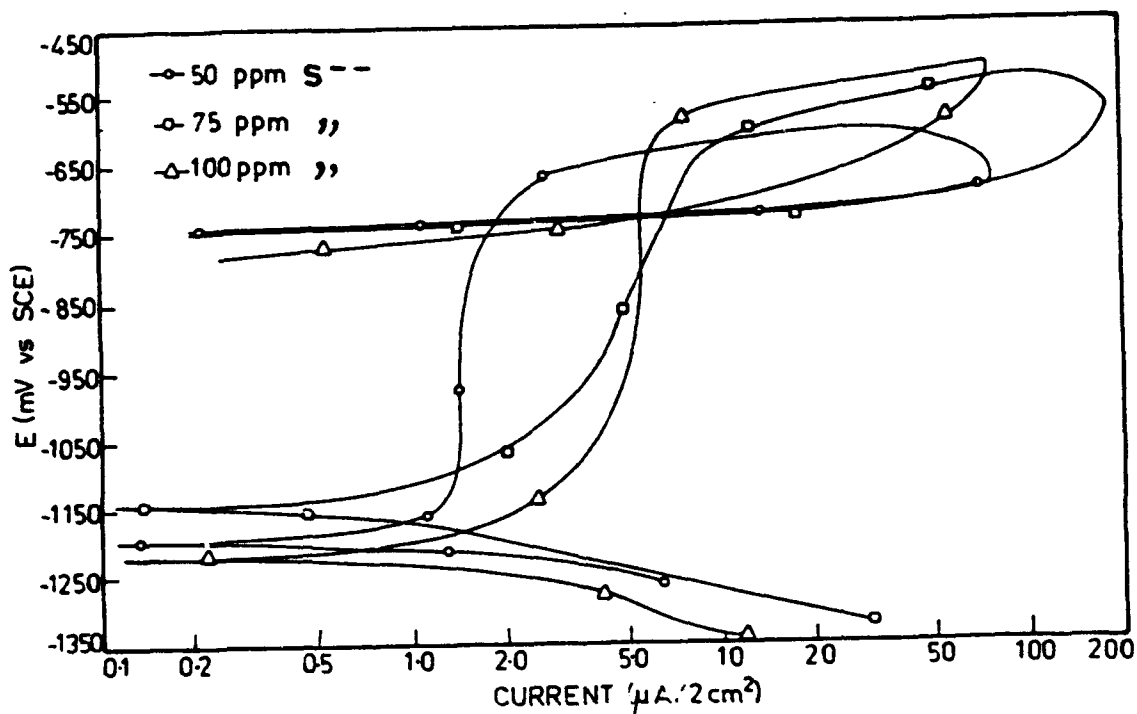


Fig.I(b) : Polarisation behaviour of H₂O Al in synthetic seawater containing sulfide.

Corrosion Protection of Submerged Steel Structures by the combined use of Protective Coatings and Impressed Current Cathodic Protection

**Mikko Arponen
Rautaruukki Oy
Research Centre
P.O. Box 93
SF-92101 RAAHE FINLAND**

Abstract

Application of protective coatings and cathodic protection is a well-known corrosion control method for steel structures subjected to aqueous immersion. In this present study, the corrosion performance of different types of paint systems on carbon steel substrates has been investigated.

The tests were carried out in the laboratory with specimens immersed in synthetic sea water, and polarised to a potential of - 1000 mV and - 1200 mV (SCE). The duration of the test was six months, after which the disbonding of the paint films was determined as the loss of adhesion occurring round an artificially formed holiday. The degree of blistering was recorded also.

The test results showed that coal tar epoxy paints, epoxy powder paints, and the almost solvent-free epoxy paint had the best corrosion resistance on steel surfaces. The use of zinc-rich paints for cathodically protected marine steel structures is questionable. Zinc reacts easily under alkalic conditions with hydroxide ions formed at the point of the defect and may cause abnormal disbonding of the coating.

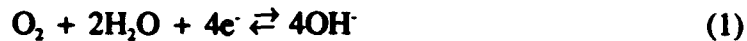
The film thickness and the surface roughness have a great influence on the paint performance. The role of the steel grade on the performance of paint films is of minor significance but in certain cases, weathering steels may offer a better choice for painted steel structures under cathodic protection in marine conditions.

Key terms: steel, paint, cathodic protection, disbonding, blistering

Introduction

Protective organic coatings and cathodic protection are widely used to control corrosion of steel structures subjected to aqueous immersion or buried onshore conditions. Protective coatings prevent corrosion by isolating steel from the corrosive environment while cathodic protection is the use of an impressed current to prevent or to reduce the rate of corrosion of a metal in an electrolyte by making the metal the cathode.

In the presence of a defect in the coating, the metal itself is cathodically protected, but electrolyte is permitted to reach the metal surface. Under these conditions, the cathodic half reaction



prevails and causes an increase of pH value. This reaction occurs under the coating at the defect and causes an accelerated disbondment of the coating. The mechanism of the delamination process itself is poorly understood but it is thought to result from attack on either the coating or the interfacial bond by the alkaline conditions generated at the leading edge of the disbonding region¹.

When coatings are combined with cathodic protection they must possess several physical and chemical properties to be fully effective. These properties are described in several references^{2,3} and can be summarized as follows:

1. **Dielectric Strength.** The dielectric characteristics of the coating must be sufficient so that both cathodic protection potentials and current flows would not affect its ability to act as a corrosion prevention membrane.
2. **Chemical Resistance.** The coating has to be chemically resistant to high concentrations of hydroxyl ions.
3. **Adhesion.** The application of the coating on to poorly prepared surfaces will cause early coating breakdown, when subject to cathodic protection potentials.
4. **Moisture Absorption and Transfer.** The coatings should have both low moisture vapour transfer rate as well as low moisture absorption. It is a general rule of thumb that the lower the moisture vapour transfer rate of the coating, the more effective the coating.
5. **Electroendosmosis.** Where electroendosmosis may be encountered, adhesion is also very important. Electroendosmosis is defined as the forcing of water through a semi-permeable membrane by an electrical potential in the direction of the pole that has the same charge as the coating membrane. Most surface coatings are negatively charged. This being the case, coatings with a high moisture vapour transfer rate or questionable adhesion are more subject to damage and blistering by cathodic potentials.

6. **Coating Thickness.** Coating thickness is very important. Several of the above properties are directly affected by thickness.
7. **Ionic Resistance.** The coating must be resistant to the passage of ions, which may be considered part of chemical resistance.

In this present study, some of the most common paints used together with cathodic protection for submerged steel structures have been tested in laboratory experiments. The effect of surface roughness and steel grade on the disbonding of paint films have been tested.

Experimental

The test specimens were prepared from structural and weathering steel grades. The surfaces of the specimens were blasted either with a mixture of metal shot and grit or with metal shot and grit separately (Sa 2½, ISO 8501-1:1988). The chemical composition of the steels are presented in Table 1. The specimens were painted with different types of paint systems normally used for corrosion protection of submerged steel structures. The tested paint systems are listed in Table 2. The test method applied was

BS 3900: Part F10: 1985
Determination of Resistance to Cathodic Disbonding of Coatings
for Use in Marine Environments

with the exception of the electrolyte, which consisted of 3.380 kg NaCl, 0.628 kg Na₂SO₄ and 0.192 kg CaCl₂ in 160 l water. A schematic diagram of the test apparatus is presented in Figure 1 and the test vessel with the specimens and electrodes is shown in Figure 2. The anode was titanium net coated with iridium oxide. The potentials, -1.0 V and -1.2 V (SCE), were potentiostatically controlled. The currents were measured over 100 Ω resistor.

Test Results

The disbondment and the number of blisters on the paint systems are summarized in Tables 3 and 4. The measured current values are graphically presented in Figures 3 and 4. Examples of the specimens tested at -1.0 V and -1.2 V potentials (SCE) are presented in Figures 5 and 6. Scanning electron microscope pictures of the shot blasted and the grit blasted steel substrates are presented in Figure 6. The delamination of paint films on shot blasted and grit blasted specimens is shown in pictures presented in Figure 7.

Conclusions

The following conclusions can be drawn on basis of the obtained results:

1. Coal tar epoxy paints, the almost solvent free epoxy paint and epoxy powder paints have the best performance under cathodic protection conditions. The disbondment rate and the amount of blisters are smaller when compared to the other paints.
2. Although the amount of tests performed is not very comprehensive, it is very obvious that a sufficiently thick coating must be applied, preferably over 300 μm . Under practical conditions, the coating thickness applied should also probably be even greater in the vicinity of the anodes.
3. The use of zinc-rich paints for cathodically protected marine steel structures is questionable. Zinc is a so called amphoteric substance, which reacts easily with both acids and alkalis. Under alkalic conditions, the following chemical reaction will occur in defects at the coating/substrate interface:



This reaction will probably together with the cathodic half reaction (1) break the interfacial bonds and form an interfacial layer from the reaction products, which can cause a high disbonding of the coating and very large amount of blisters, see paint system 8 in Table 3. For the paint system 9 the disbondment is not very high, but the amount of blisters is as high as in the paint system 8. The disbonding of paint probably starts from the formation of blisters. The blisters appear to be formed first in the vicinity of the defect, see Figures 5 and 7. The small black spots correspond to blisters in the coating.

4. Surface roughness has a great effect on the disbonding rate. This is especially emphasized with one coat paint systems, see Table 4. A shot blasted surface is probably too smooth for thick one coat systems, but for paint systems consisting of several coats, it may be acceptable, see paint system 2 in Table 4. For practical purposes the mixture of shot and grit is probably to be recommended.
5. No clear difference between the steel grades tested could be seen in this study. More important than the steel itself is the surface pretreatment. Then may be advantages however in using weathering steels with certain types of these paints.
6. Current density, $\mu\text{A}/\text{specimen}$, is higher in one coat paint systems than in paint systems with several coats, see Figure 3. The loss of adhesion is also greater with one coat systems, see Table 4.

Discussion

The performance of coatings on cathodically protected steel structures is effected by many factors. A number of which are already mentioned above. The surface pretreatment before painting, the paint system itself and the applied potential are of great importance. The disbondment of the paint is caused by the cathodic corrosion reaction on the one hand and by the loss of adhesion, which is influenced by surface profile, film porosity etc. on the other. Different types of disbondments are illustrated in Figure 8.

Acknowledgements

I would like to express my gratitude to Kurt Blomqvist of Teknos-Winter for useful discussions and for providing figure 8. I am also grateful to Rautaruukki Oy for permission to publish these results.

References:

1. H. Leidheiser Jr, W. Wang, Corrosion Control by Organic Coatings, NACE Publication 81-84733 (1981) p.70
2. C.G. Munger, R.C. Robinson, Coatings and Cathodic Protection, NACE Materials Performance, July 1981
3. J.M. Keyman, The Effect of Overvoltage on Immersed Coating Performance, The National Corrosion Conference, Yorkshire, England, 1981

Table 1. Average chemical compositions of the steel substrates (%).

| Steel grade | C | Si | Mn | P | S | V | Cu | Cr | Ni |
|------------------------|----------|-----------|-----------|----------|----------|----------|-----------|-----------|-----------|
| ASTM A 572 Grade 50 | .151 | .424 | 1.36 | .023 | .021 | .009 | .018 | .022 | .031 |
| COR-TEN A ¹ | .070 | .434 | .418 | .104 | .017 | .007 | .424 | .580 | .275 |
| COR-TEN B ¹ | .116 | .397 | 1.16 | .011 | .023 | .060 | .242 | .500 | .186 |

¹) COR-TEN is a registered trademark of USX Corporation

Table 2. Paint systems tested.

-
1. Two pack epoxy paint; epoxy GPL
 2. Two pack almost solvent free epoxy paint; epoxy 160
 3. Resin modified two pack epoxy paint; epoxy RC
 4. Epoxy powder paint; epoxy powder OPR
 5. Two pack coal tar epoxy paint; coal tar epoxy ET1
 6. Two pack coal tar epoxy paint; coal tar epoxy RT2
 7. Two pack urethane tar; urethane tar UT
 8. Polyamide cured zinc epoxy paint; zinc epoxy RS + epoxy RC
 9. Two pack zinc rich polyamide cured epoxy paint;
zinc epoxy RG + a resin modified two pack epoxy paint; epoxy EPI
 10. 2 x polyamide cured epoxy paint; epoxy 51 MIOX + 2 x epoxy EPI
-

Table 3. Disbondment of the coating film and the amount of blistering on the paint film after cathodic disbondment test.

| Coating | Potential V/SCE | Film thickness μm | Disbondment in mm | Disbondment in mm^2 | Number and size of blisters | | | | |
|---------------------------------|--------------------|---------------------------------|---------------------------|---------------------------------|-----------------------------|-----|-----|-------|--|
| | | | | | <1 | 1-3 | 3-6 | >6 mm | |
| Epoxies: | | | | | | | | | |
| 1. Epoxy GPL | -1.0 | 347 | 19.3 | 1780 | 0 | 1 | 0 | 2 | |
| | -1.2 | 318 | 25.7 | 2880 | 0 | 8 | 11 | 2 | |
| 2. Epoxy 160 | -1.0 | 541 | 17.9 | 1565 | 0 | 0 | 0 | 0 | |
| | -1.2 | 532 | 17.6 | 1518 | 1 | 1 | 0 | 0 | |
| 3. Epoxy RC | -1.0 | 259 | 23.0 | 2383 | 6 | 1 | 4 | 11 | |
| | -1.2 | 245 | complete loss of adhesion | | >100 | 15 | 13 | 4 | |
| 4. Epoxy powder OPR | -1.0 | 307 | 19.3 | 1753 | 0 | 0 | 0 | 0 | |
| | -1.2 | 292 | 21.3 | 1776 | 0 | 0 | 0 | 0 | |
| 5. Coal tar epoxy ET1 | -1.0 | 364 | 3.9 | 168 | 0 | 0 | 1 | 0 | |
| | -1.2 | 357 | 8.6 | 502 | 0 | 0 | 0 | 0 | |
| 6. Coal tar epoxy RT2 | -1.0 | 277 | 5.0 | 238 | 0 | 0 | 0 | 0 | |
| | -1.2 | 307 | 15.0 | 1178 | 7 | 7 | 0 | 0 | |
| Urethane tars: | | | | | | | | | |
| 7. Urethane tar UT | -1.0 | 229 | 22.7 | 2385 | 28 | 50 | 1 | 0 | |
| | -1.2 | 247 | complete loss of adhesion | | 0 | 4 | 0 | 1 | |
| Paint systems: | | | | | | | | | |
| 8. Zinc epoxy RS + Epoxy RC | -1.0 | 260 | complete loss of adhesion | | >100 | 95 | 8 | 3 | |
| | -1.2 | 236 | complete loss of adhesion | | >100 | 8 | 0 | 0 | |
| 9. Zinc epoxy RG + Epoxy EPI | -1.0 | 173 | 15.2 | 1196 | >100 | 12 | 0 | 0 | |
| | -1.2 | 154 | 9.6 | 586 | >100 | 8 | 0 | 0 | |

- Preparation of steel substrates, ISO 8501-1:1988, Sa 2½

- Blasting with a mixture of metal shot and grit (= S230 and G40); $R_{\text{a}} = 40 - 60 \mu\text{m}$

Table 4. The effect of the steel grade and the surface profile on disbonding and the amount of blistering of the paint system. Cathodic protection potential -1.0 V/SCE.

| Specimen | Film thickness μm | Disbondment in mm | Disbondment in mm ² | Number and size of blisters | | | | Total number of blisters |
|-----------------|----------------------|---------------------------|-----------------------------------|-----------------------------|-----|-----|---------|-----------------------------|
| | | | | <1 | 1-3 | 3-6 | >6 (mm) | |
| 1. A1G3 A1S3 | 683 | 28.8 | 3509 | 10 | 7 | 1 | 1 | 19 |
| | 782 | Complete loss of adhesion | | 30 | 18 | 4 | 2 | 54 |
| 2. B1G3 B1S3 | 732 | 32.2 | 4316 | 75 | 3 | 0 | 0 | 78 |
| | 769 | Complete loss of adhesion | | 32 | 16 | 8 | 3 | 59 |
| 3. F1G3 F1S3 | 688 | 14.6 | 1211 | 23 | 2 | 0 | 0 | 25 |
| | 637 | Complete loss of adhesion | | 30 | 45 | 48 | 6 | 129 |
| 4. A2G3 A2S3 | 503 | 2.2 | 88 | 8 | 4 | 0 | 0 | 12 |
| | 423 | 36.1 | 5236 | 2 | 2 | 5 | 3 | 12 |
| 5. B2G3 B2S3 | 426 | 7.6 | 420 | 2 | 2 | 0 | 0 | 4 |
| | 422 | 35.7 | 5117 | 1 | 1 | 2 | 1 | 5 |
| 6. F2G3 F2S3 | 450 | 4.8 | 223 | 6 | 2 | 0 | 0 | 8 |
| | 508 | 28.7 | 3491 | 11 | 26 | 3 | 1 | 41 |

A = COR-TEN A
 B = COR-TEN B
 F = ASTM A 572 Grade 50
 G = grit blasted (G40)
 S = shot blasted (S230)

1 and 2 are paint systems; 1 = 1 x Epoxy 160
 2 = 2 x Epoxy 51 MIOX + 2 x Epoxy EPI

COR-TEN is a registered trademark of USX Corporation

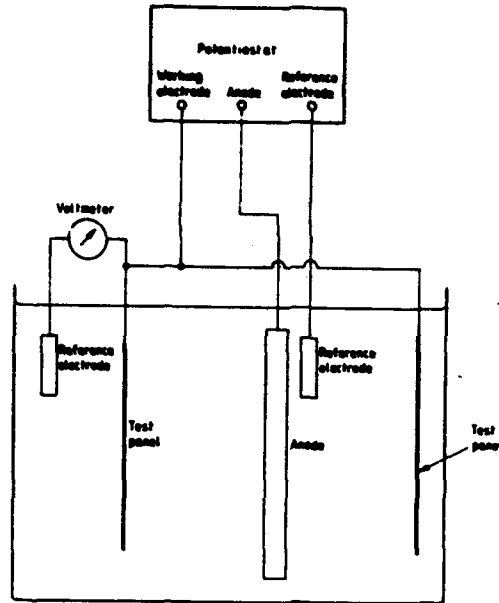


Figure 1.
Potentiostatically-
controlled cathodic
protection circuit.
BS 3900:
Part F10: 1985.



Figure 2.
Apparatus for testing
cathodic disbonding
of paint films on steel
substrates.

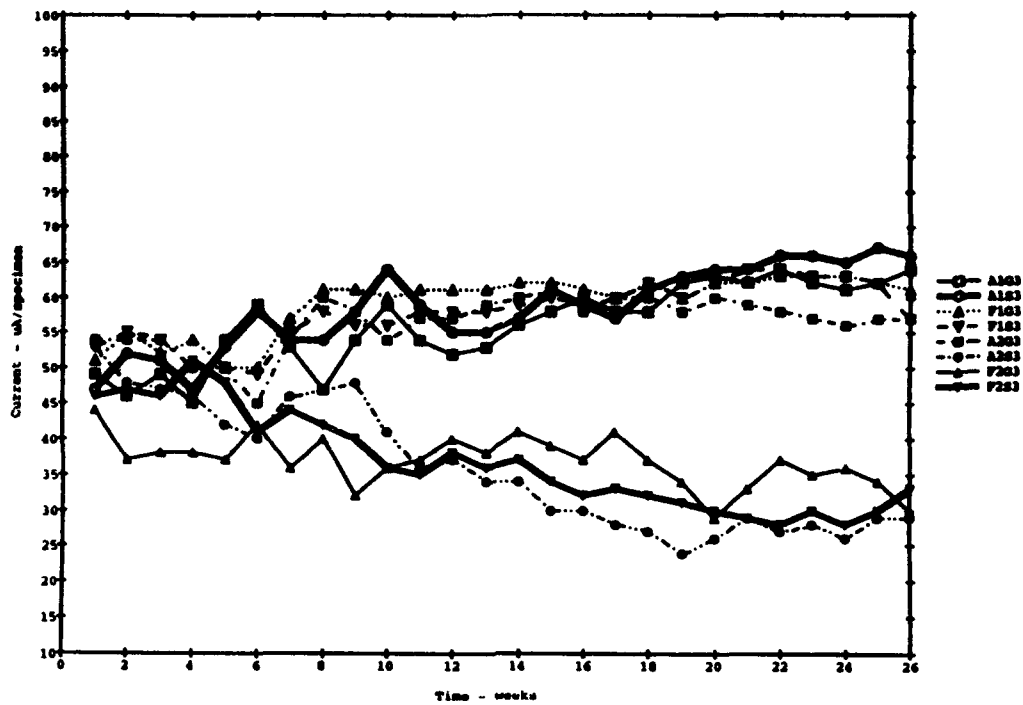


Figure 3. Average current-time curves of specimens cathodically protected at -1000 mV.
 A = COR-TEN A, F = ASTM A572 Grade 50,
 G = Grit blasted (G40), S = shot blasted (S230)
 1 and 2 are paint systems; 1 = 1 x Epoxy 160
 2 = 2 x Epoxy 51 MIOX + 2 x Epoxy EPI

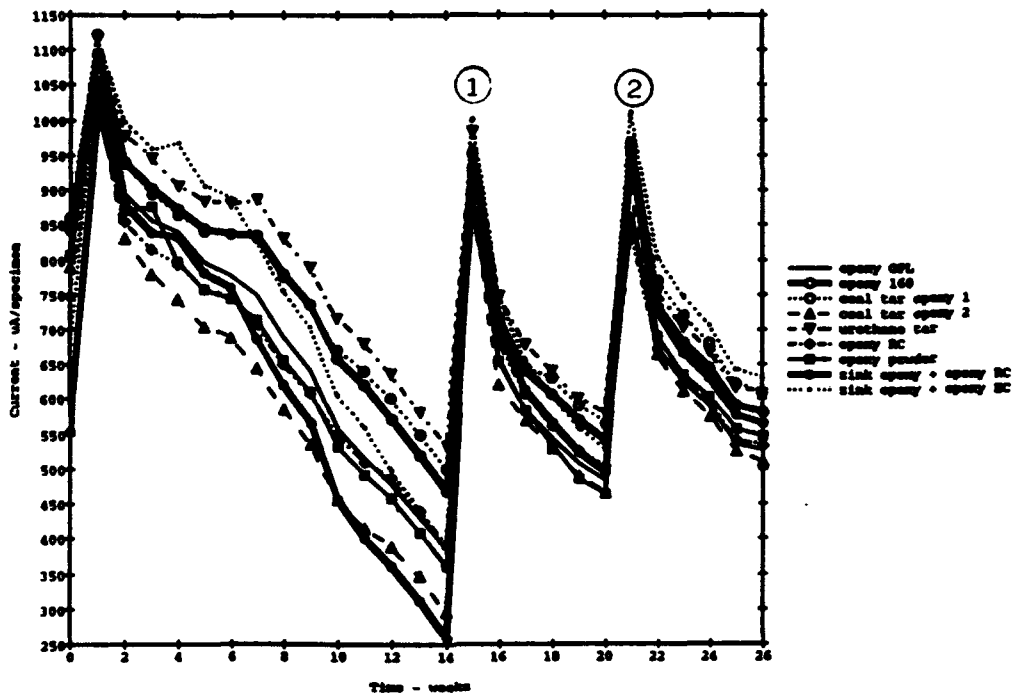


Figure 4. Average current-time curves of specimens cathodically protected at -1200 mV. Different paint systems on shot/grit blasted ASTM A572 Grade 50. The CaCO₃ in the holidays removed at the points 1 and 2.

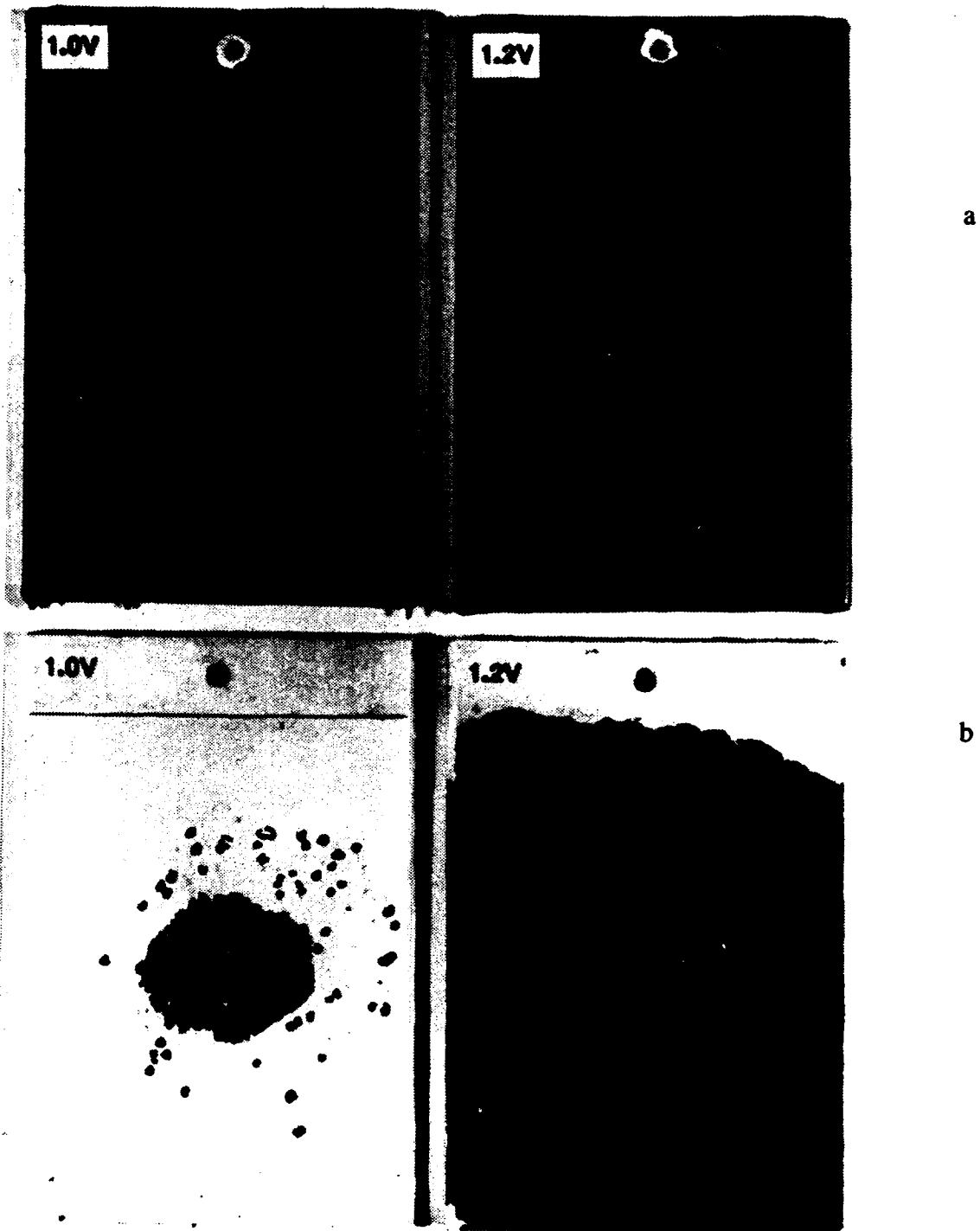


Figure 5. Disbonding of the paint film after exposure
a. Epoxy powder paint OPR
b. Zinc epoxy + Epoxy RC (Blisters are marked on the 1.0 V specimen).

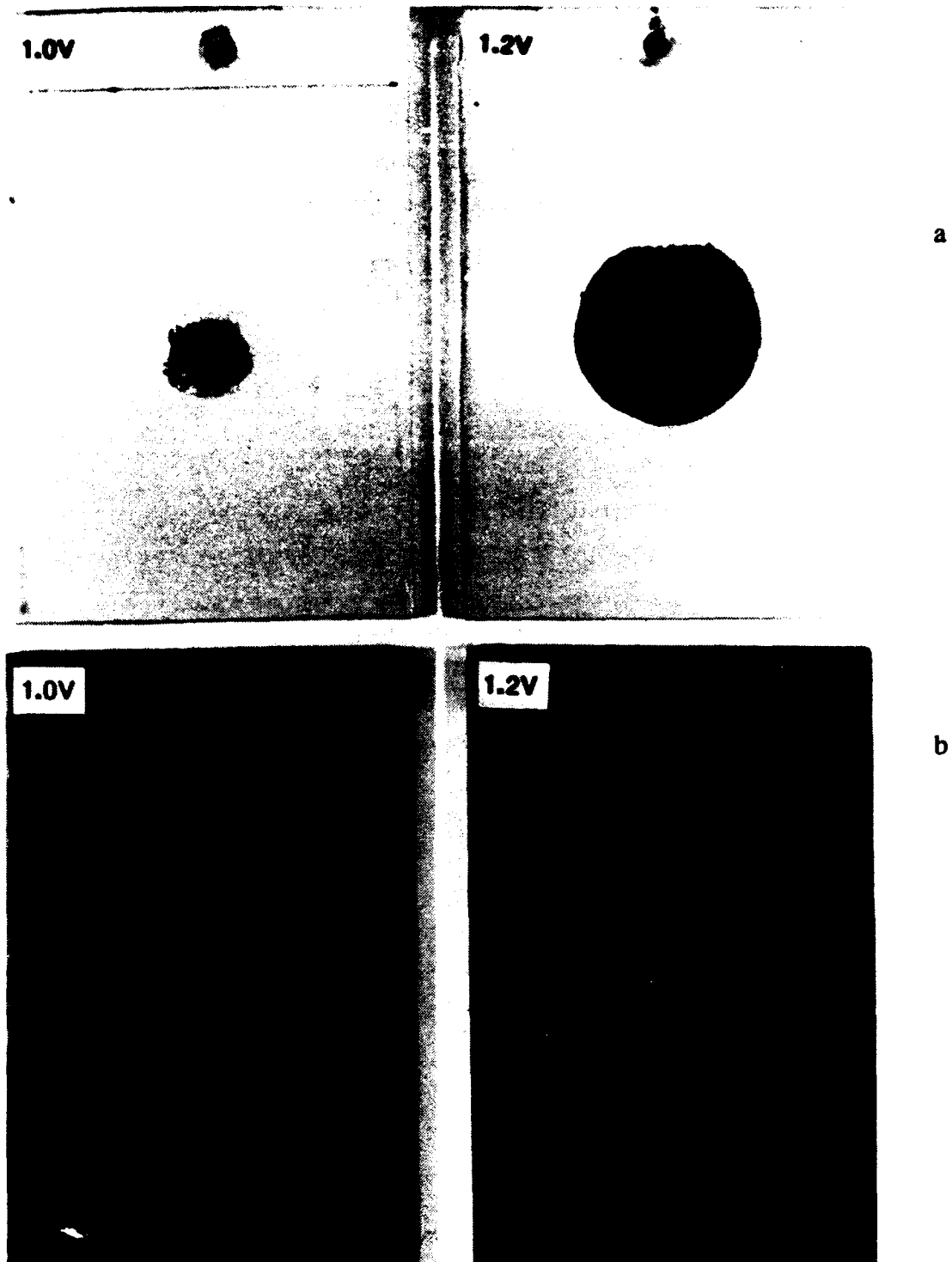
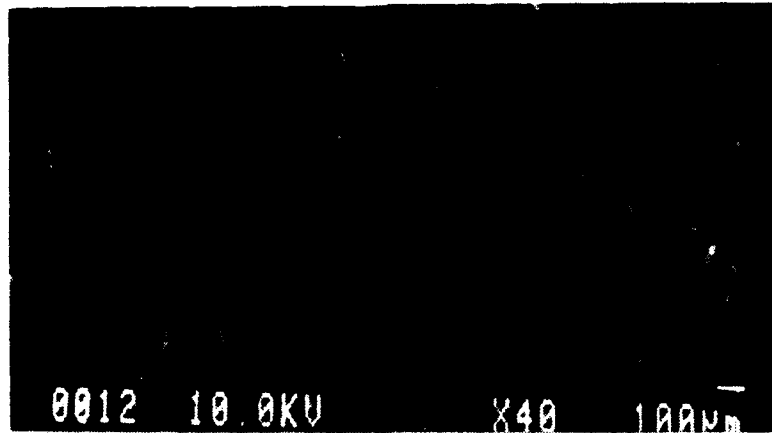
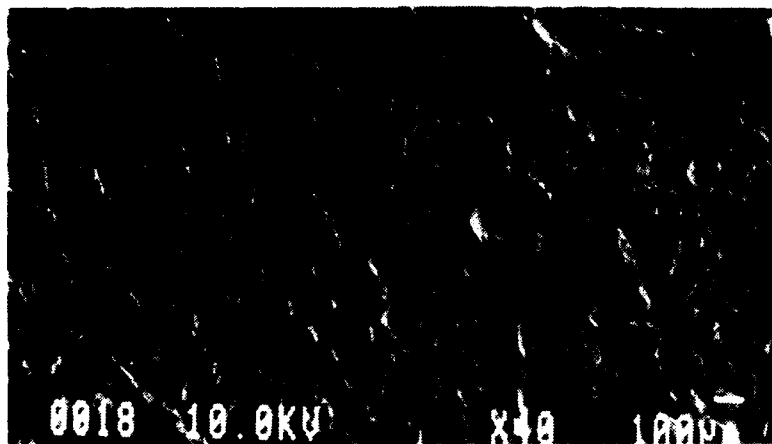


Figure 5.1. Disbonding of the paint film after exposure
a. Epoxy 160
b. Coal tar epoxy ET1



a



b

Figure 6. SEM pictures of shot blasted and grit blasted steel surfaces
a. shot blasted (S230), $R_{\text{m}} = 46 - 56 \mu\text{m}$
b. grit blasted (G40), $R_{\text{m}} = 50 - 61 \mu\text{m}$

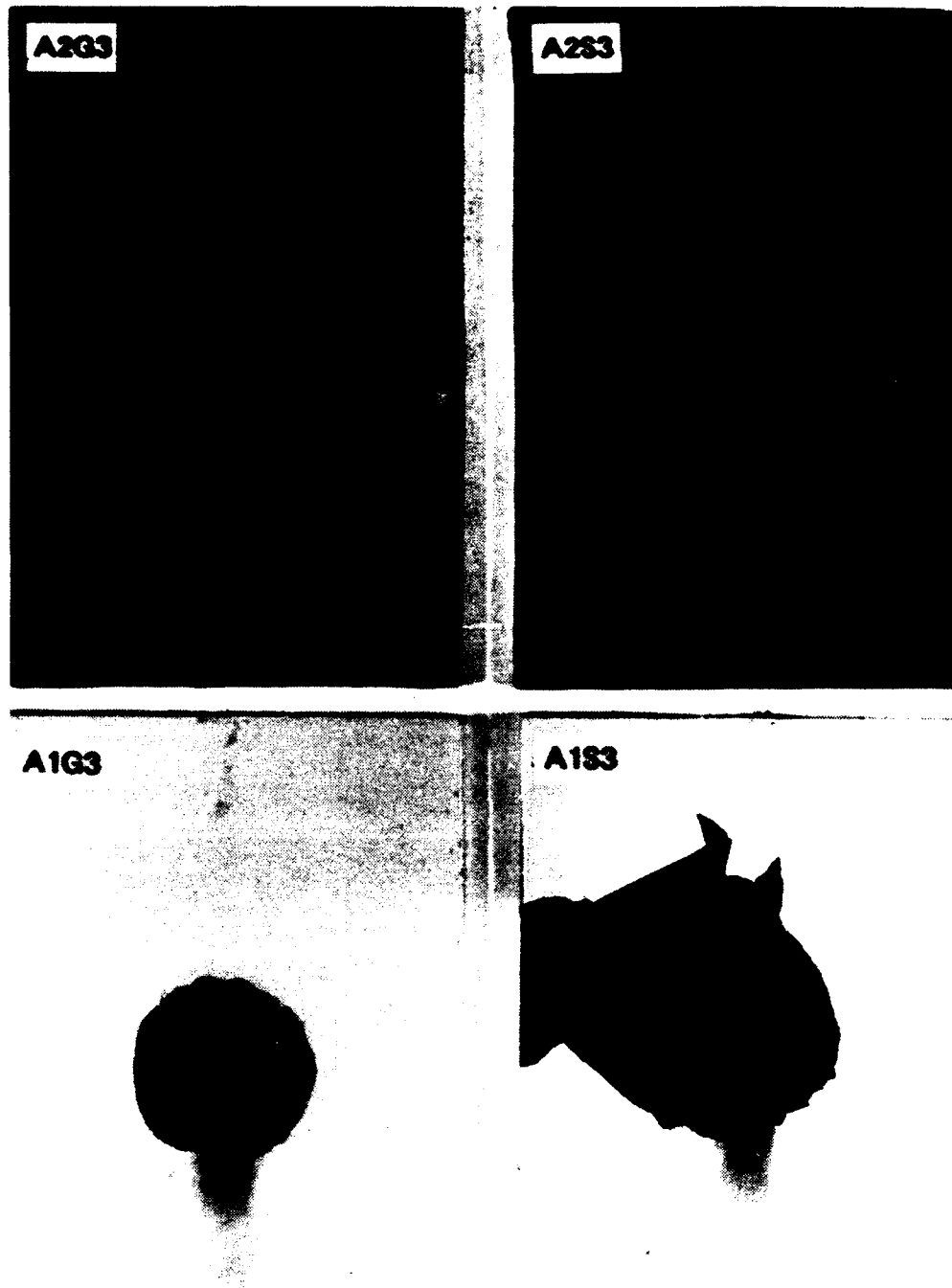
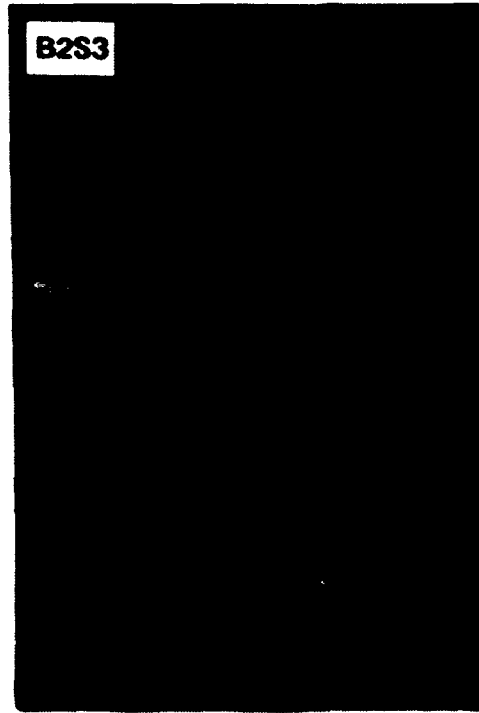


Figure 7. Disbonding of paint on grit blasted (G) and shot blasted (S) COR-TEN A surfaces

1 = 1 x Epoxy 160

2 = 2 x Epoxy 51 MIOX + 2 x Epoxy Epi



B1G3



B1S3



Figure 7.1. Disbonding of paint on grit blasted (G) and shot blasted (S) COR-TEN B surfaces.

1 = 1 x Epoxy 160

2 = 2 x Epoxy 51 MIOX + 2 x Epoxy Epi

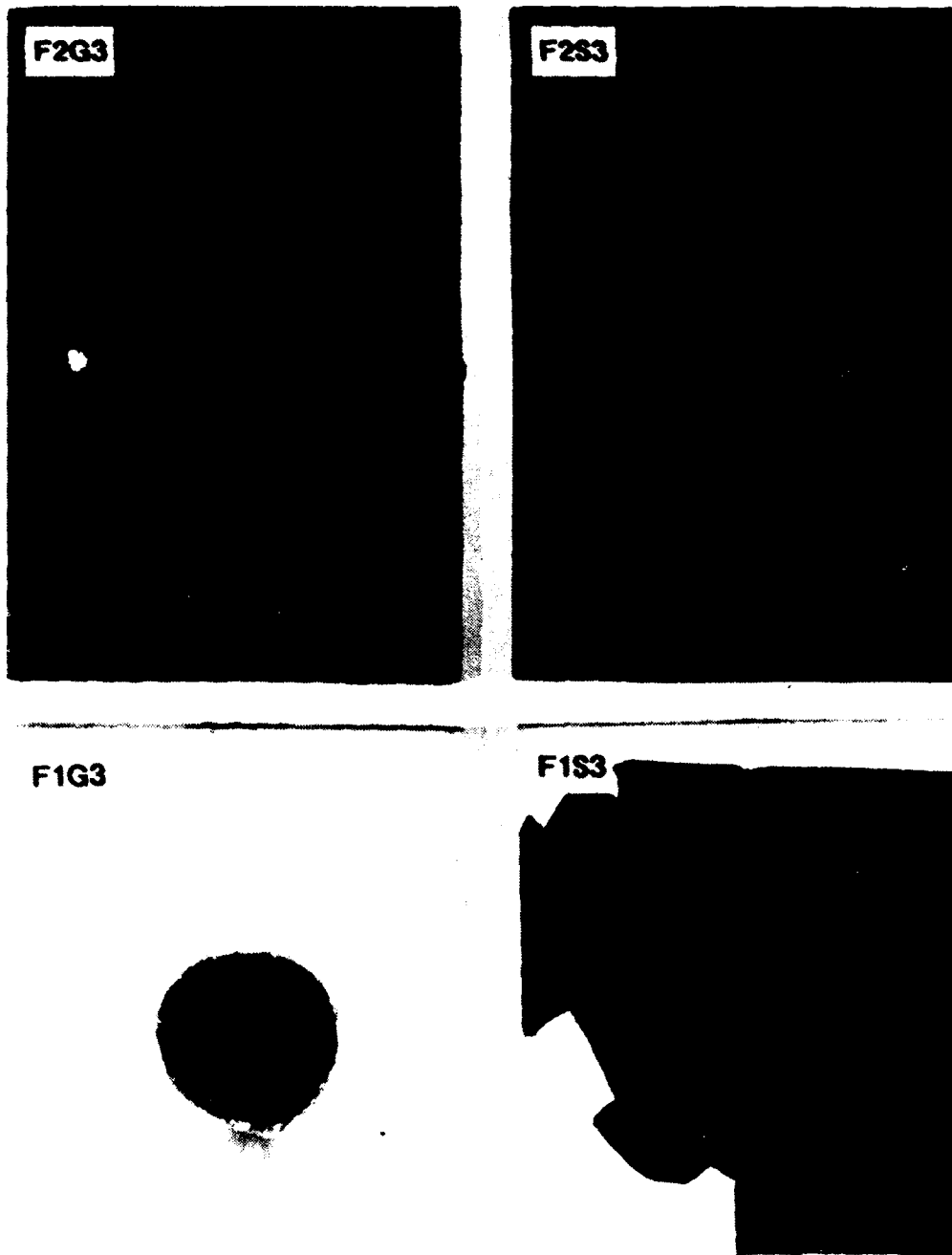


Figure 7.2. Disbonding of paint film on grit blasted (G) and shot blasted (S)
ASTM A572 Grade 50 steel.

1 = 1 x Epoxy 160

2 = 2 x Epoxy 51 MIOX + 2 x Epoxy Epi



Figure 8. Disbondment of two epoxy paint films. Dark area around the holiday is due to the cathodic corrosion reaction.

The other disbonded area is assumed to be due the through-film diffusion reactions

B 22 1x, almost solvent free epoxy 160, 607 μm , -1,5 V/SCE

D 20 2x, almost solvent free epoxy 165, 747 μm , -1,5 V/SCE

Black spots are traces of blisters on the steel substrate.

**On the Influence of Hydrostatic Pressure on the Corrosion Behaviour
of 42CD4 Steel in Natural Seawater : a Mössbauer and X-ray Study**

Jean-Marie Le Breton
Laboratoire de Magnétisme et Applications, URA CNRS 808
Faculté des Sciences de Rouen, BP 118
76134 Mont-Saint-Aignan Cedex, France

Jacques Teillet
Laboratoire de Magnétisme et Applications, URA CNRS 808
Faculté des Sciences de Rouen, BP 118
76134 Mont-Saint-Aignan Cedex, France

Dominique Festy
Laboratoire Matériaux Marins, D.I.T.I.
IFREMER Centre de Brest, BP 70
29280 Plouzané Cedex, France

Abstract

The influence of hydrostatic pressure on the composition of the rust layer of 42CD4 (AISI 4142) steel was studied in order to investigate the effect of a deep marine environment on the corrosion behaviour of this steel. The immersion simulation was realised in a high pressure vessel by hydrostatic pressure generation, with a circulating natural seawater flow in an open circuit.

The rust layer which developed on the surface of the plates was analysed by both ^{57}Fe Mössbauer spectroscopy and X-ray diffraction. For times up to 15 days, it appeared that $\gamma\text{-FeOOH}$, $\alpha\text{-FeOOH}$ and Fe_3O_4 are always present. $\beta\text{-FeOOH}$ was only observed in the inner part of the rust layer for pressures less than 3 MPa. Under atmospheric pressure (0.1 MPa), and for shorter immersion times (3 and 6 days), a paramagnetic phase was observed in the inner part of the rust layer instead of $\beta\text{-FeOOH}$. This paramagnetic phase could be an iron oxyhydroxyde precursor.

The results are interpreted by considering the influence of dissolved oxygen on the mechanisms of iron oxyhydroxyde formation. Upon increasing the activity of dissolved oxygen, the hydrostatic pressure prevents the formation of $\beta\text{-FeOOH}$; under pressures higher than 3 MPa, and for immersion times up to 15 days, $\beta\text{-FeOOH}$ is not observed in the corrosion layer.

Introduction

New developments and progresses in marine technology of immersed systems require a better understanding of material behaviour in a deep marine environment. Among the problems occurring in this media, corrosion problems are of major importance. In order to improve the behaviour of steels in great depths, and thus to increase their lifetime, the effect of the different physicochemical parameters that vary with marine depth (pH, temperature, salinity, dissolved oxygen concentration, pressure, microbiological activity...) have to be characterised independently. In this paper, we investigate the influence of hydrostatic pressure on the composition of the corrosion layer of the 42CD4 steel. Indeed, it is well known that the evolution of the corrosion of steels is essentially related to the nature of the corrosion products which appear during the process. This study completes electrochemical and mechanical measurements made on the same steel¹, which must indicate if different means of corrosion protection are necessary depending on immersion depth.

The corrosion behaviour of steels immersed in seawater or chlorinated aqueous media have been extensively studied during the last twenty years. The final corrosion products of iron are mainly ferric oxyhydroxides and magnetite. Among ferric oxyhydroxides, only the β form is specific to media containing chloride ions^{2,3}. β -FeOOH is formed on steels immersed in chlorinated solutions⁴ or in seawater after long exposure time^{5,6}. The oxyhydroxides γ -FeOOH and α -FeOOH are commonly observed on steels immersed in seawater⁶, chlorinated solutions⁷, and on steels exposed to marine atmosphere⁸⁻¹². The presence of magnetite Fe_3O_4 , which is observed in the inner part of the rust layer, is reported in some cases^{6,8,10}.

⁵⁷Fe Mössbauer spectroscopy is a very useful tool for steel corrosion studies; it allows both qualitative and quantitative analyses of the iron containing phases, and has been extensively used¹³. However, the identification of the corrosion products by Mössbauer spectroscopy can be made difficult by small particle size¹⁴⁻¹⁶ and poor crystallinity¹⁷ effects. These effects lower the Néel temperatures of iron oxyhydroxides and make the interpretation ambiguous at room temperature. In order to make it unambiguous it is necessary to perform a Mössbauer analysis at low temperature¹⁸.

The hydrostatic pressure affects all the physicochemical properties of seawater, but its influence is low except for the activity of dissolved gases, which is noticeably increased¹⁹. An increase in the dissolved hydrogen activity results in an increase of the 42CD4 steel hydrogen embrittlement¹. Another effect of hydrostatic pressure is the modification of the corrosion rate, as it has been shown for nickel²⁰ and 42CD4 steel¹ in seawater. Such a modification could be related to the preferential formation of some compounds in the rust layer. It has been demonstrated that dissolved oxygen, which influences the corrosion kinetics of steel in seawater²¹, influences the composition of the rust layer as well⁴.

Experimental

42CD4 (AISI 4142) steel plates (50mm x 33mm x 5mm) were corroded in natural seawater under pressures up to 30 MPa in order to simulate a deep marine environment. Some plates were corroded under atmospheric pressure (0.1 MPa) in a tank with a circulating natural seawater flow in an open circuit. The immersion simulation was done in a high pressure vessel by the hydrostatic pressure generation, with a circulating natural seawater flow in an open circuit. The seawater was conditioned before its introduction in the vessel so that all its physicochemical parameters were kept constant. Pressures were fixed at 3, 10 and 30 MPa, which correspond approximately to depths of 300, 1000 and 3000 m respectively. Immersion times varied between 3 and 15 days.

After the treatment, the steel plates were dried under a nitrogen atmosphere and kept in liquid nitrogen or under a primary nitrogen vacuum to prevent any evolution of corrosion products in ambient atmosphere. However, some plates were kept in ambient air after immersion and corrosion products analysed for comparison. Two zones were observed on the steel plates surface: a rust layer and a chalky deposit. The corrosion products in the rust layer, which consisted of an orange-brown powder, were removed by carefully scraping the steel plate surface and used as samples. In some cases, the superficial corrosion layer was analysed independently from the lower corrosion layer to detect any possible difference of composition with the thickness in the corrosion layer.

X-ray diffraction analyses were performed using a fast curved detector in an evacuated tank. The X-ray generator was equipped with a cobalt anticathode, using the $\text{Co}(K\alpha)$ radiation. The powders were analysed by reflexion.

Transmission ^{57}Fe Mössbauer spectroscopy analyses were performed using a conventional spectrometer with a source of ^{57}Co in a rhodium matrix. The samples contained about $10\text{mg}/\text{cm}^2$ of natural iron.

Results

X-ray Diffraction Analysis

Samples from plates corroded under atmospheric pressure (0.1 MPa)

X-ray diffraction patterns of the corrosion layer formed on the surface of steel plates corroded under atmospheric pressure for 3 and 6 days and kept under primary nitrogen vacuum are shown in Figures 1a and 1b. The corrosion products are identified to be mainly $\gamma\text{-FeOOH}$ (corresponding to the most intense X-ray diffraction lines), $\alpha\text{-FeOOH}$ and Fe_3O_4 . In both samples, NaCl lines are identified; this may result from seawater evaporation during the drying of the plates. In the sample corresponding to the plate immersed for 6 days, CaCO_3 lines are also identified (Figure 1b), which shows that a part of the chalky deposit was taken with the rust layer.

Superficial rust layer (SRL) and lower rust layer (LRL) formed on steel plates kept in a primary nitrogen vacuum after 15 days immersion were analysed. Corresponding X-ray diffraction patterns (Figures 1c and 1d) show that both the SRL and LRL contain $\gamma\text{-FeOOH}$, with $\alpha\text{-FeOOH}$ and Fe_3O_4 in lower proportions. In addition, $\beta\text{-FeOOH}$ is present in the LRL.

Analyses made with samples taken from plates kept in liquid nitrogen or in ambient atmosphere show the same results.

Samples from plates corroded under 3, 10 and 30 MPa

X-ray diffraction patterns of rust layer formed on the surface of steel plates corroded under 3, 10 and 30 MPa for 10 to 15 days are shown in Figure 2. All the samples contain $\gamma\text{-FeOOH}$, $\alpha\text{-FeOOH}$ and Fe_3O_4 . NaCl lines are also observed. $\beta\text{-FeOOH}$ is only observed in the LRL of the steel plate corroded for 15 days under 3 MPa (Figure 2b).

Mössbauer Spectroscopy Analysis

In all cases, room temperature Mössbauer spectra show only a broad non lorentzian quadrupolar doublet, which does not allow the phases to be identified unambiguously. This behaviour has been attributed to particle size effects¹⁸. In fact, from X-ray diffraction results, using the Scherrer formula, the mean particle size was determined to be 23-30 nm for all the oxyhydroxides. Thus, the analyses were performed at 60 and 77 K. At these temperatures, in these samples, $\gamma\text{-FeOOH}$ is still paramagnetic, while $\alpha\text{-FeOOH}$ and $\beta\text{-FeOOH}$ are magnetic¹⁸.

The Mössbauer spectra were fitted in each case, according to the X-ray diffraction results. The results of these fittings are summarised in Table 1.

Samples from plates corroded under atmospheric pressure (0.1 MPa)

The corresponding Mössbauer spectra, recorded at 77 K, are shown in Figure 3. The SRL of the steel plate corroded during 3 days was analysed independently from the LRL. The SRL spectrum (Figure 3a) was fitted with a broad quadrupolar doublet and a broad magnetic sextet. The hyperfine parameters of the doublet are in agreement with those of γ -FeOOH, and a good fit is achieved using a distribution of quadrupolar splittings, according to particle size effects. The hyperfine parameters of the sextet are in agreement with those of α -FeOOH. The LRL spectrum (Figure 3b) was fitted with the γ -FeOOH doublet, the α -FeOOH sextet, and a broad paramagnetic line, associated to a paramagnetic phase, named P, whose isomer shift (0.49 mm/s at 77K) corresponds to that of iron in the Fe^{3+} state.

The Mössbauer spectrum corresponding to the 6 days immersion (Figure 3c) was fitted with the same components as the LRL of the steel plate immersed for 3 days, indicating that the paramagnetic P phase is still present. The Mössbauer spectra of samples from steel plates corroded for 15 days, and kept under the different conditions described previously, were fitted with γ -FeOOH, α -FeOOH and β -FeOOH contributions (Figure 3d). The P phase contribution was not present. The hyperfine parameters of the β -FeOOH magnetic contribution agree reasonably well with values published^{22,23}. The results are identical for samples kept in different conditions, indicating that the corrosion products identified here are stable in relation to the conditioning of the plates after immersion.

A Fe_3O_4 contribution was not observed on these spectra, indicating that its Mössbauer abundance in the samples is lower than the detection limit (typically less than 2%).

Samples from plates corroded under 3, 10 and 30 MPa

A corresponding Mössbauer spectra, recorded at 60 or 77 K, are shown in Figure 4. The spectrum for the plate corroded under 3 MPa was fitted with γ -FeOOH, α -FeOOH and β -FeOOH contributions (Figure 4a). The relative proportion of the β -FeOOH contribution is lower than that of the sample corresponding to the 0.1 MPa / 15 days immersion. The Mössbauer spectra of samples from plates corroded under 10 and 30 MPa were fitted with the γ -FeOOH and α -FeOOH contributions, in the same proportions (Figures 4b and 4c). The Fe_3O_4 contribution was not observed on the spectra, indicating that its Mössbauer abundance in the samples is again less than 2%.

Discussion

From these results, it appears that the composition of the rust layer depends on both hydrostatic pressure and immersion time. The conditioning of the plates after immersion did not appear to affect the stability of the corrosion products.

While γ -FeOOH, α -FeOOH, and Fe_3O_4 phases are observed in all cases, the presence of β -FeOOH depends on both hydrostatic pressure and immersion time. This phase is only observed for pressures lower than 3 MPa, which indicates that the effect of hydrostatic pressure is to prevent its formation in the rust layer. Under 0.1 MPa, β -FeOOH is formed after 15 days in the lower part of the rust layer. For immersion times less than 6 days under 0.1 MPa, a paramagnetic phase (P phase) is observed in the lower part of the rust layer instead of β -FeOOH. This P phase is associated to an amorphous or ill-crystallised phase, which could be a precursor of the iron oxyhydroxides²⁴. In that case, the X-ray pattern would show broad and low intensity lines; this would be hard to observe when superimposed with narrow lines from crystallised phases.

These results are interpreted as being the effect of dissolved oxygen on the mechanism of oxyhydroxide formation in chlorinated aqueous media. According to the results obtained by Nomura et al.⁴, the decrease of dissolved oxygen concentration under the initial corrosion layer of iron results in the formation of a complex oxyhydroxide containing Cl⁻ ions, which converts into β -FeOOH. When dissolved oxygen can reach easily the surface, γ -FeOOH is preferentially formed. Consequently, β -FeOOH appears when the corrosion layer is sufficiently thick (or in other words when the immersion time is sufficiently long) to allow a decrease of dissolved oxygen concentration at the rust/steel interface. On the other hand, when the hydrostatic pressure increases, the dissolved oxygen activity in the corrosion layer is enhanced, γ -FeOOH is formed and β -FeOOH does not form.

Conclusion

42CD4 steel plates were corroded under pressures up to 30 MPa for times up to 15 days in natural seawater. The analysis of the rust layer formed on steel plates showed that γ -FeOOH, α -FeOOH, and Fe₃O₄ are always present, while β -FeOOH was only observed in some cases. It has been shown that both hydrostatic pressure and immersion time are parameters which influences the composition of the rust layer, by influencing the formation of β -FeOOH.

It appears that for immersion times up to 15 days, β -FeOOH can only be formed in the inner part of the rust layer of plates corroded under pressures between 0.1 and 3 MPa, corresponding to marine depths between 0 and 300 m. Increasing hydrostatic pressure prevents the formation of β -FeOOH and the composition of the rust layer is not affected beyond 10 MPa (1000 m).

The influence of hydrostatic pressure on the composition of the rust layer of 42CD4 steel has been correlated to the influence of dissolved oxygen on the mechanism of iron oxyhydroxides formation in seawater.

References

1. D. Festy, "Influence de la pression hydrostatique sur la corrosion et la protection cathodique de l'acier 42CD4 en eau de mer", Thesis, Université de Technologie de Compiègne (1991)
2. T. Misawa, K. Hashimoto, S. Shimodaira, *Corrosion Science*, 11 (1974), p. 131
3. Y. Ujihira, M. Ohyabu, *Journal de Physique, Colloque C2 40* (1979), p. 347
4. K. Nomura, M. Tasaka, Y. Ujihira, *Corrosion* 44 (1988), p. 131
5. J. Chen, Z. Cai, Z. Wang, C. Wang, H. Zhang, W. Hu, F. Yu, G. Zhang, *Proceedings of the International Conference on the Applications of the Mössbauer Effect* (Jaipur, India, 1981), p. 261
6. F. Blekkenhorst, G.M. Ferrari, C.J. van der Wekken, F.P. Ijselling, *British Corrosion Journal*, 21 (1986), p. 163
7. R.K. Nigam, U.S. Mehrotra, S. Varma, S.N. Pandey, *Proceedings of the International Conference on the Applications of the Mössbauer Effect* (Jaipur, India, 1981), p. 299
8. A.K. Singh, T. Ericsson, L. Häggström, J. Gullman, *Corrosion Science*, 25 (1985), p. 931

9. D.C. Cook, *Hyperfine Interactions*, 28 (1986), p. 891
10. K. Nomura, Y. Ujihira, *Hyperfine Interactions*, 29 (1986), p. 1467
11. A. Raman, S. Nasrazadani, L. Sharma, A. Razvan, *Praktische Metallographie*, 24 (1987), p. 535
12. S. Rezaie-Serej, D.C. Cook, *Hyperfine Interactions*, 41 (1988), p. 701
13. A. Vértes, *Hyperfine Interactions*, 45 (1989), p. 105 (and references herein)
14. A.M. van der Kraan, D. Rahner, *Physics Letters*, 20 (1966), p. 614
15. S. Mørup, M.B. Madsen, J. Franck, J. Villadsen, C.J.W. Koch, *Journal of Magnetism and Magnetic Materials*, 40 (1983), p. 163
16. S. Bocquet, S.J. Kennedy, *Journal of Magnetism and Magnetic Materials*, 109 (1992), p. 260
17. E. Murad, U. Schwertmann, *Mineralogical Magazine*, 48 (1984), p. 507
18. J. Teillet, J.M. Le Breton, D. Festy, submitted to the International Conference on the Applications of the Mössbauer Effect (Vancouver, Canada, 1993)
19. D. Festy, A.M. Beccaria, IFREMER Report 88DIT/EQE/MR14 (1988)
20. A.M. Beccaria, P. Fiordiponti, G. Mattogno, *Corrosion Science*, 29 (1989), p. 403
21. J. Sefaja, J. Malina, *Surface Technology*, 26 (1985), p. 369
22. C.W. Childs, B.A. Goodman, E. Paterson, F.W.D. Woodhams, *Australian Journal of Chemistry*, 33 (1980), p. 15
23. D. Rezel, J.M.R. Génin, *Hyperfine Interactions*, 57 (1990), p. 2067
24. J.H. Johnston, D.G. Lewis, in "Industrial Applications of the Mössbauer Effect", G.J. Long and J.G. Stevens Editors, Plenum Press, New York (1987), p. 565

Table 1- Mössbauer parameters of the constituents of the rust layer formed on 42CD4 steel plate surface in natural seawater

| Pressure | Immersion time | Temperature | Phase | IS mm/s | QS mm/s | Hf T | Mössbauer abundance | |
|----------------|-----------------|-------------|-----------------|-----------------|------------|---------|------------------------|-----|
| 0.1 MPa | 3 days (SRL) | 77 K | γ -FeOOH | 0.48 | 0.66 | ---- | 91% | |
| | | | α -FeOOH | 0.51 | -0.25 | 47.2 | 9% | |
| | 3 days (LRL) | 77 K | γ -FeOOH | 0.47 | 0.74 | ---- | 64% | |
| | | | α -FeOOH | 0.50 | -0.25 | 48.0 | 23% | |
| | | | P phase | 0.49 | 0.00 | ---- | 13% | |
| | 6 days (LRL) | 77 K | γ -FeOOH | 0.46 | 0.74 | ---- | 56% | |
| | | | α -FeOOH | 0.48 | -0.21 | 48.0 | 23% | |
| | | | P phase | 0.49 | 0.00 | ---- | 21% | |
| | 15 days | 77 K | γ -FeOOH | 0.48 | 0.63 | ---- | 82% | |
| | | | α -FeOOH | 0.44 | -0.25 | 48.4 | 10% | |
| | | | β -FeOOH | 0.58 | -0.09 | 48.4 | 3% | |
| | | | | 0.48 | -0.26 | 45.6 | 3% | |
| | | | | 0.62 | -0.39 | 42.6 | 2% | |
| | 3 MPa | 15 days | 77 K | γ -FeOOH | 0.48 | 0.62 | ---- | 93% |
| | | | | α -FeOOH | 0.44 | -0.25 | 48.1 | 4% |
| β -FeOOH | | | | 0.58 | -0.09 | 48.3 | 1% | |
| | | | | 0.48 | -0.26 | 45.6 | 1% | |
| | | | | 0.62 | -0.39 | 42.6 | 1% | |
| 10 MPa | 14 days | 60 K | γ -FeOOH | 0.49 | 0.60 | ---- | 86% | |
| | | | α -FeOOH | 0.49 | -0.25 | 48.7 | 14% | |
| 30 MPa | 10 days | 60 K | γ -FeOOH | 0.49 | 0.62 | ---- | 85% | |
| | | | α -FeOOH | 0.50 | -0.23 | 48.0 | 15% | |

Statistical errors for isomer shift (IS), quadrupolar splitting (QS) and hyperfine field (Hf):
 $\Delta IS = \pm 0.02$ mm/s ; $\Delta QS = \pm 0.04$ mm/s ; $\Delta Hf = \pm 0.1$ T.

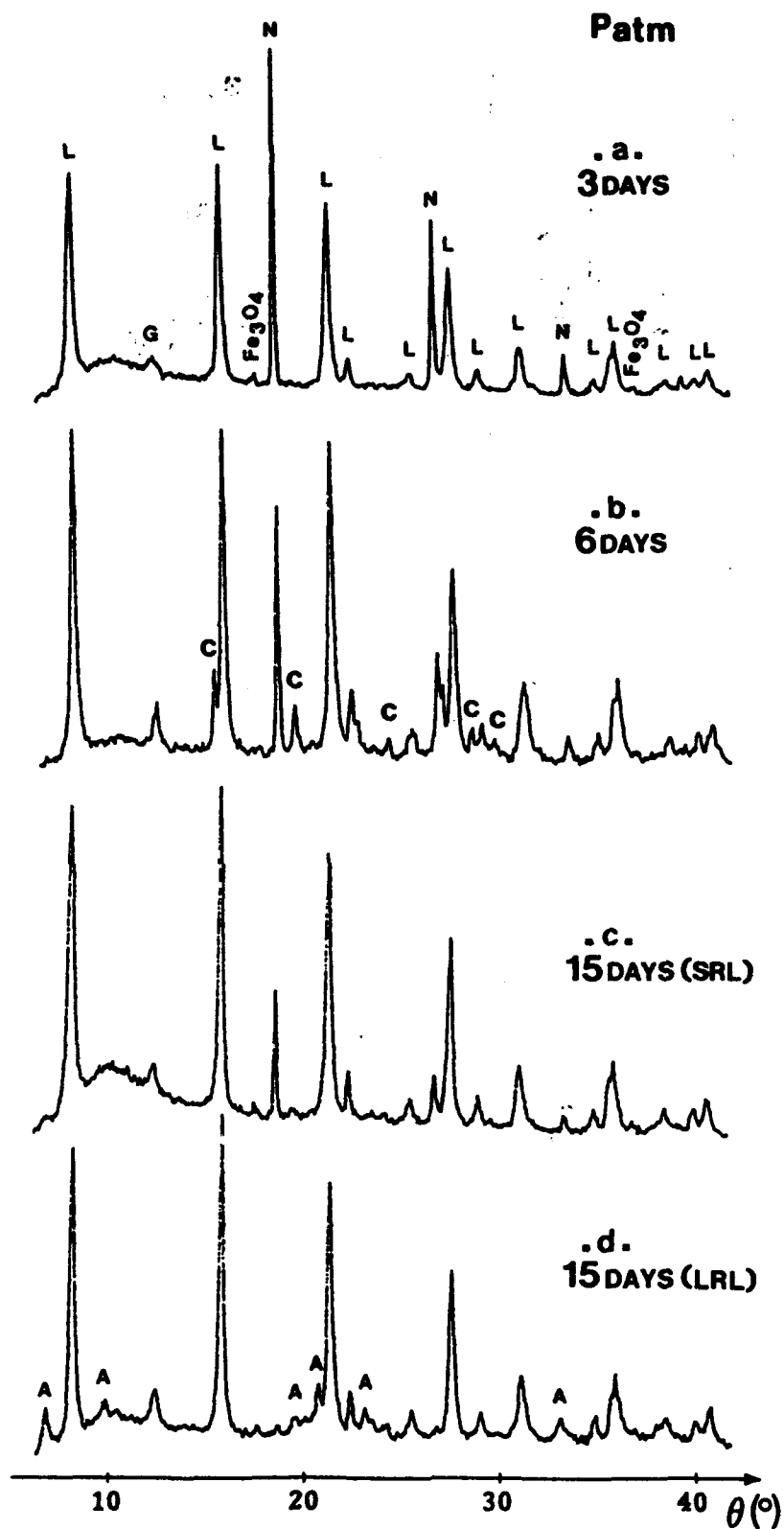


Figure 1- X-ray diffraction patterns of the corrosion layer formed on the surface of steel plates corroded under atmospheric pressure in natural seawater for 3, 6 and 15 days.

(L: lepidocrocite γ -FeOOH; G: goethite α -FeOOH;
A: akaganeite β -FeOOH; N: NaCl; C: CaCO₃)

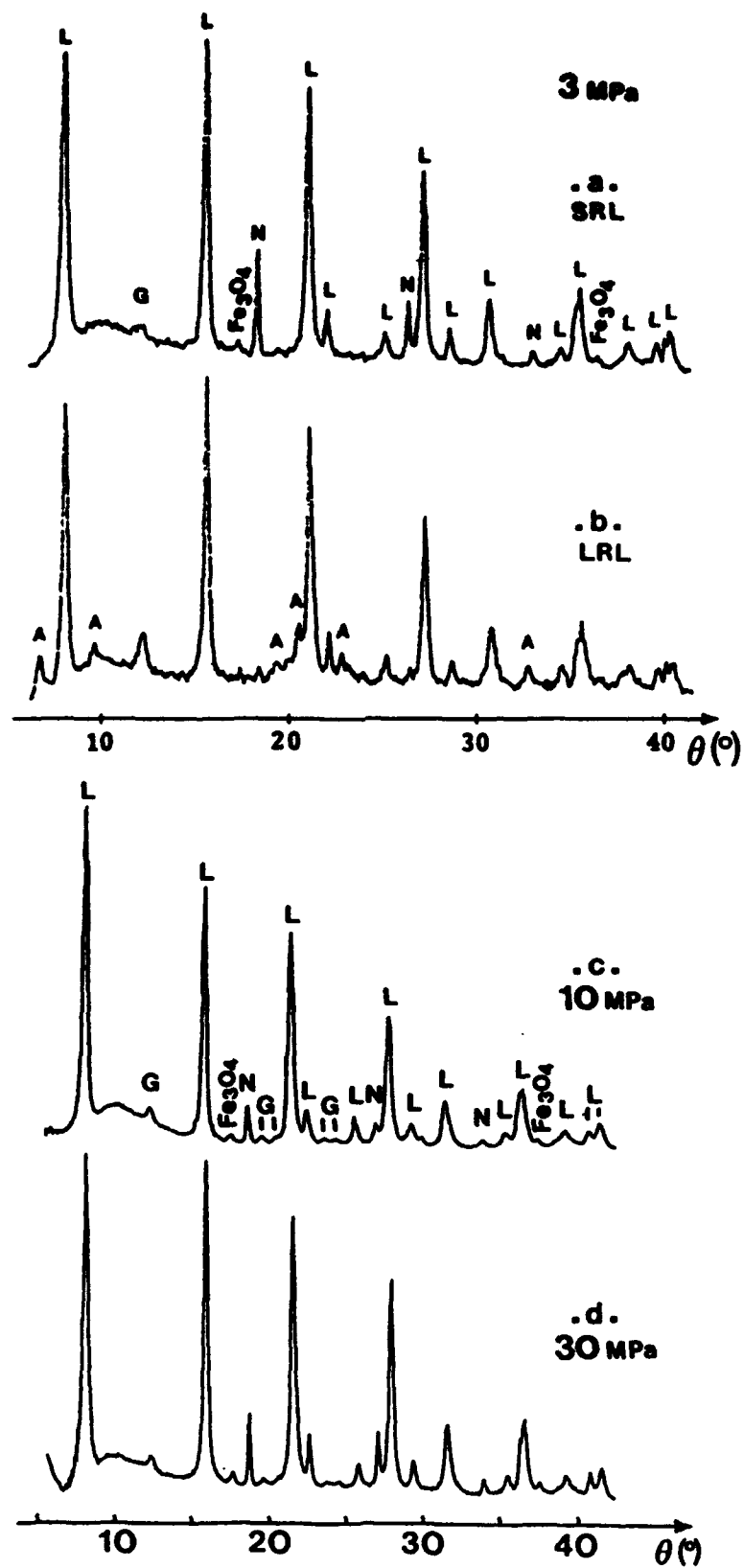


Figure 2- X-ray diffraction patterns of the corrosion layer formed on the surface of steel plates corroded under 3, 10 and 30 MPa in natural seawater for 15, 14 and 10 days respectively.
(L: lepidocrocite γ -FeOOH; G: goethite α -FeOOH;
A: akaganeite β -FeOOH; N: NaCl)

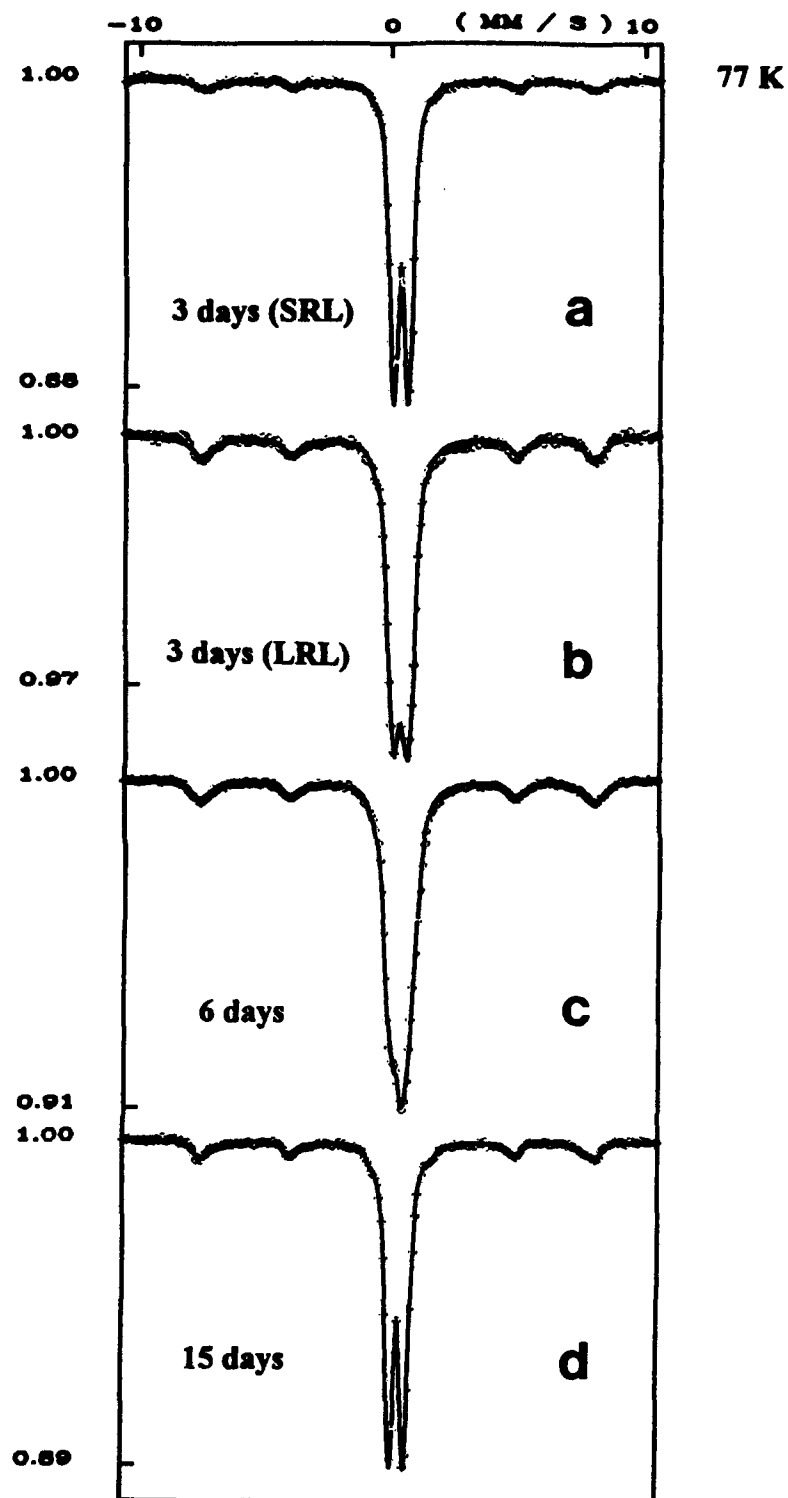


Figure 3- ^{57}Fe Mössbauer spectra of the corrosion layer formed on the surface of steel plates corroded under atmospheric pressure in natural seawater for 3 (a,b), 6 (c) and 15 (d) days.

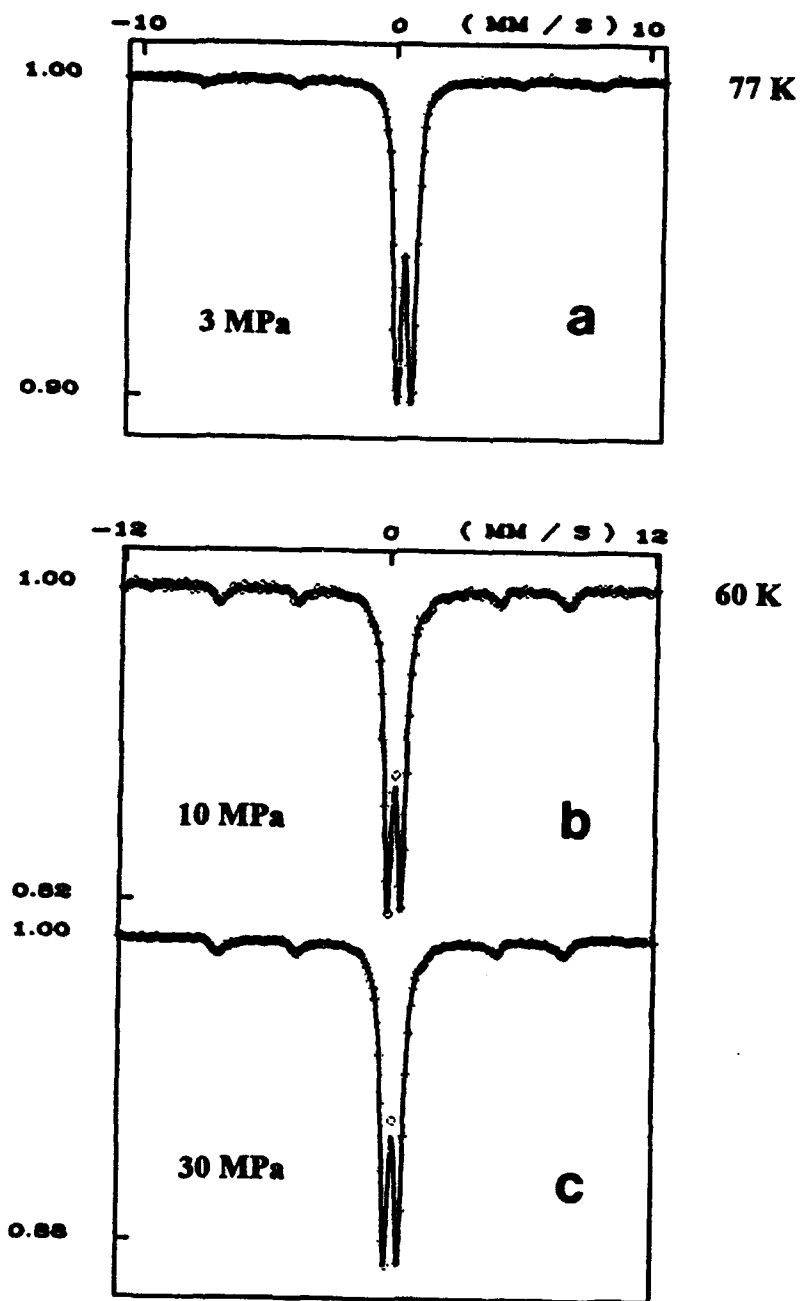


Figure 4- ^{57}Fe Mössbauer spectra of the corrosion layer formed on the surface of steel plates corroded under 3, 10 and 30 MPa in natural seawater for 15 (a), 14 (b) and 10 (c) days respectively.

Corrosion Characterization of Explosively Bonded Materials in Marine Environment

M. Lindsey

Naval Surface Warfare Center
Electrochemistry Branch (R33)
Dahlgren Division, White Oak Detachment
Silver Spring, Maryland 20903-5640

K.L. Vasanth

Naval Surface Warfare Center
Electrochemistry Branch (R33)
Dahlgren Division, White Oak Detachment
Silver Spring, Maryland 20903-5640

Abstract

Explosively bonded materials are combinations of two or more alloys which have been joined in a continuous manner by a metallurgical bond. Such explosively bonded materials possess specific properties from both alloys, usually good corrosion resistance of one alloy with the strength and economics of the other alloy. Research has been performed to characterize the bonded interface as well as the individual alloys. Electrochemical studies and atmospheric exposure tests have been performed to investigate the corrosion behavior of explosively bonded materials in a marine or seawater environment. Scanning Electron Microscopy (SEM) has been employed to examine both the interface and the surface of the alloys of these explosively bonded materials. Energy Dispersing Analysis by X-rays (EDAX) has been employed to study the interface chemical make-up. The galvanic corrosion behavior of explosively bonded materials and of conventionally coupled alloys has been studied.

Key terms: corrosion, explosive bonded material, EDAX, galvanic corrosion, interface, seawater, SEM

INTRODUCTION

Naval ships are vessels that pose complex materials selection problems. These ships must simultaneously be a reliable structure, have minimal topside weight, and withstand harsh marine environments. Unfortunately, no single structural material can satisfy all of these requirements. Materials that satisfy corrosion requirements may not meet strength requirements, materials that meet weight requirements may not meet cost restrictions. The obvious solution is the use of a variety of metals and alloys throughout the vessel, each selected for the appropriate properties for the specific component. Many dissimilar metal combinations cannot be welded by traditional methods and are joined by mechanical methods like bolting or riveting. The combination of a crevice at the joint and galvanic potential differences between these joined metals frequently results in accelerated corrosion in the marine environment. Explosive bonding of dissimilar metals appears to be the solution to this dilemma by eliminating the mechanical joints [1]. It produces a crevice-free metallurgical weld between metals that otherwise can not be welded.

The explosive bonding technique is believed to have been first suggested during the 1880's although some sources claim a later discovery date [2]. The first attempts of this type of welding occurred in the 1940's and the first patent was filed in 1960 [3]. Explosive bonding became more common in the mid sixties and today it is being utilized in a variety of applications.

Explosive bonding uses the energy of detonating explosives to produce a solid-state metallurgical bond between dissimilar metals. One metal is accelerated by explosion at a high rate over a short distance resulting in a progressive collision of that metal with the metal to which it will be bonded. The metals are forced together under several million pounds per square inch of pressure resulting in electron sharing between the metals and a bond (weld) that is typically stronger than the weaker of the parent metals. The metallurgical bond created by this process is virtually immune to crevice corrosion. The weld or bond is a solid state bond that is created in a fraction of a second without the addition of filler metals. There are many types of explosive bonding processes but the parallel arrangement process has been used exclusively in the study.

The objective of this investigation is to characterize the behavior of the interface of various explosively bonded metallic combinations in a marine environment. The interfaces have been examined by Scanning Electron Microscopy (SEM) and interfacial compositions determined by Energy Dispersing Analysis by X-rays (EDAX). The results of laboratory experiments and marine atmospheric exposure tests for selected explosively bonded materials are compared to obtain a better understanding of the corrosion resistance of the interface.

I. Experimental

A. Apparatus

The electrochemical studies were performed using an EG&G PARC Corrosion Console System 350-A (potentiostat/microprocessor) and a PARC 273 Potentiostat with corrosion software from EG&G PARC SoftCorr. Several different electrochemical cells were used to collect data in these studies. These cells were modified for use in this study. The reference electrode used was the saturated calomel electrode (SCE). A Keithley 195A Digital Multimeter was used to monitor all potentials. A Sartorius Model E1200S Balance was used to obtain all weights.

B. Materials and Chemicals

All solutions were prepared using triply distilled water obtained from a Dow Corning Still. All reagents are Analytical Reagent Grade purity. ASTM Standard D 1141-86 [4] was used to make the substitute seawater.

The materials examined in this investigation were explosively bonded metals of the following combinations:

1. Aluminum 5456: Steel A516 Gr
2. Copper-Nickel 70:30: Steel A516 Gr
3. Aluminum 5456: Titanium: Stainless Steel 304
4. Aluminum 5456: Titanium: Copper-Nickel 70:30

Other materials, including steel alloy (4340), aluminum alloys (6061), stainless steel alloy (304), and monel K 400 were examined in the same manner. These materials were mounted in Extec fast cure epoxy resins after connected to electrical wire with silver paint. The samples were polished with sandpaper of 280, 320, 400 and 600 grit and wiped with a soft cloth to a mirror shine. The polished samples were washed thoroughly with distilled water, acetone and air dried. All samples were allowed to equilibrate in ASTM substitute seawater for one hour before any electrochemical experiments were performed. There was no aeration of test solutions, and all tests were conducted under ambient conditions.

C. Methods of Investigation

This investigation included the following laboratory tests: measurement of Polarization Resistance, Galvanic Corrosion [5] and open circuit potential measurements to characterize the corrosion behavior of the bimetallic and individual components in ASTM seawater. The Constant immersion test in ASTM seawater was performed in the laboratory on the explosively bonded materials listed above. Weight loss measurements were performed on all explosively bonded materials.

Field tests were performed on the explosively bonded materials and some components of the bonded materials. Field test consisted of atmospheric exposure and seawater wet down tests. Weight loss measurements and visual observations were made after these tests were completed.

Polarization resistance technique is a method for measuring corrosion rates of materials of interest. This technique is used by applying a controlled-potential scan over a small range, in this case +/- 10 mV with respect to E_{corr} . The resulting current is linearly plotted versus potential. The slope of this potential-current plot at E_{corr} is identical to the Polarization Resistance, which is used with the Tafel Constants to determine I_{corr} . A scan rate of 0.1 mV/sec was used and the potential range of 20 mV was scanned in about 200 seconds (3 minutes). Since the applied potential is never far removed from the corrosion potential, the surface of the specimen is not destroyed or affected by the experiment, and the same sample can therefore be used for other techniques.

Galvanic corrosion measurement is differs from all other electrochemical techniques. The corrosion measuring system measures the voltage/current characteristics of two dissimilar metals immersed in a chloride medium. The corrosion measuring system primarily functions as a zero-resistance ammeter during the Galvanic Corrosion measurements. Galvanic Corrosion is the only technique in which two separate plots are produced by the 350A corrosion console. The first graph generated is the voltage versus time plot. The second graph is a plot of current versus time. From these graphs corrosion behavior for explosively bonded pairs or electrically connected alloys were determined.

Open circuit potential measurements were performed on both explosively bonded materials and single components comprising these materials. The potentials were measured over a period of time (approximately 3 months) against SCE. The corrosion behavior determined for steel explosively bonded to aluminum. repeatedly. An average corrosion rate of 1.815 mils per year was for the reactivity of each material studied in chloride medium.

The field tests employed in this study consisted of two types: atmospheric exposure (to marine environment) and seawater wet down test. The atmospheric test involved the exposure of an explosively bonded specimen to a marine environment. The samples are placed on an ASTM approved test rack and exposed to marine elements, humidity, temperature, UV radiation and stack gases (SO_2 sulfur dioxide). The samples were periodically examined by visual inspection. The seawater wet down test involved the intermittent spraying of samples with seawater (for about 10 minutes) and atmospheric exposure for about 50 minutes.

This is by far the most aggressive test used in this investigation. The samples were examined periodically for corrosion products and interfacial material failure.

The laboratory immersion test consisted of immersing specimen in ASTM substitute seawater for approximately one year. Samples were weighed and photographed before and after the year long test. These results were compared to a constant immersion field test, where similar specimens were immersed in a constant immersion seawater tank for approximately one year in another investigation [1].

Energy Dispersing Analysis by X-ray (EDAX) and Scanning Electron Microscopic (SEM) analyses were performed on the explosively bonded samples. The surface evaluation techniques were used to examine the bonded interface of the materials described above. The surface analysis yielded information on the chemical makeup of the interface layers and a visual look at these layers.

II. Results and Discussion

Corrosion phenomena at interfaces or transition joints has been very detrimental to the successful use of materials for naval applications and these are the areas where most material failure occurs. Two types of corrosion are basically responsible for this material failure, galvanic corrosion and crevice corrosion. The two work in a synergetic manner to cause material deterioration and eventually material failure. This investigation is an attempt to characterize the interface and the materials which comprise this interface and make a comparison between two types of interfaces, bonded and electrically connected interfaces. The bonded interface of the explosion welded material is both strong and resistant to corrosive environments. These traits make it a viable alternative to conventional bolted or welded interfaces. This discussion for convenience has been divided into three sections: (1) electrochemical studies (laboratory tests), (2) field tests and (3) SEM and EDAX analyses.

Section 1. Electrochemical Studies

A comparison was made between the galvanic corrosion behavior of explosively bonded aluminum alloy to steel alloy and aluminum alloy electrically coupled to steel alloy in ASTM substitute seawater. Figure 1 is a typical graphic presentation of galvanic currents versus time for aluminum alloy bonded to steel and aluminum alloy electrically coupled to steel. In the case of the electrical couple, the galvanic corrosion current measurements exhibit the classical decrease in current with respect to time following the galvanic corrosion process. As galvanic corrosion proceeds the two metals are shorted (in this case steel alloy and aluminum alloy), making them approach a mutual potential. As the potentials converge, the corresponding galvanic current decreases with time.

In sharp contrast, the explosively bonded couple generates a very negligible galvanic current that does not appreciably change with time (small magnitude of current measurements). This observation implies that no detectable corrosion occurs between the aluminum and steel interface.

Except for some surface activity in the beginning phases of testing (visible corrosion products on both surfaces in seawater), there was little fluctuation observed for the galvanic current measurements. The galvanic corrosion behavior was consistent for other alloys studied and showed similar current-time relations.

Figure 2 is a typical plot of the galvanic potentials (also measured during the galvanic experiment) as a function of time for aluminum coupled to steel. Galvanic potential measurements of electrically coupled materials showed similar behavior to that of explosively bonded materials. This comparison is quite different from the galvanic currents, where there is a drastic distinction between explosively bonded and electrically connected couples. The potentials of this connection are approximately -0.780v (vs SCE), and show constant behavior during the test range of 90 days. The fluctuation of potentials in the initial stages is consistent with the fact that surface activity is greater in the early stages of measuring. Visual observations of these materials concur with the galvanic current-time results. There were no signs of deterioration of interface where the explosively bonded materials are bonded and virtually no surface activity was observed after 45 days of testing.

Crevice corrosion occurs at an area of joining, such as at a lap joint, beneath surfaces, and spaces where collection of moisture is possible. Because of the physio-chemical nature of the explosion bond, the crevice or dead space is eliminated and thus removes one requirement for galvanic/crevice corrosive interactions.

Galvanic corrosion is the deterioration of metal as a result of the coupling of two dissimilar materials in a medium and galvanic current flow due to the difference in their potentials. The crevices allow electrolyte to collect (in this case seawater) which facilitates the galvanic corrosion process (allows a path for electrons). The elimination of the crevice, ensures the removal of this path for electrons to flow (collection of electrolyte). This agrees with the observation made by Carpenter [6] for aluminum explosively bonded to steel and in 3.5% NaCl water solution showed no accelerated corrosion along the bond zone. Naval hardware utilizing explosively bonded materials have been found to perform well in the harsh marine environments [7]. Again, the elimination of the galvanic and crevice corrosion effects are attributed to the success of explosively bonded materials.

Open circuit potential measurements (OCP) were made in ASTM substitute seawater. Each specimen was approximately $1.27\text{cm} \times 1.27\text{cm}$ and were mounted in EXTEC XL14730 Epoxy resin/XL14733 hardener. The types of specimens studied were:

- a. uncoupled aluminum
- b. uncoupled steel alloy
- c. bonded steel and copper-nickel (70%:30%)

- d. bonded steel and aluminum
- e. bonded steel/titanium/aluminum
- f. bonded aluminum/titanium/copper-nickel (70%:30%)

The open circuit potentials were measured with a Keithley 195A Digital Multimeter and a saturated calomel electrode (PAR model K0077 with vycor tip) as the reference electrode. The period of measurement was every 24 hours over a five month duration. During each measurement the vycor tip of the SCE was placed within distance of 1.48 cm from the test specimen. A volume of 250 milliliters of test solution was used for each cell. Evaporation was compensated for by the periodic addition of distilled water.

Table 1 is a list of various materials studied and their open circuit potentials. The potentials shown in Table 1 are average values of OCP over a span of thirty day. A comparative study of OCPs versus Time of aluminum, copper-nickel (70%:30%) and aluminum bonded to copper-nickel (70%:30%) has been performed. A typical plot of OCP versus Time is shown in Figure 3. The potentials for the explosively bonded pair were slightly more negative than aluminum, when compared to both of the uncoupled metals. This should be expected since copper-nickel is cathodic to aluminum and drives the potential of the bonded pair in the negative direction. The fluctuations in the initial stage of testing can be attributed to surface activity or corrosion (sample showed visible corrosion products) of the two alloys.


Another factor that contributed to this fluctuation is the fact that the bonded pair behaves like a galvanic couple. The potential of this couple is close to the open circuit potential of aluminum. The single components showed only constant behavior during the test period.

Consistent with theory, the open circuit potentials of galvanically coupled materials should change with time (shorting effect). The mechanism for this variation is that the more noble component (e.g. steel) has a tendency to drive the less noble component (e.g. aluminum) to more cathodic potentials. Open circuit potentials of single specimens should change only as the surface activity changes as a function of time (since no current is flowing between the working and reference electrodes). Because of the depletion of oxygen (stagnant solution) corrosion appears to be slow after about 45 days for the explosively bonded materials (constant behavior shown in Figure 3).

Visually corrosion products were observed on all surfaces tested. There was no sign of corrosion at the interfaces which remain unaffected by the corrosive environment. Figure 4 shows the comparative behavior of three explosively bonded materials. After about 45 days the potentials for the three explosively bonded materials converged.

TABLE 1.

OPEN CIRCUIT POTENTIAL MEASUREMENTS MADE ON VARIOUS
ALLOYS AND METALS IN ASTM SEAWATER

| <u>METALS/ALLOYS</u> | <u>POTENTIALS (VOLTS)</u> vs SCE | <u>STABILITY</u> |
|-------------------------------------|-------------------------------------|---|
| TITANIUM | +0.0989V | <p>MORE NOBLE</p>  <p>LESS NOBLE</p> |
| STAINLESS STEEL | +0.0695V | |
| MONEL | -0.1135V | |
| COPPER-NICKEL | -0.1820V | |
| CARBON STEEL | -0.7100V | |
| ALUMINUM | -0.7290V | |
| ALUMINUM:TITANIUM:STEEL | -0.685V | |
| ALUMINUM:TITANIUM: COPPER-NICKEL | -0.759V | |
| ALUMINUM:STEEL | -0.764V | |

The plot in Figure 4 suggests (1) surface activity influences the potentials in the early stages of measuring and (2) that the explosive bonded interfaces are stable in corrosive solution after about 45 days. The open circuit potential of copper-nickel is about -0.182v (vs SCE), stainless steel is +0.0695v (vs SCE) and aluminum is about -0.729v (vs SCE). The explosively bonded materials involving these combinations of individual ones have potentials between -0.750v and -0.900v (vs SCE).

Section 2. Field Tests Studies

Samples exposed to marine atmosphere were taken out after 1 year, cleaned, reweighed and photographed. The interfaces on each bonded material was examined for loss of integrity and material failure. Corrosion products were observed on the surface of the bonded materials but the interface showed no sign of material failure associated with dissimilar metals joints. From weight loss measurements, a corrosion rate of approximately 2.0 mils per year was calculated for explosively bonded material of aluminum bonded to steel.

Explosively bonded materials were subjected to two types of immersion tests. One was dynamic and the other was static, one a field test and the other a laboratory test. After an interval of one year in ASTM seawater (laboratory immersion test) the interfaces were not affected by the chloride environment.

A similar immersion test done in the field concurred with the laboratory test. The field test has been ongoing for approximately three years with no effect on the interface.

Section 3. SEM and EDAX analysis

Four explosively bonded specimens were analyzed using SEM and EDAX. The samples examined were (1) aluminum bonded to steel, (2) copper-nickel bonded to steel, (3) aluminum bonded to titanium bonded to steel, (4) aluminum bonded to titanium bonded to copper-nickel. For all but one of the samples there was an intermetallic layer at the interface. The only sample not containing at least one intermetallic layer was the copper-nickel bonded to steel specimen.

The intermetallic layer is the area where both metals are said to have formed a chemical and a physical bond. In the first specimen, aluminum bonded to steel, SEM photographs showed four distinct layers.

The four layers are aluminum (layer A), interlayer I (layer B), interlayer II (layer C), and steel (layer D). In Figure 5, three of the four layers are clearly shown. Layers B and C were found to contain aluminum surrounded by iron particles and iron surrounded by aluminum particles, good indication physical chemical bonding. There is excellent agreement between EDAX chemical spectral analysis and the SEM photographic analysis. Figure 6 is an EDAX spectra of the interlayer II showing the presence of aluminum and iron. The chemical composition of layer C is given in the inset of Figure 6. The table shows a layer rich in aluminum (73%) and iron (23%). Based on visual observations, field tests, surface analysis and electrochemical data the interface between aluminum bonded and steel performed well in aggressive marine environments.

A strong factor for the good performance of explosively bonded materials is the elimination of crevices and the use of a filler metals found in conventional welding. This eliminates the synergistic effect of galvanic (dissimilar metals) and crevice (the collection of seawater in unreachable spaces) corrosion. The fact that a chemical bond is formed at the interface ensures non-separation of the metals by mechanical means only. With a welded or bolted joint configuration, this assurance cannot be made. Figures 7 and 8 are SEM photographs of aluminum bonded to titanium and copper-nickel, and EDAX of the interface between aluminum and titanium. The SEM photograph shows very distinct bonding patterns between the three metals.

These strong interfacial patterns underscore the fact that there is no limit to the combination of materials that can be joined through explosive bonding.

Based on the corrosion tests and EDAX data, there are endless possibilities for use of these materials in aggressive environment. Their usage will definitely improve service life cycles of structures and equipment exposed to marine environment.

The only explosively bonded material without an intermetallic layer is copper-nickel bonded to steel. The performance of this material in the marine environment was comparable to the other materials with distinct interlayers.

The EDAX spectral analysis showed no interlayer but near the interface a composition of copper (65%), nickel (28%), and traces of iron, silicone and aluminum on the copper-nickel side. The composition on the steel side is iron (94%) with traces aluminum and silicone. The explanation is that the interlayer is present but indistinguishable. The fact that there is some sharing of trace metals is a good indicator that a minute indiscreet layer might exist.

III. Conclusions

Based on the results obtained from the field tests and electrochemical studies, it can be concluded that explosively bonded materials perform well in chloride/marine environments. When galvanic and crevice corrosion are major concerns in material selection, explosively bonded materials appears to be an attractive alternative. The data presented in this paper provide evidence for the use of explosively bonded materials in marine environments for naval applications where conventional joints have not been successful.

The electrochemical studies show that (1) explosively bonded materials do not behave like traditional galvanically coupled components and (2) the galvanic potentials are fairly stable in seawater (chloride medium).

The field tests results agree with the electrochemical studies and show that explosively bonded materials do perform well in real time marine environment.

The surface analysis results show strong evidence of chemical and physical interactions between explosively bonded components. The EDAX analysis shows an interlayer (Figure 6) rich in both components (aluminum and iron). This fact suggests that the interface is a combination of both alloys. The surface analysis also suggests that a variety of alloy combinations are possible and the similar interfacial mixing is achieved. Recent efforts have proven that molybdenum can be bonded by the explosive bonding process [9].

IV. References

1. Oberle, Hugues, Masters of Science Thesis, "Combined Influence of Heat and Immersion Corrosion on the Tensile-Shear Strength of Aluminum-Steel Explosively Welded Plates", Florida Atlantic University, December 1991.
2. Keelean, Michael R., Masters Thesis, "Microscopic Investigation of Interface Corrosion of Steel-Aluminum Explosively Bonded Material Exposed to Periodic Seawater Spray", Naval Postgraduate School, September 1976.
3. US Patent No. 3,137,937, "Explosive bonding", June 1964.
4. ASTM 1991 Annual Book of Standards, Section 11, Water and Environmental Technology, Volume 11.02 Water (II), D-19 on Water, D 1141-90, pp 423-4, Philadelphia, PA 19103, 1991.
5. Model 350A Corrosion Measurement System Operating and Service Manual, EG&G Princeton Applied Research, USA, 1980.
6. Carpenter, S.H., "Explosive welding: a review", Shock waves and high-strain rate phenomena in metals, International conference on metallurgical effects, pp. 941-959, 1980.
7. Lindsey, N., "Corrosion Study of Materials used in the Manufacture of Grounding/Bonding Straps for Naval Applications", unpublished report from NSWC, pp. 34, White Oak, MD 20903-5000.
8. Banker, J. G. and C. R. McKenney, "Explosion-Bonded Metals for Marine Structural Applications" paper presented to the Society of Naval Architects and Marine Engineers, San Diego, CA., 18 November 1970.
9. Sharp, William F., "The Explosion Cladding Process", Engineering Designer, September/October 1979.

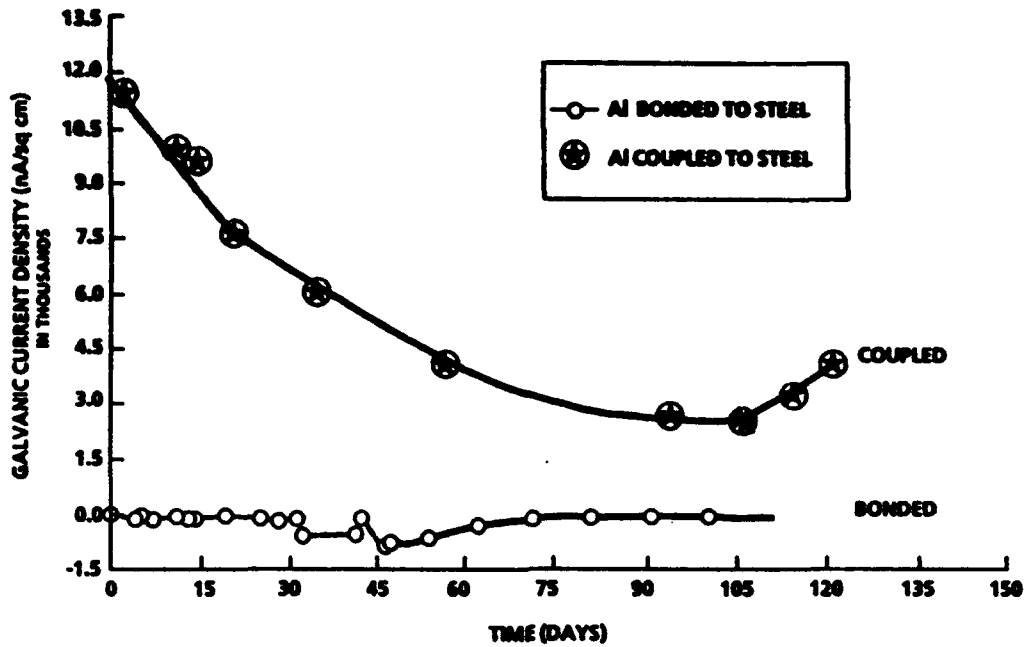


FIGURE 1. GALVANIC CORROSION CURRENTS OF BIMETALLIC MATERIALS IN ASTM SUBSTITUTE SEAWATER VERSUS EXPOSURE TIME

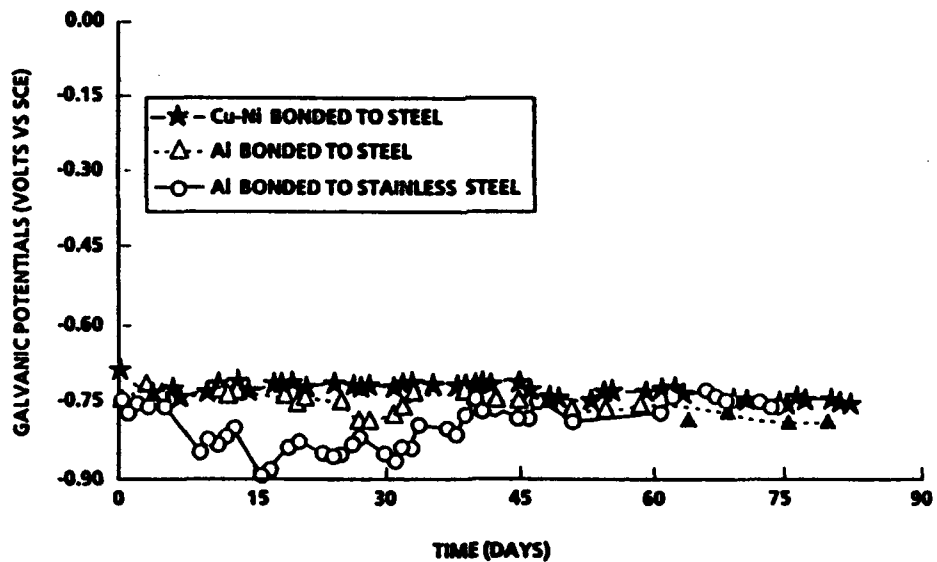


FIGURE 2. GALVANIC POTENTIALS OF EXPLOSIVE BONDED MATERIALS IN ASTM SUBSTITUTE SEAWATER AS A FUNCTION OF TIME. A COMPARATIVE STUDY

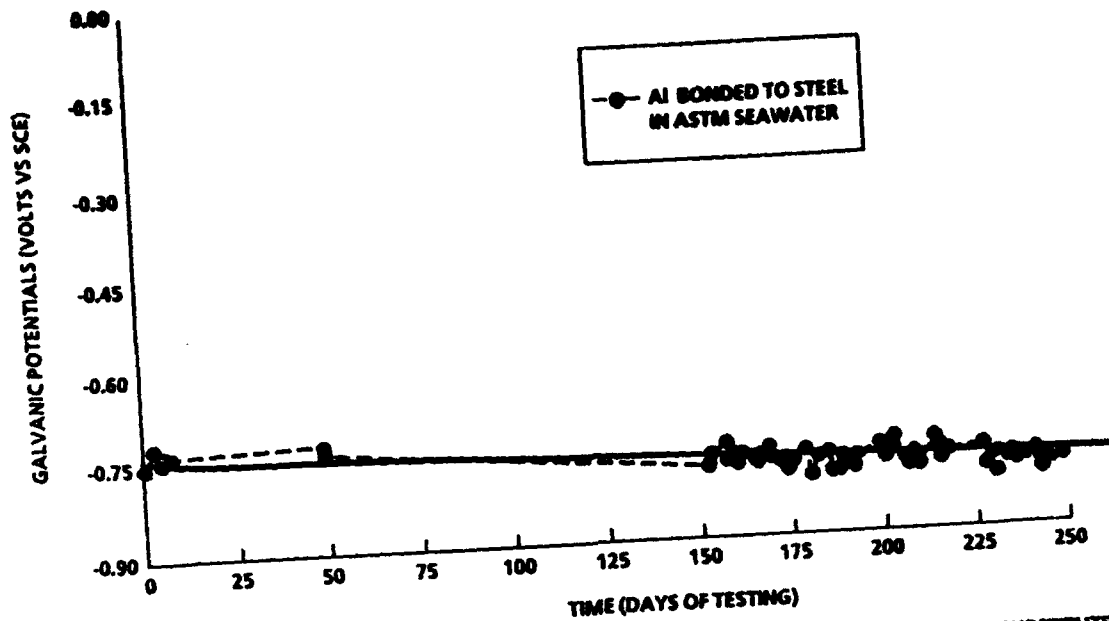


FIGURE 3. OPEN CIRCUIT POTENTIAL MEASUREMENTS OF BIMETALLIC MATERIAL IN ASTM SUBSTITUTE OCEAN WATER AS FUNCTION OF TIME

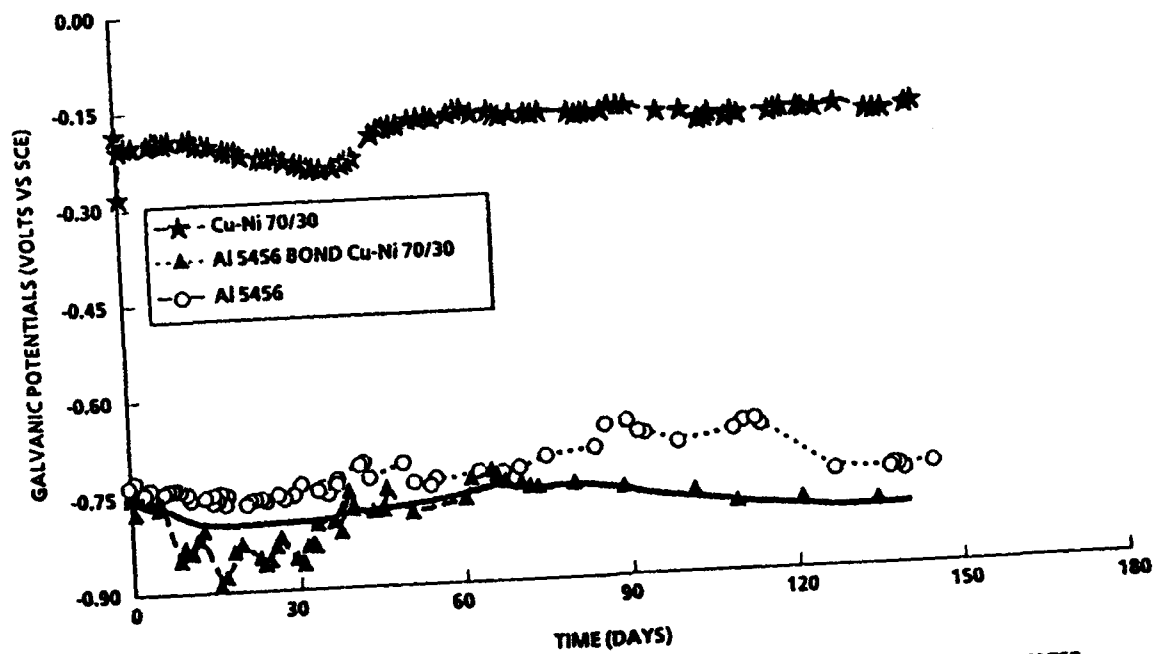


FIGURE 4. OPEN CIRCUIT POTENTIALS OF SELECT MATERIALS IN ASTM SUBSTITUTE OCEAN WATER AS FUNCTION OF TIME

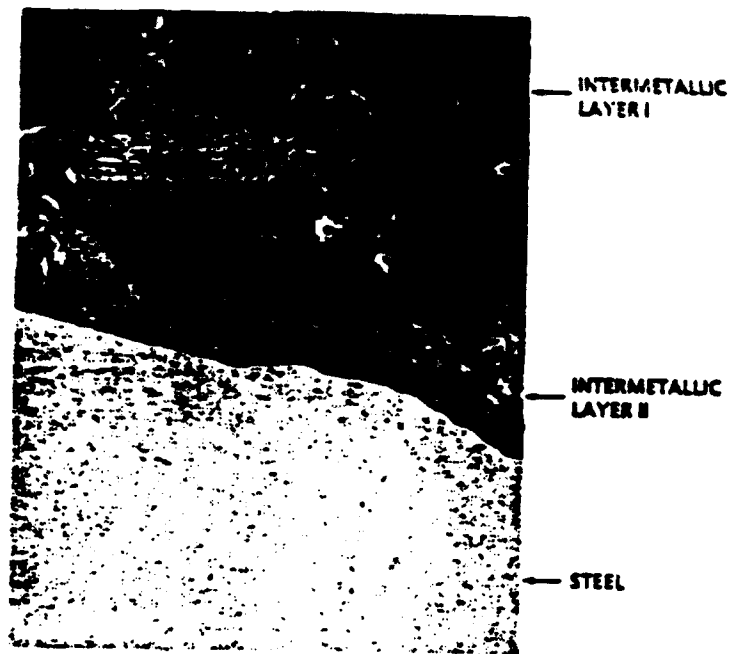
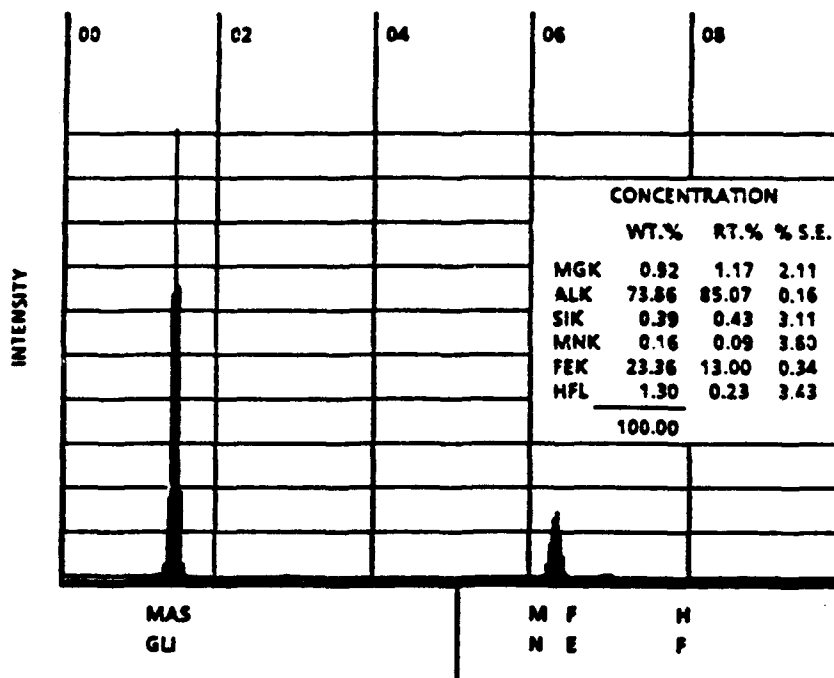


FIGURE 5. SEM PHOTOGRAPH OF ALUMINUM BONDED TO STEEL INTERFACE AT 500X (POLISHED SURFACE)



CURSOR (KEV) = 05.120

ENERGY (KEV) ATOMS PRESENT

FIGURE 6. EDAX SPECTRUM OF INTERLAYER AREA II OF Al BONDED STEEL (POLISHED SURFACE)

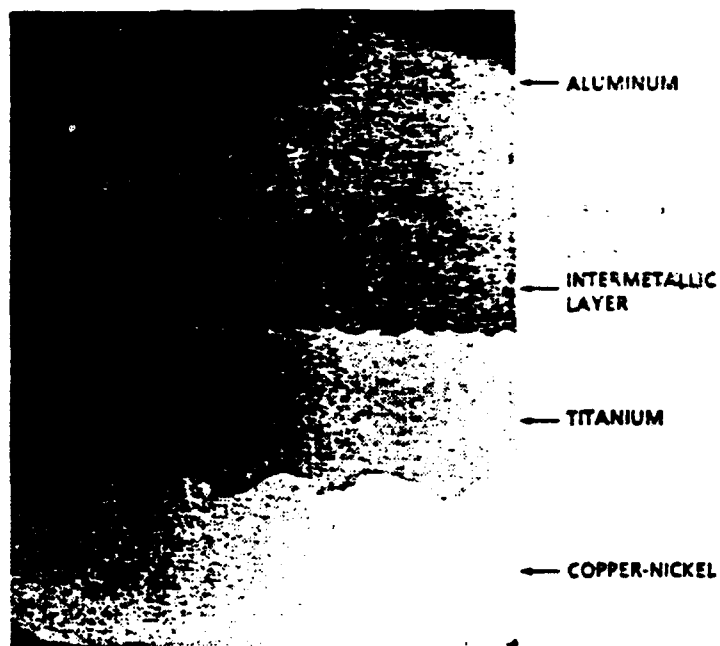
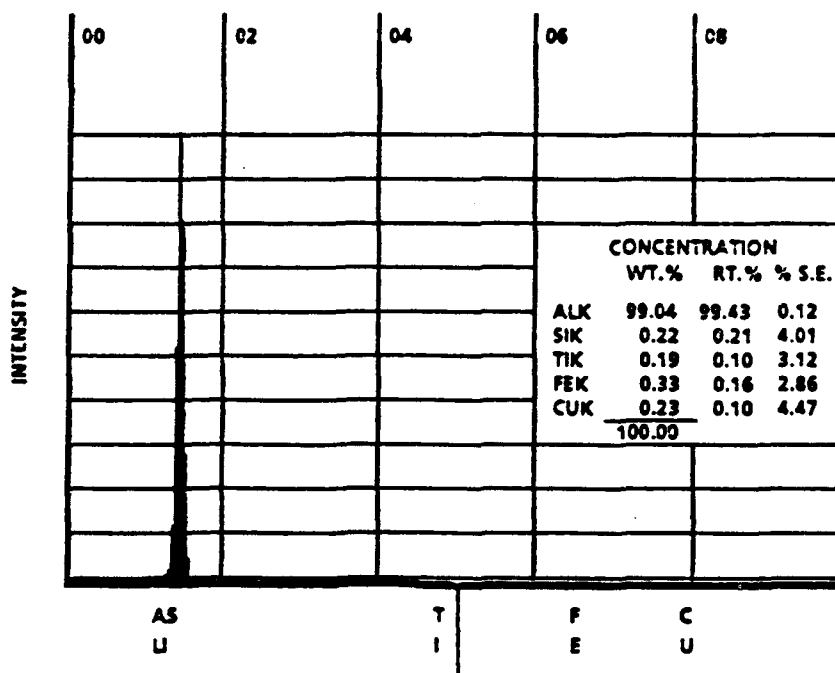


FIGURE 7. SEM PHOTOGRAPH OF ALUMINUM BONDED TO TITANIUM BONDED TO COPPER-NICKEL AT 15X (POLISHED SURFACE)



CURSOR (KEV) = 05.120

ENERGY (KEV) ATOMS PRESENT

FIGURE 8. EDAX SPECTRUM OF INTERLAYER (E) 0.5 X 0.5 MM AREA

Corrosion and Stress Corrosion Cracking of a Marine Steel in Artificial and Natural Sea Water

M. A. Golozar

Materials Engineering Department,
Isfahan University of Technology,
Isfahan, IRAN.

A. Saatchi

Materials Engineering Department,
Isfahan University of Technology,
Isfahan, IRAN

Abstract

In order to determine the Stress Corrosion Cracking susceptibility of a selected marine steel with and without welding, using various welding techniques, the following tests were performed: Constant strain tests were carried out in Persian Gulf for seven months. In the laboratory, slow strain rate tests were done in natural sea water and in 3.5% NaCl solution. Also in laboratory corrosion rates of the base metal and weld metals were measured using weight loss measurements and electrochemical polarization tests. In addition, Scanning Electron Microscopy was employed to investigate the nature and characteristics of the fracture surfaces of tested specimens. The results indicated that: 1. all the weld metal zones were anodic compared to the base metal, thus corroded with a higher rate. 2. Arc welding with coated electrode exhibited better mechanical and corrosion properties, compared with the other welding techniques which were used in this research work. Neither the steel nor its weldments showed any sign of SCC susceptibility.

Key terms: Stress Corrosion Cracking, Marine Steel, Weldments, Persian Gulf

Introduction

Stress Corrosion Cracking (SCC) often causes unexpected costly failures. This is due to the lack of visual evidence of corrosion as compared with uniform and localized corrosion. SCC is a cracking phenomenon under conjoint action of tensile stress and corrosion, which happens for some metals in specific environments. In other words there are three main factors acting together in SCC. 1. Tensile stress, which can be working or designed stress, residual and thermal stresses due to welding and other operations. 2. corrosion environment which will be affected by major and minor chemical composition, temperature, velocity or turbulence, and even biological activities of the environment. 3.

The susceptibility of the metal to SCC, which can be affected by the chemical composition, micro structure, thermal and mechanical operations.

Sea water is a complex biochemical broth. Its nominal chemical composition is 2.9%NaCl plus 0.4%MgSO₄, but in reality it contains trace of just about everything one can imagine⁽¹⁾. Its high chlorinity makes it corrosive to most of metals and alloys. Chloride also causes localized corrosion and SCC in many metals. The action of biological organism also create a complex situation for predicting the performance of alloys in sea water. So whereas there are cases that the results of SCC of steel in national sea water is identical to the results in 3.5% NaCl solution,^(2,3) there are other cases where different behavior has been reported⁽⁴⁾.

The purpose of this research was to evaluate the SCC susceptibility of a domestically produced selected marine steel and its weldments in Persian Gulf water. Also the effects of various welding techniques were studied. Constant strain tests were performed in Persian Gulf for 7 months. In laboratory, Slow Strain Rate (SSR) tests were performed in natural sea water and also in 3.5% NaCl solution. In addition, the corrosion rates of the base metal and the weld metal were measured using weight loss and electrochemical polarization tests. Optical and Scanning Electron Microscopes were also employed to investigate the micro structure of weld metal, heat affected zone (HAZ) and fracture surfaces of the specimens, respectively.

Experimental

Specimens preparation. The specimens for various tests were cut from 6 mm plate of the selected marine steel. The chemical composition and mechanical properties of this steel are shown in Tables 1 and 2 respectively. For weldments the one sided V notch was used. The specimens were pre heated to about 150 °C prior to welding. The low hydrogen electrodes were dried at 100 °C before being used for welding. The following welding techniques were used: For constant strain tests : 1. Metal Arc with coated electrode type AWS6013, 2. Tungsten Metal Arc with uncoated electrode made from the base plate steel, 3. Metal Arc with coated electrode type super S1100, 4. Acetylene gas welding using filler metal from the base steel. For immersion, polarization and SSR tests the following testing procedures were used: 1. Arc Weld using coated electrode type AWS7016-1, 2. Tungsten Metal Arc with inert gas and coated electrode type OK73-08.

Immersion Tests, Immersion tests were used to measure the corrosion rate of the base metal, with and without welding, using ASTM G1 standard. The specimens dimensions were 20x50x2 mm.

Polarization Tests. Cathodic and anodic polarization of the steel and weld metals were determined by potentiodynamic technique based on ASTM G5-87. Corrosion rate of the specimens were also calculated using linear polarization technique. The electrochemical measurements were performed using standard potentiostat, Wenking model ST72, with Ag/AgCl reference electrode.

Constant Strain SCC Tests. Fig. 1 shows the details and the type of the specimen which were used for these experiments. Constant Strain SCC tests were performed according to ASTM G39. The specimens were exposed to Persian Gulf water, in Bandar Abbas Coasts at various depths of 5, 7, and 9 meters for 7 months. The applied stress on all the specimens were yield stress of the steel (54 Kg mm²). In order to avoid galvanic and crevice corrosion the nuts and bolts at both ends of the specimens were covered with a special antirust marine primer.

Slow Strain Rate (SSR) Tests. Fig. 2 shows the details of the specimens which were used in SSR tests. For these tests a SSR testing machine, based on the recommendation of the Parkins⁽⁵⁾, was designed and constructed. The strain rate used was 3×10^{-6} sec⁻¹. This was based on the previous results obtained^(6,7). Stress - strain curves for specimens without welding and welded in the gauge length area using various techniques were obtained. These curves were plotted in various conditions including: air, seawater and 3.5% NaCl solution. The fracture surfaces of the SSR specimens were studied using a Scanning Electron Microscope, JEOL model S6400.

Results and DISCUSSION

Fig. 3 shows the corrosion rate of the specimens with and without welding in Persian Gulf water and a 3.5% NaCl solution as determined by Laboratory Immersion Test. It is shown that welding has decreased the corrosion rate. Inspection of the specimens indicated that the weld metal has corroded preferentially and cathodically protected the base metal. This is obviously related to the electrode composition and does not seem to be influenced by welding technique (compare specimen 1 and 3, i.e. same electrode, but different welding technique). Electrode material in specimen 4 contained some Cu and Ni and therefore resulted in less protection and thus higher corrosion rate (Compare specimens 2 and 4, i.e. same welding technique but different electrode materials).

Fig. 4 shows the potentiodynamic polarization curves of the base metal and weld metals, in Persian Gulf water and in a 3.5% NaCl solution. All the data on these curves have been summarized in

table 3. The corrosion rates obtained for the base metal and weld metal using linear polarization technique are also summarized in Table 3. It is noted that all the specimens show a lower corrosion rate in Persian Gulf water as compared with 3.5% NaCl solution. It is also noted that the corrosion potential of the weld metals are more active than the base metal and thus the weld metal can cathodically protect the base metal. These are in agreement with corrosion rates obtained by immersion tests.

Fig. 5 shows the typical constant strain specimens immersed at depths of 5, 7 and 9 meters below sea water surface for 7 months in Persian Gulf (Banda Abasi Co. Ltd. area) and after removing. Severe swelling was observed in Persian Gulf water specimens, they were not tested. No cracking was observed in neither of specimens. These results indicate that neither the base metal, nor the weld specimens were susceptible to SCC in Persian Gulf water.

Fig. 6 shows the stress - strain curves for the steel with and without welding, as was obtained by SSR testing machine. The specimens were tested in air as well as in Persian Gulf water and 3.5% NaCl solution. The results of these curves are summarized in Fig. 7. It is noted that only for materials without welding, there is significant reduction in ductility of the specimen tested in air as compared with sea water and 3.5% NaCl solution. Although this is not to that extent to be related to SCC susceptibility.

Fig. 8 shows the typical SEM of the fractured surfaces of the specimens with and without welding, tested by SSR testing machine in air, Persian Gulf water and a 3.5% NaCl solution. All the fractured surfaces showed dimpled fracture and indicated extensive ductility which is the evidence of non susceptibility to SCC. In Fig. 8C there are areas which were suspected as being cleavage brittle fracture. Inspecting the corresponding stress - strain curve in Fig. 7, clearly indicated the lack of any differences in mechanical properties of specimens tested in air compared with Persian Gulf water and 3.5% NaCl solution. Therefore, it was clearly concluded that such areas as in Fig. 8C were due to the corrosion products and not due to brittle fracture.

Conclusion

1. All the weld metals were anodic to the base metal and provided protection for it. The degree of protection depended upon the composition of the electrode and was independent of welding technique.
2. Constant strain specimens immersed in Persian Gulf water at

the depths of 5, 7 and 9 meters, for 7 months, also did not show any indication of SCC susceptibility, for the steel with and without welding.

3. SSR test results did not show any indication of SCC susceptibility for the steel with and without welding.

4. SEM fractographs of fractured surfaces of SSR tests also did not show any indication of SCC susceptibility for the steel with and without welding.

5. Neither the base metal nor its weldments were susceptible to SCC in Persian Gulf water

References

1. G. A. Gehring, *Materials Performance*, 9 (1987): p. 9.
2. G. Sandoz, *Stress Corrosion Cracking in High Strength Steels and in Titanium and Aluminum alloys*, B. F. Brown, Ed., Naval Research Laboratory, (1972).
3. G. Sandoz, *Metallurgical Transactions*, 2 (1971): P. 1055.
4. H. P. Lockie, A. W. Loginow, *Corrosion*, 14 (1968): P. 291.
5. R. N. Parkins, *ASTM STP 665*, (1979): P. 2-25.
6. M. Sobhani, M.Sc. Theses (1990), Materials Engineering Department, Isfahan University of Technology, IRAN.
7. M. Sobhani, M. A. Golozar, A. Saatchi, *First Symposium on the Iraian Industrial Corrosion*, IRAN, (1992)

Table 1. Chemical composition of the selected marine steel

| Element | C | Mn | Si | P | S | Cr | Ni | Cu | Fe |
|---------|-------|-------|-------|-------|-------|-------|-------|-------|-----|
| Wt.% | 0.251 | 0.741 | 0.549 | 0.013 | 0.013 | 0.985 | 0.594 | 0.394 | Bal |

Table 2. Mechanical properties of the selected marine steel

| | | |
|-----------------------|---------------------|-------|
| Density | g cm ⁻³ | 7.85 |
| Hardness | RB | 92 |
| Fracture Strength | Kg mm ⁻² | 65 |
| Modules of Elasticity | Kg mm ⁻² | 13890 |
| Tensile Strength | Kg mm ⁻² | 79 |
| Yield Strength | Kg mm ⁻² | 54 |

Table 3. Data obtained from polarization and immersion tests

| Corrosion environment | Polarization test | | | Immersion test |
|--|--------------------------|---|-----------|----------------|
| | E _{corr.} mv | I _{corr.} μA cm ⁻² | CR mpy | CR mpy |
| Selected steel without welding | | | | |
| Persian Gulf water | -688 | 26 | 11.8 | 2.1 |
| 3.5%NaCl solution | -658 | 38.2 | 17.3 | 3.7 |
| Welded steel, Metal Arc with coated electrode, OK 73/08 | | | | |
| Persian Gulf water | -694 | 24.6 | 11.1 | 1.95 |
| 3.5%NaCl solution | -689 | 48.8 | 22.1 | 2.62 |
| Welded steel, Metal Arc with coated electrode, AWS 7016-1 | | | | |
| Persian Gulf water | -709 | 32.2 | 14.6 | 1.7 |
| 3.5%NaCl solution | -693 | 183.2 | 82.2 | 1.26 |
| Welded steel, Tungsten Arc with uncoated electrode, AWS 7016-1 | | | | |
| Persian Gulf water | -728 | 26 | 11.8 | 1.71 |
| 3.5%NaCl solution | -719 | 40.2 | 18.2 | 1.2 |

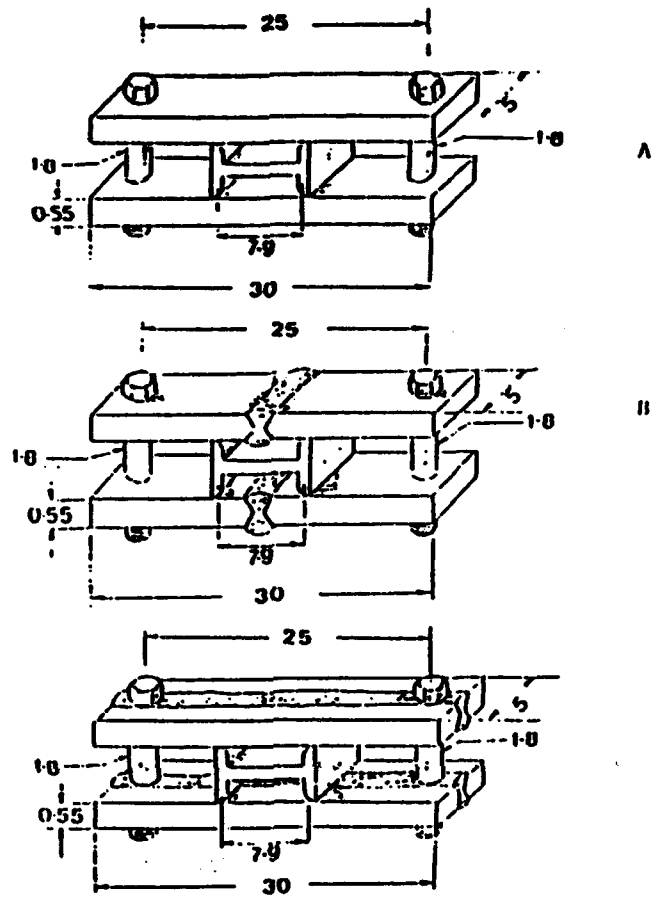


Fig. 1. the details of design of constant strain test specimens used in this study, (a) without welding, (b) transverse welds, (c) longitudinal welds.

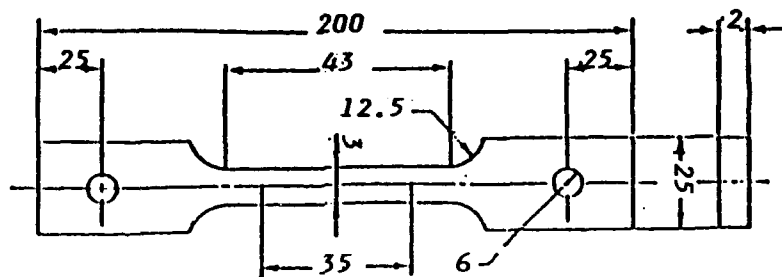


Fig. 2. The details of the tensile specimens used in SSR tests.

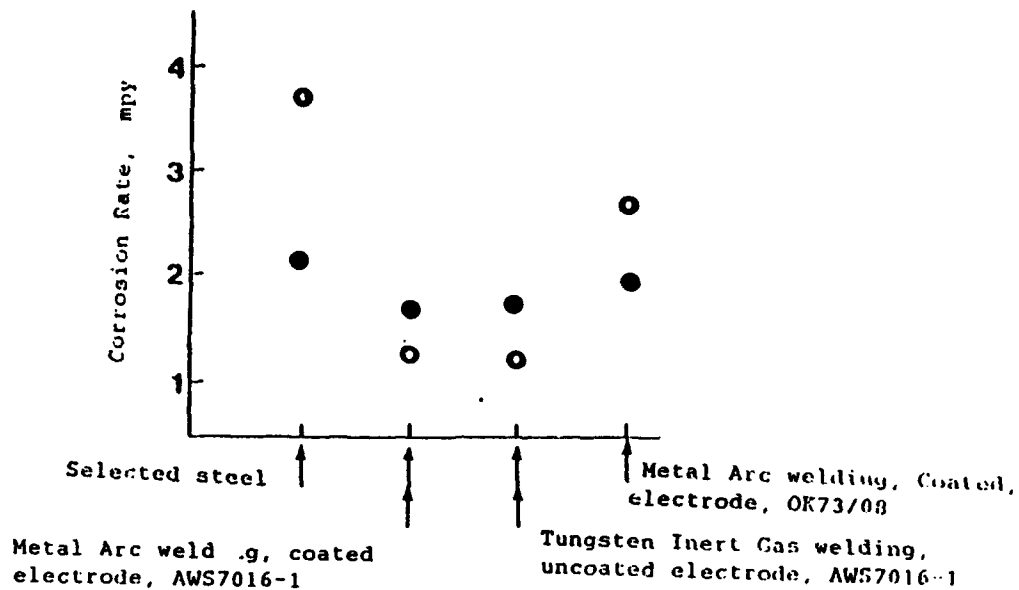


Fig. 3. Corrosion rate of the steel and its weldments as determined by immersion tests. Duration of the test: 45 days. ● Persian Gulf water, ○ 3.5%NaCl solution.

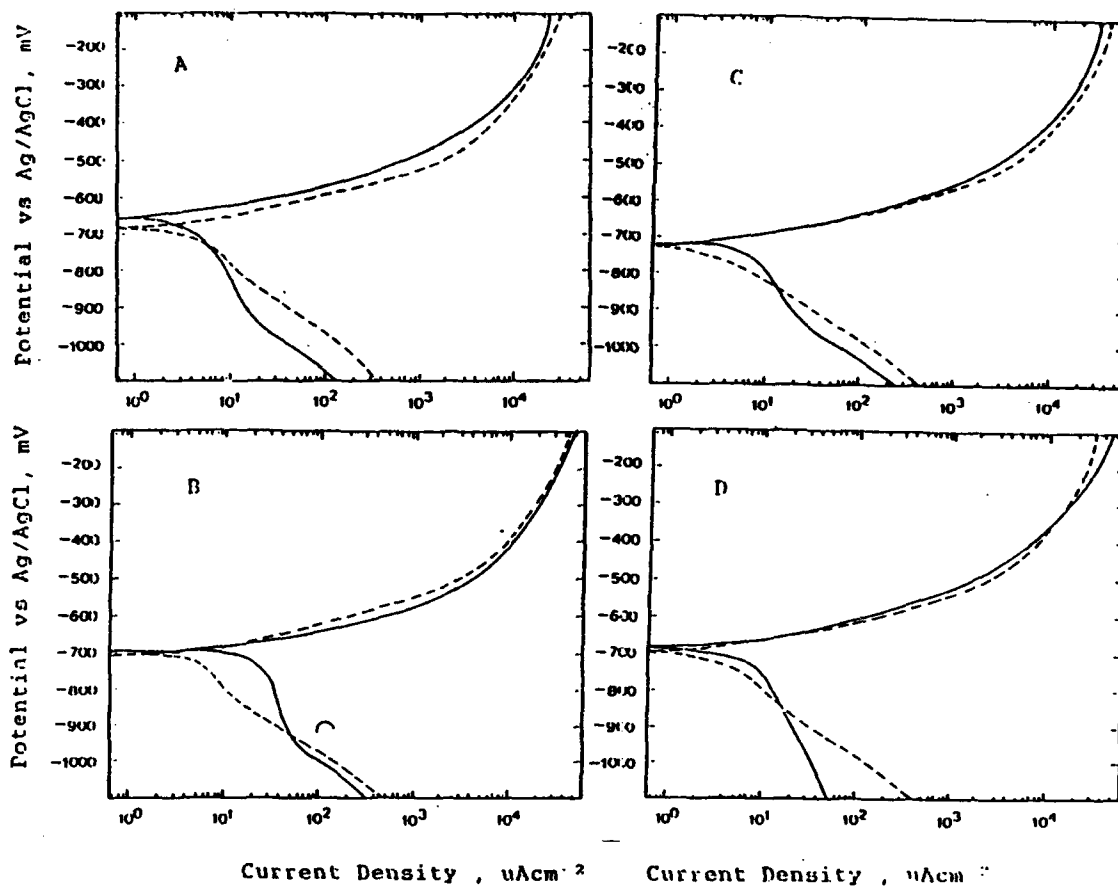


Fig. 4. Potentiodynamic polarization curve of the steel and the weld metals. (a) the steel, (b) Metal Arc welding with coated electrode AWS 7016-1, (c) Tungsten Inert Gas welding with uncoated electrode, (d) Metal Arc welding with coated electrode AWS 7016-1. Persian Gulf water, — 3.5%NaCl solution.

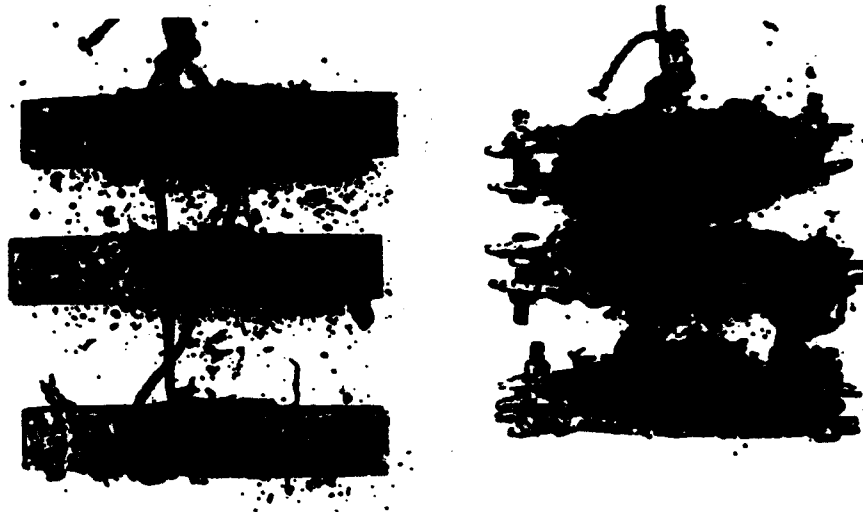


Fig 5

Fig. 5. The typical constant strain specimens immersed at the depth of 5, 7, and 9 meters for 7 months in Persian Gulf (Bandar Abbas), before and after cleaning.

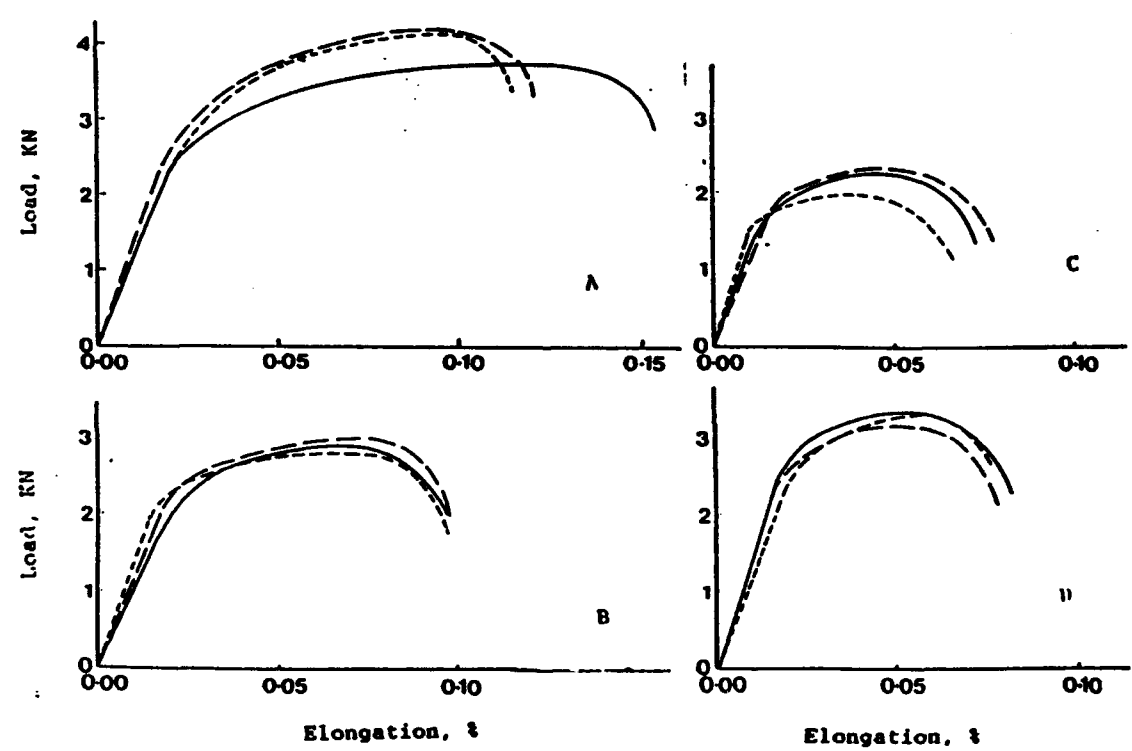


Fig. 6. Stress strain curves for tensile specimens as used by SSR testing machine with and without welding. (a) without welding, (b) Metal Arc welding with coated electrode AWS 7016-1, (c) Metal Inert Gas welding with uncoated electrode AWS 7016-1, (d) Metal Arc welding with coated electrode AWS 7016-1.
 — Air, Persian Gulf water, 3.5%NaCl solution.

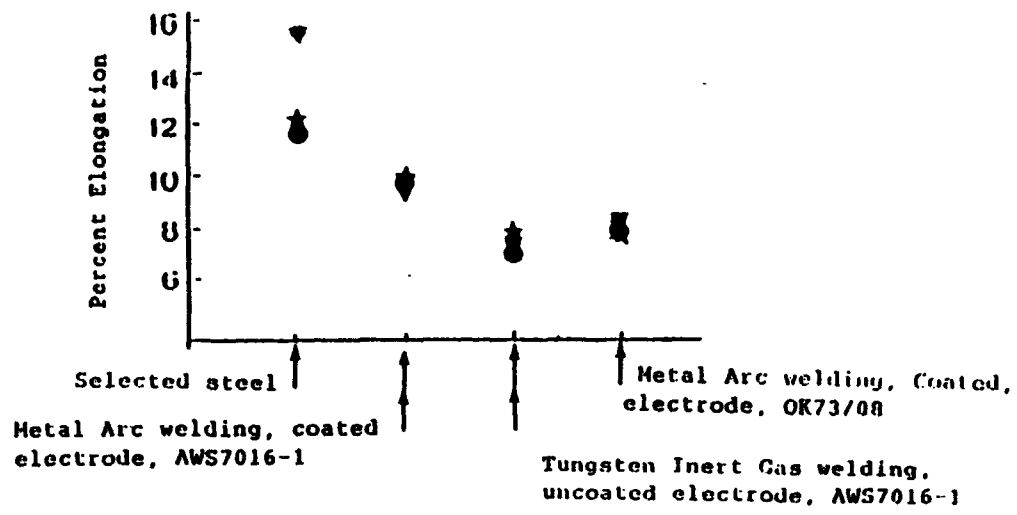


Fig. 7. Elongation to fracture obtained from tests of welds as shown in Fig. 6.

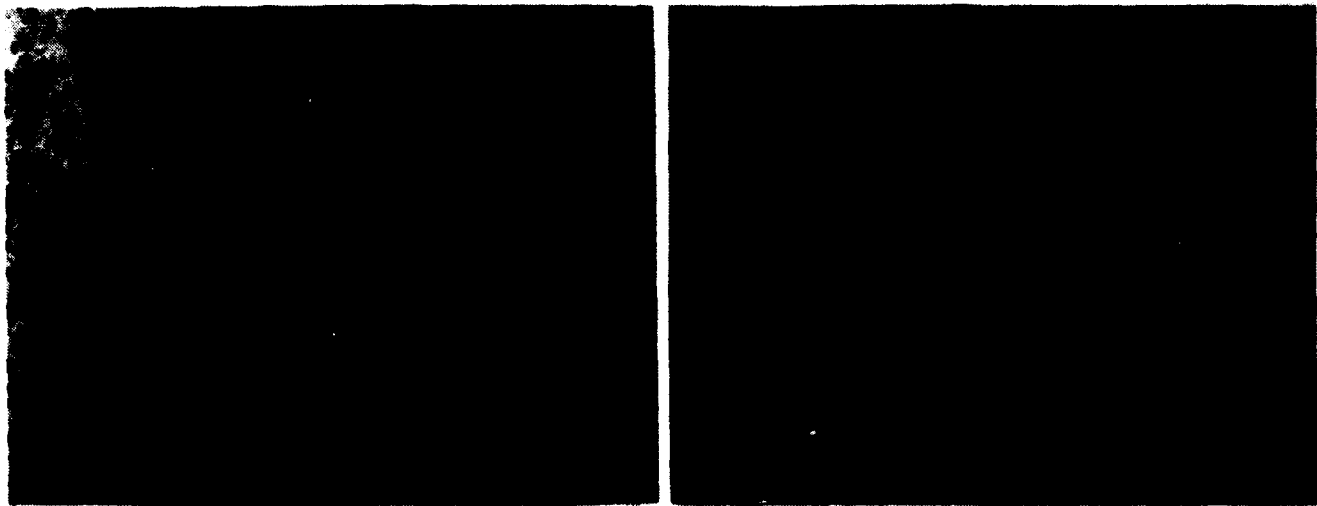


Figure 8a



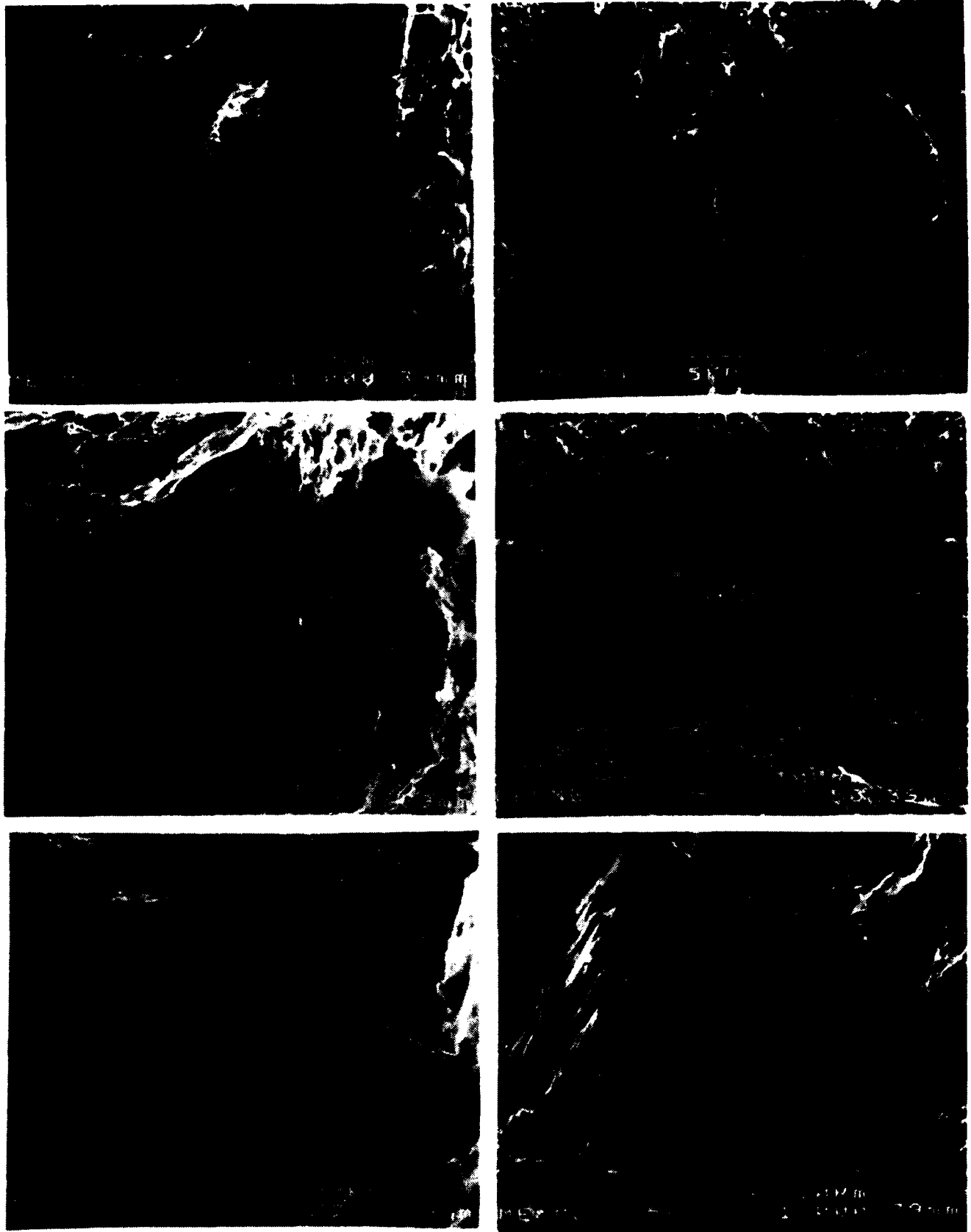


Fig.8. The typical SEM fractographs of the fractured surfaces of the tensile specimens with and without welding, as obtained by SSF tests. Top to bottom in: Air, Persian Gulf water, and 3.5%NaCl solution. (a) without welding, (b) Metal Arc welding with coated electrode AWS 7016-1, (c) Metal Inert Gas welding with uncoated electrode AWS 7016-1.

Environmental Degradation of Polymer Matrix Composite Exposed to Seawater

Victoria Stolarski
Department of Chemistry
Texas A&M University
College Station, TX 77843

Alan Letton
Polymer Technology Consortium
Texas A&M University
College Station, TX 77843

Walter Bradley
Department of Mechanical Engineering
Texas A&M University
College Station, TX 77843

L. R. Cornwell
Department of Mechanical Engineering
Texas A&M University
College Station, TX 77843

Abstract

This study focuses primarily on the effects of biofouling, (such as barnacles, algae, etc.) on composite surfaces which have been submerged in the Gulf of Mexico for six months. Adapting a technique developed by Perkinson¹, the surface of submerged samples are compared, using Fourier-transform infrared spectroscopy, to control samples previously subjected to a distilled water environment. Quantitative examination of the resulting infrared spectra gives insight into the negligible chemical changes taking place on the composite surface. Optical microscopy is also used to explore macroscopic degradation.

Key terms: polymer composite, FTIR, biofouling, degradation

Introduction

As our natural resources begin to diminish, oil companies will inevitably need to drill to deeper ocean depths. Hence, revolutionary changes must be made to replace heavy traditional materials with lighter, more buoyant, high strength alternatives, such as Fiber Reinforced Plastics, for oil drilling platforms. However, testing must be done to assure the stability and reliability of the polymer composites in a harsh seawater environment. Much work has been done to understand the effects of moisture absorption on the physical properties of high performance polymer composites. Most notably, Antoon and Koenig^{2,3} have examined the reversible and irreversible property losses due to plasticization by water of a diglycidylether of bisphenol-A (DGBA) epoxy resin as examined by Fourier-transform infrared spectroscopy (FTIR). Apicella and Nicolais⁴ also examined this plasticization phenomena using a tetraglycidyl-4,4'-diaminodiphenylmethane (TGDDM) resin crosslinked with diaminodiphenyl sulfone (DDS) in their book chapter. However, little work has been done to examine the effects of biofouling on epoxy resin or composite properties. Our work addresses the use of FTIR spectroscopy to examine the effects of microorganisms in Texas gulf water on several glass and fiber reinforced polymer composites.

Experimental

Seven polymer composite systems were obtained from Dow Chemical and submerged off the Texas coast for six months. System 1 is a TGDDM epoxy crosslinked with DDS and enhanced with T2C145 graphite fibers. System 2 is also a TGDDM/DDS epoxy with an aramid network and IM7 graphite fibers. IM7 graphite fibers were also used in System 3 but the epoxy is the tricyclic hydrocarbon, fluorene, again crosslinked with DDS. Systems 4 and 5 are glass reinforced with vinylester resins. They are Derakane 410 and 511 respectively. Systems 6 and 7 are also the Derakane vinylester resins but are reinforced with graphite fibers 410 and 511 respectively. Samples from each system were set aside prior to submersion in the Gulf for control purposes. However, to factor out the water contribution to surface alterations, the controls were submerged in distilled water. All samples were air dried for at least seventy-two hours before FTIR preparation. All other chemicals and solvents were obtained from Aldrich® and used as received.

Absorbance spectra in the mid-infrared region using 200 sample and reference scans at 4 cm^{-1} resolution were obtained using a Fourier-transform infrared spectrometer from Bio-Rad (FTS 60A). A difference spectra was generated by subtracting the normalized submerged spectra from the normalized control spectra⁵. Peak shifting, appearance, or disappearance indicates changes on the molecular level⁶.

Results and Discussion

Samples taken out of the gulf water were covered with algae, barnacles, and other unidentifiable organic matter. To prepare the samples for microscopic work, they were rinsed with swiftly running tap water to remove the algae coating. (Figure 1).

Optical microscopy showed no notable surface destruction (50-100x) (Figures 2-4). For spectroscopic work, the barnacles were removed with a nylon brush.

Initially, ATR spectra were attempted. Since the quality of the resultant spectrum is proportionate to the contact area between the sample and the prism, composite warpage, though minimal, gave unsatisfactory results. Adequate spectra were obtained by using an adaptation of a procedure developed by Perkinson¹. This includes filing the composite surfaces, removing any graphite or glass fibers from the filings, mixing them with spectrum grade KBr, and running pellets in transmission mode (Figure 5). Peak assignments were made using several sources⁷⁻⁹.

To test the sensitivity of the technique to changes on a molecular level, a TGDDM/DDS sample was subjected to chemical degradation by submersion in a fuming sulfuric acid (15% SO₃/H₂SO₄) environment for 24 hours. Figure 8 shows the resulting spectra before and after imposed degradation. The appearance of large peaks at 1266 and 1233 cm⁻¹ are attributed to sulfonation of the phenyl rings on the epoxy backbone. Furthermore, a decrease in the *para* semi-stretch region, 1516 and 822 cm⁻¹, confirms a decrease in the amount of *para* substituted rings as the sulfonation takes place. The 1023 cm⁻¹ peak is characteristic of a symmetric sulfite ion stretch. Lastly, the 1596 cm⁻¹ asymmetric phenyl stretch is enhanced due to the increase of electronegativity differences between the substituents once the sulfite ions are added to the ring. Included also are pictures by optical microscopy of the surface after acid degradation (Figure 6&7).

Transmittance spectra were run on the control and submerged composite surfaces of the seven different systems (Figures 9-15). Systems 1 and 7 show an epoxy peak at 890-906 cm⁻¹ in the submerged but not control samples (Figures 9 & 15). This could be attributed to either epoxy ring formation or incomplete cure. Since the submerged and control composites are the same resin systems, but not necessarily from the same plaque, curing variations will be present and are the most probable cause of the 906 cm⁻¹ peak. More over, the ring strain in the epoxy moiety makes it energetically more favorable to break than form a ring, making production by biofouling highly unlikely. With complete overlap of the neighboring peaks in System 1, there is a noticeable reduction in the intensity of the asymmetric phenyl stretching peak (1603 cm⁻¹). As a molecule loses its dipole moment, it becomes less sensitive to infrared measurement. Should there be a decrease in hydrogen bonding to the adjacent sulfone or amine groups, the dipole should also decrease, minimizing the intensity of the asymmetric stretching. The 1628 cm⁻¹ band represents the bending mode of water. Its decrease indicates less residual water in the submerged sample than the control. This alludes to a point discussed by Southwell et al. in their studies of biofouling effects of carbon steel specimens¹⁰. They suggested that marine fouling can have protective effects against corrosion, providing a coating against ions in the ocean water. Thus, the thick biofouling layer of the submerged specimen could have prevented intercalation of water into the composite.

Most of the fingerprint region in System 2 displays an increase after gulf water submersion (Figure 10) This is also the case for System 6 (Figure 14). On the other

hand, Systems 4, 5 and 7 displays frequency shifting due to influences on the ester linkages (Figures 12, 13, & 15). The shift of the 1390 cm^{-1} OCH_2 wagging peak in System 4 is sensitive to dipolar interactions and dependent on conformation. The shift to higher wavenumber alludes to lower energy conformation at the ester linkage within the submerged sample. Systems 5 and 7 both show significant change in the 1417 cm^{-1} region. This could be a result of deformation to the ester-methylene linkages of the vinyl ester backbone.

The difference spectra of System 3 shows submersion only effects the 1428 cm^{-1} peak attributed to CH_2 deformations (Figure 11). This is not surprising as the fluorene based epoxy is hydrophobic, inhibiting water plasticization and exhibits greater bond strength.

Conclusions

The effects of biofouling on the polymer composite samples over a period of six months as seen by FTIR is relatively minimal. It is difficult to differentiate between the effects of non-reversible plasticization and that strictly from the biofouling. However, the fluorene based resin showed the least amount of change due to its hydrophobic nature. Work by Connolly¹¹ and Fried¹² has also shown that many polymers can withstand exposure to marine environments for periods up to thirteen years with minimal surface effects or loss of mechanical properties. The few differences seen between control and submerged samples is more likely from processing differences and irreversible plasticization than from the biofouling.

Acknowledgements

The authors would like to extend their appreciation to A. Clearfield, J. Narney, N. Prakash, and M. Paramasivam for their contributions to this work.

References

1. J. L. Perkinson, Govt. Rep. Announce (US), 71 19, (1971): p. 88.
2. M. K. Antoon, J. L. Koenig, T. Serafini, J. Polym. Sci., Polym Phys. Ed., 19, (1981): p. 1567.
3. M. K. Antoon, J. L. Koenig, J.L. J. Macromol. Sci., Rev. Macromol Chem., C19, (1980): p. 135.
4. A. Apicella, and L. Nicolais, Advances in Polymer Science. 72, (1985): p. 69.
5. J. L. Koenig, Advances in Polymer Science, 54, (1984): p. 87.
6. H. H. Willard, L. L. Merritt, et. al. Instrumental Methods of Analysis Wadsworth Publishing Co. California, (1988), pp. 287-305.
7. R. J. Morgan, E. T. Mones, J. Appl. Polymer Sci. 33, (1987): p. 999.

8. E. Mertz, J. L. Koenig, *Advances in Polymer Science*. 75, (1986): p. 73.
9. N. B. Colthup, L.H. Daly, S. E. Wiberley, Introduction to Infrared and Raman Spectroscopy. Academic Press, New York, (1990), pp.260-385
10. C. R. Southwell, et.al. *Materials Protection*, 4, (1965): p. 30.
11. R. A. Connolly, *Mat. Research Stds.* 3, (1963): p.193.
12. N. Fried, et. al. , *Marine Technology*. 3, (1966): p. 321.

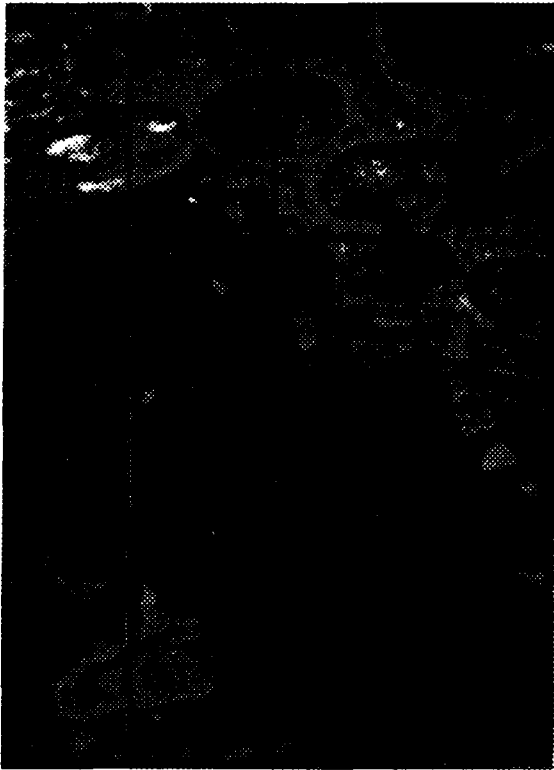


Figure 1. TGDDM/DDS Composite after tap water rinse. 50x.



Figure 2. TGDDM/DDS Composite after tap water rinse viewed through chipped barnacle. 50x.

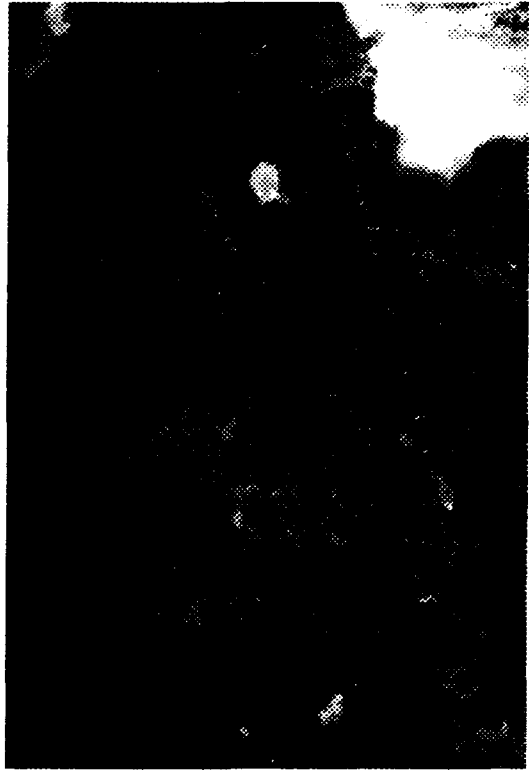


Figure 3. TGDDM/DDS Composite viewed through chipped away barnacle. 100x

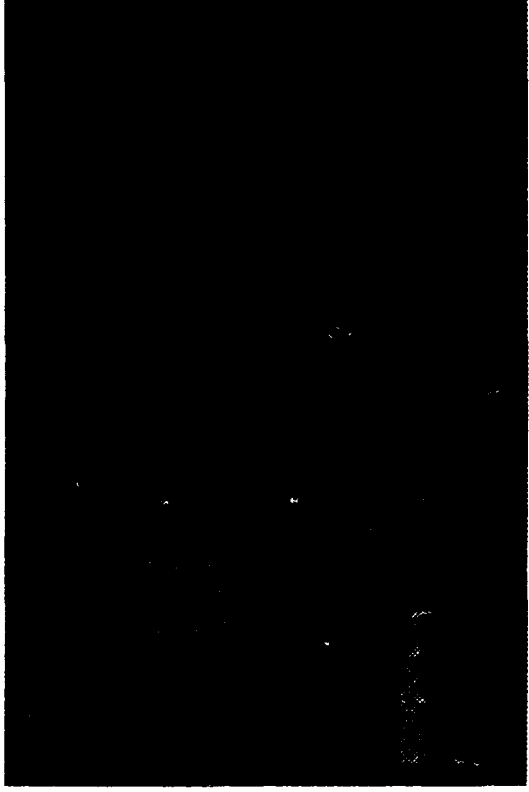


Figure 4. TGDDM/DDS Composite control. 50x.



Figure 5. TGDDM/DDS Composite after FTIR sample preparation. 50x.

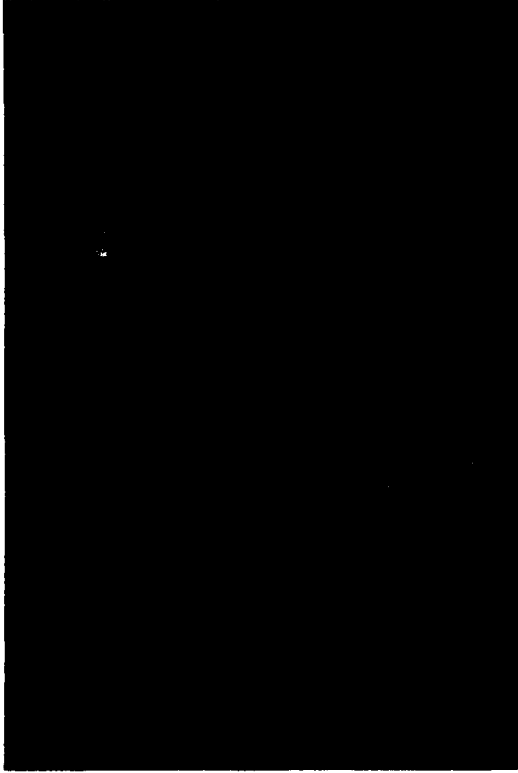


Figure 6. TGDDM/DDS Composite after imposed degradation by fuming sulfuric acid. 50x.



Figure 7. TDGGM/DDS Composite after imposed degradation by fuming sulfuric acid. 100x.

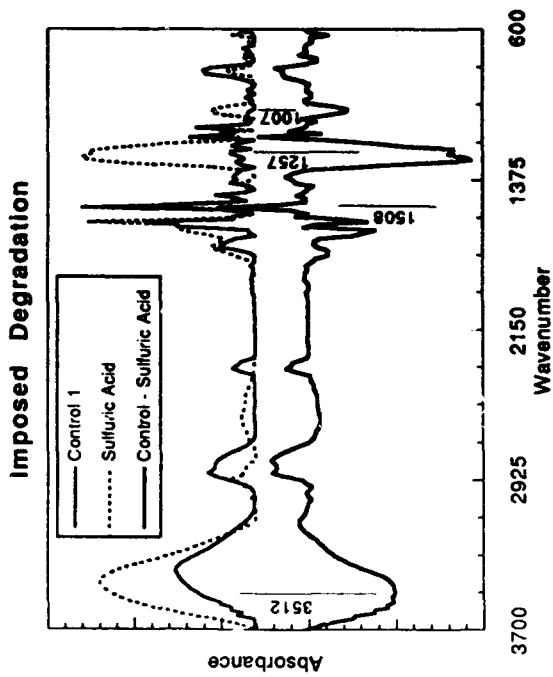


Figure 8. Absorbance and Difference spectra for System 1 control and sample subjected to fuming sulfuric acid environment.

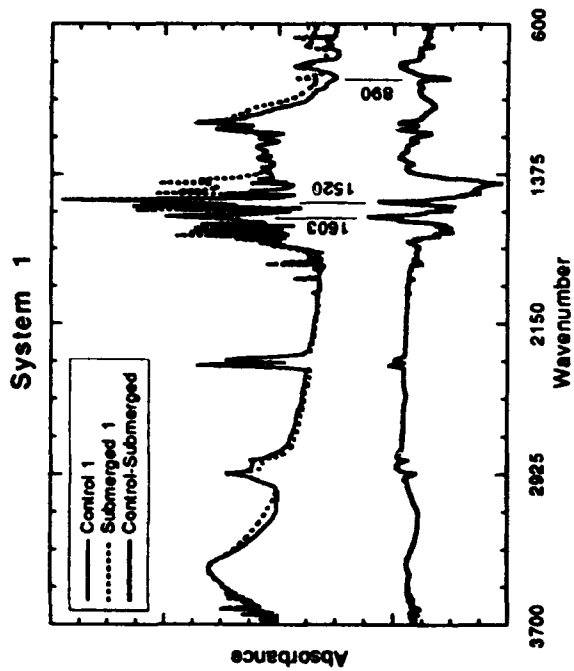


Figure 9. Absorbance and Difference spectra for System 1.

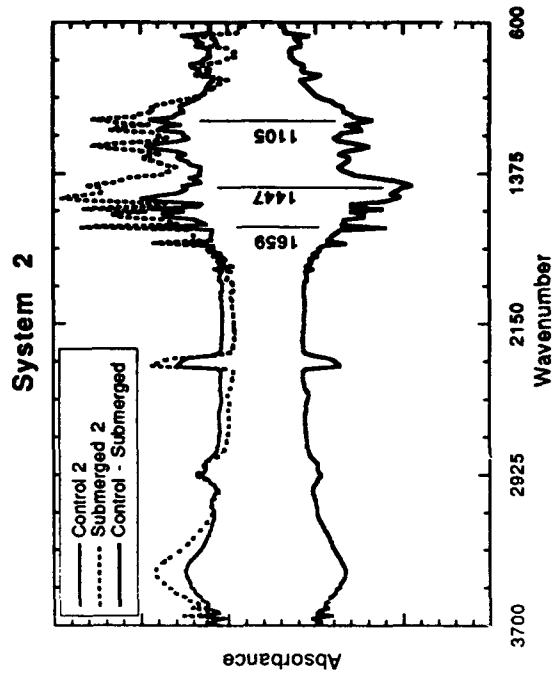


Figure 10. Absorbance and Difference spectra for System 2.

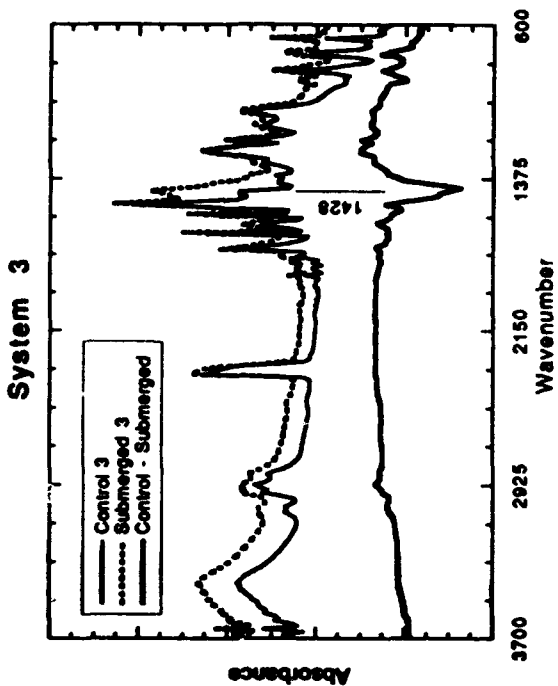


Figure 11. Absorbance and Difference spectra for System 3.

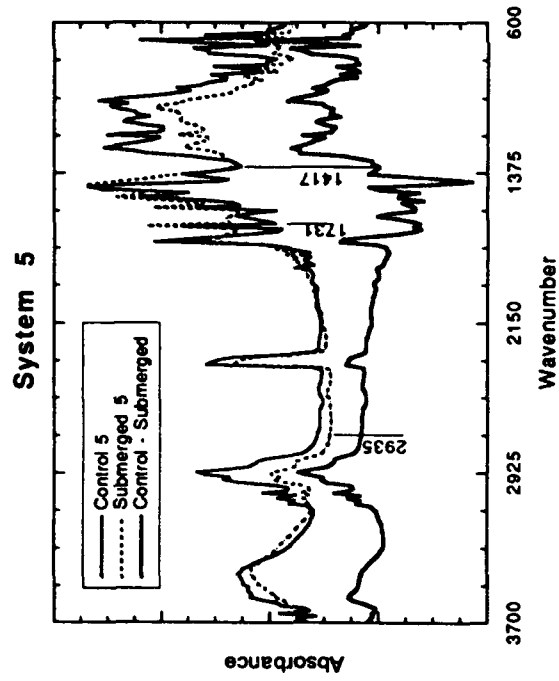


Figure 12. Absorbance and Difference spectra for System 4.

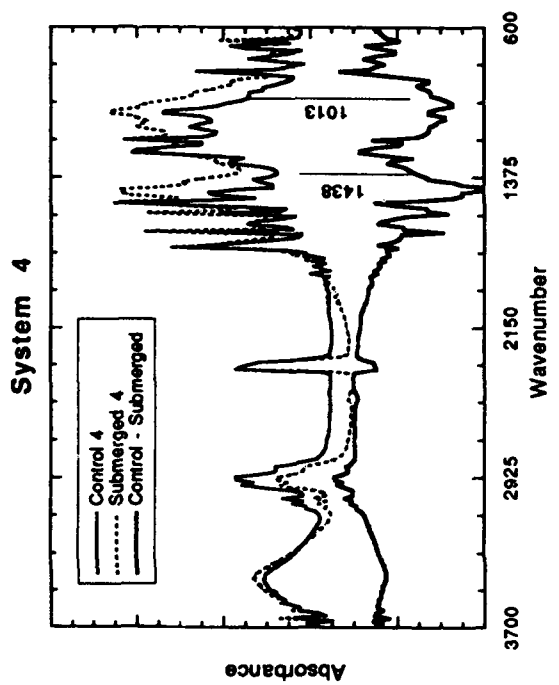


Figure 13. Absorbance and Difference spectra for System 5.

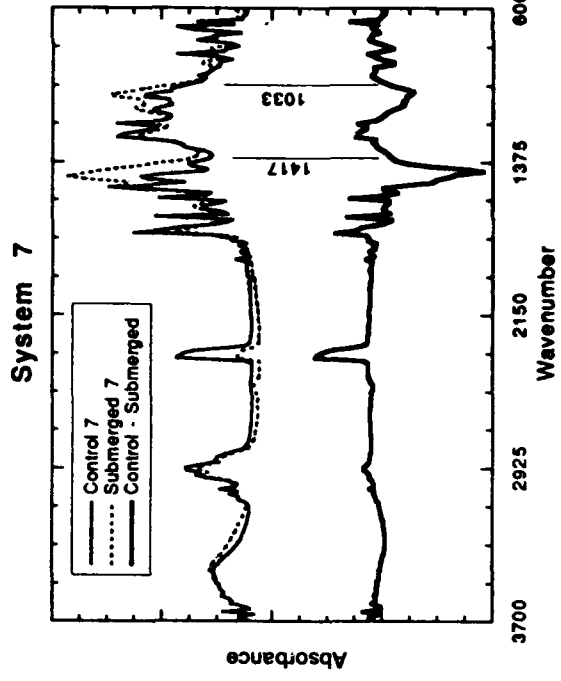


Figure 14. Absorbance and Difference spectra of System 6.

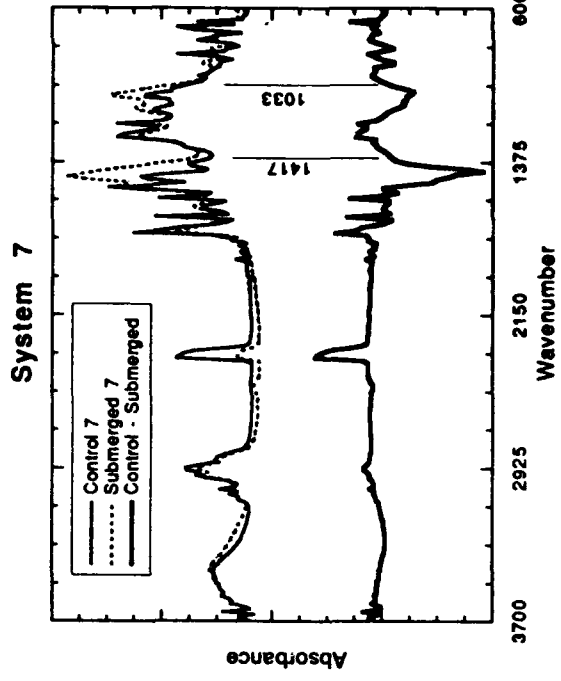


Figure 15. Absorbance and Difference spectra for System 7.

The Impact Of Alloying Elements On Microbiologically Influenced Corrosion – A Review

Brenda Little and Patricia Wagner
Naval Research Laboratory
Stennis Space Center, MS 39529 U.S.A.

Michael McNeil
Nuclear Regulatory Commission
Washington, D. C. 20555

Florian Mansfeld
University of Southern California
Los Angeles, CA 90089

Abstract

Alloying elements are added to metals to improve workability, electrical properties and corrosion resistance. Alloying elements also alter the formation, chemical composition, thickness and tenacity of corrosion products and may increase or decrease susceptibility to microbiologically influenced corrosion (MIC). The influence of alloying elements on MIC are reviewed for stainless steels, copper, nickel, aluminum and titanium alloys.

Key terms: microbiologically influenced corrosion, alloys, sulfate-reducing bacteria, corrosion product mineralogy.

Introduction

Microbial biofilms develop on all surfaces in contact with aqueous environments. Chemical and electrochemical characteristics of a metal substratum influence the formation rate and cell distribution of microfouling films in seawater during the first hours of exposure. Electrolyte concentration, pH, organic and inorganic ions also affect microbial settlement. Biofilms produce an environment at the biofilm/metal interface that is radically different from that of the bulk medium in terms of pH, dissolved oxygen, and inorganic and organic species.¹ Reactions within biofilms can control corrosion rates and mechanisms. The term microbiologically influenced corrosion (MIC) is used to designate corrosion resulting from the presence and activities of microorganisms within biofilms. The reactions are usually localized and can include: 1) sulfide production, 2) acid production, 3) ammonia production, 4) metal deposition, as well as 5) metal oxidation and reduction.

Commercially pure metals may contain a variety of impurities and imperfections which influence all types of corrosion. In general, as purity increases, the tendency for a metal to corrode reduces proportionately.² However, high purity metals frequently have low mechanical strength, leading to the use of alloying elements to improve mechanical, physical and fabrication characteristics. Nearly all metals and alloys exhibit a crystalline structure.² If an alloying element is added to a base metal, the crystal structure may remain essentially stable and produce a solid solution or single phase. Two or more phase structures can result with some alloy combinations. More than one phase in an alloy usually produces poorer corrosion resistance.

Copper and Nickel Alloys

Copper alloys are frequently used for seawater piping systems and heat exchangers due to their good corrosion resistance combined with mechanical workability, excellent electrical and thermal conductivity,

ease of soldering and brazing, and resistance to macrofouling. In oxygenated seawater a film of cuprous oxide, cuprite (Cu_2O), forms on copper alloys. Copper ions and electrons pass through the film. Copper ions dissolve and precipitate as $\text{Cu}_2(\text{OH})_3\text{Cl}$, independent of alloy chemistry. Alloying nickel and small amounts of iron into copper results in a single phase structure and increases resistance to turbulence induced corrosion. CDA 706 (88.5% Cu, 10% Ni, 1.5% Fe) has been shown to be the most corrosion resistant copper alloy for seawater service.³

Copper alloys are vulnerable to biocorrosion. Differential aeration, selective leaching, underdeposit corrosion and cathodic depolarization have been reported as mechanisms for MIC of copper alloys. Pope et al.⁴ proposed that the following microbial products accelerate localized attack: CO_2 , H_2S , NH_3 , organic and inorganic acids, metabolites that act as depolarizers, and sulfur compounds such as mercaptans, sulfides and disulfides.

In the presence of sulfides, copper alloys form a porous layer of cuprous sulfide with the general stoichiometry $\text{Cu}_2\text{-xS}$, $0 < x < 1$. Copper ions migrate through the layer, react with more sulfide, and produce a thick black scale. McNeil and Odom⁵ described a model that predicts sulfide-induced corrosion in the presence of SRB. Corrosion is initiated by sulfide-rich reducing conditions in the biofilm where the oxide layer is destabilized and acts as a source of metal-containing ions. The authors concluded that if any reaction of metal oxide with sulfide has a high negative standard free energy of reaction, SRB-related MIC will occur. If the reaction has a high positive standard free energy of reaction, this form of corrosion will not occur. Negative standard free energies of reactions were used to predict SRB-MIC for copper alloys. Analysis of sulfide corrosion products recovered from corroding copper alloys confirmed the prediction. Specific copper sulfides have been suggested as fingerprints for SRB sulfide production. Chalcocite (Cu_2S) and covellite (CuS_{1+x}) are frequently identified in copper corrosion products associated with SRB.⁶ Djurleite ($\text{Cu}_{31}\text{S}_{16}$) formation has been reported for copper/nickel alloys.

It has been argued that if the copper sulfide layer were djurleite, the sulfide layer would be protective. Even if such a sulfide film were technically passivating, the film's mechanical stability is so poor that sulfide films are useless for corrosion protection. McNeil et al.⁶ reported that sulfide corrosion products on 99 copper were consistently non-adherent, while those on 90/10 and 70/30 copper/nickel were adherent in SRB laboratory cultures and in natural waters.

Nickel minerals have not been found in corrosion products on 90/10 or 70/30 copper/nickel alloys.⁷ Selective dealloying of zinc, nickel and iron from copper alloys has been reported by several investigators.^{8,9} Little et al.⁹ demonstrated dealloying of nickel from a 90/10 copper/nickel in association with SRB. Wagner et al.⁸ described dealloying of nickel in 70/30 copper/nickel exposed to flowing natural seawater.

SRB are not necessary for MIC induced pitting of copper alloys. While the role of the biofilm in copper pitting is not entirely clear, it appears that the presence of the biofilm contributes to corrosion by maintaining enhanced local chloride concentrations and differential aeration cells.¹⁰ Pope¹¹ documented MIC of 90/10 copper/nickel, admiralty and aluminum brass, and welded aluminum bronze at electric generating facilities using fresh or brackish cooling waters. Most of the copper/nickel tubes had underdeposit corrosion due to formation of deposits by slime-forming organisms in association with iron- and manganese-depositing bacteria. Ammonia-producing bacteria were isolated from scale and organic material on the admiralty brass tubes suffering ammonia-induced stress corrosion cracking. Mansfeld and Little reported that 5 copper alloys exposed to natural seawater were colonized by bacteria within 3 weeks, independent of alloy composition.¹² Corrosion rates were higher in natural seawater compared

with artificial seawater for all copper alloys exposed. Intergranular corrosion and denickelification of 70/30 copper/nickel was observed after 1 month.

Nickel alloys, including Monel 400 (66.5% Ni, 31.5% Cu, 1.25% Fe), are used extensively in highly aerated fast-moving seawater environments as evaporators, heat exchanger pumps and valves, diffusers for steam nozzles in steam ejectors and turbine blades. Uhlig and co-workers¹³ calculated that a critical nickel concentration of 35% was required for passivity. Nickel alloys containing less than this amount behave like copper. The formation of the protective film on nickel is aided by the presence of iron, aluminum and silicon. In high velocity seawater, nickel alloys are superior to predominantly copper alloys because the protective surface film remains intact under highly turbulent and erosive conditions.

Monel 400 is susceptible to pitting and crevice corrosion attack where chlorides penetrate the passive film. Sulfides can cause either a modification or breakdown of the oxide layer. Schumacher¹⁴ reported that Monel 400 was susceptible to underdeposit corrosion and oxygen concentration cells formed by bacteria. Gouda et al.¹⁵ demonstrated pitting of Monel 400 tubes exposed in Arabian Gulf seawater where pits developed under deposits of SRB and nickel was selectively dealloyed. Little et al.⁹ reported selective dealloying in Monel 400 in the presence of SRB from an estuarine environment.

Pope¹¹ reported a case study from nuclear power plants in which severe pitting corrosion associated with dealloying was observed under discrete deposits on Monel heat exchanger tubes. Deposits formed by iron- and manganese-depositing bacteria in association with SRB contained large amounts of iron and copper, significant amounts of manganese and silicon, and reduced amounts of nickel. No evidence for MIC in nickel-chromium (Inconel) and nickel-chromium-molybdenum (Hastelloy) has been reported. Hastelloy C (54% Ni, 15% Cr, 16% Mo, 4% W, 5% Fe) shows outstanding resistance to pitting or crevice attack in seawater.

Stainless Steels

The corrosion resistance of stainless steels (SS) is due to the formation of a thin passive chromium-iron oxide film at additions of chromium in amounts of 12% or more. Metal-depositing organisms, important in MIC of stainless steels, may catalyze the oxidation of metals, accumulate abiotically oxidized metal precipitates, or derive energy by oxidizing metals. Dense deposits of cells and metal ions create oxygen concentration cells that effectively exclude oxygen from the area immediately under the deposit. Underdeposit corrosion is important because it initiates a series of events that are, individually or collectively, extremely corrosive.¹⁶ In an oxygenated environment, the area immediately under the deposit becomes a relatively small anode compared to the large surrounding cathode. Cathodic reduction of oxygen may result in an increase in pH of the solution in the vicinity of the metal. The metal will form metal cations at anodic sites. If the metal hydroxide is the thermodynamically stable phase in the solution, metal ions will be hydrolyzed by water with formation of H⁺ ions. If cathodic and anodic sites are separated from one another, the pH at the anode will decrease and at the cathode will increase. The pH within anodic pits depends on specific hydrolysis reactions.¹⁷ The lowest pH values are predicted for alloys containing chromium and molybdenum.

One of the most common forms of MIC attack in austenitic SS is pitting at or adjacent to welds¹⁸ at the heat affected zone, the fusion line and in the base metal. Borenstein¹⁹ made the following observations for MIC in 304L (18% Cr, 9% Ni, .03% C, bal. Fe) and 316L (17% Cr, 12% Ni, 2.5% Mo, .03% C, bal. Fe) weldments: both austenite and delta ferrite phases may be susceptible; combinations of filler and base materials have failed, including matching, higher and lower alloyed filler combinations; and solution annealing and pickling may produce welds that are less susceptible. A lack of

sensitization in austenitic welds did not ensure protection. Additionally, surface conditions commonly associated with corrosion resistance, such as heat tint, and those related to residual stresses, including gouges and scratches, may increase susceptibility. Kearns and Borenstein²⁰ state that welds having filler metal compositions matching the base metal have lower corrosion resistance than fully annealed base metal due to lack of homogeneity and the microsegregation of chromium and molybdenum. Chemically depleted regions can be much more susceptible to localized attack. Stein²¹ reported that MIC susceptibility of base metal related to weld area was not related to sensitization but to the microstructure produced during the manufacturing process. Reannealing reduced the severity of the pitting corrosion. Videla et al.²² observed that sensitization heat treatments with related carbide precipitation lowered pitting corrosion resistance of 304 and 410SS in the presence of SRB and aggressive anions.

Stainless steels containing 6% or more molybdenum were once thought to be immune to MIC because molybdenum increases the resistance of austenitic SS to chloride and acid solutions. However, Scott and Davies²³ documented MIC in an austenitic 904L SS (20% Cr, 25% Ni, 4.5% Mo, 1.5% Cu, 0.02 max. C, bal. Fe) used in a tube and shell heat exchanger for cooling sulfuric acid in brackish and seawater applications. The failure occurred within two weeks of startup and was accompanied by attack of welds and crevice corrosion. Little et al.²⁴ observed deep etching of SMO254 SS (20% Cr, 18% Ni, 6.5% Mo, 0.75% Cu, 0.2% N, bal. Fe) after exposure to both an iron/sulfur-oxidizing mesophilic bacterium and a thermophilic mixed SRB culture.

Ennoblement of corrosion potential (E_{corr}) for stainless steels during exposure to natural seawater has been reported by several investigators.^{1,25,26} The practical importance of ennoblement is increased probability of localized corrosion as E_{corr} approaches the pitting potential (E_{pit}). Thermodynamic and kinetic factors have been discussed, including increase of the partial pressure of oxygen, a decrease in interfacial pH and organometallic catalysis. An increase of the partial pressure would move the reversible potential of the oxygen electrode in the noble direction, but cannot be used to explain large shifts in E_{corr} . A local decrease in pH would produce the same effect. Local acidification would move E_{pit} in the negative direction to potentials significantly below the reported E_{corr} values. Johnsen and Bardal²⁷ reported that E_{corr} approached -50 mV (vs saturated calomel electrode (SCE)) after 28 days for SS that contained 1–3 w/o molybdenum. In contrast, SS containing 6 w/o molybdenum reached values of $+50$ – 150 mV vs. SCE in the same time period. Early reports suggested that molybdenum was not found in the passive layer for alloys containing up to 5.2% molybdenum.²⁸ Recently, Olefjord and Wegrelius²⁹ studied the influence of molybdenum and nitrogen on the corrosion behavior of high alloyed SS containing 6% molybdenum. Passive layers contained 8–14% molybdenum. Since ennoblement is more pronounced for high molybdenum SS, molybdenum may play a role in the acceleration of the cathodic reaction leading to ennoblement of E_{corr} .

Aluminum and Aluminum Alloys

The corrosion resistance of aluminum and its alloys is due to an aluminum oxide passive film. Anodizing produces thicker insulating films and better corrosion resistance. The natural film on aluminum alloys can be attacked locally by halide ions. The susceptibility of aluminum and its alloys to localized corrosion makes it particularly vulnerable to MIC. Most reports of MIC are for aluminum (99%), 2024 and 7075 alloys used in aircraft or in underground fuel storage tanks.³⁰ Localized corrosion attributed to MIC occurs in the water phase of fuel-water mixtures in the bottom of tanks and at the fuel-water interface. Contaminants in fuel include surfactants, water, and water soluble salts that encourage growth of bacteria. Two mechanisms for MIC of aluminum alloys have been documented: production of water soluble organic acids by bacteria and fungi, and formation of differential aeration cells.

Titanium and Titanium Alloys

There are no case histories of MIC for titanium and its alloys. Schutz³¹ reviewed mechanisms for MIC and titanium's corrosion behavior under a broad range of conditions. He concluded that at temperatures below 100°C titanium is not vulnerable to iron/sulfur-oxidizing bacteria, SRB, acid-producing bacteria, differential aeration cells, chloride concentration cells and hydrogen embrittlement. In laboratory studies, Little et al.²⁴ did not observe any corrosion of Grade 2 titanium in the presence of SRB or iron/sulfur oxidizing bacteria at mesophilic (23°C) or thermophilic (70°C) temperatures. Using the model of McNeil and Odom⁵ one would predict that titanium would be immune to SRB induced corrosion. There are no standard free energy reaction data for the formation of a titanium sulfide. If one assumes a hypothetical sulfide product to be titanium sulfide, the standard enthalpy of reaction is +587 kJ. While standard free energies of reaction are not identical to standard enthalpies of reaction, it is still unlikely that titanium will be derivatized to the sulfide under standard conditions of temperature and pressure.

Conclusions

MIC is localized corrosion documented in failures of engineering materials. Alloying elements affect susceptibility to MIC by providing a corrosion-resistant single phase and by affecting reaction kinetics. However, in practical cases, the primary effect of alloying elements is to stabilize a protective film either mechanically or chemically. Additions of nickel and iron improve the mechanical properties of copper alloys but may increase susceptibility to MIC. Molybdenum found in the passive layer on stainless steel alloys may influence ennoblement of E_{corr} .

Acknowledgments

This work was supported by the Office of Naval Research, Program Element 0601153N, through the NRL Defense Research Sciences Program. Approved for public release; unlimited distribution. NRL Contribution Number NRL/PP/7333-93-0008.

References

1. B. Little, R. Ray, P. Wagner, Z. Lewandowski, W. C. Lee, W. Characklis, F. Mansfeld, *Biofouling*, 3 (1991): p. 45.
2. *Corrosion Basics-An Introduction* (Houston, TX: National Association of Corrosion Engineers, 1984), p. 49.
3. J. F. D. Bates, J. M. Popplewell, *Corrosion*, 32 8 (1975): p. 269.
4. D. H. Pope, D. J. Duquette, A. H. Johannes, P. C. Wayner, *Materials Performance*, 23 4 (1984): p. 14.
5. M. B. McNeil, A. L. Odom, "Prediction of Sulfiding Corrosion of Alloys Induced by Consortia Containing Sulfate Reducing Bacteria (SRB)," *International Symposium on Microbiologically Influenced Corrosion (MIC) Testing*, (Miami, FL: ASTM, 1992).
6. M. B. McNeil, J. M. Jones, B. J. Little, *Corrosion*, 47 9 (1991): p. 674.
7. J. Jambor, private communication, 1990.
8. P. Wagner, B. Little, R. Ray, J. Jones-Meehan, "Investigations of Microbiologically Influenced Corrosion Using Environmental Scanning Electron Microscopy," *CORROSION/92*, paper no. 185 (Houston, TX: National Association of Corrosion Engineers, 1992).
9. B. Little, P. Wagner, R. Ray, M. McNeil, *Marine Technology Society J.*, 24 3 (1990): p. 10.

10. H. H. Paradies, I. Hansel, W. Fischer, D. Wagner, "The Occurrence of a Severe Failure of Water Supplies in a County Hospital," International Copper Research Institute, Project No. 404 (1990).
11. D. H. Pope, *Microbial Corrosion in Fossil-Fired Power Plants – A Study of Microbiologically Influenced Corrosion and a Practical Guide for its Treatment and Prevention*, (Palo Alto, CA: Electric Power Research Institute, 1987).
12. F. Mansfeld, B. Little, *Electrochimica Acta*, 37 12 (1991): p. 2291.
13. H. H. Uhlig, W. R. Revie, *Corrosion and Corrosion Control: an Introduction to Corrosion Science and Engineering*, Third Edition, (New York, NY: Wiley-Interscience, 1985).
14. M. Schumacher, *Seawater Corrosion Handbook*, (Park Ridge, NJ: Noyes Data Corporation, 1979).
15. V. Gouda, I. Banat, W. Riad, S. Mansour, *Corrosion*, 49 1 (1993): p. 63.
16. L. L. Shreir (ed.), *Corrosion, Vol. 1 & 2, Corrosion Control*, (London, UK: Newnes-Butterworth, 1977).
17. T. P. Hoar, *Disc. Faraday Soc.*, 1 (1947): p. 299.
18. G. Kobrin, *Materials Performance*, 15 7 (1976): p. 38.
19. S. W. Borenstein, *Materials Performance*, 30 1 (1991): p. 52.
20. J. Kearns, S. Borenstein, "Microbially Influenced Corrosion Testing of Welded Stainless Alloys for Nuclear Power Plant Service Water Systems," CORROSION/91, paper no. 279 (Houston, TX: National Association of Corrosion Engineers, 1991).
21. A. A. Stein, "Metallurgical Factors Affecting the Resistance of 300 Series Stainless Steels to Microbiologically Influenced Corrosion," CORROSION/91, paper no. 107 (Houston, TX: National Association of Corrosion Engineers, 1991).
22. H. A. Videla, M. F. L. deMele, D. A. Moreno, J. Ibars, C. Ranninger, "Influence of Microstructure on the Corrosion Behavior of Different Stainless Steels," CORROSION/91, paper no. 104 (Houston, TX: National Association of Corrosion Engineers, 1991).
23. P. J. B. Scott, M. Davies, *Materials Performance*, 28 5 (1989): p. 57.
24. B. Little, P. Wagner, R. Ray. "An Experimental Evaluation of Titanium's Resistance to Microbiologically Influenced Corrosion," CORROSION/92, paper no. 173 (Houston, TX: National Association of Corrosion Engineers, 1992).
25. S. C. Dexter, G. Y. Gao, *Corrosion*, 44 (1988): p. 717.
26. V. S. Scotto, R. Di Cintio, G. Marcenaro, *Corrosion Science*, 25 3 (1985): p. 185.
27. R. Johnsen, E. Bardal, *Corrosion*, 41 (1985): p. 296.
28. A. E. Yaniv, J. B. Lumsden, R. W. Staehle, *J. Electrochemical Society*, 124 4 (1977): p. 490.

29. I. Olefjord, L. Wegrelius, "Passivation of High Alloyed Stainless Steels," Symposium on Modifications of Passive Films (Paris, France, 1993).
30. R. C. Salvarezza, H. A. Videla, *Acta Cientifica Venezolana*, 35 (1984): p. 244.
31. R. W. Schutz, *Materials Performance*, 30 1 (1991): p. 58.

Early Stages of Bacterial Biofilm and Cathodic Protection Interactions in Marine Environments

Héctor A. Videla
Bioelectrochemistry Section. I.N.I.F.T.A.
University of La Plata.
C.C. 16 suc. 4, La Plata 1900. Argentina

Sandra G. Gómez de Saravia
Bioelectrochemistry Section. I.N.I.F.T.A.
University of La Plata.
C.C. 16 suc. 4, La Plata 1900. Argentina

Mónica F.L. de Mele
Bioelectrochemistry Section. I.N.I.F.T.A.
University of La Plata.
C.C. 16 suc. 4, La Plata 1900. Argentina

Abstract

The effect of cathodic protection on the early stages of bacterial biofilm formation on stainless steel was studied at different temperatures. The influence of the applied potential on pure *Vibrio alginolyticus* and mixed SRB (*Desulfovibrio vulgaris* and *Desulfovibrio desulfuricans*) biofilms was assessed using saline media, in laboratory experiments under controlled conditions. Interactions between cathodic protection and bacterial settlement and growth, calcareous deposits, and current densities were successively analyzed. For aerobic bacteria, cathodic protection diffculted adhesion to the metal surface only at the early stages of biofilm formation. Higher current densities are generally required in the presence of biofilms.

Key terms: cathodic protection, biofilm, seawater, calcareous deposits.

Introduction

Cathodic protection (CP) is particularly attractive in marine environments or certain kinds of soils where the medium conductivity is high enough to obtain a uniform current distribution over the metal surface to be protected. It has been described¹⁻³ as an effective method of protecting stainless steel (SS) structures immersed in seawater against crevice corrosion.

CP is generally accomplished by impressing an external current to the metal, opposing the naturally occurring corrosion current. Thus, the cost of this protective method will mainly depend on the amount of the current to be applied to the metallic structure to be protected^{3,4}.

CP alters the ionic concentration at the interface increasing hydroxyl ions concentration. The consequent pH increase diminishes the solubility of calcium and magnesium at the interface favoring the precipitation of a calcareous scale⁴⁻⁶.

The current required to polarize the structure depends on the electrochemical properties of the metal to be protected and the type of film formed under CP. It has been reported^{4,7,8} that the properties of this film in natural seawater are influenced by microbial adhesion processes. Moreover, microbial adsorption depends on the electrochemical characteristics of the polarized interface⁹.

As the adhesion of aerobic microorganisms frequently shifts the corrosion potential in the anodic direction^{1,4,10} the amount of applied current required to polarize the structure to a pre-selected potential could also depend on the amount of microbial settlement. CP seems to be effective for controlling the growth of aerobic bacteria in carbon structures immersed in seawater whereas it could favour the growth of sulfate reducing bacteria (SRB)¹¹.

The goal of this paper is to assess the interrelationships between CP on SS samples and pure aerobic and mixed anaerobic bacterial settlement and reproduction and calcareous deposits structure. The influence of seawater temperature on these interactions will also be studied under laboratory well controlled conditions.

Experimental

A. Microorganisms

Pure *Vibrio alginolyticus* (*V. alginolyticus*) and mixed SRB *Desulfovibrio vulgaris* (*D. vulgaris*) and *Desulfovibrio desulfuricans* (*D. desulfuricans*) were used in the experiments. *V. alginolyticus* was isolated from polluted harbor seawater and was maintained in nutrient agar with the addition of 3 % NaCl. Experiments were made using synthetic seawater supplemented with 1 g/l of yeast extract. Cell number in the culture media were initially c.a. 10⁶ cells/ml.

D. vulgaris and *D. desulfuricans* were maintained in a medium containing 35% of synthetic seawater with 1 g/l of yeast extract, 0.2 g/l sodium lactate, 0.005 g/l Na₂HPO₄, 0.05 g/l NH₄Cl, 0.001 g/l Na₂SO₃. This medium was also used as culture medium in the SRB experiments. In this case, after SRB inoculation, 10 % of the medium was removed and replaced by fresh medium every 24 h.

The initial pH of all the solutions was adjusted to 7.5 by adding 0.1 N NaOH solution.

B. Metal samples

Metal specimens were AISI⁽¹⁾ 304L SS (50 x 20 x 1 mm). They were mechanically polished with different grits of silicon carbide paper (240, 400, 600) and later with alumina paste (1 μm grain size). After polishing, samples were cleaned and degreased with acetone, and finally rinsed with distilled water prior to their exposure to the bacterial suspension.

C. Exposure times

Metal specimens were exposed to SRB cultures for 7 or 15 days. Shorter immersion times (2, 4, 18, 24 and 48 h) were used in the case of *V. alginolyticus* experiments.

D. Cathodic protection conditions

SS samples were cathodically polarized to -0.7 V against a saturated calomel electrode (SCE) using a potentiostat and a platinum counter electrode.

E. SEM observations

After exposure, and in order to preserve biological material, specimens were successively fixed with 2% glutaraldehyde solution in synthetic seawater, washed with distilled water, dried through an acetone series to 100%, and finally, critical point dried. To assess metal attack, samples were polished with alumina (1 μm) to remove biological and inorganic deposits from the surface. Later, samples were cleaned and degreased with acetone and finally rinsed with distilled water. SEM observations were made using a JEOL⁽²⁾ JSM-T 100 microscope.

(1) American Iron and Steel Institute, Washington, DC.

(2) JEOL LTD, 1418 Nakagami Arishima, Tokyo 196, Japan.

F. Cell enumeration methods

1. "In situ" enumeration. It was made through a direct cell count method using epifluorescence microscopy. After exposure, the samples were removed, stained with 0.01% acridine orange for 5 minutes, rinsed in sterile synthetic seawater to remove loose cells, and examined under ultraviolet light with an epifluorescence microscope at 400X. Cells were counted in 12 randomly chosen 0.0464 cm² fields per sample.

2. "Ex situ" enumeration. For viable counts, samples were washed in sterile synthetic seawater and thereafter scraped with a scalpel. The resulting suspension was transferred into a tube containing 10 ml of sterile seawater. Enumeration of cells was made by a standard plating method for viable counts. Colonies were counted after 48 h of incubation at 28C.

Results

V. alginolyticus sessile cell counts on 304 SS specimens after 2 and 4 h of immersion at 12 C are shown in figure 1. The number of bacteria attached to the SS surface diminished when CP was applied. Sessile cell numbers decreased from 2.4×10^3 cells/cm² to 1.2×10^2 for a 2 h exposure time. A longer exposure period (4h) did not result in an increase of sessile *V. alginolyticus*.

Experiments made at two different temperatures (12 C and 20 C) for SS specimens exposed for 18 h to a *V. alginolyticus* culture, are compared in Table 1. A reduction in the cell numbers can be noticed when the temperature was increased.

CP effect on a 2 h old *V. alginolyticus* biofilm at 12 C is shown in Table 2. To analyze the balance between desorption + detachment vs. reproduction, biofilmed specimens were immersed in sterile medium, to avoid the readsorption of cells. For unprotected samples the number of bacteria slightly increased in the sterile media (desorption + detachment are slightly lower than reproduction). Conversely, an important decrease in the number of attached cells with respect to the initial value was observed when CP was applied. Thus, it can be inferred that desorption and detachment seemed to be enhanced and reproduction was reduced by CP.

Experiments made at 12 C for longer exposures (Fig. 2) showed that the number of cells attached on the unprotected samples at this temperature increased to reach a steady value (c.a. 10^4 cells/cm²) after 24 h, and remained nearly constant afterwards. For this temperature the number of attached cells is markedly lower than that obtained at 20 C (see Table 1). When the samples were cathodically protected immediately after the immersion in the culture medium a lower number of attached cells with respect to that observed without protection is again observed. Conversely, when the metal coupons remained 48 h immersed but, alternating the first 24 h unprotected and protected for the next 24 h, it could be noticed that no reduction in the number of cells was found with respect to the unprotected SS samples for 48 h. It is likely that when a steady biofilm is obtained, the effect of cathodic protection is not so relevant as in the early stages of biofilm growth.

Current density vs. time curves for SS in synthetic seawater (Fig. 3) show the characteristic shoulder shape related to the nature of the calcareous deposits formed under these experimental conditions. It can also be noticed a different shape of the curve and a non-well defined transient time, when bacteria are present in seawater. SEM observations showed that pioneer bacteria are covered by calcareous deposits (Figs. 4 and 5). When cell detachment occurs, cavities reproducing bacterial shapes can be observed, revealing a discontinuity in the calcareous deposit structure (Fig. 6).

Results of Fig. 3 show that after the immersion in the inoculated seawater, current decreases sharply and then, when the biofilm is formed it began to increase reaching finally a steady

state value which duplicates that of the control. Experiments made at 12 C, i.e., when the growth of biofilm is slow, did not show this current increase in the same period.

Attachment of mixed cultures of SRB to SS specimens was analyzed at longer exposure periods than *V. alginolyticus*. After seven days of immersion a high number of cells (larger than 10^4 cells/cm²) was found on the SS samples. No reduction in the number of sessile cells was observed when CP was applied for periods of 7 days and longer. Localized attack has been found on samples with and without cathodic protection. Small pits, which were frequently covered by bacteria were observed by SEM (Fig.7). A slight current density increase was recorded after two days of immersion for the protected samples.

After 15 days exposure the number of cells markedly increased and thick biofilms were covering the metal surface (Fig. 8). Beneath the biofilm and on the metal surface an inorganic film, firmly adhered to the metal and small pits could be observed when the biofilm was removed (Fig. 9).

Discussion

The attachment of bacteria to an unfouled metal surface is preceded by initial processes of transport and adsorption of organic molecules. These processes are followed by the growth of attached bacteria which results in an increase of attached cells and associated material and the detachment of portions of the biofilm. Consequently, the accumulation of cells in the metal/solution interface is the result of the balance of several processes¹²:

$$\frac{dX_c}{dt} = \underset{\text{adsorption}}{ra_c} - \underset{\text{desorption}}{rd_c} + \underset{\text{growth - detachment}}{X_c \text{ tot } (K_g - K_d)}$$

ra_c : adsorption rate for cells

rd_c : desorption rate for cells

X_c : cell concentration at the substratum

K_g : probability of cell growth

K_d : probability of cell detachment

t: time

Sorption related processes are considered to be dominant within a short period of time. For instance, in the case of *Pseudomonas aeruginosa* at 25 C this period is about 100 minutes after the immersion of the unfouled specimens. Growth related processes begin to contribute to the accumulation in later stages. Adsorption influences the rate of the induction and growth phases but does not influence the plateau biofilm accumulation¹².

Present results obtained with *V. alginolyticus* show that a relevant decrease in the cell number due to the application of CP occurs during the first hours after immersion (the extent of the period depends on temperature). Considering the model previously mentioned¹³, adsorption processes may be dominant in this period. Thus, CP should affect adsorption processes, reducing the number of adsorbed cells. Induction and growth periods (but not the steady phase of growth) are considered to be dependent on the number of attached cells. Thus, the effect of CP on the cell growth is appreciable for those periods (see Table 2). Conversely, CP effects are not significant in the biofilm steady state (in this case adsorption process is not relevant). Consequently, it could be inferred that CP affects adsorption processes that influence bacterial growth until steady state is reached.

Although the number of SRB attached bacteria was high after 7 days both for protected and unprotected samples, biofilms did not reach the stationary phase after this period. Consequently, adsorption processes are not reduced by CP in the case of SRB. It was not found an increase in sessile SRB cells when CP was applied as it has been previously reported¹². However, shorter exposure periods must be assayed in the future.

SRB metabolites facilitate metal attack (small pits were observed in the metal surface, Fig. 9). This effect could not be eliminated with the application of CP levels used in this work.

The current density vs. time curve for SS in synthetic seawater shows the characteristic shape related to the formation of the calcareous deposits. The time necessary to reach a steady state, could be associated with the kinetics of the deposit formation which is modified in the presence of organic material confirming previous results^{6,7}. The evolution of the current density as a function of time (Fig. 3) shows a similar behavior to that observed with natural biofilms, when low current densities are necessary to maintain cathodic protection^{1,4}. Similar depolarization effects have been extensively reported^{1,4,10,13} for several metals immersed in seawater. In all cases the increase in current density occurred when the biofilm became established¹⁴. It was suggested¹ that this effect could be attributed to an enhancement of the oxygen reduction by the biofilm. Edyvean et al.⁷, suggested that organic material slows down precipitation process.

Results reported in this paper offer evidence on the interactions between bacterial fouling, cathodic protection and calcareous deposits: i) Aerobic bacterial adsorption is reduced by the application of CP while anaerobic bacterial adsorption did not seem to be diminished; ii) current values are modified by depolarization effects due to the aerobic biofilm; iii) aerobic and anaerobic biofilms alter the calcareous deposits structure; iv) current values are decreased by calcareous film formation.

Conclusions

- CP inhibits aerobic bacterial adsorption and growth at the early stages of biofilm formation.
- After reaching a steady biofilm CP effects are not relevant.
- The reduction of bacterial adhesion can be due to an interference of CP in the adsorption processes.
- At low temperatures, when growth rate is low, the CP effect is more significant.
- For low current values, biofilms can modify calcareous deposits structure.
- In the presence of aerobic bacterial biofilms formed at 20 C, higher current densities are needed to protect SS samples, increasing CP costs.

Acknowledgements

This research project is financially supported by the Universidad Nacional de La Plata and the Consejo Nacional de Investigaciones Científicas y Técnicas (CONICET). The authors wish to acknowledge Merck Química Argentina for the supply of analytical reagents and culture media used in this work. Dr. Robert G.J. Edyvean (Department of Chemical Engineering, the University of Leeds, UK) is also gratefully acknowledged for his valuable discussions.

References

1. R. Johnsen, E. Bardal, "Effect of a microbiological slime layer on stainless steel in natural seawater", CORROSION/86, paper no. 227 (Houston, TX: National Association of Corrosion Engineers, 1986).
2. T.S. Lee, A.H. Tuthill, *Materials Performance*, 22 1 (1983): p. 48.

3. M.H. Peterson, T.R. Lennox, *Corrosion*, 29 (1973): p. 406.
4. S.C. Dexter, S.H. Lin, *International Biodeterioration & Biodegradation*, 29 (1992):p. 231.
5. W.H. Hartt, C.H. Culberson, S.W. Smith, *Corrosion*, 40 11 (1984): p. 609.
6. S.H. Lin, S.C. Dexter, *Corrosion*, 44 9 (1988): p. 615.
7. R.G.J. Edyvean, A.D. Maines, C.J. Hutchinson, N.J. Silk, L.V. Evans, *International Biodeterioration & Biodegradation*, 29 (1992): p. 251.
8. B. Little, P. Wagner, D. Duquette. *Corrosion*, 44 5 (1988): p. 270.
9. H.P. Dahr, D.W. Howell, J.O'M. Bockris, *Journal of Electrochemical Society*, 129 (1982): p. 2178.
10. A. Mollica, E. Traverso, G. Ventura, Electrochemical monitoring of the biofilm growth on active passive alloy tubes of heat exchanger using seawater as cooling medium, in Proc. 11th International Corrosion Congress, Florence, Italy, 4, p.341, 1990.
11. J. Guezennec, *Biofouling*, 3 (1991): p. 339.
12. A.E. Escher, "Colonization of a smooth surface by *Pseudomonas aeruginosa*: Image Analysis Methods. Doctoral dissertation. Montana State University, Bozeman, MT (1987).
13. G. Hernandez, W.H. Hartt, H.A. Videla, "Biofilms and their influence on cathodic protection: a literature survey", Proc. 1st Pan American Corrosion and Protection Congress, Vol. II (1992): p. 391.
14. H.A. Videla, S. Gómez de Saravia, M.F.L. de Mele, G Hernández, W.H. Hartt, "The influence of microbial biofilms on cathodic protection at different temperatures", CORROSION/93, paper no. 486 (Houston, TX: National Association of Corrosion Engineers, 1993).

TABLE 1

Effect of Cathodic Protection on *V. alginolyticus* settlement on 304L SS immersed for 18 h in synthetic seawater at different temperatures

| Protection | Cell numbers/cm ² | |
|-------------|------------------------------|-----------------------|
| | 12 C | 20 C |
| Unprotected | 1.07 x 10 ⁴ | 1.4 x 10 ⁸ |
| Protected | 7.30 x 10 ² | 3.0 x 10 ⁷ |

TABLE 2

Effect of Cathodic Protection on sessile *V. alginolyticus* growth on 304L SS. T=12 C.

| Protection | Cells/cm ² |
|--|-----------------------|
| 2 h without CP | 1.9 x 10 ² |
| 4 h without CP | 3.4 x 10 ² |
| 2 h without CP + 2 h without CP in sterile media | 2.1 x 10 ² |
| 2 h without CP + 2 h with CP in sterile media | 26.3 |

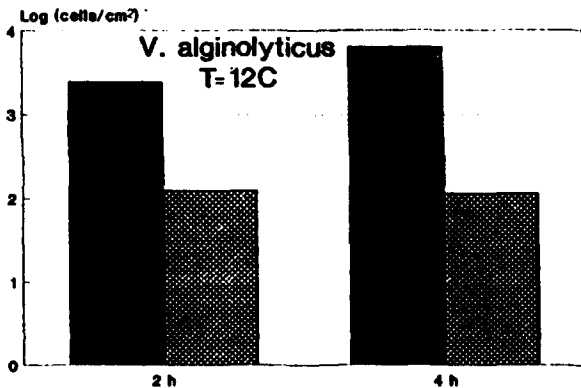


Fig 1: Log (cell number/cm²) vs. exposure time plot. AISI 304L SS specimens were immersed in a 24 h old culture of *V. alginolyticus* in synthetic seawater (▨) with CP (-0.7 V); (■) without CP. Incubation temperature: 12 C. (From Ref. 14 with permission of NACE).

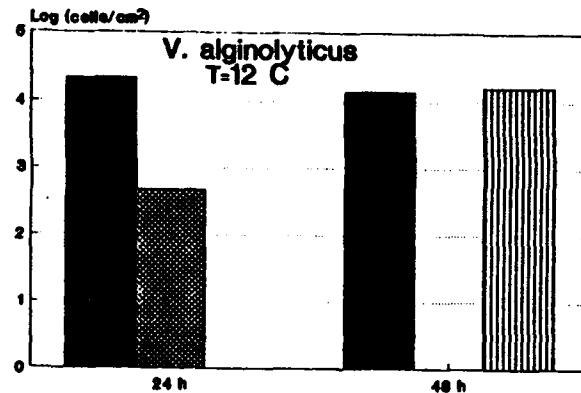


Fig 2: Log (cell number/cm²) vs. exposure time plot. AISI 304L SS specimens were immersed in seawater inoculated with *V. alginolyticus*: (▨) with CP (-0.7 V); (■) without CP; (▤) 24 h without CP and 24 h with CP. Incubation temperature: 12 C.

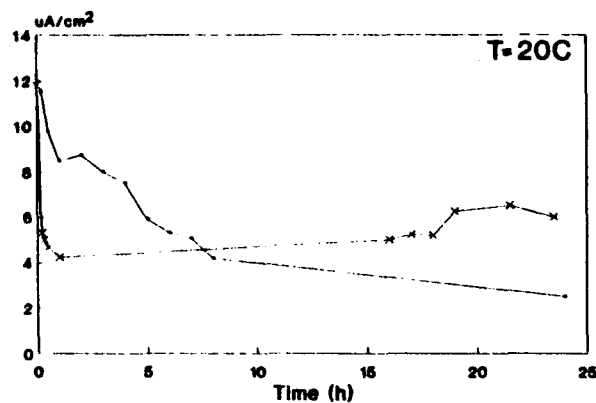


Fig 3: Current density vs. time plot of a cathodically protected AISI 304L SS immersed in: (■) sterile synthetic seawater and (x) synthetic seawater inoculated with *V. alginolyticus*. Incubation temperature: 20 C. From Ref. 14 with permission of NACE)



Fig 4: SEM microphotograph of a cathodically protected AISI 304L SS specimen after a 4 h exposure to a 24 h old culture of *V. alginolyticus* in synthetic seawater. Bacteria are covered by calcareous deposits. Magnification X 10,000 .

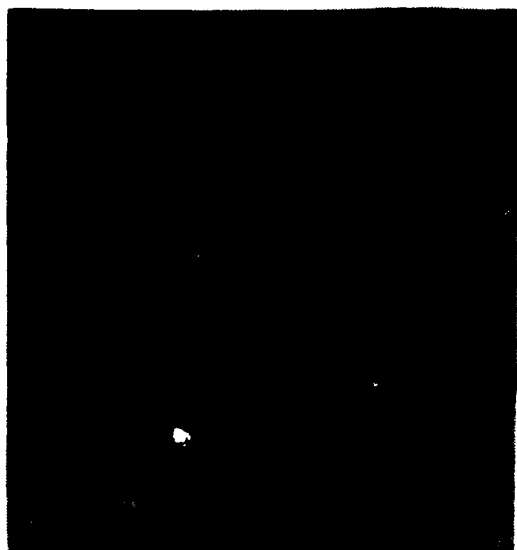


Fig 5: SEM microphotograph of a cathodically protected AISI 304L SS specimen after a 4 h exposure to a 24 h old culture of *V. alginolyticus* in synthetic seawater. Magnification X 10,000.

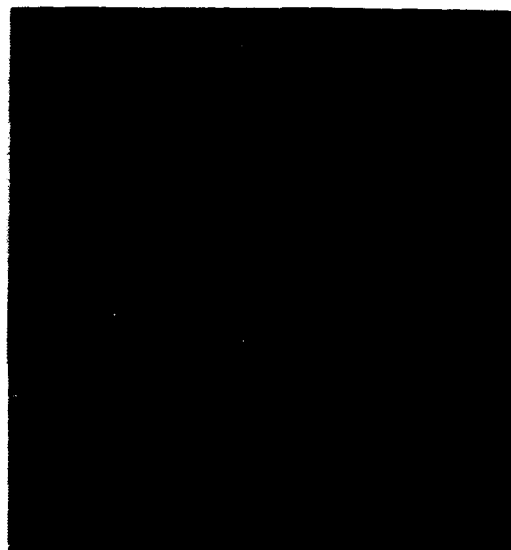


Fig 6: SEM microphotograph (topographical image); experimental conditions as in Fig. 5. Cavities reproducing bacterial shapes can be seen at the right side of the picture.



Fig 7: SEM microphotograph of an AISI 304L SS specimen (without CP) after a 7 days exposure to a mixed SRB culture. Localized attack beneath bacterial film can be seen. Magnification X 5,000.

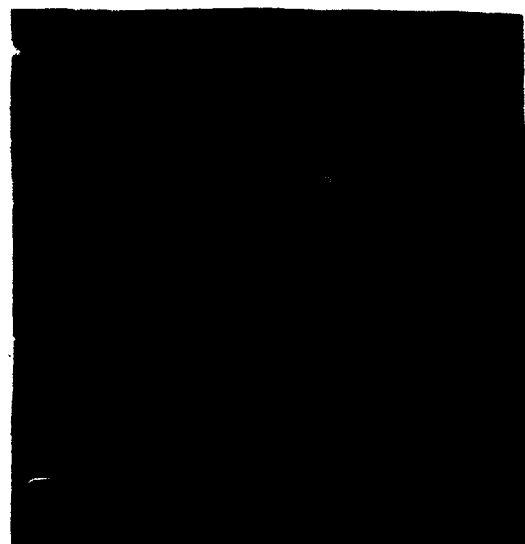


Fig 8: SEM microphotograph of a cathodically protected AISI 304L SS specimen after a 15 days exposure to a mixed SRB culture. The vertical arrows indicate the biofilm thickness. Magnification X 3,500.

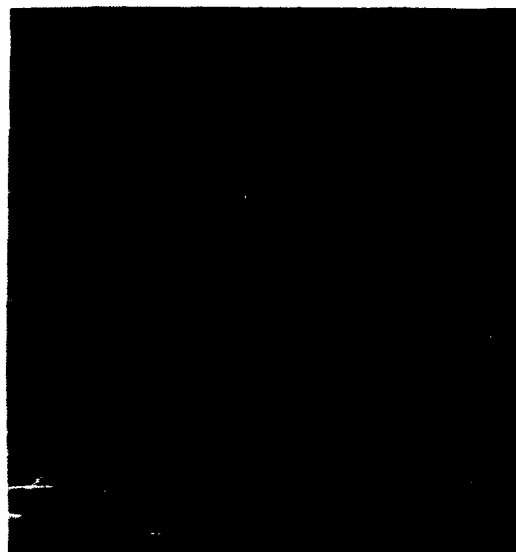


Fig. 9: SEM microphotograph (topographical image) of an AISI 304L SS specimen (without CP) after a 15 days exposure to a mixed SRB culture. The biofilm was removed and a small pit can be seen. Magnification X 5,000.

Factors Contributing to Ennoblement of Passive Metals Due to Biofilms in Seawater

P. Chandrasekaran
Graduate College of Marine Studies
University of Delaware
Lewes, DE 19958. U.S.A.

S.C. Dexter
Graduate College of Marine Studies
University of Delaware
Lewes, DE 19958. U.S.A.

ABSTRACT

Ennoblement of the corrosion potential on passive metals due to the action of biofilms is a widely recognized phenomenon. The presence of peroxide as a by-product of bacterial metabolism has been verified in biofilms formed in two widely separated geographical locations. Experiments with enzymes indicated that some dissolved oxygen is necessary in the bulk solution. Abiotic simulation experiments demonstrated, however, that an acid pH at the metal-biofilm interface is also necessary for the observed amount of ennoblement on platinum to be achieved. EDAX data show the presence of manganese, iron and sulfur in mature biofilms on platinum. A multi-layered model is described, encompassing both the acid and neutral pH schools of thought for ennoblement. The model features aerated, near neutral pH conditions in the outermost layer, with peroxide being produced and regulated by the respiratory enzyme system of the aerobic organisms. The model requires decreasing oxygen and pH as one proceeds into the biofilm, becoming predominantly low oxygen (or anaerobic) and acid pH at the metal-biofilm interface. It is suggested that the mechanism of ennoblement involves a synergistic effect of peroxide and acid pH at low oxygen within near the metal surface.

Key words: Ennoblement, peroxide, pH, dissolved oxygen, EDAX, enzyme, passive metal, interfacial chemistry.

INTRODUCTION

Ennoblement of passive metals due to biofilm formation is well documented as reviewed by Chandrasekaran and Dexter¹. Even though this phenomenon is widely recognized, no mechanism has been agreed upon so far. Several workers^{2,3} have suggested a decrease in pH of a biofilm as a major contributor to ennoblement. Chandrasekaran and Dexter¹ have identified and measured the presence of low milli-molar levels of H₂O₂ in marine biofilms. It was argued that the presence of H₂O₂ and reduction in pH contribute synergistically towards shifting the open circuit potentials (OCP) in the positive direction. The production of H₂O₂ in a biofilm was rationalized on the basis of the respiratory enzyme system of the bacteria, macrocyclic organo metallic catalysis and electrochemistry¹. Presence of peroxide in biofilms was speculated by Salvago et al⁴ as a reason for ennoblement. The presence of acid producing microbes in the biofilm was also reported¹. Recently a new hypothesis for ennoblement mechanism has been put forth by Mollica⁵ and Eashwar⁶, in which the biofilm pH is considered to be neutral for ennoblement. Mollica⁵ measured the OCP of stainless steel in seawater acidified down to pH 5. Since the OCP did not rise to the level observed for biofilms, he ruled out the possibility of acidification as a mechanism for ennoblement. Mollica⁵ hypothesized that ennoblement is due to depolarization of the cathodic oxygen reaction

by bacterially produced catalytic enzymes with a maximum efficiency at pH near 8. Eashwar⁶ pointed out that bacterially produced enzymes are active only at near neutral pH, and he hypothesized that the siderophores produced by bacteria would be important to ennoblement.

In the present work the contribution of H_2O_2 towards ennoblement was further investigated. Two sites were selected for carrying out the ennoblement mechanistic studies. One site was on the lower Delaware Bay, at College of Marine Studies (CMS) Facilities at Lewes, DE and the other one was a tropical environment at Offshore Platform and Marine Electrochemistry Center on the Gulf of Mannar, a unit of Central Electrochemical Research Institute at Tuticorin, India. Platinum coupons were exposed for marine biofilm development, and for ennoblement mechanistic studies.

EXPERIMENTAL PROCEDURE

Platinum coupons were prepared according to fabrication procedures described previously¹. The seawater characteristics during exposure in Delaware Bay were: temperature 22 - 26°C, pH 7.7 to 8.1, salinity 25 to 31 parts per thousand, oxygen air saturated at 5 to 8 ppm and H_2O_2 below the detection limit of the peroxidase enzyme strip. Biofilms of 30 to 160 μm thickness with macroscopically complete coverage⁷ have typically developed in this water. These films are usually so thick that it is impossible to count all the microorganisms. Epifluorescence microscopy at 1000X after staining with DAPI reveals a diverse microflora ranging from coccoidal bacteria to short and curved rods to other filamentous forms. The concentrations of organisms in the surface layers of the films vary from 3×10^5 to 2×10^6 cells cm^{-2} of coupon surface. The numbers are significantly higher than this in those areas covered by microcolonies. The biofilms grown in this study were not specifically analyzed, but were assumed to be similar to those described above. The water characteristics at Tuticorin during the exposure were: temperature 25.6 to 27.4°C, dissolved oxygen 6 ppm, salinity 33.2 to 33.9 parts per thousand and H_2O_2 below the detection limit of the peroxidase enzyme strip. Biofilms formed in Tuticorin waters on platinum in the present studies were not analyzed. It is expected, however, that they should be similar to those already characterized from those same waters by Maruthamuthu, et al⁸. They found that the ratio of heterotrophic bacteria to thiosulfate oxidizing bacteria was high initially, but decreased significantly as the biofilm matured. They also reported that low biofilm pH was a significant feature of microbial fouling in Tuticorin harbor waters.

The open circuit potentials of these coupons were measured using high impedance digital voltmeter, with SCE for reference. At Delaware, electrochemical experiments were conducted using an IBM computer with PARC 342 software controlled 273A potentiostat (EG & G, Princeton Applied Research) with standard accessories and cell set up. This set up was used for E_{corr} measurements at various combinations of pH, H_2O_2 and oxygen. Cyclic voltammetry was carried out using IBM Instruments Inc. EC 225 Voltammetric Analyzer with Hewlett Packard Moseley Division X-Y recorder. Platinum was used for working and counter electrodes, and SCE for reference. During all the experiments, the seawater dissolved oxygen and pH were measured. Measurement of dissolved oxygen was carried out using a YSI model 57 oxygen meter and the pH was measured using Fisher digital pH meter. H_2O_2 indicating peroxidase enzyme strips (E. Merck) were used in measuring H_2O_2 in a biofilm. The presence of H_2O_2 was indicated by a change in color of the strip, and the concentration range of H_2O_2 was indicated by the intensity of the color developed.

A series of experiments was carried out to decrease the peroxide concentration in a biofilm which caused ennoblement on platinum, and to record the effect of that decrease on the OCP of the electrode. In order to do this, beef liver catalase (Sigma Chemical Co.) at a concentration of 0.5 mg ml^{-1} was added to the seawater surrounding the ennobled electrode. The catalase added should dismute any peroxide it came in contact with. The hope was that through a combination of diffusion of 1) peroxide out of the biofilm into the bulk solution and

2) catalase into the biofilm, the peroxide concentration would be reduced enough to affect its contribution to ennoblement. Similar concentrations of both active and deactivated (control) catalase were added. The deactivated catalase control was achieved by exposure to sunlight under aerated conditions⁹. Seawater with catalase was exposed for two hours to artificial sunlight produced by Phillips cool-white fluorescent lamps at an irradiance of 900 $\mu\text{Einsteins m}^{-2} \text{sec}^{-1}$. Enzyme activity¹⁰ was measured using a Bausch and Lomb spectrophotometer operating at a wavelength of 240 nm and connected to a strip chart recorder. A calibrated level of absorbance was first established for 30% peroxide with 7.5 pH, 1M NaCl and 0.1M Na_2HPO_4 buffer in quartz cuvettes. When active enzyme was added, that absorbance decreased with time, while additions of deactivated enzyme did not change the absorbance.

A Philips model 501 Scanning electron microscope (SEM) with Energy dispersive X ray analyzer (EDAX) model 9100 was used for surface analysis. Biofilmed platinum coupons from natural seawater exposure were dehydrated by placing in a vacuum chamber for about 30 minutes without any other pretreatment or coating. The imaging capability of SEM was used to choose the location on the surface, and EDAX was used to identify the elements present in the biofilm at that location.

RESULTS

OCP values and H_2O_2 concentration were measured for biofilmed platinum at the Delaware and Tuticorin locations in natural seawater. Platinum OCP values are shown in Figure 1. To verify the presence of H_2O_2 in a natural biofilm, H_2O_2 indicating enzyme strips were used. For mature biofilms from Delaware Bay seawater a H_2O_2 concentration range of 1.3 to 6.6 mM was measured, whereas the concentration range of H_2O_2 was 1.3 to 2.6 mM during the initial stages of biofilm formation at Tuticorin.

Cyclic voltammetry was carried out on biofilmed platinum coupons. The characteristic cyclic voltammogram as shown in Figure 2 was produced with a scan rate of 50 mV/sec over the potential range from -400 to +600 mV SCE. In all the scans using biofilmed platinum coupons the characteristic oxidation peak at about 0.35 V SCE in the forward scan and the reduction peak at -0.15 V SCE in the reverse scan were observed to be reproducible. Chandrasekaran and Dexter¹ identified the peak at 0.35 V as H_2O_2 oxidation and the peak at -0.15 V as oxygen reduction. Abiotic experiments on 600 grit polished bare platinum electrodes were carried out to simulate the cyclic voltammogram of a biofilmed platinum. Various combinations of oxygen, pH and H_2O_2 were used in trial and error method. Peroxide additions were made in appropriate volumes to one liter of seawater, and the concentration was expressed in mM units. The voltammogram of a biofilmed platinum coupon from Figure 2 was not fully reproduced until the seawater was deaerated to an oxygen concentration below 0.6 ppm, with 8.2 - 9.8 mM H_2O_2 added at pH 2.8 - 2.9 as shown in Figure 3. An independent set of experiments was carried out to determine the OCP of platinum in deaerated seawater (0.55 ± 0.5 ppm O_2) at various combinations of pH and H_2O_2 . The results are shown in the form of a bar graph in Figure 4. Starting at condition 1 to the left in the diagram, the OCP is shown for platinum at pH 8.3. A reduction in pH to 5 (condition 2) produced a jump in OCP to over 300 mV. Addition of 8.2 mM peroxide at pH 5 gave no further increase in potential (condition 3). A further decrease in pH to 2.9 without peroxide addition increased the potential to about 350 mV, but it was not until a combination of pH 2.9 and 8.2 mM peroxide was tried that the potential of over 400 mV observed on biofilmed platinum was obtained (condition 5).

A typical catalase enzyme activity measurement using spectrophotometer is shown in Figure 5. The decrease in absorbance over time after adding active catalase is directly related to dismutation of H_2O_2 by the active enzyme. In contrast, no decrease in absorbance is noted upon addition of inactivated enzyme. The decay in OCP values of ennobled platinum electrodes exposed to active and inactive forms of catalase were also recorded. Due to

dismutation of H_2O_2 by active catalase, OCP values were expected to drop more rapidly upon active catalase exposure than inactive catalase exposure. However, the rates of decay in OCP values were comparable in both exposures (data not shown). To understand more about this anomaly, studies were conducted to periodically measure the solution chemistry and the catalase activity. Hourly measurements of catalase activity showed that the enzyme remained active for nearly 10 hours in seawater. This indicated that the decay in OCP for first 10 hours after addition of active enzyme could be taken as due to dismutation of H_2O_2 . A closer look at the inactive enzyme experiment revealed that the enzyme precipitated out of solution and formed a thin continuous film on the surface of the solution. Active enzyme did the same thing after the first 10 hours. Experiments were further conducted using an ennobled biofilmed coupon exposed to active catalase enzyme. Periodic measurements of OCP, bulk solution pH and dissolved oxygen were recorded. The data are shown in Figure 6. At first the potential decreased with no change in dissolved oxygen. As the 10 hour limit approached, however, the dissolved oxygen fell rapidly. This corresponded to the active-inactive transition of the enzyme and the formation of the surface film. Subsequent immersion of catalase treated coupons in natural seawater brought the OCP back to their original ennobled values, after a period of time. This was attributed to a recovery of normal biofilm chemistry.

When a biofilm was formed on platinum at the CMS location, the color of the coupon changed from silvery in appearance to golden yellow, to reddish to brown as it matured, having a brown black and mixed appearance after several months. The color of the biofilm on platinum provided clues for identifying the elements present in the film. Typical EDAX data are shown in Figures 7 and 8 for elements present in a relatively younger (one week) and mature biofilms (four months) respectively developed on platinum from natural seawater. Manganese, iron and sulfur were found in mature biofilm whereas these elements were absent in the younger biofilms. The presence of Mn, Fe, and S in mature biofilms was used in identifying the clues to the chemistry of the biofilm and the bacterial metabolism. The other elements in these EDAX diagrams were not considered significant as they were present either in seawater or in the platinum substratum.

DISCUSSION

Figure 1 showed the OCP values for platinum in Tuticorin waters to be considerably lower than those in Delaware. The reasons aren't very clear. Since the duration of exposure was only 20 days at Tuticorin the biofilms probably weren't mature enough to give a maximum concentration of H_2O_2 , and thereby a higher OCP value. Probably the microbial population itself is widely different between these two locations contributing to this low amount of ennoblement. However, identification of measurable quantities of H_2O_2 at both locations is considered to be significant.

Results from the abiotic simulation experiments shown in Figure 4 verify the synergistic effects of pH and H_2O_2 in creating the ennoblement phenomenon. The level of ennoblement and the positions of the predominant cyclic voltammetry peaks found in the presence of natural biofilms were reproduced only when the proper combination of pH, H_2O_2 , and low oxygen were established in bulk seawater. Under natural biofilm conditions, however, only the chemistry immediately adjacent to the metal surface needs to be at the specified combination of pH, H_2O_2 , and oxygen.

Figure 6 showed a rapid decrease in dissolved oxygen of the solution roughly coinciding with the active-inactive transition of the enzyme and formation of the surface film. It is thought that elimination of oxygen from the solution was brought about by a combination of blocking dissolution of oxygen from the atmosphere by the inactive enzyme film and scavenging of oxygen from solution by the biofilm. The loss of dissolved oxygen as well as peroxide contributed to the rapid decay of OCP values. This leads to the important conclusion that at least

some dissolved oxygen in the bulk seawater is necessary for ennoblement. Once oxygen is eliminated from the system, the respiratory system of the aerobic organisms will also cease from producing peroxide, and the synergistic effects of peroxide and pH will be lost.

The EDAX data in Figures 7 and 8 showed the elements present in young and mature biofilms on platinum. All the elements except the relatively large quantities of manganese, iron and sulfur can be accounted for by their presence in seawater or in the substratum. The occurrence of manganese, iron and sulfur can be explained partly due to microbial metabolism and partly due to favorable chemistry for precipitation. The EDAX data provide information neither on the oxidation state of these elements nor on the stoichiometry of the compounds, so it is possible that both oxidized and reduced forms of these elements could be present depending on the chemistry involved. The color changes in the biofilm from yellow to red to brown and black are generally consistent with the EDAX data. Yellow might correspond to a predominance of sulfur compounds^{11,12} (perhaps pyrite or marcasite), while the reds and browns could correspond to iron and manganese¹¹⁻¹⁵ compounds such as limonite, goethite, hematite or pyrolusite.

Since the pH of the biofilm is proposed to be either acidic or neutral according to the different theories of ennoblement, let us next consider two different pH ranges and the general reactions that are possible in each. First assume the pH of the entire biofilm to be acidic. Ferrous and manganous ions would be dominant in the anaerobic layers of the biofilm¹¹⁻¹⁴. In the aerobic layer, however, due to presence of oxygen, ferrous and manganous ions would be oxidized to ferric and manganic¹¹⁻¹⁴. But at acidic pH iron and manganese have a high solubility^{11-14,16}. This would make accumulation of iron and manganese by precipitation in the biofilm unlikely, in contrast to the EDAX observation. Acidic pH would also not support the presence of active respiratory enzymes in a biofilm^{6,17}. Even though an acid pH would seem to be important to ennoblement, it is inconsistent with an active respiratory enzyme system and with the EDAX data. Hence we believe, that the entire biofilm cannot be acidic.

Next assume the pH of the entire biofilm to be neutral. This condition would support an active enzyme system in controlling the peroxide concentration in the aerobic layers of the biofilm. This would also support the precipitation of iron and manganese in a biofilm, because iron and manganese are practically insoluble at neutral pH (10^{-15} M at pH 7)^{11-14,18}. However, we were unable to simulate a fully ennobled electrode or the proper peaks in the cyclic voltammogram at neutral pH¹. Hence the neutral pH model also fails to explain all the observations.

Since neither the acidic nor neutral pH model alone, can explain all the observations, we propose a combination of these acidic and neutral conditions in explaining the ennoblement. The most realistic model would seem to involve a multi-layered biofilm, in which aerobic, microaerobic, and anaerobic layers would work together in creating a favorable chemistry for ennoblement. The chemistry in the outer portions of the biofilm is expected to be close to that of normal bulk seawater. Oxygen would be consumed in these outer layers, allowing iron and manganese reducers to proliferate in the microaerobic or anaerobic regions of the film. H_2O_2 produced in the aerobic portion of the film during respiration would diffuse into the biofilm toward the metal substratum.

It is well known that manganese and iron reducers do not gain as much energy in reducing these elements as they would in the use of oxygen as an electron acceptor^{19,20}. This means that these microorganisms must use large quantities of iron and manganese for their metabolism, which would be consistent with measurable concentrations of manganese and iron in a mature biofilm as shown by EDAX. Starkey and Halvorson²¹ have explained iron reduction in nature as an indirect microbial process in which the microorganisms decreased the pH and oxygen concentration in their environment creating conditions favorable for reduction of $Fe(OH)_3$. Manganese and iron reduction take place in acidic environments^{11-14,18,22}, and there are many possible reactions in a biofilm which can

lead to increasing acidity. These include the production of acid due to hydrolysis of iron and manganese oxides¹⁴ in the aerobic portion of the biofilm, oxidation of reduced metabolic products either by peroxide or by oxygen at the oxic-anoxic interface²⁴⁻²⁷, oxidation of sulfides by ferric and manganic²⁸ and production of acidity due to heavy metal adsorption by hydrous manganese dioxide^{14,29}. Bacterial metabolism itself might contribute to the low pH by secreting various acidic metabolites^{1,20,31}. This would lead to an acidic microaerobic layer where iron and manganese would be readily available¹⁶ for microorganisms as electron acceptors. The acidity produced within the biofilm can be expected to spread toward both the metal-biofilm and biofilm-seawater interfaces. However, the buffering capacity of seawater should keep the pH in the outer portions of the biofilm near neutral, while the buffering capacity is much more likely to be overcome in the small portion of liquid trapped near the metal surface, leading to a low pH at the metal-biofilm interface.

Thus, this multi-layered model predicts that there will be sharp gradients of oxygen, pH and perhaps peroxide through the biofilm thickness. It would also allow for point to point variations in chemistry parallel to the metal-film interface. The model would accommodate micro-niches for a wide variety of microorganisms, from aerobes to anaerobes to coexist in consortia, all contributing to ennoblement by working together to change the chemistry at the biofilm-substratum interface. The model accommodates both the acid and neutral pH schools of thought. It requires aerated, neutral pH conditions with active enzyme systems in the outer layers of the film, with low oxygen, acidic conditions predominating at the metal-film interface.

SUMMARY AND CONCLUSIONS

The developing model for a biofilm capable of ennobling the OCP of passive metals and alloys features a multi-layered structure with aerated, near neutral pH conditions in the outermost layer. Approaching the metal surface, the model requires decreasing oxygen and pH, with peroxide playing an important synergistic role. The peroxide is hypothesized to come from both the respiratory enzyme system of the aerobic organisms in the biofilm and the electrochemical reduction of oxygen. The accumulation of Fe, Mn and S compounds in mature biofilms is consistent with this structure, and there may also be a synergistic relationship between these compounds and peroxide in establishing the low pH conditions required by the model at the metal-film interface. Specific conclusions from this work are:

1. H_2O_2 was found in measurable quantity in the biofilms at both locations, where ennoblement studies were conducted.
2. Under our conditions, only a combination of low oxygen and acidic pH with milli-molar concentrations of peroxide can produce the observed amount of ennoblement.
3. Mature biofilms formed in lower Delaware Bay waters had elevated quantities of Mn, Fe and S compared to young films.
4. From the catalase enzyme experiment it can be inferred that the presence of dissolved oxygen in the bulk solution is required for ennoblement.

ACKNOWLEDGEMENTS

This work was sponsored by the Office of Naval Research under contract number 01490J1947. The authors would also like to thank Prof. Dr. G.V. Subba Rao, Director, Central Electrochemical Research Institute for allowing the former author P.C to use his laboratory facility at OPMEC during his visit to India late November, 1992. M. Eashwar, Scientist at OPMEC, Tuticorin is acknowledged for the ennoblement data on platinum.

REFERENCES

1. P. Chandrasekaran and S.C. Dexter, NACE Paper No. 493, CORROSION/93, Houston, TX.
2. S.C. Dexter and S.H. Lin, Proc. 7th Intl. Cong. on Marine Corrosion and Fouling, Valencia, Spain (1988).
3. R.A. Buchanan, P. Li, X. Zhang, N.D.E. Dowling, E.E. Stansbury, J.C. Danko and D.C. White, Electrochemical Field Studies of Freshwater Microbiologically Influenced Corrosion. A Progress Report to the EPRI, Dec. 1989.
4. G. Salvago, G. Fumagalli, G. Taccani, P. Cristiani and G. Rocchini, Electrochemical and corrosion behaviour of passive and fouled metallic materials in seawater, In European federation of corrosion publications, No. 8, Microbial Corrosion, Proceedings of the 2nd EFC workshop Portugal, 1991. Eds C.A.C. Sequeira and A.K. Tiller, Published for the European Federation of Corrosion by the Institute of Materials, 1992.
5. A. Mollica, International Biodeterioration and Biodegradation, 29, 213 - 229, 1992.
6. M. Eashwar and S. Maruthamuthu, The ennoblement phenomenon: critical analysis and a hypothetical model, unpublished manuscript.
7. S.C. Dexter and H.J. Zhang, Effect of biofilms, sunlight and salinity on corrosion potential and corrosion initiation of stainless alloys, EPRI final report NP - 7275, Research project 2939 - 4, 1991.
8. S. Maruthamuthu, M. Eashwar, S. Sebastin Raja and K. Balakrishnan, Effects of microfouling and light/dark regimes on corrosion potentials of two stainless alloys in seawater, CORROSION-ASIA (organised by NACE, Houston, TX) 7-11 september 1992, Singapore.
9. R.L. Mitchell and I.C. Anderson, Science, Vol. 150, pp.74.
10. Worthington Manual, Enzymes related biochemicals, Worthington biochemical corporation, Freehold, NJ, U. S. A. 07728.
11. K.H. Nealson, The Microbial Iron Cycle, Chapter 6, in Microbial Geochemistry Ed. W. E. Krumbein, Blackwell Scientific, Boston p. 159 - 190, 1983.
12. H.L. Ehrlich, The Geomicrobiology of Iron, In Geomicrobiology, pp. 165-201, Marcel Dekker, New York, 1981.
13. K.H. Nealson, The Microbial Manganese Cycle, Chapter 7 in Microbial Geochemistry Ed. W.E. Krumbein, Blackwell Scientific, Boston, p. 191-222, 1983.
14. H.L. Ehrlich, The Geomicrobiology of Manganese, In Geomicrobiology, pp. 203-249, Marcel Dekker, New York, 1981.
15. Manual of Mineralogy (after J.D. Dana), 20th Edition, Eds. C. Klein and C.S. Hurlbut, jr. John-Wiley and Sons, 1985.
16. G.M. Gadd, Metal Tolerance, Chapter 7 in Microbiology of Extreme Environments pp. 178-210, Ed. C. Edwards, McGraw-Hill Publishing Company, 1990.
17. A.L. Leninger, Chapter 9, In Principles of Biochemistry, pp. 207-247, Worth Publishers, Inc., New York, 1982.
18. W.C. Ghiorse, Chapter 6 In Biology of Anaerobic Microorganisms Ed. A. B. Zehnder, Wiley Series in Ecological and Applied Microbiology, pp. 305 - 331, Wiley - Liss, A John Wiley and Sons Inc. Publication, New York (1988).
19. T.D. Brock and M.T. Madigan, Biology of Microorganisms, 5th Edition, pp. 552-597, Prentice-Hall, Englewood Cliffs, New Jersey 07632, U.S.A. 1988.
20. T.D. Brock and M.T. Madigan, Biology of Microorganisms, 5th Edition, pp. 789-792, Prentice-Hall, Englewood Cliffs, New Jersey 07632, U.S.A. 1988.
21. R.L. Starkey and H.O. Halvorson, Soil Sci. 24, 381 - 402, 1927.
22. W.H. Koppenol, Bioelectrochemistry and Bioenergetics 18 (1987), 3 - 11, A section of J. Electroanal. Chem and Constituting Vol. 232 (1987).

23. T.D. Brock and M.T. Madigan, *Biology of Microorganisms*, 5th Edition, pp. 598-656, Prentice-Hall, Englewood Cliffs, New Jersey 07632, U.S.A., 1988.
24. C.C. Gilmour, *Effects of Acid Deposition on Microbial Processes in Natural Waters*, Chapter 2 In *Environmental Microbiology*, Ed. Ralph Mitchell, Wiley-Liss, A John-Wiley and Sons, Inc. Publication, 1992.
25. J.L. Crolet, S. Daumas and M. Magot, pH regulation by sulfate-reducing bacteria, NACE Paper No. 303, CORROSION/93, Houston, TX.
26. G.W. Luther III, G. Catalano, G.J. De Lange and J.R.W. Woittiez, *Marine Chemistry*, 31, pp. 137-152, 1990.
27. P. Behra and L. Sigg, Evidence for Redox Cycling of Iron in Atmospheric Water Droplets, *Letters to Nature*, *Nature*, Vol 344, pp. 419, 29 March 1990.
28. B. Thamdrup, K. Finster, J.W. Hansen, and F. Bak, *Applied Environmental Microbiology*, Vol. 59, No. 1, Jan. 1993, pp. 101-108.
29. R.M. McKenzie, Proton release during adsorption of heavy metal ions by a hydrous manganese dioxide, *Notes in Geochimica et Cosmochimica Acta*, Vol. 43, pp. 1855-1857.
30. W.J. Ingledew, *Acidophiles*, Chapter 2 in *Microbiology of Extreme Environments* Ed. C. Edwards, McGraw-Hill Publishing Company, 1990.
31. B.J. Little, P.A. Wagner, W.G. Characklis and W.C. Lee, *Microbial Corrosion*, Chapter 16, In *Biofilms* Eds. W.G. Characklis and K. C. Marshall, A Wiley-Interscience Publication, John-Wiley and Sons, Inc. 1990.

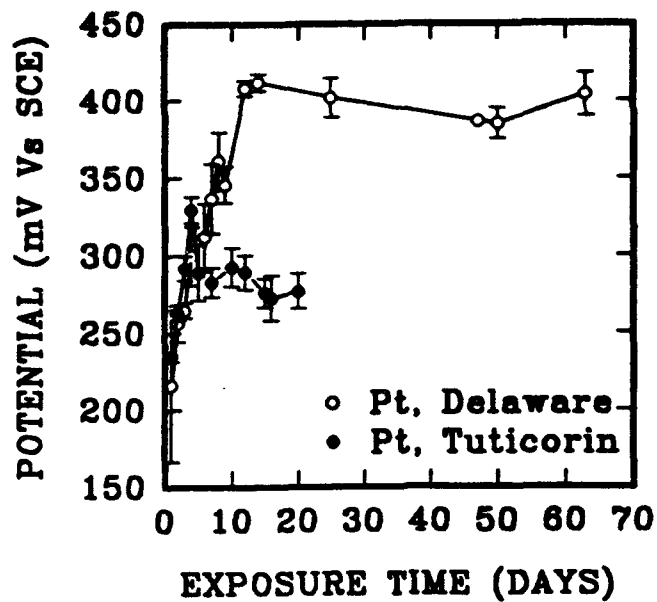


FIGURE 1. Ennoblement data on platinum at two geographical locations.

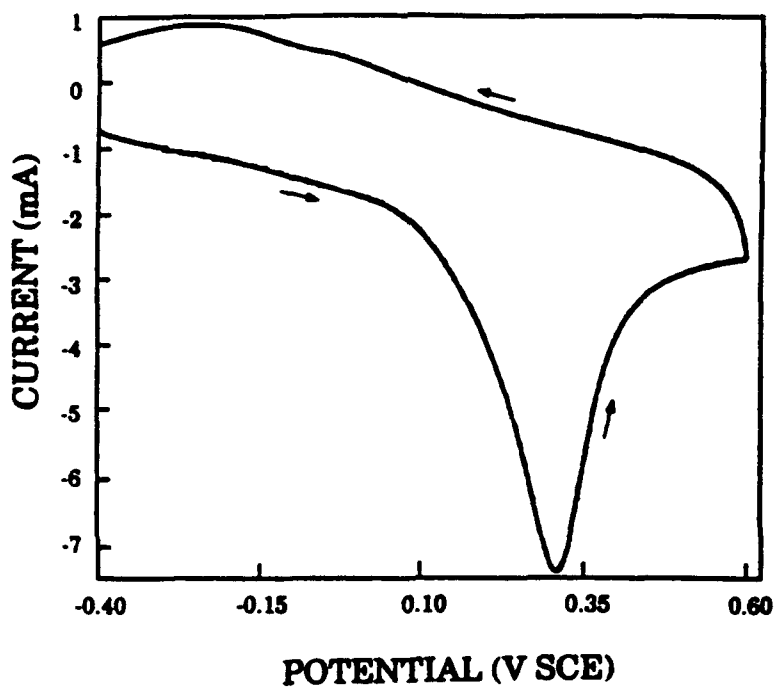


FIGURE 2. Cyclic voltammogram of a biofilmed platinum electrode in natural seawater. (Scan rate 50 mV/sec)

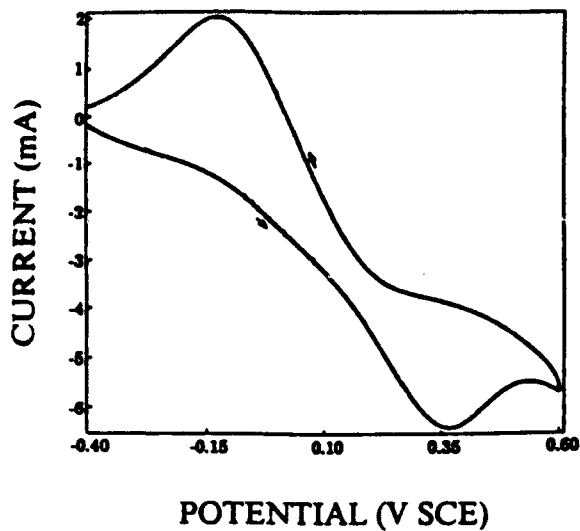


FIGURE 3. Cyclic voltammogram of a bare platinum electrode, produced using the chemistry thought to exist in a biofilm (H_2O_2 peak at close to 0.35 V, Oxygen peak at -0.15 V, Scan rate 50 mV/sec).

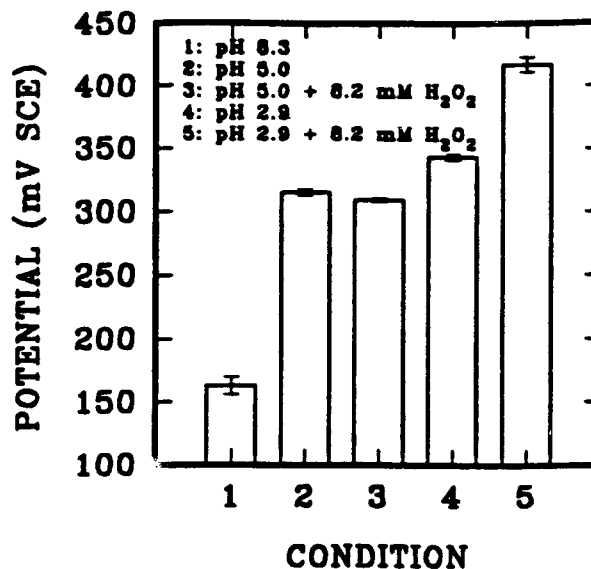


FIGURE 4. OCP of platinum in deaerated (0.55 ± 0.05 ppm O_2) natural seawater at various pH and peroxide levels.

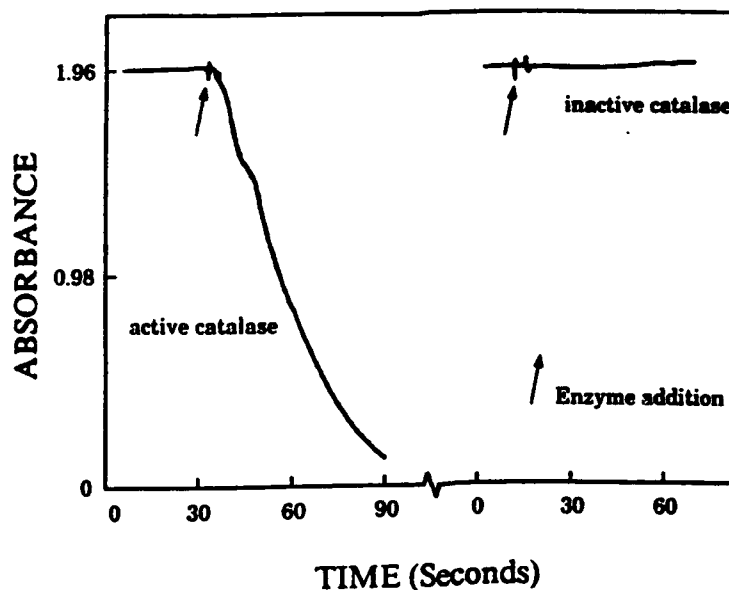


FIGURE 5. Typical spectrophotometer data, showing change in absorbance (or peroxide concentration) upon addition of active or inactive catalase enzyme.

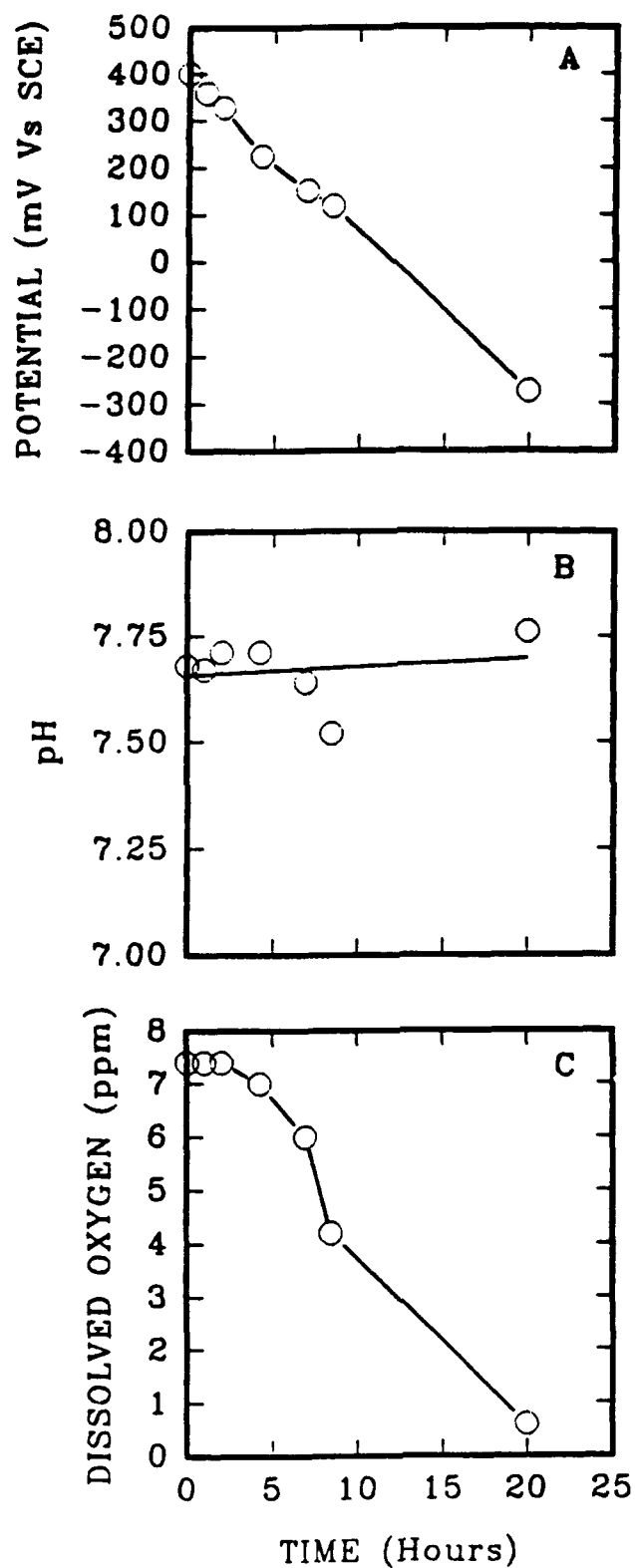


FIGURE 6. Effect over time of adding active catalase to the bulk solution on A). OCP of ennobled platinum electrode, B). pH of the bulk solution and C). dissolved oxygen in the bulk solution.

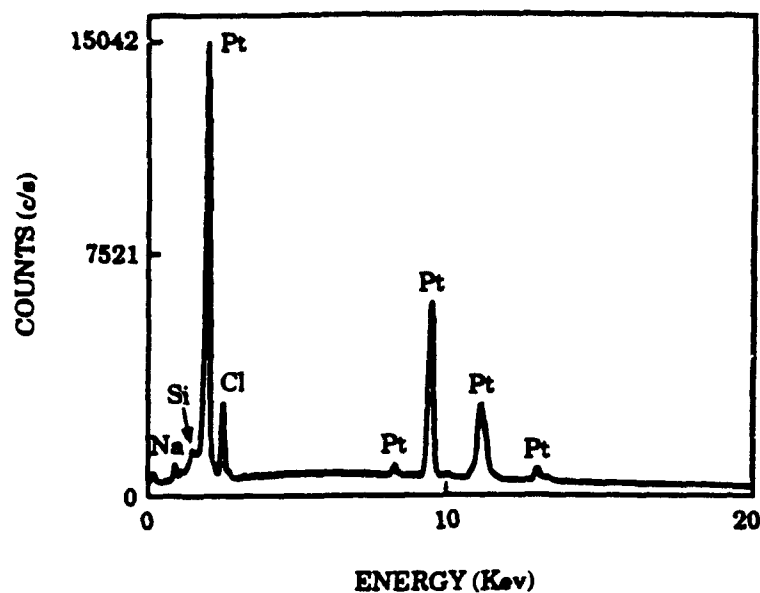


FIGURE 7. EDAX data showing elements present in a one week old biofilm on platinum.

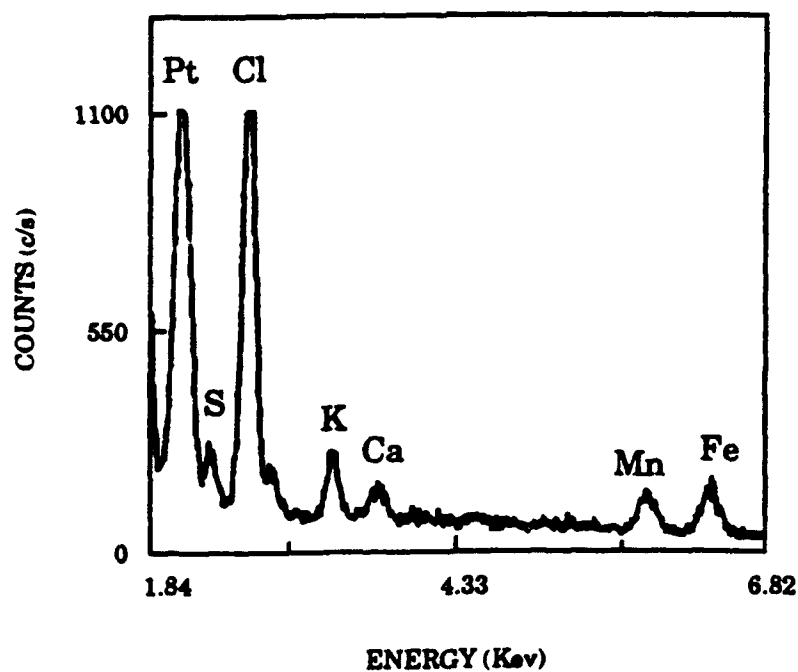


FIGURE 8. EDAX data showing elements present in a nearly four month old biofilm on platinum.

Ennoblement of Stainless Alloys by Marine Biofilms: An Alternative Mechanism

M Eashwar and S Maruthamuthu
Offshore Platform and Marine Electrochemistry Centre
CECRI Unit, Harbour Area
Tuticorin 628 004, India

S Sathyanarayanan and K Balakrishnan
Corrosion Science and Engineering Division
Central Electrochemical Research Institute
Karaikudi 623 006, India

Abstract

Biofilms from Tuticorin seawater caused appreciable ennobling of titanium in the presence of moderate illumination that allowed diatoms to grow in association with bacteria. In the dark and with high light levels, ennobling was hindered. Based on present results and other literature data, it is hypothesised that pH's close to neutral trigger the ennoblement phenomenon. Anodic polarization data show that ennobling is accompanied by a decrease in passive current, i_p , and an increase in the critical pitting potential, E_{cpp} , suggesting that passivity enhancement by microbially produced inhibitors could be the major mechanism.

Introduction

Numerous reports have been made over the years, from geographically distant sea locations, that biofilms typically shift the corrosion potential of stainless¹⁻⁸ alloys in the noble direction, often by as large as 300 mV. This shift, an ennoblement, increases (i) the³ susceptibility to corrosion of anode materials in galvanic couples and (ii) the current density required to maintain stainless alloys cathodic.

While there is controversy^{9,10} over the major mechanism of ennoblement on the one hand, observations by some workers that¹¹⁻¹³ ennoblement is small or none with biofilms of certain areas add up to the anomaly on the other.^{7-9,12} Further, data on the effect of light on corrosion potentials^{7-9,12} are conflicting.

In this paper, the corrosion potential of a stainless alloy is investigated in relation to light level and the composition of microfouling. The anodic behaviour of an ennobling stainless alloy is also studied by electrochemical techniques since earlier works have not considered this aspect.

Experimental Procedures

Corrosion Potential Measurements

Titanium (grade 2) was chosen for the present study. The coupons, measuring 50 x 25 x 1 mm, were polished, decreased in acetone and rinsed in distilled water before use. Electrical lead to the coupons was made with copper wire, and a lacquer coating insulated the bimetallic junction.

Biofilms were allowed to develop on the titanium coupons under three different light conditions. Natural seawater was brought into the laboratory by the continuous pumping facility at OPMEC, Tuticorin.

Exposure # 1 utilized a large (750L capacity, rectangular) tank filled almost to the top with seawater. Water was pumped in, and removed by gravity flow ensuring good replacement twice a day. By virtue of placement of the tank outdoors, the water in the tank received illumination direct from the sun. The intensity of light just above the water surface (about 1 foot from the position of the coupons) varied between 20,000 and 35,000 lux during most part of the day on gloomy days. On bright sunny days, the light level was about 50,000 lux or higher.

The other two exposures were made in 50L tanks in the laboratory where seawater was renewed once in 24 hours. One was kept in a dark room (to exclude diatoms) while the other was placed close to the northern windows of the laboratory in such a manner that the light level just above the water surface was low to moderate, between 2,000 and 4,000 lux at day time. This condition was sufficient to ensure appreciable diatom representation in the biofilm.

The properties of seawater during the study period were as follows: salinity = 32.7 to 34.1; DO = 6 mg/L; pH = 8.1 to 8.2. Temperature in the smaller tanks varied between 25.2 and 25.8°C at night and 26.5 to 27.7°C during day. The readings in the large tank were about the same as in the smaller tanks at night, but higher by 1 to 2°C in day hours.

For each exposure condition, five coupons were used for measuring corrosion potential. The coupons were suspended from wooden planks and the potentials recorded by using a high impedance voltmeter in conjunction with a saturated calomel electrode (SCE). These measurements in the large tank were timed at 05.00, 11.00, 17.00 and 21.00 hrs in order to observe possible variations in response to the photo-period. In the indoor experiment, recordings were spaced 24 hours during the first 5 days, and 2 to several days subsequently.

The microfouling that formed on titanium coupons was not

specifically characterised since an earlier investigation⁸ covering two seasons has brought out the successional patterns in biofilm formation under low-light and alternate light/dark conditions in Tuticorin waters.

Electrochemical Measurements

Cyclic anodic polarization was performed on a bare titanium coupon and two biofilmed titanium coupons. These later coupons were ennobled by 125 mV and 215 mV upon exposure to the indoor tank receiving moderate light level, for respective periods of 7 and 15 days. An EG & G PARC Potentiostat (model 173) and Universal Programmer (model 175) were used for determining passive current (i_p) and critical pitting potential (E_{cpp}). Anodic polarization was scanned (1 mV/sec) from a potential 100 mV negative to the open circuit potential. The critical pitting potential was taken as that potential coincident with a sharp rise in current marking the transition from passive to transpassive behaviour.

Results

Corrosion Potentials

Results of titanium exposure to the large tank (high illumination) are presented in Figure 1. Potential variations up to 200 mV or more are noted between the period of maximum illumination and the period of darkness. Note that this effect is obvious even before the time required for biofilm formation. This figure also shows that the fluctuations are much reduced with time, upon aging of the biofilm.

Potentials of titanium in the indoor exposures were remarkably affected by the illumination factor. At the end of the exposure period, all of the coupons exposed to low light contained reasonable numbers of diatoms (about $10^2 / \text{cm}^2$), whereas those in the dark did not. Figure 2 shows that an appreciable ennobling (by about 240 mV) results in presence of diatoms. Light/dark variation in potential was usually small (30 to 40 mV), and all data presented in Figure 2 are those recorded in day light. Potentials in the dark are shifted by only 50 mV, to be eventually reduced after 7 days.

Pitting Scans

Cyclic anodic polarization curves for bare and biofilmed titanium coupons are shown in Figure 3. There is an appreciable shift in the critical pitting potential from +200 mV (bare coupon) to about +660 mV and +800 mV after 7 and 15 days of biofilm formation respectively. Note that this improvement in the E_{cpp} is accompanied by a decrease in the passive current, i_p .

Discussion

Present results are consistent with our earlier observation⁸ that

an appreciable and consistent ennobling requires the presence of diatoms in biofilms. In that study conducted on titanium and 304 stainless steel the corrosion potentials of sea-immersed coupons were ennobled in day hours, with corresponding dip in values at night. These potential excursions were in sharp contrast to the trend shown for stainless alloys in Delaware waters 9,14. Data presented in Figure 2 are in harmony with the observations by Motoda et al.⁷ and Little et al.¹², to be complementary to the objection raised against the low pH mechanism.

In our earlier investigation that is referred to above⁸, the coupons were immersed in natural seawater below OPMEC platform, the illumination level being comparable to that imparted on coupons of the indoor exposure of the present study (2000 to 4000 lux). This light level has no major influence on corrosion potential of stainless steel in the absence of biofilms. Fig.1, however, shows that high light intensities can probably interfere with the ennobling phenomenon. The potentials for titanium as negative as those shown by Mansfield et al.¹³ from Port Hueneme waters are very likely to have been caused by excessive light. Also possible is that some¹⁴ if not all of the potential dip observed by Dexter and Zhang¹⁴ in day hours could have been due to this effect.

Exposure of titanium to Tuticorin harbour waters in the dark does not result in sustained ennoblement (Figure 2) as already shown⁸. This observation is in agreement with that of Little et al.¹² for biofilms from Gulf of Mexico waters. Quite large^{1,2,9} ennobling, on the contrary, has been noted by several authors whose exposure condition utilized substantially low light, at the exclusion of diatoms.

We suggest a model that provides for settling the conflicting corrosion potential behaviour quoted above. The Tuticorin seawater biofilm is arguably more acidic than a "normal" biofilm, by increased⁸ presence of acid producing, thiosulphate oxidising, bacteria. Assuming difference in biofilm pH as the major criterion for the observed variability, we hypothesis that (i) ennoblement is to be expected with any biofilm whose pH is neutral or close to it and (ii) loss or absence of ennoblement is caused by acidic or alkaline shifts, i.e. unfavourable pH's. This model implies that, with an acidic biofilm, ennobling occurs in day light when the diatoms neutralize the acid pH. The opposite trend should be expected with neutral pH biofilms. Here, photosynthesis will result in alkaline pH's contributing to the loss. Figures 4a, 4b and 4c are three hypothetical configurations depicting E_{corr} behaviour in response to biofilm pH. The first of this shows a typical Mediterranean profile. The ennobling here is large with a narrow scatter in values. Present authors presume this to be an effect of persistent neutral pH conditions throughout the exposure. Figures 4b and 4c represent Delaware and Tuticorin

situations respectively. Note that the scatter in E_{corr} is typically large due to sunlight, i.e. photosynthesis. Positive and negative E_{corr} shifts are reversed, as shown by the corresponding dark and open zones. Our hypothesis predicts nobler shift in E_{corr} (an ennoblement) to occur at pH's close to neutral, no matter when this is achieved.

Absence of ennoblement in the Gulf of Mexico waters¹² may also be understood in terms of the neutral pH theory. Little observed biofilm pH to be unvarying from that of the bulk seawater (pH 8) in experiments with continuous lighting. This pH¹⁵ is considerably lower than that measured by Terry and Edyvean¹⁵ or the pH_9 value thought to exist in Delaware biofilms exposed to light⁹. Sustained ennobling was observed by Little only under such conditions. The E_{corr} was rapidly ennobled in the dark, quite similar to the occurrence in Tuticorin in harbour waters⁸. Little observed that biofilm pH in the dark was non-uniform, varying between 5.4 and 9.2. The fact that she measured high concentration of organic carbon in the Gulf of Mexico waters probably reflects enhanced heterotrophic bacterial activity and hence large acid production. This presumption would both vindicate the absence / loss of ennoblement in dark and explain why the interfacial pH was not raised high enough by light.

Results of anodic polarization (Figure 3) clearly reveal that the ennoblement process involves (i) a decrease in i_p and (ii) an increase in $E_{c_{pp}}$, both parameters indicating an enhancement of passivity. The fate of i_p for ennobling stainless alloys has not been measured by earlier workers. Scotto et al.¹⁶ calculated i_p from weight loss data and concluded that the value was nearly the same for stainless steels immersed in artificial seawater as for those ennobled by biofilms. Such calculations can be misleading, since the weight loss data provide little information regarding the electrochemical parameters of stainless alloys. Malik et al.¹⁷, for instance, found that the losses in weight on SS 316 in chloride media about were nearly the same for pH variations from 4 to 9, whereas the $E_{c_{pp}}$ varied drastically. The large positive shift in critical pitting potential during ennoblement further questions the validity of the low pH mechanism, since it is well documented that the $E_{c_{pp}}$ for 304 and 316 stainless steels is shifted to more negative values by reduced pH.

Several authors^{13,14,17} have noted that a minor amount of ennobling usually occurs during the first few hours or days of exposure to synthetic chloride media and/or natural seawater. This shift, which does not require the presence of biofilms, is generally thought to indicate that the alloy is passivated. Present authors are of the opinion that microorganisms accomplish a further improvement in passivity by producing specific inhibitors which are retained in the biofilm matrix. It follows from the neutral pH model that the production and/or efficiency of

such inhibitors is crucially controlled by biofilm pH.

One important aspect with our mechanism concerns disagreement of the passivity improvement concept with the prevalent, generalized notion that biofilms eventually cause corrosion by shifting E_{corr} into E_{cnp} range. We do not know, however, a reference from the ennoblement literature where pitting corrosion on biofilmed surfaces and not crevice corrosion beneath washers and/or lacquer coating has been demonstrated. As a matter of fact, biofilms usually shift the E_{corr} of certain alloy to potentials more positive than their E_{cnp} values without causing pitting. Speculation as to how this can happen cannot easily be accounted for by other mechanisms.

Acknowledgements

This work was supported by the Department of Science and Technology, New Delhi, through grant No. YSP/L91/90. The authors are thankful to the Director, CECRI for permission to communicate the results, and to the Scientist-in-Charge, OPMEC for support.

References

1. A.Mollica, A.Trevis, "The Influence of Microbiological Film on Stainless steels in Natural Seawater", Proc. 4th Int. Cong. on Marine Corrosion and Fouling (Antibes, France, 1976), p.351.
2. R.Johnson, E.Bardal, Corrosion 41(1985) : p.286.
3. S.C.Dexter, G.Y.Gao, Corrosion 44(1988) : p.717.
4. O.Varjonen, T.Hakkarainen, E.L.Murmiaho, Lassila, M.Salkinoja Salonen, "The Brackish water Biofilm Stainless Steels : An Electrochemical and Morphological Study", Microbial Corrosion, Eds. C.A.C Sequeira, A.K.Tiller (London : The Metals Society, 1988), p.164.
5. H.A. Videla, M.F.L de Mele, G.Barankevich, "Biofouling and Corrosion of Stainless Steel and 70/30 Copper-Nickel Samples After Several Weeks of Immersion in Seawater", CORROSION/89, Paper No.291, (Houston, TX : NACE, 1989).
6. J.R.Scully, H.P.Hack D.G.Tipton, Corrosion 41(1985) : 462.
7. S.Motoda, Y.Sazuki, T.Shinohara, S.Tsujikawa, Corrosion Science 31(1990) : p.515.
8. S.Maruthamuthu, M.Eashwar, S.Sebastin Raja, K.Balakrishnan, Biofouling (1993), accepted
9. S.C.Dexter, H.J.Zhang, "Effect of Biofilms on Corrosion

Potential of Stainless Alloys in Estuarine Waters", Proc. 11th Int. Corrosion Congress. (Florence : Association Italiana di Metallurgia, 1990), p.333.

10. A.Mollica, International Biodeterioration and Biodegradation 29(1992) : p.213.
11. F.Mansfeld, R.Tasi, H.Shih, B.J.Little, R.Ray, P.Wagner, "Results of "Exposure of Stainless Steels and Titanium to Natural Seawater", CORROSION/90, Paper No.190, (Houston, TX : NACE, 1990).
12. B.J.Little, R.Ray, P.Wagner, Z.Lewandovski, W.C.Lee, W.G.Characklis, F.Mansfeld, Biofouling 3(1991) : p.45.
13. F.Mansfeld, R.Tasi, H.Shih, B.J.Little, R.Ray, P.Wagner, Corrosion Science 33(1992) : p.445.
14. S.C.Dexter, H.J.Zhang, "Effect of Biofilms, Sunlight and Salinity on Corrosion potential and Corrosion Initiation of Stainless Alloys", Final Project Report No. 29394 (Lewes : Univ. of Delaware, 1991).
15. L.A.Terry, R.G.J.Edyvean, "Influence of Microalgae on the Corrosion of Structural Steel", in Corrosion and Marine Growth of Offshore Structures, eds. J.R.Lewis, A.D.Mercer (London : Society of Chemical Industry, 1984), p.38.
16. V.Scotto, R.Di Cintio, G.Marcenaro, Corrosion Science, 25 (1985) : p.185.
17. A.U.Malik, P.C.Mayan Kutty, N.A.Siddiqi, I.N.Andijani, S.Ahmed, Corrosion Science, 33(1992) p.1809.

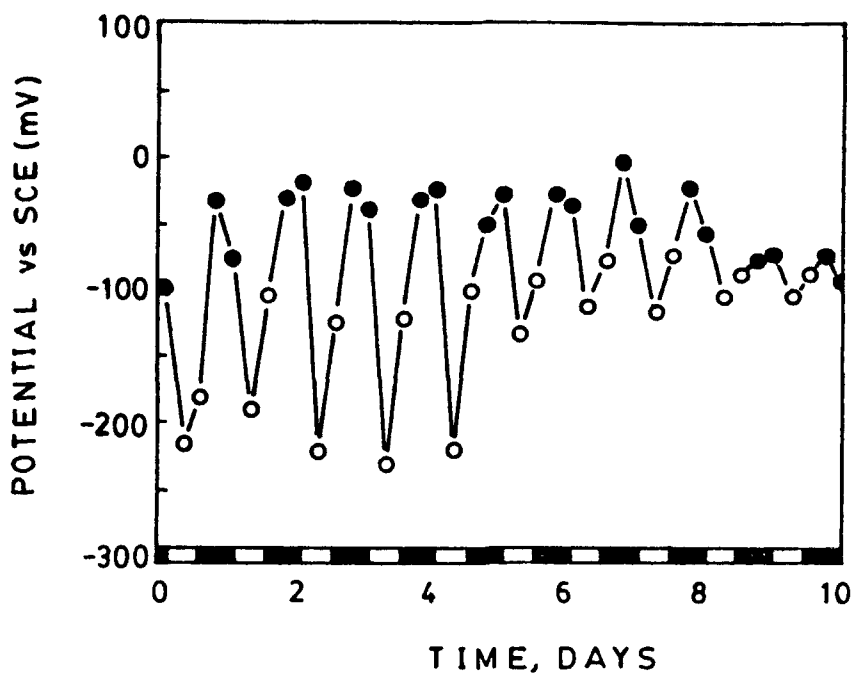


Fig.1 : Potential excursions on a titanium coupon exposed outdoors. Dark circles are values taken at night; open circles, day.

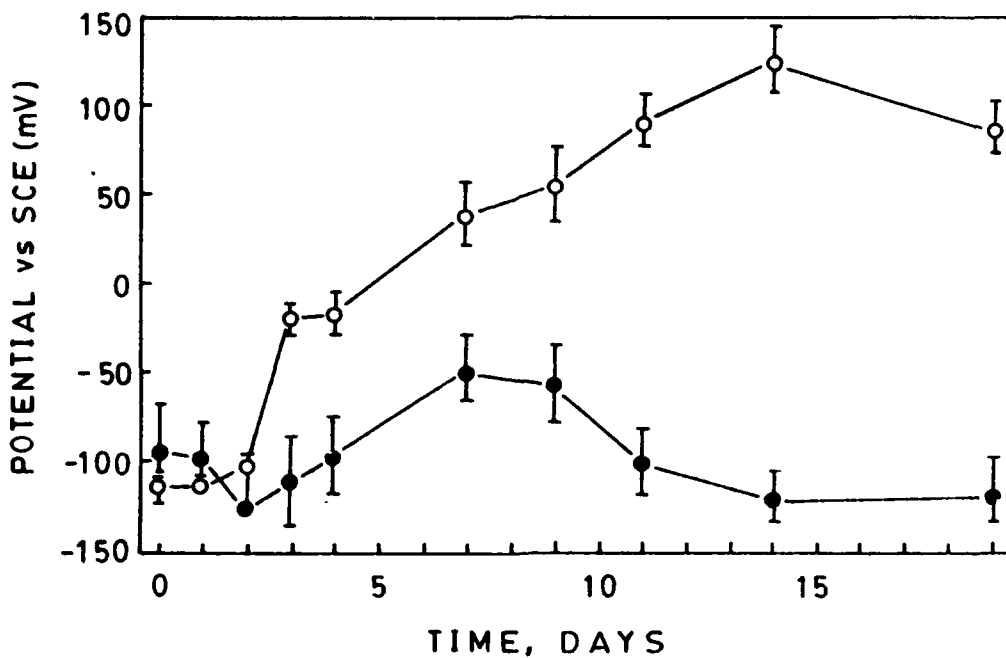


Fig.2 : Potentials measured on five titanium coupons. Dark circles represent values in the dark tank; open circles, illuminated tank.

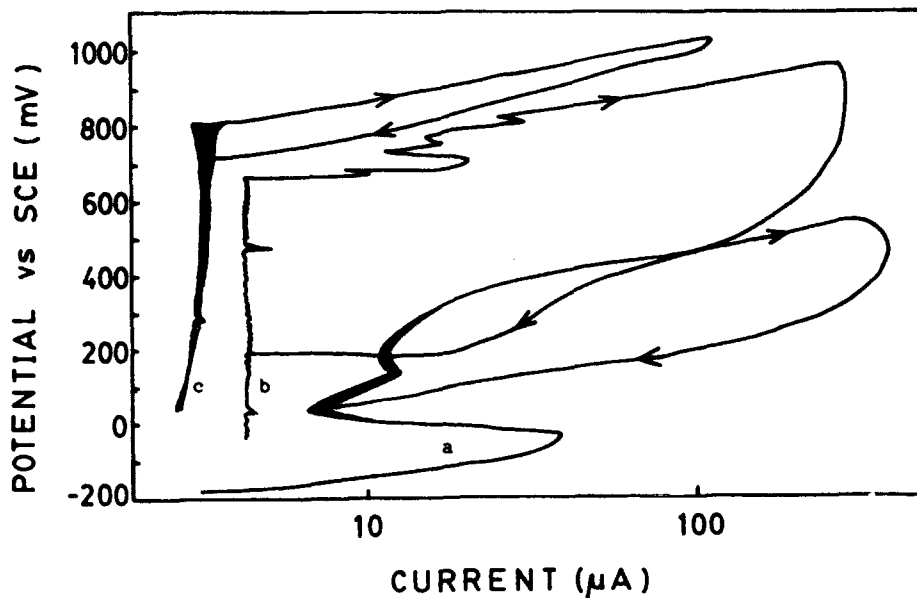


Fig.3 : Anodic polarization curves for titanium.
 a = bare titanium; b = biofilmed titanium ennobled by 125 mV
 c = biofilmed titanium ennobled by 215 mV

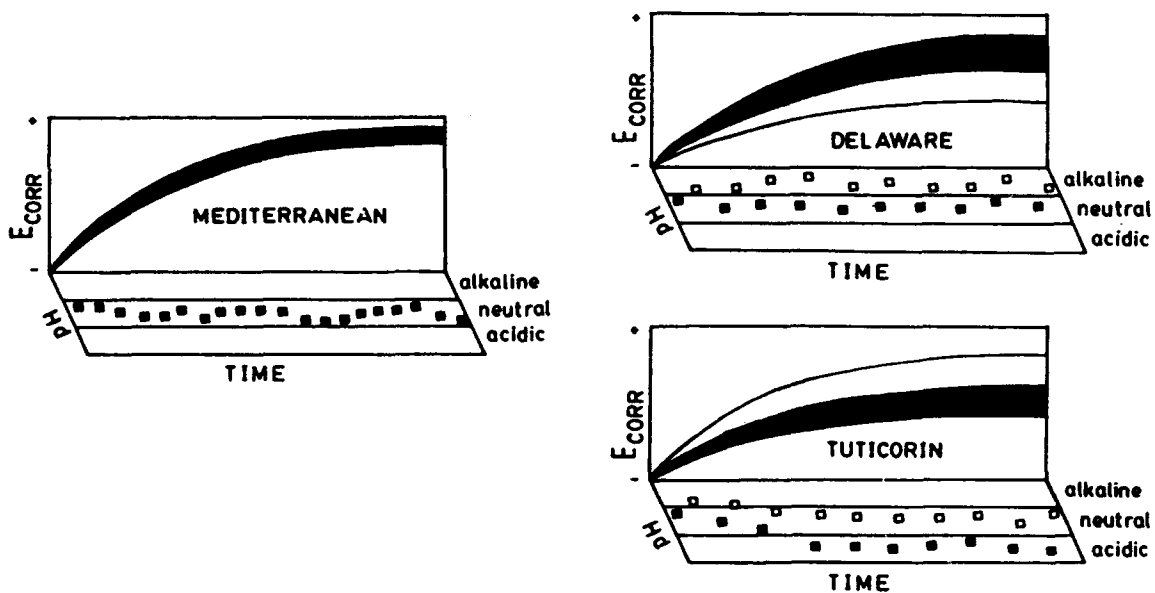


Fig.4 : Three hypothetical configurations depicting E_{corr} profiles in response to biofilm pH

**Characterization of the Bio-Film Formed on a Steel Electrode in Seawater
by Analyzing the Mass Transport of Oxygen**

Dominique Festy
IFREMER, Centre de Brest
29280 Plouzané, France

Florence Mazeas
IFREMER, Centre de Brest
29280 Plouzané, France

Mama El Rhazi
UPR15 CNRS
Physique des Liquides et Electrochimie
4 Place Jussieu, 75252 Paris Cedex 05, France

Bernard Tribollet
UPR15 CNRS
Physique des Liquides et Electrochimie
4 Place Jussieu, 75252 Paris Cedex 05, France

Abstract

The stainless steel electrode is polarized at a potential corresponding to the diffusion plateau of the oxygen and the limiting current is analyzed for different immersion times in natural seawater. The variation of the limiting current with time (in days) is due to the bio-film formation and so the modification of the mass transport properties through this bio-film.

Key terms : bio-film, mass transport, impedance

Introduction

Microbiologically influenced corrosion is due to the presence of micro-organisms which forms a bio-film on a metal surface and leads to changes in the rates and sometimes also the types of the electrochemical reactions which are involved in the corrosion processes. Electrochemical techniques are able to provide reliable information but the complexity of the corrosion phenomena combined with the complexity of the bio-film had limited the proposed mechanisms^{1,2}. In the present paper, a rotating disk electrode in stainless steel is polarized in natural seawater at a potential corresponding to the reduction plateau of the oxygen. The oxygen current is limited by the mass transport and in particular by its transport through the bio-film. In this case the information obtained are not concerned by the corrosion process but only by the presence of the bio-film. Of course each measurement is performed on a short time in order to neglect the formation of calcareous deposits. An accurate formula is used in order to analyze the data, but the scattering of the experimental data limited until now the conclusions.

I. Theoretical Analysis : Diffusion Transport through a Porous Layer

In a first step the bio-film is considered as a porous non reacting layer covering the metallic interface, it may slow down the mass transfer rate of diffusing species and in particular of oxygen. This decrease includes the effect of the layer permeability D_f/δ_f where D_f is the apparent diffusion coefficient through the layer and δ_f the layer thickness. Transient techniques such as the electrochemical or the electrohydrodynamical (EHD) impedance measurements provide, in principle, an evaluation of the diffusion time constant δ_f^2/D_f and thus, by combining the steady-state and transient data, a separate determination of δ_f and D_f is available.

A. Steady-state

The system under investigation is schematized in Figure 1. The concentration gradient is distributed between the fluid and the porous layer. Therefore two mass balance equations can be written :

(i) In the porous layer, the concentration distribution is only determined by the molecular diffusion.

(ii) In the fluid, the concentration distribution is governed by the convective diffusion.

The steady-state current may be analytically determined³ :

$$i^{-1} = i_L^{-1} + i_k^{-1} + i_{\Omega \rightarrow \infty}^{-1} \quad (1)$$

where i_L is the limiting diffusion current at Ω on the metallic surface free from porous layer, i_k is the "kinetic" current, i.e. that given by the transfer reaction by assuming the mass transfer process in volume is infinitely fast and $i_{\Omega \rightarrow \infty}$ is the limiting current when the whole concentration distribution is located within the porous layer, i.e. when angular speed $\Omega \rightarrow \infty$.

The interest of using reciprocal values as in equation (1) is that an experimental plot of i^{-1} vs $\Omega^{-1/2}$ must provide a straight line parallel to the Levich linear variation which passes through the origin.

When the experiment is performed on the diffusion plateau ($k^{-1} \rightarrow 0$), the ordinate value of the intercept of this straight line gives $I_{\Omega \rightarrow \infty}^{-1}$ that is proportional to the layer permeability D_f/δ_f ($I_{\Omega \rightarrow \infty} = (n F C_N D_f)/\delta_f$, with C =concentration).

B. Electrohydrodynamical Impedance

The electrohydrodynamical (EHD) impedance, i.e. the frequency response of an electrochemical system to a perturbation of the angular speed (Ω) of a rotating disk electrode is now a well-known technique for an heterogeneous reaction on a uniform accessible interface^{4,5}. The unsteady convection diffusion equation links the concentration field to the velocity in the diffusion layer. The normal velocity is $v_z(t) = \alpha(t)z^2$ (with α =constant, z =normal distance) and the mass transport transfer function $Z_c = (\Delta(dc/dz) / \Delta\alpha)$ had been calculated and tabulated in references 4 and 5 versus the dimensionless frequency $pSc^{1/3}$ for a uniform accessible bare electrode (with $p=\omega/\Omega$, ω =pulsation, Sc =Schmidt number).

The hydrodynamic transfer function ($Z_{HD} = \Delta\omega/\Delta\Omega$) had been calculated from the Navier-Stokes equation^{4,5}.

In potentiostatic regulation, on the diffusion plateau, if the effect of the double layer capacitance is neglected we have :

$$Z_{EHD} = \Delta I/\Delta\Omega = n F D Z_c Z_{HD} \quad (2)$$

In the case of a porous non reacting layer covering the electrode³ :

$$Z_{EHD} = \frac{n F Z_c Z_{HD}}{\left(\text{ch} \left(s_f^{\frac{1}{2}} \right) \left(1 - \frac{\delta_f D}{D_f \delta_N} \Gamma \left(\frac{4}{3} \right) \theta'(0) \frac{\text{th} \left(s_f^{\frac{1}{2}} \right)}{s_f^{\frac{1}{2}}} \right) \right)} \quad (3)$$

where $(-1/\theta'(0))$ is the dimensionless convective Warburg impedance⁶ and $s_f = j\omega \delta_f^2/D_f$.

This last expression had been simulated (figure 2) for different angular velocities. In contrast with the simple behaviour on bare electrode, the data are no more reducible by the dimensionless frequency $p = \omega/\Omega$. An increase of Ω produces a shift of the Bode diagrams toward smaller p values, other parameters being kept constant.

II. Experimental

The stainless electrode being polarized in natural seawater at a potential (-750 mV/ECS) corresponding to the diffusion plateau of oxygen, the steady current is recorded versus the square-root of the angular speed of the rotating disk electrode (figure 3). The curve obtained immediately after the immersion is a straight line with a non-zero intercept at $\Omega = 0$, corresponding to a non diffusional component of the current, this one is probably due to the hydrogen current. The curve obtained two days after the immersion is no more a straight line

but has a clear curvature in agreement with the expression (1). Then the steady results must be analyzed by considering an expression as :

$$I = I_0 + (I^{-1}_{\Omega \rightarrow \infty} + I^{-1}_L)^{-1} \quad (4)$$

where I_0 is the hydrogen current.

I_L , the Levich current, is proportional to $\Omega^{1/2}$ ($I_L = K\Omega^{1/2}$), then three different parameters can be fitted from the experimental results : I_0 , $I_{\Omega \rightarrow \infty}$ and K . A fitting procedure is used for each set of experimental results and the agreement between the experimental points and the fitted curve is excellent, then the expression (4) can be used in order to analyze the steady current.

On figure 4, $(I - I_0)^{-1}$ is plotted versus $\Omega^{-1/2}$, I_0 had been determined with a fitting procedure. These results correspond to those plotted on figure 3.

On figure 5, the three fitted parameters (I_0 , $I^{-1}_{\Omega \rightarrow \infty}$ and K^{-1}) are plotted versus the immersion time. Each point corresponds to a different sample, this procedure decreases the risk of modifying the bio-film by experiments, on the opposite the reproducibility from one sample to another one is not very good.

The dispersion of the results for the hydrogen current (figure 5a) is decreasing with time but the average value seems constant. So the active area of the stainless steel electrode is not modified by the presence of the bio-film.

$I^{-1}_{\Omega \rightarrow \infty}$, so the inverse of the layer permeability, is increasing fastely during the first four days and then decreases to zero before to increase again (figure 5b). Two time constants are appearing in the developments of the bio-film, the first one just after the immersion and the second one for an immersion time longer than five days. This critical time of four days had been observed previously by measuring the open circuit potential⁷.

The dispersion of the Levich constant (figure 5c) is linked as the current I_0 to the dispersion of the active area but also to a possible variation of the seawater oxygen concentration.

The steady-state measurements being not completely understood, in particular due to the dispersion of the results, the transient techniques and in particular the EHD impedance cannot be analyzed quantitatively. Nevertheless, the EHD impedance obtained after 21 days of immersion has qualitatively the properties of an EHD impedance of an electrode coated by a porous layer (figure 6).

III. Conclusion

The analysis of the oxygen current measured on a steel electrode seems a promising way to characterize the mass transport through the bio-film. A procedure in order to reduce the scattering of the experimental results is in progress. Nevertheless, the present data show the modification of the bio-film after four or five days and a particular attention will be devoted to this first bio-film development.

References.

1. F. Mansfeld, B. Little, *Corrosion Science*, 32 (1991): p. 247.
2. B. Little, P. Wagner, F. Mansfeld, *Material Science Forum*, 111-112 (1992): p. 1.
3. C. Deslouis, B. Tribollet, M. Duprat, F. Moran, *J. Electrochemical Society*, 134 (1987): p. 2496.
4. B. Tribollet, J. Newman, *J. Electrochemical Society*, 130 (1983): p. 2016.
5. C. Deslouis, B. Tribollet, "Advances in Electrochemical Science and Engineering" (Vol 2, edited by Tobias and Gerischer, VCH Weinheim, New York, 1991), p. 264.
6. B. Tribollet, J. Newman, *J. Electrochemical Society*, 130 (1983): p. 822.
7. R. Holthe, E. Bardal, P.O. Gartland, *Corrosion/88*, paper n° 293 (Houston, TX : National Association of Corrosion Engineers, 1988).

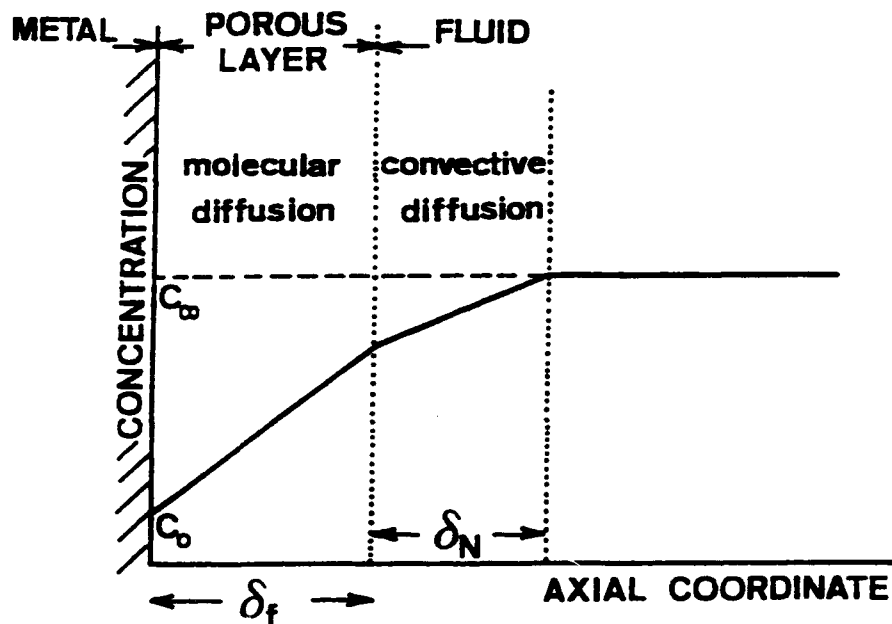


Figure 1 : Variation of the concentration versus the axial coordinate.

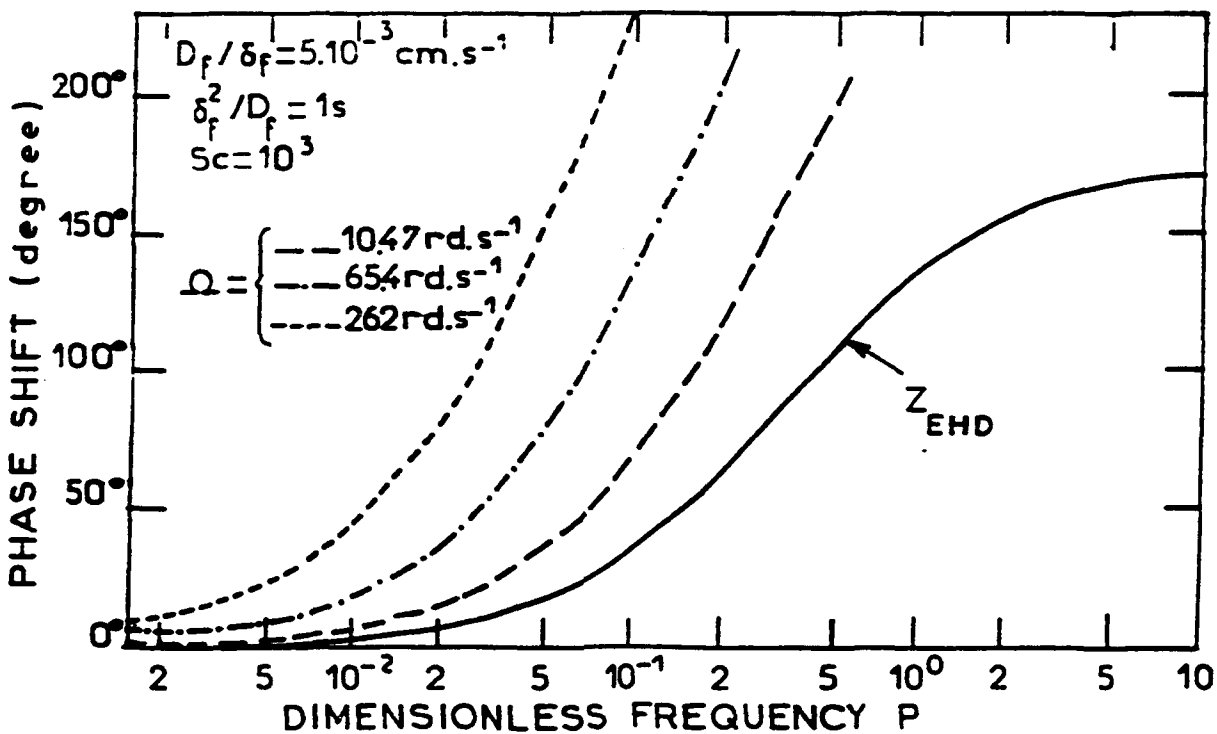
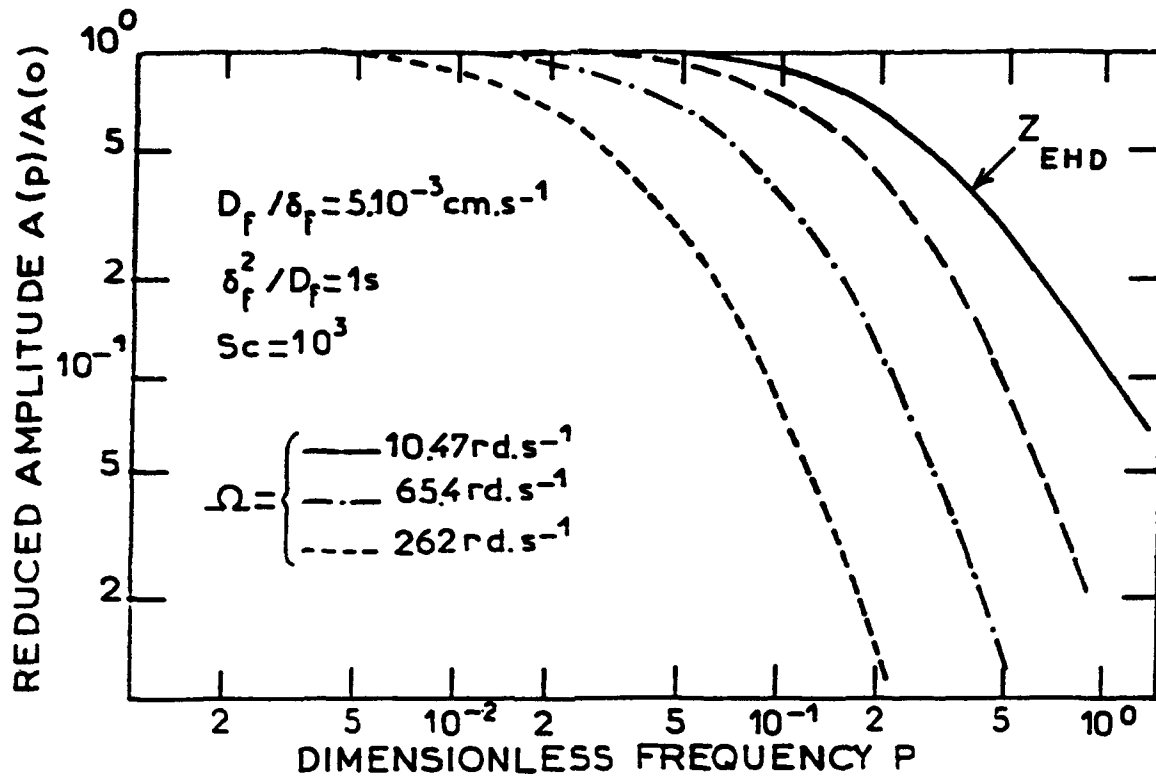


Figure 2: From equation (3), EHD impedance versus the dimensionless frequency p for different rotation speeds. The curve in full line is the EHD impedance on a bare electrode.

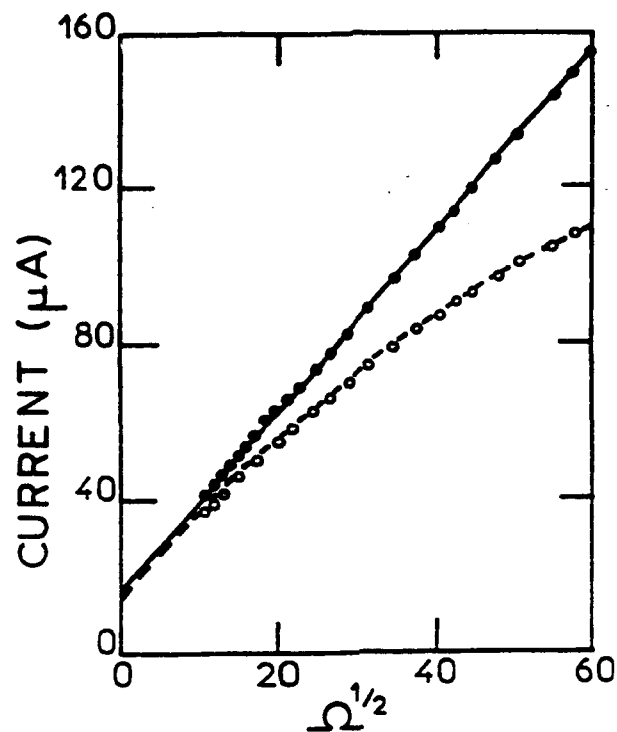


Figure 3 : Variation of the limiting current versus the square-root of the rotation speed. (•) corresponds to the curve recorded immediately after the immersion, (o) corresponds to the curve recorded two days after the immersion.

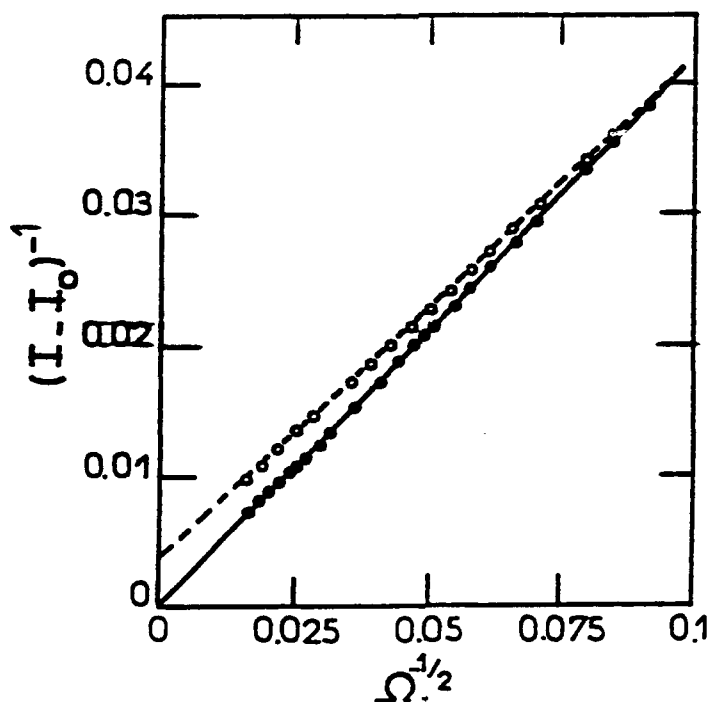


Figure 4 : Variation of the inverse of the oxygen current versus the inverse of the square-root of the rotation speed. (•) corresponds to the curve recorded immediately after the immersion, (o) corresponds to the curve recorded two days after the immersion. The same data are plotted on figures 3 and 4 in different coordinates.

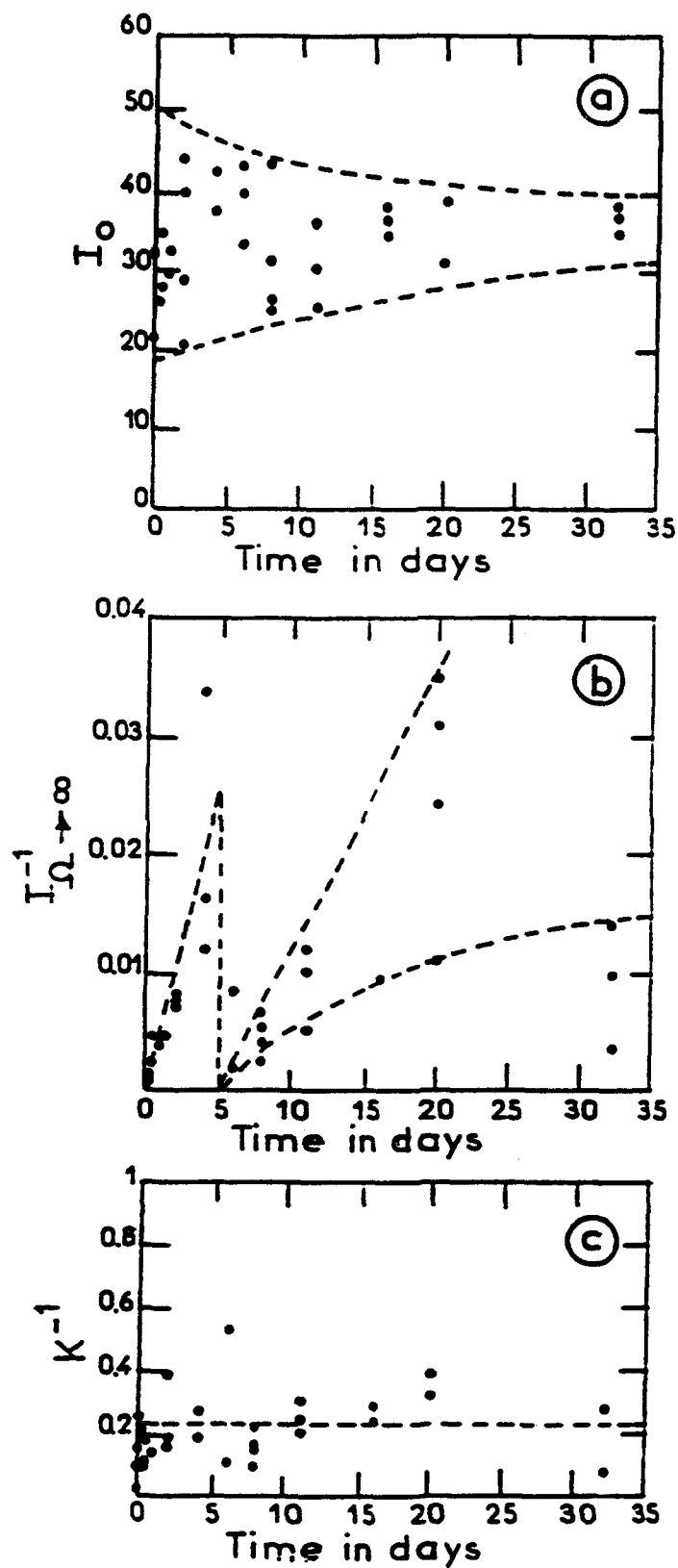


Figure 5: Variation of the fitted parameters versus time. (a) corresponds to the hydrogen current, (b) corresponds to $I_{\Omega \rightarrow \infty}^{-1}$ which is proportional to the layer permeability and (c) corresponds to the inverse of Levich constant.

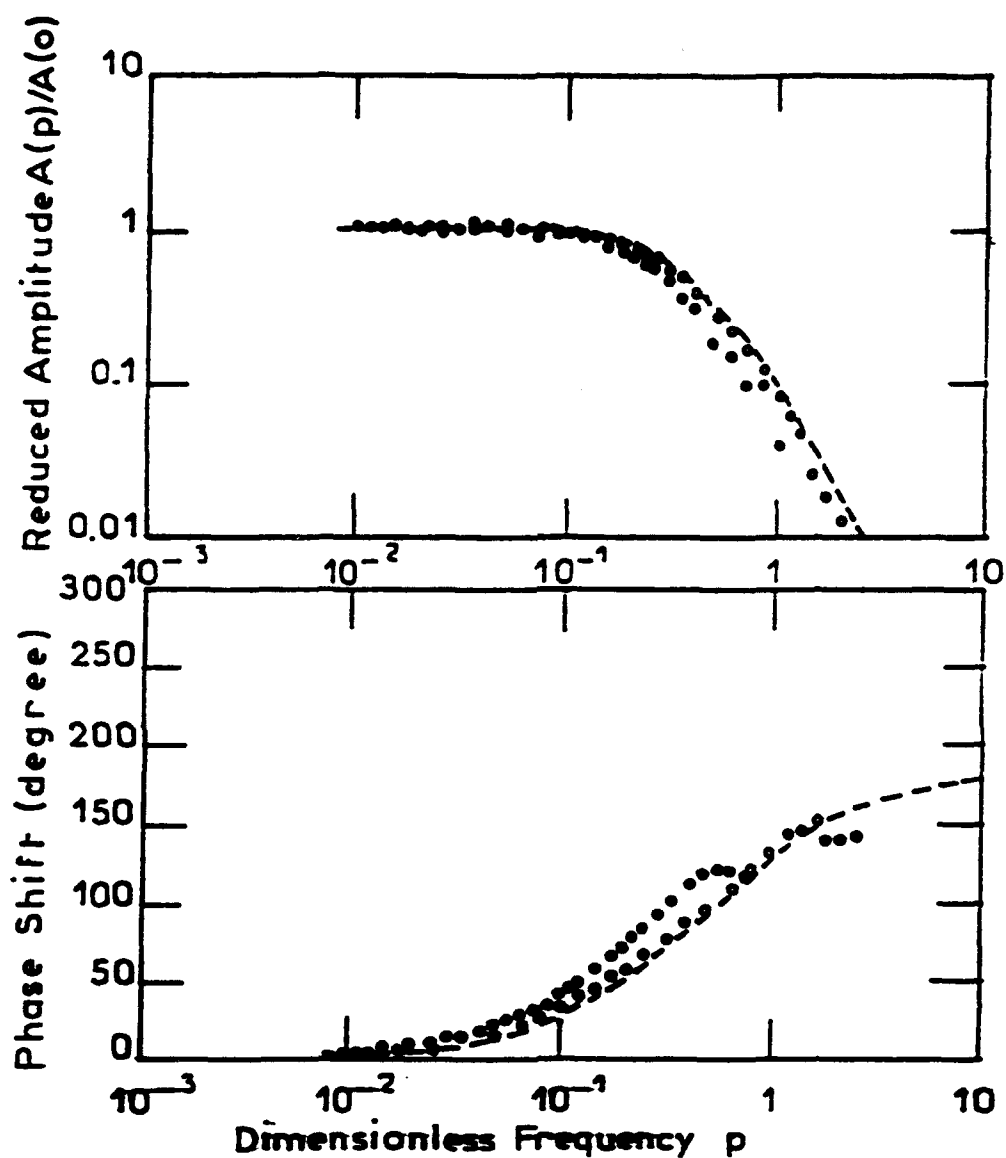


Figure 6: Experimental EHD impedance obtained after an immersion time of 21 days. The curve in dashed line is the theoretical curve on a bare electrode for a Schmidt number of 700 (corresponding to the oxygen), (o) corresponds to the experimental EHD impedance at 120 rpm, (•) corresponds to the experimental EHD impedance at 1200 rpm.

Microfouling Induced Corrosion of Alloys*

Z. Ying
Qingdao Research Institute for Marine Corrosion
Central Iron & Steel Research Institute
Wheat Island, Qingdao, Shandong
People's Republic of China 266071

Wing Qiu
Biology Department
Qingdao Ocean University
Qingdao, Shandong
People's Republic of China 266071

Abstract

Weight loss measurement, electrochemical techniques, scanning electron microscopy (SEM) and X-ray diffraction analyses were made in the study of the effect of Thiobacillus thioparus (T.p.) and Thiobacillus ferrooxidans (T.f.) bacteria on mechanisms of Microbiologically Induced Corrosion (MIC) of Cr-Ni-Mo-V steel and SS316L.

Experimental results showed that both bacteria attached to the surface of these alloys and induced localized change of the constituents of the electrolyte, pH and oxygen levels. These changes lead to changes in the rates and the types of the electrochemical reaction of alloys. T.P. excretes H_2SO_4 and forms a slime layer. T.f. oxidizes Fe^{+2} to Fe^{+3} and it can form tubercles. In cultures of T.p., the pitting resistance of SS316L was found to be lower, I_{pass} and E_{corr} higher, accompanied by the formation of an active peak and a decrease in the passive range. T.f. had no obvious effect on SS316L.

Key terms: Biodeterioration, Corrosion, Microfouling, Thiobacillus.

* Project supported by National Natural Science Foundation of China (NNSFC)

Introduction

Early in 1895 Dutch biologist M. W. Beijerinck proposed that biological activity on the surface of metals is one of the important factors for corrosion. After nearly a century, especially after 1970, scientists in biology, chemistry and materials engineering have done much research on Microbiologically Influenced Corrosion (MIC) or biodeterioration [1-6]. A large percentage of available literature deals with corrosion involving anaerobic, sulfate reducing bacteria (SRB). Sulphur-oxidizing bacteria, especially those that are acid producers and acidophilic, such as members of the genus Thiobacillus, are particularly noteworthy [7-10]. The corrosive effects of the Thiobacilli can mainly be attributed to their ability to produce sulphuric acid and to oxidize Fe^{+2} to Fe^{+3} . Biological corrosion of steels is mainly due to microbes and their biocoene succession. When steels were exposed in water, it was microbes that first attached to the surface of steel which was determined by the chemotaxis of organisms. As the biofilm formed, it created a localized region (or niche) next to the metal surface in which the chemistry, pH and oxygen level of the

electrolyte were altered, leading to changes in the rates and the types of electrochemical reactions which are involved in the corrosion processes.

The purpose of this work was to investigate the mechanism of MIC on a Cr-Ni-Mo-V steel and SS316L in cultures of Thiobacillus thioparus (marine) and Thiobacillus ferrooxidans (continent) and to provide basic data for the development of new materials with anticorrosion and antifouling properties.

Experimental Methods

Thiobacillus thioparus was isolated from rust of steel in sea water and cultivated in cultures, a technology described by T. Y. Xue [11]. The composition of the culture medium was Na₂S₂O₃.5H₂O, 10.0g; K₂HPO₄, 4.0g; KH₂PO₄, 4.0g; NH₄Cl, 0.4g; MgSO₄.7H₂O, 0.8g; FeSO₄; MnSO₄, seawater 1000ml. pH6, 27C(±1C). Thiobacillus ferrooxidans was isolated from Co mine effluent according to the procedures of W. M. Yan [12]. The composition of the culture medium was (NH₄)₂SO₄, 3.0g; KCl, 0.1g; K₂HPO₄, 0.5g; MgSO₄.7H₂O, 0.5g; Ca(NO₃)₂, 0.01g; distill water, 700ml; 10N H₂SO₄, 1ml; 14.78% FeSO₄.7H₂O Solution, 300ml pH2.5, 30C(±1C).

The compositions of the alloys used were as follows:

| Alloys | Composition (W %) | | | | | | | | | |
|------------|-------------------|------|------|-------|-------|-------|-------|-------|------|-------|
| | C | Si | Mn | P | S | Cr | Ni | V | Mo | Zr |
| Cr-Ni-Mo-V | 0.135 | 0.52 | 1.03 | 0.022 | 0.008 | 0.67 | 1.2 | 0.035 | 0.10 | -- |
| SS316L | 0.006 | 0.57 | 1.01 | 0.019 | 0.016 | 17.15 | 12.50 | -- | 2.56 | 0.002 |

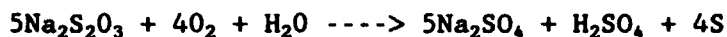
The tests were conducted in cultures of T.p. and T.f. and in sterile medium. The tests have run for 9 days. The electrodes for electrochemical test were made according to National Standard GB4334.9-84 [13]. The samples of SS316L were passivated in 30% HNO₃ at 60°C for 1 hr before testing, exactly 1 cm² of area was exposed to the solutions. Samples were ground on SIC grinding paper to grit size of 600#. Corrosion potentials and potentiodynamic polarization curves were measured with an EG&G PARC corrosion measuring system (Model 351). A scan rate of 20 mv/min. Impedance was measured with a Solartron 1250 instrument. For all electrochemical tests, the saturated calomel electrode (SCE) was used as reference electrode and platinum electrode as counter electrode.

Cr-Ni-Mo-V steel samples exposed 9 days in media inoculated with the bacterium have been analyzed by D/max-V B rotating anode X-ray diffraction instrument made by Japan Recom Motor Corporation to analyze compositions of rust.

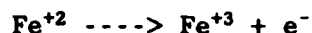
Coupons were examined by SEM periodically during the experiment (two hours, five hours, four days, eight days). SEM coupons were prepared by dipping in a fixative composed of 2.5% glutaraldehyde, dehydrating with 50%, 70%, 80%, 90%, 100% alcohol and critical point drying from CO₂. Coupon surfaces were coated with gold before examination with SEM.

Results and Discussion

The two bacteria used have different metabolic characteristics. Thiobacillus thioeparus produces sulfuric acid and elemental sulfur and derives energy from the oxidation of Sodium Thiosulfate.



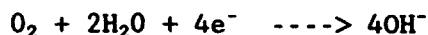
Thiobacillus ferrooxidans gets energy by oxidizing ferrous to ferric.



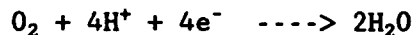
Corrosion under the slime layer

Surfaces of the Cr-Ni-Mo-V steel coupons exposed in Thiobacillus thioeparus were inspected with SEM. There were bacteria attached on 2-hour coupon [14]. It was found that a biofilm formed on the 3- and 4-day coupons. The potentials of Cr-Ni-Mo-V steel greatly shifted (Figure 1). Figure 3 shows that cathodic current density increased. Impedance got smaller (Table 1), which resulted in increase in the Corrosion rates. Anodic Tafel slope gradually increased. Black rust contained Fe_3O_4 , FeSO_4 , FeO , FeS and etc. (Table 2).

When a metal is immersed in natural seawater and other aqueous systems, the dissolution of metal will take place according to the following equations:



Thiobacillus thioeparus attached to the surface of Cr-Ni-Mo-V steel excretes H_2SO_4 and S, forms slime layer, and results in localized changes of the electrolyte, pH and oxygen levels. It was found that the pH decreased from 6 to 4.5 during the duration of the tests. Increase in cathodic current density and decrease in cathodic slope indicated that H^+ within slime layer can be utilized by equations given below:



The existence of the bacterium provides strongly corrosive agent H_2SO_4 , enhances cathodic depolarization and increases active dissolution of anode. The whole reaction was under cathodic control. After forming a slime and rust layer, the rate of corrosion was under cathodic-anodic mixed control. The corrosion ability of thiobacillus thioeparus was weakened by the buffered materials K_2HPO_4 and KH_2PO_4 . The experimental results confirm that the bacterium is more corrosive than natural seawater and medium.

Susceptibility of passive film to bacteria

From Figure 7, we can see that Thiobacillus thioeparus attached to the surface of SS316L in about two hours, and they multiplied on the surface of 5 hour coupon (Figure 8). The slime layer on the 9-day coupon was sparse from Figure 9. One

of three repeated tests found pits. Corrosion potentials of SS316L shifted slightly noble, as shown in Figure 2. Pitting resistance of the passive film decreased (Table 1). Figure 4 showed potentiodynamic polarization curves of SS316L in sterile medium and in the culture of T.p. Pitting curves for SS316L in Thiobacillus thioparus culture showed the formation of an active peak, increase in I_{pass} , and decrease in the passive range.

The sterile medium contains 0.6M NaCl+ 0.03M $Na_2S_2O_3$. Newman et al. found that thiosulfate will induce pitting of SS304 when sufficient chloride ion is present. 0.25M NaCl+0.01M $Na_2S_2O_3$ is a very severe pitting environment for SS304 at 25C. The existence of bacteria made system more complicated by excreting H_2SO_4 and S. Garner [17] found that thiosulfate pitting can occur in the absence of chloride, when sufficient sulfate is present. In this work, it was found that the pitting susceptibility of SS316L increased when sufficient chloride ions 3.6% were present and the $SO_4^{-2}/S_2O_3^{-2}$ ratio reached a certain range. Electrodes were placed into cell in the logarithmic growth period of the bacteria. After 3-4 days, bacterial growth reached stable period, and the bacteria excreted a large amount of H_2SO_4 . The $SO_4^{-2}/S_2O_3^{-2}$ ratio increased greatly. Anions like Cl^- and SO_4^{-2} electromigrate and absorb at the pit site, which becomes acidified. The acidified environment decreases activation energy of dissolution of the passive film. It has been argued that thiosulfate will decompose to form elemental sulfur [16, 18] and H_2S [19], and thus promote anodic dissolution.

Numerous reports show a rapid ennoblement of E_{corr} during the first days of exposure for stainless steels in natural seawater [20-26]. Dexter and Gao [25] concluded that the increase of E_{corr} for the samples of SS316 was due to an increase of the rate of the cathodic reduction of oxygen at a given potential. It is microbes that first attach to the surface of samples, when steel is exposed to natural seawater. Thiobacillus thioparus is one of them, and laboratory works have shown that the potentials of SS316L shift slightly in the noble direction, this is in agreement with work as described above, but we found no obvious increase of cathodic current density. This suggests that electrochemical evaluation of other marine bacteria, such as Thiobacillus thiooxidans and Desulforibrio desulfuricans should be done. All these bacteria can bring about changes of cathodic process. Other papers showed a decrease in E_{corr} for SSs in cultures of SRB [3,5]. In this work the corrosion potential of SS316L was in the range of pitting potential, and this may bring about localized corrosion of SS316L. The corrosion behavior of SS316L in T.f. culture was similar to that in dilute H_2SO_4 solution with Fe^{+3} . T.f. attached to the surface of SS316L as shown in Figure 10, however, no significant effect on the pitting resistance was detected from Figure 6.

Effect of ferric ion

It has been found that Thiobacillus ferrooxidans attached to the surface of Cr-Ni-Mo-V steel in two hours [14]. Pitting corrosion increased during the period of test. The acidity of electrolyte and anodic depolarization of Thiobacillus ferrooxidans made Cr-Ni-Mo-V steel into a highly active state, and the potential, E_{corr} , shifted in the active direction (Figure 1). Figure 5 showed that Cr-Ni-Mo-V steel corroded at a constant rate in cultures of T.f. After removing red rust from the surface of steel, it was found that there were 10 pits/cm² (1mm deep) on the surface. The composition of red rust was mainly Fe_2O_3 (Table 2).

There are different opinions about the effect of ferric ion on corrosion of steel. Little et al. [8] demonstrated that microbial oxidation of Fe^{+2} to Fe^{+3} resulted in red deposits that covered 75% of the surface of the electrode. The accumulated ferric hydroxide created differential aeration cells. But Kino et al. [7] suggested that ferrous iron in equilibrium with metallic iron will be oxidized by Thiobacillus ferrooxidans, resulting in ferric ion which oxidizes the metal. Thus Thiobacillus ferrooxidans recycles the ferric ions required for the initial attack. Under the same experimental conditions, the result of iron plate in the culture of T.f. have been obtained in the presence of high ferric ion concentration (44g/L).

The results presented here have shown that bacteria attached to the surface of steel and oxidized Fe^{+2} to Fe^{+3} . The ferric compounds precipitated around the cells and accumulated as tubercles. The material under the tubercles became the anode of the cell, while the area away from the tubercles became the cathode. The mechanism of corrosion is simply the formation of a differential aeration cell due to the uptake of oxygen by the microbial colony and cathodic reaction, the oxygen concentration under these conditions becoming depleted.

Conclusions

1. Two bacteria attached on the surface of Cr-Ni-Mo-V steel can form a niche which has the different constituents, pH et al., T.p. formed slime layer, T.f. formed tubercles. Both accelerated corrosion of Cr-Ni-Mo-V steel.
2. The pitting curves for SS316L in T.p. showed the formation of an active peak, an increase in I_{pass} , a decrease in the passive range. T.f. had no obvious effect on SS316L.
3. Electrochemical techniques, SEM and X-ray diffraction proved the difference between two bacteria.
4. A bacterium has different effects on different alloys.

References

1. Daniel H. Pope, D.J. Duquette, Materials Performance, 24 4 (1984): p.14.
2. P.J.B. Scott, J. Goldie, M. Davies, Matls. Perf. 31 1 (1991): p. 88.
3. G. Hernandez et al., "Biological Microfouling Formation and Corrosion of 316L Stainless Steel: Role of poison alloying elements" International Corrosion and Protection Symposium (Xia Men) (1988): p. 664.
4. L. JRenhao, Ou Jiawei, Proceedings of the National Conference on Corrosion Science and Protection Technology, Science Press, (1966): p. 122.
5. C. Ringas, F.P.A. Robinson, Corrosion, 44 6 (1988): p. 386.
6. Tang Heqing et al., Journal of Chinese Society of Corrosion and Protection, 111 (1991): p. 46.
7. P. Bos, J. G. Kuenen, Microbial Corrosion, Proceedings of the conference sponsored and organized jointly by the National physical laboratory and the metals society held at NPL Teddington in 8-10 March, The Metals Society, London (1983): p. 18.
8. B.J. Little, P. A. Wagner, An Electrochemical Evaluation of Microbiologically Induced Corrosion by two Iron-Oxidizing Bacteria CORROSION/86, paper no. 122. (Houston, TX: Nat. Assoc. Cor. Eng., 1986).
9. Xu Huaishu, Ji Weischang, Journal of Ocean University of Qingdao, 19 1 (1989): p. 104.
10. W. P. Iverson, AD752599, (1971).

11. Xue Tingyao, Marine Microbiology, Science Press, Beijing, (1959): p. 194.
12. Zheng Shimin, Yan Wangming Autotrophic Microbiology, Science Press, Beijing, (1983).
13. The national standard of China, GB 4334.9-84 stainless steel-Measurement of pitting potential?
14. Peng Shaojun, Bachelor Thesis, Microfouling Effect on the corrosion of steels (unpublished) (1990)
15. A.J. Sedriks, Corrosion of stainless steel, John Wiley, N.Y.(1979): p. 19.
16. R.C. Newman, H.S. Isaacs, B. Alman, Corrosion, 385 (1982): p. 261.
17. A. Garner, Corrosion, 41 10 (1985): p. 587.
18. R. C. Newman, Corrosion, 41 8 (1985): p. 450.
19. D. Tromans, L. Frederick, Corrosion, 40 12 (1984): p. 633.
20. V. Scotto, R. Decintio, G. Marcenaro, Corros. Sci. 253 (1985): p. 185.
21. R. Johnsen, E. Bardal, Corrosion, 415 (1985): p. 296.
22. R. Johnsen, E. Bardal, "The effect of a microbiological slime layer on stainless steel in natural seawater" CORROSION/86, paper no. 227. (Houston, TX: National Association of Corrosion Engineers, 1986).
23. H.A. Videla, M.F. L. De mele, G. Branke Vich, Microfouling of several metal surfaces in polluted seawater and its relation with corrosion" CORROSION/87, paper no. 365. (Houston, TX: Nat. Assoc. Cor. Eng., 1987).
24. A. Mollica, G. Ventura et al., Int. Bioderlor. 24 (1988): p. 221.
25. S. C. Dexter, G.Y. Gao, Corrosion 44 6 (1988): p. 717.
26. A. Mollica, A. Trevis et al., Corrosion 45 1 (1989): p. 48.

Table 1 The impedance Rp (ohm·cm²)

| | T.p. | | | T.f. | | |
|------------|---------|-------|--------|---------|-------|--------|
| | sterile | 1 day | 5 days | sterile | 1 day | 5 days |
| 316L | 22000 | 9550 | 11000 | 32000 | 18000 | 28000 |
| Cr-Ni-Mo-V | 103 | 101 | 8.6 | 108 | 67 | 63 |

Table 2 The compositions of rust

| | | | | | | | |
|------|--------------------------------|---------------------|-------------------|--------------------------------|-----|------------------|-------|
| T.f. | Fe ₂ O ₃ | Fe(OH) ₂ | FeO | | | | |
| T.p. | Fe ₂ O ₃ | FeS | FeSO ₄ | Fe ₃ O ₄ | FeO | FeS ₂ | FeOOH |

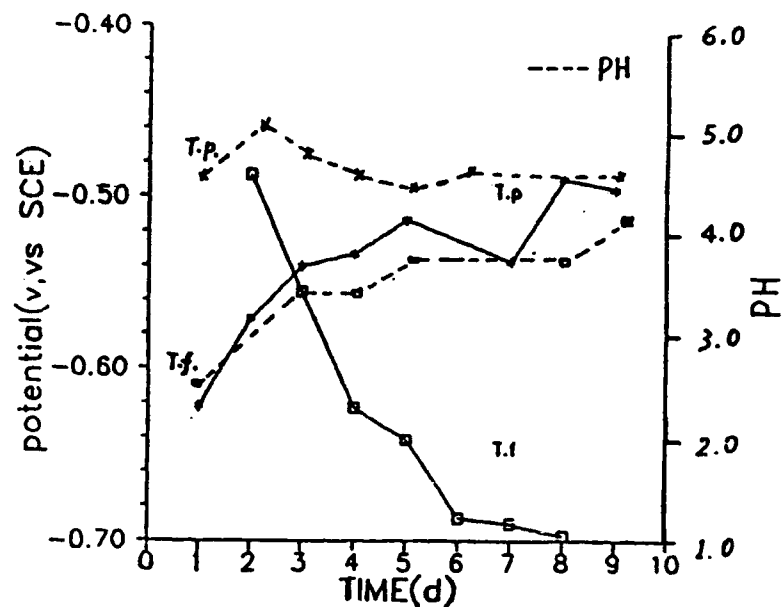


Fig.1 Corrosion potential and PH vs time for Cr-Ni-Mo-V steel in the culture of T.p. and T.f.

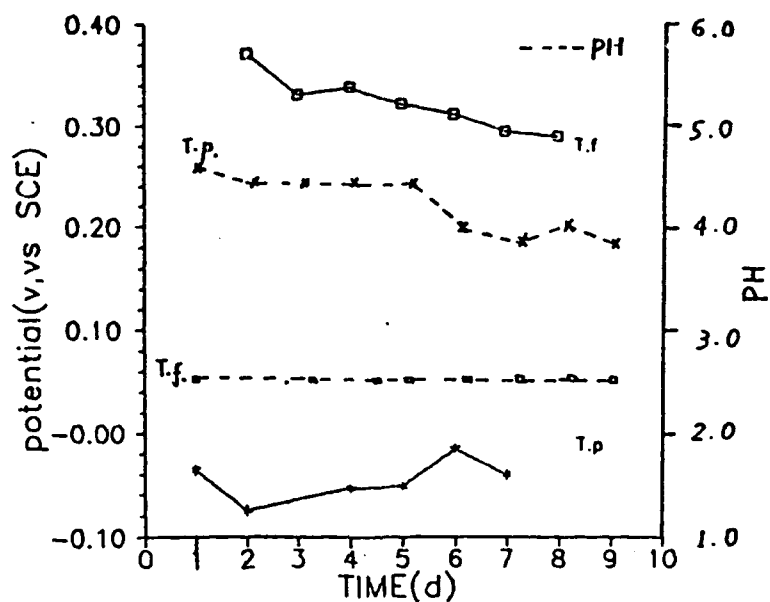


Fig.2 Corrosion potential and PH vs time for SS316L in the culture of T.p. and T.f.

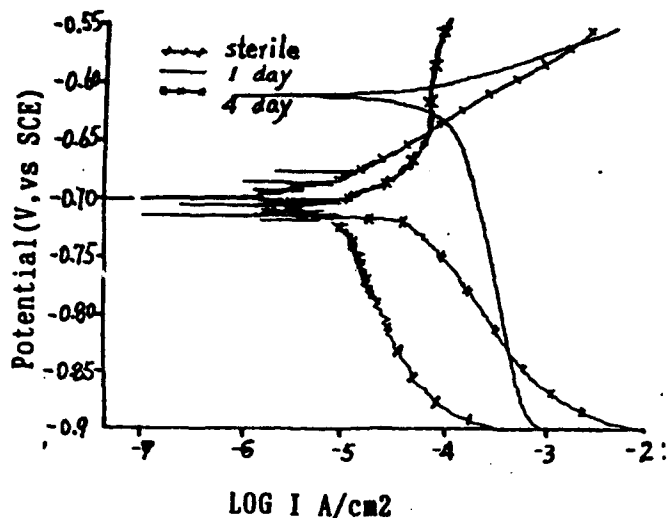


Fig.3 Polarization curves of 945 steel in sterile medium and in the culture of T.p.

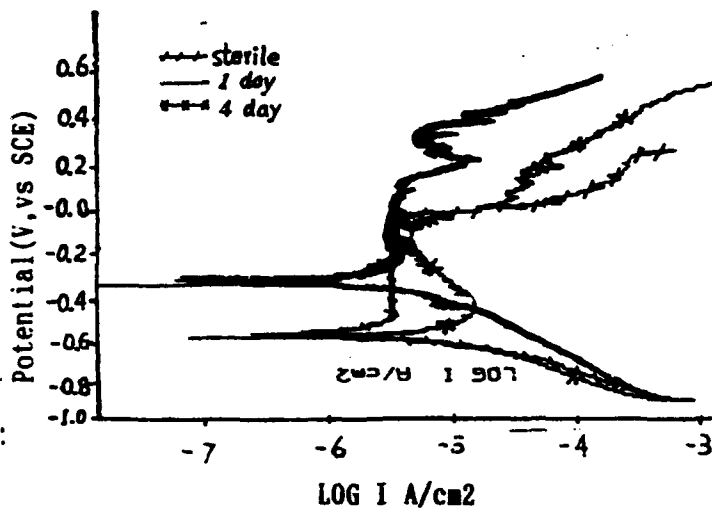


Fig.4 Polarization curves of SS316L in sterile medium and in the culture of T.p.

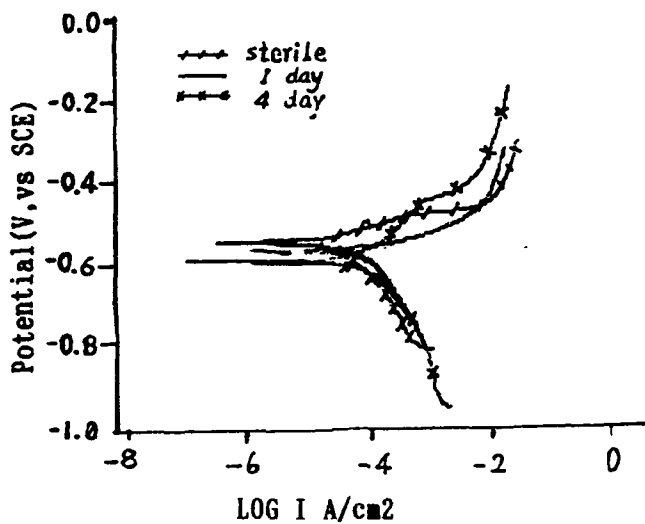


Fig.5 Polarization curves of 945 steel in sterile medium and in the culture of T.f.

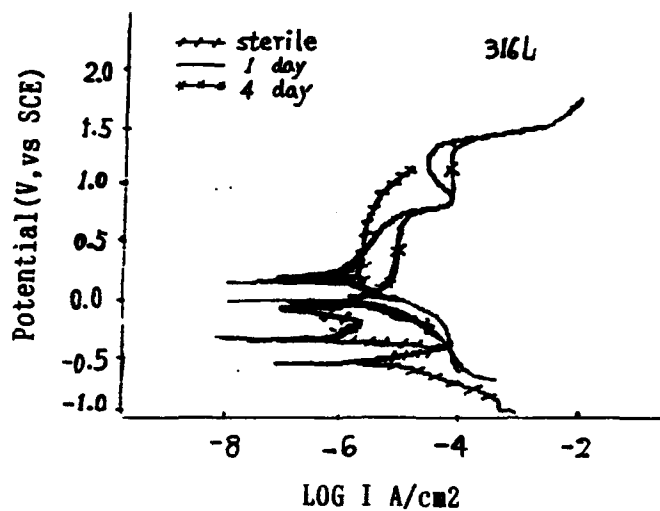


Fig.6 Polarization curves of SS316L in sterile medium and in the culture of T.f.

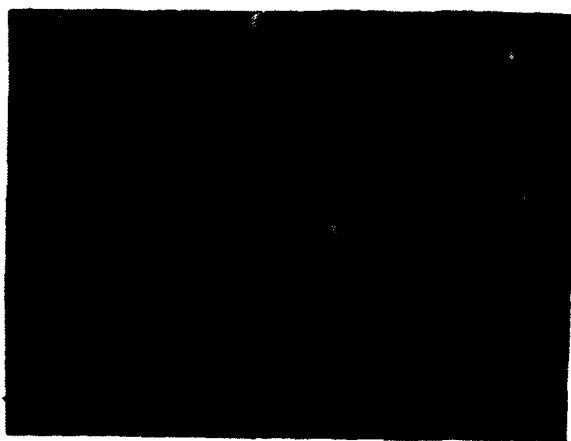


Fig.7 Scanning electron micrograph of T.p. attached on the surface of SS316L after 2 hours



Fig.8 Scanning electron micrograph of T.p. attached on the surface of SS316L after 5 hours

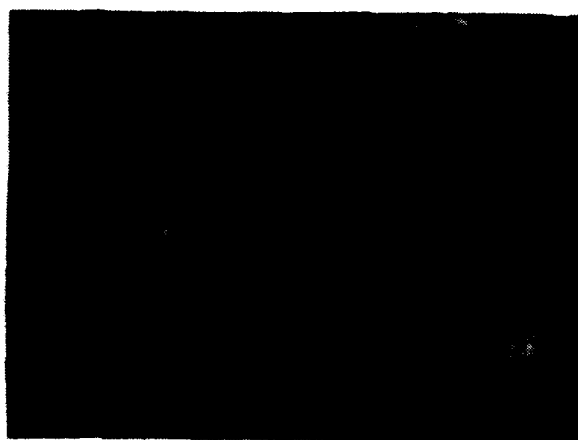


Fig.9 Scanning electron micrograph of T.p. attached on the surface of SS316L after 9 days

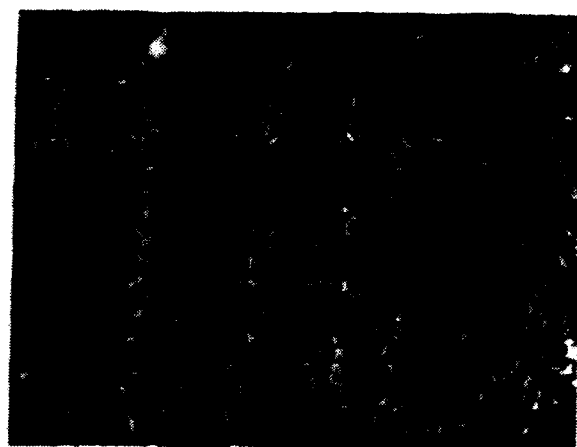


Fig.10 Scanning electron micrograph of T.f. attached on the surface of SS316L after 4 days

Microbiological Aspects of the Low Water Corrosion of Carbon Steel

Iwona B Beech, Sheelagh A Campbell and Frank C Walsh
Electrochemistry and Microbiology Group, Department of Chemistry,
University of Portsmouth,
St. Michael's Building, White Swan Road,
Portsmouth PO1 2DT, UK

Abstract

These studies were undertaken to elucidate the significance of microbial consortia in localised, low water marine corrosion of carbon steel. Microorganisms present in biofilms formed on steel were isolated, enumerated and identified. Corrosion products accumulated in biofilms were analysed and electrochemical measurements were performed under laboratory conditions to determine the extent of corrosion in the presence of pure and mixed microbial isolates.

The results of microbiological studies showed the presence of diverse bacterial genera such as sulphate reducing bacteria (SRB), *Pseudomonas* and *Vibrio* as well as different species of the same genus in biofilms removed from the surface of steel. No simple correlation was found between bacterial numbers and observed corrosion levels. However, the composition of microbial consortia appeared to be linked with the degree of corrosion. There was a tendency for bacterial species of the same genus to be associated with non-corroding sites, whereas mixed populations were always detected in samples from corroding sites. The number of SRB was higher in the biofilms recovered from sites which experienced high rates of corrosion. Although the SRB count was moderate to low, the bacteria showed high metabolic activity.

Phase analysis of the surface products revealed differences between samples from non-corroding and corroding sites. The former consisted largely of oxyhydroxides with some magnetite; the latter showed the presence of iron sulphides. Electrochemical measurements of average corrosion rates showed that SRB in pure and mixed cultures were aggressive to steel and a dependence between the exposure time and the observed level of corrosion was noted.

The results emphasise the importance of the composition of microbial consortia and their metabolic activity in the process of marine biocorrosion.

This project has been sponsored by British Steel Technical, UK.

Key terms: marine corrosion, microbial corrosion, localised corrosion, biofilms, carbon steel.

Introduction

The occurrence of highly localised, low water corrosion of carbon steel piling has recently been reported in many European harbours. Steel manufacturers have launched a programme of investigation in order to determine the cause of this accelerated corrosion. Studies involved installation of test panels and continuous, on-line corrosion monitoring, using a variety of electrochemical techniques. In addition, parameters such as temperature, pH and sulphate content of the water were also measured. The sections of piles retrieved for replacement were examined for the presence of residual stresses. Data obtained from tests did not provide a satisfactory explanation of the observed phenomena. Corrosion rates calculated on the basis of performed measurements were much lower compared to observed levels of metal deterioration, estimated as 3mm/year. Analysis of the results indicated that factors other than those commonly considered as instigating corrosion of carbon steel in marine environment were contributing to the process. The involvement of a biological contribution has been suggested as one of the possible mechanisms contributing to the corrosion of piles. Numerous studies report cases of microbially influenced corrosion of steel in marine habitats. The role of anaerobic sulphate-reducing bacteria (SRB), aerobic *Pseudomonas* and facultatively anaerobic *Vibrio* spp. has often been emphasised. The deleterious influence of SRB on steel corrosion is unequivocally accepted. Marine *Vibrio* species are reported to enhance the adhesion of SRB to steel surfaces thus increasing metal corrosion^{1,2,3}. *Pseudomonas* are prevalent in all aquatic environments where their primary role in corrosion appears to be in colonising metal surfaces, creating oxygen-depleted microenvironments for SRB growth, initiating differential aeration cells and excreting corrosive acids^{4,5}. The accelerated corrosion of stainless steel in seawater by marine *Pseudomonas* spp and its exopolymers has also been demonstrated⁶. It is widely accepted that microbial consortia present as a biofilm on the metal surface are able to influence corrosion process. Moreover, is often found that the rate of corrosion in mixed cultures is greater than in pure cultures and that synergistic effects operate. Although the complexity of interaction between microbial populations within a biofilm is well appreciated no documented information exists regarding biofilm/substrate interactions occurring in the presence of more than two bacterial genera. In the field of microbially induced corrosion, very few studies deal with corrosion of steel in mixed cultures^{7,8,9}. Prior to this investigation no work focusing on the importance of the composition of microbial communities in marine corrosion appears to have been reported.

Experimental

Procedures for Microbial Sampling and Sample Treatment

Biofilm samples were collected, on two separate visits, from the sheet piling wall from corroding and non-corroding sites (S1 and S2 respectively) at a variety of tidal and low water levels and from inpanels, outpanels and web regions of the piles. In the case of each sample taken

from the piling wall, an area of approximately 25 cm² was cleared by removing the products of macrofouling. The exposed biofilm remaining in direct contact with the surface was removed with a sterile cotton swab and the swab was placed in a sterile medium for protection and preservation. In subsequent laboratory studies, cotton tips were removed, placed in a known amount of sterile water and homogenised by vortexing to achieve a uniform bacterial suspension. A known amount of this suspension was then spread-plated on four different types of solid growth media such as marine agar, yeast agar, *Pseudomonas* isolation agar and total count agar (Difco) for the purpose of detection and enumeration of aerobic bacteria and fungi. An aliquot of the biofilm suspension was transferred into a liquid, deoxygenated growth medium (Postgate's medium B¹⁰ supplied by SGS Redwood Ltd., UK) for detection of sulphate reducing bacteria. All procedures were carried out aseptically.

Sediment samples were recovered from the sea bed along the length of the piling at regular intervals of 25 metres. Samples were placed in pre-weighed, sterile plastic containers, reweighed and after resuspension in a known volume of sterile water, processed as described for biofilms.

Bacterial Enumeration and Identification

Bacterial enumeration was performed by the viable count method. The inoculated plates were incubated for 48 hours at 25°C. The colonies were counted twice after periods of 24 h and 48 h and then the counts were normalised to either the surface area of samples (in order to give the number of bacterial cells per cm²), or to the bulk (for determination of the number of cells per milligramme of sediment).

Preliminary identification of aerobic bacteria in both biofilms and sediment samples was accomplished by studying the morphology of colonies and determining Gram reaction and motility of the cells using both light and epifluorescence microscopy. Further identification was carried out by the API (Analytical Profile Index) tests API20E and API20NE (Bio Merieux Ltd). SRB in biofilms and in the sediment samples were enumerated by the "dilution to extinction" method¹¹.

Electrochemical Measurements

A series of electrochemical measurements were performed to determine the behaviour of steel in pure and mixed bacterial cultures. Measurements were made at a temperature of 22°C using a three electrode cell. A steel working electrode was fabricated by encapsulating non-corroded steel piling material in epoxy resin to expose a 1 cm² disc; this was polished down to a sub-micron surface finish on wet alumina and degreased in trichloroethane before use. A large surface area platinum mesh counter electrode was used. The reference electrode was a

saturated calomel type which communicated to a point ca 1 mm away from the working electrode surface via a luggin capillary to minimise uncompensated IR drop between working and reference electrodes. The electrolyte was either Postgate medium C¹⁰ or seawater taken from the vicinity of tested sites. The water was strained and autoclaved before measurements and was used either in the sterile conditions (control experiments) or it was inoculated with bacteria isolated from biofilms recovered from corroded piling. Several types of measurements were made:

- (a) steady state potentiodynamic sweep were used to obtain current-potential curves
- (b) observed Tafel regions from (a) were extrapolated to the corrosion potential to obtain an estimate of corrosion rate.
- (c) a linear polarisation instrument was used to monitor corrosion rates.

In addition, two other strains of SRB were tested to serve as a frame of reference in order to establish the aggressiveness of the tested strain. These other strains were associated with severe cases of marine corrosion of mild steel, one in Indonesia and the other in Alaska. SEM micrographs of steel sections exposed to these three different strains were taken to supplement electrochemical data.

Surface Analysis

Corrosion products present in biofilms removed from sites S1 and S2 were characterised by Energy dispersive X-ray analysis (EDXA) and X-ray diffraction techniques. Typical samples recovered from corrosion and surface products were analysed by a scanning X-ray diffractometer using Co radiation to obtain an approximate interplanar spacing in the range of 1.0 to 8.0 Å (corresponding to a 10 deg to 120 deg scattering angle range).

Results and Discussion

Bacterial Assessment

The results of bacterial assessment are presented in Tables 1 and 2 for samples taken on the first visit and in Tables 3 and 4 for samples collected on the second visit. The outcome of these microbiological studies revealed that the biofilms removed from the surface of steel piling contained diverse bacterial genera as well as different species of the same genus. These microbial consortia consisted of aerobic and anaerobic bacterial cells and products of cell metabolism known as extracellular polymeric matrix (EPM).

Sulphate-reducing bacteria. SRB were found in the sediment along the whole length of the piling. The number of cells detected in sediment was similar irrespective of the sampling site and equalled 10⁵ cells/mg of wet mud. SRB were also isolated from biofilms removed from the surface of the piling. No growth of SRB was detected in samples collected on the first site

visit with the exception of samples H and M which were obtained from the area around the hole in the out panel at the low water level (Table 1). All but one sample collected on the second site visit (approximately two months later) contained SRB. The number of SRB varied depending on the sampling region (Table 3). Typically, there was a greater number of SRB associated with corroding areas of piling than with the areas which did not exhibit signs of corrosion. SRB have a very high requirement for iron; actively corroding areas of piling are likely to provide higher concentrations of ferrous ions than non-corroding sites thereby encouraging the proliferation of SRB. The high bacterial presence would tend to depolarise the cathodic reaction kinetics, leading to increased corrosion rates. The lack of detection of SRB in samples collected during the first visit could be related to the physiological status of cells and their abundance in the proximity of the surface. It is likely that the population of the SRB is subjected to seasonal variations and that the numbers present in biofilms were below the detection level.

Pseudomonas and *Vibrio* species. The presence of bacteria implicated in marine corrosion of steel, in biofilms removed from the piling, indicates that the microbial component may play a significant part in observed, localised corrosion. The composition of microbial consortia varied depending of the region from which samples were taken (Tables 2 and 4). Biofilms recovered from sites which did not exhibit corrosion showed the prevalence of either *Pseudomonas* or *Vibrio species* (Tables 1 and 3 respectively). In the later case the number of SRB detected in these samples was one or two orders of magnitude lower than in samples from corroded areas. The number of aerobic bacteria counted was also lower except for sample 2 (Table 3).

The results presented in Table 1 appear to indicate a lack of correlation between the total number of aerobic cells and corrosion. It is more likely that the composition of the consortia and its metabolic activity will determine the aggressiveness of the environment at the surface of steel¹². Indeed, samples recovered from the corroding areas showed the presence of more than two microbial species including yeast (Tables 1 and 3). However, the number of cells in these samples was always relatively high.

Electrochemical Measurements

A series of experiments utilising the Tafel extrapolation technique were applied to a sterile seawater control and to seawater inoculated at the level of 10^5 cells/cm³ with pure and mixed cultures of SRB, *Vibrio* and *Pseudomonas* isolated from the surface of piling material. As shown in Table 5, the infected electrolyte samples each gave rise to a modest increase in the estimated corrosion rate at short times. After 21 hours, the SRB, *Vibrio* and *Pseudomonas* mixture showed a drop in the corrosion rate which may be attributed to the temporary

formation of a protective surface film. The Tafel extrapolation technique also showed comparatively little change in the corrosion rate over a six-day period. Due to technical problems associated with the application of this technique (e.g. the time required for repetitive measurements, the need for uncompensated IR drop correction and the large perturbations from the open-circuit potential involved), the linear polarisation method was preferred for monitoring studies. Figure 1 shows the mean corrosion rate as a function of time over a period of 15 days in Postgate medium C as found by a linear polarisation technique. The corrosion rates for the sterile and infected media are comparable for an initial period of approximately 3 days. Thereafter, the infected sample shows a marked increase in corrosion rate, reaching a relatively high level of >11 mpy (mils per year) after day 9. During this time the control (sterile) sample shows a relatively small increase in corrosion rates over the range 0.6 to 2 mpy. It should be noted that these results relate to initially smooth, polished samples; in practice, a significant roughening would result in an increase in the observed corrosion rate due to an enhanced surface area. Another experiment utilised a 100 cm³ sterile sea water electrolyte which was inoculated with 1 cm³ of sludge taken from a biofilm removed from an outpan on site S1. As shown in figure 2, the mean corrosion rate (measured by a linear polarisation resistance technique) showed a similar trend to the behaviour of steel in Postgate medium C infected with SRB. The initial rate was relatively low (1.3 mpy) but a rapid increase occurred after a 3 to 4 day period. At a sufficiently long time (more than 25 days), the corrosion rate became relatively steady at a level of approximately 14 mpy. The data in figures 1 and 2 demonstrate the importance of time-dependent studies of microbial corrosion in this system and the shortcomings of rapid tests.

In auxiliary laboratory experiments, SRB isolated from biofilms removed from sheet piling gave rise to particular high corrosion rates comparing with Alaskan and Indonesian strains (as measured by LPR). SEM studies supported electrochemical data showing that biofilm formation and corrosion of steel surface underneath of the biofilm was greater in the case of Portsmouth strain than that observed for Alaskan and Indonesian strains at longer times¹³.

Energy Dispersive X-ray Analysis and X-Ray Diffraction Analysis

A number of samples of surface products were analysed from three sites and typical results are summarised in Table 6. The majority of samples showed appreciable sulphur and chlorine contents, while some samples contained calcium and occasionally magnesium. The sulphur levels tended to be highest in the samples taken from test site S1. The diffraction patterns are rendered complex by the presence of minerals, organic and amorphous material. Phase identification is also hindered by the large number of components and wide ranges of stoichiometry. However, samples taken from outpan and inpan sections at site S1 showed the presence of iron sulphides and relatively high magnetite levels. The presence of iron sulphides

in several samples was confirmed by the evolution of hydrogen sulphide on addition of hydrochloric acid and by the evolution of nitrogen effervescence during an azide spot test. Several peaks were not readily identified using JCPDS assignments. Diffraction patterns from site S2 and from general surface corrosion products showed the presence of large amounts of iron oxyhydroxides and moderate magnetite levels. Additional analyses are required to determine whether these corrosion products were biogenically produced.

Conclusions

1. Although the SRB count was moderate to low, the bacteria were shown to be very active metabolically. Auxilliary experiments demonstrated that, in comparison with other SRB species associated with the corrosion of mild steel, the strain isolated from biofilms taken from a corroded sheet piling proved to be highly aggressive.
2. The analysis of biofilm samples revealed the presence of different species of aerobic bacteria belonging to the genera *Pseudomonas* and *Vibrio* which are reported to be associated with corrosion of steel in aquatic environments. No simple correlation was found between numbers of aerobic bacteria and observed corrosion levels. However, there was an indication that the composition of the microbial consortia was linked with the degree of corrosion. There was also a tendency for bacterial species of the same genus to be associated with non-corroding sites whereas mixed genera were always found in samples from corroding sites.
4. EDX analysis showed the presence of relatively high levels of sulphur in surface products taken from both sites S1 and S2, the values lying within the range 0 % to 8 %. There was a tendency for site S1 to show higher sulphur levels.
5. Phase analysis of the surface products by XRD, although problematic due to appreciable levels of amorphous, organic (including microbial EPM) and mineral components, clearly showed differences between products from S2 and S1 sites. The former consisted largely of iron oxyhydroxides with some magnetite; the latter showed additional XRD peaks partly attributable to iron sulphides.
6. Electrochemical measurements of averaged corrosion rate showed that:
 - (a) sterile and SRB infected Postgate's media give rise to comparable corrosion rates (1 mpy) at short times (up to 3 days). At longer times, the SRB infected medium showed a rapid increase in corrosion rate with time.
 - (b) in seawater inoculated with biofilm suspension, the corrosion also showed a marked increase following a short (4 day) induction period.

In view of the obtained results it may be concluded that microbial consortia can significantly contribute to the process of localised marine corrosion of steel. Further work involving sampling from different UK harbours in order to extend the present findings and elucidate biocorrosion mechanisms is in progress.

The authors are grateful to British Steel Technical, Swinden Laboratories, U.K. for financial support and to Mr K. Johnson and Dr V. Chun in the Corrosion Section of this company for their valuable technical advice.

References

1. C. C. Gaylarde, H. A. Videla, *International Biodeterioration* 23 (1987): p. 91.
2. C. C. Gaylarde, J. M. Johnston, Anaerobic metal corrosion of cultures on bacteria from estuarine sediments. (Biologically Induced Corrosion. NACE-8, Houston, Texas, 1986), p. 137.
3. C. C. Gaylarde, J. M. Johnston, *International Biodeterioration Bulletin* 18 (1982): p.111.
4. H. A. Videla, S. G. Gomez de Saravia, M. F. L. de Mele, P. S. Guiamet, "Bioelectrochemical assessment of biofilm effect on MIC of two different steels of industrial interest". *Corrosion* 90, Paper No 123, NACE, Houston, 1990.
5. R. A. King, R. D. Eden, *Biocorrosion, Biodeterioration Society occasional publication No 5*, (C.C. Gaylarde and L.H.G. Morton eds.), 1989, p. 134.
6. D. C. White, D. E. Nivens, A. T. Nichols, B. D. Mickall, J. M. Kerger, P. D. Henson, G. G. Geesey, K. C. Clarke, "Role of aerobic bacteria and their extracellular polymers in the facilitation of corrosion". *Biologically Induced Corrosion, NACE-8, NACE, Houston, Texas, 1986*, p. 233.
7. N. J. E. Dowling, J. Guezennec, D. C. White, *Microbial problems in the offshore oil industry*, E.C. Hill, J.L. Shennan and R.J. Watkinson, eds. (John Wiley and Sons Ltd., Chichester, England, 1987), p. 27.
8. C. C. Gaylard, H. A. Videla, "Synergistic action of bacteria on the corrosion of mild steel in a marine medium". *Proceedings of the 7th International Congress on Marine Corrosion and Fouling, 7-11 November, 1988, Valencia, Spain*.
9. C. C. Gaylarde, J. M. Johnston, *Microbial Adhesion to Surfaces*, R.C.W. Berkeley et al., eds., (Ellis Horwood, Chichester, 1980), p. 511.
10. J. R. Postgate, *The Sulphate Reducing Bacteria*, (Cambridge University Press, London, 1984).
11. I. B. Beech, R. Edyvean, *International Biodeterioration and Biodegradation*, in press.
12. A. Steele, I. B. Beech, *International Biodeterioration and Biodegradation*, in press.
13. C. W. S. Cheung, I. B. Beech, F. C. Walsh, *International Biodeterioration and Biodegradation*, in press.

Table 1 Aerobic and Anaerobic Bacteria (SRB) Detected in Biofilms Removed from the Surface of Steel Piling (1st Sampling on first site visit)

| Sample | Total number of aerobic bacteria No. cells x 10 ² /cm ² ± (SD) | | SRB no. cells x 10 ³ /cm ² | Bacterial genes |
|-----------|---|--------|--|--------------------|
| D OC1/TL | 3.97 | 0.4 | ND | PsI Y |
| F OC1/TL | >>4.00 | - | ND | PsIII VII |
| G OC1/TL | >>4.00 | - | ND | PsIII VII |
| O ONC1/TL | >>4.00 | - | ND | PsII,III |
| C IC1/TL | 3.21 | (0.59) | ND | PsI,III Y |
| N INC1/TL | 2.87 | (0.24) | ND | PsII Y |
| V INC1/TL | 0.10 | (0.02) | ND | ND |
| W IC1/TL | 2.50 | (0.16) | ND | VII |
| A WC1/TL | 3.73 | (0.23) | ND | PsI, VII Y |
| E WC1/TL | 3.46 | (0.46) | ND | PsIII VII Y |
| T WNC1/TL | 0.10 | (0.02) | ND | PsI |
| B CA1/ZTL | 1.84 | (0.22) | ND | PsI VII Y |
| H OAH1/LW | 3.74 | (0.36) | 0.4 | VII |
| L ONC2/LW | 2.32 | (0.16) | ND | PsI |
| M OAH1/LW | >>4.00 | - | 0.4 | PsI VII |
| Q OA1/LW | 2.32 | (0.28) | ND | PsI VII |
| R ONC1/LW | >>4.00 | - | ND | PsI VII Y |
| X OTP1/LW | >>4.00 | - | ND | PsI VII |
| Y OTP1/LW | 1.32 | (0.18) | ND | PsII VIII |
| S INC2/LW | 3.20 | (0.31) | ND | PsI |
| J WC1/LW | >>4.00 | - | ND | PsI VIII Y |
| K WNC1/LW | 0.90 | (0.08) | ND | PsI VIII |
| P WNC2/LW | >>4.00 | - | ND | PsI |
| U WA1/LW | >>4.00 | - | ND | PsI VII |

WC -web corroded OC -outpan corroded
WNC-web non corroded ONC -outpan non corroded
TP -test panel IC -inpan corroded
LW -low water INC -inpan non corroded
TL -tidal level H -hole
A -active

PsI -*Pseudomonas luteola* PsII -*Pseudomonas paucimobilis*
PsIII -*Pseudomonas cepacia* VII -*Vibrio fluvialis*
PsI -*Pseudomonas fluorescens* VIII -*Vibrio analgaliticus*
Y -yeast species

Numbers 1 and 2 indicate sampling sites as described in procedures.

Table 2 Percentage of Aerobic Bacteria Detected in Biofilms Removed from the Surface of Steel Piling (1st Sampling on first site visit)

| Sample | PsI | PsII | PsIII | PsI | VII | VIII | Y |
|-----------|-----|------|-------|-----|-----|------|----|
| D OC1/TL | 0 | 0 | 0 | 90 | 0 | 0 | 10 |
| F OC1/TL | 0 | 0 | 2 | 0 | 98 | 0 | 0 |
| G OC1/TL | 0 | 0 | 5 | 0 | 95 | 0 | 0 |
| O ONC1/TL | 0 | 80 | 20 | 0 | 0 | 0 | 0 |
| C IC1/TL | 0 | 0 | 7 | 80 | 0 | 0 | 13 |
| N INC1/TL | 0 | 85 | 0 | 0 | 0 | 0 | 15 |
| V INC1/TL | 0 | 0 | 0 | 0 | 0 | 0 | 0 |
| W IC1/TL | 0 | 0 | 0 | 0 | 100 | 0 | 0 |
| A WC1/TL | 10 | 0 | 0 | 10 | 50 | 0 | 30 |
| E WC1/TL | 0 | 0 | 2 | 0 | 95 | 0 | 3 |
| T WNC1/TL | 100 | 0 | 0 | 0 | 0 | 0 | 0 |
| B CA1/ZTL | 5 | 0 | 0 | 0 | 50 | 0 | 45 |
| H OAH1/LW | 0 | 0 | 0 | 0 | 100 | 0 | 0 |
| L ONC2/LW | 100 | 0 | 0 | 0 | 0 | 0 | 0 |
| M OAH1/LW | 60 | 0 | 0 | 0 | 40 | 0 | 0 |
| Q OA1/LW | 60 | 0 | 0 | 0 | 40 | 0 | 0 |
| R ONC1/LW | 80 | 0 | 0 | 0 | 10 | 0 | 10 |
| X OTP1/LW | 70 | 0 | 0 | 0 | 30 | 0 | 0 |
| Y OTP1/LW | 0 | 85 | 0 | 0 | 0 | 15 | 0 |
| S INC2/LW | 100 | 0 | 0 | 0 | 0 | 0 | 0 |
| J WC1/LW | 50 | 0 | 0 | 0 | 0 | 45 | 5 |
| K WNC1/LW | 90 | 0 | 0 | 0 | 0 | 10 | 0 |
| P WNC2/LW | 100 | 0 | 0 | 0 | 0 | 0 | 0 |
| U WA1/LW | 70 | 0 | 0 | 0 | 30 | 0 | 0 |

For key see Table 1

Table 3 Aerobic and Anaerobic Bacteria (SRB) Detected in Biofilms Removed from the Surface of Steel Piling (2nd Sampling on second site visit)

| | Total number of aerobic bacteria No. cells x 10 ² /cm ² ± (SD) | | SRB no. cells x 10 ³ /cm ² | Bacterial genus |
|----------------|---|-------|--|--------------------|
| | | | | |
| 1 OC1/LW | 26.8 | (3.7) | 0.4 | ViI,II PsI,II |
| 2 ONC1/LW | 28.2 | (2.4) | 0.004 | ViI,II |
| 3 WHC1/LW | 27.4 | (3.5) | 4 | PsI,II ViI,II |
| 4 WNC1/LW | 3.8 | (0.7) | 0.04 | ViI,II |
| 5 OC1/LW | 28.5 | (1.4) | 4 | PsI,II ViI,II |
| 6 WC1/LW | 31.4 | (3.3) | 4 | PsI,II, ViI,II |
| 7 WC1/LW | 28.4 | (2.8) | 4 | PsI,II ViI |
| 8 WC1/LW | 38.3 | (4.1) | 4 | PsI,II ViI |
| 9 ONC2/LW | 2.8 | (0.3) | 0.4 | ViI,II |
| 10 OC1/2/LW | 42.4 | (3.1) | 4 | PsI,II ViI,II |
| 11 WNC2/LW | 10.6 | (1.8) | 0.4 | ViI,II |
| 12 ONC2/LW | 9.5 | (0.8) | 0.4 | ViI,II |
| 13 TP14/2TL | 8.9 | (0.6) | 0.04 | ViI,II |
| 14 TP25/2TL | 11.0 | (1.2) | 0.04 | PsI |
| 15 TP18/2/LW | 16.6 | (3.7) | ND | PsI |
| 16 TP23/2/LW | 18.2 | (3.2) | 0.4 | PsI |
| 17 TP26/2/1mBL | 13.3 | (2.6) | 4 | PsI ViI |
| 18 TP15/2/LW | 17.6 | (3.1) | 0.04 | PsI ViI |

WC -web corroded
WNC -web non corroded
TP -test panel
LW -low water
TL -tidal level
A -active

OC -outpan corroded
ONC -outpan non corroded
IC -inpan corroded
INC -inpan non corroded
H -hole

PsI -*Pseudomonas luteola*
ViI -*Vibrio fluvialis*

PsII -*Pseudomonas paucimobilis*
ViII -*Vibrio anguillarum*

Numbers 1 and 2 indicate sampling sites as described in procedures.

Table 4 Percentage of Aerobic Bacteria Detected in Biofilms Removed from the Surface of Steel Piling (2nd Sampling on second site visit)

| Sample | PsI | PsII | ViI | ViII |
|----------------|-----|------|-----|------|
| 1 OC1/LW | 30 | 30 | 25 | 15 |
| 2 ONC1/LW | 0 | 0 | 40 | 60 |
| 3 WHC1/LW | 70 | 5 | 10 | 15 |
| 4 WNC1/LW | 0 | 0 | 35 | 65 |
| 5 OC1/LW | 0 | 70 | 20 | 10 |
| 6 WC1/LW | 40 | 20 | 30 | 10 |
| 7 WC1/LW | 50 | 10 | 40 | 0 |
| 8 WC1/LW | 45 | 20 | 35 | 0 |
| 9 ONC2/LW | 0 | 0 | 45 | 55 |
| 10 OC1/2/LW | 40 | 20 | 15 | 25 |
| 11 WNC2/LW | 0 | 0 | 45 | 55 |
| 12 ONC2/LW | 0 | 0 | 35 | 65 |
| 13 TP14/2TL | 0 | 0 | 40 | 60 |
| 14 TP25/2TL | 100 | 0 | 0 | 0 |
| 15 TP18/2/LW | 100 | 0 | 0 | 0 |
| 16 TP23/2/LW | 100 | 0 | 0 | 0 |
| 17 TP26/2/1mBL | 70 | 0 | 30 | 0 |
| 18 TP15/2/LW | 60 | 0 | 40 | 0 |

For key see Table 3

Table 5 Corrosion Rates of Steel Piling in Seawater Estimated from Tafel Extrapolation Measurements

| Electrolyte condition | Corrosion rate after 1 hour /mpy | Corrosion rate after 21 hours /mpy |
|--|----------------------------------|------------------------------------|
| Sterile control | 1.3 ± 0.2 | 1.2 ± 0.2 |
| Sterile plus <i>Pseudomonas</i> * | 1.8 ± 0.2 | 2.4 ± 0.3 |
| Sterile plus SRB* | 1.6 ± 0.2 | 2.1 ± 0.3 |
| Sterile plus <i>Vibrio</i> * | 1.9 ± 0.2 | 2.5 ± 0.3 |
| Sterile plus SRB* plus <i>Vibrio</i> * plus <i>Pseudomonas</i> * | 2.0 ± 0.2 | 0.8 ± 0.1 |

* the bacteria were inoculated at an approximate level of 10^5 cells per cm^3 in the case of each genera

Table 6. Energy Dispersive X-Ray Analysis of Fragments of Surface Products

| Site | Fe | Cl | S | Ca | Mg |
|--|----|-----|-----|-----|-----|
| S2 (low-corrosion) | 89 | 2.7 | 1.5 | 6.5 | - |
| | 92 | 6.1 | 0.2 | 1.8 | - |
| | 87 | 5.7 | 3.2 | 3.9 | - |
| | 79 | 9.1 | 5.0 | 7.0 | - |
| | 94 | 3.4 | 1.0 | 2.0 | - |
| S1 (high corrosion) | 96 | 0.5 | 3.6 | - | 0.4 |
| | 89 | 2.4 | 7.9 | - | 0.8 |
| | 93 | 3.1 | 2.1 | 2.2 | - |
| | 95 | 0.9 | 4.1 | - | - |
| Patch panel (outpanel near site S1) | 90 | 2.4 | 5.1 | - | - |
| | 91 | 2.7 | 6.2 | - | - |
| | 87 | 1.3 | 8.5 | 0.6 | - |
| | 94 | 0.7 | 4.2 | 0.2 | 0.2 |

Samples containing high levels of Si have been omitted.

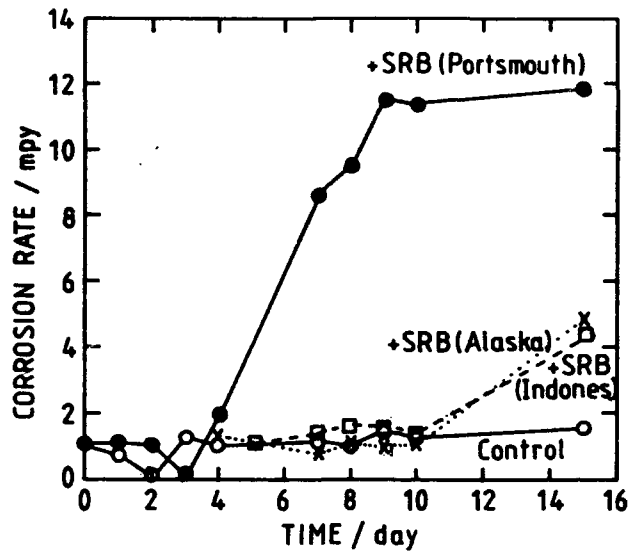


Figure 1 Mean Corrosion Rate (via LPR in mils per year) as a Function of Time for Steel Piling in Postgates Medium C at 22°C. The difference between a sterile control and electrolyte inoculated at a level of 10^5 cells/cm³ with SRB isolated from various sources. At early times, all the corrosion rates are comparable and some data points have been omitted for clarity. (Static flow conditions).

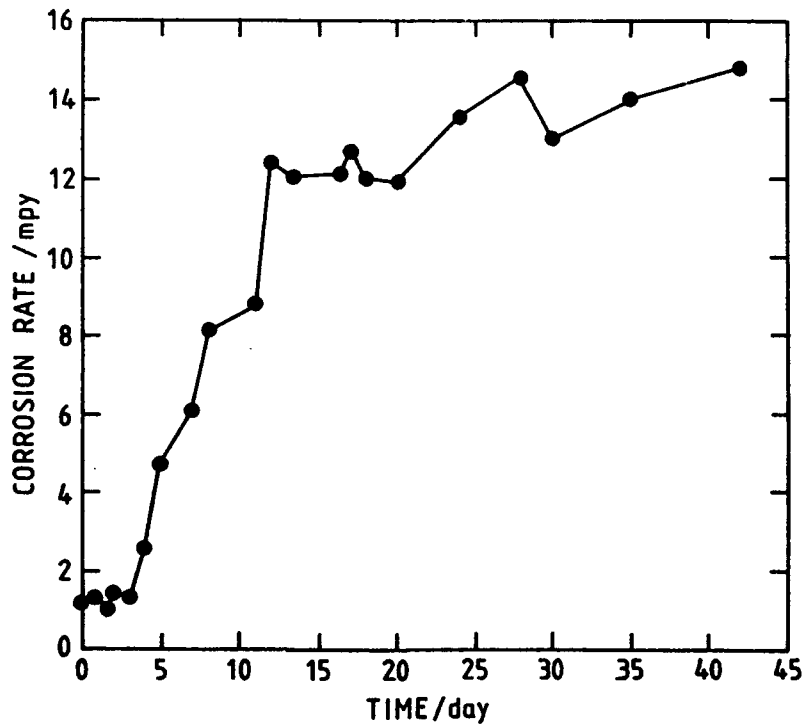


Figure 2 Mean Corrosion Rate versus Time for Steel Piling in Seawater. 100 cm³ electrolyte was inoculated with 1 cm³ sludge/biofilm material from a corroding outpan section at test site S1 (Static flow conditions).

Anaerobic Corrosion of Steel by Phototrophic Sulphur Bacteria

M Eashwar, S Maruthamuthu and S Sebastin Raja
Offshore Platform and Marine Electrochemistry Centre
CECRI Unit, Harbour Area
Tuticorin 628 004, India

S Venkatakrishna Iyer
Central Electrochemical Research Institute
Karaikudi 623 006, India

Abstract

Putrid models with Tuticorin seawater revealed a novel type of anaerobic corrosion. Decomposition of macrofouling organisms resulted in spectacular colouration of putrid seawater exposed to light. Putrid cells in the dark did not show pigmentation and accounted for very low rates of steel corrosion. The microorganisms responsible for colouration as well as corrosion enhancement were identified as the photosynthetic sulphur bacteria. Chemical analysis indicated that these bacteria accelerated corrosion by anaerobic oxidation of sulphide to elemental sulphur under photic conditions.

Introduction

The putrid model offers a convenient way for evaluating¹⁻³ marine alloys in media represented mixed microbial populations. The predominance of sulphur cycle in putrid systems can be illustrated by the transformation of atomic ratio of elements from O:C:N:P = 240:106:16:1 under aerobic conditions to S:C:N:P = 60:106:16:1 under anaerobic conditions⁴.

Until recently, the corrosivity of putrid seawater³ was related directly to the amount of sulphide. Eashwar *et al.*³ have however shown that the role of sulphur oxidising bacteria, e.g. thiobacilli, could be more important. The authors concluded from that study that sulphide had an inhibitory action on steel under anaerobic conditions.

In preliminary studies with Tuticorin seawater, we observed that decomposition of organic matter regularly resulted in bright colouration of putrid water. Furthermore, rates of³ corrosion were considerably higher than those in an earlier test³. Microscopic examination of the coloured seawater revealed the abundant presence of pigmented microorganisms which apparently were phototrophic sulphur bacteria. A detailed investigation was taken up to examine a possible role for these bacteria in steel corrosion.

Experimental Procedures

Corrosion Measurements

The composition of the steel used is shown in Table 1. Sheets (1.1mm thick) were cut into coupons that measured 50mm by 15 mm. They were picked, polished, degreased, weighed and stored in desiccators until use.

Eight macrofouling species (Table 2) served as the inoculum with which seawater was made putrid. Corrosion cells were set-up in 3L culture flasks. Each species was allowed to stagnate and decompose in 5% (wt./vol.) ratios with freshly sampled seawater. A control environment was also used in which the cell received only seawater. Six coupons (from 2 cells) were withdrawn at desired periods for assessment of corrosion by weight loss. Potentials of the steel were measured using a high impedance voltmeter and an SCE, utilizing a series of 1L flasks with appropriate additions of the decomposing species.

Two series of corrosion tests were performed. The first was designed to evaluate the corrosivity of putrid seawater as a function of time. In the second, the effect of light was specifically examined by placing putrid cells in (i) the dark and (ii) alternate light/dark (12/12) condition. Illumination (diffuse sunlight) level varied between 2,000 and 8,000 lux in day hours.

Solution Chemistry Changes

Chemical analyses were carried out in 1L flasks. At various stages of the putrefaction sequence, seawater was withdrawn for various chemical determinations. The first series of corrosion tests was complemented by oxygen and pH measurements only. In tests examining the effect of illumination, several other parameters were also considered. Sulphate, thiosulphate and sulphide were determined according to Grasshoff⁵. Estimation of elemental sulphur was done by the colorimetric method after Stal et al.⁶

Microbiological Studies

Putrid seawater samples were regularly observed under the microscope for the presence of photosynthetic sulphur bacteria. Pigmentation, morphology and motility were recorded for various species.

Characterization of some isolates was carried out according to Pfenning and Truper⁷, proceeding from agar shake dilution in the defined media. Purified cultures were scaled up to larger volumes. Light absorption maxima were recorded on a Shimadzu (model 160 UV) spectrophotometer.

Results

Corrosion

A remarkable feature with all of the putrid cells exposed to light was the spectacular colouration of seawater. The period for colouration was normally between 6 and 8 days from the commencement of decomposition, but took 10 days in presence of G. corticata. Initially the colour was purple/pink, but this transformed to green by 20 days.

Values of solution pH as a function of time are shown in Figure 1 for control seawater and seawater solutions with 5% decomposing macroorganisms. The pH of seawater with no macro species decreased from 8.1 to 6.87 in 37 days. This decrease was dramatic in the presence of decomposing organisms and, in general, the lowest pH was measured between the 2nd and 3rd day of the putrefaction process. Thereafter, the pH restored slowly to neutral values. As seen in Figure 1, return of pH to neutral was least in the C. peltata cell and most rapid in the one with G. corticata. With the latter, the seawater became alkaline; the pH rise in the cell with decomposing sponge was also somewhat peculiar in that the values crashed down a second time after 12 days' putrefaction.

There was no trace of dissolved oxygen in any of the putrid cells after 36 hours. As a matter of fact, only the C. peltata cell contained any oxygen (0.6 mg/L) at 48 hours. Values recorded at 24 hours correlated well with the corresponding drop in pH. The least concentrations (1.2 and 1.3 mg/L) were noted for the oyster (C. cucullata) and the red weed (G. corticata) which interestingly produced the most acidic conditions. The values for other cells during the same period were 1.7 (Sargassum sp.), 1.8 (T. anhelans) and 2.4 (C. peltata).

Figure 2 illustrates the fate of steel, in terms of corrosion rates, in the control and putrid cells. In presence of all decomposing species, with one obvious exception, G. corticata, the steel exhibited very low rates of corrosion during the first 5 days. Values were less than 10 mdd, the least being 2.81 mdd with Sargassum sp. This was quite unexpected because these rates were lower than those in the control cell. Corrosion, however, increased dramatically between 5 and 20 days, i.e. during the period when the seawater in the cells became intensely coloured. This high rate was sustained till the completion of the experiments (32 days). In contrast to other species, G. corticata was responsible for a high amount of corrosion initially, which further increased in the later periods. The rate at 20 days was an imposing 63.34 mdd which was considerably higher than that caused by other decomposing species.

Potentials of steel for the corresponding conditions are shown in Figure 3. There was no appreciable change in steel potential in

the control cell (-750 to -765 mV vs SCE). Onset of decomposition, however, caused potentials to rapidly shift in the positive direction. Barring a minor negative shift between 12 and 16 days, the potentials of steel in the sponge cell moved progressively more positive and reached -610 mV at 40 days. With the other species, potentials drifted negatively after the initial positive shift, either transiently (Sargassum sp. and C. peltata) or permanently (C. cucullata).

Figure 4 shows that light had a crucial role on the rate of corrosion of steel. In general, corrosion was 2 to 3 times higher in presence of light. Data for G. corticata were again one exception, the corrosion acceleration by light being only moderate. This fact illustrates that the high rate of attack was governed by some, as yet undetermined, "corrosive" chemical release by this species.

Solution Chemistry

pH measured in the dark (D) and alternate light/dark(L/D) cells with 5% decomposing C. peltata are shown in Figure 5. The pH in the L/D cell dropped more slowly, restored to neutral more quickly and further moved on the alkaline side.

Light had a conspicuous and remarkable effect on the speciation of sulphur in putrid seawater. Figure 6 shows the levels of sulphate, thiosulphate, sulphide and elemental sulphur as a function of time. There was a small increase in sulphate concentration after 24 hours, and it decreased thereafter. Whereas sulphate in the dark cell depleted progressively, values in the L/D cell fluctuated throughout. A different trend was noticed with thiosulphate concentration. Values increased in both the cells until about 9 days. Thereafter, a marked reduction in thiosulphate occurred in the presence of light, contrary to the further increase and thereafter a relatively constant trend in the dark.

Evolution of sulphide occurred faster in presence of light. Following the peak at 9 days, sulphide was used up at a remarkably high rate in the L/D cell until about 20 days. Between 20 and 37 days, however, values remained less variable. Sulphide reached its peak by 13th day in the dark cells, but there was no obvious loss as that noted in the L/D cell. Perhaps the most note worthy feature was the variable manner in which sulphur formed in the D and L/D cells. Levels of sulphur were very low throughout the experimental period in the D cell. Note that a dramatic increase in sulphur concentration occurred in the L/D cell at the period corresponding to sulphide depletion.

Phototrophic Sulphur Bacteria

The purple/pink photosynthetic sulphur bacteria that initially started to colour the putrid seawater exposed to light were readily recognised as members of the family Chromatiaceae by the

characteristic absorption maximum at the 830 nm region. Sulphur was noted as highly refractile globules inside their cells. The first to appear (after 6 to 7 days) was a highly motile species, circular to ovoid, which kept swarming in the whole vessel (Thiocystis gelatinosa). Another Chromatiaceae representative was a larger, non-motile, rod-shaped organism which occurred in aggregates of hundreds to thousands of cells (Thiodydion sp.). This species was in particular responsible for the intense colouration of the walls of flasks to which they adhered. These two species occurred in all putrid cells no matter what decomposing macrofouling species they contained, and persisted till the 3rd week.

A purple red sulphur bacterium, different from the ones mentioned above, appeared in the G.corticata cell. This species was spiral, motile, and stored sulphur outside the cells. Globules of sulphur were found in the medium or along the peripheral part of their cells. Placement of this species as Ectothiorhodospira mobilis was suggested by 1. formation of sulphur globules outside the cells, 2. colour of the species, and 3. absorption spectrum (Figure 7) revealing 2 major peaks, one at 849 and the other at 799 nm.

Microscopic observations of green water showed the presence of a non-motile, rod shaped green bacterium, Chlorobium limicola. In addition to this species, many filamentous gliding bacteria occurred. These forms were mostly confined to the walls of the vessels. Absorption spectrum of C.limicola culture is shown in Figure 8.

Discussion

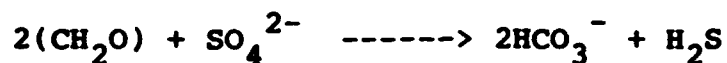
The photosynthetic sulphur bacteria play an important role not only in the sulphur cycle but also in the synthesis of organic matter in aquatic environments. It is generally accepted that the phototrophic sulphur bacteria occur in much greater abundance⁸ in freshwater and estuarine habitats than in the open ocean. As a result, studies of photosynthetic sulphur bacteria in the marine environment are rather limited.

Traditionally, studies on the isolation of phototrophic sulphur bacteria from the marine environment have utilized sea-bed sediment as the only source of inoculum. A rather different source of inoculum, namely marine sponges,¹⁰ was first employed by Eimjellen⁹ and later by Imhoff and Truper¹⁰. Eimjellen isolated Chlorobium limicola and Thiocystis sp. from Halichondrium panicea. Attempts by the latter workers with 4 species of marine sponges confirmed the earlier findings. Isolation of phototrophic sulphur bacteria from seawater or marine organisms other than sponges has not been ventured yet. The successful use of putrid systems in enriching photosynthetic sulphur bacteria has been demonstrated in this work.

Since the location of seawater and marine species sampling was open ocean that receives good flushing by tidal currents, the occurrence of phototrophic sulphur bacteria in the macro species and/or the oxygenated is conceivably clear. This is contrary to the likelihood envisaged by many workers, notably Truper¹¹, Imhoff⁸ and Madiyan¹² that open sea locations are generally devoid of anaerobic sulphur bacteria. These bacteria have, however, been stated to occur regularly in marine sediment, in association with the sulphate-reducing bacteria. Since it is now well established that oxygenated parts of the ocean do contain sulphate-reducing bacteria (in a dormant state), it can be hypothesised that the anaerobic, phototrophic sulphur bacteria would also be present in such waters.

Much of the variable effects of light in regard to sulphur chemistry and corrosion are by reactions inherent of photosynthetic sulphur bacteria. As a matter of fact, profound differences in sulphur speciation become obvious only after about 5-7 days of putrefaction, when these bacteria started to flourish in the L/D cells occurred as the preliminary step followed by intense sulphate reduction. Hydrogen

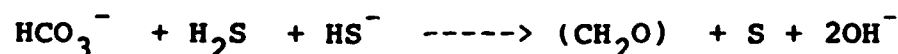
sulphide in the putrid seawater can be liberated from decaying protein as well as through bacterial sulphate reduction. Biomass in its proteins contains on the average 1% bound (organic) sulphur⁴. Liberation by putrefaction would yield approximately 10g H₂S per 1000g of biomass. If, however, the same amount of biomass is channeled into bacterial sulphate reduction, according to



(where CH₂O is a general average formula for biomass that allows to estimate stoichiometrics), it could in principle yield 570g H₂S per 1000g of biomass. The lower level of sulphide measured during the earliest stage of putrefaction probably implies an importance for sulphide liberation from tissues since the sulphate reduction reaction is theoretically not expected at the stage.

A rapid increase of pH in the L/D cells is clearly an effect of the photosynthetic sulphur bacteria. At pH's close to 7, when the PSB start to bloom, sulphide would occur as HS⁻ (50%) and H₂S (50%). Phototrophs, however, consume stoichiometrically the undissociated species¹³. Withdrawal of CO₂ and H₂S will lead to hydroxyl ions and hence to an increase of the pH.

The overall reaction catalysed by the photosynthetic sulphur bacteria can be hypothesised to occur as :



(the formula in the parenthesis again means cell material). Data

for sulphide and sulphur (Figure 6) are in excellent agreement with the suggested reaction. Note from the same figure that a significant increase in sulphate concentration has not occurred during the sulphide oxidation phase (L/D cell) contrary to the generalized⁷ implication which envisages sulphate as the ultimate end product. In seawater environments, however, incomplete oxidation of sulphide (to sulphur) is more¹³ prevalent than complete oxidation as suggested¹⁴ by Pfennig¹³ and later confirmed by van Gernerden et al.¹⁴

The suggested reaction would also account for the higher corrosive action of putrid seawater in the L/D cell. Sulphur is extremely¹⁵ corrosive to steel as experimentally demonstrated by Schaschl¹⁵. Since the photosynthetic bacteria carry out such a type of reaction resulting in the yield of elemental sulphur it is concluded that these organisms were responsible for the accelerated corrosion of steel in the cells exposed to light. Research is under way with pure cultures of PSB to establish the findings presented here.

References

1. K.D.Efird, T.S.Lee, Corrosion, 35 (1979) : p.79.
2. C.J.Thomas, R.G.J.Edyvean, R.Brook, Biofouling, 1 (1988) : p.65.
3. M.Eashwar, P.Chandrasekaran, G.Subramanian, K.Balakrishnan, Corrosion, 49 2 (1993).
4. E.K.Dunrsma, R.Dawson, Marine Organic Chemistry (Amsterdam : Elsevier, 1981) p.395.
5. K.Grasshoff, M.Ehrhardt, K.Kremling, Methods of Seawater Analysis, 2nd edition (Weinheim : Verlag Chemie, 1983).
6. L.J.Stal, H.van Gernerden, W.E.Krumbein, FEMS Microbiology Ecology, 31 (1985) : p.111
7. N.Pfennig, H.G.Truper, "Anoxygenic Phototrophic Bacteria", Bergey's Manual of Systematic Bacteriology Vol 3, eds. J.T.T.Staley, M.P.Bryant, N.Pfennig, J.G.Holt (Baltimore : Williams & Wilkins, 1989) p.1635.
8. J.F.Imhoff, "Halophilic phototrophic Bacteria", Halophilic Bacteria Vol-1F, ed. Rodriguez - Valera, (Boca Raton : CRC Press Inc, 1988) p.85.
9. K.E. Eihmjellen, Acta Chem Scan, 21 (1967) : p.2280.
10. J.F.Imhoff, H.G.Truper, Microbial Ecology, 3 (1976) : p.1.

11. H.G.Truper, *Helgolander Wiss Meeresunters*, 20 (1970) : p.6.
12. M.T.Madigan, "Microbiology, Physiology and Ecology of phototrophic Bacteria", *Biology of Anaerobic microorganisms*, ed. A.J.B. Zender (New York : John Wiley and Sons, 1988) p.40.
13. N.Pfennig, *Ann Rev Microbiol*, 31 (1977) : p.275.
14. H.van Gernerden, R.de Wit, S.Caroline, R.A.Herbert, *FEMS Microbiology Ecology*, 62 (1989) : p.111.
15. Schaschl, *Materials Performance*, 19 7 (1980) : p.9.

Table 1 : Composition of the steel (% weight)

| C | Mn | Si | S | P | Fe |
|-----|------|-------|-------|------|-----------|
| 0.1 | 0.46 | 0.074 | 0.028 | 0.07 | remainder |

Table 2 : List of macrofouling species

| Species | Group |
|---------------------------------|-------------------------------------|
| 1. <i>Hypnea valentiae</i> | -----> Rhodophyta, the red weeds |
| 2. <i>Gracilaria corticata</i> | |
| 3. <i>Sargassum sp.</i> | -----> Phaeophyta, the brown weeds |
| 4. <i>Padina pavonica</i> | |
| 5. <i>Caulerpa peltata</i> | -----> Chlorophyta, the green weeds |
| 6. <i>Ulva lactuca</i> | |
| 7. <i>Crassostrea cucullata</i> | -----> Mollusca, oysters |
| 8. <i>Tedanus anhelans</i> | -----> Porifera, sponges |

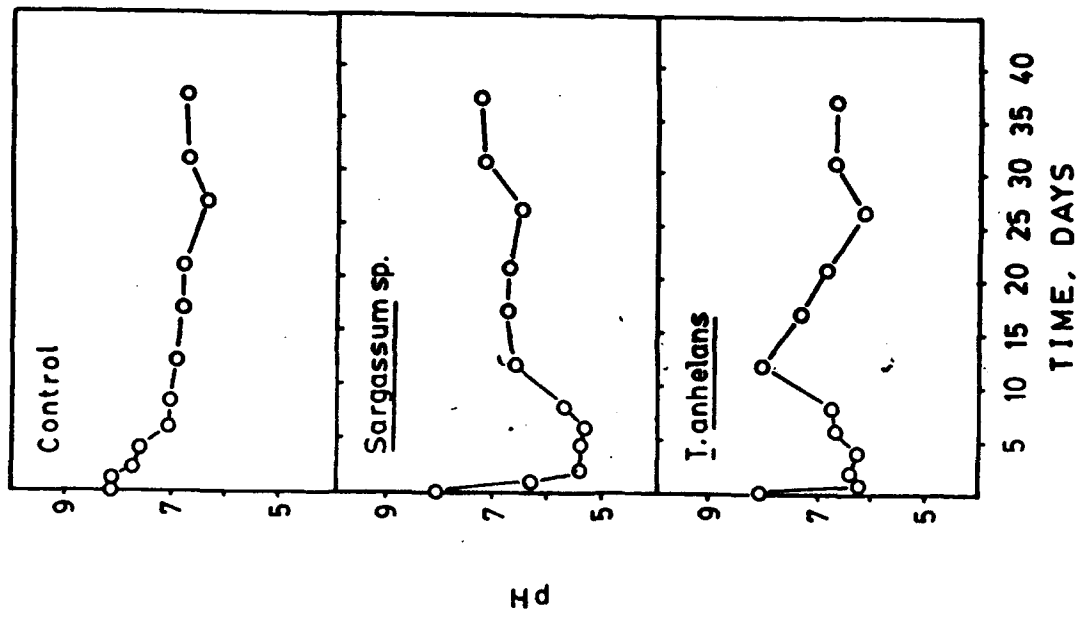
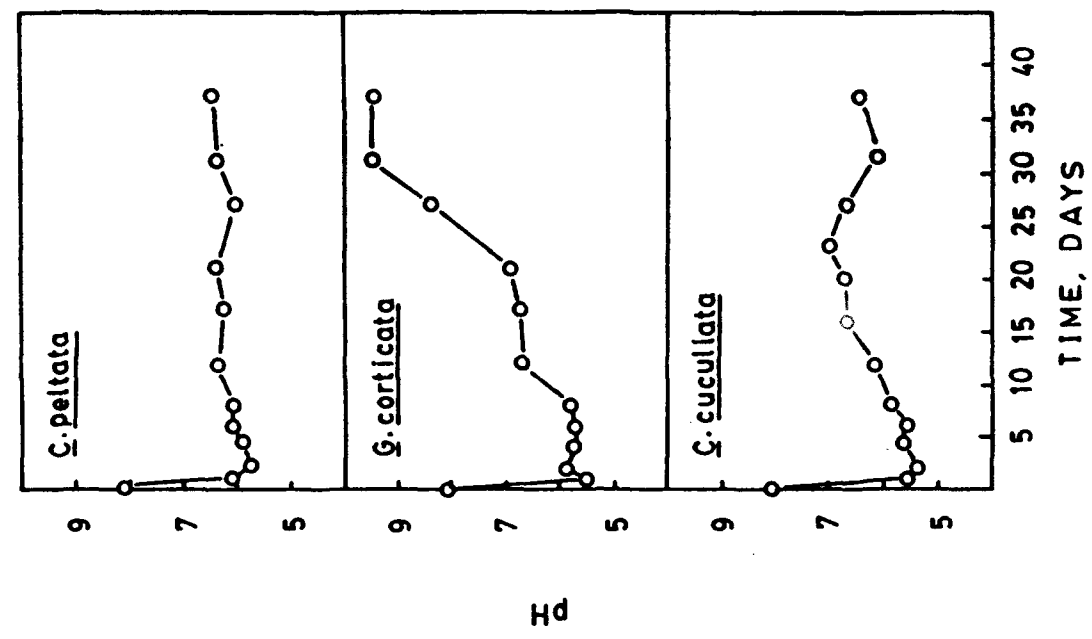


Fig. 1 : pH as a function of time in decaying cultures of macrofouling organisms.

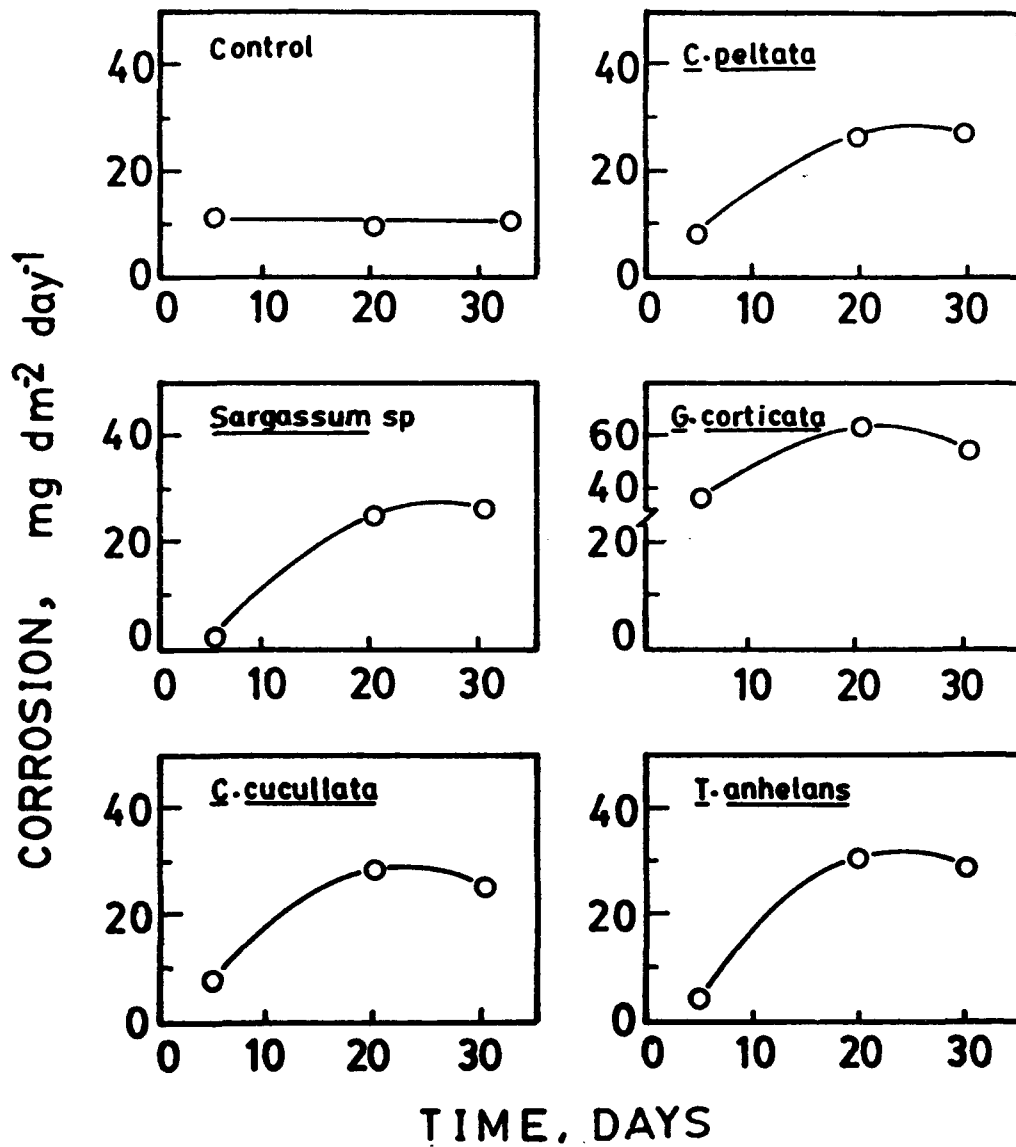


Fig.2 : Rates of corrosion as a function of time in decaying cultures of macrofouling organisms

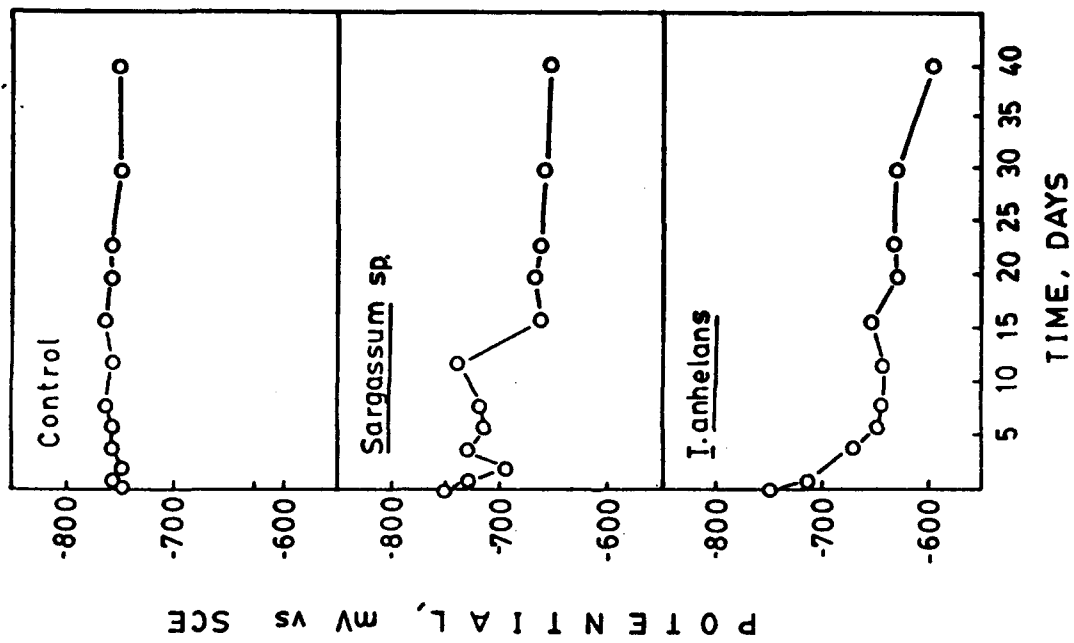
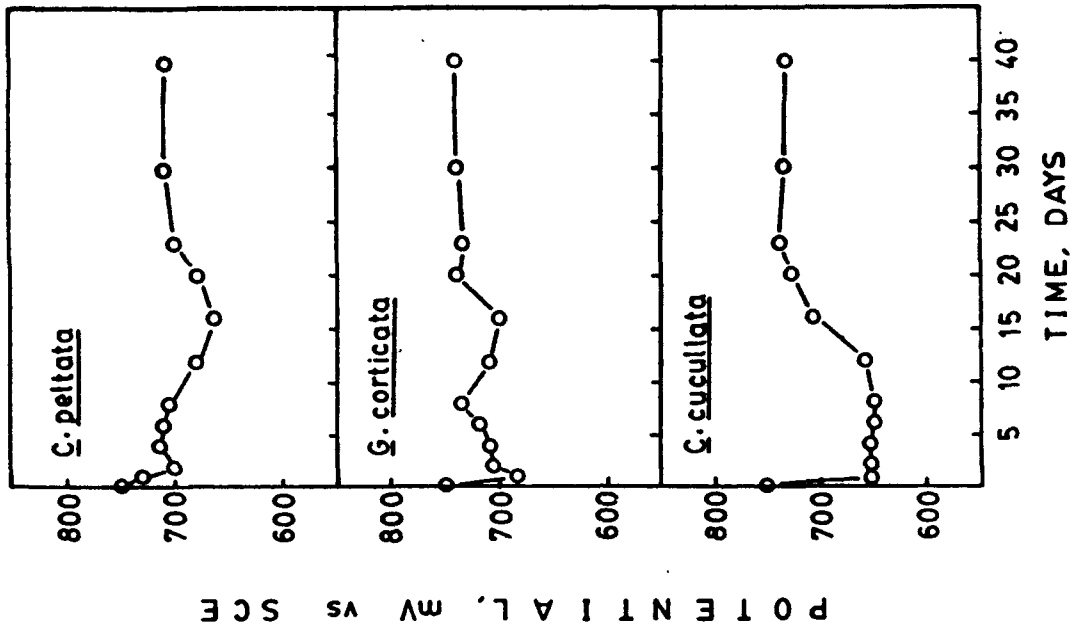


Fig.3 : Corrosion potential as a function of time in decaying cultures of macrofouling organisms

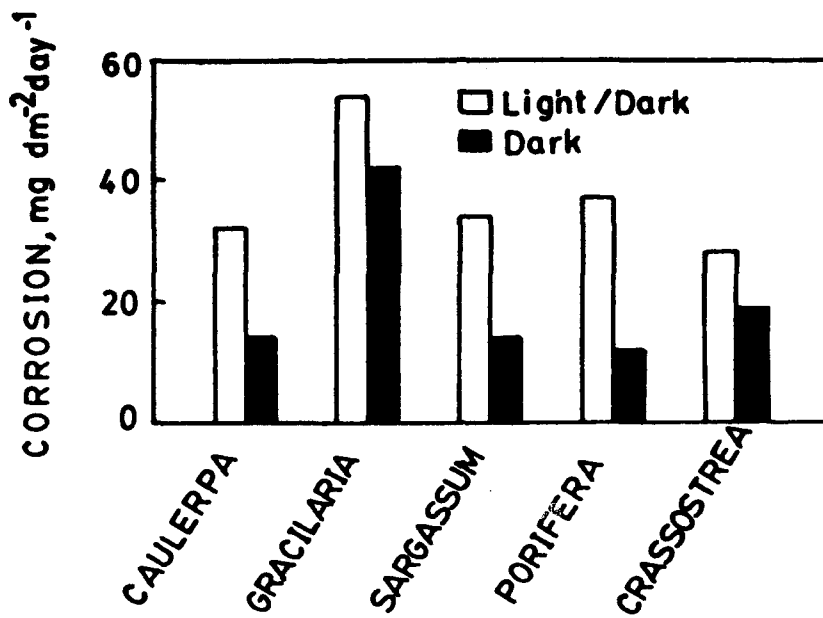


Fig.4 : Effect of light on corrosion in putrid systems

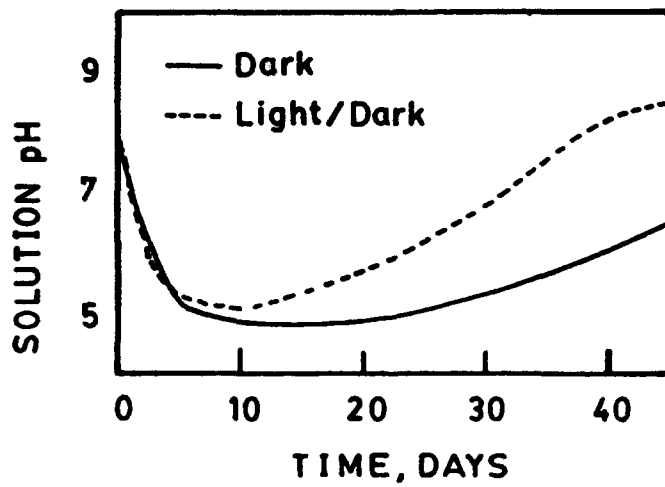


Fig.5 : Effect of light on pH of putrid seawater

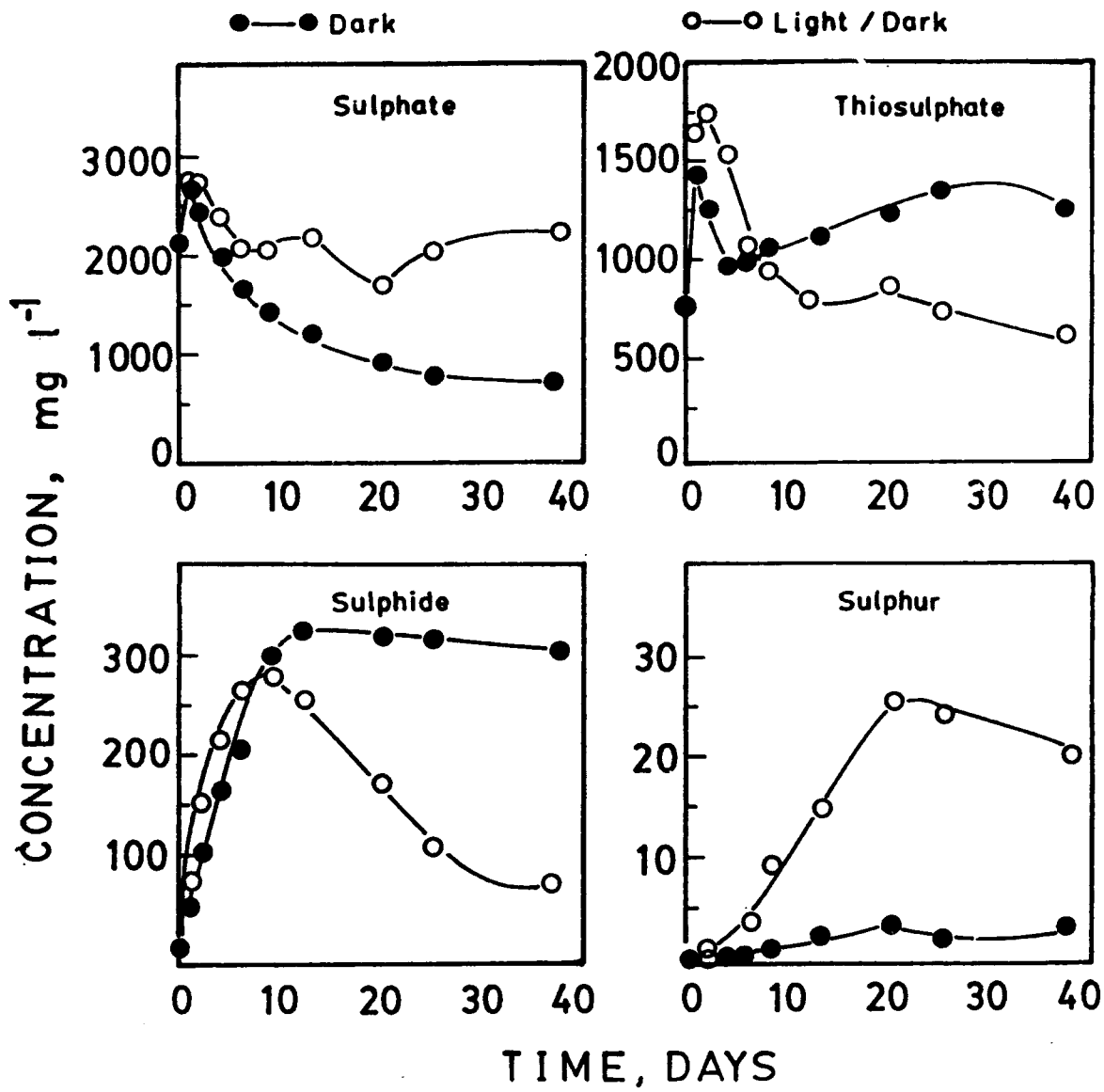


Fig.6 : Effect of light on sulphur speciation in putrid seawater

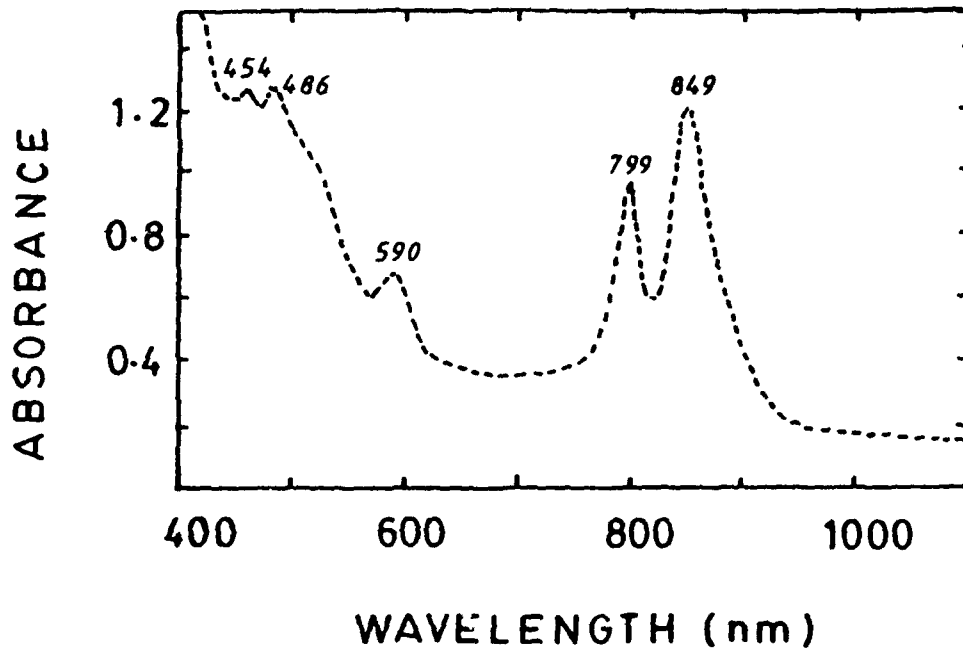


Fig.7 : Absorption spectrum for E.mobilis.

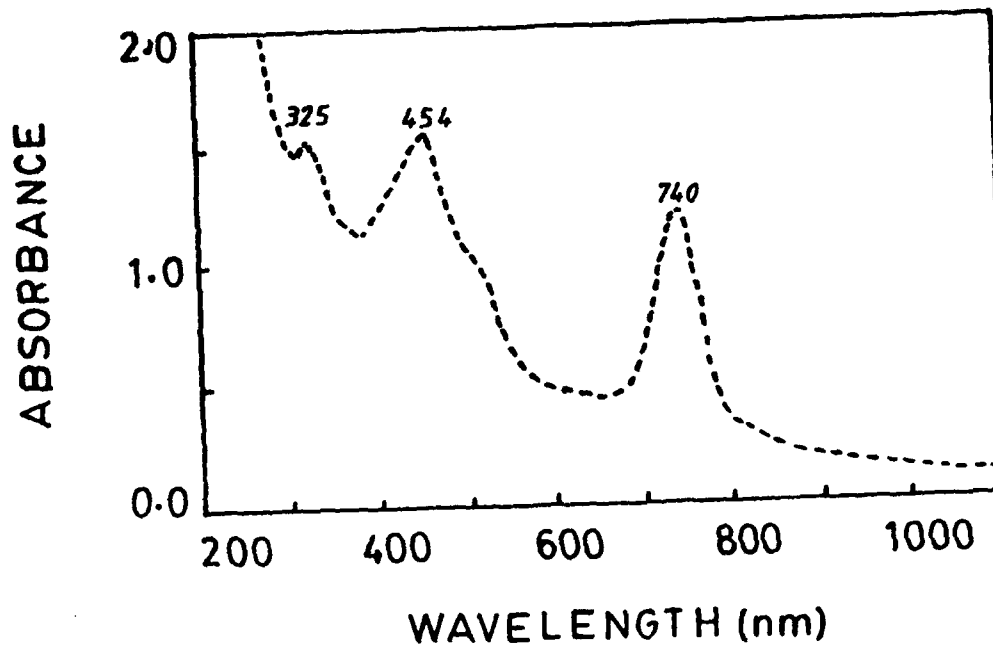


Fig.8 : Absorption spectrum for C.limicola.

Effect of Biofilms on Crevice Corrosion of Stainless Alloys in Coastal Seawater

Hong-Ji Zhang
College of Marine Studies
University of Delaware
Lewes, DE 19958

S. C. Dexter
College of Marine Studies
University of Delaware
Lewes, DE 19958

Abstract

Effect of biofilms on crevice corrosion of stainless alloys in coastal seawater has been investigated for stainless alloys S31603, S31703, and N08904 using remote crevice assembly technique. It was found that for S31603 and S31703 biofilms only slightly decreased initiation times; for N08904 biofilms moderately decreased initiation times. Biofilms were found to greatly increase the crevice corrosion propagation rate for all three alloys as measured by maximum and average penetrations, weight losses and corrosion current densities. The decrease of initiation times was due to ennoblement of E_{corr} and the increase in propagation rate was caused by cathodic depolarization, both due to the action of biofilms.

Key words: biofilm, crevice corrosion, stainless alloy, seawater, current density, initiation, propagation, weight loss

Introduction

Biofilms can shift the open circuit potential (E_{oc}) of stainless alloys in the noble direction in: seawater¹⁻⁶, brackish water and fresh water^{7,8}. While much has been published¹⁻⁸ about the effect of this E_{oc} ennoblement on pitting, less is known about its effect on crevice corrosion. Johnsen and Bardal⁴ pointed out that E_{oc} ennoblement should increase the tendency for crevice corrosion initiation as well as for pitting. Likewise, Scotto et al⁶ suggested that an increase in cathodic reduction rate of oxygen caused by bacteria should increase localized corrosion of passive metals in natural seawater. Dexter et al⁹ showed that bacteria in the crevice solution could contribute to the depletion of oxygen, potentially decreasing crevice initiation times.

Kain and Lee¹⁰ studied the crevice corrosion of S31600 and N08904 in natural and artificial seawaters using the remote crevice assembly technique. They found that for S31600 the initiation time in natural seawater was almost same as that in artificial seawater, while the total corrosion current in natural seawater was one order of magnitude higher than that in

artificial seawater; for N08904 the initiation time in natural seawater was 10 % of that in artificial seawater and the total current in natural seawater was two orders of magnitude higher than that in artificial seawater. Valen¹¹ also used a remote crevice assembly device to study the crevice corrosion of S31603 in natural and artificial seawaters. He found that the current density for S31603 in natural seawater was two orders of magnitude higher than that of S31603 in artificial seawater although the cathode-to-anode area ratio was 20 times larger in artificial seawater than in natural seawater. Mollica et al¹² studied the effect of temperature on crevice corrosion of stainless steels (SS) in natural seawater. Their results showed that as temperature increased from 25 to 40 °C the corrosion for SS with intermediate resistance decreased one to two orders of magnitude, but the corrosion for SS with low resistance like S31600 remained unchanged. They attributed the difference to the activity of biofilms at 25°C. Gallagher et al¹³ studied crevice corrosion of stainless steels in natural, transported and artificial seawaters using a multiple crevice assembly device. They found that crevice corrosion of a range of steels was dramatically less in artificial seawater than in natural seawater. They attributed the difference to the microorganisms in natural seawater.

Zhang and Dexter¹⁴ used traditional and remote crevice assembly techniques to study crevice corrosion for S30400, S31603, S31703, S31803, and N08904 in natural and control coastal seawaters. They found that biofilms had little effect for S30400 and S31603 but had considerable effect for S31703 and N08904. The control water produced by 0.2 μ m filtering alone was effective in maintaining a biofilm free condition for only about 500 hours. They suggested that more effective control methods were needed.

There are two purposes for this paper. The first purpose is to present data on the effect of marine biofilms on crevice corrosion of stainless alloys using a more effective control method, which combined pasteurization of the natural seawater at 80°C for four hours with periodic replacement of cathodes. The second purpose is to present data on the effect of biofilms on propagation of crevice corrosion by using coupons on which corrosion had been pre-initiated galvanostatically. S31603 (316L) was selected because of its low resistance to crevice corrosion in seawater. S31703 (317LM) and N08904 (904L) were used as examples of newer alloys with intermediate resistance to crevice corrosion in seawater, and N08367 (AL 6XN) with 6 % Mo was used as a more crevice resistant control for comparison. Tests were done in natural coastal seawater and in the control water prepared as above to kill most microorganisms without altering the water chemistry.

Experimental

The compositions of the alloys are shown in Table 1. The annular electrodes (31.7 mm OD, 9.6 mm ID, 3 mm thickness) used as anodes were purchased from Metal Samples Co., Inc., Munford, AL. The large panels of the same alloys (152 x 101 x 2 mm) used as cathodes were donated by Allegheny Ludlum Steel Corp., Brackenridge, PA. All samples were prepared before testing by surface grinding through 320 grit silicon carbide paper, degreasing with soap and water, and rinsing in distilled water.

Coastal seawater was obtained at the tidal part of the Broadkill River where it enters the

lower Delaware Bay. This water had the following characteristics: temperature, 22 to 26°C; salinity, 25 to 31 parts per thousand (ppt); oxygen, air saturated (5 to 8 ppm); and pH 7.7 to 8.1; all varying daily with tidal cycle and fresh water run-off. The water was brought to the lab where the tests were done in a 34 liter polypropylene tray at 21 to 23°C. The water was continuously refreshed by a gravity feed and overflow system at a rate to replace the entire volume once a day.

To separate the effect of microorganisms from that of water chemistry, a control water with much reduced numbers of microorganisms was needed. The control water was produced using a four hour pasteurization of the natural water. Due to the large volume (34 liters) of water needed for these tests, more stringent preparation of the water was not practical. The control water was first stored in autoclave sterilized bottles, and then fed into a covered 34 liter polypropylene tray in which the control experiments were done. The control water was changed every three days using a gravity feed and overflow system.

Remote crevice assembly technique was used. Each annular shaped anode with a spot welded nickel wire was mounted in an epoxy resin mold as shown in Figure 1. Delrin washers were prepared as shown in Figure 1. The anode-washer assembly was fastened together using a titanium fastener insulated with heat shrink tubing and tightening to an initial torque of 7.3 Nm. The assembly was re-tightened after two days and before the actual experiment began. The spot welded wire was used both to secure the assembly to a wooden rack and to provide the connection between anodes and cathodes. The first 104 mm of cathodes were immersed in the test solution. Two nickel wires spot welded to the top of each cathode panel had the same functions described above. The cathode-to-anode area ratio was 30:1.

In control tests the cathodes and anodes were exposed in control water prepared as above. The cathodes were replaced when control water was changed. The removed cathodes were immersed in 60°C fresh water for at least an hour, then naturally air-dried for future use. Three samples for each material (one for N08367) were used both in control and natural seawaters.

Two sets of experiments were performed. The first set was to study the effect of biofilms on initiation and propagation of crevice corrosion, while the second set was to investigate the effect of biofilms on propagation of crevice corrosion using pre-initiated anodes and pre-nobled cathodes. The corrosion of the anodes in the second set was galvanostatically initiated at 40 mA for 30 minutes; under those conditions there was little sample to sample variation. The cathodes were immersed in natural coastal seawater for about three weeks until the potentials were near +400 mV SCE.

Open circuit potentials were measured vs. SCE using a digital voltage meter. The currents between the cathode and anode members were assessed using a zero-resistance ammeter (model AM 1000) made by Thurston/Bell Associates, Inc. The initiation time for each sample was taken as the time when the corrosion current increased suddenly and remained above zero.

Cathodic polarization experiments for cathodes at the end of the immersion tests were computer controlled through an EG&G PARC 273A potentiostat with PARC 352 software. The potential was scanned from 100 mV positive to E_{corr} to -1000 mV SCE with a 0.15 mV/sec rate.

The depth of attack was measured for each sample after the experiment using a needle point dial gauge. Both maximum and average depths of attack were recorded. The average depth was obtained from 10 to 34 measurements for a given sample depending on the extent of attack. The percentage of corroded area under washer (PCA) for each anode was also measured. Weight losses for the anode members were determined by subtracting the final weight to the nearest 0.01 g from the original weight. Corroded anodes were cleaned by soap and brush, rinsed in distilled water, and air-dried before weight measurement.

The biofilm thickness was measured using a stereo microscope to focus sequentially on the biofilm surface and the bare metal surface with a precision of $\pm 3\mu\text{m}$. The biofilm was then fixed with 4% glutaraldehyde and stained with 0.1mg/ml 4',6-diamidino-2-phenylindole (DAPI). The apparent bacterial concentration in the surface layers of the film was determined using epifluorescence microscopy.

Results

Effect of Biofilms on Initiation of Crevice Corrosion.

Table 2 gives initiation times under natural initiation conditions. For S31603 and S31703, the initiation times for the natural samples were almost the same as those for the control samples. Natural sample No.2 of N08904 did not corrode at all during the test period. The initiation times for natural samples No.1 and 3 were less than 40% of those for the control samples.

Effect of Biofilms on Propagation of Crevice Corrosion.

Table 3 gives weight losses, PCA and maximum and average depths of attack for the anodes under natural initiation conditions. In general, crevice propagation was much faster in natural seawater than in control water. Weight losses of all samples in natural seawater were one to two orders of magnitude more than those of the samples in control seawater. For S31603 and S31703, PCAs of samples in natural seawater were generally much larger than those of samples in control seawater. PCAs for natural samples No.1 and No.3 of N08904 were 80%, while PCAs for control samples No.2 and No.3 of N08904 were unmeasurable. For all alloys maximum and average depths of attack in natural seawater were one to two orders of magnitude larger than those in control seawater.

Table 4 gives weight losses, PCA and maximum and average depths of penetration for the pre-initiated anodes. Weight losses of all natural samples were one to two orders of magnitude more than those of the control samples. For all alloys PCAs of samples in natural seawater were generally much larger than those of samples in control seawater and maximum and average depths of attack in natural seawater were one to two orders of

magnitude larger than those in control seawater. Results show the same general trend as the data in Table 3 except that the effect of biofilms was more noticeable here.

Figures 2 through 4 show measured corrosion current densities under natural initiation conditions. Due to the logarithmic scale no data is shown until the initiation of crevice corrosion. Figures 2 and 3 show that the current densities of three samples of S31603 and S31703 in natural seawater were at least one order of magnitude higher than those of the same alloy in control water. The current densities for N08904 in natural seawater (Figure 4) were nearly three orders of magnitude higher than those of the control sample. Figure 5 shows a typical E_{corr} vs. time record for S31703 under natural initiation conditions. E_{corr} of the natural sample first reached 100 mV SCE, then decreased to -100 mV SCE or below after initiation. The control process of changing water and cathodes caused the fluctuation in E_{corr} of the control sample.

Figures 6 through 8 show measured corrosion current densities for S31603, S31703 and N08904 in the pre-initiated experiments. The current densities for S31603, S31603, and N08904 in natural seawater were two, two and a half, and three orders of magnitude larger respectively than those in control seawater. The current densities for control samples here were smaller than those for the control samples in Figures 2 to 4. Figure 9 shows typical potential vs. time records for S31703 in the pre-initiated experiments. After the natural and control samples began to corrode, the E_{corr} stayed around -50 and -200 mV SCE respectively.

Figure 10 shows cathodic polarization curves for the cathodes of S31703 at the end of the pre-initiated experiments. At any given potential above -600 mV SCE current densities for the natural cathodes were higher than those for the control cathodes.

Biofilm Analysis

The biofilm thicknesses for all cathode panels were $45 \pm 25 \mu\text{m}$. The biofilm thickness was difficult to measure on the control panels. The filtration procedure for producing the control water removed most of the suspended particles as well as the bacteria. Therefore the film that might form in the control water was transparent, making it difficult to focus on the top surface. The biofilms on the control samples were much thinner (less than $10\mu\text{m}$) than those on the natural samples.

The surface bacterial concentrations for natural and control N08367 samples were $2.1 \times 10^6 \text{cm}^{-2}$ and $1.4 \times 10^5 \text{cm}^{-2}$ respectively in the naturally initiated experiments; the bacterial concentrations for natural and control N08367 samples were $1.1 \times 10^6 \text{cm}^{-2}$ and $2.5 \times 10^5 \text{cm}^{-2}$ respectively in the pre-initiated experiments.

Discussion

From the data in Table 2 for S31603 and S31703, the initiation times for the natural samples were almost same as those for the control samples. For N08904 the initiation times for the natural samples were much shorter than those for the control samples. At the time of

initiation the current densities for the natural samples were at least one order of magnitude higher than those for the control samples. This is consistent with the results of Zhang and Dexter¹⁴. The S31603 data of Kain and Lee¹⁰ and Valen¹¹ gave the similar kind of conclusion, whereas the N08904 data of Kain and Lee¹⁰ showed that the initiation time in natural seawater was only 10% of that in artificial seawater compared to 40% shown here.

From the data in Tables 3 and 4, and Figures 2 and 6, the propagation of corrosion for S31603 natural samples was one to two orders of magnitude faster than that for the control samples. In Figure 2 the fluctuation in current density for the control sample was magnified due to the use of log scale. Valen¹¹ showed that the current density of the S31603 samples in natural seawater was more than two orders of magnitude higher than that of the samples in artificial seawater even though the cathode/anode ratio in artificial seawater was 20 times larger than that in natural seawater. Gallagher et al¹³ found that there was almost no crevice corrosion for S31603 in artificial seawater. In this work the corrosion depths for the control samples were very shallow, whereas PCAs for the control samples were quite large and in one case it was 65%. Apparently artificial seawater is less corrosive than the pasteurized control seawater used in this work. The reason for this difference is unknown, but was probably related to the fact that the chemistry of the control water used here was different from that of artificial seawater. Organic chemicals in the control water here were more than those in artificial seawater. The S31603 control samples here had less corrosion than those reported in the previous paper of Zhang and Dexter¹⁴. The difference seems due to that the control method used here was more effective.

From the data in Tables 3 and 4, Figures 3 and 4 and Figures 7 and 8, the corrosion rates for S31603 and N08904 in natural seawater were one to two and a half and two to three orders of magnitude higher than that in control seawater respectively. It is very hard to compare the data of N08904 with those from Gallagher et al¹³ because they did not give specific values for PCA and depths; but it seems that the results for N08904 here were consistent with their results. The results here also agree with those of Kain and Lee¹⁰ and Zhang and Dexter¹⁴.

According to the mixed potential theory, anodic currents must be equal to corresponding cathode currents under open circuit conditions. The steady potentials for the natural and control samples were -50 and -200 mV SCE respectively (see Figure 9). At these two potentials, the current densities of the natural and control cathodes for S31703 in Figure 10 were $1.77 \times 10^{-2} \text{ A/m}^2$ and $2.1 \times 10^{-4} \text{ A/m}^2$ respectively. Due to the 30:1 cathode/anode ratio, $1.77 \times 10^{-2} \text{ A/m}^2$ for the natural cathode corresponded to 0.53 A/m^2 for the natural anode; $2.1 \times 10^{-4} \text{ A/m}^2$ for the control cathode was equal to $6.3 \times 10^{-3} \text{ A/m}^2$ for the control anode. The current densities for the natural anodes in Figure 7 were about 0.5 A/m^2 , which was in excellent agreement with 0.53 A/m^2 calculated above. The current densities for the control anodes in Figure 7 were about 0.003 A/m^2 , which was of the same order of magnitude as 0.0063 A/m^2 estimated above. Therefore, the calculated current densities for the anodes from cathodic polarization curves were in excellent agreement with those measured using the zero-resistance ammeter.

Theoretically, the higher E_{corr} is the higher the probability of crevice corrosion and the

shorter the initiation time should be. The ennoblement of E_{corr} by biofilms, therefore, should reduce the initiation times of crevice corrosion, which was generally true in the present experiments. For S31603 and S31703 with low crevice corrosion resistance, even without E_{corr} ennoblement, crevice corrosion initiated readily. The biofilms in our experiment slightly decreased the average initiation time for S31603 and S31703 from 255 to 223 hours. For N08904 with medium crevice corrosion resistance, it should again take longer for samples to corrode without the effect of biofilms. The initiation times for N08904 in Table 2 showed a mixed result. For the two natural and two control samples that showed initiation, biofilms decreased the average initiation time from 1377 to 425 hours. A larger set of samples, however, would be needed to give a more definitive result.

In contrast to the case of initiation, biofilms increased the current density during crevice corrosion by at least one order of magnitude for S31603, S31703 and N08904 in this work. This resulted in large difference in weight loss as well as in maximum and average depths of penetration for all three alloys tested as shown in Tables 3 and 4. The increase in propagation was caused by depolarization of cathodic reaction as shown in Figure 10 and in agreement with the data published by other authors^{3,15,16}.

The control water combined with replacing cathodes in this work provided effective control condition. This method was much more successful than that using 0.2 μm filtration¹⁴.

Conclusions

1. Marine biofilms slightly decreased the average initiation times of crevice corrosion for S31603 and S31703. The decrease of the initiation times by the biofilms was due to the ennoblement of E_{corr}
2. The biofilms increased the propagation rate of crevice corrosion on S31603, S31703, and N08904 by one to three orders of magnitude. The increase of the propagation rate was caused by the cathodic depolarization by the biofilms.
3. The method that combined 4 hour pasteurization of seawater and replacing cathodes provided a very effective control.

Acknowledgment

This research was supported by NOAA Office of Sea Grant, U.S. Department of Commerce under Grant No. NA16RGO162-01. The U.S. Government is authorized to produce and distribute reprints for governmental purposes, not withstanding any copyright notation that may appear hereon. Authors also thank Allegheny Ludlum Steel for donating samples.

References

1. A. Mollica and A. Trevis. Proceedings of the 4th International Congress on Marine Corrosion and Fouling. 1976, p.351.

2. S. C. Dexter. Biofouling, in press.
3. R. Holthe, E. Bardal and P. O. Gartland. Time dependence of cathodic properties of stainless steels, titanium, platinum and 90/10 CuNi in sea water. Corrosion/88, paper No.393, (Houston, TX:NACE, 1988).
4. R. Johnsen and E. Bardal. Corrosion, Vol. 41, 1985, p.296.
5. S. C. Dexter and G. Y. Gao. Corrosion, Vol. 44, 1988, p.717.
6. V. Scotto, R. Di Cintio, and G. Marcenaro. Corrosion Science, Vol. 25, 1985, p.185.
7. S. C. Dexter and H-J Zhang. Effect of Biofilms on Corrosion Potential of Stainless Alloys in Estuarine Waters. Proc. 11th Intl. Corrosion Congress, Florence, 1990, p.333.
8. S. C. Dexter and H-J Zhang. Proc. Microbially Influenced Corrosion and Biodeterioration, N. J. Dowling, M. W. Mittelman and J. C. Danko, edited, 1990, 7-1.
9. S. C. Dexter, K. E. Lucas, and G. Y. Gao. The Role of Marine Bacteria in Crevice Corrosion Initiation, Proc. Biologically Induced Corrosion, S. C. Dexter, edited, p.144, (Houston, TX:NACE,1986)
10. R. M. Kain and T. S. Lee. Recent Development in Test Methods for Investigating Crevice Corrosion, ASTM STP 866, Philadelphia,1985, p.299.
11. S. Valen. Thesis, Norwegian Institute of Technology, Department of Materials and Processes, Trondheim, 1966.
12. A. Mollica, A. Trevis, E. Traverso, G. Ventura, G. GE Carolis and R. Dellepiane. Corrosion, Vol. 44, 1988, p.194.
13. P. Gallagher, R. E. Malpas, and E. B. Shone. Bri. Corrosion Journal, Vol. 23, 1988, p.229.
14. Hong-Ji Zhang and Stephen. C. Dexter. Corrosion/92, paper No.400, Nashville, 1992.
15. A. Mollica and U. Montini. Unpublished data, 1973.
16. S. Motoda, Y. Suzuki, T. Shinohara and S. Tsujikawa. Corrosion Science, Vol. 31, 1990, p.515.

TABLE 1.
CHEMICAL COMPOSITION OF STAINLESS ALLOYS
(% by Weight)

| UNS | Cr | Ni | Mo | Cu | C | Si | Mn | S | P | N | Co |
|--------|-------|-------|------|------|-------|------|------|--------|-------|-----|-----|
| S31603 | 16.23 | 10.11 | 2.10 | 0.36 | 0.022 | 0.43 | 1.84 | 0.001 | 0.034 | .04 | .22 |
| S31703 | 18.29 | 16.27 | 4.36 | 0.17 | 0.024 | 0.48 | 1.66 | 0.025 | 0.020 | .09 | .31 |
| N08904 | 19.00 | 24.30 | 4.28 | 1.38 | 0.012 | 0.36 | 1.59 | 0.0003 | .019 | .06 | .29 |
| N08367 | 20.28 | 23.82 | 6.22 | 0.30 | 0.018 | 0.49 | 0.36 | 0.0004 | .022 | .23 | NA |

NA: Not Available

TABLE 2.
Effect of Biofilms on Initiation Times

| CATHODE/ANODE = 30 INITIAL TORQUE 7.3 Nm | | TEST ALLOYS | | | | | | | | |
|--|---------|-------------|-------------|-------------|-------------|-------------|-------------|-------------|-------------|-------------|
| | | S31603 1 | S31603 2 | S31603 3 | S31703 1 | S31703 2 | S31703 3 | N08904 1 | N08904 2 | N08904 3 |
| INITIATION TIME (Hours) | Natural | 182 | 155 | 244 | 244 | 244 | 267 | 333 | >1862 | 517 |
| | Control | 182 | 420 | 182 | 267 | 298 | 182 | NA* | 1353 | 1400 |

* Data not available

TABLE 3.
Propagation of Crevice Corrosion in Naturally Initiated Tests

| TEST ALLOYS | REMOTE CREVICE CORROSION ASSEMBLY CATHODE/ANODE = 30 INITIAL TORQUE = 7.3 Nm | | | | | | | |
|----------------|--|---------|----------|---------|-----------------------|---------|-----------------------|---------|
| | PROPAGATION | | | | PARAMETERS | | | |
| | Weight Loss (gram) | | PCA* (%) | | Maximum Depth (mm) | | Average Depth (mm) | |
| | Natural | Control | Natural | Control | Natural | Control | Natural | Control |
| S31603-1 | 1.11 | 0.09 | 80 | 55 | 1.52 | 0.14 | 0.39 | 0.04 |
| S31603-2 | 1.16 | <0.01 | 80 | <1 | 1.27 | <0.01 | 0.47 | <0.01 |
| S31603-3 | 1.04 | 0.08 | 90 | 55 | 0.81 | 0.14 | 0.36 | 0.04 |
| S31703-1 | 0.97 | 0.05 | 80 | 60 | 1.98 | 0.09 | 0.34 | 0.04 |
| S31703-2 | 0.70 | 0.04 | 65 | 35 | 0.94 | 0.13 | 0.30 | 0.03 |
| S31703-3 | 0.83 | 0.01 | 75 | 50 | 1.17 | 0.05 | 0.29 | 0.02 |
| N08904-1 | 0.53 | NA** | 80 | NA** | 1.30 | NA** | 0.21 | NA** |
| N08904-2 | 0 | <0.01 | 0 | <1 | 0 | <0.01 | 0 | <0.01 |
| N08904-3 | 0.55 | <0.01 | 80 | <1 | 0.94 | <0.01 | 0.17 | <0.01 |

* Percentage of Corroded Area Under the Washer

** Data Not Available

TABLE 4.
Propagation of Crevice Corrosion on Pre-initiated Samples

| TEST ALLOY | REMOTE CREVICE CORROSION ASSEMBLY CATHODE/ANODE = 30 INITIAL TORQUE=7.3 Nm | | | | | | | |
|---------------|--|---------|----------|---------|-----------------------|---------|-----------------------|---------|
| | PROPAGATION | | | | PARAMETERS | | | |
| | Weight Loss (gram) | | PCA* (%) | | Maximum Depth (mm) | | Average Depth (mm) | |
| | Natural | Control | Natural | Control | Natural | Control | Natural | Control |
| S31603-1 | 0.88 | < 0.01 | 90 | 53 | 1.61 | < 0.01 | 0.46 | < 0.01 |
| S31603-2 | 0.79 | < 0.01 | 67 | 65 | 1.28 | < 0.01 | 0.44 | < 0.01 |
| S31603-3 | 0.87 | 0.05 | 73 | 38 | 1.75 | 0.64 | 0.50 | 0.11 |
| S31703-1 | 0.60 | < 0.01 | 85 | 25 | 1.40 | < 0.01 | 0.22 | < 0.01 |
| S31703-2 | 0.66 | < 0.01 | 93 | 5 | 1.30 | < 0.01 | 0.23 | < 0.01 |
| S31703-3 | 0.58 | < 0.01 | 80 | 20 | 1.78 | < 0.01 | 0.24 | < 0.01 |
| N08904-1 | 0.51 | < 0.01 | 65 | 0 | 1.16 | < 0.01 | 0.26 | < 0.01 |
| N08904-2 | 0.67 | < 0.01 | 75 | 1 | 1.35 | < 0.01 | 0.27 | < 0.01 |
| N08904-3 | 0.60 | < 0.01 | 95 | 0 | 1.04 | < 0.01 | 0.19 | < 0.01 |

* Percentage of Corroded Area under the Washer.

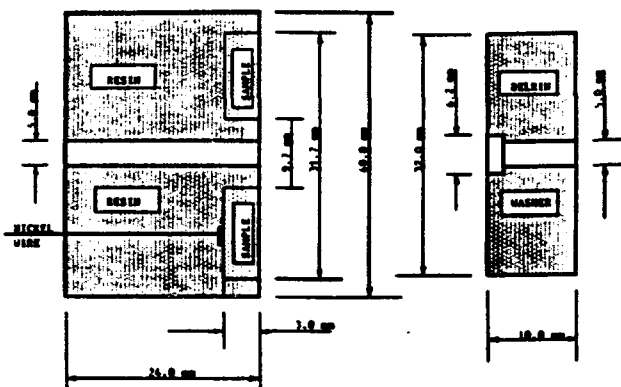


Figure 1. Configurations of the anode and crevice-forming washer in remote crevice assembly.

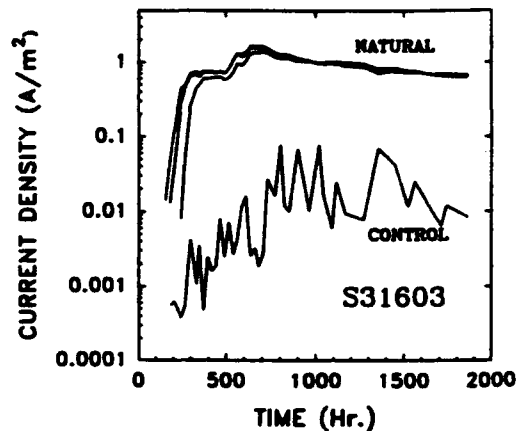


Figure 2. Current density vs. time for S31603 in naturally initiated tests.

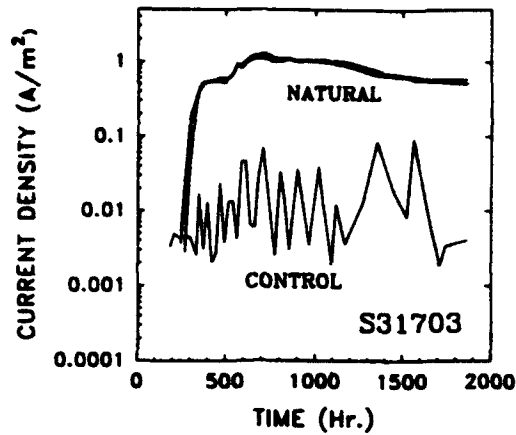


Figure 3. Current density vs. time for 31703 in naturally initiated tests.

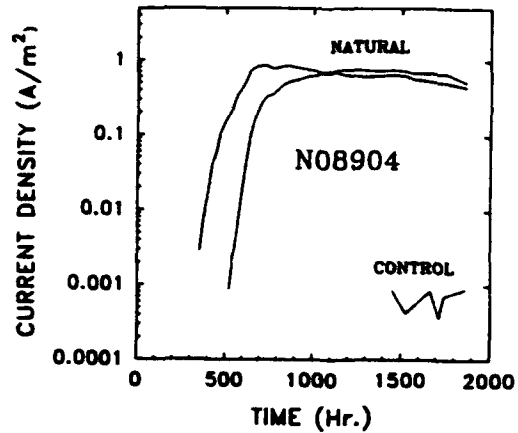


Figure 4. Current density vs. time for N08904 in naturally initiated tests.

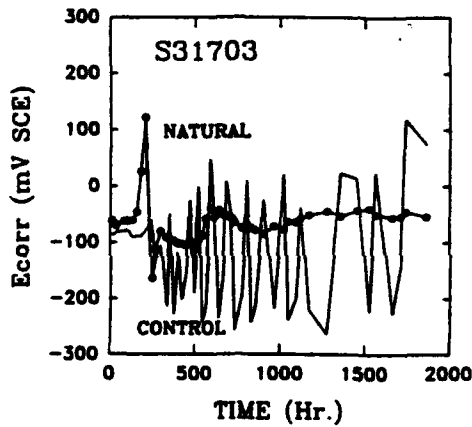


Figure 5. E_{corr} vs. time for S31703 in naturally initiated tests.

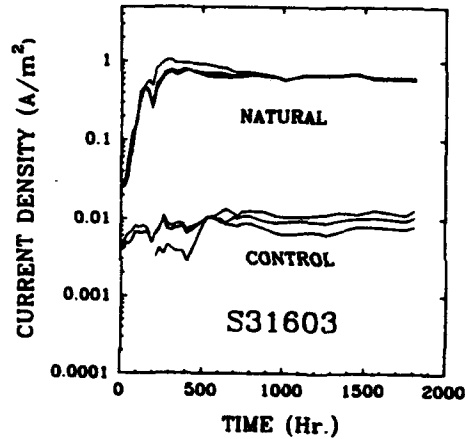


Figure 6. Current density vs. time for pre-initiated coupons of S31603.

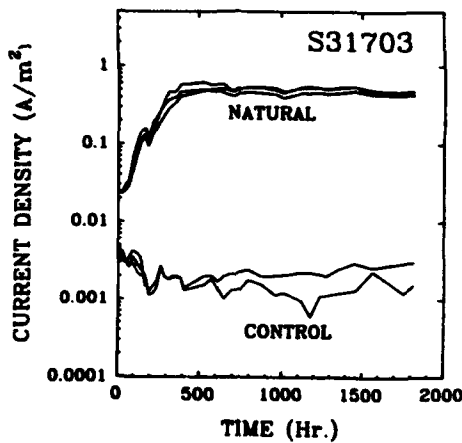


Figure 7. Current density vs. time for pre-initiated coupons of 31703.

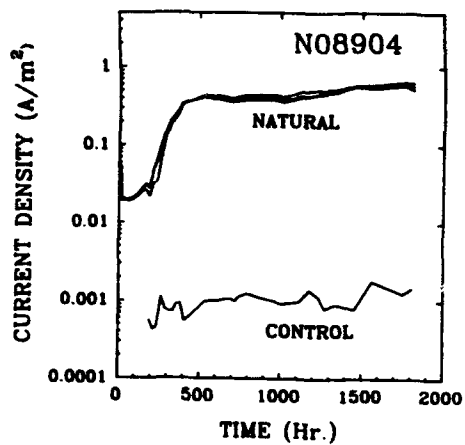


Figure 8. Current density vs. time for pre-initiated coupons of N08904.

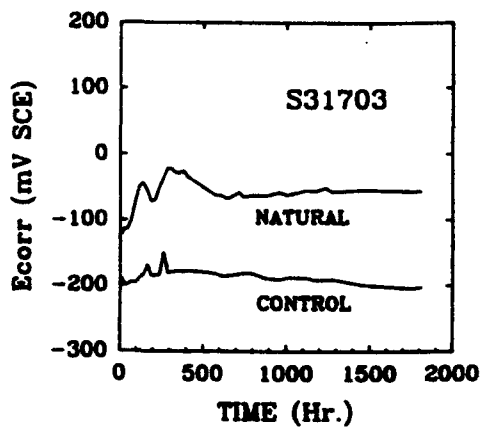


Figure 9. Corrosion potential vs. time for pre-initiated coupons of S31703.

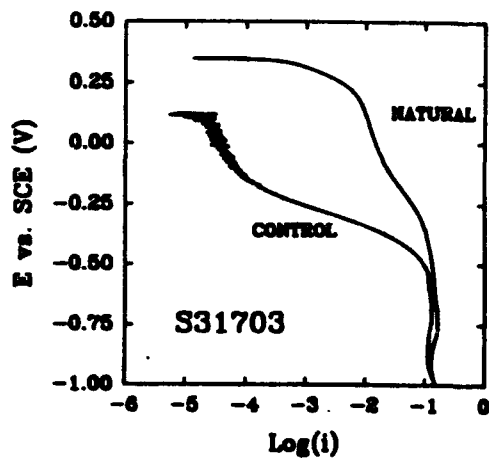


Figure 10. Cathodic polarization curves for the cathodes of 31703 at the end of the pre-initiated tests.

Role of the Metal Uptake by the Mycelium of the Fungus Hormoconis resinæ
in the MIC of Aluminum Alloys

B.M. Rosales
CITEFA-CONICET
Zufriategui 4380
(1603) Villa Martelli, Argentina

Andrea Puebla
CITEFA
Zufriategui 4380
(1603) Villa Martelli, Argentina

Daniel Cabral
Fac. Cs. Exactas
Ciudad Universitaria- Pabellon 2
(1428) Capital, Argentina

Abstract

The purpose of this work was to determine whether any interaction existed among the fungal biomass of Hormoconis resinæ and the metal ions present in the environment. That could help to clarify its relative role in the mechanism of acceleration of the microbially influenced corrosion (MIC) of Al alloys observed under their fungal mats. This problem is generally observed in military aviation due to the longer land periods at room temperature than in the commercial aircrafts, thus providing more appropriate conditions for growth.

Keywords: MIC, fungal biofilm, metal uptake, aluminum alloys.

Introduction

The increasing interest devoted to the study of biofilms present in different industrial systems, suggests the importance of the analysis of their effect on metallic corrosion. The accumulation of microbial biomass generally causes problems related to the decrease in the performance and life time of equipment^{1,2,3}.

Biofilms also produce potential benefits in natural and industrial media in removing or degrading toxic contaminants, in fermentation processes and in other biotechnological applications^{2,4}.

The uneven affinity⁵ determined for the fungus Hormoconis resinæ on different metal ions suggested the interest of analysing the influence of its fungal biomass on the localized attacks observed on aluminum alloys. This behaviour of the mycelium of the fungus is very similar to that shown by the polymeric extracellular material produced by various bacteria and by the cell walls of other fungi, in the presence of heavy metals, and could be used by living organisms to decrease the toxicity of a given environment².

According to our previous electrochemical results^{7,9,10} the aqueous media of the cultures become modified by metabolic activity of the fungus, favouring pitting nucleation on Al alloys. Once this attack is initiated, the growth of a biomass able to produce specific metal ions uptake would shift the reaction equilibrium in the sense of simulating its selective dissolution.

The results would be the exposition of fresh areas of the alloy, instead of its repassivation produced in the same medium in the absence of fungal proliferation and biomass formation.

Furthermore, the sensing ability of some microbes would explain why certain alloys that undergo MIC in the presence of a given microbial culture stimulate their growth⁴ while non affected alloys stop it.⁴ The polygonal way followed by hyphae of Hormoconis resiniae growing on Al alloys, connecting second phases distant 50 μm , suggests a long distance chemotropic effect.⁵

The selective attack on those phases and the high uptake observed for the metals conforming them seems to indicate that the MIC could be dependent of a biological driving force. This sensing ability seems to be similar to cases mentioned in the literature, where certain bacteria complex toxic metals dissolved in the environment they colonize, or use them as oligoelements necessary to their metabolism, through the production of polymeric extracellular material².

Experimental

An inoculum of suspended spores was prepared from the biomass grown by inoculation of a Bushnell-Hass¹² nutrient solution, without FeCl_3 , diluted to 1:10 with distilled water and Jet A 1 kerosene. The spore concentration was $2.5 \cdot 10^6$ viable spores per ml.

Batch cultures of the diluted mineral medium additioned with 32 mg of Na^+ , Mn^{+2} , Mg^{+2} , Cu^{+2} , Zn^{+2} , Fe^{+3} and Al^{+3} were sterilized by autoclaving.

Batteries of 5 erlenmeyer flasks, of 125 ml, containing 25 ml of each mineral media were inoculated with 1 ml of the spores suspension.

Three flask of each set, not seeded with the fungus, were the blank for the microbial growth. Another set of 5 flasks with 25 ml of the nutrient solution was used as control in the absence of the metal ions. All the flasks were then additioned with 10 ml of Jet A 1 kerosene, previously sterilized by filtration through millipore membrane of 0.45 μm pore size. Incubation at 30°C was followed by visual observations to determine the amount of growth at different times. The pH of the aqueous phases was determined with Merck sticks, only when appreciable changes were observed.

After the stationary phase was attained in all media, the mycelia were separated by filtration through paper Whatman N° 42, washed with distilled water and dried at 65°C up to constant weight.

Analysis of the metal uptake by the biofilms and of the remaining ions in the respective nutrient media were performed by spectrometry of atomic absorption.

Four Al alloys (Table I) inoculated with droplets of the spores suspension in distilled water were used to verify previous results, concerning chemotropism of Hormoconis resiniae⁵. The metal samples were polished up to 0.25 μm diamond paste. Jet A1 was used as carbon source, the incubation temperature was 30°C and test duration 4 days.

SEM Philips 515 coupled to an EDAX 9100 was applied on the biological sludges grown, after critical point drying and metalizing with Au.

Results

The amount of fungal growth observed was summarized in Table II. The low amount of growth produced great relative errors in the weight determinations of the biomass formed. The respective uptake, included in Table II, were also low giving not quantitative figures. SEM-EDAX determinations were used as complementary techniques to establish differences in the morphology and uptake ability of the micelya grown in the presence of the distinct cations. The SEM aspect of the mycelia was different for the distinct aqueous media and for the surfaces in contact with the aqueous and kerosene phases. Typical micrographs are shown in Fig. 1. EDAX on the areas that were in contact with the aqueous phases, gave evidence of the metal fixation by the biomass. Uptake was only observed for ions with charge +2 and +3 while Na^+ was not detected. This results are in good agreement with those determined by atonic absorption. The drop test on metal surfaces during 4 days gave paterns of the initial steps in growth as those shown in Fig. 2.

At the very initial stage of mycelium formation the hyphal trace and branching on the surface can be followed by SEM-EDAX providing good correlation between corrosion and growth. It is clear from Figs. 2 a) and b) that corrosion is localizied in the contact areas with hyphae producing corrosion products that mask them. This effect is evident in Fig. 2 b) where in various points there are fungal hyphae emerging from the corroded surface of the alloy. EDAX on the mycelium shown in Fig. 2 a) reveals other components from the fungus espureous to the alloy. EDAX on second phases of those Figs. show appreciable amounts of different elements which could promote a chemotropic response during hyphal growth.

In Fig. 2c the effect of the aqueous medium in the drop test where the mycelium is growing evidences the great contrast in aggressiveness with respect to the direct contact with hyphae. In this micrograph only an homogeneous selective dissolution of the second phases can be noticed on the alloy while in Fig. 2 a) and b) only few of these phases remained out of the way of the hyphae.

Discussion

EDAX determinations on the metals with the initial fungal growth showed the presence of second phases components in small regions where individual hyphae changed in direction or converged. That suggested a chemotropic effect of the metal surface on the hyphae development which would be associated to the growth control by a chemosensor.

From the stationary cultures, on the contrary the uptake observed could be the result of a biological activity of the fungus or only the chemical effect of the polymer conforming the mycelium. In fact the main component of the hyphal walls, kitine, has the ability to fix ions specially those with high charge. This behaviour would not be a consequence of a biological function of the fungus but only the result of an ion exchange reaction on the hyphal walls surface. This was verified through the measurement of metal ions uptake by the mycelium of the fungus Rhizopus arrhizus performed on living and died cultures⁹. Similar results, allowed to discard biological effects, as could be nutritional requeriments of oligoelements or chelation as a detoxification mechanism of the environment².

Furthermore, the exopolymers which promote attachment on metallic surfaces affect the distribution of the metal ions at the solution-surface interphase when corrosion occurs¹⁹. For instance Cu^{+2} is preferently fixed with H^+ release from an exopolymer of a "Pseudomonas like" bacterium, which in turn

favors copper dissolution producing further binding and acidification. Dissolution would proceed until all binding sites are saturated or the metal surface is depleted.

Mixed cultures produce exopolymers with different affinities for a given metal ion causing uneven distribution which determine anodic areas under the biofilm with the strongest affinity for the ion. This condition will persist up to saturation of the binding sites in the polymer. Once saturated the biofilm could polarize the anodic reaction slowing the ions diffusion to the bulk solution.

Among the chemical gradients analysed in connection with fungal chemotropism, the oxygen positive effect and negative autotropism caused by some of their own metabolites are the most frequently reported. At the beginning of such property study, characterized by a low density population, the negative autotropic effect was dominant to the oxygen one, but subsequent orientation of growth was determined by the oxygen concentration gradient. This extremely important tropic response provides ecological control due to its survival value¹⁴. The experience design could some times produce misleading results associated to the powerful effect of oxygen, as was reported in the perforated plate and slide experiments of Stadley¹⁵ for determination of different chemotropic responses.

The hyphal branching and direction of hyphal growth are very important mechanisms in the fungal colonization of solid substrata. In young mycelia two mechanisms control the site of germ-tube emergence and negative autotropic reactions between germ-tube hyphae. Spacing between neighboring hyphae depends of the nutrient availability and negative autotropism between them. This last is not observed at the center of mature colonies. Branching is controlled by a biomass sensor in fungi¹⁶. The mechanism proposed to explain its role suggests that vesicles concerning the tips extension would be involved¹⁷. The knowledge of the mechanism that regulates hyphal branching would clarify the effect of mycelial morphology on culture rheology¹⁸.

Kropf et al¹⁹ demonstrated that in Achlya bisexualis an inward moving electrical current precedes branching evidencing the sites of branch formation.

Since the initial proposal of Lund²⁰ about the electrical nature of the space localization of growth, strong evidence has been obtained that many cells produce extracellular electrical currents, of definite polarity, related to anatomy and function²¹. The basic observations concerned chemotropic growth of the rhizoid of Blastocladiella emersonii in gradients of nutrients (Pi and amino acids) and of proton-conducting ionophores. In both cases the rhizoids grew up to the gradient being quite unlike those cells grown in DM2 medium²¹. Robinson et al²² showed that gradient of a calcium ionophore polarizes the germination of certain fungi and the effect of electrical fields on plant growth can be explained in terms of the enhancement of local calcium fluxes. Harold et al²¹ reported that growth of the rhizoid of Blastocladiella organisms is markedly oriented by gradients of proton conducting ionophores, certain nutrients and a mixture of amino acids. This means that the rhizoid serves to transport nutrients to the thallus and that chemotropic growth of the rhizoid results from modulation of the proton current through the growing cell.

Even when from the literature³ it appears that only the Mastigonycotina present chemotropism, the precedent results supports the hypothesis of a biological effect of the solid substratum on the pattern followed by fungal

hyphae during the first steps in growth. The presence of chemical heterogeneities, segregated as second phases on metals, originate uneven electrical potential distribution which could be detected by specific chemosensors.

The distances among these phases are in an order of magnitude of 10 to 50 μm , which could allow their detection by the typical biological sensors.

Poor nutrient media used facilitates the observation of the spatial arrangement of the hyphal growth, outwards from the inoculum centre. The reason for this distribution was interpreted as a negative autotropism of the branch hyphae to metabolites produced by the fungus²³. On the contrary, Robinson²⁴ suggested a positive chemotropism to oxygen which would operate, from the side of the hyphal tip to the higher oxygen concentration, at over a much longer range (a few millimeters?) than the detection mechanism for gem-tube emergence under influence of neighbouring spores (up to around 50 μm)²⁵.

Further research work is required to determine whether the nature of the mycelium effect on MIC of the Al alloys has any biological component.

On the contrary a conclusive result is the strong corrosive effect of the hyphae contact on the alloys, which was previously associated to different causes: high local acidic metabolites concentration and differential aereation^{7,11}. The hypothesis of another chemical effect, associated to the interaction of the biopolymer⁵ conforming the hyphal wall with metal ions originated during corrosion⁵, which would displace de dissolution equilibrium reaction, also requires further investigation.

References

1. D.E. Kleme and R.A. Neihof. Biocides for control of bacteria in fuel tanks. Report of Naval Research Laboratory Progress, Dec., USA (1975).
2. M.J. Brown and J.N. Lester. Metal removal in activated sludge: the role of bacterial extracellular polymers. Water Research, 13 (1979): p. 818.
3. M. Tsezos, B. Volesky. The mechanism of uranium biosorption by Rhizopus arrhizus. Biotechnology and Bioengineering. XXIV (1982): p. 385.
4. G. Bitton and V. Freihofer, Microb. Ecol., 4 (1978): p. 119.
5. B.M. Rosales. Microbial corrosion of Al alloys under a fungal biofilm, Proc. 11th. Int. Corrosion Congress, Italy. Vol.4 (1990): p. 359.
6. E.S. Ayllón, O.A. Biscione and B.M. Rosales. Proc. 6th. International Congress on Marine Corrosion and Fouling, Marine Biology, Grece, (1984): p. 417.
7. E.S. Ayllón and B.M. Rosales. Corrosion of AA 7075 Al alloy in media contaminated with Cladosporium resinae, Corrosion, NACE, 44 (1983): p. 638.
8. O.A. Biscione, M.A. Caria and B.M. Rosales. Microbial corrosion of a Sn base alloy. Int. Biodtn., 23 (1987): p. 159.
9. M.C. Leiro and B.M. Rosales. The predominance of microbial growth vs. metallurgical characteristics in the corrosion of 2024 Al alloy through electrochemical data. Corrosion'86, NACE, Paper 124, Texas, USA, (1986).
10. B.M. Rosales and E.R. de Schiapparelli. A corrosion test for determining the quality of maintenance in jet fuel storage. Mater. Perf., 19 N° 8, (1980): p. 41.
11. D.J. Hansen, D.J. Tighe-Ford and G.C. George. Role of the mycelium in the corrosive activity of Cladosporium resinae in a Dieso-water system. Int. Biodtn. Bull., 17, 4 (1981): p. 103.
12. L.D. Bushnell and H.F. Hass. The utilization of certain hydrocarbons by

- microorganisms. *J. Bact.*, 41 (1941): p. 653.
13. G.G. Geesey, M.W. Mittelman, T. Iwaka, P.R. Griffiths. Role of bacterial exopolymers in the deterioration of metallic copper surfaces. *Materials Performance*. NACE. Febr. (1986): p. 37.
 14. P.M. Robinson. Chemotropism in fungi. *Trans. Br. mycol. Soc.* 6x, 2 (1973): p. 303.
 15. D.R. Stadler. Chemotropism in Rhizopus nigricans: the staling reaction. *J. Comp. Physiol.* 39 (1952): p. 449.49.
 16. A.P.J. Trinci. Regulation of hyphal branching and hyphal orientation. *Syposium of Br. Mycol. Soc.* 2 (1983): p. 23.
 17. J.I. Prosser, A.P.J. Trinci. A model of hyphal growth and branching. *Journal of General Microbiology*, 111 (1979): p. 153.
 18. B. Metz. From pulps to pellet. PhD Thesis. Technical University of Delft. The Netherlands (1976).
 19. D.L. Kropf, M.D.A. Lupa, J.H. Caldwell, F.M. Harold. *Science*. 220 (1983): p. 1385.
 20. E.J. Lund. Bioelectric fields and growth. University of Texas Press. Austin (1947).
 21. R.L. Harold, F.M. Harold. Orient growth of Blastocladiella emersonii in gradients of ionophores and inhibitors. *J. of Bacteriol.* 144, 3 (1980): p. 1159.
 22. K.R. Robinson, R. Cone. Polarization of fucoid eggs by a calcium ionophore gradient. *Science* 207 (1980): p. 77.
 23. J.F. Clark. On the toxic properties of some copper compounds with special reference to Bordeaux mixture. *Botanical Gazetti.* 33 (1902): p. 26.
 24. P.M. Robinson. Oxygen positive chemotropic factor for fungi? *New Phytologist*, 72 (1973); p. 1.349.
 25. P.M. Robinson, D. Park, T.A. Graham. Autotropism in fungal spores. *J. of Exp. Botany*, 19 (1968): p. 125.

Table I. Chemical Composition of the Alloys (w/w %)

| Alloy | Zn | Cu | Mn | Si | Mg | Fe | Cr | Ti | Al |
|-------|------|-------|-------|------|-------|------|-------|-------|------|
| 7005 | 4.7 | 0.05 | 0.45 | 0.10 | 1.2 | 0.18 | 0.16 | 0.03 | rest |
| 7075 | 5.2 | 1.6 | 0.09 | 0.23 | 2.6 | 0.24 | 0.13 | 0.02 | rest |
| 2024 | 0.12 | 4.5 | 0.53 | 0.14 | 1.5 | 0.29 | ---- | 0.02 | rest |
| 1050 | 0.01 | 0.002 | 0.004 | 0.10 | 0.002 | 0.21 | 0.001 | 0.022 | rest |

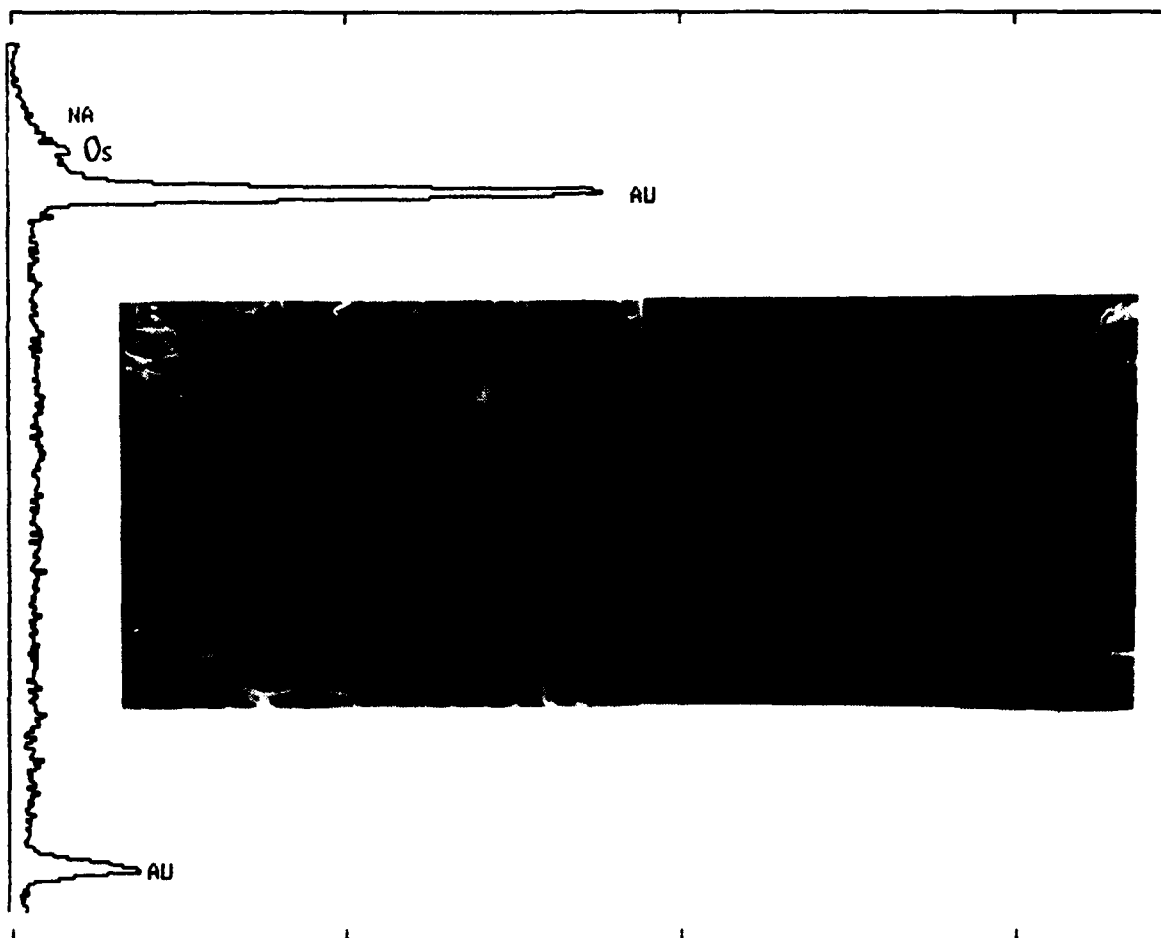
Table II. Amount of Growth of Homeconis resiniae, pH of the Aqueous Media and Metal Uptake by the Mycelium for Different Incubation Times.

| Aqueous Media | 12 Days | | 30 Days | | 60 Days | | 120 Days | | M ²⁺ uptake |
|----------------------|---------|-----|---------|-----|---------|-----|----------|-----|------------------------|
| | Growth | pH | Growth | pH | Growth | pH | Growth | pH | |
| Nutrient Solution | + | 6.5 | + | 6.0 | + | 6.0 | + | 4.5 | - |
| " + Na ⁺ | + | 6.5 | + | 6.5 | + | 5.5 | + | 5.0 | - |
| " + Mn ⁺² | +/- | 6.5 | + | 6.0 | + | 6.0 | + | 4.5 | +/- |
| " + Mg ⁺² | +/- | 6.5 | + | 6.5 | +++ | 5.5 | +++ | 4.0 | + |
| " + Cu ⁺² | - | 6.5 | - | 6.0 | - | 6.0 | - | 6.0 | - |
| " + Al ⁺³ | - | 6.5 | + | 6.5 | ++ | 5.5 | ++ | 3.5 | + |
| " + Fe ⁺³ | +/- | 6.5 | + | 6.5 | +++ | 5.5 | +++ | 4.0 | + |
| " + Zn ⁺² | - | 6.5 | +/- | 6.0 | +/- | 6.0 | + | 4.5 | + |

* All the interphase aqueous solution-kerosene occupied.

Fig. 1. SEM-EDAX of Hormoconis resinae mycelium formed in the presence of M^{+n} ions.

a) Na^+



(a) Reproductive structures

Fig. 1 b)

Mg⁺²

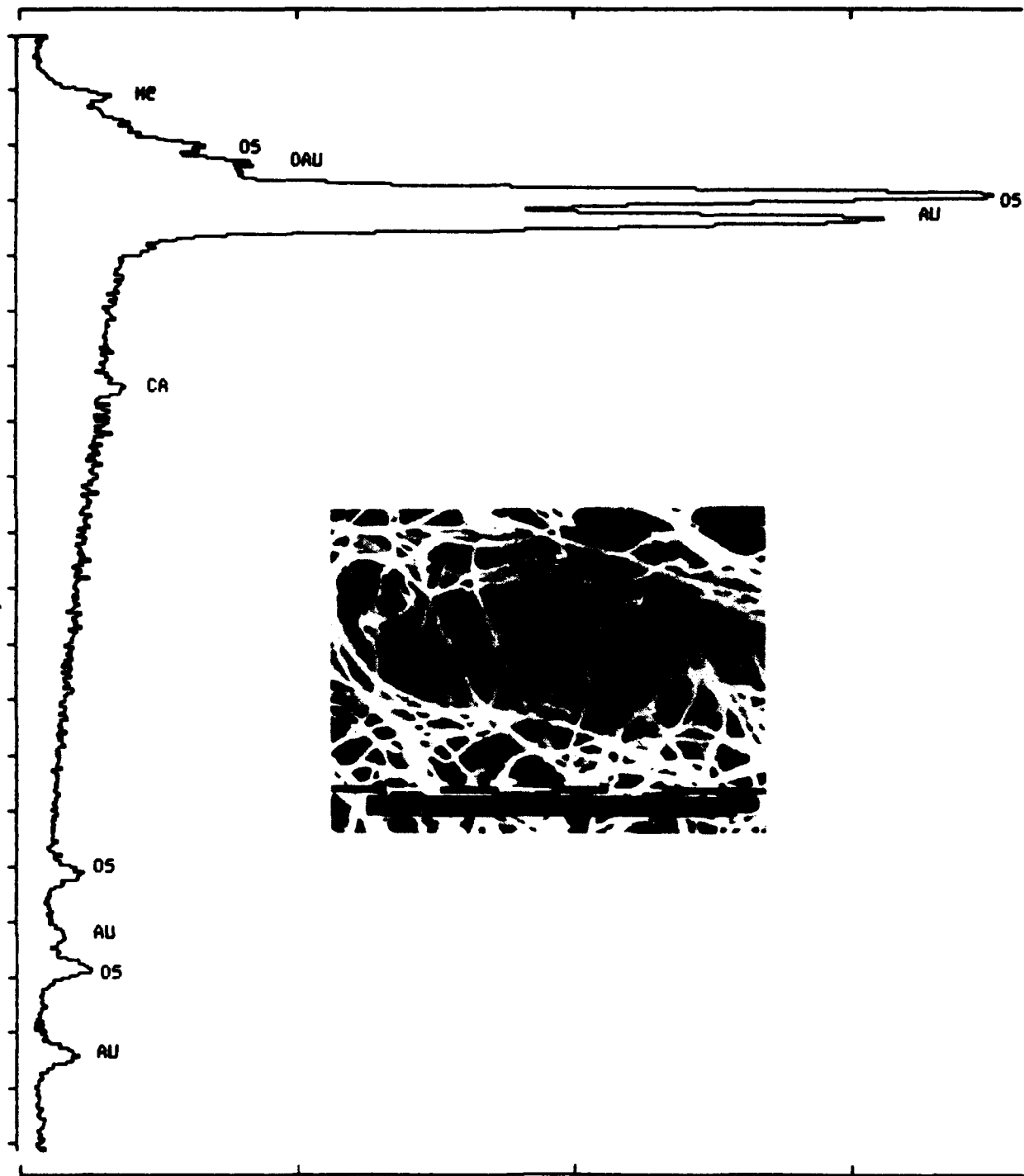


Fig. 1 c)

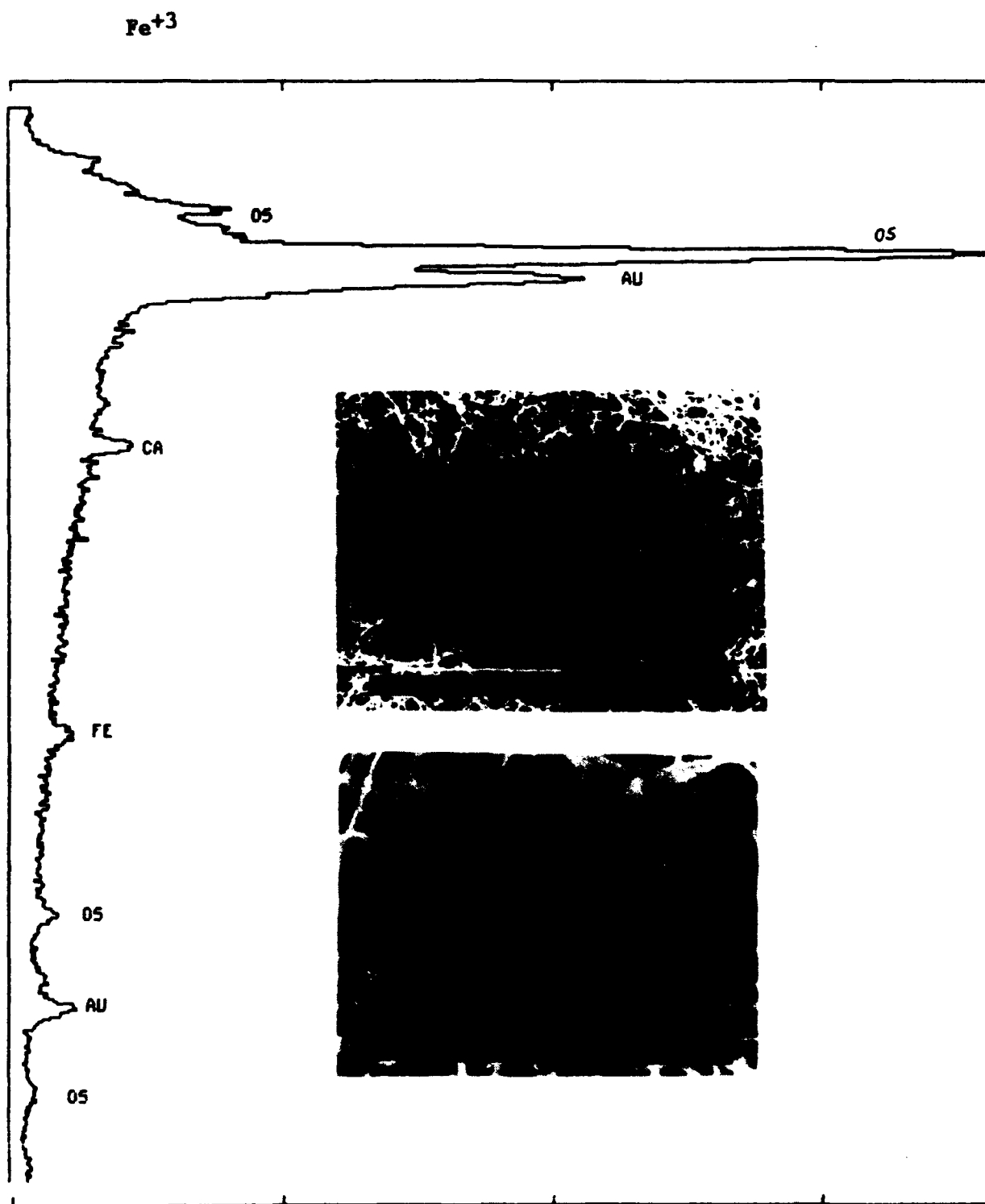
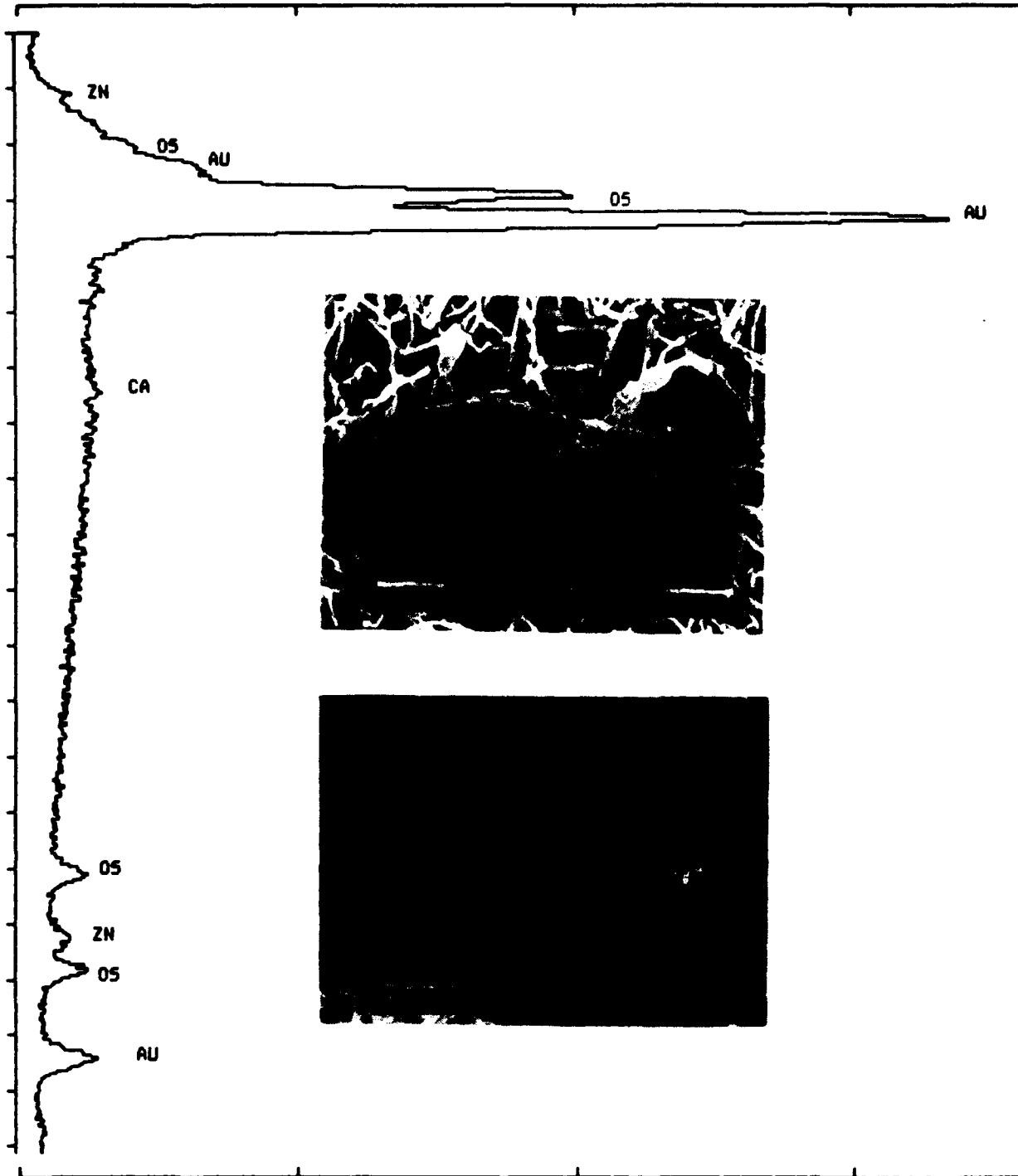


Fig. 1 d)

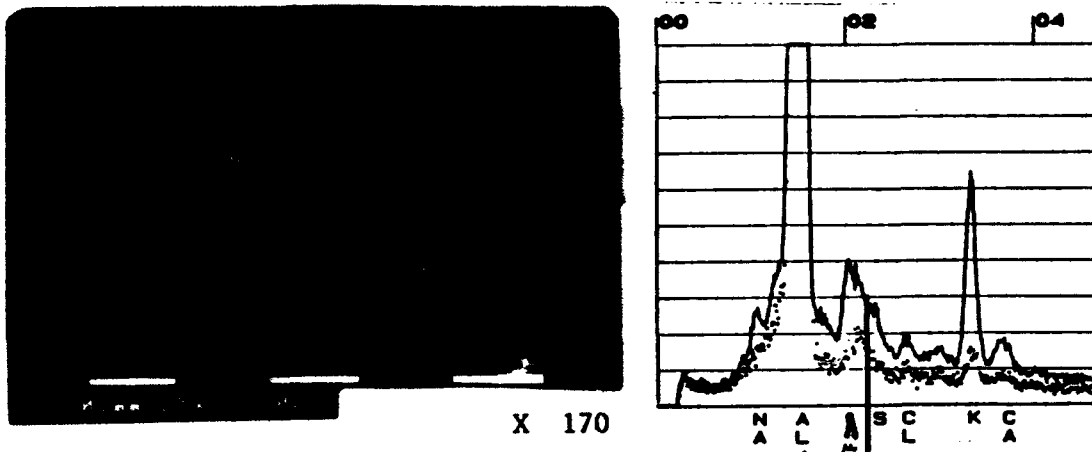
Zn⁺²



(a) Reproductive structures

Fig. 2. SEM-EDAX of the *Hormoconis resinae* mycelia formed during 4 days on Al alloys.

a) 1050 alloy in contact with the mycelium



EDAX on a second phase

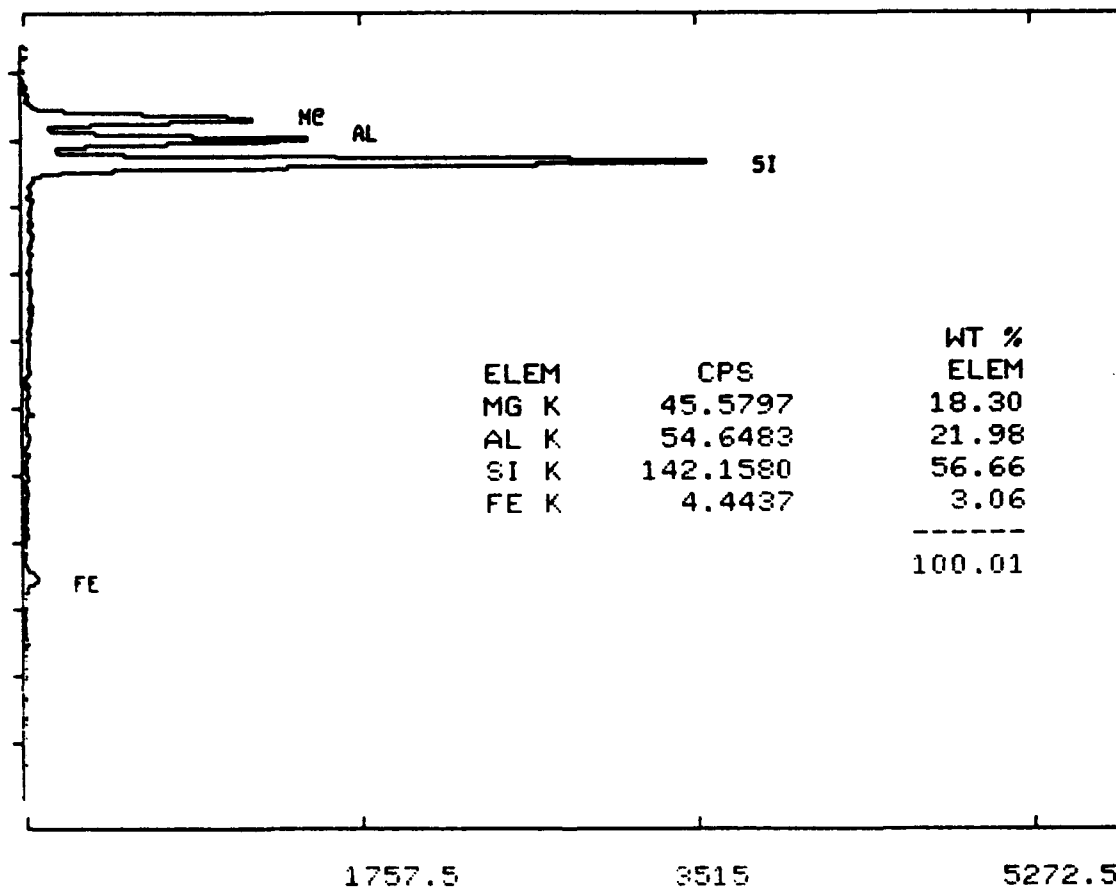
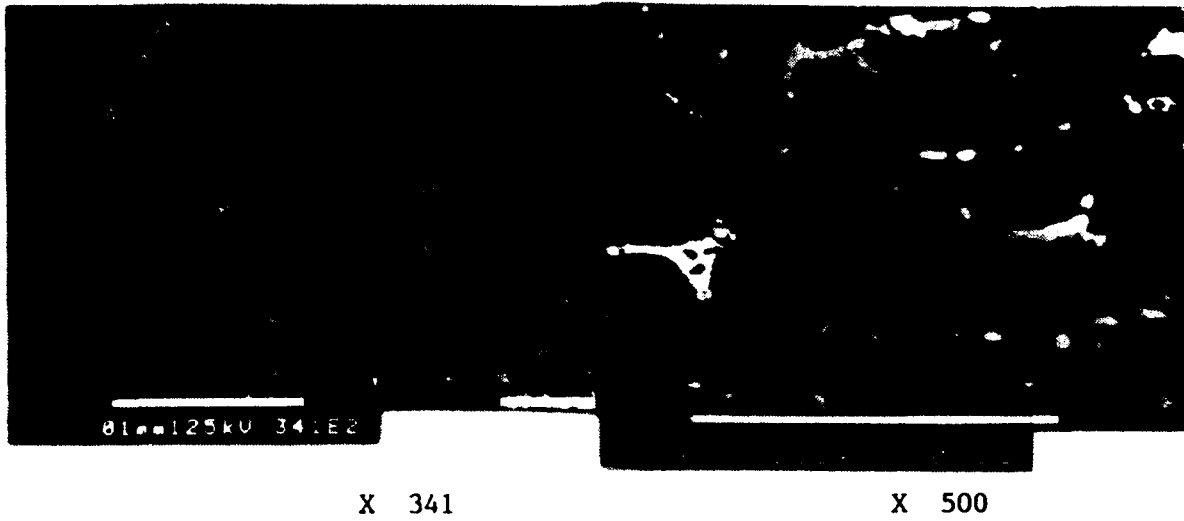


Fig. 2 b) 2024 alloy with and without mycelium



EDAX on a second phase

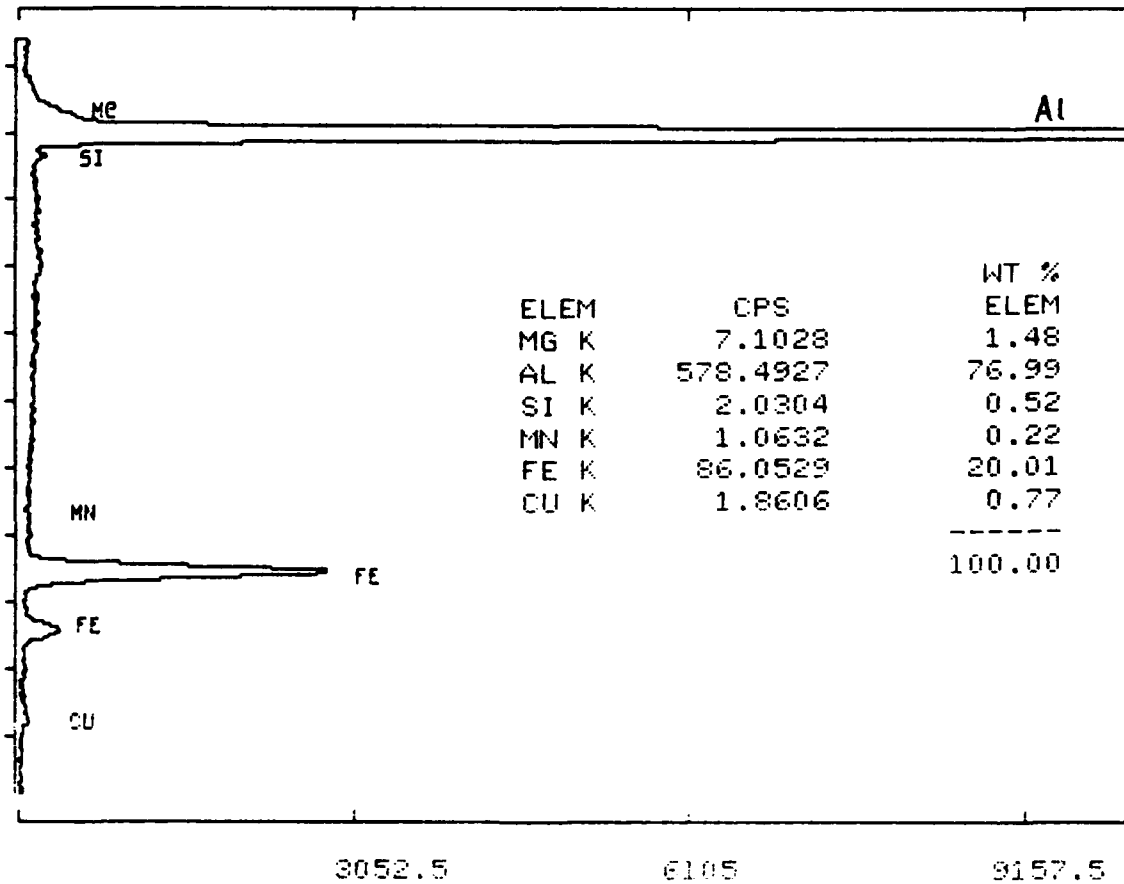
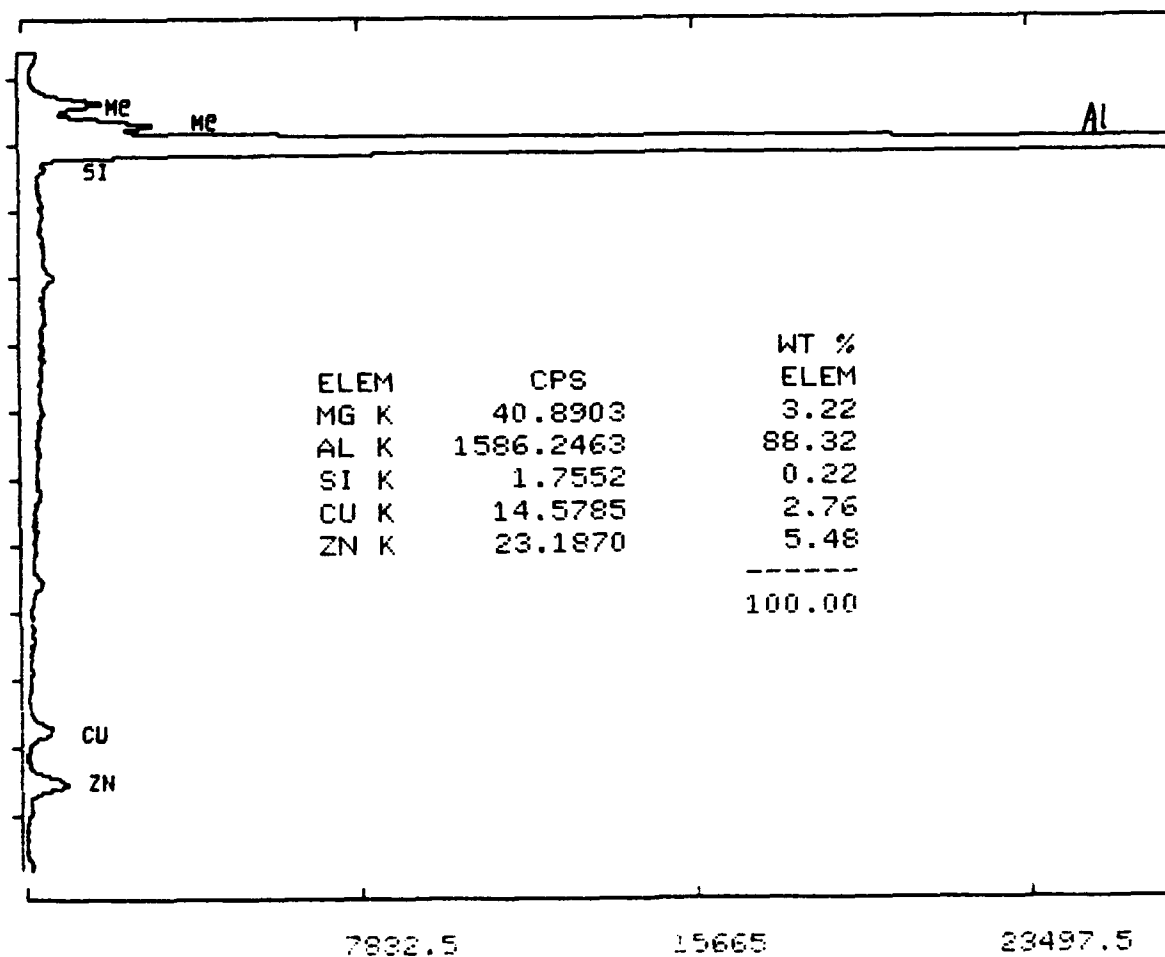


Fig. 2 c) 7075 alloy under the drop. No contact with hyphae.



EDAX on a second phase



**Electrochemical Noise Analysis as an indicator
of Microbiologically Induced Corrosion**

A. Saatchi
Materials Engineering Department
Isfahan University of Technology
Isfahan, Iran

T. Pyle
Center for Materials Technology
Curtin University of Technology
Perth, WA, Australia

A. P. Barton
School of Biomedical Sciences
Curtin Univ. of Tech.
Perth, WA, Australia

Abstract

The open circuit potential fluctuations (electrochemical-potential noise) of identical pairs of steel electrodes in sea water containing sulphate-reducing bacteria (SRB) has been recorded for as long as twelve months. The potential/time plots, recorded at one or two samples per seconds, were transformed into frequency-domain (spectral-density) curves using the maximum-entropy method (MEM). Also the root mean square (RMS) of the noise levels were calculated. The RMS values of the signals, which were initially steady at around 0.03 mV, started to increase to up to 0.07 mV after about 6 months, thus indicating the start of the localized corrosion process. The spectral-density curves also indicated the existence of specific and consistent patterns for the various stages of the tests in the high frequency range (100-1000 mHz) of the spectrum. The culture medium, added periodically to support the growth of the bacteria, suppressed the signals, which was due to the corrosion inhibiting effect of the yeast extract in the culture medium. After each feeding, it usually took three weeks before the RMS values reached the values prior to the addition of the culture medium to the system. Occasionally, the open-circuit potential of the cell rose to a much higher levels, with corresponding higher values of RMS. This effect has been related to the bacterial-growth stage and other changes occurring at the metal/solution interface. Despite the fact that the corrosion product in this system, after twelve months exposure, was a thick sludge, the 0.07 mV RMS values could still be detected. This could be due to the dynamic action of the bacteria on the corrosion process. These preliminary results indicate the potential of electrochemical-noise analysis for the detection of microbiologically-induced corrosion.

Introduction

Corrosion of iron and steel under anaerobic conditions in the presence of sulphate-reducing bacteria (SRB) is well documented[1]. Based on the electrochemical theory of corrosion, de-aerated soils of near-neutral pH are not expected to be corrosive to iron and steel. However, if the soil contains SRB and a source of sulphates, rapid corrosion has been found to occur[1]. The aim of the present study was originally to explore the possibility of differentiating between biological and non-biological corrosion, using electrochemical technique. In fact, at the present time, there is no available electrochemical technique which can accurately determine the location on the steel structure where SRB are actively causing corrosion. Electrochemical noise has been discussed by some as a promising technique for the detection of the bacterial corrosion[2,3].

Electrochemical noise is simply fluctuations in cell current and electrode potential of an electrochemical cell, and is related to the changes that are occurring at the metal solution interface. The analysis of the electrochemical noise can provide information concerning the nature of the reactions that are occurring at the interface[4,5]. Noise analysis is very well developed in various fields (electronics, chemistry, biology and electrochemistry). In particular, it seems that this method can give information which cannot be reached by normal impedance measurements. Therefore, there is an increasing interest to apply electrochemical noise analysis to corrosion science and engineering[6,7].

In this work the open circuit potential fluctuations (electrochemical noise) of identical pairs of electrodes in sea water containing SRB has been recorded for as long as 12 months. In order to correlate the changes in electrochemical noise to corrosion rate and corrosion morphology and to link the results to the influence of SRB, the following tests were also performed: The motility of SRB's were checked periodically by phase microscopy, Preweighted coupons were exposed to corrosion cell. These coupons were taken out of the cell periodically for scanning electron microscopy (SEM) of the biofilm, SEM of the corroded surface, X-ray diffraction of the corrosion products, and corrosion rate determination using weight loss measurements. The details of these tests has been described before[8]. In this work low frequency (1 to 1,000 mHz) potential noise of SRB influenced corrosion of steel are reported. These preliminary results indicate the possibility of detection of microbial corrosion using electrochemical noise analysis exist.

Experimental Procedure

The steel samples were exposed to 2 liters of sea-water containing the modified Postgate B culture medium to support the growth

of the bacteria. The top of the cell was covered with about 1 cm thick layer of liquid paraffin to prevent oxygen diffusion from the air into the cell. The cells were initially contaminated with SRB strains. SRB were isolated from 3 separate oil and gas rigs located in the North-west of Western Australia. All of these strains were *Desulfovibrio Salixgins*. The number of cells in the inoculum was of the order of 10^9 per ml. 500 ml of the test solution was replaced with fresh culture medium every 30 days. The cells were in duplicate and also a sterile cell of the same composition was used for comparison. The details of the anaerobic environment is according to the recommendations of Stott et al (9) and has been described before[8].

The open circuit potential between two identical steel electrodes in the cell was measured using a high impedance voltmeter. The voltmeter output was connected to an IBM-PC compatible computer and a Metrabyte [10] DAS-8PGA analog to digital converter board (12 bit resolution, 4ms acquisition time and +/-10 mV to +/-10v input ranges). Time records consisted of up to 16200 data points taken at sampling frequencies in the range 1 to 10 Hz. Time records were taken for about 12 hours per day up to 12 months.

The time records were transformed to the frequency domain, to give both power density and amplitude spectra, using the maximum entropy method (MEM) developed by Burg [11]. The MEM technique was preferred to the alternative Fourier Transform Technique as it inherently produces smoother spectra, without apparent loss of information [12], and is simpler to use when the number of data points is not a power of 2. All calculations have been carried out with double precision floating point arithmetic, to minimize rounding off errors, and the data was corrected for linear drift prior to calculation of Root Mean Square (RMS) of noise levels and transformation to the frequency domain. As the frequencies beyond the limits of the experiment cannot realistically be computed, the frequency domain was restricted to a lower limit of $1/t$ where 't' is the length of the time record in seconds, and an upper limit of the Nyquist frequency $1/2f$, where 'f' is the sampling frequency. Six coefficients (poles) were used to calculate the power density and amplitude spectra as it was found that a greater number of poles did not alter the spectra significantly, other than producing less smooth results.

Results and discussion

Fig.1 shows the typical variation of the RMS values of the open circuit potential fluctuations (noise levels) just before and after 6 months exposure. For the periods less than about 6 months, the RMS values were very low and almost constant at about 0.03 mV. This corresponds to very low corrosion activities associated with the passive state. From 6 months and onwards and usually 3 weeks after feeding, the RMS values started to fluctuate around 0.03 mv, and reached to the maximum 0.07 mv. A typi-

cal time record at this stage is also shown in Fig.2. The open circuit potential is not steady and changes with a regular pattern. This behavior is indicative of a repetitive passive break down and repair process, i.e. a localized corrosion stage. These results are in agreement with the results obtained by Stott et al[9]. Fig.3 shows the typical spectral density curve for the periods less than and longer than 6 months, indicating different frequency composition in these two stages. especially in the high frequency range (100-1000 mHz) of the spectra. Although this indicate different corrosion processes for periods less than and longer than 6 months, their significance remains to be further investigated.

From 6 months and onwards the spectral density curves also indicated the existence of a specific and consistent peak structure in the high frequency range of the spectra, fig.4 and thus a specific corrosion process. The notable exception to this behavior were: 1. When there was a dramatic change in the open circuit potential, such as in fig.5, and, 2. When the time record showed a temporary low frequency and high amplitude fluctuations, such as in fig.6. These two instances obviously indicate a dramatic change occurring in the corroding interface, and thus different peak structure in the spectra. The former case has been observed by others [13] and has been related to the bacterial growth, changes of the local environment induced by the metabolic activities of the bacteria and the resulting corrosion effect of the metal, whereas the significance of the latter remains to be investigated.

Feeding the bacteria, by replacing 25% of the total volume of the cell with fresh culture medium, caused the suppression of the signals to the RMS values of 0.03 mv. It usually took about 3 weeks before the RMS values reached the values prior to the addition of the culture medium to the system. This can be related to the corrosion inhibiting effect of the yeast extract in the culture medium [9]. Thus when this substance is consumed, then the corrosion activities and therefore the RMS values start to increase again.

Despite the fact that the corrosion product in this system was a thick sludge, the 0.07 mv RMS values was steady after 12 months of exposure. This could be due to the dynamic effect of the bacteria on the corrosion process and is in contrast to the behavior of non-biological systems where the RMS values decay after the build-up of the corrosion products [13]. These preliminary results indicate the potential of the electrochemical noise analysis to detect and monitor of MIC.

Conclusion

The analysis of the electrochemical potential noise of identical pair of steel electrodes in an anaerobic environment containing

SRB indicated the generally accepted behavior of this type of corrosion, i.e.:

1. A long incubation time in the passive state before the start of the localized corrosion processes.
2. Occasional bacterial growth and dramatic changes occurring in the corroding interface.
3. Suppression of corrosion activities after addition of the culture medium to the cell, due to the corrosion inhibiting effect of the yeast extract in the culture medium.

The analysis of the electrochemical potential noise also indicate:

4. The existence of a specific and consistent pattern for various stages of the tests in the high frequency range of the spectral density curves.
5. The existence of a steady signals after long exposure time and the build up of a thick sludge.

These preliminary results indicate that the analysis of the electrochemical noise offer promise for the detection of microbiologically influenced corrosion

References

1. S.C. DEXTER, in Metals Handbook, vol. 13,p.119,ASM,(1988).
2. W.P. IVERSON and L.F. HEVERLY, Corrosion Monitoring in Industrial Plants using NDT and Electrochemical Methods,ASTM STP908, G.C. MORGAN Ed. p.459,Philadelphia (1986).
3. W.P. IVERSON and L.F. HEVERLY, Biologically Induced Corrosion, NACE-8, C. DEXTER Ed.,National Association of Corrosion Engineers, Houston (1986).
4. G.C. BARKER, J. Electroanal. Chem. vol.21,p.127 (1969).
5. G. BLANC, I. EPELBOIN, G. GABRIELLE and M. KEDDAM, J. Electroanal. Chem. vol.75, p.97 (1977).
6. U. BERTOCCI, Corrosion 89, paper No. 24, NACE, HOUSTON (1989).
7. C. GABRIELLI, F. HUET, M. KEDDAM, R. Oltra, corrosion, vol. 46,p. 346 (1990).
8. A. SAATCHI, T. PYLE, A.P. Barton, and W. VAN BRONSVIJK, Electrochemical Noise Analysis of Anaerobic (bacterial) Corrosion of Steel, J. of Eng'g. of IRI, vol.4, p.53 (1991).
9. J.F.D. STOTT, B.S. SKERRY and R.A. KING, The use of Synthetic Environments for Corrosion Testing, ASTM STP970, P.E. FRANCIS and T.S. LEE, Eds., ASTM, p98, Philadelphia (1988).
10. Metrabyte Corp., Taunton, MA (1990).
11. J.P. BURG, Modern Spectrum Analysis, D.G. CHILDERS ed. p42,IEEE, New York (1978).
12. R.A. COTTIS and C.A. LOTO, Corrosion, vol.46, p.12 (1990).
13. X. ZHANG, R.A. BUCHANAN, E.E. STANSBURY and N.J.E. DOWLING,Corrosion/89, paper No.512.
14. A. SAATCHI, T. PYLE, A.P. BARTON, and W. VAN BRONSVIJK, A Comparative Study of a Biological and a Non-biological Corrosion System using Electrochemical Noise Analysis, Submitted for publication.

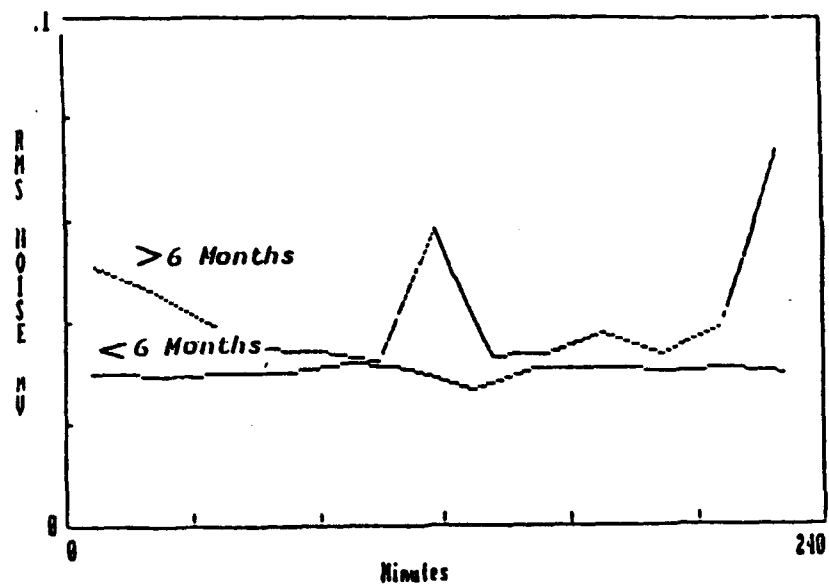


Fig.1. Typical variation of the RMS values of the potential noise levels just before and after 6 months.

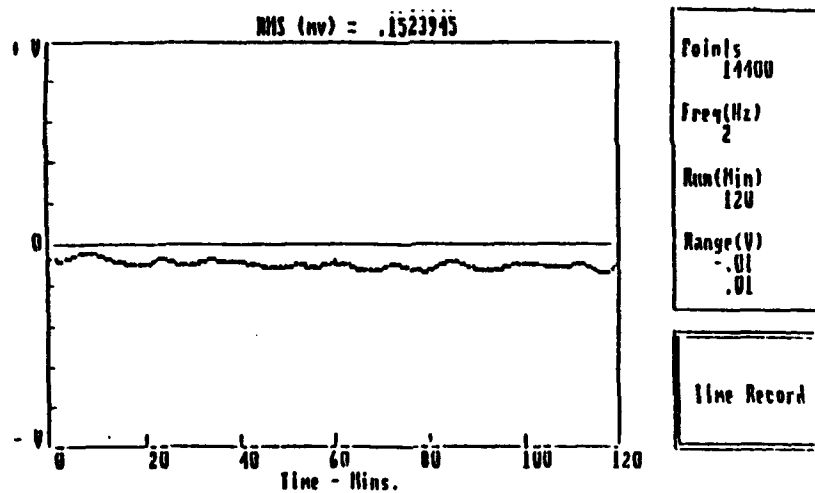


Fig.2. Typical time record, after 6 months exposure and usually 3 weeks after feeding the bacteria.

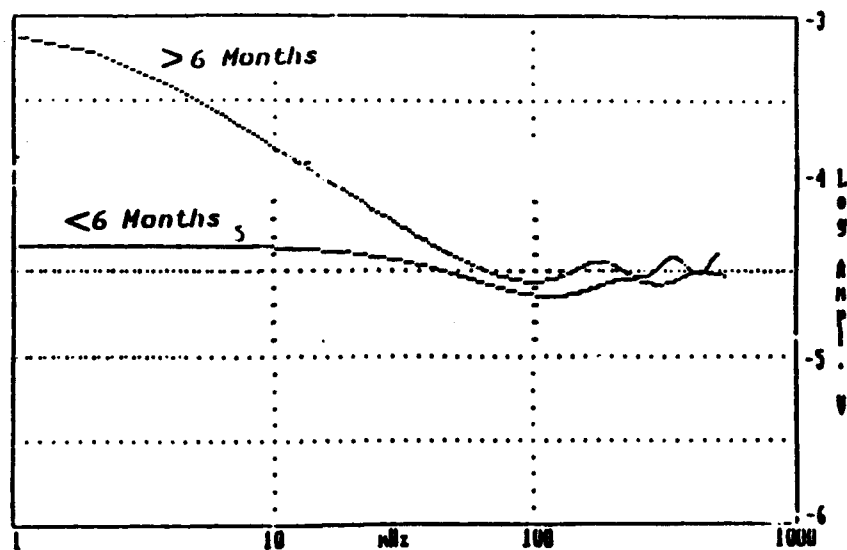


Fig. 3. Typical spectral density curves of the potential noise of the steel electrodes for periods before and after 6 months exposure.

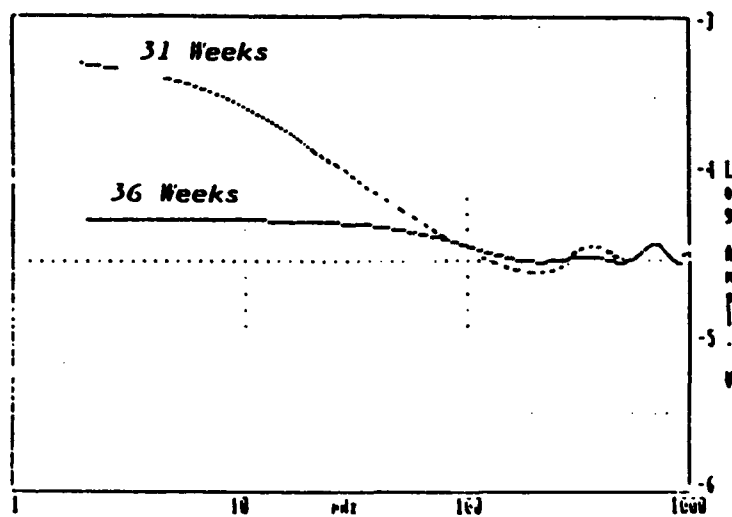


Fig. 4. Spectral density curve of the potential noise of the steel electrodes at various times after 6 months exposure, indicating a specific and consistent pattern in the high frequency range.

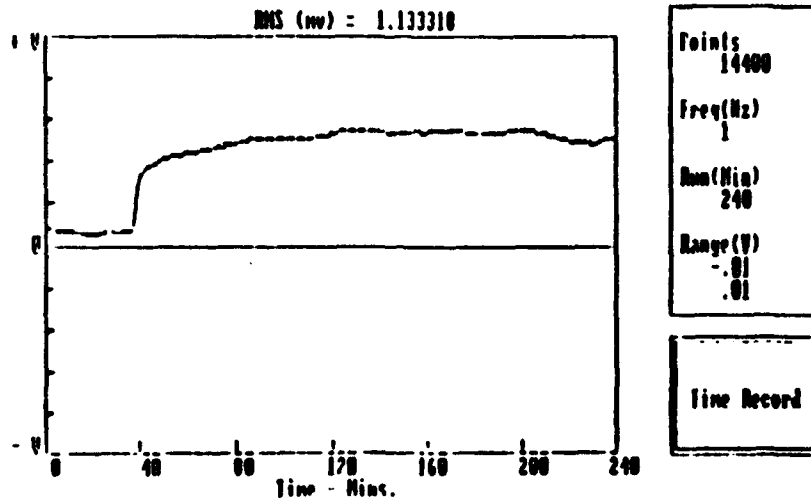


Fig.5. Time record showing a dramatic change in the open circuit potential of the steel electrodes.

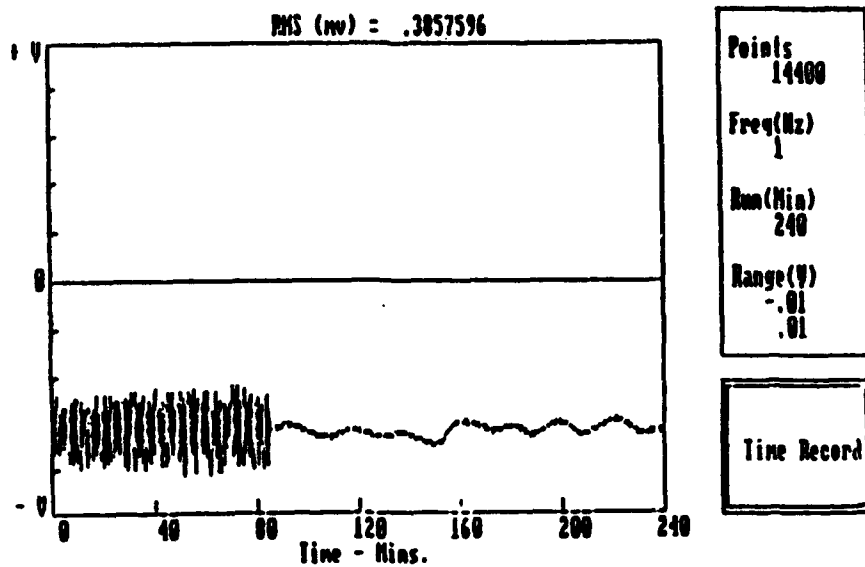


Fig.6. Time record showing a temporary high amplitude low frequency fluctuations in the open circuit potential.

Use of Nucleic Acid Probes in Assessing the Community Structure of Sulfate-Reducing Bacteria in Western Canadian Oil Field Fluids.

**Donald W. S. Westlake
Julia M. Foght
Phillip M. Fedorak
University of Alberta
Edmonton, AB
Canada, T6G 2E9**

**Gerrit Voordouw
University of Calgary
Calgary, AB
Canada, T2N 1N4**

**Thomas R. Jack
NOVA HUSKY Research Corporation
2928 16th Street NE
Calgary, AB
Canada, T2E 7K7**

Abstract

The [NiFe] hydrogenase gene probe is specific for sulfate-reducing bacteria (SRB) of the Desulfovibrio genus. It can be used to identify the presence of cells of this genus in samples obtained from oil field fluids and biofilms. The presence of other SRB species in these environments is evident because many SRB isolated from these oil fields did not react with the [NiFe] hydrogenase gene probe. The development of a chromosomal deoxyribonucleic acid (DNA) hybridization technique, reverse sample genome probing (RSGP), permits rapid identification of different bacteria in a sample with a single probing step. The application of this technique to 31 Alberta oil field samples indicated that there were at least 20 genetically distinct SRB in these samples. This diversity was verified by analysis of 367 samples prepared from 56 sites representing 7 different oil field locations. Two distinct SRB communities were detected in these samples: one from saline environments and the other from fresh water environments. The application of these techniques to the examination of sessile and related planktonic populations indicate that only a few of the planktonic SRB population dominated the sessile SRB flora.

Key terms: hydrogenase, nucleic acid, probes, SRB, planktonic, biofilms

I. Introduction

In the oil industry the anaerobic sulfate-reducing bacteria (SRB) have long been associated in the oil industry with the corrosion of metals and the souring of producing reservoirs. The production of H₂S as a microbial respiratory product, and the presence of an active hydrogen metabolism, via the enzyme hydrogenase, are the primary metabolic activities by which these bacteria act in microbial influenced corrosion and reservoir souring. SRB have been identified as being very important agents in the turnover of organic matter in aquatic sediments¹. These relationships have stimulated research on the classification, detection and monitoring of SRB in industrial and environmental systems.

Taxonomic studies based on classical bacteriological techniques^{2,3} and 16S rRNA sequencing studies⁴ suggest that there are at least eight different taxonomic groups of SRB. While the Desulfovibrio genus represents a phylogenetically coherent group of SRB it shows a greater diversity than is normally encountered in other eubacterial genera⁵. Most SRB cannot use complex sources of organic matter for growth. The majority use low molecular compounds, e.g. fatty acids and alcohols, as a source of carbon and energy, and some can also obtain energy from the oxidation of hydrogen. The SRB can be divided into two nutritional groups: those that incompletely oxidize electron donors to acetate, and those that completely oxidize electron donors to CO₂. The acetate-producing bacteria also grow faster than the acetate-oxidizing SRB and therefore will become predominant under most enrichment conditions.

It has been hypothesized^{6,7} that substrates which support SRB growth in reservoirs are the products of the incomplete oxidation of organic matter introduced via injection waters by other reservoir bacteria (e.g. clostridia) or by the incomplete oxidation of reservoir hydrocarbons (e.g. n-alkanes) by aerobic hydrocarbon-degrading bacteria.

There is no single medium however which will support the growth of such a diverse bacterial flora or even just the variety of SRB which have been reported to be present in environmental samples. Therefore a variety of media of different compositions must be used to grow and evaluate community structure of bacterial populations. In addition the presence of viable but non-culturable cells are present in natural environments⁸ demonstrates the need for techniques which can determine species composition without requiring growth in the laboratory. Considering the diversity of SRB reported in ecosystems, information about the structure of SRB communities is required if we are to understand and control the

bacterial activities in oil field environmental and industrial ecosystems. It is probable that not all of the SRB found in an oil reservoir are involved in the souring or corrosion processes.

The traditional technique for detecting and monitoring levels of SRB is the most probable number (MPN) method. This is a statistical method involving the serial dilution of samples in an iron-rich medium containing sulfate and lactate as the carbon source. Growth is indicated by the development of a black iron-sulfide precipitate and requires incubation periods of up to 4 weeks duration. Studies^{9,10} comparing the rate of sulfate-reduction and viable numbers of SRB as determined by the MPN method indicate this method grossly underestimates the *in situ* SRB population. This difference is the result of the presence of newly discovered nutritional types of SRB and the difference in growth rates of diverse physiological types of SRB which make it impossible to design a single medium to support the growth of all the SRB present.

Recently direct methods which do not require bacterial growth have been developed based on the detection of cellular components characteristic of SRB. For example, such techniques rely on the reaction of antibodies with cell surface components specific to SRB; the detection of APS reductase, an enzyme present in all SRB; and a chemical test for the activity of the enzyme hydrogenase¹¹ which is present in almost all SRB as well as other oil field bacteria (e.g. *Shewanella* spp.). These direct detection methods significantly reduce the time involved, requiring only a few hours instead of weeks to obtain data on SRB numbers. However they do not provide information on the types or diversity of SRB present, i.e. community structure.

The application of nucleic acid hybridization techniques can supply information on the genetic diversity of SRB as well as monitor the presence, appearance or disappearance of a given SRB species in an environmental community. These techniques are based on the fact that complementary nucleic acid sequences, i.e. either DNA or RNA (ribose nucleic acids), hybridize with each other and under defined conditions this reaction can be made very specific and quantitative. This technique also can be used to identify the presence of a given species via the detection of its DNA in a mixture of nucleic acids extracted from an environmental population. This approach has been used by Genprobe (San Diego, CA, USA)¹² for the preparation and marketing of chemiluminescent probes specific for ribosomal RNA representing different species of SRB. This technique using general and specific 16S rRNA probes together with

fluorescent microscopy was used to visualize specific SRB populations in developing and established biofilm populations¹³.

This paper presents information on the application of new nucleic acid hybridization techniques to the assessment of the community structure of SRB present in fluids (planktonic) and biofilms (sessile) in western Canadian oil field environments.

II. Methods

A. Microbiological

The techniques used for isolation of SRB field cultures and for growth of known cultures of SRB obtained from culture collections have been published^{14,15,16}. Cultures were grown at a temperature and a salinity close to that of the field conditions from which the samples were obtained. The following criteria were used in assessing culture purity: colonial and cell morphologies; lack of growth when incubated under aerobic conditions; the analysis of DNA restriction profiles assayed with hydrogenase genes and 16S rRNA probes, and via DNA homology reactions. Because these isolates were not assigned to genera they were designated "lac", "pro", "dec", "ben", "ace" and "eth" to indicate that they were purified from lactate, propionate, deconoate, benzoate, acetate or ethanol enrichments, respectively. Serial numbers were also assigned (e.g. "lac 5", "ben 1") to denote different, non-cross reacting hybridization groups or "standards".

B. Molecular biological

The methods used for DNA isolation and the preparation of hydrogenase gene probes have been published¹⁴. The fact that total chromosomal DNA can be used as a gene probe is well established in the literature. Such techniques however preclude the distinction between strains with highly homologous genomes. The term "standard" was used to represent all closely hybridizing strains and therefore different standards show little or no cross-hybridization.

DNA from unknown organisms can be probed sequentially with labelled DNA from standards of interest. However such a process is time consuming when a large number of samples are to be surveyed. Therefore the sample itself was labelled and used to probe a "master filter" containing dots of DNA from bacteria relevant to the environment being examined. Once a master filter has been prepared for an environment this reverse sample genome probing (RSGP) procedure allows for the analysis

of a DNA preparation in a single step rather than the usual multistep process¹⁵. New standards, as they are isolated, can be readily added to master filters. The techniques used for the isolation of DNA from plugs, i.e. the sessile flora, are under development and modification.

The process used for the preparation and the utilization of a master filter is described in Figure 1. Using oil field fluids or plug scrappings as inocula, enrichment cultures are established on the six carbon sources listed in the microbiological section. After a suitable incubation period, pure cultures of SRB are isolated from these enrichment cultures using standard microbiological methods. DNA is recovered from these isolates and it is denatured by heating. A small amount of the denatured DNA is spotted onto a membrane filter and it is treated with ultra-violet light to anneal the DNA to the filter. A master filter contains many of these spots or "dots" of DNA from pure cultures recovered from environmental sources and/or culture collections.

Subsequently, DNA is recovered from other enrichments, SRB cultures or extracted directly from environmental samples, denatured and labelled with ³²P-phosphate. This radioactive DNA is used as a probe and reacted with the master filter. After suitable incubation, the master filter is washed to remove any radioactive DNA which has not hybridized with the standard DNA dots. The filter is then exposed to x-ray film and the presence and location of radioactive material is detected as a black spot on the film after it is developed. This procedure yields qualitative results, that is it detects the presence of specific SRB, as well as qualitative results, that estimate the abundances of specific SRB in the population. Both results provide information on the SRB community structure.

III. Results and Discussion

Some examples of the types of hybridization which can be obtained with the RSGP procedure are shown in Figure 2. Panels A and B are representative of the results obtained with a labelled probe from a pure isolate. The failure of the DNA from the unknown SRB to react with standards in panel A indicates that the isolate is new and its DNA could be added as a new standard to the master filter. In panel B, however, the reaction of the probe with standard #3 indicates that it is identical to or very closely related to that standard. The reaction in panel C is typical of probes prepared from an enrichment culture containing a mixture of SRB. The appearance of three black spots indicate that SRB in the mixed culture are closely related or identical to standards 1,13 and 20. However a completely negative reaction in panel C, providing the source is known to

contain SRB, indicates that new SRB types are present. Microbiological investigations should be undertaken to recover the SRB for possible inclusion in the master filter. The reaction shown in panel D, i.e. no self-hybridization, indicates that there was possibly a problem with the hybridization assay and the sample should be re-examined.

Once these master filters are established for a given environment they can be used to assess community structure without involving growth procedures. That is, the DNA may be recovered directly from fluids by centrifugation or adsorption techniques to collect the bacteria, or from biofilms, plugs, tubercles or metal scrapings. This procedure provides data on community structures as they exist in nature.

The selectivity of the [NiFe] hydrogenase probe as a specific detector for members of the Desulfovibrio genus is established by the data presented in Table 1. There is no reaction of this probe with SRB representing 4 other SRB genera. The positive reaction of this probe with almost half of the planktonic oil field isolates examined, isolated from 7 different sites, indicate that members of the Desulfovibrio genus are a predominant species in these western Canadian oil field fluids.

The data presented in Figure 3 summarize the difference between the planktonic SRB community structure found in fluids from saline and freshwater fluids. These fluids were obtained from 56 sites in seven different oil field locations and analyzed using published nucleic acid probe techniques^{14,15,16}. There is a slightly greater diversity of SRB species in the saline environments yielded 24 different standards whereas the freshwater sites yielded only 17 different standards. The SRB population of saline environments contained any combination of the following 16 standards (lac4, lac5, lac6, lac10; eth3; ben1, ben3; dec1, dec3, dec8; pro1, pro4, pro12; or ace1, ace3, ace4); whereas freshwaters contained any combination of the following 10 standards (lac1,2, lac7, lac17; ben6; dec4, dec6, dec7; pro5, pro10; or ace5). There were a few standards (lac3, lac12, lac15, lac21; eth2; or ben4) which could be found in either environment. That is, the salinity of the environment is a very important factor in determining the community structure of the SRB population.

A comparison of the SRB community structure in planktonic and sessile (biofilm) SRB flora is described in Figures 4 and 5. In both biofilm systems studied (sites WW5 and WW14) the SRB planktonic population has a similar distribution of the 11 SRB standards detected with no standard consisting of >2% fraction of the SRB population. However when the sessile (biofilm) population of the respective planktonic samples were

examined certain SRB from the planktonic population dominated. In sample WW5 standards lac6 and eth3 were predominant at > 4% incidence and lac24 at >10% incidence. The sessile population from sample WW14 showed two SRB, lac3 and lac24, with incidence levels >4%. This information suggests that only specific SRB from the planktonic flora become predominant in a sessile population. All these standards react strongly with the [NiFe] hydrogenase probe and therefore are members of the Desulfovibrio genus. The predominance of certain SRB in the sessile community flora might be a result of differences in growth rates of planktonic flora when present in a biofilm (sessile) structure. It also is possible that the dominant biofilm SRB are those that are active in microbial influenced corrosion.

The variations observed in the duplicate sessile sample (Figure 4) indicate that further work has to be done to refine the technique used for examining sessile flora community structure.

The information presented shows that nucleic acid probe techniques can be used to analyze the community structure of SRB in planktonic and sessile (biofilm) systems. The development of the RSGP technique allows for the rapid assessment of environmental community structure without having population structure biased by growth procedures.

IV. References

1. B.B. Jørgensen, *Nature (London)*, 292 (1982): p. 643.
2. F. Widdel, T.A. Hansen, "The dissimilatory sulfate-reducing Bacteria", *The Prokaryotes*, Second Edition. 1991, (Springer-Verlag, New York), p. 583.
3. F. Widdel, F. Bak, "Gram-negative mesophilic sulfate-reducing bacteria", *The Prokaryotes*, Second Edition. 1991, (Springer-Verlag, New York), p. 3352.
4. R. Devereux, M. Delaney, F. Widdel, D.A. Stahl, *Journal of Bacteriology*, 171 (1989): p. 6689.
5. R. Devereux, S.H. He, C.L. Doyle, S. Orkland, D.A. Stahl, J. LeGall, W.B. Whitman, *Journal of Bacteriology*, 172 (1990): p. 3609.
6. V.A. Kuznetsova, A.D. Li, *Mikrobiologiya*, 32 (1964): p. 274.
7. A.M. Jobson, F.D. Cook, D.W.S. Westlake, *Chemical Geology*, 24 (1979): p. 355.
8. D.B. Roszak, R.R. Colwell, *Microbiological Reviews*, 51 (1987): p. 365.
9. B.B. Jørgensen, *Geomicrobiology*, 1 (1978): p. 49.
10. G.R. Gibson, R.J. Parkes, R.A. Hebert, *Journal of Microbiological*

Figure 1. Preparation and utilization of a master filter

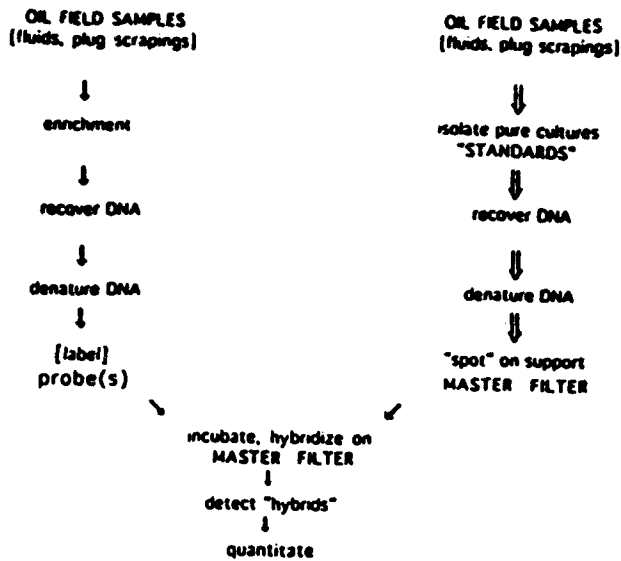


Figure 2. Examples of different types of hybridization in RSGP analyses.

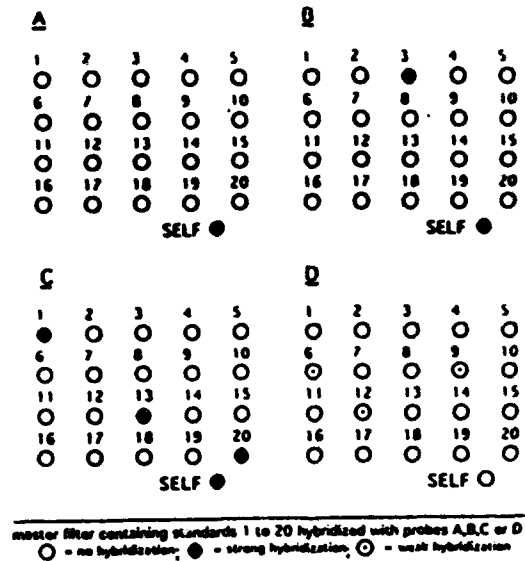


Table 1. Distribution of [NiFe] hydrogenase gene in sulfate-reducing bacteria.

| SRB | number tested | HYDROGENASE GENE* | | |
|---------------------------------------|----------------------|-------------------|--------------------|----------|
| | | [NiFe] | [NiFeSe] | [Fe] |
| Desulfovibrio spp. | 22 | + | (+ or -) | (+ or -) |
| Desulfosarcina variabilis | 1 | - | - | - |
| Desulfococcus multivorans | 1 | - | - | - |
| Desulfobulbus propionicus | 1 | - | - | - |
| Desulfotomaculum ruminus | 2 | - | - | (+ or -) |
| "Desulfovibrio bearsi" ^{***} | 1 | (+ or -) | - | - |
| "Desulfovibrio sapovorans" | 1 | - | - | - |
| "Desulfovibrio thermophilis" | 1 | - | - | - |
| oil field isolates - planktonic | > 300 ^{***} | + | nd ^{****} | (+ or -) |

*+ = strong hybridization; (+ or -) = some cultures +, others -; - = no hybridization

** taxonomy of species in quotations needs re-evaluation (3)

*** approximately 45% of oil field samples reacted with [NiFe] probe

**** not determined

Figure 3. SRB community structure of saline and freshwater oil-field communities.

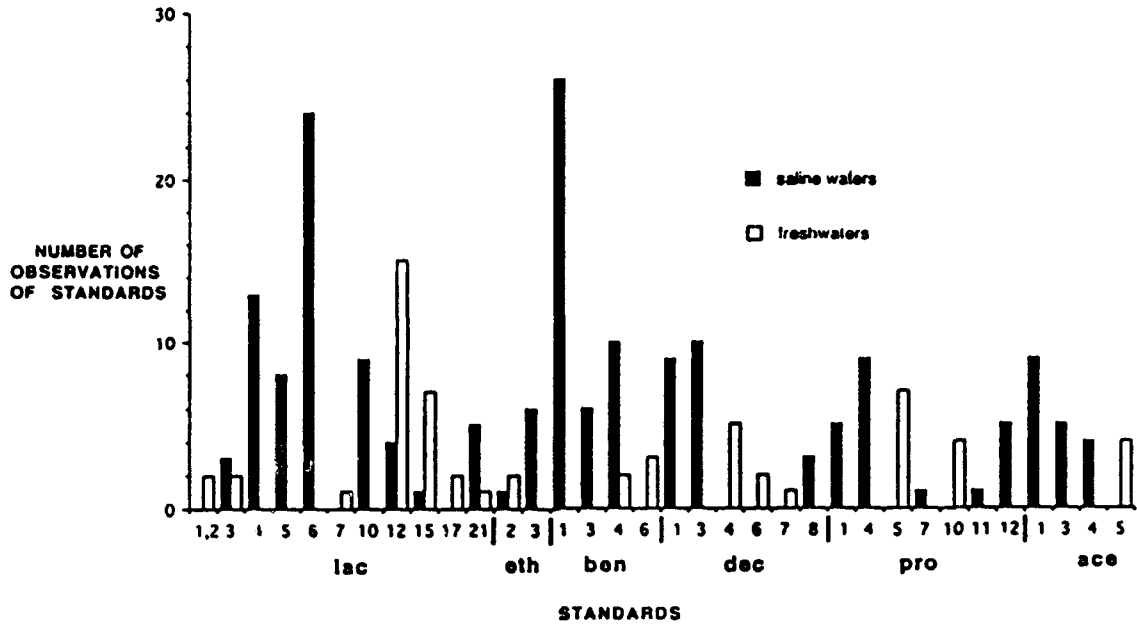


Figure 4. Fraction of SRB standards in waterplankton SRB populations (sample WW5)

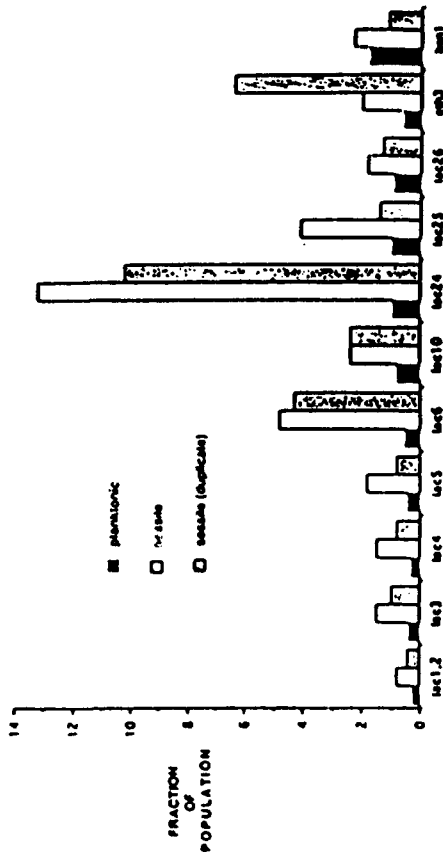
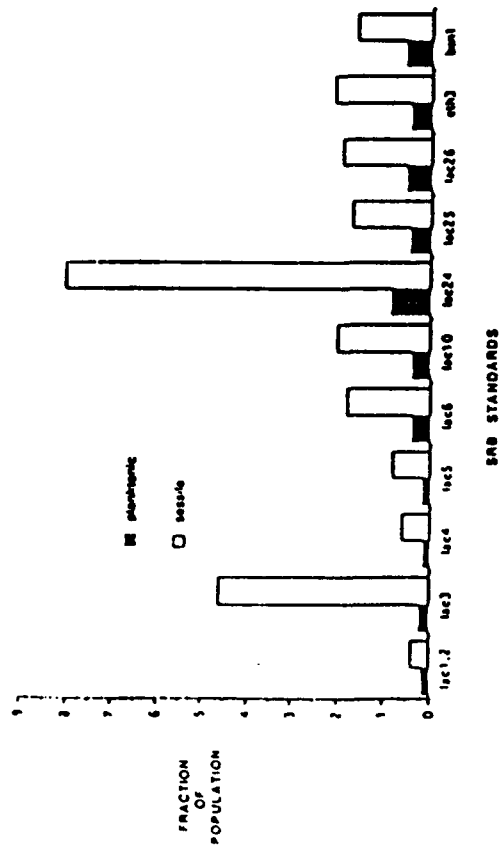


Figure 5. Fraction of SRB standards in waterplankton SRB populations (sample WW14)



Control of Microbial Biofilm by Electrically-Enhanced Biocide Treatment

**Bill Costerton
Center for Biofilm Engineering
Montana State University
409 Cobleigh Hall
Bozeman, MT 59717-0398 U.S.A.**

Abstract

Direct examination of surfaces in industrial aquatic systems clearly shows the presence of slime-enclosed bacterial biofilms and it is axiomatic that it is these adherent populations that are involved in fouling, souring, and corrosion. It is now widely acknowledged that bacteria within these biofilms are inherently resistant to very high concentrations of biocides and that routine biocide treatment usually kills planktonic (floating) cells, and gives the illusion of control of bacterial processes, but fails to kill these biofilm bacteria. We have developed a novel technology in which very weak DC electric fields are used to overcome the diffusion resistance implicit in the biofilm made of growth and thus allow conventional biocides to penetrate microbial biofilms and kill biofilm bacteria.

Key terms: biocide, electric field, biofilm, bacteria

Introduction

Bacteria in all aquatic systems examined to date show a pronounced tendency to adhere to available surfaces and their subsequent growth and slime production lead to the development of bacterial biofilms.¹ Bacteria within these biofilms have been unequivocally shown to be inherently resistant to both biocides² and antibiotics^{3,4} so that 500-1500 times more of the antibacterial agents is required to kill biofilm cells compared to the amount necessary to kill planktonic (floating) cells of the same species. We have discovered that the diffusion resistance implicit in the biofilm mode of growth^{1,5} can be overcome by the imposition of a relatively weak DC electric field so that biofilm bacteria can readily be killed by concentrations of biocides only 1.0-2.0 times those necessary to kill planktonic cells of the same organism.⁶

Material and Methods

The modified Robbins device (MRD) described in Nickel *et al.*⁴ was further modified, as shown in Figure 1, to produce the electrical MRD (eMRD). An environmental isolate of *P. aeruginosa* that exhibited excellent adhesion characteristics was selected for this study and we determined its MIC for Kathon (1 ppm), glutaraldehyde (5 ppm), and quaternary ammonium compound - dimethyl ammonium chloride (10 ppm) in classical tests involving laboratory-grown planktonic cells. This organism was grown in M-56 medium⁷ and passed through paired eMRD devices at a rate of 60 ml/hour by the use of a peristaltic pump. In some cases the two electrodes of the eMRD were connected to a power supply that produced a field strength of 12 V/cm and a current density of 2.1 mA/cm² and the polarity of the electrodes was reversed every 64 seconds. After exposure to planktonic cells of the environmental strain of *P. aeruginosa* in flowing M-56 medium pairs of studs were removed from the eMRD at intervals and numbers of living bacteria within their adherent biofilms were determined by the quantitative recovery methods described by Nickel *et al.*⁴

Results

When planktonic cells of the environmental strain of *P. aeruginosa* were passed through a pair of eMRD devices, only one of which was connected to a power supply, these organisms colonized the stainless steel studs with equal avidity (Figure 2). The biofilm developed very rapidly in the presence or absence of the DC electric field and the confluent mature biofilm was produced in 24 hours. When 1.0 MIC of glutaraldehyde (5 ppm) or of Kathon (1 ppm) were added to each of two pairs of colonized eMRD's, at 26 hours, the biofilm cells were completely killed in 12 hours (Kathon) or in 24 hours (glutaraldehyde). In the absence of the DC electric field neither of these biocides produced a significant decrease in the number of living biofilm bacteria when assessed at 24 hours. The quaternary ammonium compound was similarly effective in killing all of the biofilm bacteria on stainless steel studs in the eMRD when it was used in the presence of the DC electric field.

Discussion

Davis and his colleagues^{8,9} have shown that planktonic bacteria can be killed by electric currents alone and they have invoked a mechanism involving iontophoresis. Other workers¹⁰ have used iontophoresis to deliver effective concentrations of an antibiotic into the middle ear. The "bioelectric" effect that we describe in this paper has an entirely different basis in that, in our system, the DC electric field alone has no deleterious effect on bacteria. However, the DC field facilitates the efficacy of antibacterial agents in penetrating microbial biofilms and killing biofilm bacteria. This effect of the DC field is universal in that it enhances the killing of biofilm bacteria by all biocides and antibiotics tested to date and in that it also enhances the efficacy of these antibacterial agents in killing bacterial and fungal spores. We expect that this novel bioelectric technology will be very useful. The simple generation of weak DC fields

on fouled metal surfaces will allow the complete control of biofilm bacteria by easily attained concentrations of conventional biocides.

Acknowledgements

I am profoundly grateful to Dr. Tony Khoury for his research collaboration and the Brian Ellis and Kan Lam for their excellent technical assistance.

References

1. J.W. Costerton, K.-J. Cheng, G.G. Geesey, T.I. Ladd, J.C. Nickel, M. Dasgupta, and T.J. Marrie, Bacterial biofilms in nature and disease. *Ann. Rev. Microbiol.*, 41 (1987): p. 435.
2. I. Ruseska, J. Robbins, J.W. Costerton, and E.S. Lashen, Biocide testing against corrosion-causing oil field bacteria helps control plugging. *Oil and Gas J.*, March 8 (1982): p. 253.
3. H. Anwar, M.K. Dasgupta, and J.W. Costerton, Testing the susceptibility of bacteria in biofilms to antibacterial agents. *Antimicrob. Agents Chemother.* 34 (1990): p. 2043.
4. J.C. Nickel, I. Ruseska, and J. B. Wright, *et al.*, Tobramycin resistance of *Pseudomonas aeruginosa* cells growing as a biofilm on urinary catheter material. *Antimicrob. Agents Chemother.* 27 (1985): p. 619.
5. W.W. Nichols, M.J. Evans, M.P.E. Slack, and H.L. Walmsley, The penetration of antibiotics into aggregates of mucoid and non-mucoid *Pseudomonas aeruginosa*. *J. Gen. Microbiol.* 135 (1989): p. 1291.
6. S.A. Blenkinsopp, A.E. Khoury, and J.W. Costerton, Electrical enhancement of biocide efficacy against *Pseudomonas aeruginosa* biofilms. *Applied and Envir. Microbiol.* 58 (1992): p. 3770.
7. B.C. Carlton, and B.J. Brown, Gene mutation, In P. Gerhardt, R.G.E. Murray, R.N. Costilow, E.W. Nester, W.A. Wood, N.R. Krieg, and G.B. Phillips (ed.), *Manual of methods for general bacteriology*, (Washington, D.C.: American Society for Microbiology, 1981), p. 222.
8. C.P. Davis, S. Weinberg, M.D. Anderson, G.M. Rao, and M.M. Warren, Effects of microamperage, medium, and bacterial concentration on iontophoretic killing bacteria in fluid. *Antimicrob. Agents & Chemother.* 33 (1989): p. 442.
9. C.P. Davis, N. Wagle, M.D. Anderson, and M.M. Warren, Bacterial and fungal killing by iontophoresis with long-lived electrodes. *Antimicrob. Agents & Chemother.* 35 (1991): p. 2131.
10. I.W. Chang, Y.B. Cho, and S.C. Lim, Iontophoretic application of cefotiam hydrochloride into inner ear through round window membrane. *Chonnam J. Med. Sci.* 2 (1989): p. 141.

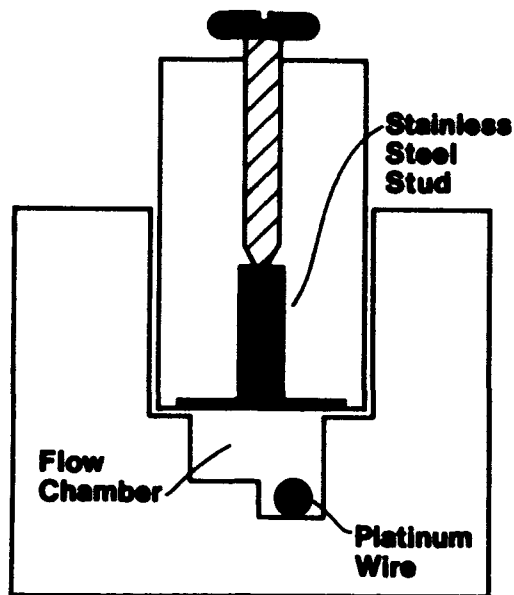


Figure 1 Cross-sectional diagram of an electrified MRD showing the configuration of the perspex structure and the flow chamber and the relative position of the stainless steel stud and the platinum wire. Direct current was applied, with reversal of polarity each 64 s, to the stainless steel stud (via its retaining screw) and the platinum wire, which serve as the two electrodes needed to generate the electric field.

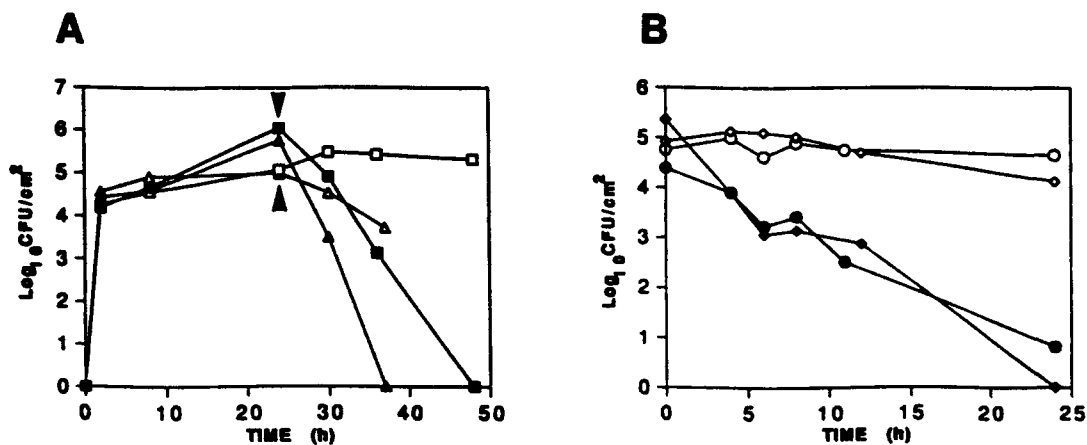


Figure 2 Effect of a DC electric field on the development and growth of a biofilm of *P. aeruginosa* cells on the stainless steel studs of eMRD devices. Biofilm developed equally in the presence (■; ▲) or absence (□; △) of the electric field, but when glutaraldehyde (5 ppm) or Kathon (1 ppm) were added to the systems at 24 hours (arrows) the combined effect of the DC field and the glutaraldehyde (■) killed all of the biofilm bacteria in 24 hours, while the combined effect of the DC field and the Kathon (▲) killed all of the biofilm bacteria in 12 hours. The biocides alone, without the DC field, had no significant effect on the biofilm bacteria.

Use of a Biofilm Electrochemical Monitoring Device for an Automatic Application of Antifouling Procedures in Seawater.

Alfonso Mollica

C.N.R. - Istituto per la Corrosione Marina dei Metalli
Via De Marini, 6 - Torre di Francia.
16149 Genova - Italy

Giovanna Ventura

C.N.R. - Istituto per la Corrosione Marina dei Metalli
Via De Marini, 6 - Torre di Francia.
16149 Genova - Italy

Abstract

In previous works the phenomenon of the oxygen reduction depolarization induced by the biofilm presence on active-passive alloys was utilized to make electrochemical devices able to monitor the biofilm growth on surfaces of a series of active-passive alloys exposed in seawater.

In particular a very simple device constituted by a galvanic couple between a stainless steel pipe and a suitable sacrificial anode was studied: the measurement of the change in time of the galvanic current was utilized for the monitoring of the first phase of the biofilm growth and its destruction by a biocide treatment.

The same device was utilized in this work to automatically guide the application of a chlorine treatment in order to control biofilm growth at a very thin level, in view of a possible application in condensers utilizing seawater as a cooling medium.

Results of field tests indicate that such a device is able to automatically control the biofilm amount at a level which can be selected between $10^6 + 10^7$ bacteria/cm² and, at the same time, to minimize the biocide addition.

Key terms: biofilm, biocide, monitoring, seawater.

Introduction

It is well known that the growth of biofilm on pipe walls of condenser utilizing seawater as a cooling medium causes a reduction of the thermal exchange and an increase in the friction factor: that means a costly reduction of the plant efficiency.

It follows that antifouling procedures, mainly based on the addition of biocides in solution, must be applied, causing often problems of environmental impact.

Biofouling monitoring devices able to provide, in situ and in real time, information about the biofilm status can help to optimize the application of antifouling procedures and, as a consequence, to minimize the environmental impact.

For this purpose, some attempts were made to realize simple biofilm monitoring electrochemical devices (1-3).

These devices are based on the following effect of the biofilm growth: the presence of biofilm causes a depolarization of the oxygen reduction on the surface of many active-passive alloys like Stainless steels, Ni-Cr, Ni-Cu, Titanium...

It follows that, apart from the increasing risk of Microbial Induced Corrosion (MIC) on the above mentioned alloys, the galvanic current between these alloys and other less nobles materials coupled with them increases during the phase of the biofilm growth: a correlation between galvanic current and biofilm growth can, hence, be thought.

To control if an electrochemical device, simply based on the reading of the galvanic current, can successfully be utilized for the biofilm monitoring on a series of active-passive alloys in seawater, we made several tests (1,3) utilizing a Stainless Steel pipe coupled with an iron anode as a monitoring device.

It was shown that, by following in time the trend of the galvanic current, correct information about the effect of continuous and intermittent chlorine treatments on the biofilm growth and destruction on Stainless Steel surfaces are obtained.

In addition, it has been proven that this technique can be utilized as a very early warning of the first phases of the biofilm growth because an increase of one order of magnitude of the galvanic current signalizes the increase of the bacterial population from, about, 10^6 to 10^7 bacteria/cm². Taking into account that the proposed device provides an electrical signal of the biofilm growth and its destruction, we can now imagine it will be possible to utilize this signal to guide the application of a biocide treatment in such a way to automatically obtain both the control of the biofilm at a selected thin layer and the minimisation of the biocide additions. At the same time the MIC risk will be reduced.

The aim of this work is to control if electrochemical biofilm monitoring devices can be utilized for this purpose.

Materials and Methods

Several loops, like that shown in Fig.1, were utilized for the present study.

In each loop natural seawater flows once-through inside a Stainless Steel pipe (20Cr-24Ni-6Mo, 24 mm: internal diameter, 140 cm length) and a brass (Cu/Zn-70/30) pipe in series. The two pipes are connected through a resistor ($R = 10$ ohms) and the galvanic current flowing between them can be obtained by measuring the potential difference (δV) across R .

Five equal loops were mounted in series as shown in Fig.2.

The measure of the galvanic current on the last loop (loop N° 5) was recorded versus exposure time and utilized to guide, through an automatic controller, an intermittent injection of biocide into the flowing seawater.

The biocide injection started when δV surpassed a first selected value (δV_{max}) and stopped when δV fell down to a second selected value (δV_{min}).

Sodium hypochlorite was utilized as a biocide and its concentration in the stock solution was calculated to obtain a nominal chlorine concentration of 1 ppm in the flowing seawater.

The biocide was injected in between the first and the second loop, so that the chlorine treatment was applied to loops 2, 3, 4 and 5, for an overall pipe length of about 16 meters.

Loop 1 was utilized as a control of the efficiency of the automatic antifouling treatment.

The test lasted about 3 months; during the test the seawater temperature decreased from 21 to 14°C.

The seawater velocity inside the stainless steel pipes was 0.5 m/s.

Finally: several flat stainless steel samples were added to each loop for SEM and EDX analysis of the biofilm.

Results

Figure 3 shows the trend of the galvanic current (or δV) versus time for the untreated loop 1 and for the automatically chlorinated loop 5.

The graph indicates that in untreated seawater (curve A) the galvanic current between the stainless steel and the copper alloy increases more than one order of magnitude during the first week of exposure as a result of the initial biofilm growth on the stainless steel surfaces; a partial decrease of the galvanic current can be observed later as a consequence of the increase in time of the biofilm layer which causes, in turn, a lowering of the oxygen reduction limiting current due to both the increase of the diffusion layer and to a partial oxygen consumption by bacteria.

The effect of the automatic chlorination is described by curve B: each sharp decrease of the galvanic current signalizes when a chlorine addition in seawater was automatically applied.

We normally set the controller schematized in Fig.2 in such a way to activate the biocide injection when the galvanic current surpassed 0.7 mA and to stop when the galvanic current fell down to 0.3 mA; sometimes, during the test, the above mentioned limits were temporarily changed.

During the test the chlorination was automatically applied for an overall time of about 18 hours.

Figure 4 shows, in expanded time scale, an example of the galvanic current trend versus time when chlorination is applied.

Desultory readings of the galvanic currents on the other loops, between the chlorine injection point and the controller, indicated that the currents were progressively increasing from loop 2 to loop 5 during all the phases of the automatic biocide treatment.

At the end of the test, the settlement on treated and untreated loops was observed.

Figure 5 shows a picture of the aspect of two pipe segments which clearly indicates that the automatic chlorine treatment strongly reduced the fouling amount on the stainless steel surfaces; the fouling reduction, measured as a ratio between the fouling dry weights in untreated and treated loops, is about 100.

The Scanning Electron micrographs in Figure 6 show the typical aspect of the fouling after about 3 months of exposure in untreated and treated seawater: it can be seen that, in automatically treated seawater, on the Stainless steel surfaces remain only a few bacteria and a thin, non continuous, deposit layer.

Regarding the bacterial density: many of the SEM observations on randomly chosen fields indicate only a residual bacteria mean density of the order of 10^6 bacteria/cm².

Regarding the nature of the deposit: the EDX analysis (Figure 7) show that only a minor presence of silicon can be observed on the surfaces exposed in treated seawater.

Discussion

In a previous work (3), studying the relationship between galvanic current and biofilm growth, we utilized a normalized and dimensionless index $\Theta(t)$ defined through the expression:

$$\Theta(t) = \frac{I_g(t) - I_{gmin}}{I_{gmax} - I_{gmin}} \quad (1)$$

where I_{gmin} and I_{gmax} are the values of galvanic current measured, respectively, in absence and in presence of a fully developed biofilm on stainless steel surfaces and $I_g(t)$ is the instantaneous value of the galvanic current.

It was observed that the fluctuation of $\Theta(t)$ between 0 and 1 corresponded to a fluctuation of the bacterial population density between 10^6 to 10^7 bacteria/cm².

Looking at the graphs in Fig.3 we can assume, for the present test, $I_{gmin}=0.05$ mA and $I_{gmax}=1.2$ mA.

It follows that the two limits of the galvanic currents normally imposed when the automatic chlorination is applied (0.3 and 0.7 mA) allow a controlled fluctuation of Θ between, about, 0.2 and 0.6 and, therefore, a low residual bacterial population of some 10^6 bacteria/cm² should be expected at the end of the test.

Effectively, this is the order of magnitude of the observed mean bacterial population density after 3 months of treatment.

It means that simple electrochemical devices can be utilized to guide the biocide treatment in such a way to control the first phase of the biofilm growth up to a selected level.

In addition: a control by an electrochemical device seems to be able to minimize the biocide additions in seawater.

Figure 8 shows an elaboration of data plotted in Figure 3: in this graph the interval between two subsequent chlorinations, in function of the exposure time, is reported.

It can be seen that, at the beginning of the test, one chlorination about every 2 days is automatically imposed by the electrochemical device; the interval increases in time and, at the end of the test, only one chlorine treatment every 5-6 days is sufficient to maintain the galvanic current within the chosen limits.

It suggests that the biological activity tends to decrease in time: this indication is consistent with the observed decrease of the seawater temperature from 21 to 14°C during the test.

In other words: a very simple electrochemical device seems to be sensitive to the effect of environmental parameters on the biological activity and, therefore, able to automatically adapt the biocide additions in function of the actual and local needs.

Conclusions

The change in time of the galvanic current in a simple electrochemical device constituted by a galvanic couple between a stainless steel pipe and a Copper based alloy as anode, due to the oxygen reduction depolarization induced by the biofilm growth on the stainless steel surfaces, was utilized to automatically guide a chlorine treatment in order to control the biofilm growth at a very thin level and in view of a possible application in condensers utilizing seawater as a cooling medium.

For this purpose two levels of the galvanic current, within the values assumed in presence and in absence of a fully developed biofilm on stainless steel surfaces, were selected: the chlorine treatment automatically started every time the galvanic current reached the prefixed maximum value and lasted until it descended below to a second, minimum, value.

Results of field tests indicate that such a device is able to automatically control biofilm growth at levels between $10^6 + 10^7$ bacteria/cm² and to minimize the biocide additions.

References

1. A. Mollica, E. Traverso, G. Ventura, "Electrochemical monitoring of the biofilm growth on active-passive alloy tubes of heat exchanger using seawater as a cooling medium", Proc. of 11th Int. Corrosion Congress, (Florence, Italy, Associazione Italiana di Metallurgia, 1990), 4, p.341.
2. G. Licina, G. Nekoksa, G. Ward, "An Electrochemical Methods for monitoring the development of biofilms in cooling water", Proc of Int. Congress on Microbially Influenced Corrosion, (Knoxville, TN, USA, N.J. Dowling, N.W. Mittleman, J.C. Danko Eds, 1990), 5, p.41.
3. A. Mollica, G. Ventura, "Electrochemical monitoring of the biofilm growth and corrosivity in seawater: effect of intermittent chlorination", Proc. of 8th Int. Congress on Marine corrosion and Fouling, (Taranto, Italy, 1992), in press.

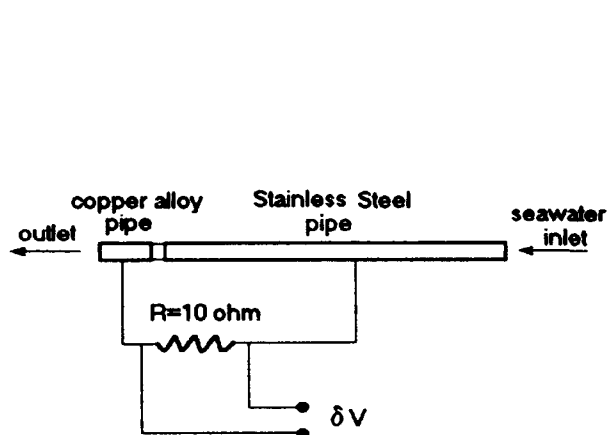


Figure 1 - Scheme of a loop

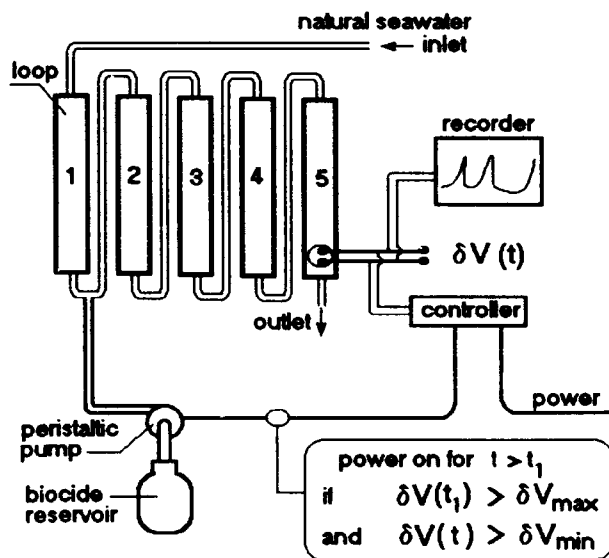


Figure 2 - Scheme of the plant

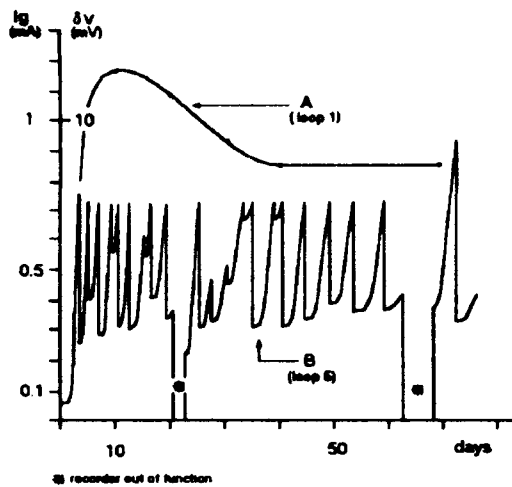


Figure 3 - Trend of the galvanic current in untreated (curve A) and automatically chlorinated (curve B) seawater.

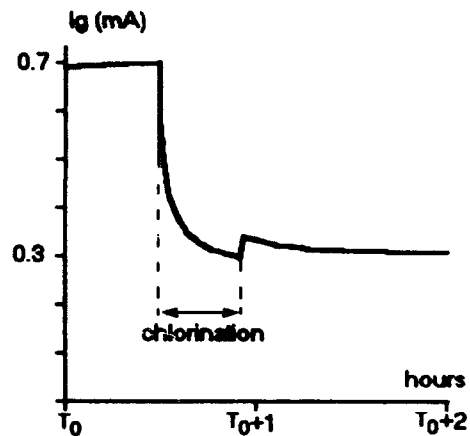


Figure 4 - An example of galvanic current decay during an automatic chlorination.

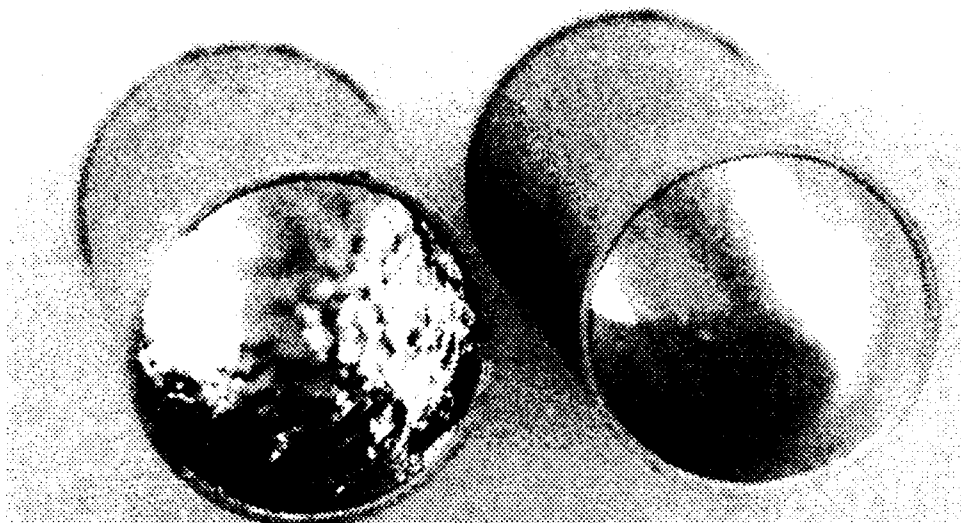


Figure 5 - Aspect of the pipe internal walls after three months of exposure to untreated (on the left) and automatically chlorinated seawater (on the right).

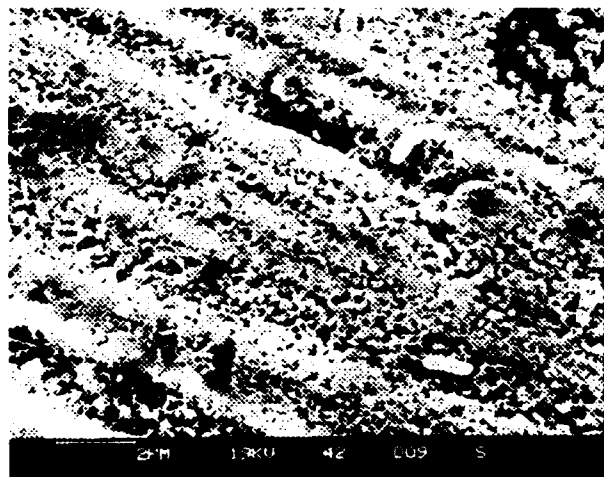
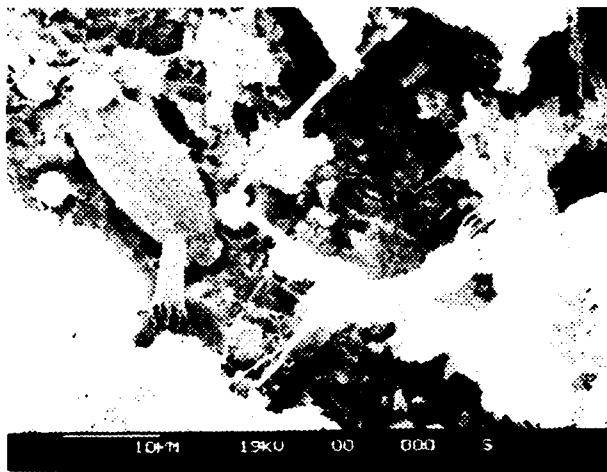


Figure 6 - Scanning Electron micrographs of samples after three months of exposure to untreated (on the left) and automatically chlorinated seawater (on the right).

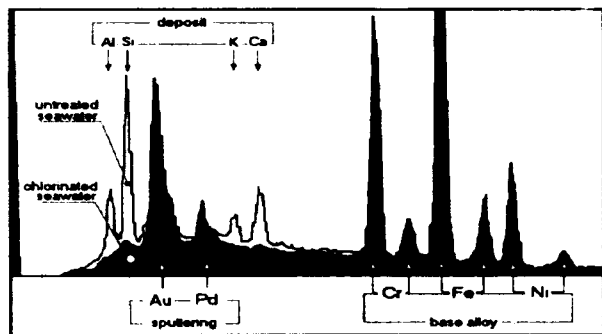


Figure 7 - EDX analysis on samples after three months of exposure to untreated and automatically chlorinated seawater.

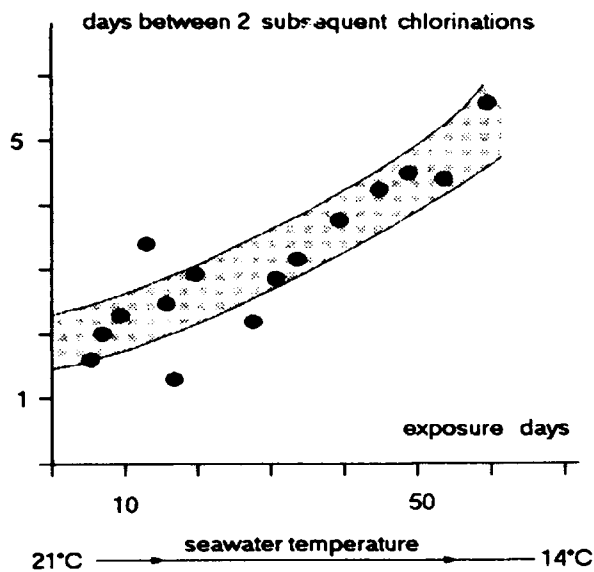


Figure 8 - Interval between two subsequent automatic chlorinations versus exposure time.

Results of Electrochemical Monitoring of Microbiological Activity*

G. Nekoksa and G. Licina

* Paper not available at time of publication.

An Investigation of Biologically Induced Corrosion in Wastewater Lift Stations

H. Saricimen

King Fahd University of Petroleum and Minerals Box 1686
Dhahran 31261, Saudi Arabia

M. Shamim

King Fahd University of Petroleum and Minerals
Dhahran 31261, Saudi Arabia

M. Maslehuddin

King Fahd University of Petroleum and Minerals
Dhahran 31261, Saudi Arabia

Abstract

An investigation of wastewater lift stations in residential areas of Jubail Industrial City (JIC) in 1985, showed that some of the lift stations were severely corroded, particularly at unsubmerged surfaces, in less than six years after construction. The concrete walls showed severe sulfate attack up to about 20 mm depth from the exposed surface. Ductile iron and galvanized steel items corroded by sulfuric acid attack and exhibited generalized pitting with pit depths ranging between 50 to 150 mpy. In order to supplement the findings of the above investigation, coupons of various metallic and non-metallic materials as well as mild steel coupons coated with eight different high quality coatings were placed above water line in one of the lift stations inspected.

The weight loss results of 87-day exposure of the uncoated coupons showed that brass, ductile iron, galvanized steel and cast iron had high corrosion rates ranging between 17 to 50 mpy in the sewer atmosphere. Aluminium was moderately attacked by crevice corrosion under sludge deposits. Stainless steel Type 316, polyvinyl chloride (PVC) and fibre reinforced plastic (FRP) did not show any significant deterioration in the sewers.

The coated coupons were evaluated visually and by electrochemical techniques after 490 days of exposure to the sewer environment. The results showed that the two best performing coatings in the wastewater lift stations were vinyl ester and polyamide cured epoxy.

Key terms: biological corrosion, wastewater lift station, sewage, coating performance.

Introduction

An investigation [1] of wastewater lift stations in residential areas of JIC in 1985, showed that some of the lift stations were severely corroded, particularly at unsubmerged surfaces, in less than six years after construction. The coal tar epoxy coating on concrete walls and ductile iron pipes, and zinc coating on galvanized steel items deteriorated badly and became ineffective. The concrete walls showed [1,2] severe sulfate attack up to about 20 mm depth from the exposed surface. Ductile iron and galvanized steel items [1,3] corroded by sulfuric acid attack and exhibited generalized pitting with pit depths ranging between 50 to 150 mpy.

Until 1902, corrosion in sewer systems was thought to involve only pure chemical reactions between hydrogen sulfide and concrete[4]. Recent research revealed that this type of corrosion is a combination of bacteriological and chemical reactions involving three groups of bacteria, namely aerobic thiobacillus and anaerobic desulfovibrio and desulfotomaculum.

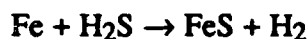
Generally, microorganisms may initiate corrosion of metals by: (1) production of oxidizing agents, (2) forming differential oxygen or chemical concentration cells, (3) removing hydrogen

(electrons) from the surface of metal and/or (4) interfering with the formation or destruction of protective films on metal surfaces.

In aerobic corrosion, sulfuric acid, which is produced by thiobacillus bacteria on aerobic (unsubmerged) surfaces in sewer systems, causes the most severe corrosion of metals as well as deterioration of concrete. Domestic sewage normally contains a few parts per million H_2S , around 20 mg/l of inorganic sulfates and 6 mg/l of organic sulfur compounds at the beginning. As sewage becomes septic, the bacteria *Desulfovibrio desulfuricans* and *D. desulfotomaculum* reduce sulfates to sulfides [4,5,6] and produce more of hydrogen sulfide. Hydrogen sulfide exists in the solution in both ionized and molecular form; the latter is released into the sewer atmosphere. The actual rate of hydrogen sulfide generation and subsequent emission are influenced by (1) biological oxygen demand (BOD), (2) pH, (3) temperature, (4) flow velocity, (5) retention time and (6) turbulence of wastewater. Biological oxygen demand is a measure of anaerobic condition and potential for sulfide generation in wastewater. For every $10^\circ C$. increase in effluent temperature over $20^\circ C$, there is a 100% increase in effective BOD. Optimum sulfide generation takes place when wastewater pH lies between 6.5 and 8.5. Liberation of generated H_2S into atmosphere increases with decreasing pH[4]. The buildup of hydrogen sulfide in the sewer atmosphere depends upon its rate of generation and its oxidation by absorbed oxygen before it escapes out of the effluent. The extent of oxygen absorption is dependent upon the effluent flow velocity. While a high effluent velocity restricts the release of H_2S into the atmosphere, a high turbulence on the contrary increases the rate of H_2S emission [4,7].

Substantial amount of released H_2S is absorbed by the moisture film present on the unsubmerged surfaces of the sewer system. Aerobic bacteria, *Thiobacilli concretivorans*, *Thiooxidans* and *Neapolitanas* [4] then oxidize the absorbed H_2S into sulfur compounds and sulfuric acid. This may result in ultimate H_2SO_4 concentration of about 5%, and the pH may drop to as low as 1 on aerobic (unsubmerged) surfaces even when the pH of wastewater stream is only 6-7 [4].

The other common form of bacteriological corrosion in sewer systems is anaerobic corrosion. The most common anaerobic corrosion is caused by direct reaction of H_2S . Hydrogen sulfide in an aqueous environment in the relative absence of oxygen reacts with iron to form iron sulfide according to:



At pH values around 7 and above (a favorable pH for growth of *Desulfovibrio*), ferrous sulfide is precipitated close to anodic areas to form a protective film [8]. On prolonged exposure to bacterial cultures, the film becomes detached, causing formation of FeS/Fe couple and a corresponding increase in the corrosion rate.

In addition, there are other mechanisms identified to have significant contribution to corrosion of metals in anaerobic environments. Microorganisms, for example, due to their active metabolic processes, can develop oxygen or ion concentration cells on metal surfaces. Metal goes into solution at the anodic areas of low oxygen concentration under the mass of microorganisms. Von Wolzogen Kuhr and van der Vlug [9] showed that sulfate reducing bacteria (SRB) which contain the molecular-hydrogen-activating enzyme hydrogenase remove hydrogen from the surface of iron (cathodic depolarization) and utilize it for the reduction of sulfate. As electrons are removed, more iron goes into solution. Iverson [10] identified iron phosphide (Fe_2P), in the corrosion product of mildsteel. He reported that anaerobic corrosion by SRB is caused by a highly active volatile phosphorous compound which reacts with bulk iron to form Fe_2P .

This paper reports the results of a study to determine the performance of various structural materials and coating systems in a domestic wastewater lift station located at about 2 km from the Western Coast of the Arabian Gulf. Structural details of the lift station were reported in an

earlier publication [2]. The lift station has been in service since 1982. At the time of this investigation the lift station was in service for about three years.

Experimental Program

The experimental program consisted of exposure of coupons in the lift station, visual inspection, analysis of coupons by gravimetric and metallographic techniques, and electrochemical measurements in order to evaluate the performance of materials and coatings in sewage environment.

Preparation and Exposure of Coupons

Uncoated coupons of various metallic and non-metallic materials as well as mild steel coupons coated with eight different high quality coatings were placed above water line in one of the lift stations inspected. The coupons of size 2 x 3 inches were prepared from structural materials used in the lift station and from alternative materials as shown in Table 1. After initial weighing, they were fixed in triplicates to a wooden rack and installed in the lift station by hanging from a nylon rope above the water level at two meters from the manhole entrance. The uncoated coupons were exposed to sewer environment for 87 days and then retrieved for inspection and analysis.

Mild steel coupons of 2 x 3 inches coated with eight different coatings, ie., two kinds of vinylester, high performance coal-tar epoxy, high built micacious iron primer based on chlorinated rubber, polyamide cured epoxy, amine adduct cured coal-tar epoxy, amine cured epoxy resins, and polyamide cured epoxy coating, were provided by three internationally known manufacturers. The coated coupons were then fixed in triplicates to wooden racks and installed above water line in the lift station. They were retrieved after 490 days of exposure to the environment, and evaluated for coating performance.

Monitoring and Evaluation

Gravimetric Analysis. After retrieval, the uncoated coupons were visually inspected. The severity of corrosion, color and thickness of corrosion products on the coupons were recorded. They were then cleaned with a power brush. The depth, extent and pattern of corrosive attack on the coupons were determined. The cleaned coupons were weighed to determine their final weight after exposure, and corrosion rate of each coupon was calculated in mils per year (mpy). Corrosion rate of the coupons was calculated according to:

$$CR \text{ (mpy)} = \frac{(W_i - W_f) \times 1000 \times 365}{A \times d \times t}$$

where mpy = corrosion rate in mils per year
 W_i and W_f = initial and final weight in grams
A = exposed surface area in square inches
t = exposure time in days
d = density in grams per cubic cm.

Chemical Analysis. Corrosion products collected from guide tubes and pump discharge pipes in the lift station were analyzed by X-ray diffraction and X-ray fluorescence techniques. Samples of wastewater from the lift station were analyzed in the laboratory for pH, biological oxygen demand (BOD) chemical oxygen demand (COD), sulfide, sulfate, chloride, total solids, oil and grease, dissolved oxygen and bacteria. The results of chemical analysis were reported in earlier publications [1-3].

Metallographic Analysis. Metallographic samples were prepared from corroded ductile iron discharge tube (DI) and galvanized steel guide tube (GS) in the lift station. Samples of 1 x 2 cm size were cut with a diamond saw, mounted in epoxy, and polished to 0.5 micron (μm). They were examined using a Jeol JSM 840 Model Scanning Electron Microscope installed with Energy Dispersive X-ray Diffraction (EDX) capability.

Coated Coupons

Preliminary Observation and Surface pH. The coated coupons were examined for their general condition and surface deposits. The pH of the surface moisture was measured using narrow-range pH papers. The coupons were then washed with tap water and dried in a desiccator before further observations.

Visual Observations. Visual inspection of coated coupons was conducted using the guidelines in Section 8 of NACE RP-02-81 [11]. These standards recommend establishing a grading system for visual evaluation of coating deterioration and suggest ASTM standards for grading various types of coating deterioration. The ASTM standards consist of photographic references representative of degrees of coating deterioration. The following inspections were carried out and an optical microscope was used whenever recommended: (1) Rusting, ASTM D610, (2) Blistering, ASTM D714, (3) Checking, ASTM D660, (4) Cracking, ASTM D 661, (5) Flaking, ASTM D 772, and (6) Erosion, ASTM D 662.

The visual inspection results were recorded in a modified version of the form specified in ASTM 1150-74. Miscellaneous defects and damages such as microscopic pinholes, mechanical wear not related to erosion by fluid, and microscopic scratches were observed during inspection at 10-diameter magnification under microscope. These were arbitrarily graded on a numerical scale from 10 to 0, based on the approximate area affected.

Electrochemical Measurements. The coated coupons were immersed in a 0.5M NaCl solution. Small coating damages at corners and edges on some of the coupons were repaired by water resistant silicone sealant, prior to immersion. Their open circuit potentials[12] were measured with respect to a standard calomel electrode by means of EG&G Princeton Applied Research Potentiostat/Galvanostat Model 273 interfaced with an Apple IIc computer for automatic data acquisition and plotting using Parc M332 software. The potential variation during the first 15 minutes after immersion was monitored and recorded every five seconds since a rapid change in potential was expected to occur during this interval. Thereafter, potential variation was monitored and recorded every 20-25 seconds for one hour. For coupons still showing a fluctuating potential or a substantial rate of change of potential after one hour of testing, potentials were monitored and recorded every five minutes for durations of 8-12 hours. Finally the potentials were monitored and recorded every 24 hours for seven days and every 72-100 hours for about 22 days. The daily potential measurements were supplemented with determinations of coating resistance[12] using a Beckman Model HD100 digital multimeter.

Results and Discussion

Visual Inspection and Gravimetric Analysis of Uncoated Coupons

The results of visual inspection and gravimetric analysis of uncoated coupons are summarized in Table 2. The study showed unsuitability of metallic materials such as ductile iron galvanized steel, brass and aluminium as structural materials in aerobic environment in the lift station without adequate protective coating. Ductile iron and galvanized steel corroded by generalized pitting; brass corroded by dezincification (dealloying) and pitting, and aluminium corroded mainly by crevice corrosion.

Metallographic investigation of corroded ductile iron and galvanized steel coupons using SEM and EDX techniques (Figures 1 and 2) showed that main corrosive species were sulfur

containing compounds, most probably, H_2S and H_2SO_4 . Two layers of corrosion products were identified on the DI coupon (Figures 1a and 1b). The top layer (150 to 400 μm thick) generally had low sulfur content throughout the bulk of the layer (Figure 1e), except at few locations along the outermost periphery, where sulfur content was relatively high (Figure 1f). Very few spherical carbon particles (Figure 1a) were present embedded in the top layer indicating corrosion reaction mechanism involve outward migration of iron atoms to react with corrosive species at the surface. The EDX spectra showed the presence of sulfur, some silicon and manganese in this layer (Figure 1f). The innermost corrosion layer (300 to 650 μm thick) exhibited the propagation of corrosion into ductile iron (Figures 1a, 1d). The EDX spectra showed the presence of relatively higher sulfur and silicon in this corrosion layer in addition to some potassium, phosphorous and chloride (Figures 1g to 1i). The results indicate that corrosion of DI in aerobic environment in the lift station occurred due to two major factors: (1) sulfuric acid and (2) galvanic effect at iron/graphite interfaces in the ductile iron. Corrosion starts at locations with relatively high cathodic/anodic ratio, i.e., locations with high population of graphite particles, and progresses deeper as pits along graphite spheres. Thus corrosion forms 200-300 μm deep and 50-400 μm wide pits (Figures 1a, 1d).

Chloride ions might also have contributed to the corrosion of DI coupons. Chloride ions are strong depassivating species for iron based alloys. They react with iron to produce chlorides (ferrous and ferric) and ultimately oxides of iron. The corrosion products most probably consisted mainly of ferric oxyhydroxide (Fe_2OOH), ferric oxide (Fe_2O_3) at the outer layer and magnetite and ferrous oxide (FeO) at the inner layer. Sulfur was most probably in the form of iron sulfate (Fe_2SO_4) and iron sulfide (FeS) in both corrosion layers. There was not enough evidence, however, to show that phosphorous had significant contribution to corrosion of the DI coupon in this case.

Corrosion of the GS coupons was mainly due to sulfur containing species and chloride dissolved in the wastewater (Figure 2b). The top 20-to-25 μm thick layer of the zinc coating (Figure 2a) corroded producing probably various zinc compounds such as sulfide, sulfate of chloride and oxide of zinc as corrosion products (Figure 2b). The corroded zinc layer developed wide and deep cracks, and exposed the intact layer underneath (Figure 2d) to further corrosive attack. The uncorroded zinc layer developed fine cracks throughout the whole thickness of the coating as seen in the micrograph (Figure 2a).

Visual Inspection of Coated Coupons

The generic type, curing agents, percent volume of solids, surface preparation requirements, number of coats, dry film thickness and finish color of each tested coating are presented in Table 3. Visual assessment of the coatings using ASTM standard photographic references are presented in Figure 3. A rating of zero indicates complete failure and ten represents no failure. A close look at Figure 3 indicates that rusting is the most predominant type of deterioration among these coatings. However, rusting has led to coating failure over the entire coupon surface in only two cases: C3 and C4. These two coating systems have failed due to severe corrosion under the coating film leading to blistering, cracking, and flaking of the film over the entire surface [13]. The other coating systems appear to be in far better condition showing only minor deterioration at a few isolated locations. The results are summarized in Table 4. Based on the visual assessment, the eight coatings can be rated as follows in descending order of performance: C7>C2>C6>C1>C5>C8>C3>C4.

Electrochemical Test Results of Coated Coupons

Electrochemical tests were conducted on six of the eight coupons. The two coupons not included are those whose coatings had completely failed during field exposure (C3 and C4). The tests resulted in short- and long-term data. The short-term data consist of potential vs. time graphs showing (1) variation in potential during the first 15 minutes after immersion (2) the variation in potential during the next one hour, and (3) the variation during longer periods (between 2 and 12 hours, depending on the nature of the coating). The long-term data consist of

graphs showing variation of potential and coating resistance with time for 29 days. The short-term potential behavior of a coating is an aid to determining the presence of pinholes or defects. These may be either original or developed during field exposure. Long-term test results are expected to give an idea of the overall protective characteristics of the coating. The variation of potential and coating resistance are summarized in Table 5. Long-term potential and resistance variation of the coatings are shown in Figures 4-6. Based on these results, the six coatings are rated as follows in descending order of performance: C2>C5>C7>C6>C1>C8.

Evaluation of Test Results for Coated Coupons

The results obtained from visual and electrochemical tests and other data are presented in Table 6. The table does not include data on the two coatings which completely failed in the field exposure and did not enter electrochemical testing. The table indicates that the two tests (visual and electrochemical) yielded slightly different results. However, both of them rated C8 as the poorest of the six coatings under consideration. This coating is a coal tar epoxy resin, which is not recommended for wastewater service due to its limited resistance to H₂S and H₂SO₄ exposure. In order to get an overall performance rating of the six coatings, based on both the tests, a point system has been used. Each coating has been awarded points on a scale of 1 to 6, depending on its performance rating in individual tests. The coating securing the highest points is considered to be the best. The results are shown in Table 6. The last column of this table indicates that C2 is the best of all the coatings and that C7 is the second best. Based on the results of visual and electrochemical tests the coatings can thus be grouped as follows:

| | | |
|-----|--------------|-----------|
| (a) | Best | C2 and C7 |
| (b) | Satisfactory | C6 and C5 |
| (c) | Poor | C1 and C8 |
| (d) | Rejected | C3 and C4 |

CONCLUSIONS

1. Ductile iron, galvanized steel and brass coupons corroded severely by general and pitting corrosion and/or selective leaching, and are unsuitable for such service without adequate coating. The aluminium coupons showed crevice corrosion under sludge deposits, while the stainless steel coupons developed very minor corrosion at crevices. The latter is the most corrosion resistant metal in sewage environment. The PVC and GRP coupons also were unaffected in the sewage environment.
2. The corrosion of the coupons was caused mainly by hydrogen sulfide, sulfuric acid and chloride ion attack. Corrosion of the DI coupons progressed faster at locations of high graphite/iron ratio. Although phosphorous was detected in the corrosion products, there was not enough evidence to show that it took effective part in the corrosion reactions. The GS coupons corroded by corrosion of the zinc layer first by hydrogen sulfide, sulfuric acid and chloride ions. The corroding zinc layer cracked and exposed fresh zinc layer underneath to further corrosive attack by the environment.
3. Visual and electrochemical assessment of performance of mild steel coupons coated with eight different coatings from three well-known manufacturing companies showed that C2, vinylster, and C7, a polyamine cured epoxy, coatings were the best performers in H₂S and H₂SO₄ environment in sewage lift stations.

Acknowledgement

The authors wish to acknowledge the support of the Royal Commission for Jubail and Yanbu, General Directorate for Jubail Project, for this work under KFUPM/RI Project No. 25016.

REFERENCES

1. H. Saricimen, M. Shamim, M. Maslehuddin, and I.M. Allam, Final Report, "Research Study of Corrosion in Wastewater Lift Stations," King Fahd University of Petroleum and Minerals Research Institute, Dhahran, Saudi Arabia (1985).
2. H. Saricimen, M. Shamim and I.M. Allam. "Case study of deterioration of concrete in sewage environment in an Arabian Gulf country," *Durability of Building Materials*, 5 (1987), 145-154.
3. H. Saricimen, M.B. Mohammed, M. Shamim and B. Wascik. "A case study of corrosion of metallic structures in Sewage Systems in Arabian Gulf." The proceedings of the 4th ME Corrosion Conference, 11-13 Jan. 1988, Bahrain, part 2, pp. 193-205.
4. B. Appleton. Acid test for Middle East drain brains. *New Civil Engineering*, (Feb. 1976), pp. 20-23.
5. S.P. Ewing. "Electrochemical Studies of the Hydrogen Sulfide Corrosion Mechanics," *Corrosion*, 11, (1955), pp. 497-501t.
6. D.H. Hope, D.J. Duguet, A.H. Johannes, and P.C. Wayner. Microbiologically influenced corrosion of industrial alloys. *Material Performance*, (April 1984), pp. 14-18.
7. A.F.G. Rossouw. Corrosion in Sewers. Report, National Building Institute, Pretoria, South Africa, (1979).
8. W.P. Iverson. "Mechanism of anaerobic corrosion of steel by sulfate-reducing bacteria." *Material Performance*, (Mar. 1984), pp. 28-30.
9. C.A.H. Von Wolzogen Kuhr, and L.S. van der Vlugt. De Grafitering von Gietzer als electrobiochemich Process in anaerobic Gronden (Graphitization of cast iron as an electrobiochemical process in anaerobic soils). *Water (the Hague)*, 18, 16, (1934), 147-165 (Received from Clearinghouse for Federal Scientific and Technical Information, US Department of Commerce, Springfield, Virginia).
10. Iverson, W.P. and G.L. Olson. "Anaerobic corrosion by SRB due to highly reactive volatile phosphorous compound, microbial corrosion," Proceedings of the conference sponsored and organized jointly by the NPL and the Metals Society, held at NPL Teddington on 8-10 (March 1983).
11. NACE RP-02-81, Section 8; Published by National Association of Corrosion Engineers (1981).
12. J.H. Payer. "Electrochemical Methods for Coatings Study and Evaluation," *Electrochemical Techniques for Corrosion*, NACE/76 Meeting (Houston, TX: National Association of Corrosion Engineers, 1976).
13. Henry Leidheiser, Jr. "Towards a Better Understanding of Corrosion Beneath Organic Coatings," *Corrosion*, 39, 5, (May 1983).

Table 1. Uncoated corrosion coupons tested in the lift station

| Material | Description | In Use | Alternative |
|--|--|--------|-------------|
| 1. Galvanized steel (I) | Cut from galvanized guide tube; 2x3 inches size | Yes | - |
| 2. Galvanized steel (II) | Galvanized chain link, taken from the chain used to lift the submersible pumps | Yes | - |
| 3. Ductile Iron | Cut from ductile iron discharge pipe; 2x3 inches size | Yes | - |
| 4. Polyvinyl Chloride (PVC) | Cut from PVC pipes used for inlet pipe to the lift station | Yes | - |
| 5. AISI 316 SS | Cut from commercially available SS plate; 2x3 inches size | - | Yes |
| 6. Aluminium | Cut from commercially available aluminium plate; 2x3 inches size | - | Yes |
| 7. Brass | Cut from commercially available brass plate; 2x3 inches size | - | Yes |
| 8. Glass fibre reinforced plastic (GFRP) | Cut from commercially available GFRP pipe | - | Yes |

- = Not applicable

Table 2. Summary of uncoated coupon test results

| Coupon | Description of Corrosion | Corrosion rate MPY | Description of Deposits |
|------------------|---|--------------------|--|
| Ductile Iron | 40 mils deep pits | 17.5 | 1 mm thick. Loose light brown top, black bottom |
| Galvanized Steel | 20-40 mils deep pits | 14.5-19.4 | <1/2 mm thick, Brown top layer. Black lower, layer |
| Aluminium | Thinning and Grooving | 7 | No deposits. Light staining |
| Brass | General and pitting corrosion, and selective leaching | 24.6 | Some whitish deposits. Thin film distributed in patches, golden and brown coloration |
| AISI 316 SS | Mild crevice | 0.85 | No deposits |
| PVC | None | 0 | No deposits |
| GRP | None | -4.8 | Weight gain due to water absorption |

Table 3. Types and characteristics of tested coatings

| Code | COATING SYSTEM DESCRIPTION | | Volume % Solids | | Color of finish | Recom- mended sub- strates | Surface Prepre- ration | Dry film thickness (μm) | | Remarks |
|------|---|--|-----------------|----------|-------------------|-------------------------------------|---|---|----------|---|
| | Primer (1st coat) | Top coat 2nd coat | 1st coat | 2nd coat | | | | 1st coat | 2nd coat | |
| C1 | Vinyl ester with binder | N/A | 100% | N/A | White | Steel | SA2.5 | 200-300 | N/A | One coat system |
| C2 | Vinyl ester with binder | N/A | 100% | N/A | White | Steel | SA2.5 | 200-300 | N/A | One coat system |
| C3 | A high performance coal tar epoxy, consisting of two components | Same as first coat | 71% | N/A | Black | Steel | SA2.5 | 100-200 | 100-200 | |
| C4 | High build micaceous iron oxide primer based on chlorinated rubber | High build chlorinated rubber with inert pigments | 42% | 35-41% | Metallic white | Steel | SA2.5 | 75-100 | 60-75 | |
| C5 | A two component, high build, polyamide cured epoxy coating | Same as first coat | 72% | 72% | Black | Steel | SA2.5 | 125-150 | 125-150 | |
| C6 | A solvent free two pack compound based on epoxy resins, cured with amine hardner | A solvent free amine cured, two component epoxy resins coating | 100% | 100% | Greenish grey | Concrete steel | SA2.5 for steel. For concrete, see remarks column | 3000 to 5000 | 7450 | Surface prep. for Concrete: -Free from litanice by sand blasting. -Moisture content concrete should be max. 4%. |
| C7 | A polyamine cured epoxy coating | N/A | 100% | N/A | White | Steel | SA2.5 | 300 | N/A | One coat system |
| C8 | Amine adduct cured coal tar epoxy | N/A | 54% | N/A | Black | Steel | SA2.5 | 200 | N/A | Same as above |

N/A = Not applicable

Table 4. Visual assessment of coating deterioration

| Code | Condition of coating upon retrieval | pH of Surface Moisture | Rusting ASTM D610 | Blistering ASTM D714 | Checking ASTM D660 | Cracking ASTM D661 | Flaking ASTM D772 | ERrosion ASTM D662 | Microscopic Pinholes | Mechanical Wear | Microscopic Scratches |
|------|---|------------------------|--------------------|----------------------|--------------------|--------------------|-------------------|--------------------|----------------------|-----------------|-----------------------|
| C1 | Patches of black sludge deposits on surface | 6-7 | E=9 C=0 S=10 | 10 | 10 | 10 | 10 | 10 | 5-6 | 10 | 10 |
| C2 | Thin pasty deposits all over | 6-7 | 10 | 10 | 10 | 10 | 10 | 10 | 8-9 | 7 | 4 |
| C3* | Same as above, and softened coating | 6-7 | 0 | * | * | * | * | * | * | * | * |
| C4* | Same as above | 6-7 | 0 | * | * | * | * | * | * | * | * |
| C5 | Thin layer of clear deposits | 6 | E=9 C=0 F=10 | 10 | 10 | 10 | 10 | 10 | 10 | 10 | 10 |
| C6 | Thin layer of clear deposits in some areas | 6 | 10 | 10 | 10 | 10 | 10 | 10 | 5-6 | 10 | 10 |
| C7 | Same as above | 4-5 | 10 | 10 | 10 | 10 | 10 | 10 | 10 | 10 | 10 |
| C8 | Same as above | 6-7 | E=0 | 10 C-1 S=10 | 10 | 10 | 10 | 10 | 10 | 10 | 10 |

E = Edges; S = Flat Surface; C = Corners or projections; * = Since coating had completely failed, grading of deteriorations other than rusting was not possible.

Table 5. Summary of electrochemical test data

| Code | Film Thickness (µm) | Initial Potential | | Potential Drop | | Potential Regain | | Final Drop in Potential | | Resistance variations | | | Conclusion | |
|------|---------------------|-------------------|-----------|----------------|------------------|------------------------|-----------------------------|-------------------------|-----------------|-----------------------|---------------------|-----------------|------------|---|
| | | Initial -mv | Final -mv | Difference mv | Drop rate mv/min | Regained potential -mv | Final Drop potential mv/min | Av. Value -mv | Drop Rate mv/hr | Initial Value M-Ω | Initial Drop to M-Ω | Regained to M-Ω | | Final Average Value |
| C1 | 200-300 | a) 210 | 480 | 270 | 18 | - | - | 620 | - | - | 5 M-Ω | * | 5-8 M-Ω | Initial permeability is higher than C5 but lower than C6. Film breakdown started in field exposure. |
| | | b) 480 | 645 | 165 | 0.34 | - | - | - | - | - | 10 M-Ω | ? | ? | |
| C2 | 200-300 | a) 414 | 414 | 0 | 0 | - | - | ? | - | >20 | ? | ? | ? | Initial permeability very low and no pinholes present initially. It appears that coating is still absorbing water and point of breakdown is not reached. For definite conclusion more testing is necessary. |
| | | b) 414 | 450 | 50 | | | | | | | | | | |
| C5 | 250 | 1) 395 | 636 | 241 | 5.35 | 205 | 0.011 | * | * | >20 | 11.8 M-Ω | >20 M-Ω | >20 M-Ω | Permeability of sound coating is low but pinholes are present. Point of coating breakdown not yet reached. |
| | | 2) 636 | 700 | 64 | 0.08 | | | | | | | | | |
| C6 | 3500 | 654 | 960 | 306 | 12 | 465 | 0.52 | 620 | 1.23 | ? | 0 K-Ω | 16 K-Ω | 4-5 K-Ω | Permeability high due to pinholes. Point of breakdown after 24 hrs. of lab test. |
| | | 425 | 500 | 75 | 0.5 | 300 | 3.33 | 535 | <3.25 | >20 | - | >20 M-Ω | 0.18 M-Ω | |
| C7 | 300 | | | | | 005 | 0.065 | | | | | | | Permeability very low, no voids and pinholes in the beginning. Coating film breakdown started after 450 hrs. in the test. |
| C8 | 200 | 548 | 618 | 70 | 0.7 | * | * | 625 | 0.015 | >20 M-Ω | * | * | 4-6 M-Ω | Permeability moderate but film breakdown has started during field exposure |

* = Drop/Regain not noticed. ? = Not clear. - = Not measured/calculated. M-Ω = Mega-Ohms. K-Ω = Kilo-Ohms.

Table 6. Evaluation of coating test results

| Coating System | Generic Type | Visual inspection | | Electrochemical | | Total Points | Overall Rating |
|----------------|-----------------------------------|-------------------|--------|-----------------|--------|--------------|----------------|
| | | Rating | Points | Rating | Points | | |
| C1 | Vinyl ester | 3 | 4th | 2 | 5th | 5 | 4th |
| C2 | Vinyl ester | 5 | 2nd | 6 | 1st | 11 | 1st |
| C5 | Polyamide cured epoxy coating | 2 | 5th | 5 | 2nd | 7 | 3rd |
| C6 | Amine cured epoxy resin | 4 | 3rd | 3 | 4th | 7 | 3rd |
| C7 | Polyamide cured epoxy | 6 | 1st | 4 | 3rd | 10 | 2nd |
| C8 | Amine adduct cured coal-tar epoxy | 1 | 6th | 1 | 6th | 2 | 5th |

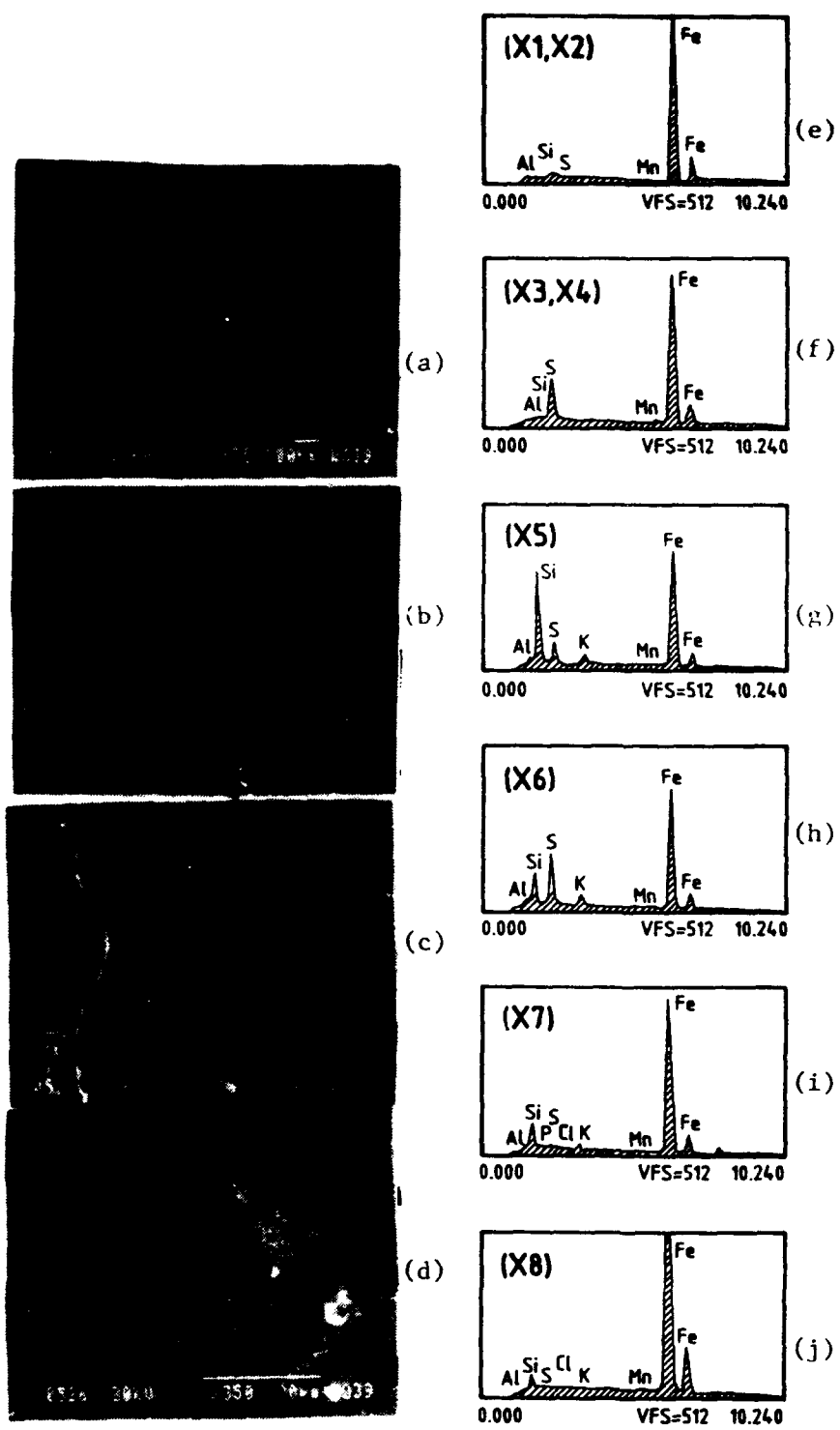


Figure 1: (a),(b), (c) and (d) SEM micrograph of a polished section showing corrosion of ductile iron in the lift station. (e) through (j) EDX spectra of corresponding points as marked on the micrographs.

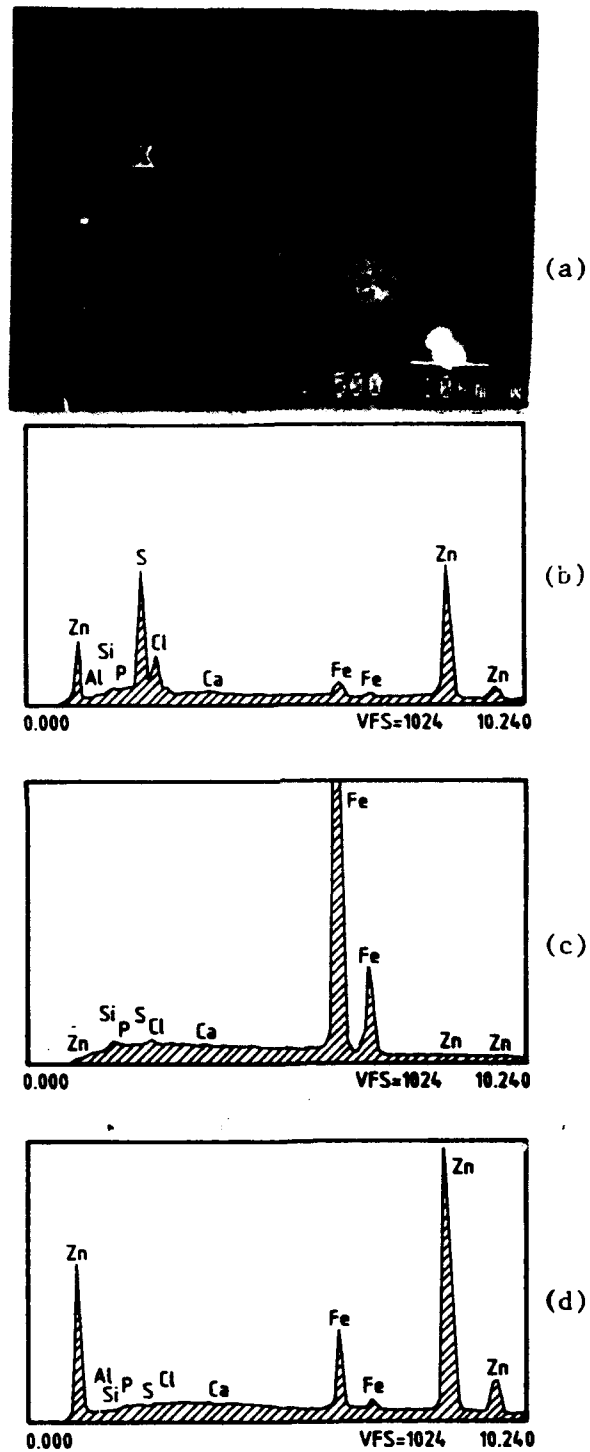


Figure 2: (a) SEM micrograph of a polished section showing corrosion of galvanized steel coupon in the lift station. (b) through (d) EDX spectra at points (X1) through (X3) as marked on the micrograph.

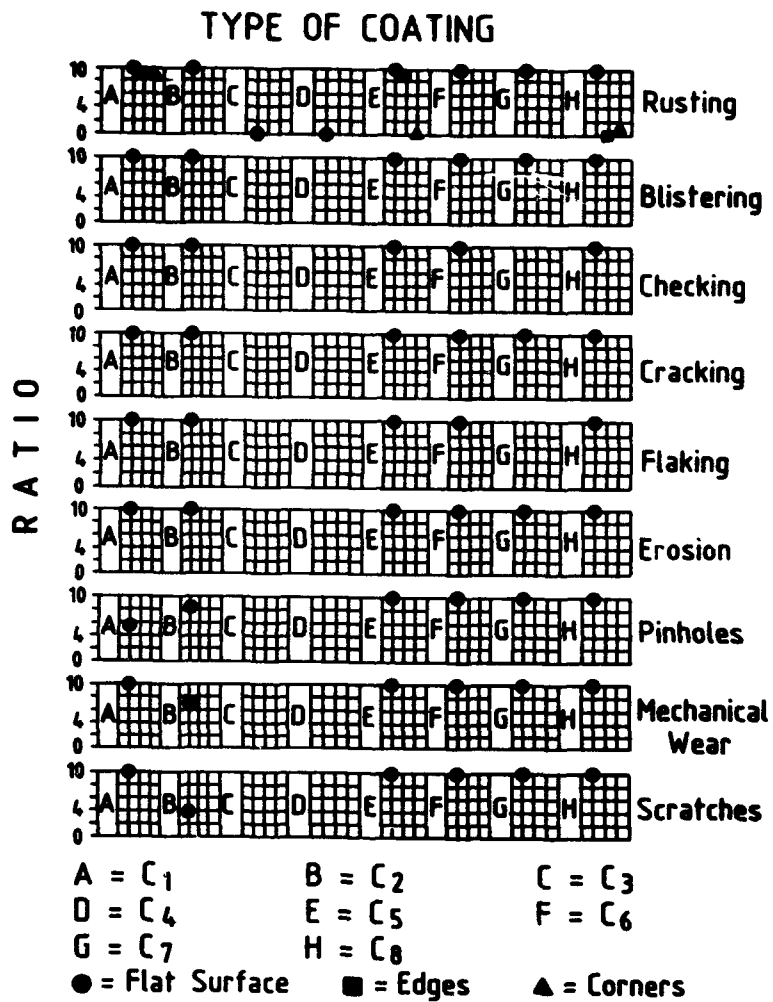


Figure 3: Visual assessment of coating deterioration.

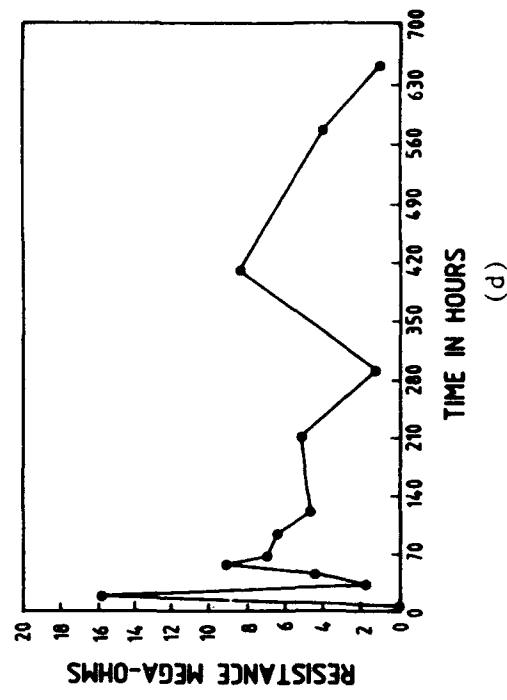
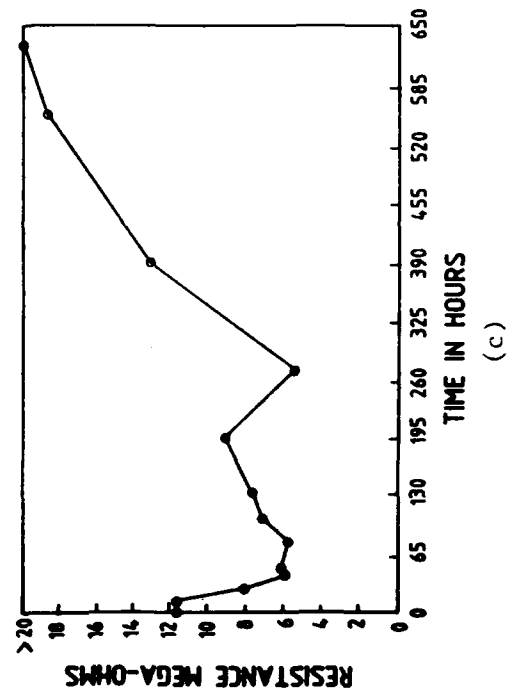
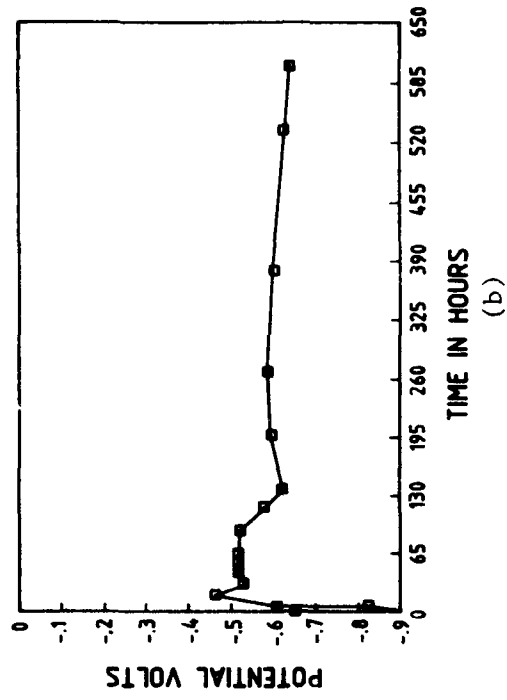
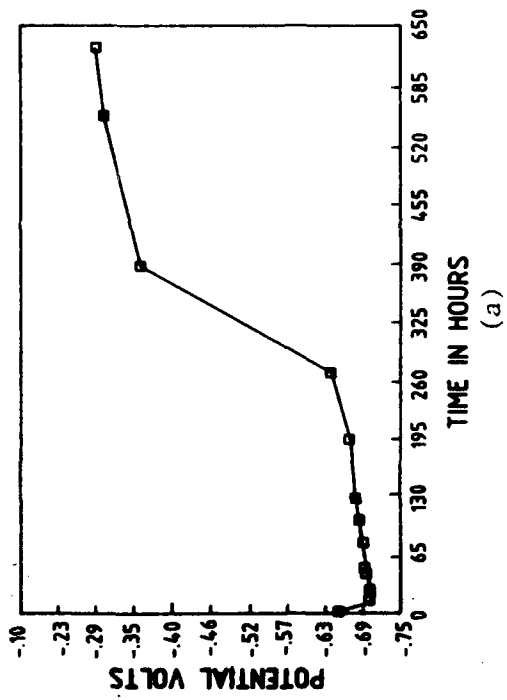


Figure 4: Long-term potential and resistance variation. (a) and (c) Coating C1, and (b) and (d) Coating C2.

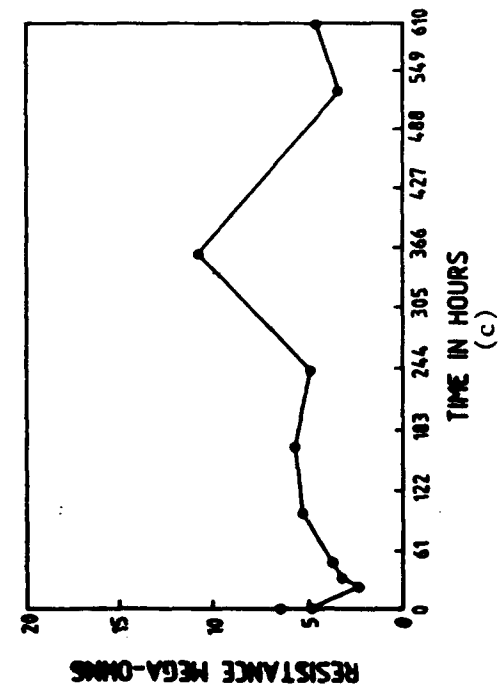
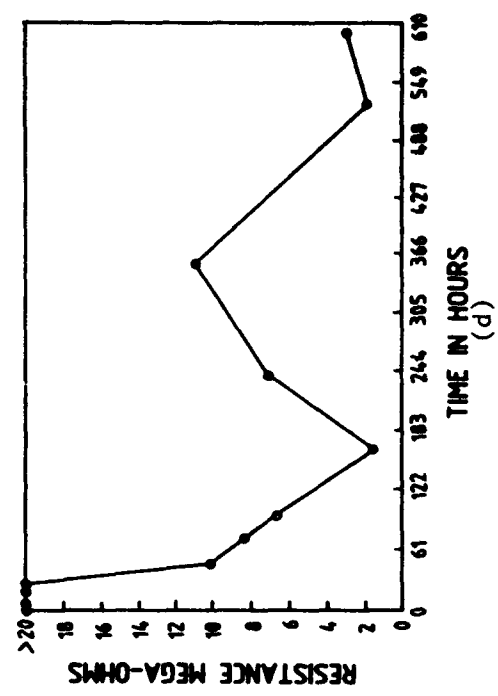
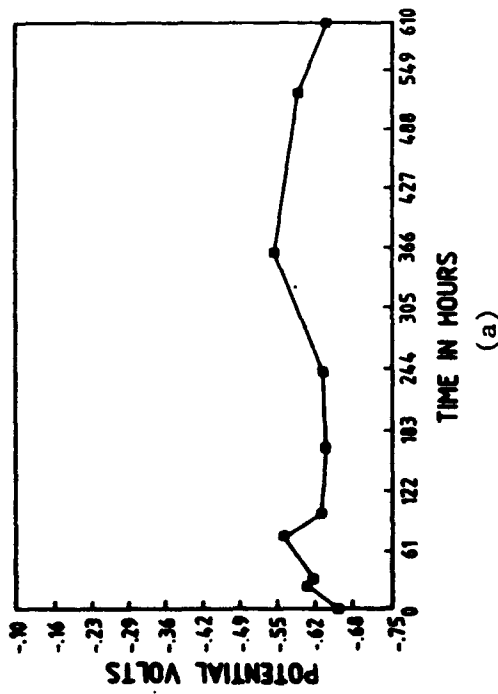
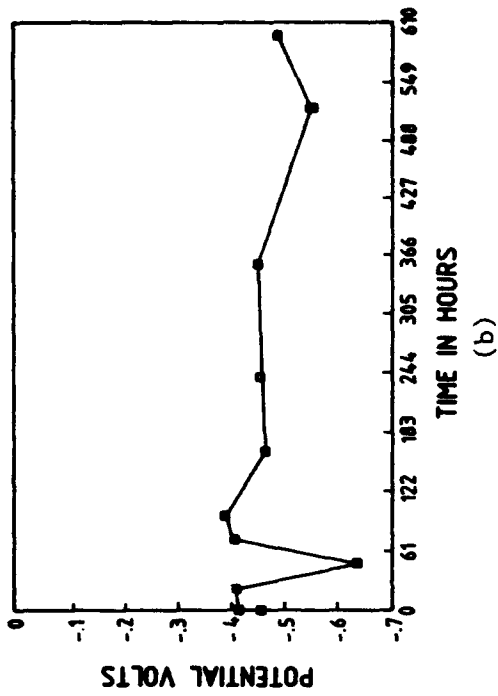


Figure 5: Long-term potential and resistance variation: (a) and (c) Coating C5, and (b) and (d) Coating C6.

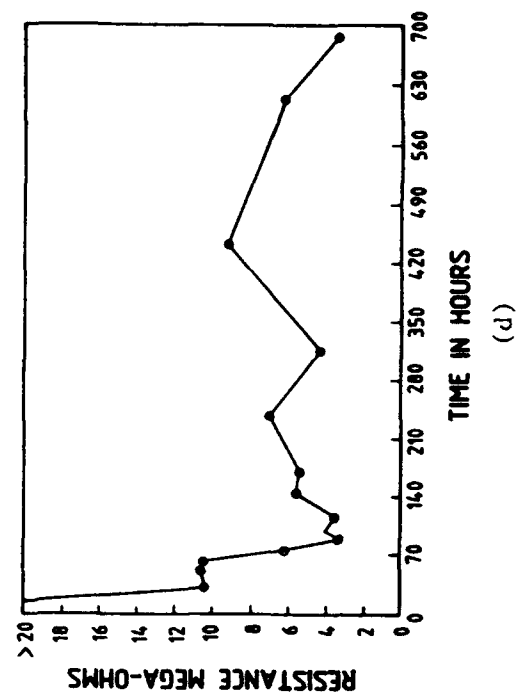
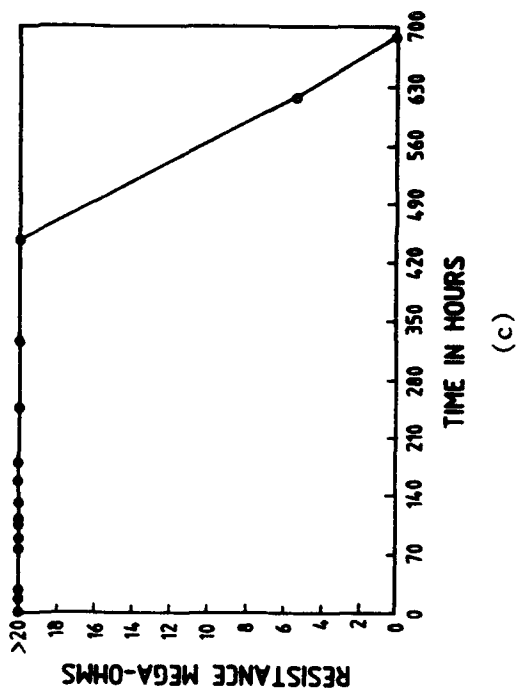
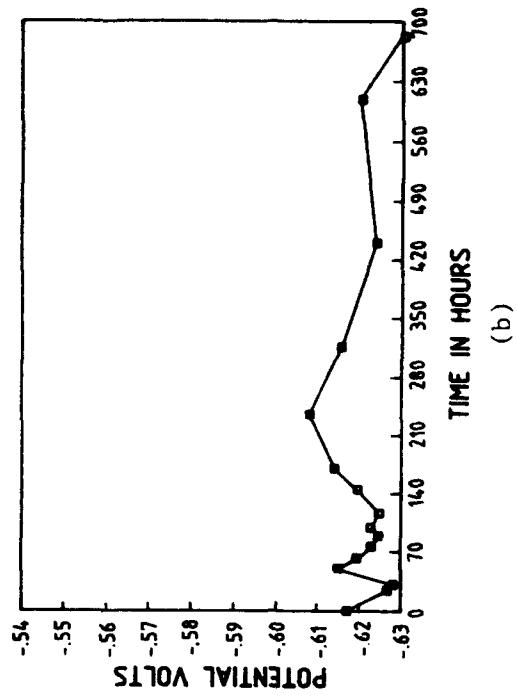
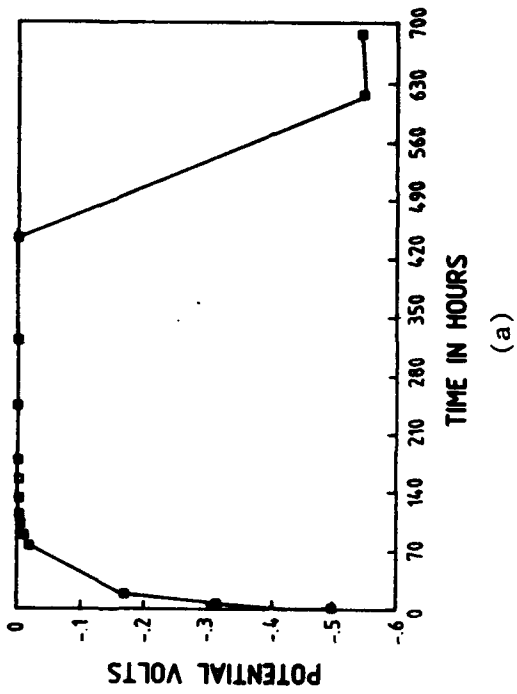


Figure 6: Long-term potential and resistance variation: (a) and (c) Coating C7, and (b) and (d) Coating C8.

**An ^{18}O /SIMS Study of Oxygen Transport in Thermal
Oxide Films Formed on Silicon**

R.J. Hussey
Institute for Microstructural Sciences
National Research Council of Canada
Ottawa, Canada K1A 0R9

G.I. Sproule
Institute for Microstructural Sciences
National Research Council of Canada
Ottawa, Canada K1A 0R9

D.F. Mitchell
Institute for Microstructural Sciences
National Research Council of Canada
Ottawa, Canada K1A 0R9

M.J. Graham
Institute for Microstructural Sciences
National Research Council of Canada
Ottawa, Canada K1A 0R9

Abstract

The growth and transport in oxide films formed on (100) silicon (p-type) in oxygen at 10 torr (1.33 kPa) at temperatures of 950 and 1050°C were studied using the ^{18}O /SIMS technique. Samples were oxidized sequentially, first in $^{16}\text{O}_2$ and then in $^{18}\text{O}_2$, for various times totalling up to 48 h to produce films in the thickness range 2-100 nm. Parabolic and parabolic oxidation kinetic behaviour, derived from the SIMS data, were shown at 950 and 1050°C, respectively. Sputter profiles of both ^{18}O - and ^{16}O -containing species (Si_2O^+) showed the distribution of each within the thin oxide films. The ^{18}O is localized in the vicinity of the gas-oxide interface (so-called surface region) and at the Si-SiO₂ interface (so-called interface region). The concentration of ^{18}O in both regions increases with increasing time of exposure to $^{18}\text{O}_2$, but the rate of increase of ^{18}O in the interface region and its proportion relative to the surface region are greater. The maximum in the SIMS profile of the ^{18}O -containing species in the surface region indicates that oxygen has diffused through the oxide during oxidation. The SIMS data suggest that the inward diffusion probably occurs along short circuit paths such as micropores extending to the Si-SiO₂ interface.

Key terms: silicon, thermal oxide, kinetics, SIMS, oxygen transport

NRC No. 35737

Introduction

Thermally formed silicon dioxide on Si has been studied for many years because of its use in the fabrication of silicon-based devices. Current interest is being maintained by industrial requirements for very thin dielectric SiO₂ films for submicron-scale integrated circuits. In 1965 Deal and Grove¹ showed that the oxidation growth kinetics in dry oxygen could be expressed by a linear-parabolic equation for films thicker than about 30-50 nm. Since that time there have been many attempts to model the oxidation behaviour for thicknesses >30 nm, where the data deviate from the linear-parabolic relationship. There is still much discussion regarding the most appropriate model to explain the kinetic behaviour²; there appears to be no general agreement regarding further experimentation to resolve the issue. More recently, transport mechanisms during thermal oxide growth have been studied using ¹⁸O as a tracer. These studies³⁻⁸ have shown that inward oxygen diffusion occurs. The determination of the ¹⁸O distribution within the oxide film also provided valuable additional information on the oxidation mechanism. The present paper deals with the oxidation of Si(100) over the oxide thickness range 2-100 nm at 950 and 1050°C and an oxygen pressure of 10 torr (1.33 kPa) using the ¹⁸O/SIMS technique⁹ developed for metal-oxygen systems. Molecular species of the type M₂O⁺ rather than the usual O⁻ ions were profiled to elucidate the transport properties in the oxide and to substantiate the oxide growth mechanism.

Experiment

Samples (approximately 3 cm²) were cut from a 4 inch double-sided polished wafer of p-type, Si(100), resistivity 6-10 Ω-cm (impurities >1 ppm by weight are: C 2, N 4, O 34). They were etched for 1 min in 1% HF, rinsed with doubly-distilled water and subsequently dried in a jet of Zero Gas compressed air and inserted immediately into a high vacuum oxidation apparatus. The HF etch removes the native oxide completely, leaving a stable, hydrogen-terminated surface^{10,11}. Oxidation experiments were carried out for various times at 950 and 1050°C at a system pressure of 10 torr (1.33 kPa). Prior to each experiment the reaction chamber was exposed to oxygen at about 1 torr (133 Pa) for 15 min. All samples were heated to temperature in O₂ and allowed to cool in O₂ at the end of the experiment; they were usually oxidized sequentially, first in ¹⁶O₂ (containing <3 ppm H₂O) and then in ¹⁸O₂ (nominally 97.0-99.0% ¹⁸O and containing a few μm H₂O). Oxidized samples were examined by SIMS depth profiling to determine the oxygen distribution. The SIMS analyses were performed as described previously⁹, except that sputtering was done with 1 keV xenon ions at 33° off the sample normal. SIMS profiles were obtained for all oxidized samples and the results are presented as atomic concentration versus sputter time in minutes. The profile for the species containing ¹⁶O is: ²⁸Si₂¹⁶O⁺ (mass 72); the corresponding profile for that containing ¹⁸O is: ²⁸Si₂¹⁸O⁺ (mass 74). The profile for ²⁸Si₃⁺ (mass 84) is a convenient indication of the Si-SiO₂ interface, since there is no Si₃⁺ signal from the oxide. The mass 74 signal was corrected for the contribution of the ³⁰Si²⁸Si¹⁶O⁺ and ²⁹Si₂¹⁶O⁺ signals by subtracting 6.96% of the mass 72 peak. A

suitable value for the sensitivity of the mass 84 signal was found to be 3% of the mass 72 or mass 74 signals.

Results and Discussion

Kinetics

It was not possible to determine the oxidation kinetics by continuous oxygen uptake measurements. Oxide film thicknesses were estimated instead from the mass 84 profile produced during SIMS analysis of each oxidized sample. The maximum in the mass 84 was determined to be indicative of the position of the Si-SiO₂ interface. The rationale for using the mass 84 maxima is described in the Appendix. The film thickness was calculated from the average sputter rate (nm/min), which was determined by comparing oxide thicknesses of many samples oxidized at both 950 and 1050°C measured by transmission electron microscopy (TEM) with sputter times at the mass 84 maximum. Figures 1 and 2 show the kinetic data thus obtained for 950 and 1050°C for a series of samples oxidized from a few minutes up to 48 h. Each point on the graph represents a separate experiment. "Intermediate points" for each experiment were determined from the SIMS data from the area under the mass 72 (²⁸Si₂¹⁶O⁺) profile. This area gives the percentage of the total oxide film present as ¹⁶O-oxide and thus the extent of oxidation at the changeover from ¹⁶O₂ to ¹⁸O₂. The calculated sputter time at the gas change is approximately the same for any given exposure time in ¹⁶O₂. Both the final and intermediate points for each experiment at 950°C are shown in Figure 1 (as a circle and a cross, respectively). The data points from zero time to 12 h may be best fitted to a parabolic rate equation (solid line), while the data from 20 h onwards show a good fit to a linear rate equation (dashed line) as demonstrated by least squares fits to these data. The final and intermediate points for the data at 1050°C are identified in Figure 2 (again as a circle and a cross, respectively). In contrast to the 950°C data there is no obvious long term linear region and the data at all times are best fitted to a parabolic rate relation as shown by the solid line in Figure 2.

In many studies the Deal-Grove equation¹

$$x^2 + Ax = B(t + t_0) \quad (1)$$

where x is the oxide thickness, t is the oxidation time, t_0 is the initial oxidation time corresponding to the initial oxidation thickness and B and (B/A) are the parabolic and linear rate constants, respectively, has been used to describe the oxidation kinetics. This equation can be used in its limited form for thinner films

$$x = (B/A)(t + t_0) \quad (2)$$

to get the value of the linear rate constant, (B/A), from the kinetic data at 950°C (dashed line in Figure 1). This equation is appropriate even if there is an initial parabolic region. A value of 0.012 nm/min is obtained. An estimate from other data by van der Meulen gives a value for the rate constant of 0.03 nm/min¹². The oxidant in this case, however, was a 1% O₂/N₂ mixture at 1 atm (100 kPa) total pressure. With regard to the initial data at 950°C, which conforms very closely to parabolic behaviour, the Deal-Grove equation can be further simplified to the form

$$x^2 = Bt \quad (3)$$

where t_0 is essentially zero under the present sample preparation procedures. The value of the parabolic rate constant, B, is found to be equal to 0.67 nm²/min ($\equiv 0.11 \text{ \AA}^2/\text{sec}$ at 1 torr, where B is directly proportional to pressure¹). This value is very similar to those calculated by Adams et al.¹³ from a collection of published data extrapolated to 953°C and 1 torr ranging from 0.08-0.25 $\text{\AA}^2/\text{sec}$. Adams et al. found that their data fitted closely to a parabolic rate law, apart from a short initial deviation, for oxide thicknesses up to about 11 nm.

The value for B derived from the 1050°C kinetic data is 3.54 nm²/min. This value and that calculated at 950°C above also agree closely with those extracted by Han and Helms¹⁴ from fitting a parallel oxidation model to experimental growth rates from various authors. In the case of the 1050°C data, there is no obvious linear region, but as Han and Helms point out a linear region between two parabolic regions would be of short duration at increasing temperature and decreasing pressure.

SIMS Data

Analysis of the SIMS profiles for samples oxidized only in ¹⁸O₂ permits the ¹⁶O content of the oxide films to be determined¹⁵. After allowing for the ¹⁶O content of the ¹⁸O₂ and for the fact that the HF pretreated surface is essentially oxide-free, there remains a small amount of ¹⁶O. It is believed that this arises from exchange of ¹⁸O in the film with ¹⁶O from atmospheric water vapour during transfer to the SIMS system¹⁶. The oxides produced at both 950 and 1050°C are very clean; they are contaminated only with adventitious C on the surface as well as ~0.4 at% N within the bulk (as detected by XPS). The N impurity concentration is most likely due to trace amounts within the oxygen gas (¹⁸O₂).

Examples of SIMS profiles for samples oxidized at both 950 and 1050°C for short and long times are shown in Figures 3a and b, respectively. In Figure 3a the sample was oxidized at 950°C for 24 h in ¹⁶O₂ and 12 h in ¹⁸O₂ to produce an oxide 39.1 nm thick. In Figure 3b the sample was oxidized at 1050°C for 2 h in ¹⁶O₂ and 1 h in ¹⁸O₂ to produce an oxide 26.7 nm thick. The Si₂¹⁸O⁺ SIMS profiles show that the ¹⁸O is

concentrated in two distinct regions in the oxide film, namely, in the vicinity of the O_2 - SiO_2 (so-called surface region⁷) and Si - SiO_2 (so-called interface region⁷) interfaces. For relatively thin oxides grown over short times with proportionally large $^{18}O_2$ exposure times, the two regions show some overlap. For thicker films and relatively long oxidation times, however, the two ^{18}O regions are well-separated. The percentage of ^{18}O in the oxide at both 950 and 1050°C is similar for a given ratio of oxidation time in $^{16}O_2$ to that in $^{18}O_2$, showing that the oxidation process does not change with time.

The amount of ^{18}O in the surface and interface regions increases with increasing time of exposure to $^{18}O_2$. This is shown in Figures 4a and b for samples oxidized at 950 and 1050°C for a fixed time in $^{16}O_2$ and increasing times in $^{18}O_2$. This observation is in agreement with the results of Rochet et al.⁴ for oxidation pressures of 0.1 to 100 torr (0.0133 to 13.3 kPa) for oxide thicknesses of 5 to 260 nm grown at 930°C and with those of Han and Helms⁷ at 1 atm pressure (100 kPa) and 1000°C for thicknesses in the range 5-15 nm. Han and Helms determined that at this pressure the surface peak contains about 7% of the total ^{18}O concentration for 1 h in $^{16}O_2$ and 0.5 h in $^{18}O_2$ and an oxide thickness of 13.0 nm grown in $^{18}O_2$. The present results show, however, that for similar exposure times the surface peak comprises about 32% and 63% of the total ^{18}O concentration at 950 and 1050°C for ^{18}O -oxide film thicknesses of 1.4 and 4.8 nm respectively. Rochet et al.⁴ have determined, however, that the percentage of ^{18}O in the surface region increases with decreasing film thickness and oxygen pressure and can reach 50% for 5 nm thick films at 10 torr (1.33 kPa). The present data thus appear consistent with those in the literature.

In agreement with the data of Han and Helms⁷, Figure 4 shows that both the ^{18}O surface and interface peaks increase with increasing oxidation time. The rate of increase in the amount of ^{18}O in the interface region is greater than that in the surface region in both cases and the proportion of ^{18}O in the interface region increases with time. The inward movement of the profile maxima in the interface region reflects the increase in oxide thickness with increasing time of exposure to $^{18}O_2$ and continuing oxide formation at this interface. The increase in the amount of ^{18}O present in the surface region could be the result of the inward displacement of ^{16}O within the network oxide. Rochet et al.⁴ refer to this as a stepwise motion of network oxygen atoms. Approximate values for the network oxygen diffusion coefficients may be calculated from the surface region profiles shown in Figures 4a and b. The average values for 950 and 1050°C are found to be 2×10^{-19} and 4×10^{-18} $cm^2 sec^{-1}$, which agree with those quoted by Han and Helms⁷. The transport process is equivalent to an oxygen uptake in the oxide layer and is confirmed by the intermediate points calculated earlier (Figures 1 and 2) corresponding to the changeover from $^{16}O_2$ to $^{18}O_2$ lying on the kinetic curve defined by the final data points. If none of the ^{18}O in this region was due to oxide formation then these intermediate points would not fit on this curve.

The ^{18}O profiles obtained using the ^{18}O /SIMS technique⁹ for oxide films grown sequentially in $^{16}O_2$ and $^{18}O_2$ can be used to distinguish between lattice and short-

circuit diffusion¹⁶. The form of the ¹⁸O profiles obtained in the present case, namely localization at the O₂-SiO₂ and Si-SiO₂ interfaces, indicates that during oxidation oxygen has migrated through the film by short circuit diffusion to form new oxide at the Si-SiO₂ interface. These short circuit paths may be pores or channels extending to the Si-SiO₂ interface. Irene^{17,18} has postulated the existence of fine pores to explain the kinetic growth behaviour of SiO₂ films at temperatures in the range 780 to 980°C at 1 atm (100 kPa). Such micropores have been observed directly by TEM and have been found to be of the order of 1 nm in diameter for 9 nm thick oxide films grown in dry oxygen¹⁹. Such pores could allow rapid transport of oxidant to the Si-SiO₂ interface, short circuiting the slower lattice diffusion, particularly at lower temperatures.

Conclusions

The oxidation kinetics of Si(100) at 950°C in 10 torr (1.33 kPa) O₂ are consistent with linear oxide growth for oxide thicknesses exceeding about 20 nm. For thicknesses from 2-20 nm, and for the entire thickness range at 1050°C, the kinetics conform closely to a parabolic rate equation. SIMS analyses have confirmed that oxidation occurs by oxygen transport through the growing oxide film. New oxide is formed in the outer part of the film, but the predominant reaction is that of oxide formation at the Si-SiO₂ interface. The SIMS data also support the view that short circuit diffusion via fine micropores in the oxide film predominates under the present conditions.

Acknowledgments

The authors would like to thank J.A. Bardwell for valuable discussions, J. McCaffrey for his skilful TEM determination of oxide thicknesses and Northern Telecom Ltd., Nepean, Ontario, for the kind donation of the Si wafers.

Appendix

The Si₃⁺ (mass 84) or Si₄⁺ (mass 112) intensity-depth profiles can be used to give an indication of the position of the Si-SiO₂ interface, as the intensity rises abruptly when the Si substrate has been reached. Four different points on the mass 84 and mass 112 profiles, namely, the mass 84 maximum, 50% of the mass 84 maximum, the mass 112 maximum and 50% of the mass 112 maximum, were selected as possible indicators of the Si-SiO₂ interface. The sputter times for four samples oxidized at 950°C were determined at each of the four points and these values were plotted against the oxide thickness of each sample as determined from XPS. Details of the method used to calculate oxide thicknesses from XPS are given elsewhere²⁰. The data points for the mass 84 maximum from each sample showed the closest extrapolation through zero thickness and this point on the mass 84 profiles was therefore taken as

the most appropriate indication of the Si-SiO₂ interface. Figure A1 (short term) shows a typical mass 84 profile (in count rate per second versus sputter time) in the vicinity of the Si-SiO₂ interface for a sample oxidized for a total of 1.1 h at 950°C. The sputter time at this maximum is converted to oxide thickness using the sputter rate calculated from a comparison of sputter times at this point with oxide thicknesses obtained from transmission electron micrographs of fracture sections of samples oxidized for different times at both 950 and 1050°C.

For oxide thicknesses greater than about 25 nm at either 950 or 1050°C, there is no clear maximum in the mass 84 profile as shown in Figure A1 (long term) for a sample oxidized for a total time of 36 h at 950°C. In such cases the position of the Si-SiO₂ interface is estimated as follows. The statistical average of the difference between the sputter times at 85% of the Si₂¹⁸O⁺ (mass 74) maximum (position P1, Figure A2) prior to the mass 84 maximum and at the mass 84 maximum (position P2, Figure A2) is determined from the SIMS data for short term experiments. (85% of the signal in the region of an oxide-substrate interface has been found by experience to be a position close to this interface for oxide-metal systems.) This difference value (P2 - P1) is then added to the sputter time at 85% of the mass 74 maximum for the long term experiments to give the estimated sputter time for the mass 84 maximum. The value is 0.6 min ($\sigma = 0.4$ min) for the 950°C data and 1.2 min ($\sigma = 0.6$ min) for the 1050°C data.

References

1. B.E. Deal, A.S. Grove, *J. Appl. Phys.*, 36 (1965): p. 3770.
2. J. Blanc, *The Physics and Chemistry of SiO₂ and the Si-SiO₂ Interface*, (Ed. C.R. Helms, B.E. Deal: Plenum, 1988), p. 1.
3. E. Rosencher, A. Straboni, S. Rigo, G. Amsel, *Appl. Phys. Lett.*, 34 (1979): p. 254.
4. F. Rochet, B. Agius, S. Rigo, *J. Electrochem. Soc.*, 131 (1984): p. 914.
5. J.A. Costello, R.E. Tressler, *J. Electrochem. Soc.*, 131 (1984): p. 1944.
6. J.D. Cawley, J.W. Halloran, A.R. Cooper, *Oxid. Met.*, 28 (1987): p. 1.
7. C.-J. Han, C.R. Helms, *J. Electrochem. Soc.*, 135 (1988): p. 1824.
8. S. Rigo, *The Physics and Chemistry of SiO₂ and the Si-SiO₂ Interface*, (Ed. C.R. Helms, B.E. Deal: Plenum, 1988), p. 75.
9. D.F. Mitchell, R.J. Hussey, M.J. Graham, *J. Vac. Sci. Technol.*, A1 (1983): p. 1006.
10. P. Jakob, P. Dumas, Y.J. Chabal, *Appl. Phys. Lett.*, 59 (1991): p. 2968.
11. M. Offenbergl, M. Liehr, G.W. Rubloff, *J. Vac. Sci. Technol.*, A9 (1991): p. 1058.
12. Y.J. van der Meulen, *J. Electrochem. Soc.*, 119 (1972): p. 530.
13. A.C. Adams, T.E. Smith, C.C. Chang, *J. Electrochem. Soc.*, 127 (1980): p. 1787.
14. C.-J. Han, C.R. Helms, *J. Electrochem. Soc.*, 134 (1987): p. 1297.
15. R.J. Hussey, D.A. Bisailion, G.I. Sproule, M.J. Graham, *Corrosion Science*, in press.
16. A. Atkinson, *Rev. Mod. Phys.*, 57 (1985): p. 437.

17. E.A. Irene, *J. Appl. Phys.*, 54 (1983): p. 5416.
18. E.A. Irene, *J. Electrochem. Soc.*, 125 (1978): p. 1708.
19. J.M. Gibson, D. Dong, *J. Electrochem. Soc.*, 127 (1980): p. 2722.
20. D.F. Mitchell, K.B. Clark, J.A. Bardwell, W.N. Lennard, G.R. Massoumi, I. Mitchell, to be published.

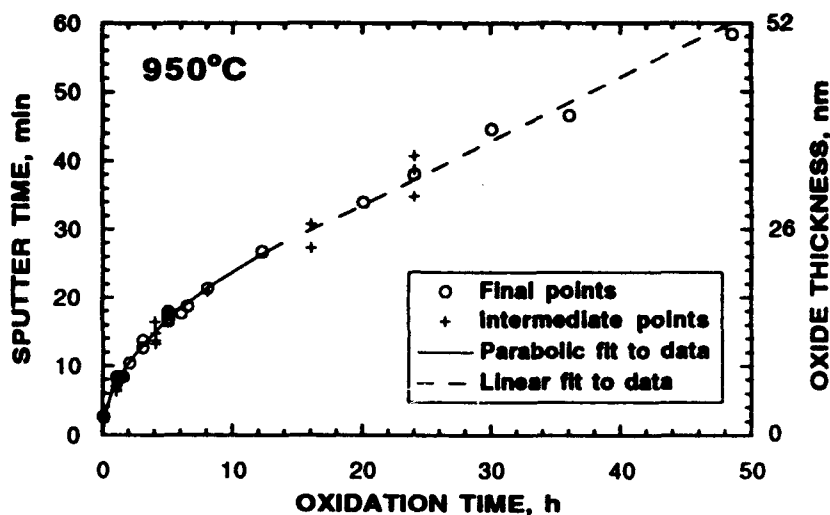


Fig. 1. Oxidation kinetics of (100)Si at 950°C and 1.33 kPa O₂ pressure. The final points (circles) were determined from the maxima in the Si₃⁺ SIMS profiles, which indicate the position of the Si-SiO₂ interface. The intermediate points (crosses) were determined from the area under the mass 72 (Si₂¹⁶O⁺) profile, which gives the percentage of the total oxide present as ¹⁶O-oxide and thus the amount formed at the changeover from ¹⁶O₂ to ¹⁸O₂. The solid and dashed lines are parabolic and linear least squares fits to the data.

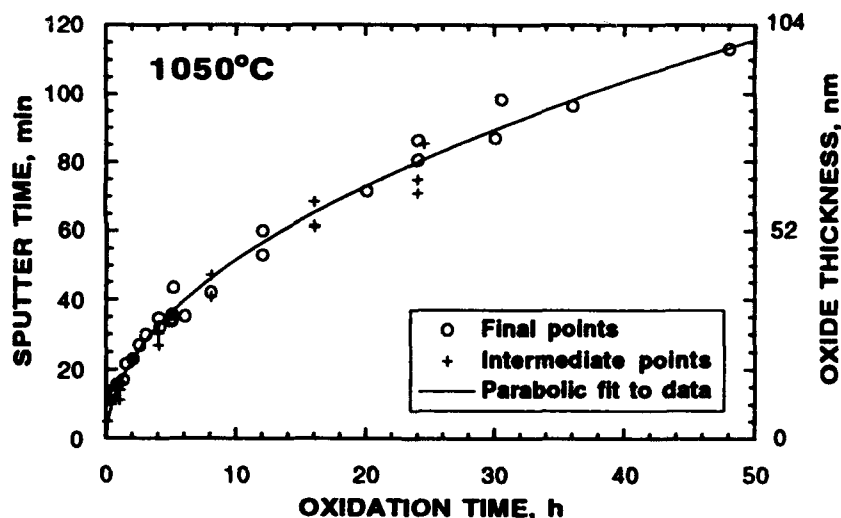


Fig. 2. Oxidation kinetics of (100)Si at 1050°C and 1.33 kPa O₂ pressure. The final points (circles) were determined from the maxima in the Si₃⁺ SIMS profiles, which indicate the position of the Si-SiO₂ interface. The intermediate points (crosses) were determined from the area under the mass 72 (Si₂¹⁶O⁺) profile, which gives the percentage of the total oxide present as ¹⁶O-oxide and thus the amount formed at the changeover from ¹⁶O₂ to ¹⁸O₂. The solid line is a parabolic least squares fit to the data.

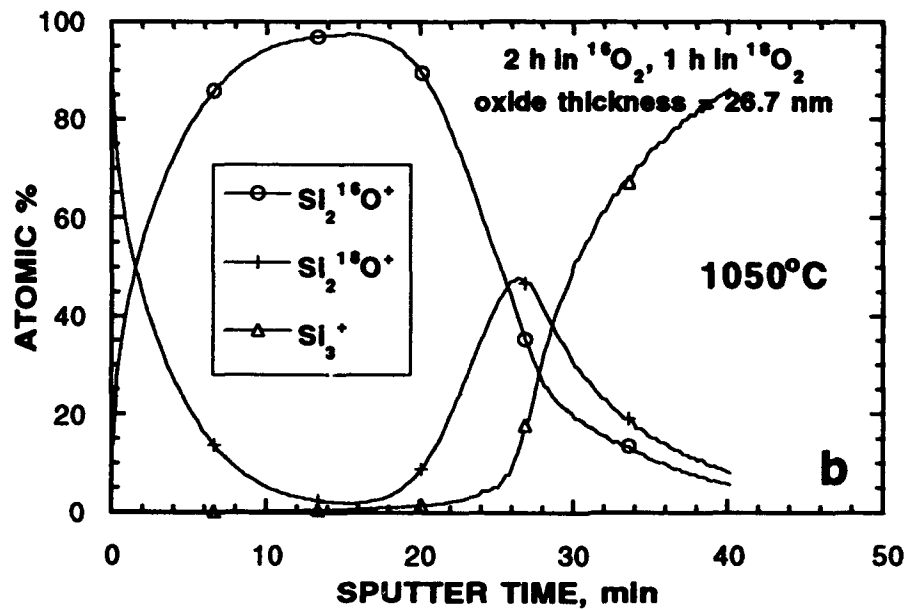
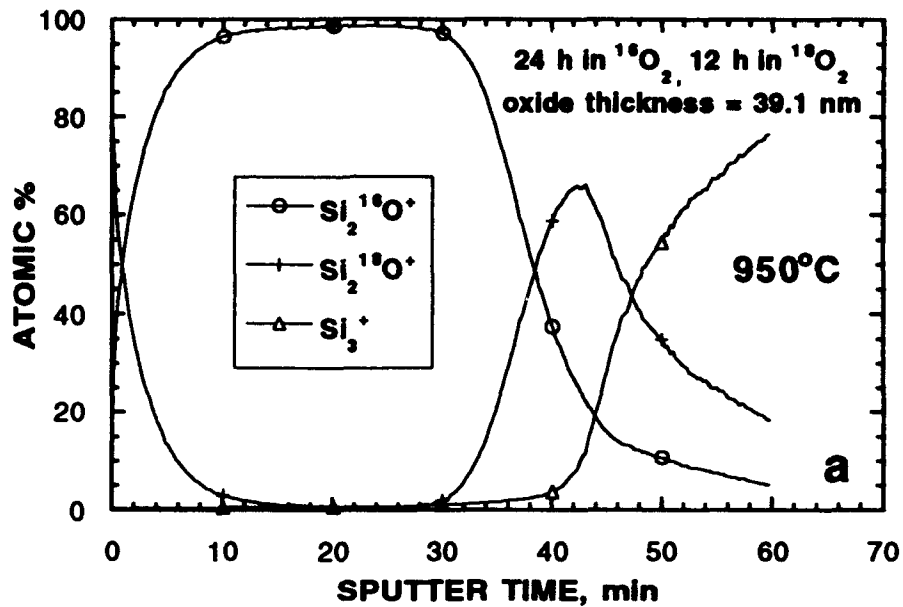


Fig. 3. SIMS composition-depth profiles for oxide films formed on (100)Si at 1.33 kPa O_2 pressure (a) at 950°C after 24 h in $^{16}\text{O}_2$ and 12 h in $^{18}\text{O}_2$; total oxide thickness is 39.1 nm and (b) at 1050°C after 2 h in $^{16}\text{O}_2$ and 1 h in $^{18}\text{O}_2$; total oxide thickness is 26.7 nm.

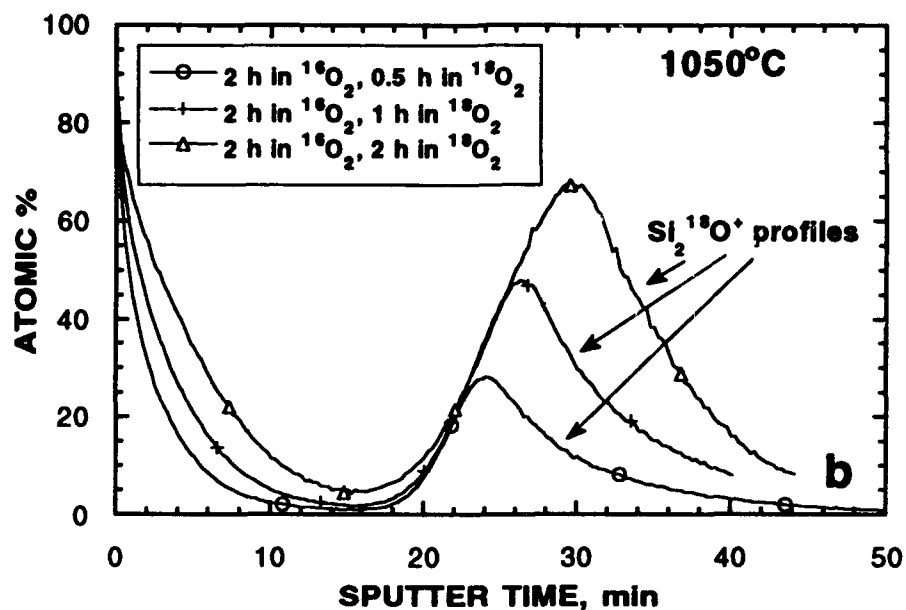
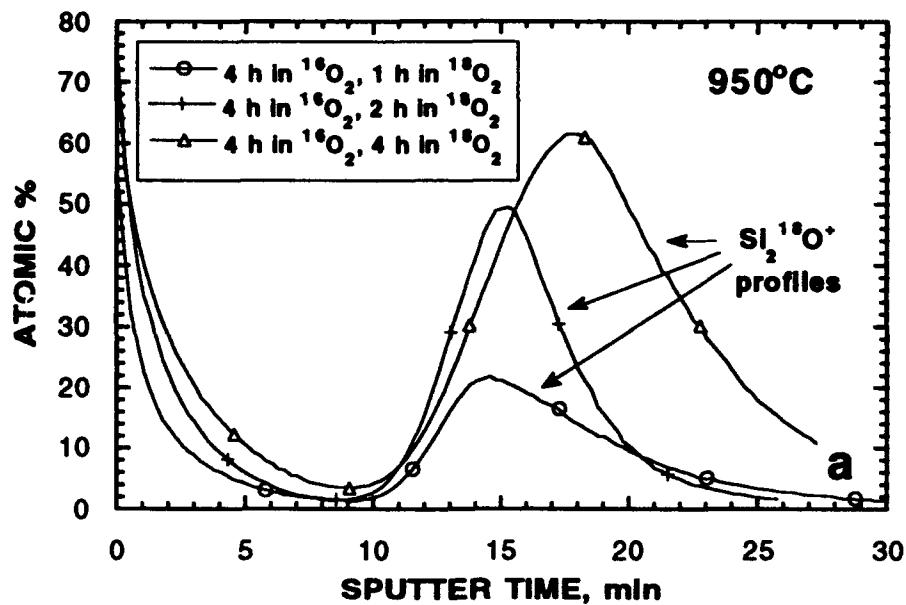


Fig. 4. SIMS composition-depth Si₂¹⁸O⁺ profiles for oxide films formed on (100)Si at 1.33 kPa O₂ pressure (a) at 950°C after 4 h in ¹⁶O₂ and 1, 2 and 4 h in ¹⁸O₂ and (b) at 1050°C after 2 h in ¹⁶O₂ and 0.5, 1 and 2 h in ¹⁸O₂.

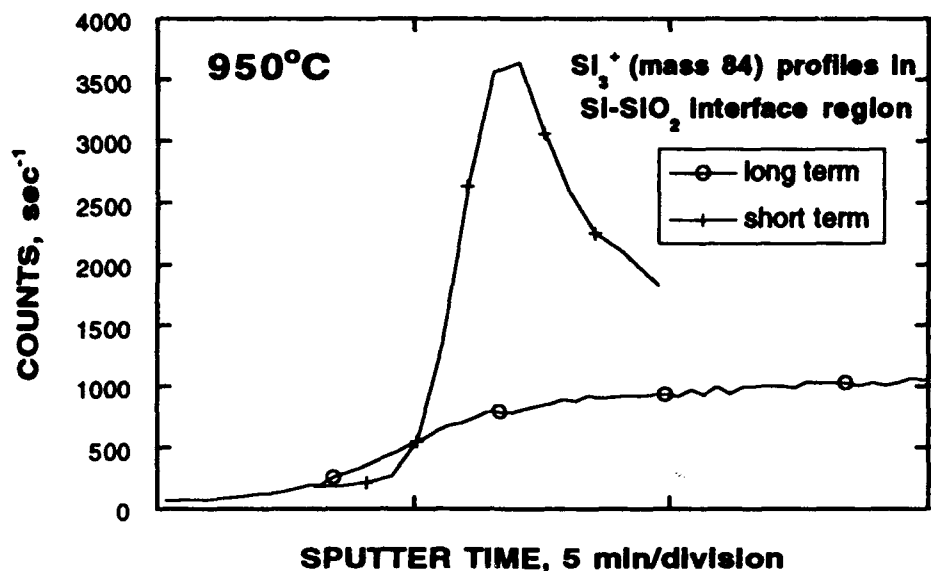


Fig. A1. SIMS intensity-depth Si_3^+ (mass 84) profiles in the Si-SiO₂ interface region for Si(100) oxidized at 950°C and 1.33 kPa O₂ pressure for (a) the short term (1.1 h) and (b) the long term (36 h). (The long term profile has been truncated for plotting convenience.)

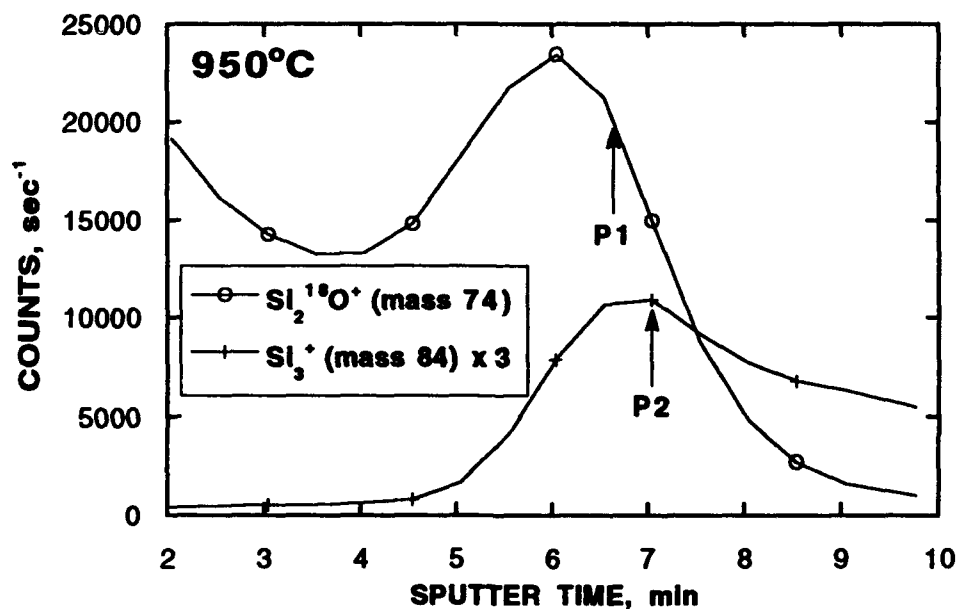


Fig. A2. SIMS intensity-depth profiles for Si(100) oxidized at 950°C and 1.33 kPa O₂ pressure for 1.1 h showing 85% of the $\text{Si}_2^{18}\text{O}^+$ (mass 74) maximum (position P1) prior to the Si_3^+ (mass 84) maximum and the Si_3^+ (mass 84) maximum (position P2).

SNMS Studies on the Oxidation Behaviour of Titanium Aluminides

W.J. Quadakkers
A. Elschner¹⁾
N. Zheng
H. Nickel
Research Centre Jülich
Institute for Reactor Materials
PO Box 1913
5170 Jülich, FRG

¹⁾ Bayer AG
4150 Krefeld, FRG

Abstract

The oxidation behaviour of TiAl-base intermetallics was investigated at 800°C in air with main emphasis being placed on the effect of niobium additions on the scale growth mechanisms. For this purpose titanium-aluminum alloys with various additions of niobium were investigated during cyclic oxidation or exposure times up to 3000h. The scale growth mechanisms during the early stages of oxidation were studied by a two-stage oxidation technique using ¹⁸O tracer. The scales formed during this oxidation process were analysed by SNMS. Nitrogen, which is known to significantly influence the oxidation behaviour of titanium aluminides, was found to form nitrides at the metal/oxide interface. Niobium was incorporated predominantly in the titanium dioxide and in the nitride-containing layer at the oxide/metal interface. The positive effect of niobium on the oxidation resistance is believed to be caused by a decreased oxygen vacancy concentration in the titanium dioxide due to niobium doping of the rutile lattice. A stabilizing effect of niobium on the nitride-containing layer might play an additional role.

Key terms: titanium aluminide, oxidation, ¹⁸O-tracer, SNMS

Introduction

Intermetallic phases on the basis of γ -TiAl are considered as construction materials for cases where low density in combination with high mechanical strength is a major design requirement ¹. A drawback for the application of titanium aluminides in high temperature components is their poor resistance against oxidation at temperatures above 700°C ^{2,3}. A special property of TiAl-based intermetallics is that the oxidation behaviour in air considerably differs from that in oxygen ^{4,5}. The mechanisms which are responsible for this effect have however not yet been elucidated. In most cases the presence of nitrogen in the surface oxide scales could not clearly be detected by conventional light and electron optical analysis methods. Considerable effort has been devoted to the improvement of the oxidation behaviour of TiAl-based intermetallics by ternary and quaternary alloying additions. The literature data concerning the effect of the various additions is somewhat controversial, but it seems generally accepted that additions of the element niobium significantly increase the oxidation resistance of intermetallics based on γ -TiAl ^{4,5,6,7}. Several mechanisms have been proposed for this effect, the exact mechanisms however, are not yet clarified.

In the present study, the formation and growth of oxide scales on γ -TiAl is studied at 800°C. Emphasis was placed on the effect of niobium additions on the early stages of oxidation. For this purpose the oxide scales were analysed by secondary neutral mass spectrometry (SNMS). This analysis technique was used to determine the niobium distribution in the various oxide phases and to analyse the incorporation of nitrogen in the corrosion scales, which appears to be extremely difficult with conventional light and electron optical analysis methods.

Experimental

The following alloying compositions were studied in respect to their long time oxidation resistance: Ti 50Al, Ti 48Al 2Nb, Ti 47.5Al 5Nb and Ti 45Al 10Nb (additions given in atomic %). The alloys were produced by induction melting in an argon atmosphere.

Specimens 15 mm in diameter and 2 mm in thickness were prepared from the cast ingots and then ground and polished to a 1 μ m diamond finish. The oxidation and spalling kinetics were investigated in still air at 800°C for exposure times of 3000h. During this exposure weight changes were determined in regular time intervals after cooling of the specimens to room temperature. Specimens were examined before and after oxidation using optical metallography, scanning electron microscopy (SEM) with energy dispersive x-ray analysis (EDX), electron microprobe analysis (EPMA) and x-ray diffraction (XRD).

To obtain more detailed information on the early stages of oxidation, specimens of alloy Ti 47.5Al 5Nb were oxidized by a two stage oxidation method at 800°C. In this technique the materials were first oxidized in air for 10 min, 0.5h, 2h, 5h or 24h, and subsequently in a gas consisting of 16% of ^{16}O , 4% of ^{18}O and 80% of ^{14}N for 20 min, 1h, 4h, 10h or 48h. The scales formed during this oxidation process were then analysed by secondary neutral mass spectrometry (SNMS) (Leybold, INA3). The primary energy of the Ar-plasma was 800 Volts. Details of the two-stage oxidation technique⁸ and the quantification methods used for the SNMS analyses have been published elsewhere⁹. The quantified oxygen tracer profiles were recalculated to an ^{18}O content of 20% in the second oxidation stage, i.e. the presented data show the results which would have been obtained if the oxygen in the second oxidation stage had been only ^{18}O instead of an ^{18}O -enriched gas⁹. The SNMS results obtained for Ti 50Al have been presented recently¹⁰ and therefore the present paper will only deal with the niobium-containing alloy.

Results

Effect of Niobium on Oxidation Behaviour

Figure 1 shows the oxidation behaviour of Ti 50Al and the three niobium-containing alloys during oxidation at 800°C in air. The scale on the binary alloy showed spallation even at the first interruption of the experiment for weight measurement i.e. the scale growth which actually occurred in the period before the first interruption for weight measurement was significantly larger than indicated by the first data point in Figure 1. All niobium containing alloys showed lower growth rates and a significantly better scale adherence. The scale growth rates decreased with increasing alloy niobium content.

Figure 2 shows the cross section and the corresponding X-ray mappings of the scale on Ti 47.5Al 5Nb after 3000h oxidation, measured by EPMA. These results, in combination with XRD data illustrate that there is an almost continuous layer of Al_2O_3 near the oxide surface. On top of this a thin layer of TiO_2 is visible. In both

layers no niobium seems to be present. Beneath the alumina-based layer, a mixed scale has been formed with titania as the dominant phase. Niobium is present in this layer especially near the scale/gas interface where again more alumina is present. XRD revealed the presence of small amounts of TiN and Ti₂AlN; these phases however, could not be localized by EPMA or SEM/EDX.

Studies of Scale Formation by SNMS

Figure 3 shows an SNMS depth profile of the oxide layer on the alloy with 5% Nb after two-stage oxidation for 10 min / 20 min at 800°C. The results clearly show the formation of an alumina-based scale at the surface and at the interface with the alloy. Between these regions a titanium-rich scale is formed. At the scale / alloy interface a nitrogen-rich layer has been formed which is rich in titanium. Niobium is only present in the inner part of the scale. The ¹⁸O-enrichment near the scale/alloy interface (Figure 4) illustrates that during the second stage of oxidation the scale has grown by short circuit oxygen diffusion⁸; the enrichment near the scale/gas interface might be caused by cation diffusion or oxygen lattice diffusion⁸.

After 0.5h / 1h two stage oxidation aluminium oxide is still present at the scale surface (Figure 5) whereas the aluminium peak in the inner part of the scale has disappeared. The ¹⁸O is still enriched at the oxide surface (Figure 6) whereas at the inner scale side it becomes more evenly distributed rather than forming a clear peak. The nitrogen-rich layer is present near the scale/metal interface and the niobium is distributed in a similar way as shown in figure 3. An interesting difference is that the nitrogen enrichment and the dip in the aluminium profile coincide after 30 minutes exposure whereas after 1.5 h they are separated.

The scale depth profiles after 2h / 4h two-stage oxidation looked very similar to those after 0.5h / 1h. A clear change in the growth processes occurred however, after longer oxidation times as illustrated in Figure 7. After a total of 15h the formation of a titanium oxide became visible on top of the initially formed outer alumina layer. The ¹⁸O profile (Fig. 8) showed a more pronounced peak at the outer scale side than in the previous examples, apparently due to outward diffusion of titanium. Again the niobium is only present in the titanium-rich oxide and nitride layer, whereas in the outer alumina and titania, no niobium is detected, which is in agreement with the EPMA analysis of the specimen which was oxidized for 3000h (Figure 2). An interesting feature is that the niobium becomes enriched in the alloy immediately beneath the nitrogen-rich layer (Figure 7). Very similar observations with respect to element depth profiles and isotope distributions were made after two stage oxidation for 24h / 48h.

Discussion and Conclusions

The long time experiments confirm that the niobium-containing titanium aluminides possess considerably better oxidation resistance at 800°C than Ti 50Al (Figure 1). The decrease in scale growth rates due to niobium additions is not due to a switch-over from titania to alumina-based surface scales: as in the case of binary titanium aluminides^{2,7} the scales are multiphase titania / alumina based mixtures, but with a significantly lower growth rate. SNMS analyses revealed, that in the early stages of oxidation at 800°C, the alloy containing 5 At.-% niobium forms an alumina-based surface scale (Figure 3). At this stage of oxidation the scale formation is very similar to that of Ti 50Al¹⁰. Beneath the outer alumina scale, a layer rich in titanium nitride is formed. Alumina formation leads to aluminium depletion and consequently to a decrease in aluminium activity in the subsurface zone. The resulting increase in oxygen activity causes the alumina to become unstable at the oxide/alloy interface relative to titania² and therefore this latter oxide is formed (Figure 3). Initially this

formation of titania beneath the alumina in turn leads to a relative increase in aluminium activity and subsequently to formation of aluminium-rich oxide between the titania and the nitrogen-containing layer (Figure 3). On further exposure the alumina and titania at the inner scale side become intermixed (Figure 4). According to Becker et al.¹¹ titania has a significant solubility for alumina which increases with decreasing oxygen partial pressure, i.e. under the prevailing conditions the solubility would be larger in the inner scale side than near the scale/gas interface. Consequently the alumina layer which initially forms can at first coexist with the titania which has been formed beneath it. As the scale thickens, the oxygen partial pressure in the inner scale side decreases and therefore the solubility of alumina in titania increases. This means that the alumina would be "attacked" at the interface between the two oxides. By this means, the barrier function of the alumina is deteriorated and titanium cations can diffuse outward (Figure 5).

The scale composition on Ti 47.5Al 5Nb in the early stages of oxidation is similar to that on Ti 50Al¹¹ with the difference that niobium is clearly present in the titanium oxide and nitride (Figures 5 and 7). In addition, the titania-rich scale on the niobium-containing alloy grows much slower than in the case of Ti 50Al^{7,10,11}. An explanation for this technologically important effect could be, that niobium decreases the oxygen vacancy concentration in the rutile lattice due to its higher valency compared to that of titanium. Consequently oxygen inward diffusion decreases and so the scale growth is slower than in the case of Ti 50Al.

For this last mentioned alloy it was shown¹⁰ that, contrary to the niobium-containing material, the initially-formed nitride becomes oxidized after longer times as soon as the growth of titania becomes the dominating process in scale growth kinetics. In the niobium-containing alloy the nitride layer remains intact due the slower ingress of oxygen through the titania. The reason for the presence of the nitride-rich layer also after longer times in Ti 47.5Al 5Nb, in contrary to Ti 50Al¹⁰, might also be due to a stabilizing of the titanium nitride by incorporation of niobium. In that case the nitride containing layer at the scale/metal interface of Ti 47.5Al 5Nb might also act as a barrier layer which could be a further reason for the improved oxidation resistance compared to Ti 50Al. Because of a lack of prevailing data for the effect of niobium on the thermodynamic stability of titanium nitride, it cannot be determined with certainty whether this effect really plays a significant role.

For a correct interpretation of the measured depth profiles it is important to note, that in SNMS studies nitrogen is an element which is difficult to quantify¹². Therefore it cannot be assumed that the maximum concentration of the nitrogen peak at the scale/metal interface is really around 10 to 20 At.-% as measured in the presented SNMS profiles (Figures 3, 5, 7). Recent results of detailed microstructural studies using SEM and TEM¹³ indicate that the nitrogen-containing layer consists of an alumina/nitride mixture. According to XRD-results a ternary nitride, Ti₂AlN, is present in addition to the binary TiN.

An interesting observation is, that after longer exposure times niobium becomes enriched in the alloy immediately at the interface with the nitride-rich layer (Figure 7). This may be caused by one of the following mechanisms:

- if aluminium and titanium are incorporated in the oxide scale to a larger extent than niobium (compared with the relative concentrations in the alloy), the two first-mentioned elements will be "depleted" in the alloy relative to niobium. This would lead to an apparent niobium "enrichment" in the surface near diffusion zone in the alloy.
- the SNMS profile in Figure 7 indicates that the niobium solubility in the titanium nitride is higher than in the titanium oxide. After the initially formed niobium-containing nitride starts to become oxidized, an excess amount of niobium will be present. As niobium seems to have no solubility in the alumina (Figures 5

and 7), it can either be oxidized or diffuse through the nitride zone into the alloy. Apparently the oxygen partial pressure in the inner part of the scale is too low for niobium to become oxidized and therefore it diffuses back into the alloy.

Acknowledgements

The authors are grateful to the "Deutsche Forschungsgemeinschaft" which has partly funded the presented investigations. Thanks are due to Mr. Beyss, KFA/IFF and Dr. Beavan, GKSS for supplying the alloys, Mr. Baumanns, KFA/IRW for carrying out the oxidation experiments, Mr. Grübmeier and Mr. Mostert, KFA/IRW for carrying out the EPMA studies.

References

1. M. Yamaguchi, High temperature Intermetallics (London, 30 April-1 May 1991, Proceedings, The Royal Society) p. 15
2. A. Rahmel, P. Spencer, Oxid. of Met. 35 (1991): p. 53
3. A.K. Misra, Metall. Trans. 22A (1991): p. 715
4. M. Khobaib, F. Vahldiek, 2nd Int. SAMPE Metals Conference (August 2-4, 1988, Proceedings) p. 262
5. M. S. Choudhury, H.C. Graham and J.W. Hinze, in Properties of High Temperature Alloys, Ed. Z.A. Foroulis, F.S. Pettit, The Electrochem. Soc., 1976, p. 668
6. G.Welsch, A.I.Kahveci, Oxidation of High Temperature Intermetallics (Ed. by T.Grobstein and J. Doychak, The Minerals Metals & Materials Society, 1989) p. 207
7. U. Figge, W.J. Quadackers, H. Schuster, F. Schubert, EUROCORR 92 (Espoo, Finland, 31 May - 4 June, 1992, Proceedings Vol.I) p. 591
8. W.J. Quadackers, H. Holzbrecher, K.G.Briefs and H. Beske, Oxid. Met. 32 (1989): p. 67
9. W.J.Quadackers, A.Elschner, W.Speier and H.Nickel, Applied Surface Science 52 (1991): p. 271
10. U. Figge, A. Elschner, N.Zheng, H. Schuster, W.J.Quadackers, Arbeitstagung "Angewandte Oberflächenanalytik" (22-25 June 1992, Jülich FRG, Proceedings in Fresenius J. for Anal. Chem.) in press
11. S. Becker, A. Rahmel, M. Schorr, and M. Schütze, Oxid. of Met., 38 (1992): p. 425
12. K.H. Müller, K. Seifert, M. Wilmer, J. Vac. Sci. Technol. A3 (1985): p. 1367
13. W.J.Quadackers, N. Zheng, Research Centre Jülich, FRG, to be published

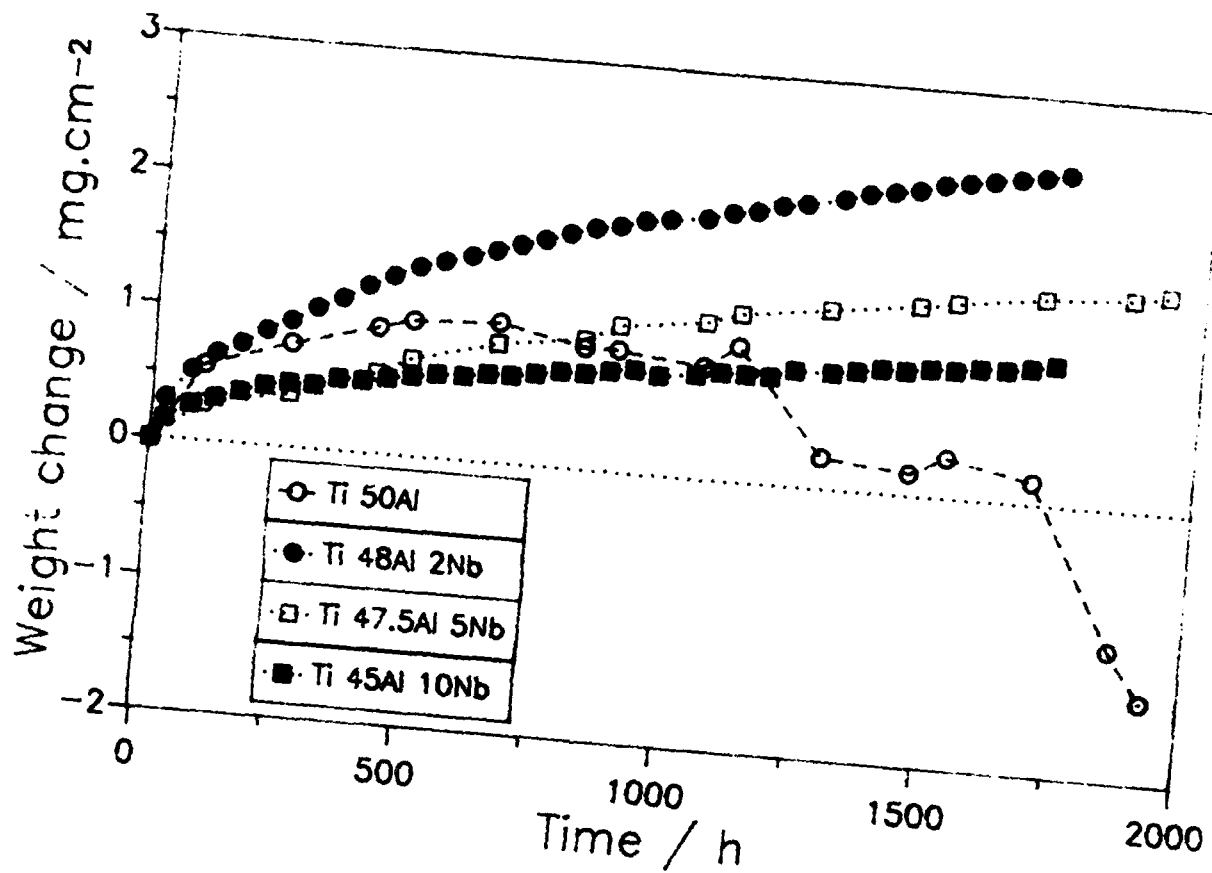


Figure 1: Weight change as a function of time for Ti 50Al and three niobium-containing titanium aluminides during oxidation at 800°C in air

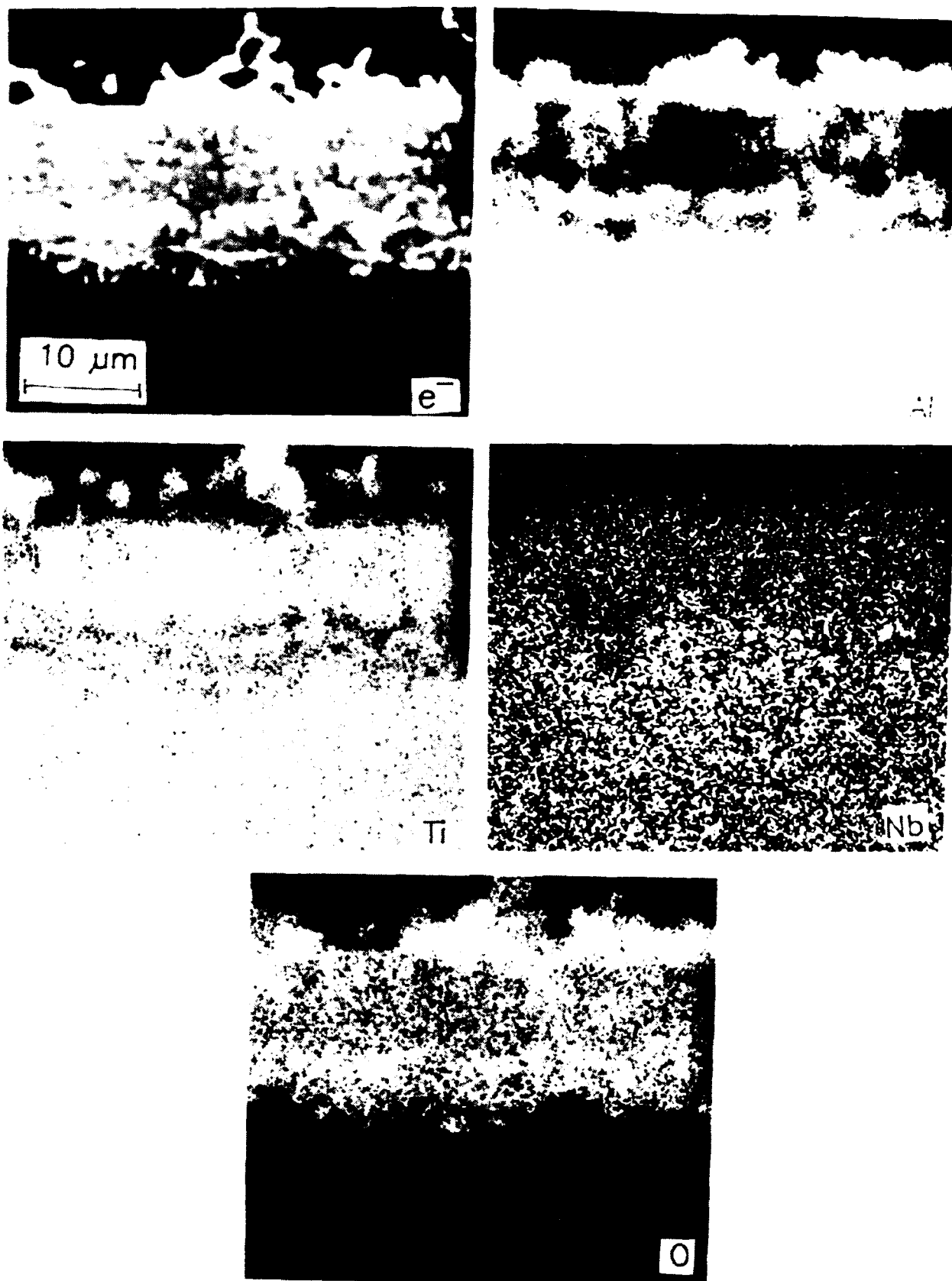


Figure 2: Element distributions (EPMA) in cross section of oxide scale formed on Ti 47.5Al 5Nb after 3000 h oxidation in air at 800°C

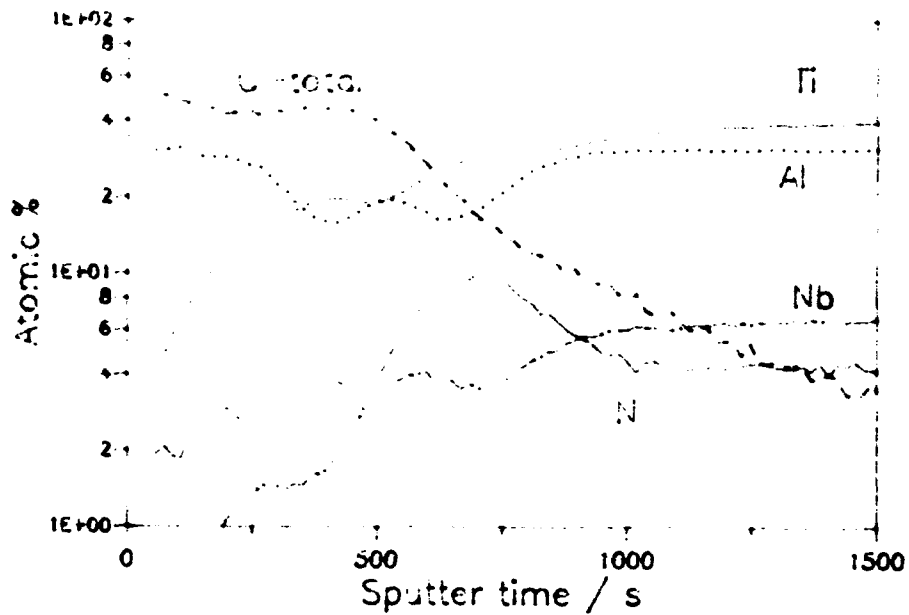


Figure 3: SNMS analysis of Ti 47.5Al 5Nb after two-stage oxidation (10 min. / 20 min.) in air and air + ^{18}O at 800°C

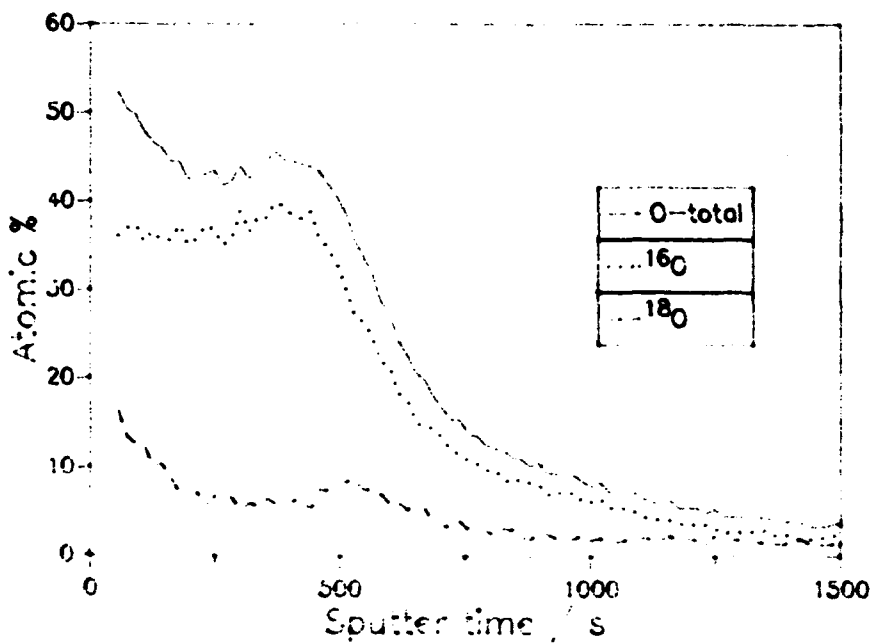


Figure 4: Similar to Figure 3, showing oxygen isotope distributions

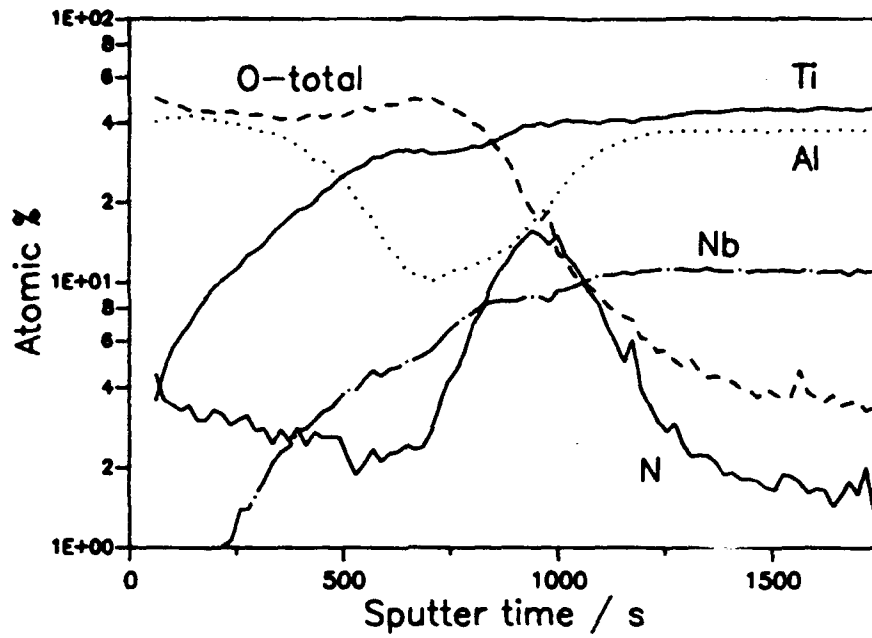


Figure 5: SNMS analysis of Ti 47.5Al 5Nb after two-stage oxidation (0.5h / 1h) in air and air + ^{18}O at 800°C

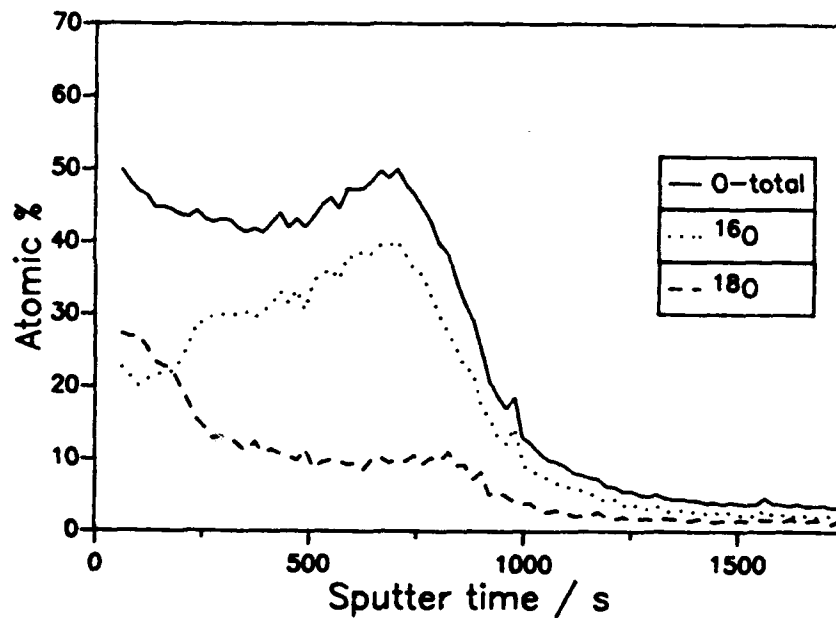


Figure 6: Similar to Figure 5, showing oxygen isotope distributions

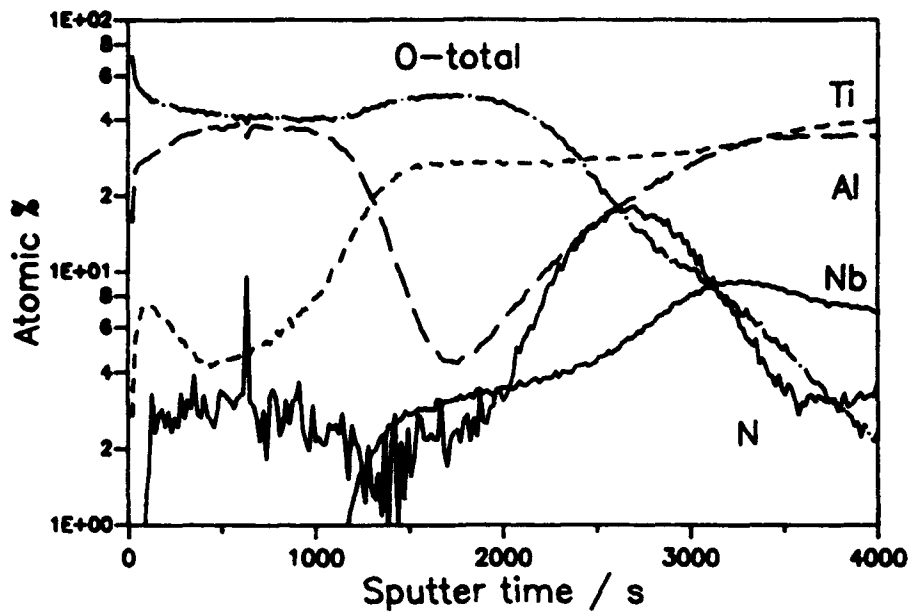


Figure 7: SNMS analysis of Ti 47.5Al 5Nb after two-stage oxidation (5h / 10h) in air and air + ^{18}O at 800°C

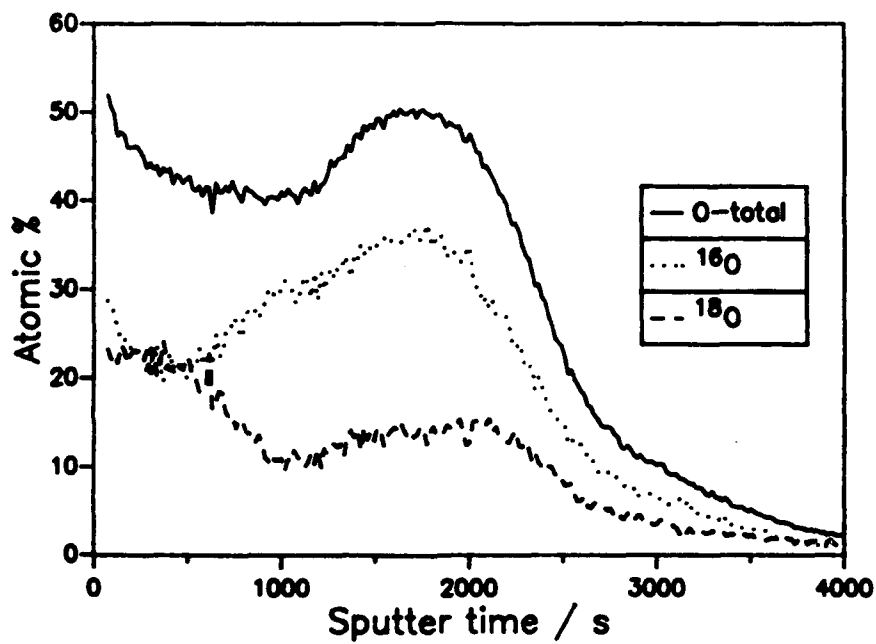


Figure 8: Similar to Figure 7 showing oxygen isotope distributions

Growth Mechanism of Alumina Scales on FeCrAl Alloys

Mohamed Boualam

Laboratoire de Génie Mécanique pour les Matériaux et les Structures,
Université de Technologie de Compiègne, B.P. 649
60206 Compiègne Cédex (France)

Gérard Béranger

Laboratoire de Génie Mécanique pour les Matériaux et les Structures,
Université de Technologie de Compiègne, B.P. 649
60206 Compiègne Cédex (France)

Michel Lambertin

Laboratoire de Génie Mécanique pour les Matériaux et les Structures,
Université de Technologie de Compiègne, B.P. 649
60206 Compiègne Cédex (France)

Elisabeth Sciora

Université de Bourgogne, Laboratoire de Recherches sur la Réactivité
des Solides, B.P. 138, 21004 Dijon Cédex (France)

Rex J. Hussey

NRC, Institute for Microstructural Sciences, Ottawa, Ontario,
K1A 0R6 (Canada)

Don F. Mitchell

NRC, Institute for Microstructural Sciences, Ottawa, Ontario,
K1A 0R6 (Canada)

Michael J. Graham

NRC, Institute for Microstructural Sciences, Ottawa, Ontario,
K1A 0R6 (Canada)

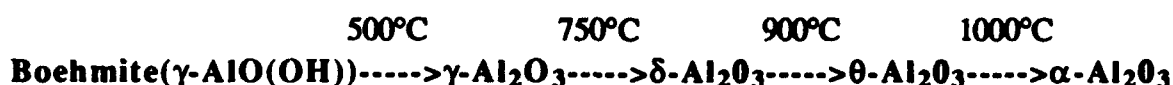
Abstract

The high temperature (850-1100°C) mechanism of oxidation of FeCrAl alloy (doped with Zr and mischmetal) was studied in air (synthetic) and in oxygen. Kinetic measurements show that the parabolic law is obeyed after several hours of oxidation ; the oxidation rate is modified at 950-1100°C. Morphological changes are observed. At low temperature, the oxide surface is covered with platelets (whiskers), whereas at high temperature small equiaxed crystals are obtained. These results may be related to the oxide phases present. At low temperature a transitional alumina (likely θ -Al₂O₃) grows, while at high temperature α -Al₂O₃ forms. These phases are not produced initially ; during the first stage, γ -Al₂O₃ is always observed but is transformed at a rate which depends on the temperature. When longer oxidation runs (up to 120 hours) are performed at low temperature, the transformation of θ -Al₂O₃ into α -Al₂O₃ increases with time. All these results clearly demonstrate that α -Al₂O₃ is the stable phase. In order to better understand the oxidation mechanism, oxidation experiments were performed in ¹⁶O₂/¹⁸O₂ and the scales subsequently analyzed by SIMS. The results show that the α -Al₂O₃ scales grow by inward transport of oxygen. In addition, stress measurements by X-ray diffraction were performed : for very thin oxides, stresses were measured in the alloy immediately beneath the scale. The data indicate that the tensile stress in the alloy decreases regularly with oxidation temperature and that a change in preferred orientation in the alloy occurs during oxidation runs up to 950°C.

Key terms : FeCrAl Alloys, Oxidation, Morphology, Structure, Diffusion, Stress measurement

Introduction

Among the MCrAl alloys, the ferritic ones (Fe-based) have been and continue to be extensively studied : protective scales (i.e α - Al_2O_3) are generally developed on their surface during oxidation at high temperature. However, various alumina phases may form, depending on different parameters such as the temperature, the atmosphere, the alloy composition or the duration of oxidation. The theoretical thermal stability of these aluminas may be summarized as follows :



The transition temperatures which are indicated above are approximate and are dependent upon the experimental conditions.

A literature review was recently published by PRESCOTT and GRAHAM¹, which included different research works devoted to the identification of various alumina phases grown on different alloys. The transition aluminas (γ , δ or θ - Al_2O_3) are mainly observed at low temperature (below 900 or 1000°C)²⁻⁷ or during a transient stage at the beginning of the oxidation reaction⁸⁻¹². At higher temperature microscopical studies^{7,12,13} have shown that the transformation of transition aluminas into α -alumina is generally accompanied by a modification of the oxide morphology . Transition aluminas are generally observed in the form of whiskers whereas α -alumina is present as equiaxed small crystals.

Considering the growth mechanism, it is generally assumed that transition aluminas form by outward cation diffusion¹⁴. In contrast, α -alumina generally forms by predominantly inward oxygen diffusion^{15,16,17}.

In this paper we will report a study of the high temperature oxidation of a FeCrAl ferritic alloy. Morphological observations and structural analyses have been emphasized.

Experimental

The alloy which was used in this work was a ferritic steel, the main alloying elements being chromium and aluminum. Its composition is given in Table 1. Zirconium additions stabilize the alloy and prevent the precipitation of chromium carbide. Cerium and lanthanum are incorporated to improve the oxidation resistance, especially when

temperature cycles are applied. Coupons (25x10 mm) were cut from thin foils (50 μm thick). Before oxidation they were degreased in trichloroethane, rinsed in alcohol and dried. They then were put in an alumina crucible and introduced into the furnace.

Oxidation experiments were made in air at 850, 900, 950, 1000, 1050 and 1100°C. Oxidation times varied between a few minutes and 120 hours. Short oxidation runs (< 2 hours) were performed and the kinetics recorded with a microbalance.

The scale morphology was observed by scanning electron microscopy (SEM). The structure of the scales was analyzed by X-ray diffraction or electron diffraction and scale composition was determined by X-ray spectrometry.

Some particular experiments were performed to determine the diffusion mechanism. For this, specimens were prior oxidized in $^{16}\text{O}_2$ and then in $^{18}\text{O}_2$. Secondary ion mass spectrometry (SIMS) was used to allow the determination of the location of the ^{18}O isotope and to distinguish which diffusion mechanism is involved in the oxidation process.

Results

Influence of Temperature

In order to establish the influence of temperature on the oxidation rate, morphology and structure of the alloy, samples were oxidized in air for 24 hours in the temperature range 850-1100°C. Morphological observations of the oxide surface are reported in Figure 1. At 850°C, it can be seen that the oxide scale is thin ; the grain boundaries of the metallic substrate are still visible. The oxide surface is smooth and mainly consists of very small crystals. Some platelets (also called whiskers) may be observed. They are more developed at 900°C and at that temperature cover the entire surface of the alloy. The grain boundaries of the metal are not discernable which suggests that the oxide scale is thicker than at 850°C. After oxidation at 950°C, a modification of the scale surface is observed ; the oxide is mainly in the form of small equiaxed crystals and only a small number of whiskers is observed. The whiskers disappear completely after oxidation at 1000°C or at higher temperature and the size of the equiaxed crystals increases. The oxides which formed were identified by X-ray diffraction. At low temperature ($\leq 900^\circ\text{C}$) only a few diffraction lines are observed (Table 2). They are more numerous at higher temperature. It may be observed that the interplanar distance 2.732Å, which is present at low temperatures, disappears at

temperatures above 950°C. The comparison of these experimental data with the values given in the ASTM files allows us to conclude that at low temperature a transition alumina ($\theta\text{-Al}_2\text{O}_3$) is formed on the alloys whereas $\alpha\text{-Al}_2\text{O}_3$ is produced at higher temperatures. Both oxide structures are observed at 950°C which is a transition temperature (Fig.2).

In order to verify that only aluminum oxide is formed, some scales were analyzed after dissolution of the alloy in a methanol - 10% bromine solution. It was verified by X-ray spectrometry that aluminum only is present (as metal) in the scale.

Influence of Oxidation Time

Taking into account the previous results, longer oxidation runs were performed. The scales were characterized by using the same observation and analysis techniques. It was clearly observed that if $\theta\text{-Al}_2\text{O}_3$ is present after 24 hours of oxidation, it is partially transformed into $\alpha\text{-Al}_2\text{O}_3$ by 48 hours. The transformation is practically complete after 120 hours at 900°C.

The First Stages of Oxidation

Short oxidation runs were made at different temperatures. The kinetic results (weight gain versus time) are reported in Figure 3. Microscopical observations show clearly that the kinetic transition occurring after a short time at 900 and 950°C corresponds to a morphological change and to the beginning of the formation of whiskers. Electron diffraction analysis after very short oxidation runs (5 minutes) shows that γ -alumina forms during the early stages of the reaction, whatever the temperature.

Discussion

All the results show that the morphology and the structure of the alumina which forms are strongly related and that two main parameters must be taken in account : the reaction time and the temperature. At the beginning of the reaction (≤ 5 minutes) a transition alumina ($\gamma\text{-Al}_2\text{O}_3$) is formed on the alloy. At low temperature (900-950°C) it transforms more or less rapidly into another transition oxide, $\theta\text{-Al}_2\text{O}_3$. That transformation is accompanied by a kinetic transition (acceleration) and a morphological change of the scale (beginning of the formation of whiskers). A second transformation from θ into $\alpha\text{-Al}_2\text{O}_3$ occurs after 24 hours or more. At higher temperature ($\geq 1000^\circ\text{C}$), both

structural transformations ($\gamma \rightarrow \theta \rightarrow \alpha\text{-Al}_2\text{O}_3$) are very rapidly completed (≤ 15 minutes).

Whiskers are observed on the surface only when the θ phase is present. All the results clearly show that $\alpha\text{-Al}_2\text{O}_3$ is the only stable structure. That phase is always obtained at long oxidation times. Experimental results show that it is not observed at the lowest temperature (850°C): this is probably because the transformation rate is very low. To confirm the stability of the corundum structure, experiments were performed as follows: specimens were oxidized for a short time (1 hour) at high temperature (1100°C) to develop an $\alpha\text{-Al}_2\text{O}_3$ scale. Then the oxidation temperature was lowered in the range 850 to 900°C and the reaction continued up to 24 hours. The $\alpha \rightarrow \theta$ transformation was never observed, which indicates that, when it is formed, the corundum phase is stable even at low temperature.

Oxidation mechanism

If one considers all the experimental results (oxidation kinetics, oxide morphology and structure) which were obtained in this study, it may be supposed that a change in the oxidation mechanism occurs between 900 and 1000°C . As mentioned in the Introduction it was shown in other systems that at low temperature cationic diffusion is the main process whereas at higher temperature the reaction proceeds by oxygen diffusion. In order to test this hypothesis, two-stage ^{18}O /SIMS experiments were performed at 1100°C . The specimens were first oxidized in $^{16}\text{O}_2$ and then in $^{18}\text{O}_2$. After reaction, the oxide scales were analysed by SIMS. The results showed that at 1100°C ^{18}O is concentrated close to the internal interface of the oxide scale (Fig.4). As the oxidation in $^{18}\text{O}_2$ was performed during the second stage of the experiment, it means that inward diffusion of oxygen occurred.

Stress Measurements

The last point which was considered in this work was to estimate the mechanical state (and particularly the stress level) of the system. As the scale thickness was too thin for reliable stress measurements to be obtained, we evaluated the stresses in the alloy, close to the alloy-oxide interface. The technique which was used was X-ray diffraction. All the measurements were made at room temperature, on the non-oxidized alloy and after oxidation for 24 hours at 900 and 1100°C (1). As can be seen (Table 3) the stresses are compressive in the non-oxidized alloy. After oxidation at 900°C , the stress level measured in

(1) For these experiments, samples 1.2 mm thick were used.

the alloy is practically equal to zero. This means that compressive stresses developed in the scale. If one considers that growth stresses are negligible (due to outward diffusion), the result is in good agreement with the respective values of the expansion coefficients of the metal and of the oxide. After oxidation at 1100°C, tensile stresses are measured in the metal, which means that compressive stresses, higher than at 900°C, develop in the alumina scale. It may be concluded that they are the result of the combination of compressive growth stresses (due to inward oxygen diffusion and scale formation at the internal interface) and of compressive stresses developed during cooling.

Conclusions

In this work, on the high temperature oxidation of a FeCrAl ferritic alloy, we have shown that the structure and the morphology of the oxide which forms on the alloy are strongly related. They depend simultaneously on the reaction temperature and time of oxidation. In all cases γ -Al₂O₃ is observed after very short times (a few minutes). After 24 hours, θ -alumina is identified at low temperature ($\leq 900^\circ\text{C}$), whereas the α -phase is observed at high temperature ($\geq 1000^\circ\text{C}$). This latter oxide is in the form of small equiaxed grains; with the former, platelets (whiskers) are seen on the surface. After longer oxidation runs, the main oxide is α -Al₂O₃. All these results show clearly that α -Al₂O₃ is the most stable phase. Diffusion experiments show that at 1100°C α -Al₂O₃ grows by oxygen inward diffusion.

Compressive residual stresses are always measured after oxidation and cooling, which are higher at 1100°C than at 900°C. This result must be related to the diffusion processes which are different in the different temperature domains.

References

- 1 R. Prescott, M.J. Graham, *Oxid. Met.*, 38 3/4 (1992): p.233.
- 2 G.C. Wood, B.Chattopadhyay, *Corros. Sci.*, 10 (1970): p.471.
- 3 G.C. Wood, B.Chattopadhyay, *Oxid. Met.*, 2 (1970): p.373.
- 4 R.E. Grace, A.E. Seybolt, *J. Electrochem. Soc.*, 105 (1958): p.582.
- 5 T.Nakagama, K. Kaneko, *Corrosion*, 26 7 (1970): p.187.

- 6 P.A. van Manen, E.W.A. Young, D. Schalkoord, C.J. Van der Wekken, J.H.W. de Wit, Surf. Interface Anal., 12 (1988): p.391.
- 7 P.T. Moseley, K.R. Hyde, B.A. Bellamy, G. Tappin, Corros. Sci., 24 6 (1984): p.547.
- 8 J.L. Smialek, R. Gibala, Met. Trans., 14 A10 (1983): p.2143.
- 9 C.J.P. Steiner, D.P.H. Hasselman, R.M. Spriggs, J. Amer. Ceram. S c., 54 8 (1971): p.412.
- 10 J. Peters, H.J. Grabke, Werkst. Korros., 35 (1984): p.385.
- 11 T.A. Ramanarayanan, M. Raghavan, R. Petkovic-Luton, JIMIS-3, Trans. of the Japan Inst. of Metals, Suppl. (1983): p.199.
- 12 E.J. Felton, F.S. Pettit, Oxid. Met., 10 3 (1976): p.184.
- 13 G.C. Rybicki, J.L. Smialek, Oxid. Met., 31 3/4 (1989): p.275.
- 14 M.J. Graham, J.I. Eldridge, D.F. Mitchell, R.J. Hussey, Mater. Sci. Forum, 43 (1989): p.207.
- 15 K.P.R. Reddy, J.L. Smialek, A.R. Cooper, Oxid. Met., 17 5/6 (1982): p.429.
- 16 J. Jedlinski, R. Borchardt, Oxid. Met., 36 3/4 (1991): p.318.
- 17 R. Prescott, D.F. Mitchell, M.J. Graham, Paper n° 133, Corrosion 92, National Association of Corrosion Engineers (1992).

Table 1 : Composition of the alloy

| | | | | | | | | |
|-------------|-----------|-----------|-----------|-----------|-----------|-----------|-----------|-----------|
| Elmt | C | Si | S | P | Mn | Cr | Ni | Ti |
| wo% | 0.025 | 0.56 | 0.001 | 0.0014 | 0.29 | 22.38 | 0.17 | 0.004 |
| Elmt | Al | Cu | Co | Ce | La | N | Zr | |
| wo% | 4.71 | 0.01 | 0.017 | 0.021 | 0.011 | 0.0023 | 0.23 | |

Table 2 : X-ray diffraction lines determined after 24 hours of oxidation

| 850°C | 900°C | 950°C | 1000°C | 1100°C | oxide phase |
|--------------|--------------|--------------|---------------|---------------|----------------------|
| - | - | 3.49 | 3.49 | 3.49 | α |
| 2.732 | 2.732 | 2.736 | - | - | θ |
| - | - | 2.55 | 2.55 | 2.55 | α |
| 2.393 | 2.393 | 2.37 | 2.37 | 2.37 | α or θ |
| - | - | 2.09 | 2.09 | 2.09 | α |
| - | - | 1.74 | 1.74 | 1.74 | α |
| - | - | 1.604 | 1.606 | 1.607 | α |
| 1.405 | 1.405 | 1.407 | 1.409 | 1.407 | α or θ |
| - | - | 1.377 | 1.375 | 1.375 | α |

Table 3 : Stress level measured in the alloy before and after oxidation

| Oxidation conditions | No oxidation | 900°C | 1100°C |
|-----------------------------|---------------------|--------------|---------------|
| Stress level Mpa | -200 | 0 | 300 |

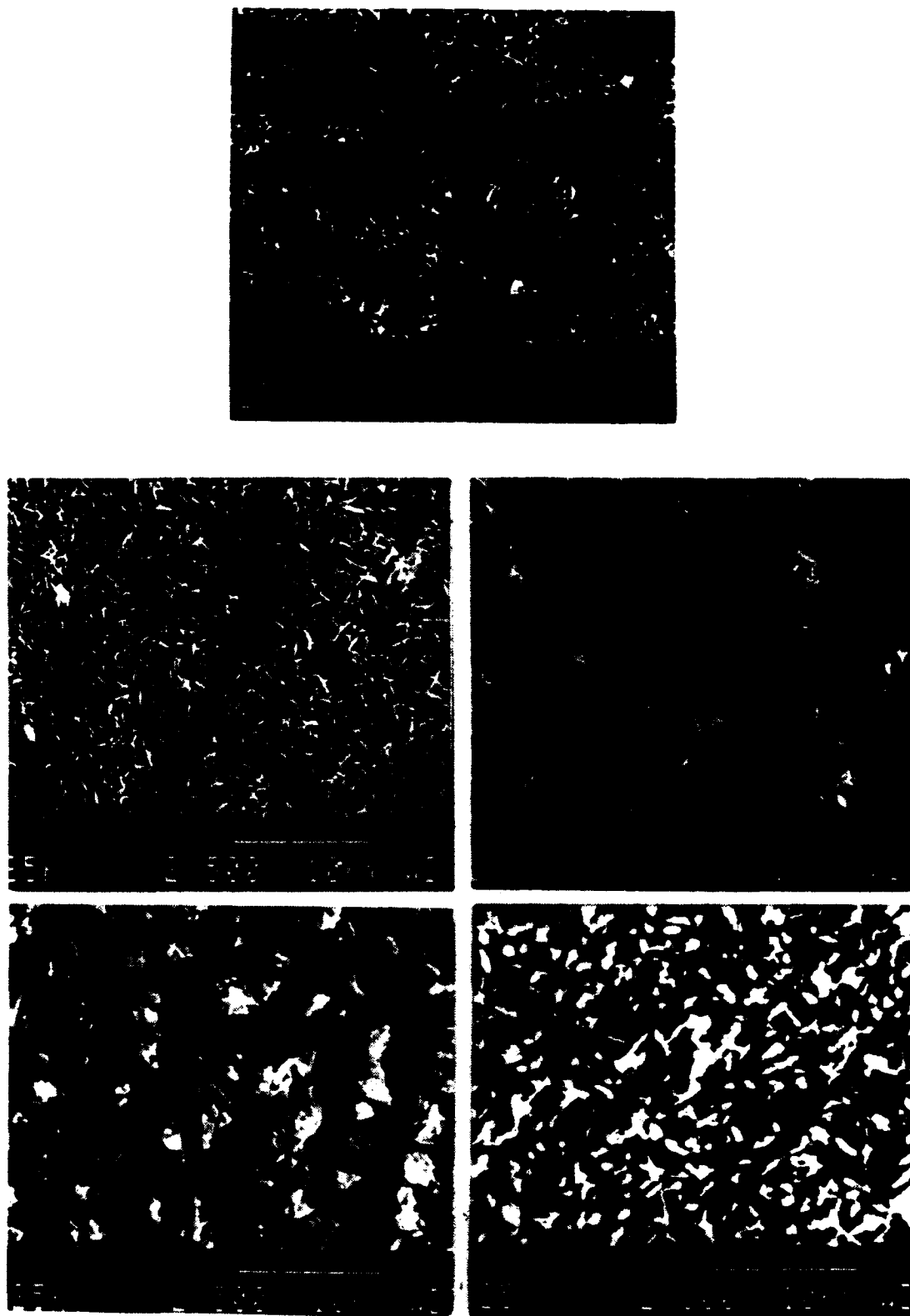


Figure 1 : Morphology of surface oxide formed after 24 hrs oxidation.

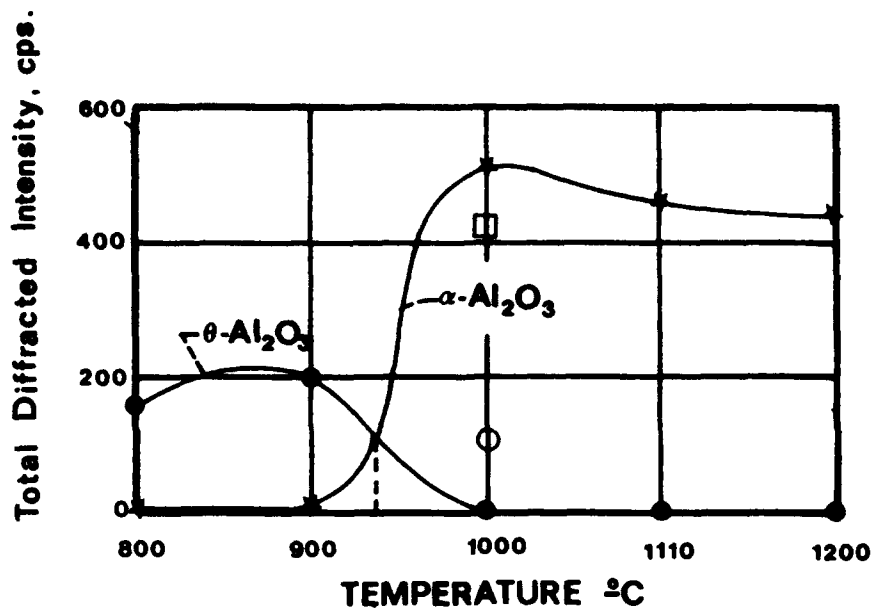


Figure 2 : Relative amounts of alumina phases grown at different temperatures¹³.

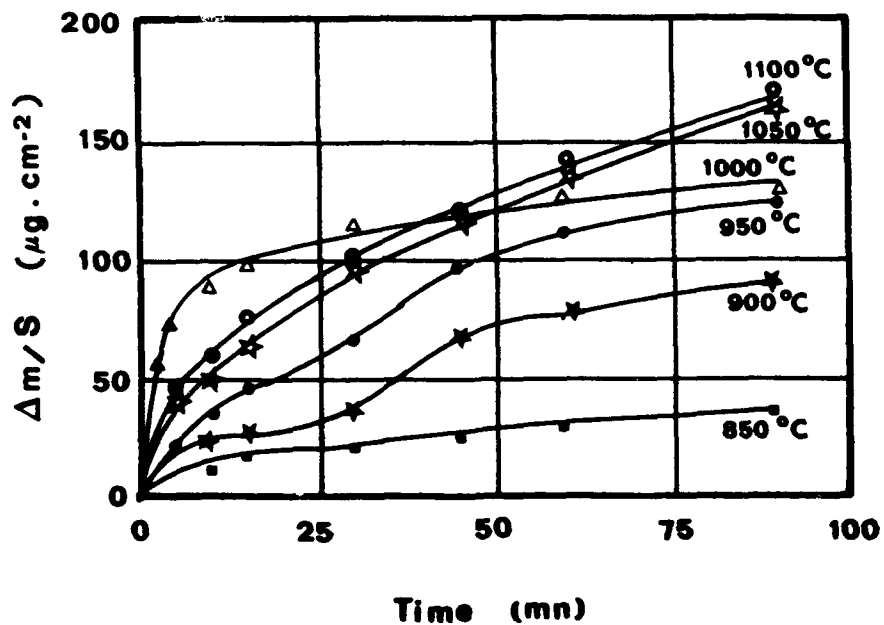


Figure 3 : Oxidation kinetics of FeCrAl alloy at different temperatures.

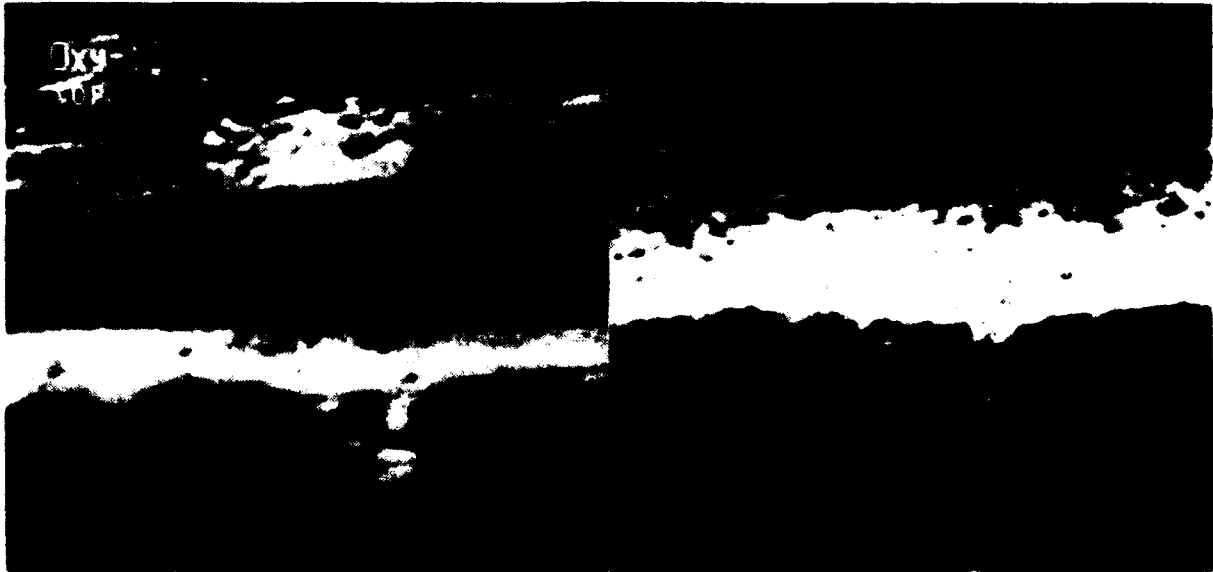


Figure 4 : SIMS analysis of samples oxidized in oxygen 16 then in oxygen 18 ;
Taper cross-section after oxidation at 1100°C.

Passive Film Studies Using Neutron Reflectivity

L. A. Krebs and J. Kruger
The Johns Hopkins University
Dept. of Materials Science and Engineering
Baltimore, MD 21218

G. G. Long
National Institute of Standards and Technology (NIST)
Ceramics Division
Gaithersburg, MD 20899

D. G. Wiesler, J. F. Ankner, C. F. Majkrzak, and S. K. Satija,
National Institute of Standards and Technology (NIST)
Reactor Radiation Division
Gaithersburg, MD 20899

Abstract

Spin-polarized neutron reflectivity is employed to characterize the passive film on iron. Thermal neutrons are used to probe the nuclear and magnetic scattering density profiles in the film and substrate, and to establish parameters for the metal-oxide interface and the oxide surface. Three surface film conditions are considered: the native oxide layer, the in-situ passive layer, and the same passive layer ex-situ. Complementary data are obtained using x-ray reflectivity in the ex-situ cases.

The thickness of the passive layer and the underlying iron layer, surface and interfacial roughness, and magnetic properties are some of the parameters available through the neutron reflectivity technique. Changes in scattering density due to removal of the passivated sample from the in-situ environment may be detectable as well. Determination of the magnetic characteristics of the passive film may be especially useful in determining the film composition and structure. This project is funded by the National Science Foundation under grant number DMR-9108368.

Key terms: spin-polarized neutron reflectivity, passivity, iron, in-situ

Introduction

The true nature of the passive film on metals and alloys has been a source of controversy since the phenomenon was first observed. We hope to resolve some the characteristics of the passive film on iron using spin-polarized neutron reflectivity. The neutron reflectivity technique allows us to study the passive film at the film surface and the film-metal interface, both in-situ and ex-situ. Using this technique we obtain information regarding the characteristics of the passive film: thickness, surface and interfacial roughness, and profiles of the nuclear and magnetic scattering densities. We also employ x-ray reflectivity to complement and confirm the neutron reflectivity data.

The use of spin-polarized neutrons to probe the scattering densities of the passive layer allows us to determine, for example, whether the film is ferromagnetic. If it can be shown that the passive film on iron is ferromagnetic, then the number of possible models for passivity would be greatly reduced¹. By collecting data on the native oxide, the in-situ passive film, and the same film ex-situ, reflectivity can also be used to explore changes in films that are removed from solution and dried after passivation.

The derivation for neutron reflectivity is similar to the conventional treatments of electromagnetic optics². Descriptions of neutron reflectivity theory and techniques are available from several sources³⁻⁵. Interested readers are directed to these references.

Experiment

A neutron beam can travel through perfectly crystalline materials such as silicon with a negligible amount of attenuation or small angle scattering. The samples and electrochemical cell for our study were designed to take advantage of this fact, such that the attenuation and increased background signal due to inelastic and incoherent scattering in an aqueous medium are avoided.

The sample consists of a 12 nm layer of iron sputter-deposited onto a 10 cm-diameter single crystal Si wafer. An earlier sample design¹ used in this experiment had a 30 nm layer of aluminum oxide followed by a 30 nm layer of iron sputter-deposited onto the Si substrate¹. The aluminum oxide layer was intended to act as a barrier to protect the silicon wafer against hydrogen diffusion during cathodic reduction. However, we have found that by keeping the reduction time short, the barrier layer can be eliminated without ill effect. The effects due to the altered sample configuration are discussed below.

The iron surface with its native oxide intact provided the starting point for our study. First x-ray, then spin-polarized neutron reflectivity data were taken for this case. Next neutron reflectivity was performed on the passivated surface in-situ. Finally, the sample was removed from the cell, rinsed with purified water, and dried quickly in a stream of N₂ gas in preparation for the ex-situ passive film data collection, using first neutron, then x-ray techniques. The native oxide and the ex-situ passive film were both exposed to the ambient environment for the duration of the data collection, roughly 12 hours for each neutron reflectivity scan.

The sample was clamped to a polytetrafluoroethylene cup fitted with a Pt counter electrode and a saturated calomel reference electrode (SCE) to form the body of a sealed electrochemical cell approximately 100 ml in volume. Our earlier cell¹ allowed the aqueous solution to be exposed to air, which affected the passive film formation. Ex-situ data were collected on the air-formed oxide, using the technique described below, before the cell was filled with solution.

For the in-situ portion of the experiment, all potentials were measured versus SCE. The solution was a pH 8.2 borate buffer. The solution was made oxygen-free by bubbling water-saturated N₂ gas through the holding vessel before transferring the solution to the cell. After cathodically reducing the surface for seven minutes at -1.0V to remove the native oxide, the system was stepped to a passivating potential of +0.750V⁶. Neutron reflectivity data were collected after the initial film growth phase was completed, as indicated by the leveling off of the current density at a suitably low value (about 0.1 $\mu\text{A}/\text{cm}^2$). Data collection continued over a period of roughly 12 hours while the system was held under potentiostatic control.

Data were taken on the BT-7 polarized neutron reflectometer⁷ at the NIST Research Reactor in Gaithersburg, MD. The entire cell assembly was placed in the neutron beam on a rotating stage. The axis of rotation was the vertical (z) axis, parallel to and centered on the face of the sample. The beam entered the Si wafer edge-on (nearly normal incidence to the edge), and was then reflected from the sample surface at glancing angles. In this configuration the in-situ experiment can easily be performed without the noise and signal loss associated with inelastic and incoherent scattering in water.

The entire cell was placed in a constant magnetic field of 225 G directed parallel to the sample surface. The sample was then exposed to spin-polarized neutrons of wavelength 2.37 Å. Data were collected by measuring the reflected beam intensity as a function of incident angle for spin states both parallel and anti-parallel to the applied magnetic field during θ - 2θ scans in the vicinity of the critical angle for total external reflection, θ_c . Identical scans were performed for each case discussed: the native oxide, the in-situ passive layer, and the ex-situ passive layer. For a ferromagnetic material such as iron, differences in the total scattering densities are seen by the two polarized spin states. Therefore, two reflectivity curves are produced to describe each case.

In addition to the neutron reflectivity data collected on the ex-situ films, x-ray reflectivity scans were also performed. Using a stationary anode machine producing x-rays of wavelength 1.54 Å, the iron surface with its native oxide was examined to confirm layer structure. The identical examination was performed again on the ex-situ passive layer after the neutron reflectivity scans were completed. While x-rays and neutrons scatter from different atomic components, the data sets can be handled in same fashion, resulting in complementary scattering density profiles for the sample in the ex-situ cases. These data are especially helpful in confirming layer thickness and interfacial roughness parameters.

Results

Figure 1 shows the most recent data for the native oxide film, the electrochemically produced in-situ passive film, and the rinsed and dried ex-situ passive film on the iron sample described above. The data are given in terms of the momentum transfer Q versus the logarithm of the reflected intensity. Q is related to the incident angle θ by the expression

$$Q = 2k_0 \sin\theta, \quad (1)$$

where k_0 is the incident wavevector magnitude. In all cases the sample was exposed to a magnetic field of 225 G parallel to the plane of the surface. The two plots indicate the reflectivities of neutrons polarized parallel to the applied magnetic field, or "spin-up" (part (a)), and those polarized anti-parallel, or "spin-down" (part (b)). It can be seen immediately that the air-formed oxide originally on the surface differs from the passive film. In our previously reported work¹, no difference in the native oxide and the passive film was apparent. This may be accounted for by the changes in both sample and electrochemical cell configuration.

Work in progress includes fitting a model to each of the reflectivity plots shown in Figure 1, and to the x-ray reflectivity data (not shown). Each model is based on a scattering density profile; total scattering density as a function of depth into the sample. The models are derived using fitting programs developed by Ankner and Majkrzak⁸. Previous modelling attempts based on the more complex sample configuration have been discussed elsewhere¹. By starting with a thinner iron layer, and removing the aluminum oxide barrier layer entirely, the overall thickness of the sample was greatly reduced, and two interfaces were eliminated. Consequently, the reflectivity patterns are less complex than those reported earlier. The data discussed here, obtained by neutron and x-ray reflectivity, should lead to reliable models for the passive film on iron, both in-situ and ex-situ.

Conclusion

Spin-polarized neutron reflectivity appears to be a useful method for determining the nuclear and magnetic properties of the passive film on iron. X-ray reflectivity data can be used to supplement some of the neutron reflectivity results. Knowing in particular the magnetic properties of this film may help reduce the number of possible structure models.

A sufficiently large magnetic scattering density detectable in a sample polarized in a relatively small magnetic field is an indication of ferromagnetism. Two iron oxides known to be ferromagnetic are magnetite (Fe_3O_4) and maghemite ($\gamma\text{-Fe}_2\text{O}_3$)⁹. If the film proves to be ferromagnetic, it would support models calling for a single layer of Fe_3O_4 , or an $\text{Fe}_3\text{O}_4/\gamma\text{-Fe}_2\text{O}_3$ bi-layer¹⁰. There is some concern that what may appear as ferromagnetism in a bulk oxide will instead become superparamagnetism in a thin film¹¹. If this is the case for the passive film on iron, it will be extremely difficult to apply a polarizing magnetic field strong enough to observe any changes in magnetic scattering density.

References

1. L.A. Krebs, J. Kruger, G.G. Long, J.F. Ankner, C.F. Majkrzak, S.K. Satija, D.G. Wiesler, Proc. Of the Symposium on Oxide Films on Metals and Alloys, 92-22, (Pennington, NJ: The Electrochemical Society, 1992): p. 580.
2. M. Born and E. Wolf, Principles of Optics, (Oxford: Pergamon Press, 1980).
3. C.F. Majkrzak and G.P. Felcher, Mater. Res.Soc. Bull., 15, 11, (1990): p. 65.
4. J. Penfold and R.K. Thomas, J. Phys. C, 2, (1990): p. 1369.
5. T.P. Russell, Mat. Sci. Rep., 5, (1990): p. 171.
6. M. Nagayama and M. Cohen, J. Electrochemical Soc., 109, (1962): p. 781.
7. C.F. Majkrzak, Physica B, 173, (1991): p. 75.
8. J.F. Ankner and C.F. Majkrzak, in "Neutron Optical Devices and Applications," Vol. 1738, SPIE Conference Proceedings, in press.
9. J.W. Murray, Marine Minerals, 6, (Washington D.C.: Mineralogical Soc. of America, 1979): p. 47.
10. J. Kruger, International Materials Reviews, 33, (1988): p. 113.
11. M.E. Brett, K.M. Parkin, M.J. Graham, J. Electrochem. Soc., 133, (1986): p. 2031.

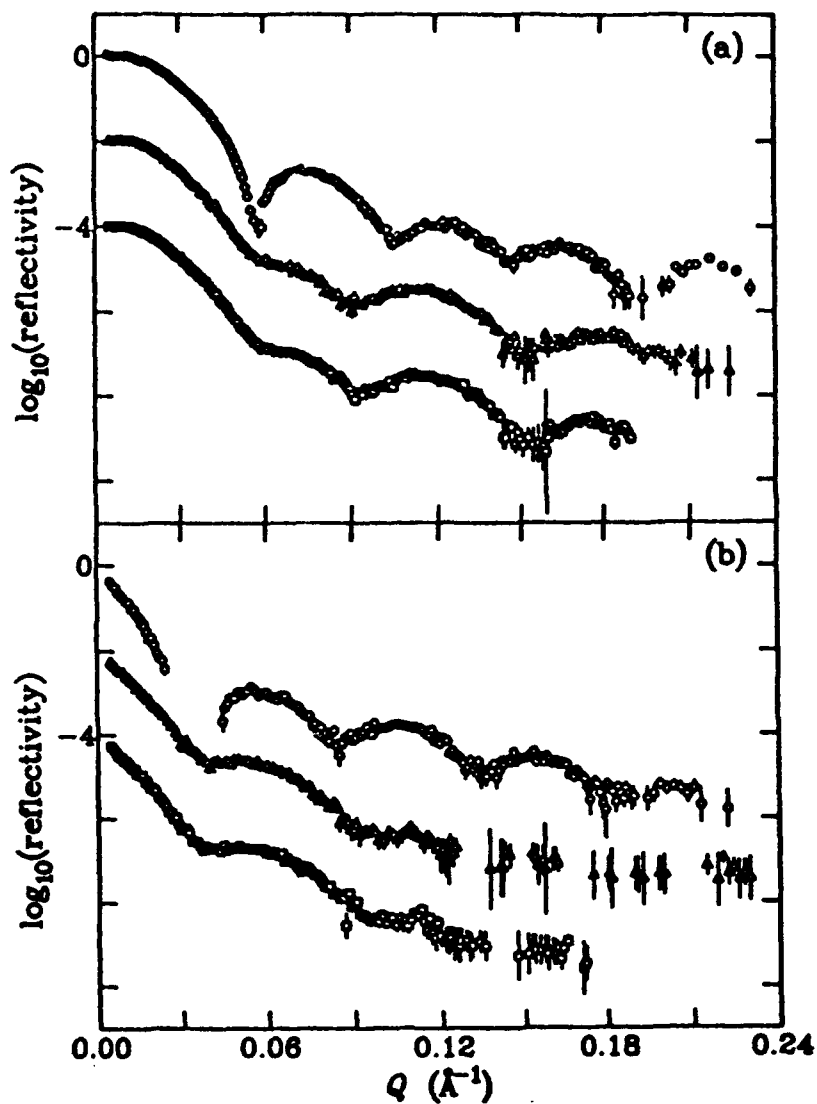


Figure 1. Spin-polarized neutron reflectivity data for various surface films on an iron substrate. The native oxide is represented by circles, the in-situ passive film by triangles (offset by two orders of magnitude), and the same passive film ex-situ by squares (offset by four orders of magnitude). Part (a) shows data for neutrons polarized parallel to an applied magnetic field, part (b) shows the same for neutrons polarized anti-parallel.

**Corrosion of Iron in Electrolytic Anhydrous Methanol Solutions
with and without Complexing Agents**

Kunitsugu Aramaki
Keio University
Hiyoshi, Yokohama, Japan

Makoto Sakakibara
Keio University
Hiyoshi, Yokohama, Japan

Hiroshi Nishihara
Keio University
Hiyoshi, Yokohama, Japan

Abstract

Corrosion of iron in an anhydrous methanol solution of 0.1M LiClO₄ (< 150 ppm of water) was investigated by impedance and polarization measurements and x-ray photoelectron spectroscopy (XPS). Under a dry argon atmosphere (< 0.01 ppm O₂ and < 50 ppm H₂O) in a dry box, an iron electrode was abraded with alumina powder, rinsed with anhydrous methanol, and then immersed in the methanol solution. The impedance of this electrode was measured in the solution under the argon atmosphere with a frequency response analyzer. The corrosion rate obtained from the impedance at the open-circuit potential decreased with an increase in the immersion time, suggesting the formation of a barrier layer on the surface. Results of XPS measurements demonstrated that a precipitate of ferrous methoxide forms on the iron surface.

Effects of complexing agents like 1,10-phenanthroline and 2,3-dimercapto-1-propanol on the corrosion rate of iron in the anhydrous methanol solution were studied by polarization measurement and XPS. Little effect of the complexing agents on the cathodic hydrogen evolution was observed in the polarization curves but the anodic iron dissolution was affected by the formation of complexes through reactions with ferrous methoxide. When a soluble complex in anhydrous methanol formed at the surface, the anodic reaction was markedly stimulated. The absence of the methoxide layer on the iron surface by the formation of the soluble complex was revealed by XPS data. If an insoluble complex formed at the surface, a protective layer of the complex on the surface suppressed the anodic and cathodic processes of iron corrosion.

Key terms: iron corrosion, anhydrous methanol, impedance, polarization, x-ray photoelectron spectroscopy, ferrous methoxide, complexing agents, 1,10-phenanthroline, 2,3-dimercapto-1-propanol

I. Introduction

Most of the studies on corrosion of metals in nonaqueous solvents have been associated with the effects of additives or contaminants like water, acids, oxygen molecules, and chloride ion on active corrosion and passivity of metals.¹ Many investigations on electrochemical corrosion of iron and iron-based alloys in electrolytic methanol solutions have been focused on the influence of the water content in the solutions on their active corrosion²⁻⁵ and passivity.⁶⁻⁹ Water at less than 460 ppm in a methanol solution of 0.1M LiClO₄ is insufficient to assure stable passivation of iron.⁶ De Anna⁷ has also described that iron is always active in a 0.1M LiClO₄-methanol solution containing water at < 500 ppm. The corrosion process at a bare metal in an electrolytic anhydrous methanol solution seems to be important in understanding corrosion and passivity phenomena of metals in anhydrous nonaqueous media.

The authors have found that a passive film formed on an iron surface during its preparation by abrasion and ultrasonic cleaning on exposure to air is sufficient to protect iron from corrosion in an electrolytic anhydrous methanol solution.¹⁰ All manipulations for preparing the surface of an iron electrode must be carried out under an inert gas atmosphere.

Since anhydrous methanol can react with most protic acids like hydrochloric and carboxylic acids forming water, concentrations of the acid and water may change with an increase of time, resulting in variation of the corrosion rate. The corrosion rate of iron in an anhydrous methanol solution of 0.05M formic acid plus 0.1M LiClO₄ has been found to decrease with an increase in the immersion time because of the formation of methyl formate.¹¹ Hence, protic acids which are not reactive with methanol must be used as additives in anhydrous methanol.

In this work, impedance measurements of an iron electrode prepared under a dry argon atmosphere were performed in an anhydrous methanol solution of 0.1M LiClO₄ containing less than 150 ppm of water. Polarization measurements were carried out on the iron electrode in the methanol solution with and without a complexing agent to stimulate or suppress the corrosion of iron in anhydrous methanol. Layers formed on the iron surface were analyzed by x-ray photoelectron spectroscopy (XPS).

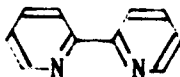
II. Experimental

A. Materials

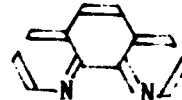
Anhydrous methanol was obtained as a reagent for high pressure liquid chromatography (Merck, < 100 ppm of water) and used without further purification. Analytical reagent grade LiClO₄ used as an electrolyte was desiccated with P₂O₅ and dissolved in anhydrous methanol at a concentration of 0.1M under a dry argon atmosphere in a dry box (< 0.01 ppm of oxygen and < 50 ppm of water). The electrolytic methanol solution was stored in the presence of 4 Å molecular sieves in the dry box. The water

content in the methanol solution, determined by the Karl-Fischer method, was maintained below 150 ppm.

High grade reagents of complexing agents, ethylene diamine $\text{NH}_2\text{CH}_2\text{CH}_2\text{NH}_2$, 2,2'-bipyridine



, 1,10-phenanthroline



acetylacetone $\text{CH}_3\text{COCH}_2\text{COCH}_3$, catechol



, 2,3-dimercapto-1-propanol

$\text{SHCH}_2\text{CH}(\text{SH})\text{CH}_2\text{OH}$ were used after drying in a desiccator. They react with ferrous ion to form stable complexes but do not with anhydrous methanol.

A cross section of an iron rod (99.99%, Johnson Matthey Chemicals, 5 mm ϕ) mounted in a Teflon holder was used as an electrode. After abrasion of the electrode surface with emery papers in air, the surface was polished with 1 μm alumina abrasive in the dry box filled with dry argon gas. The electrode was rinsed with anhydrous methanol and immediately immersed in the electrolyte methanol solution for the electrochemical measurements. All procedures were performed in the dry box.

A disk of iron (99.99%, Japan Lamp Industries, 10 mm ϕ) for XPS measurement was fixed at the end of a Teflon holder with a thermoshrinkable Teflon tube. The disk was abraded with emery papers and 1 μm alumina powder, rinsed with methanol in air or under the argon atmosphere in the dry box.

B. Preparation of Ferrous Methoxide

Ferrous methoxide $\text{Fe}(\text{OCH}_3)_2$ was prepared by the reaction of lithium methoxide with ferrous chloride in anhydrous methanol under a nitrogen atmosphere as¹²



A green crystal of the product was washed with anhydrous methanol under a nitrogen atmosphere and dried in vacuo. The product was identified by FTIR spectroscopy. This compound was susceptible not only to hydrolysis but also to oxidation with oxygen forming a brown solid of ferric methoxide. This result implies that all procedures in electrochemical and analytical measurements in this study must be performed under an inert gas atmosphere to avoid contact with air. Ferrous methoxide gradually decomposed at an elevated temperature forming a black solid.

C. Impedance Measurements

The impedance of the iron electrode in the anhydrous methanol solution of 0.1M LiClO_4 was measured at the open-circuit potential E_{oc} under the argon atmosphere in the dry box with a platinum counter electrode and a Ag/AgCl (methanol) reference electrode connected to a potentiostat, a frequency response analyzer, and a computer. Sine wave voltages (5 mV rms) between 10 kHz and 100 MHz were superimposed on the potential. The measurement was controlled with the aid of computer programs.¹³

D. Polarization Measurements

Polarization curves of the iron electrode were measured in an anhydrous methanol solution of 0.1M LiClO₄ without and with complexing agents at 25°C under the argon atmosphere in the dry box. The potential was referred to a Ag/AgCl(methanol) electrode. After immersion of the iron electrode in the solution for 1 h, the potential was changed stepwise every 60 s by 10 mV starting from E_{oc}. The cathodic and anodic curves were obtained separately. Several runs were made for each of the curves.

E. XPS Measurements

The iron disk was immersed in an anhydrous methanol plus 0.1M LiClO₄ solution without or with the complexing agent at 25°C for 5 h under the argon atmosphere in the dry box. The disk was taken off the Teflon holder and rinsed with anhydrous methanol in the dry box and then dried in vacuo overnight. The disk was mounted on a sample holder and fixed in a subchamber of an XPS spectrometer under an argon or nitrogen atmosphere using the dry box and a dry bag.

X-ray photoelectron spectra of the disk surface were measured using a JEOL JPS-90SX spectrometer with Mg K_α radiation as the x-ray source. Components of interest on the iron surface were Fe and O. The binding energies were referred to the C (1s_{1/2}) binding energy of a contaminant carbon at 284.6 eV and the resolution of binding energy was 0.05 eV. Depth profiles of Fe and O were obtained by ion bombardment with an Ar⁺ gun. The spectrum of O (1s_{1/2}) for ferrous methoxide was also recorded on the spectrometer using a disk prepared by molding with electrically conducting acetylene black.

III. Results and Discussion

A. Corrosion of Iron in an Anhydrous Methanol Solution of 0.1M LiClO₄

Figure 1(a) shows x-ray photoelectron spectra of Fe (2p) and O (1s) for the iron surface prepared by abrasion and cleaning in air and then immersed in the methanol solution under the argon atmosphere in the dry box. Depth profiles of the spectra were also shown with the sputtering time t_s. Peaks of oxidized and metallic iron appeared at about 711 and 706.9 eV of the binding energies in the spectra of Fe (2p_{3/2}). Peaks of O (1s_{1/2}) emerged at 530.5 and 531.4 eV, suggesting the formation of ferric oxyhydroxide or oxide at the surface of the iron electrode prepared in air.¹⁴ Since this oxyhydroxide or oxide on the iron surface has been proved to act as a passive film to prevent iron corrosion in the anhydrous methanol solution,¹⁰ the surface of the iron electrode must be prepared under an inert gas atmosphere.

Figure 1(b) illustrates depth profiles of the Fe (2p_{3/2}) and O (1s_{1/2}) spectra for the surface of the iron disk prepared by abrasion and rinsing with methanol under the argon atmosphere in the dry box and then immersed in the anhydrous methanol solution under the same atmosphere. A weak peak

of oxidized iron, probably ferrous ion appeared at $t_i = 0$ and 2 s. Two peaks of O ($1s_{1/2}$) emerged at about 532 and 530.5 eV in the region of t_i up to 30 s. The spectra of O ($1s_{1/2}$) will be discussed in detail later.

In order to investigate the corrosion rate of bare iron in the anhydrous methanol solution, the impedance was measured of the iron electrode in the solution under the argon atmosphere at E_{oc} . Assuming a simple equivalent circuit, parallel capacitor-resistor combination at the electrode interface, the charge transfer resistance was obtained from the impedance modulus at the maximum phase angle in the Bode diagram.¹⁵ An example of the Bode diagram for iron in the anhydrous methanol solution is shown in Figure 2. Since the faradaic conductance K_f , which is the reciprocal of the charge transfer resistance, is proportional to the corrosion rate at E_{oc} , the values of K_f were plotted against the immersion time t_i in Figure 3. The figure shows the occurrence of iron corrosion in the electrolytic anhydrous methanol solution. Though the K_f values were scattered at the initial stage of the immersion, the corrosion rate decreased with an increase of t_i . Retardation of the rate suggested that the iron surface was covered with a protective layer of corrosion product sparingly soluble in anhydrous methanol.

B. Formation of Ferrous Methoxide on the Iron Surface

Ferrous or ferric methoxide has been presumed to form on the iron surface in anhydrous methanol (< 100 ppm of water) under a nitrogen or oxygen atmosphere.⁵ Farina et al.⁶ have assumed the formation of $FeOCH_3^+$ in the process of iron corrosion in an acidified methanol solution containing 200 ppm of water. Ferrous methoxide may play an important role in the process of iron corrosion in anhydrous methanol solutions. The corrosion product was identified by comparing an x-ray photoelectron spectrum of O ($1s_{1/2}$) for the product formed on the surface in the anhydrous methanol solution with that of synthesized ferrous methoxide.

Figure 4(a) to (c) exhibit detailed x-ray photoelectron spectra of O ($1s_{1/2}$) shown in Figure 1(a) and (b) at $t_i = 2$ s and a spectrum of O ($1s_{1/2}$) for ferrous methoxide, respectively. A peak of ferrous methoxide appeared at 532.0 eV. Since the binding energy of this peak was higher than 531.4 and 530.5 eV, binding energies of peaks in the spectrum of ferric oxyhydroxide formed during the preparation of the surface in air, as shown in (a) and (c), a covalent-like bond may form between oxygen and iron atoms in the methoxide. The peak at 532.0 eV shown in (c) was apparently distinguishable from the peak at 531.4 eV in (a), judging from the reproducibility and the resolution of the binding energies.

As shown in Figure 4(b), the spectrum of O ($1s_{1/2}$) for the iron surface which was prepared by abrasion and rinsing with methanol under the argon atmosphere and then immersed in the anhydrous methanol solution under the same atmosphere revealed a peak at 532.0 eV and a shoulder at 530.5 eV. The former peak was assigned to that for atomic oxygen of the methoxide and the latter to that for oxide ion. It was concluded that ferrous methoxide forms on the bare iron surface in the anhydrous methanol

solution of 0.1M LiClO₄. Because ferrous methoxide is sparingly soluble in anhydrous methanol, a barrier layer of the deposited methoxide formed on the iron surface which protects the surface against corrosion in methanol, resulting in the decrease of the corrosion rate with an increase of the immersion time, as shown in Figure 3.

A shoulder in the spectrum of O (1s_{1/2}) for ferrous methoxide appeared at 530.5 eV as shown in Figure 4(c), being suggestive of the ferrous oxide formation in the methoxide. To elucidate a decomposition reaction of ferrous methoxide to form the oxide, the methoxide was heated at 100°C under a reduced pressure at 13.2 Pa (10⁻¹ mmHg) and any evolved gas was collected through a trap chilled with liquid nitrogen. The trapped gas was analyzed by gas chromatography. The retention time of the evolved gas agreed with that of an authentic sample of dimethyl ether. A green crystal of the methoxide changed to a black solid during this experiment. Hence, ferrous methoxide decomposes gradually forming ferrous oxide and dimethyl ether as

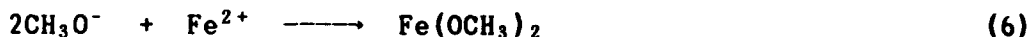


The presence of ferrous oxide observed in Figure 4(b) may be attributed to the methoxide decomposition.

If electrochemical processes of iron corrosion occur in the anhydrous methanol solution of 0.1M LiClO₄, cathodic, hydrogen evolution and anodic, iron dissolution reactions can be considered,



Methoxide ions and ferrous ion reacted immediately to form a precipitate of ferrous methoxide as



The layer of the deposited methoxide on the surface suppresses the cathodic and anodic reactions, resulting in the low corrosion rate.

C. Iron Corrosion with Complexing Agents in Anhydrous Methanol

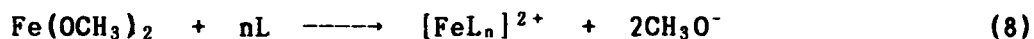
Figure 5 shows polarization curves of the iron electrode in anhydrous methanol solutions of 0.1M LiClO₄ without and with 1X10⁻⁴M of ethylene diamine, 2,2'-bipyridine, and 1,10-phenanthroline under the argon atmosphere. The curves of the electrode in the methanol solutions containing catechol, acetylacetone and 2,3-dimercapto-1-propanol at 1X10⁻⁴M are also shown in Figure 6. They react with ferrous ion to form stable complexes in aqueous solutions.¹⁶ Because these curves were not reproducible, several runs were made for each of the anodic and cathodic curves and averages of the curves are shown in the figures. Since the anodic Tafel lines could not be defined in some cases, no accurate

corrosion current densities were obtained by Tafel extrapolation. Nevertheless, these curves provided useful information for elucidating the processes of iron corrosion in an electrolytic methanol solution.

Well defined Tafel regions were exhibited in all cathodic curves. Most of the cathodic Tafel lines in the presence and absence of the complexing agents were fairly close to each other except the line for catechol. The values of the cathodic Tafel slope were markedly high, 0.59 V/decade on average, as compared with those for iron in aqueous and nonaqueous solutions of protic acids, suggesting a different mechanism for the cathodic process of iron corrosion in the methanol solutions from that of the hydrogen evolution reaction in protic acid solutions. Although dissociation constants of acetylacetone (pK_a in water = 8.93), catechol (9.19), and 2,3-dimercapto-1-propanol (8.58) in anhydrous methanol must be higher than the value of methanol (16.71)¹⁷, the cathodic reaction was unlikely associated with protons afforded by the dissociation of these compounds except catechol. Direct reduction of methanol may take place at the iron surface under no influence of protons released from complexing agents, as



The complexing agent in the anhydrous methanol solution affects the anodic polarization curve to a greater extent than the cathodic one. 2,3-Dimercapto-1-propanol remarkably accelerated the anodic process, probably forming a ferrous complex at the surface. Because this complex was dissolved into the methanol solution, it was considered that the anodic reaction was markedly stimulated by the addition of the complexing agent. Catechol formed a layer of dark red complex deposit on the surface, being rather protective against iron corrosion in methanol, as shown in Figure 6. The anodic process of iron corrosion in the methanol solution containing $1 \times 10^{-4} \text{M}$ of aprotic complexing agents was stimulated in the order, ethylene diamine < 2,2'-bipyridine < 1,10-phenanthroline. Since this order agrees with that of the stability constants for Fe^{2+} complexes of these agents in aqueous solutions ($pK = 9.72, 17.2, \text{ and } 21.0$, respectively¹⁶), the stimulation of anodic process with the complexing agent is associated with the stability of complex formation. Because the complexing agents except catechol accelerated the anodic process of iron corrosion in the methanol solutions of the agents, soluble complexes were formed by the reaction of ferrous methoxide with complexing agents, L for example, as



and ferrous ion was removed away from the surface, resulting in stimulation of the anodic process expressed by Equations (5), (6), and (8). In fact, x-ray photoelectron spectra for the iron surface previously treated with 2,3-dimercapto-1-propanol in the anhydrous methanol solution showed the presence of the ferrous complex and oxide only at the outermost layer of the surface within the sputtering time $t_s < 5 \text{ s}$, as shown in Figure 7. Since peaks of the methoxide and oxide in the spectra of O ($1s_{1/2}$) for the

iron surface immersed in the methanol solution without the complexing agent appeared even at $t_c = 30$ s, as shown in Figure 1(b), it was concluded that ferrous methoxide was dissolved into the solution from the surface by the formation of the complex.

IV. Conclusions

Ferrous methoxide forms as the corrosion product of iron in an anhydrous methanol solution of 0.1M LiClO₄ under an argon atmosphere. Because the methoxide, which is sparingly soluble in anhydrous methanol, precipitates on the iron surface forming a barrier layer, the corrosion rate decreases with an increase of the immersion time. Polarization curves of an iron electrode in the electrolytic anhydrous methanol solution containing complexing agents which form stable complexes with ferrous ion revealed that the agents affect the anodic iron dissolution process to more extent than the cathodic hydrogen evolution reaction. If soluble complexes form at the surface by reactions of the methoxide with the agents, the anodic process is stimulated. The formation of a complex insoluble in anhydrous methanol results in suppression of the anodic and cathodic processes. Direct reduction of methanol at the iron surface to form a hydrogen molecule and methoxide ion was proposed as the cathodic reaction. The methoxide ion combines with the ferrous ion afforded by the anodic process, forming ferrous methoxide.

References

1. E. Heitz, *Advances in Corrosion Science and Technology*, 4, M. Fontana, R. Staehle ed. (New York: Plenum Press 1974), p. 149.
2. P. Hronsky, *Corrosion* 37 (1981): p. 161.
3. S. Sternberg, V. Brânzoi, *Electrochim. Acta* 29 (1984): p. 15.
4. F. Bellucci, L. Nicodemo, B. Licciardi, *Corros. Sci.* 27 (1987): p. 1313.
5. U. Lechner-Knobalauch, E. Heitz, *Electrochim. Acta* 32 (1987): p. 901.
6. C. A. Farina, G. Faita, F. Olivani, *Corros. Sci.* 18 (1978): p. 465.
7. P. L. De Anna, *Corros. Sci.* 25 (1985): p. 43.
8. F. Bellucci, G. Capobianco, G. Faita, C. A. Farina, G. Farnia, F. Mazza, S. Torchio, *Corros. Sci.* 28 (1988): p. 371.
9. R. G. Kelly, P. J. Moran, *Corros. Sci.* 30 (1990): p. 495.
10. M. Sakakibara, N. Saito, H. Nishihara, K. Aramaki, *Corros. Sci.* 34 (1993): p. 391.
11. Unpublished data.
12. G. E. Calf, J. L. Garnett, *Aust. J. Chem.* 19 (1966): p. 211.
13. K. Shimura, H. Nishihara, K. Aramaki, *Boshoku Gijutsu* 35 (1986): p. 289.
14. K. Asami, K. Hashimoto, *Corros. Sci.* 17 (1977): p. 557.
15. F. Mansfeld, *Corrosion* 36 (1981): 301.
16. R. M. Smith, A. E. Martell, *Critical Stability Constants*, 2 and 3 (New York: Plenum Press 1976).
17. J. J. Christensen, L. D. Hansen, R. M. Izatt, *Handbook of Proton Ionization Heats* (New York: John Wiley & Sons 1976).

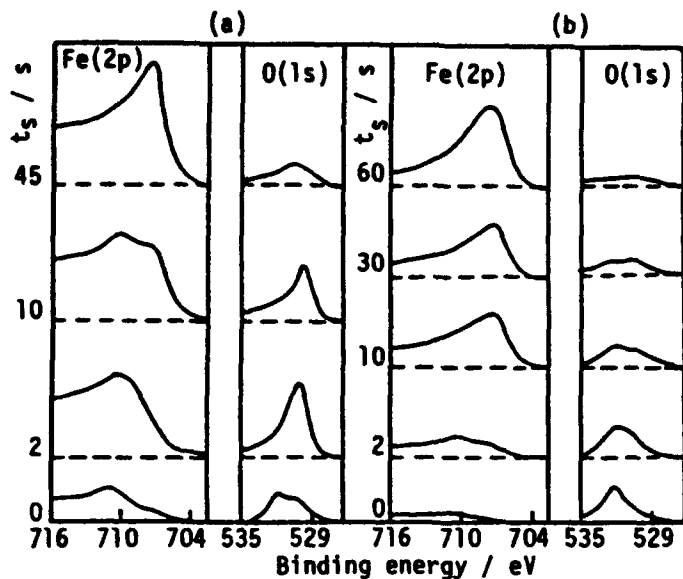


FIGURE 1. X-ray photoelectron spectra of Fe (2p) and O (1s) for the iron surface (a) prepared in air and then immersed in an anhydrous methanol solution of 0.1M LiClO₄ under an argon atmosphere and (b) both prepared and immersed in the solution under an argon atmosphere.

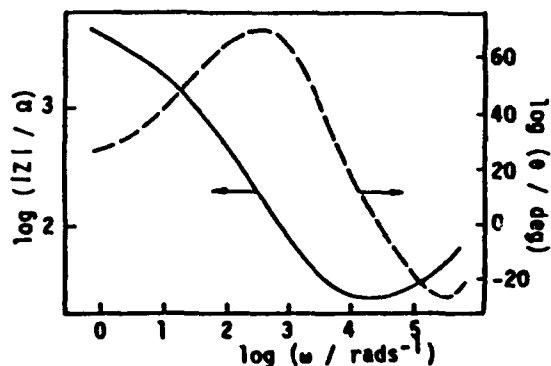


FIGURE 2. Typical Bode diagram (impedance Z , phase angle θ , and frequency ω) for iron in an anhydrous methanol solution of 0.1M LiClO₄.

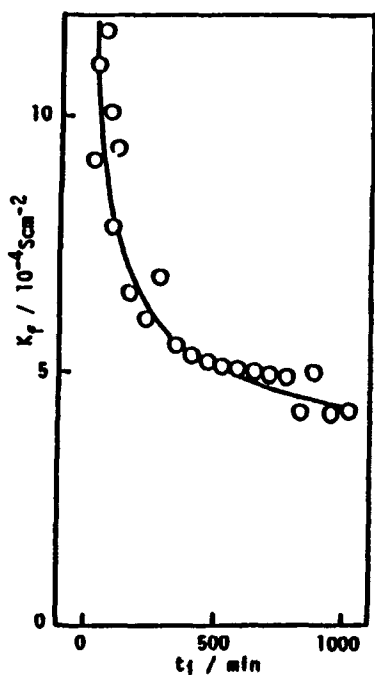


FIGURE 3. Change of the faradaic conductance K_f with the immersion time t_i for iron in anhydrous methanol solution of 0.1M LiClO₄.

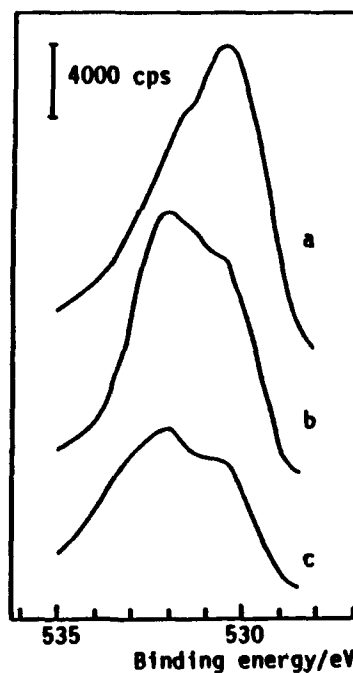


FIGURE 4. Detailed x-ray photoelectron spectra of O (1s) (a) shown in Figure 1(a) and (b) in Figure 1(b) at $t_i = 2$ s and (c) for ferrous methoxide.

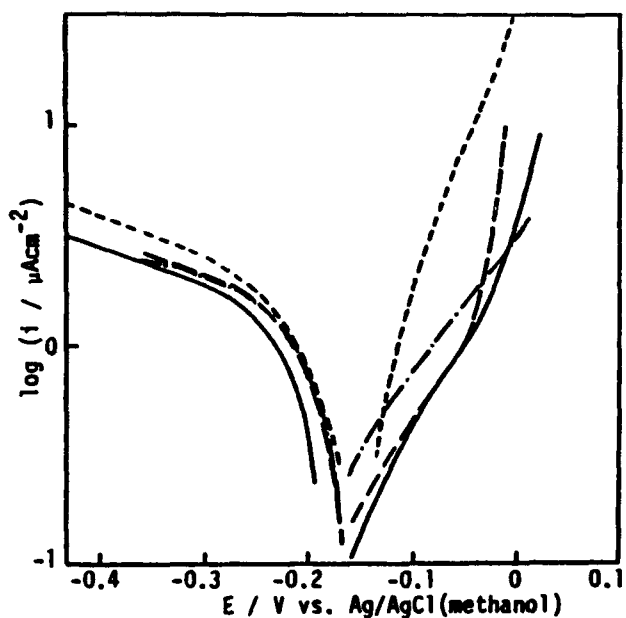


FIGURE 5. Polarization curves (potential E and current density i) of iron in methanol-0.1M LiClO_4 solutions without (—) and with ethylene diamine (---), 2,2'-bipyridine (-·-·-), and 1,10-phenanthroline (----) at $1 \times 10^{-4} \text{M}$.

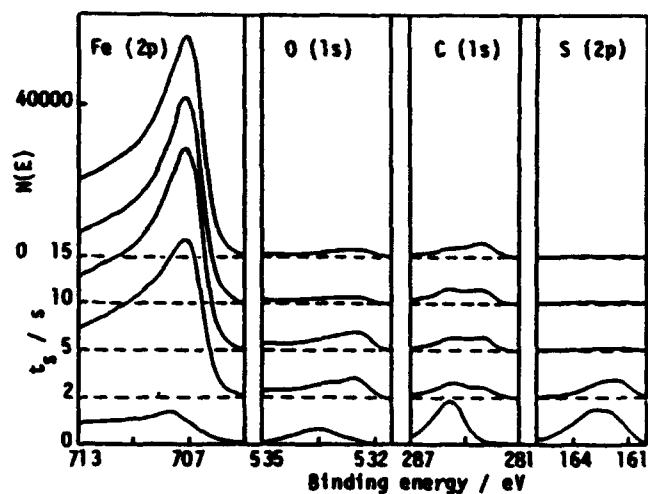


FIGURE 7. X-ray photoelectron spectra of Fe (2p), O (1s), C (1s), and S (2p) for iron treated with 2,3-dimercapto-1-propanol in the methanol solution.

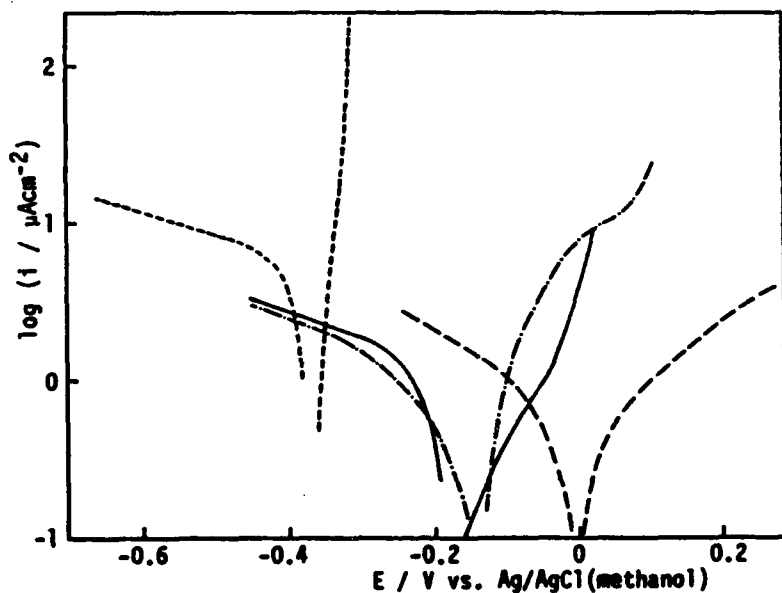


FIGURE 6. Polarization curves of iron in methanol-0.1M LiClO_4 solutions without (—), with catechol (---), acetylacetone (-·-·-), and 2,3-dimercapto-1-propanol (----) at 1×10^{-4} .

In-Situ Gravimetry of Corrosion of Iron Thin Films Combined with Surface Analytical Techniques

Masahiro Seo

Faculty of Engineering, Hokkaido University
Kita-13 Jo, Nishi-8 Chome, Kita-ku
Sapporo 060, Japan

Kengo Yoshida

Faculty of Engineering, Hokkaido University
Kita-13 Jo, Nishi-8 Chome, Kita-ku
Sapporo 060, Japan

Abstract

Corrosion and passivation of electroplated iron thin film in pH 6.48 boric acid-sodium borate solution were investigated by using the quartz crystal microbalance (QCM) technique combined with Auger electron spectroscopy (AES) for a better understanding of the corrosion of metal thin films. Moreover, the differences in corrosion behavior between iron thin films and bulk iron were examined.

The passivation potential of iron thin films was higher than that of bulk iron. Bulk iron was more easily passivated than iron thin films. No impurities were detected in iron thin film within the detection limit of AES. The differences in corrosion behavior between thin film and bulk, therefore, were attributed to a difference in structure.

The significant dissolution of iron preceded the formation of the passive film for passivation of iron thin films. The predominant process of passivation of iron thin films was the anodic deposition of ferrous ions once dissolved, which was supported by Auger results revealing the presence of significant amounts of boron in the passive film.

The anodic current of iron dissolution and cathodic current of hydrogen evolution could be separately obtained as a function of electrode potential from the mass change of iron thin films measured during galvanostatic polarization near the corrosion potential.

Key terms: quartz crystal microbalance (QCM), in situ gravimetry, iron thin films, corrosion, passivation

Introduction

In spite of many new, ex situ, surface-analytical methods such as x-ray photoelectron spectroscopy (XPS), Auger electron spectroscopy (AES), secondary ion mass spectroscopy (SIMS), and so on, detailed knowledge of the corrosion process in aqueous solution is still lacking. The quartz crystal microbalance (QCM) technique is capable of detecting small mass changes in the range of nanograms per centimeter squared from resonant frequency changes of quartz crystal. Recent application of the QCM technique to aqueous systems¹⁾⁻⁴⁾ has succeed-

ed in performing in situ gravimetry under controlled electrochemical conditions. The simultaneous measurements of mass change and electric charge would provide a better understanding of corrosion processes of metals in aqueous systems. The application of QCM, however, is limited to the corrosion of thin films and the corrosion behavior of metal thin films will not be always similar to those of bulk metals.

In this study, the corrosion and passivation of iron thin films were investigated using the QCM technique combined with AES for better understanding of the corrosion processes of iron. Moreover, the differences in corrosion behavior between thin films and bulk iron were examined.

Experimental

A QCM sensor head (5MHz, AT-cut quartz crystal) with an oscillator circuit (TPS 500, Maxtek, Inc.) was used in this experiment. Gold electrodes were evaporated on both sides of the quartz crystal in the sensor head. The geometrical surface area of the electrode was 0.50 cm^2 . According to Sauerbrey's equation⁵, the mass sensitivity of this quartz oscillator is $1.77 \times 10^{-8} \text{ g cm}^{-2} \text{ Hz}^{-1}$. The iron thin films with a thickness of about 200 nm were electroplated on one side of the gold electrodes on the quartz crystal. The electroplating was performed in $0.9 \text{ M FeSO}_4(\text{NH}_4)_2\text{SO}_4 \cdot 6\text{H}_2\text{O}$ under a constant cathodic current density of $2 \times 10^{-2} \text{ A cm}^{-2}$ for 110 s. The current efficiency for iron film formation obtained from a comparison between mass change of the QCM and cathodic charge was about 30%.

Figure 1 shows the block diagram of the electrochemical QCM system. The sensor head was mounted in an electrochemical cell, using a Teflon holder and clamps. The gold electrode covered with the iron thin film on one side of the crystal was grounded and used as a working electrode. The electrolyte solution employed for this study was boric acid-sodium borate solution of pH 6.48 which was deaerated with ultrapure nitrogen gas before and during experiments. The iron thin film immersed in pH 6.48 solution was cathodically reduced under a constant current density of $i_c = 5 \times 10^{-6} \text{ A cm}^{-2}$ for 10^3 s to remove an air-formed oxide film. After cathodic reduction, the solution was renewed and the iron thin film was polarized potentiodynamically, potentiostatically or galvanostatically.

The changes in resonant frequency of the quartz crystal due to mass change during polarization were monitored with a frequency counter and recorded on a personal computer. Simultaneously, the changes in current or potential were recorded on the same computer. Iron plates with a purity of 99.9% were used for comparison with the iron thin film and were polarized under the same experimental conditions. The depth-profiling by AES combined with argon ion-etching was performed for the iron thin film electroplated on the gold plate in place of the evaporated gold of the quartz oscillator.

Results and Discussion

Cyclic Voltammogram and Gravimetric Curves of Iron Thin Films

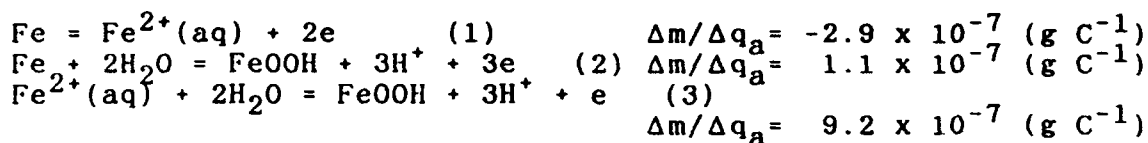
- Figure 2 shows the cyclic voltammogram (upper) and gravimetric curve (lower) of an iron thin film in pH 6.48 solution. The potential scan (10 mV s^{-1}) started in the anodic direction from the potential of natural immersion and reversed to the cathodic direction at 1.5 V (SHE). The cyclic scan was performed several times between - 0.8 V and 1.5 V (SHE). For comparison, the cyclic voltammogram of bulk iron is shown in Fig.3. The cyclic voltammogram of the iron thin film is different from that of bulk iron. The potential at maximum dissolution current for iron thin film shifts by 0.3 V to the noble direction in comparison with that for bulk iron. The passivity maintaining current of the iron thin film is higher than that of bulk iron. The corrosion behavior would depend on the impurity level and the structure of iron. Auger depth profiles of iron thin films as received indicated that no impurities such as sulfur, nitrogen, carbon and oxygen were present in the film within the detection limit of AES. The differences in corrosion behavior between iron thin film and bulk iron, therefore, will be attributed to a difference in structure, because metal thin films electroplated are amorphous or micro-crystalline in comparison with the large crystal size of bulk metals.

The gravimetric curve in Fig.2 provides the fine features of corrosion of iron thin films, responding to the cyclic voltammogram. The mass decrease is predominant in the active dissolution range, whereas a slight mass gain is observed in the active-passive transition region. The mass decrease appears again in the cathodic reduction current peak of the passive film. The net mass decrease of $6.6 \times 10^{-6} \text{ g cm}^{-2}$ is finally observed for each cycle.

Potentiostatic Polarization of Iron Thin Films - Figure 4 shows the anodic current vs. time curve (upper) and mass change vs. time curve (lower) for iron thin films subjected to potentiostatic oxidation at various potentials. The anodic current vs. time curve for bulk iron subjected to the same conditions is also shown in Fig.5. It is seen from comparison of Fig.4 (upper) and Fig.5 that the iron thin film is still active at 0 V (SHE) where the bulk iron becomes passive. In addition, in the passive region, the anodic current for bulk iron is higher than that for iron thin films at the initial stage but decreases exponentially with time. In contrast with bulk iron, the anodic current for iron thin film decreases gradually with time, after reaching a plateau. The above results indicate that the iron thin film is passivated slowly in comparison with bulk iron.

It is seen from the mass change vs. time curve in Fig.4 that the mass of the iron thin film decreases with time until the anodic current passes through the plateau region. After the plateau of anodic current, the mass increases and attains a saturation value depending on the applied potential. The mass change vs. time curve, therefore, reveals that a significant dissolution of iron precedes the passive film formation of the iron thin film.

Figure 6 shows the quantitative relation between mass change, Δm , and anodic charge, q_a required for passivation. The values of slopes, $\Delta m/\Delta q_a$ of the linear region in the curves are given in Fig.6. Assuming the possible corrosion and passivation processes of iron, the values of $\Delta m/\Delta q_a$ can be theoretically derived for the respective processes as follows.



The reaction (1) represents the dissolution of ferrous ions from metallic iron. The two possible reactions (2) and (3) will be proposed for the formation of the passive film, FeOOH. Reaction (2) means the direct formation of the passive film, whereas reaction (3) represents the indirect formation of the passive film due to anodic deposition of ferrous ions once dissolved. The slope, $\Delta m/\Delta q_a = -1.9 \times 10^{-7} \text{ (g C}^{-1}\text{)}$ of the initial mass decrease in Fig.6 deviates significantly from the theoretical slope, $\Delta m/\Delta q_a = -2.9 \times 10^{-7} \text{ (g C}^{-1}\text{)}$ of the reaction (1), suggesting that the reaction (2) proceeds simultaneously with the reaction (1). According to Kanazawa and Gordon⁶⁾, the resonant frequency of QCM in a liquid phase is influenced by the density and viscosity of the solution. This deviation may be alternatively explained in terms of the change in density or viscosity of the solution near the electrode surface due to the enrichment of ferrous ions which will result from the slow process of diffusion of ferrous ions into the bulk solution.

The slope, $\Delta m/\Delta q_a$ of the mass increase at the latter stage exceeds the theoretical slope, $\Delta m/\Delta q_a = 1.1 \times 10^{-7} \text{ (g C}^{-1}\text{)}$ of the reaction (2). Particularly, the slope, $\Delta m/\Delta q_a = 9.0 \times 10^{-7} \text{ (g C}^{-1}\text{)}$ at 0.2 V (SHE) is very close to the theoretical slope, $\Delta m/\Delta q_a = 9.2 \times 10^{-7} \text{ (g C}^{-1}\text{)}$ of reaction (3). Reaction (3), therefore, will be mainly contributing to the mass increase in the latter stage. The Auger depth profile of passive film formed at 0.8 V (SHE) on iron thin films indicated that a significant amount of boron was present in the outer layer of the passive film. The recent QCM study⁷⁾ on anodic deposition of ferrous ions in pH 6.48 boric acid-sodium borate solution suggested that the composition of deposited films was close to the equimolar mixture of FeOOH and $\text{Fe}(\text{OH})_2\text{B}(\text{OH})_4$. The maximum Auger peak-to-peak height ratio, $\text{B}(179 \text{ eV})/\text{Fe}(651 \text{ eV}) = 0.30$ in the passive film on the iron thin film exceeded the maximum value of $\text{B}(179 \text{ eV})/\text{Fe}(651 \text{ eV}) = 0.26$ in the deposited film previously reported⁷⁾, supporting strongly that reaction (3) is the predominant process for passivation of iron thin films.

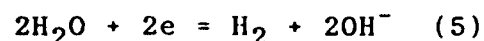
Active Dissolution of Iron Thin Films - Figure 7 shows the relation between mass change, Δm and anodic charge, q_a for iron thin films subjected to active dissolution at 0 V (SHE) and -0.2 V (SHE). The slopes of the linear relation in Fig. 7 deviate from the theoretical slope of reaction (1). The deviation may result from the deposition of ferrous hydroxide due to the enrichment of ferrous ions near the electrode surface

as explained before. The net reaction of ferrous hydroxide formation is represented as follows.



Provided that reactions (1) and (4) take place simultaneously in the active region of iron thin films, about a 20 % contribution of reaction (4) can be calculated from the slopes of the linear lines in Fig.7. However, the possibility of the resonant frequency change of QCM resulting from a change in viscosity or density of solution near the electrode surface due to enrichment of ferrous ions can not be excluded as an alternative explanation.

Figures 8 and 9 show the mass change vs. time and potential vs. time curves for iron thin films polarized galvanostatically in the anodic and cathodic directions near the corrosion potential, respectively. In Fig.8, the mass decreases linearly with time and the slope of the line increases with increasing anodic current. On the other hand, in Fig.9, the mass decreases linearly with time but the slope of the line decreases with increasing cathodic current. The following hydrogen evolution reaction (5) coupled with the reaction (1) takes place on the iron thin film when it is polarized near the corrosion potential.



The net galvanostatic current, i_g , therefore, is equal to the difference between the anodic current of reaction (1), i_a and cathodic current of reaction (5), i_c , i.e., $i_g = i_a - i_c$. At the slight polarization of the iron thin film from the corrosion potential, reaction (4) or the possibility of resonant frequency change of QCM due to the enrichment of ferrous ions can be neglected because the dissolution of ferrous ions is small. Thus, the anodic current of reaction (1), i_a can be calculated as a function of the electrode potential from the linear slope of mass change in Figs.8 and 9. Furthermore, the cathodic current of reaction (5), i_c can be calculated from the relation of $i_c = i_a - i_g$.

The values of i_a and i_c thus calculated are plotted versus electrode potential in Fig.10. The corrosion current, i_{cor} , of iron thin films at the corrosion potential, E_{cor} obtained from Fig.10 is $9.0 \times 10^{-6} \text{ A cm}^{-2}$ which was rather small compared with $i_{cor} = 1.8 \times 10^{-5} \text{ A cm}^{-2}$ of bulk iron obtained from extrapolation of the Tafel slope to the corrosion potential.

Conclusions

The following conclusions are drawn from in situ gravimetry of corrosion and passivation of electroplated iron thin films in pH 6.48 boric acid-sodium borate solution.

1. The passivation potential of an iron thin film is higher than that of bulk iron. Bulk iron is more easily passivated than the iron thin film. The difference in passivation between iron thin films and bulk iron is attributed to a difference

In structure.

2. A significant dissolution of iron precedes the passive film formation for the passivation of iron thin films. The anodic deposition of ferrous ions once dissolved from an iron thin film is the predominant process of passivation, which is strongly supported by Auger results showing the presence of significant amount of boron in passive films formed on iron thin films.

3. The possibility of deposition of ferrous hydroxide due to the enrichment of ferrous ions near the electrode surface is suggested for iron thin films subjected to active dissolution. Alternatively, it is also suggested that the enrichment of ferrous ions near the electrode influences the resonant frequency of QCM.

4. The measurement of mass change during galvanostatic polarization of iron thin films near the corrosion potential has succeeded in obtaining separately the anodic current of iron dissolution and the cathodic current of hydrogen evolution as a function of electrode potential.

References

1. O. Melroy, K.K. Kanazawa, J. G. Gordon II, D. Buttry, *Langmuir*, 2 (1986):p 697
2. A. Grzegorzewski, K. E. Heusler, *J. Electroanal. Chem.*, 228 (1987):p 455
3. L. Grasjo, M. Seo, N. Sato, *Corr. Sci.*, 31 (1990):p 299
4. L. Grasjo, M. Seo, *J. Electroanal. Chem.*, 296 (1990):p 233
5. G. Sauerbrey, *Z. Phys.*, 155 (1959):p 206
6. K. K. Kanazawa, J. G. Gordon II, *Anal. Chim. Acta*, 175 (1985):p 99
7. M. Seo, K. Yoshida, H. Takahashi, I. Sawamura, *J. Electrochem. Soc.*, 139 (1992):p 3108

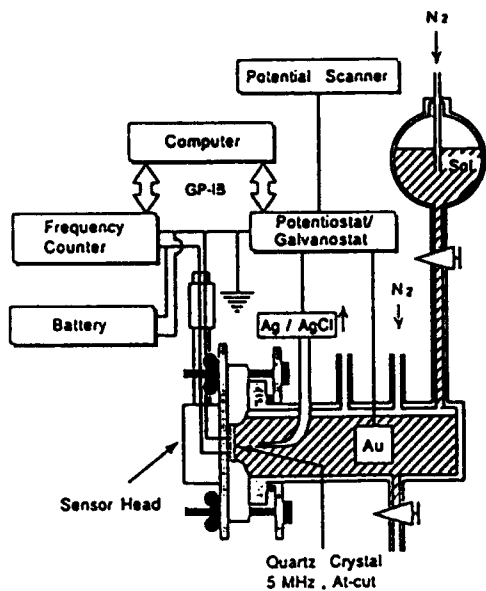


Fig.1 Block diagram of electrochemical QCM system

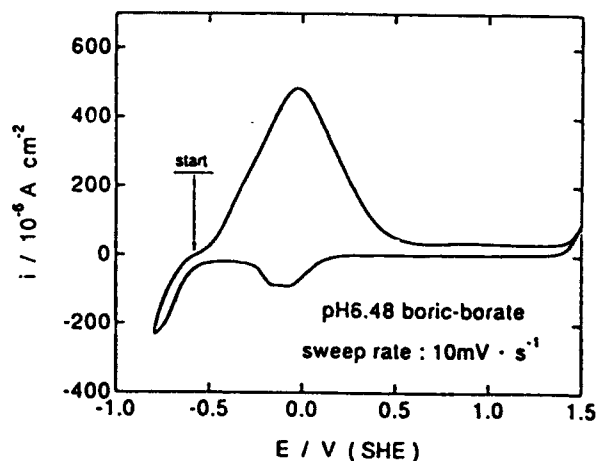


Fig.3 Cyclic voltammogram of bulk iron in pH 6.48 solution

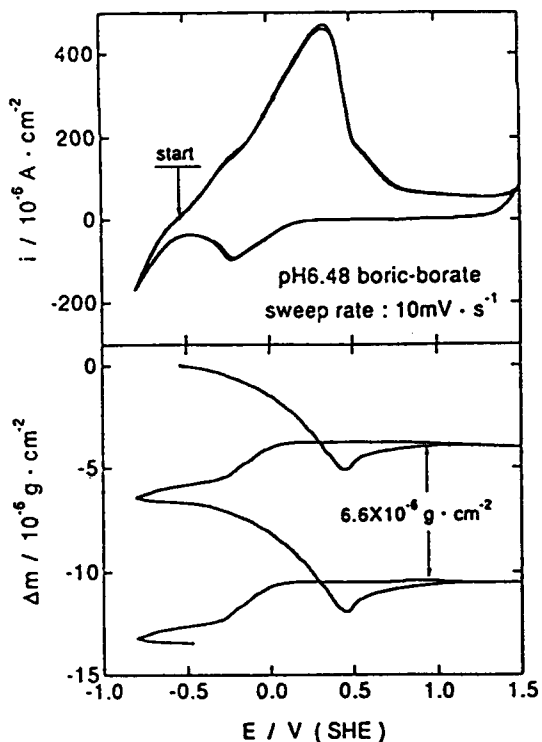


Fig.2 Cyclic voltammogram (upper) and gravimetric curve (lower) of an iron thin film in pH 6.48 solution

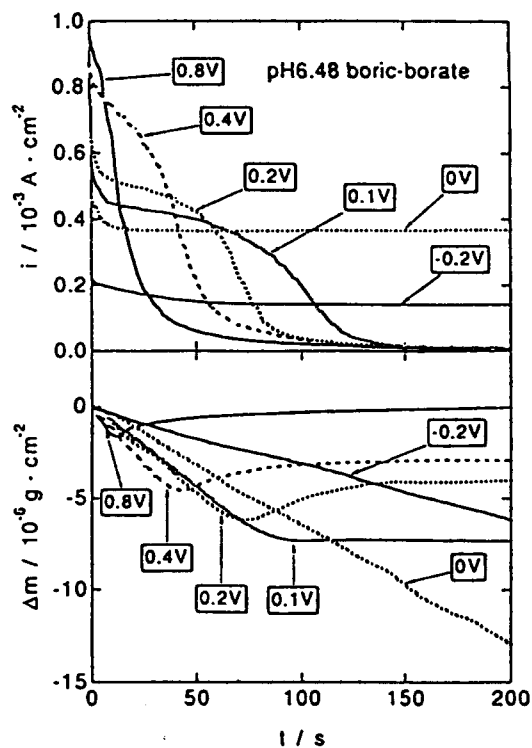


Fig.4 Anodic current vs. time curve (upper) and mass change vs. time curve (lower) of iron thin films subjected to potentiostatic oxidation at various potentials

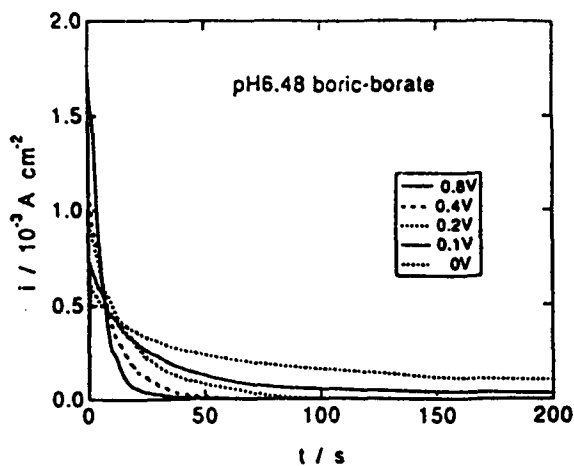


Fig.5 Anodic current vs. time curve of bulk iron subjected to potentiostatic oxidation at various potentials

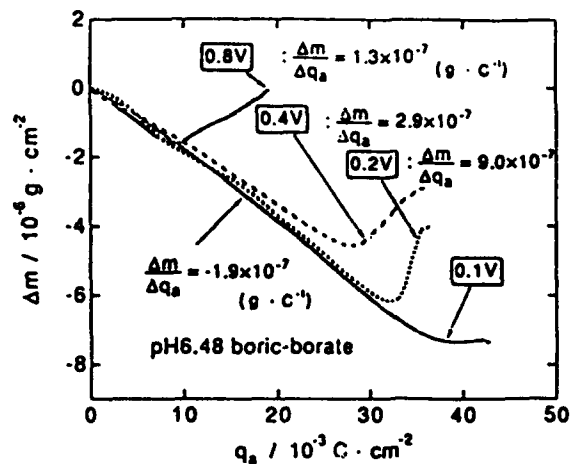


Fig.6 Relation between the mass change, Δm and anodic charge, q_a required for passivation of iron thin films

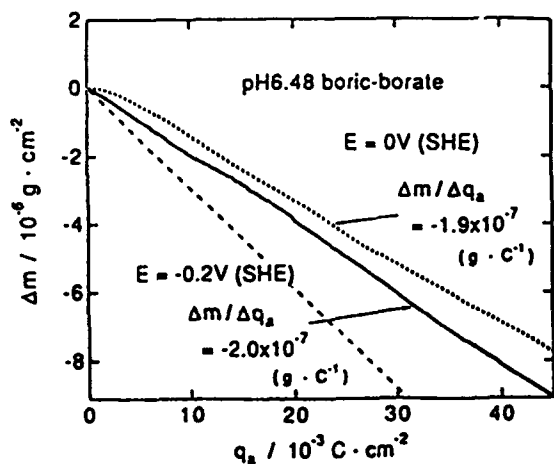


Fig.7 Relation between the mass change, Δm and anodic charge, q_a for iron thin films subjected to active dissolution at 0 V (SHE) and - 0.2 V (SHE)

Dashed line represents the theoretical slope of reaction (1)

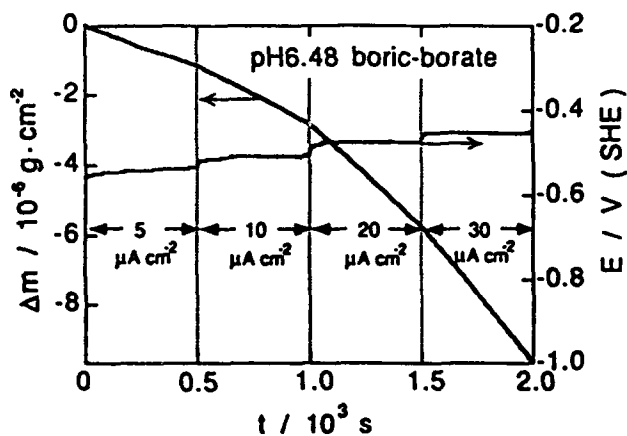


Fig.8 Mass change, Δm vs. time and potential vs. time curves for iron thin films polarized galvanostatically in the anodic direction near the corrosion potential

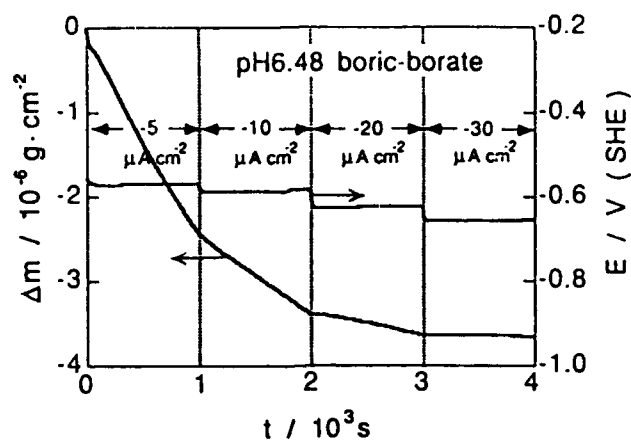


Fig.9 Mass change, Δm vs. time and potential vs. time curves for iron thin films polarized galvanostatically in the cathodic direction near the corrosion potential

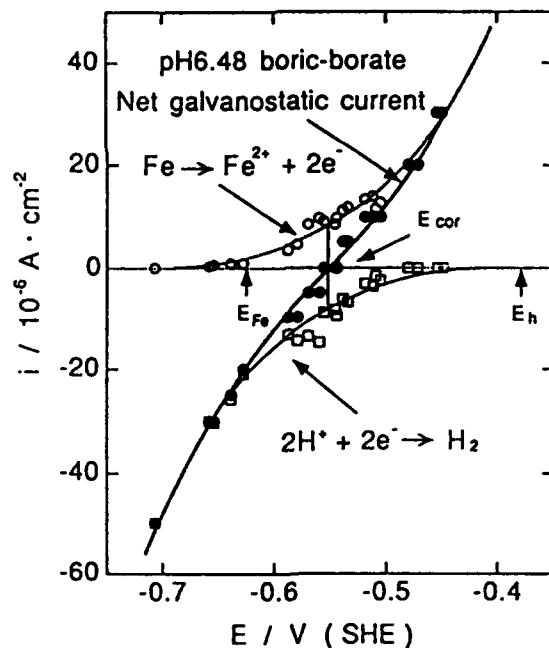


Fig.10 Anodic current of iron dissolution and cathodic current of hydrogen evolution obtained separately as a function of potential from the measurement of mass change during galvanostatic polarization near the corrosion potential

Passivation of High Alloyed Stainless Steel in HCl at 22°C and 65°C

L. Wegrelius
Department of Engineering Metals
Chalmers University of Technology
S-412 96 Gothenburg
Sweden

I. Olefjord
Department of Engineering Metals
Chalmers University of Technology
S-412 96 Gothenburg
Sweden

Abstract

A high alloyed austenitic stainless steel (20Cr18Ni6.1Mo0.2N) was exposed to 0.1 M HCl + 0.4 M NaCl at 22°C and at 65°C. Polarisation of the steel shows that it is passivated at room temperature in the potential range -200mV to 900mV (SCE). At 65°C the current fluctuates showing that initiation and repassivation of pits occur. ESCA analysis of the steel polarised to -100 mV and 500 mV (SCE) shows that the composition and thickness of the passive film is dependent on the potential and the temperature of the electrolyte. The thicknesses of the passive films formed at room temperature at the potentials -100mV and 500mV (SCE) are 12 Å and 17 Å, respectively. The films formed at 65°C are 13 Å and 19 Å at corresponding potentials.

The passive film consists of an inner oxide layer and an outer hydroxide layer. Chromium in its three valence state is enriched in both phases. The cation content of Cr^{3+} in the inner oxide formed at room temperature at -100mV(SCE) is 55 at.%. At the higher potential the Cr^{3+} content has decreased to 40 at.%. At 65°C the Cr^{3+} content in the inner oxide layer is about 45 at.% at both potentials. Molybdenum is slightly enriched in the outermost layer in its four and six valence states. The Ni contents are very low in the films formed at both temperatures. Nitride is formed at the interface between the metal and the oxide phases. The alloying elements Ni and Mo are enriched in the metal phase under the passive film. It is suggested that the repassivation properties of the steel is enhanced due to the enrichment of these elements.

Key terms: ESCA, stainless steel, passivation, hydrochloric acid, elevated temperature

Introduction

High alloyed, so called superaustenitic, stainless steels have been developed during the last decades. The development has gone from the classic AISI 304 and 316 containing 18Cr8Ni and 18Cr8Ni2.7Mo, respectively to alloys of the type 20Cr18Ni6.1Mo0.2N (UNS S31254). The driving force for the development of the steels have been the search for material with improved resistance to localised corrosion in environments containing halogen ions. Measures of the resistance to these environments are the pitting potential and the critical pitting temperature (the temperature for initiation of pitting at 400mV (SCE)). For example, the pitting temperatures of AISI 316 and UNS S31254 exposed to 1M NaCl, pH 1 are 45°C and 90°C, respectively (1). Thus, the corrosion properties of the high alloyed steels are superior to the standard materials. The influence of the alloying elements on the corrosion properties of austenitic stainless steels has so far not been clarified. It is very useful to point out some observations, which can be obtained from exposure of a series of alloys to hydrochloric acid: the polarisation diagrams show almost the same current in the passive range; the composition and the thickness of the passive films are almost the same. However, sensitivity to pitting corrosion is markedly different between the alloys. At room temperature the high alloyed steels are passivated without pitting in the whole potential range between their active dissolution and transpassive regions while the low alloyed steels are attacked at low potentials close to the active dissolution region.

Surface analysis techniques, ESCA, Auger and SIMS have shown that the passive film formed on the surface of stainless steels exposed to acids has a duplex structure. It consists of an inner barrier oxide film and an outer hydroxide film (2-23). Chromium is markedly enriched in the passive film. The Ni- content in the film is low. The outer hydroxide layer consists mainly of Cr- and Mo- hydroxide (8,12,13). The inner barrier layer consists mainly of Fe and Cr oxide containing dissolved Mo in its four valence state (5,8, 12).

ESCA analysis of stainless steels performed after polarisation to potentials in the active and passive regions shows that the measured Fe-content in the metal phase is lower than the composition of the alloy. Iron is selectively dissolved (2-8,12,13) and thereby found in the solution (14). Molybdenum and Ni are enriched in the metal phase underneath the oxide (2-8,13-17). It has been proposed (3-8,18,19) that during active dissolution and passivation of stainless steel a thin layer of an intermetallic compound is formed in the outermost layer of the metal phase. The electrochemical and corrosion properties of the steel is thereby influenced. The enrichment of the alloying elements on the surface lower the dissolution rate and enhance passivation of the alloy. The resistance to localised corrosion is increased because the enrichment of the alloying elements facilitate repassivation. It has also been proposed that Mo in the steel raises the electric field and so the dissolution occurs earlier in the repassivation process. Thus the onset of passivity is accelerated and hence the resistance to chloride induced pitting is improved (20).

The present work is a study of the surface composition of the passive film formed on the surface of a high alloyed stainless steel during exposure to hydrochloric acid at 22°C and 65°C. Attention is directed to the distribution of the elements in the passive film.

Experimental

The composition of the steel (Avesta 254 SMO) is: wt.%, 20Cr18Ni6.1Mo0.4Si0.4Mn0.7Cu0.2N0.020C-bal.Fe. The samples were polarised in deaerated 0.1 M HCl + 0.4 M NaCl at room temperature and at 65°C. The exposures were performed in an electrochemical cell directly connected to the ESCA-instrument. After polarisation of the sample it was moved to the analyser without exposure to air. The cell, made of glass and Teflon, allows the electrolyte to be heated to almost 100 °C. The potential was measured with a Calomel reference electrode located outside the cell at room temperature. All potentials in this paper are referred to the Calomel electrode. The cell is designed in a way that crevice corrosion is avoided.

The samples were pre-treated by grinding on emery paper down to 600 mesh and then by diamond-paste polishing down to 1µm, followed by ultrasonic cleaning in ethanol. The electrolyte was deaerated by Ar-bubbling for 2 hours before exposure of the sample. The sample was activated at the cathodic potential -700mV for 10 min before polarisation. The samples for ESCA-analyses were prepared by stepping the potential from the activation potential to the potentials of interest, -100mV and 500mV. The exposure time was 10 min. The polarisation was interrupted by pouring isopropyl alcohol through the cell. After rinsing the sample in methyl alcohol it was moved to the ESCA-instrument.

The ESCA-instrument (PHI 5500) was operated with its monochromised Al K α X-ray radiation. The pass energy of the analyser was 23.5 eV. The samples were analysed at the take-off angles 30°, 45° and 80°. The take-off angle is defined as the angle between the surface and the entrance to the spectrometer. The solid angle of electron acceptance was the lowest possible.

Results

Figure 1 shows polarisation diagrams recorded from the steel exposed to 0.1 M HCl + 0.4 M NaCl in the cell connected to the ESCA-instrument. The sweeping rate was 2 mV/s and the temperatures of the electrolyte were 22°C and 65°C. It appears from the figure that at room temperature the steel is passivated in the range -200mV to 900mV. The latter potential is the beginning of the transpassive range. The passive current is about 10 µA/cm². The figure shows the characteristic active passive transition at both temperatures. The passivation currents are 60 µA/cm² and 100 µA/cm² at room temperature and at 65°C, respectively. The passivation potential at room temperature is about 80mV higher than the passivation potential at 65°C. It appears from Fig.1b. that the current

fluctuates in the potential region between -100 mV and 900 mV. The minimum current in this range is about the same as the passive current obtained at room temperature. Thus, at 65°C the surface is activated and repassivated. Scanning electron microscopy analysis of the surface after polarisation shows that pits are uniformly distributed over the surface. The fluctuation of the current and the presence of deep pits after polarisation to high potentials indicate that the majority of the pits have passed through the three states: initiation, propagation and repassivation. The Tafel slope of the cathodic reaction is 140mV/decade for both exposure temperatures. The hydrogen reaction at 65°C is one order of magnitude larger than at 22°C.

The samples for ESCA-analyses were prepared by stepping the potential from the activation potential to -100 mV or 500 mV. The current versus time is illustrated in Fig.2. The steel was polarised to 500 mV at 65°C. In this case the current fluctuates due to initiation of pitting. The fact that the current decay shows that the pits are repassivated. The pits are very small and uniformly distributed over the surface. The polarisation stopped after exposure for 10 min in order to avoid uncontrolled growths of pits.

Figure 3 shows an ESCA survey scan recorded after polarisation of the sample to -100mV for 10 min at 22°C. It appears from the spectrum that photoelectron signals and Auger-electron signals from Ni, Fe, Cr, Mo, O, C, N and Cl are detected. In spite of the fact that the sample was polarised in a NaCl- containing solution Na is not detected. The binding energy (BE) of Na 1s is 1072 eV. Thus, the salt has been removed during rinsing of the sample. Chloride, on the other hand, is present in the oxide products formed on the surface during passivation.

ESCA-spectra recorded from narrow energy regions after polarisation of the steel at 65°C to -100mV and 500mV are illustrated in Fig.4a and Fig.4b, respectively. The dotted curves represent the sum of the deconvoluted peaks. It appears that both the oxide and the metallic states of Fe, Cr and Mo are detected. Nickel is present in the spectra mainly in its metallic state. The signal from Ni-oxide recorded at -100mV is very low. Nickel-hydroxide is detected after polarisation to 500mV. The oxide states of the other elements are: Fe is present in its di- and tri-valence states; the Cr-signal is divided into two signals representing Cr^{3+} in oxide and hydroxide (6,7); Mo occurs in its four and six valence states (6, 7). The oxygen signals are splitted into three peaks representing O^{2-} , OH^- and H_2O . The amount of Fe-oxide formed is higher at the higher potential. The Cr-and the O-spectra show that the hydroxide state of these elements dominate at the low potential. It will be shown that the oxide products formed on the surface consists of a duplex layer; an inner oxide layer and an outer hydroxide layer. The interpretation of nitrogen is very difficult for Mo-alloyed steels because the only available N-signal, N 1s, overlap the Mo $3p_{3/2}$ signal. The two N-signals shown in the spectra represent nitrogen in nitride (BE=397.5 eV)and ammonium (BE=400.1 eV), respectively. The figure shows a higher nitride-signal from the sample polarised to the higher potential compared to the low potential. This finding may indicate that the formation of nitride depends on the potential. The $\text{N}(\text{H}_4\text{N}^+)$ - peak is found even on the surface of non- N- containing steels. The nitrogen source is probably NO_3^- and/or NO_2^- present as impurities in the water. It is suggested that ammonium is formed during polarisation to low potentials during preparation of the sample. The recorded intensities of the metallic state of Mo is about the same. Signals representing Cl^- ions occur in the spectra. As pointed out above, Na^+ - signals were not detected. The Cl 2p signals are separated into their Cl $2p_{1/2}$ and Cl $2p_{3/2}$ peaks. The recorded signals show that Cl^- ions exist in two different states because two pares of signals are detected. The low intensity high binding energy component of Cl⁻, $\text{Cl}^-(\text{HB})$, represents Cl^- bound to N in H_4NCl . The intensity ratio between $\text{Cl}^-(\text{HB})/\text{N}(\text{H}_4\text{N}^+)$ are approximately constant for all angles.

Angle dependent ESCA-analyses have been performed after polarisations. Figure 5 illustrates the signals Cr $2p_{3/2}$, O1s, N 1s and Mo $3p_{3/2}$ recorded at the take-off angles 30°, 45° and 80° after polarisation to 500mV at 65°C. It appears that the intensity ratios $\text{Cr}^{3+}(\text{hy})/\text{Cr}^{3+}(\text{ox})$ and $\text{O}^{2-}(\text{hy})/\text{O}^{2-}(\text{ox})$ increase with decreasing take-off-angle. This is a proof for the statement above that the reaction products consists of an inner oxide layer and an outer hydroxide layer. The angle dependent intensities of the peaks from the N 1s, Mo $3p_{3/2}$ region shows that Mo^{6+} is present in the outer hydroxide layer and that $\text{Mo}^{4+}(\text{ox})$ is present in the inner oxide layer due to the fact that the intensity ratio $\text{Mo}^{6+}/\text{Mo}^{4+}$ increases with decreasing take-off angle. It also appears that $\text{N}(\text{H}_4\text{N}^+)$ is present in the outermost surface layer, because the intensity ratio $\text{N}(\text{H}_4\text{N}^+)/\text{Mo}^{6+}$ is independent of the take-off angle. Further, it appears that nitride is formed at the metal/oxide interface; the intensity ratio $\text{N}(\text{nitride})/\text{Mo}^{6+}$ increases with the take-off angle. Formation of nitride at the oxide/metal interface has been reported earlier (18).

The thickness and the composition of the films can be calculated using the formulas (4-8):

$$I_i^{ox} = \alpha D_i^{ox} Y_i^{ox} \lambda_i^{ox} \sin \theta \left\{ 1 - \exp\left(\frac{-a^{ox}}{\lambda_i^{ox} \sin \theta}\right) \right\} \exp\left(\frac{-a^c}{\lambda_i^{ox} \sin \theta}\right) \quad (1)$$

$$I_i^{me} = \alpha D_i^{me} Y_i^{me} \lambda_i^{me} \sin \theta \exp\left(\frac{-a^{ox}}{\lambda_i^{me} \sin \theta}\right) \exp\left(\frac{-a^c}{\lambda_i^{me} \sin \theta}\right) \quad (2)$$

Where I_i^{ox} and I_i^{me} are the measured intensities of element i in the oxide, ox , and the metal, me , phase, respectively. D is the atomic density of the element, Y the relative photoelectron yield factor, λ is the attenuation length of the photoelectrons, a^{ox} and a^c the thicknesses of the passive film and contamination layer, respectively.

The thickness of the oxide is obtained by dividing Eqns. 1 and 2:

$$a^{ox} = \lambda_i^{ox} \sin \theta \ln \left(1 + \frac{I_i^{ox} D_i^{me} \lambda_i^{me} Y_i^{me}}{I_i^{me} D_i^{ox} \lambda_i^{ox} Y_i^{ox}} \right) \quad (3)$$

The compositions of the two phases are:

$$C_i^{ox} = \frac{D_i^{ox}}{\sum_j D_j^{ox}} \quad \text{and} \quad C_i^{me} = \frac{D_i^{me}}{\sum_j D_j^{me}} \quad (4)$$

The potential dependence of the passive film-thickness is shown in Figs. 6a and 6b after passivation at 22°C and 65°C, respectively. It appears that the thickness of the film increases with the potential and the temperature. The hydroxide layer is about 6 Å thick and its thickness is almost independent of the potential and temperature. At the low potential, -100mV, the steel is passivated without pitting corrosion. At this potential the thicknesses of the oxide barrier phases formed at 22°C and at 65°C are 6 Å and 7 Å, respectively. Polarisation to 500mV at the two temperatures give 11 Å and 13 Å thick inner oxide layers.

The concentration obtained from the measured intensities taking into account the total thickness of the film, the electron yield factors, the take-off angle and the attenuation lengths is called "integrated concentration". It does not take into account the fact that the species are present in two different phases. On the other hand, the integrated concentration is one way to present the recorded intensities in a normalised manner. Figure 7 shows the integrated concentrations of the reaction products as function of take-off angle. The oxide products were formed on the surface of the steel during polarisation to the two potentials and the two temperatures.

It appears from the figure that the integrated concentrations of OH^- , $Cr^{3+}(hy)$, Mo^{6+} and $Mo^{4+}(hy)$ decrease with increasing take-off angle. For the species O^{2-} , $Cr^{3+}(ox)$, Fe^{ox} ($Fe^{2+}+Fe^{3+}$) and Mo^{4+} the concentrations increase with the angle. Thereby, the first group of the elements are located in the outer region of the passive film and the latter group of the elements in the inner part of the reaction products. In the case of Cl^- the tendency is not clear. It seems that the integrated concentration is independent of the take-off angle. This indicates that Cl^- ions are distributed throughout the oxide and the hydroxide layers. However, it has to be mentioned that the separation of the signals in their elementary states is very difficult due to the complexity of the spectra: the contribution of the oxygen signal representing oxygen bound to carbon in the contamination layer has to be removed (7); Ni-Auger signals overlap Fe 2p (not shown in Fig.4.) and its contribution has to be taken into consideration; the Mo 3d signal consists of overlapping spin-orbital peaks.

Figure 8 shows the concentrations of the cations in the hydroxide and in the oxide as function of potential and temperature. It appears that the Cr^{3+} is the dominating cation species in the hydroxide at both potentials and temperatures. The Cr^{3+} -content of the hydroxide products formed at room temperature is about 80 at.% and almost independent of the potential. At 65°C the Cr^{3+} -contents are slightly lower at -100mV and about the same, 80 at.%, at 500mV. The remainder cations in the hydroxide are mainly Mo^{4+} and Mo^{6+} . At the low potential the total Mo^{4+} and Mo^{6+} -contents at room temperature and at 65°C are 20 at.% and 30 at.%, respectively. The Figs. 8a and 8c indicate that the Mo^{4+} and Mo^{6+} - contents decrease with the potential. Determination of the Ni^{2+} -content is uncertain. However, the Figs.8a and 8c indicate a small amount of Ni^{2+} -ions in the hydroxide layer at 500mV.

The barrier layer consists mainly of Fe- and Cr-oxides. The Figs. 8b and 8d show that the Cr^{3+} -concentration decreases with the potential at both temperatures at the same time as the Fe^{ox} -content increases. At room temperature the sum of Cr^{3+} and Fe^{ox} is about 90 at.%. Molybdenum in its four valence state and Ni^{2+} occur in the inner oxide layer formed at -100mV. At room temperature the contents of Mo^{4+} and Ni^{2+} are about 5 at.% for each of the elements. At 65°C the cation contents of these elements are slightly higher. Further, it appears from Fig.8 that at both temperatures the contents of Mo^{4+} and Ni^{2+} in the oxide decreases with the potential. At 500 mV the concentrations of these elements are low.

Discussion

In this study a high alloyed stainless steel was polarised at room temperature and at 65°C to -100mV and 500mV for 10 min in 0.1 M HCl + 0.4 M NaCl. The steel is passivated at room temperature at both potentials and at 65°C at -100mV. The potentiostatic recording at 65°C and 500mV shows that initiation and repassivation of pits occur. The combination of high potential and high temperature was chosen in order to make it possible to analyse the composition and the thickness of the passive film during breakdown. The pits formed can be observed in a microscope, but they are small and cover only a fraction of the surface. The contribution to the ESCA-signals from the pitted areas can therefore be neglected.

The analysis shows that the thickness of the passive film increases with both the temperature and the potential. At room temperature the overall thicknesses of the surface products formed at -100mV and at 500mV are 12 Å and 17 Å, respectively. The corresponding values at 65°C are 14 Å and 19 Å.

The passive film consists of an inner barrier film of oxide and an outer film of hydroxide. Formation of the hydroxide is one of the first step in the passivation process. It is suggested that the hydroxide layer does not contribute to the limitation of the current. In stead it is the properties of the inner oxide layer which give the characteristic limitation of the current in the passive state. The inner oxide layer is formed by deprotonation of the hydroxide layer. The thickness of the hydroxide layers is found to be 6 Å. In a previous study (8) of the same material polarised at room temperature to the same potentials the composition and the thickness of the barrier layer was found to be the same as in this study. However, the thickness of the hydroxide layer was estimated to be 4.2 ± 1 Å in that study (8) compared to 6 ± 1 Å found in this study.

The hydroxide layer consists mainly of $\text{Cr}(\text{OH})_3$. The Cr^{3+} - content in the hydroxide layer is significantly higher at room temperature than at 65 °C. It was not possible to clarify any potential dependance. The standard deviations from the three measurements performed at each set of parameters are larger than the variation of the average values. Nickel can only be detected at the high potential, 500 mV, in the hydroxide layer. The Ni-spectrum shows a characteristic Ni^{2+} - hydroxide signal which make it possible to separate Ni^{2+} -hydroxide from Ni^{2+} - oxide. The angle dependent ESCA- analysis of the samples polarised to -100 mV indicates that Mo^{4+} and Mo^{6+} are present in the outer hydroxide layer. At 500 mV, Fig. 7, the contents of these species are about 1 at.% (integrated), which make it difficult to see any clear angle dependence. The analysis indicates that Fe^{2+} and Fe^{3+} are present in the oxide. However, the angle dependent ESCA-technique is in fact a relatively crude method for determination of the distribution of the elements in the oxide products. It can not be excluded that even Fe^{2+} and Fe^{3+} species are present to a low extent in the hydroxide because iron as well as the other alloying elements are dissolved through the hydroxide layer.

The enrichment of $\text{Cr}(\text{OH})_3$ and dissolution of Fe-hydroxides on the surface is unexpected from thermodynamic point of view because the solubility of $\text{Cr}(\text{OH})_3$ is larger than the solubility of Fe-hydroxides in acids (21). Thus, formation of $\text{Cr}(\text{OH})_3$ on the surface must be due to reaction kinetic factors; it is known (22) that Cr^{3+} - complexes react very slowly and thereby the $\text{Cr}(\text{OH})_3$ layer can be maintained on the surface.

The cation content of Cr^{3+} - ions in the barrier oxide layer is about 50 at.% at - 100 mV. It is slightly higher at room temperature than at 65°C. Taking into account the difference in oxide thickness it is found that the total amount of Cr^{3+} -ions in the oxide becomes the same at the two temperatures. The Fe^{ox} -concentration is about 40at.% at the low potential. Polarisation to the higher potential decreases the Cr^{3+} concentration so that Fe^{ox} becomes the dominating cation species in the oxide. The Ni^{2+} and Mo^{4+} concentrations depend on the temperature and the potential. At 500 mV the contents of Mo^{4+} and Ni^{2+} are very low at both temperatures, while at the lower potential the contents of these elements are in the range 4 to 8 at.%. The concentrations of both elements are slightly higher at 65°C than at 22 °C. The content of Mo^{4+} at the low potential is about twice as high as the Mo content of the alloy.

This study confirm earlier results (2-7) that the contents of the alloying elements, Mo and Ni, in the passive film decrease with the potential. As demonstrated the concentrations of these elements in the barrier layer is very low. Molybdenum and Ni are found in the outer hydroxide layer. It has been suggested (18) that Mo^{6+} - ions form molybdate in the outer layer and causes deprotonation of the hydroxide layer. In this study the Mo^{6+} concentrations and the hydroxide thicknesses are almost the same for all potentials and temperatures. Thereby, these results neither support nor contradict the model (18). However, it has been stated (13) that the hydroxide/oxide ratio increases with Mo^{6+} present in the hydroxide layer.

The passivation properties of stainless steels depends on the composition of the alloy, the chemical stability of the passive film, the driving force and the diffusibility of the alloying elements through the film. It is suggested that pure Cr_2O_3 should give the best protection against break down of the passive state. Pure chromium is passivated by formation of a layer of Cr_2O_3 (23), which is thinner than the thickness of the passive film formed on stainless steel. The increased thickness of the film formed on stainless steel is due to the fact that lower valence species than the dominating three valence ions of Cr and Fe are present. The presence of Fe^{2+} and Ni^{2+} ions will be accompanied by vacancies and thereby the ionic mobility will increase. It has been proposed (7) that the point defects are cancelled by the presence of higher valence ions such as Mo^{4+} in the barrier layer. Thus, the more defect free oxide will be less able to dissolve the metal.

The role of the alloying elements Mo and Ni on the corrosion properties of stainless steel is not very easy to understand from the composition of the passive film. At the highest potential and temperature where pitting is initiated but repassivation occurs the content of the alloying elements in the passive film is low. Thus, this finding indicates that the role of the alloying elements Mo and Ni is another than formation of a stable passive film. Earlier works have shown (3-7) that Fe is selectively dissolved and that the alloying elements (Cr, Ni and Mo) are enriched on the surface in their metallic states during active dissolution. It has been suggested that the enriched surface layer lower the dissolution rate and enhance the passivation of the alloy. A support for the idea can be obtained from polarisation diagrams recorded from series of alloys polarised in acid solutions (5-7,24). The polarisation diagrams show that the current in the passive range is almost independent of the alloy composition. The passivation current, the maximum current at the active passive transition, on the other hand is markedly dependent on the alloy composition. The Mo- containing alloys show at least one order of magnitude lower current than the non- Mo containing alloys. Initiation of pitting gives a surface state which is similar to active dissolution apart from the fact that the potential is higher. It is suggested that repassivation is stimulated by the anodically segregated alloying elements. The enrichment of the alloying elements under the passive film is indicated even in this study. However, it has not explicitly been shown in, because the surface is covered with a relatively thick film which make the interpretation not straight forward.

Conclusions

- The superaustenitic stainless steel, UNS S3 1254, is passivated at room temperature in 0.1 M HCl + 0.4 M NaCl. At 65 °C initiation and repassivation of pitting occur.
- The thickness of the passive film formed at 22 °C at -100 mV and at 500 mV (SCE) are 12 Å and 17 Å, respectively. The corresponding values at 65 °C are 14 Å and 19 Å.
- The passive film consists of an inner barrier oxide film and an outer hydroxide film.
- The outer hydroxide layer is 6 Å thick and its thickness is independent of the potential and temperature.
- The inner oxide barrier consists mainly of Cr and Fe-oxides. At -100 mV (SCE) Mo⁴⁺ and Ni²⁺ are present. The cation contents of these elements are in the range 4 at.% to 8 at.%. At 500 mV (SCE) the contents of Ni²⁺ and Mo⁴⁺ are lower than at -100 mV(SCE).
- The Cr³⁺ content of the inner barrier film decreases with the potential. The loss of Cr³⁺-ions is compensated with Fe²⁺ and Fe³⁺-ions.
- The hydroxide layer consists mainly of Cr(OH)₃. The other cations present are Mo⁶⁺, Mo⁴⁺ and Ni²⁺ but their concentrations are low.
- It is proposed that the alloying elements are enriched on the surface of the pits during their activation and thereby repassivation is enhanced.

Acknowledgements

The Swedish Board for Technical and Industrial Development (NUTEK) is gratefully acknowledged for financial support.

References

1. R. Qvarfort, *Corros. Sci.*, **29**, 987 (1989).
2. I. Olefjord and B-O. Elfström, 8 th Int. Symp. on Reactivity of Solids. (ed. J. Wood, O. Lindqvist, C. Helgesson and N-G. Vannerberg), p.791, Pleaum Press, NY, (1977).
3. I. Olefjord, *Materials Sci. and Eng.*, **42**, 161 (1980).
4. I. Olefjord and B-O. Elfström, *Corrosion NACE*, **38**, 46 (1982).
5. I. Olefjord and B. Brox, *Proc. 5th Passivity of Metals and Semiconductors* (ed. M. Froment), p.561, Elsevier Science Publishers, Amsterdam (1983).
6. B. Brox and I. Olefjord, *Proc. Stainless Steel'84 Göteborg*, The Institute of Metals, p.134 (1984).
7. I. Olefjord, B. Brox and U. Jelvestam, *J. Electrochem. Soc.*, **132**, 2854 (1985).
8. I. Olefjord and L. Wegrelius, *Corros. Sci.*, **31**, 89 (1990).
9. P. Brüesch and K. Müller, *Appl. Phys. A*, **38**, 1 (1985).
10. I. Olefjord, *Proc. Symp. The Application of Surface Analysis Methods to Environmental/Material Interactions*, Seattle (1990).
11. P. Marcus and J.M. Grimal, *Corros. Sci.*, **33**, 805 (1992).
12. E. De Vito and P. Marcus, to be published in *Corrosion Science*.
13. E. De Vito and P. Marcus, *Surf. Interface Anal.*, **19**, 403 (1992).

14. C. Leygraf, G. Hultqvist, I. Olefjord, B-O. Elfström, V.M. Knyazheva, A.V. Plaskeyev and Ya.M. Kolotyркиn, *Corros. Sci.*, **19**, 343 (1979).
15. I. Olefjord and B-O. Elfström, 6th European Congress on Metallic Corrosion, p.21, London (1977).
16. M. Seo and N. Sato, *Trans. Japan Institute of Metals*, **21**, 805 (1980).
17. K. Hashimoto, K. Asami, K. Kobayashi and T. Masumoto, *Sci. Rep. Res. Inst., Tohoku Univ., Ser A*, **31(1)**, 163 (1983).
18. R.D. Willenbruch, C.R. Clayton, M. Oversluizen, D. Kim and Y. Lu, *Corros. Sci.*, **31**, 179 (1990).
19. I. Olefjord and C. Clayton, *ISIJ International*, **31**, 134 (1991).
20. F.J. Graham, H.C. Brookes and J.W. Bayles, *J. Electrochem. Soc.*, **20**, 45 (1990).
21. A.E. Martell and R.M. Smith, *Critical Stability Constants*, Plenum Press, NY, p.7 (1976).
22. T.W. Swaddla and E.L. King, *Inorg. Chem.*, **4**, 532 (1965).
23. L. Björnkvist and I. Olefjord, European corrosion meeting, EUROCORR-87, Karlsruhe, FRG, DECHEMA p.325 (1987).
24. L. Wegrelius and I. Olefjord, to be published in *Corrosion Science*.

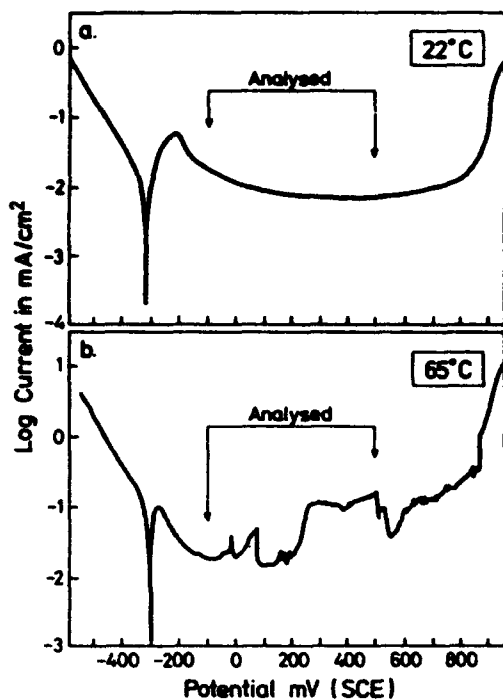


Figure 1. Polarisation curves of the alloy exposed to 0.1 M HCl + 0.4 M NaCl at 22°C and 65°C. Sweeping rate was 2.0 mV/s. The arrows mark the potentials to which the samples were polarised before surface analysis.

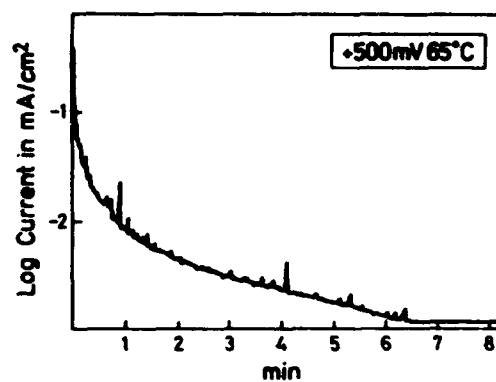


Figure 2. Current versus time for the steel polarised to 500 mV(SCE) at 65°C.

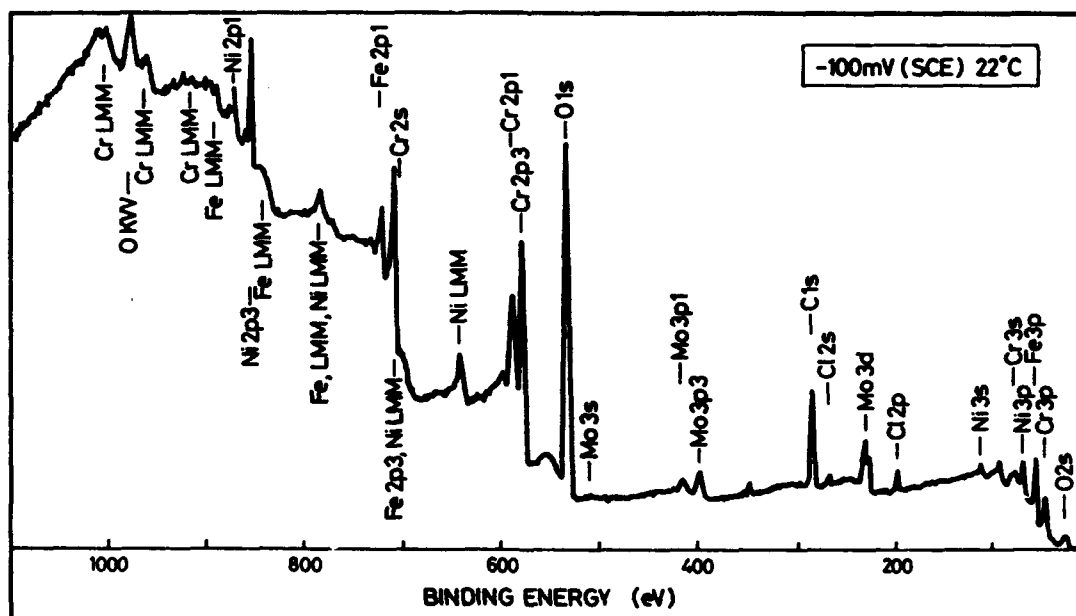


Figure 3. ESCA survey spectra recorded after polarisation of the sample to -100 mV for 10 min at 22°C.

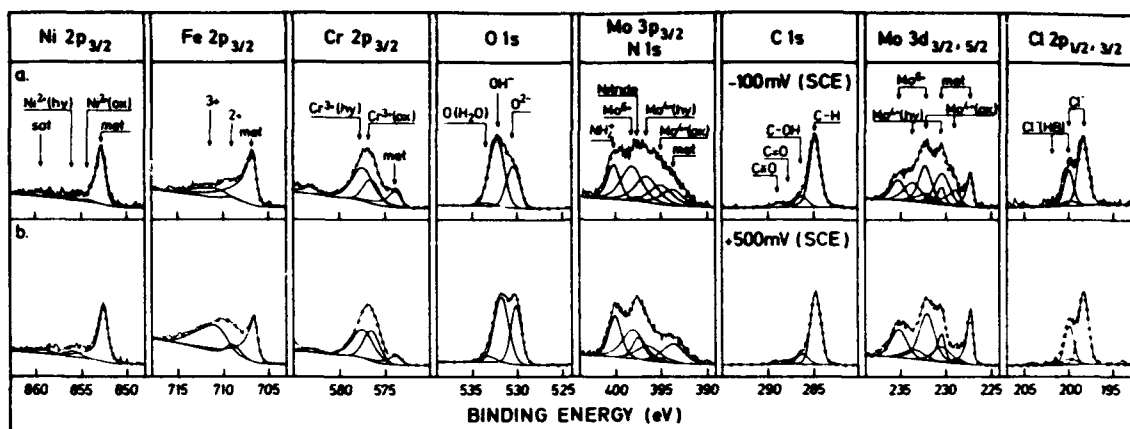


Figure 4. ESCA spectra recorded (take-off angle 45°) after polarisation of the steels at 65°C to -100 mV and 500 mV(SCE)

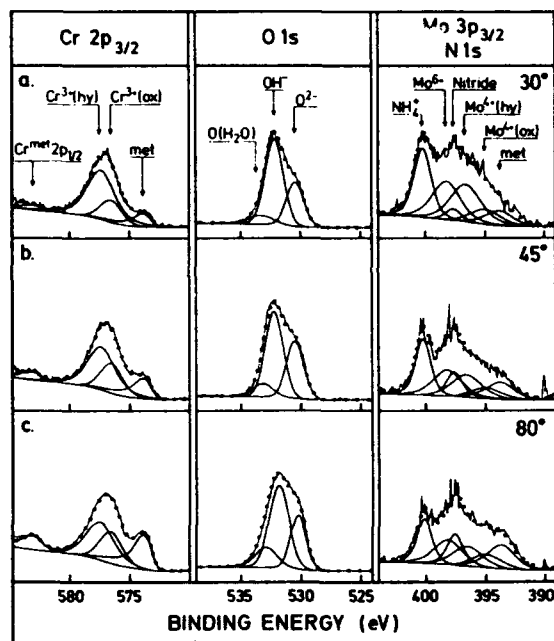
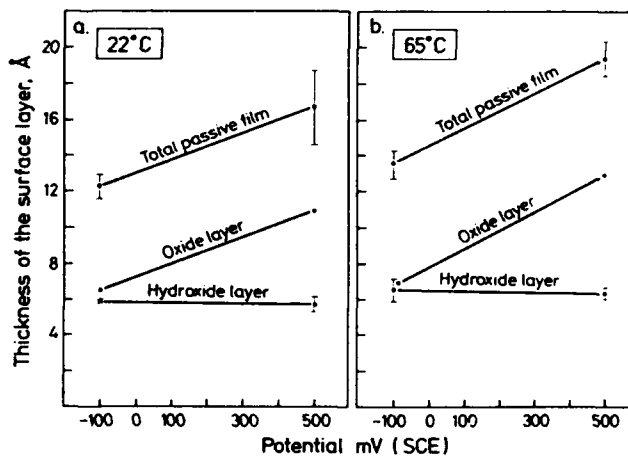


Figure 5. ESCA spectra recorded at the take-off angles 30°, 45° and 80° after polarisation to -100 mV(SCE) at 65°C.

Figure 6. The thickness of the passive films versus the potential.



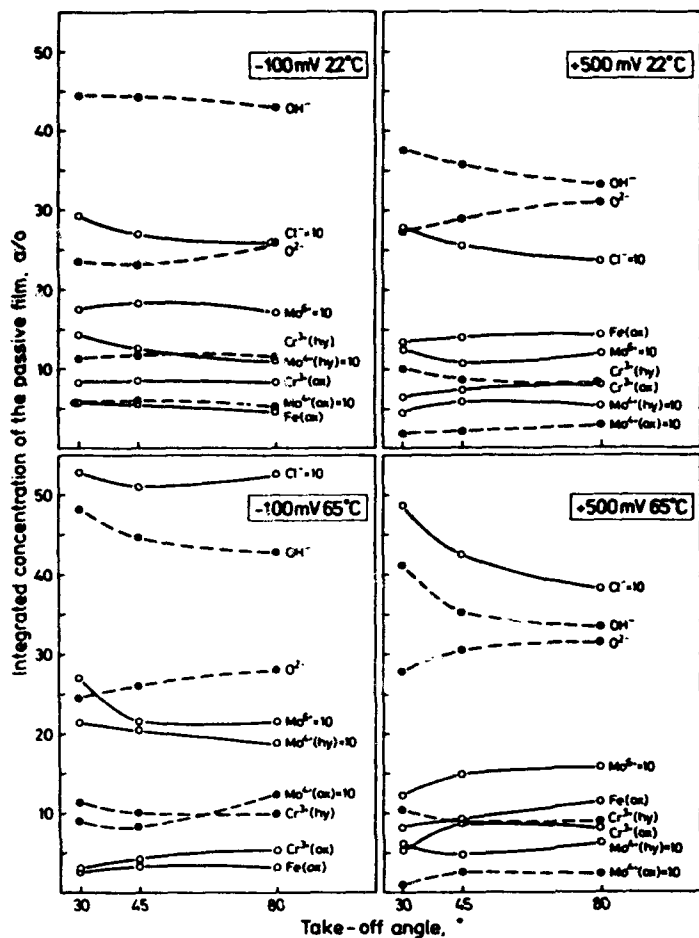


Figure 7. The integrated concentration of the passive film versus take-off angle.

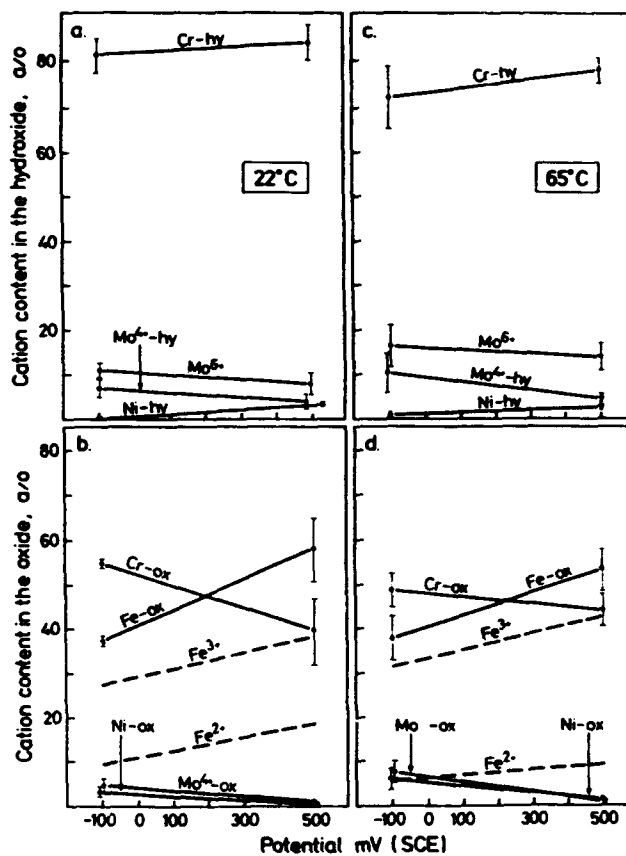


Figure 8. Cation content in the hydroxide and the oxide layers versus the potential.

XPS and Electrochemical Studies of the Dissolution and Passivation of Molybdenum-implanted Austenitic Stainless Steels

E. De Vito

Laboratoire de Physico-Chimie des Surfaces
CNRS (URA 425), Université Pierre et Marie Curie
Ecole Nationale Supérieure de Chimie de Paris
11, rue Pierre et Marie Curie, 75005 Paris, France

P. Marcus

Laboratoire de Physico-Chimie des Surfaces
CNRS (URA 425), Université Pierre et Marie Curie
Ecole Nationale Supérieure de Chimie de Paris
11, rue Pierre et Marie Curie, 75005 Paris, France

Abstract

X-ray Photoelectron Spectroscopy (XPS) was used to investigate the chemical composition and the chemical states of the passive film formed on austenitic stainless steels (Fe-19Cr-10Ni (at.%) which have been implanted with molybdenum (Mo^+ , 100 keV, 2.5×10^{16} at./ cm^2).

Prior to passivation the implanted alloy was characterized by RBS (Rutherford Backscattering Spectroscopy) and XPS. Alloys with well-defined surface concentrations of molybdenum were prepared by ion sputtering the implanted alloy in the preparation chamber of the spectrometer, to a fixed point in the implantation profile. The samples were then transferred without air exposure to a glove box with inert gas in which the electrochemical measurements were performed. After passivation, return transfer of the passivated samples was done with the same transfer device to avoid exposure to air.

In 0.5 M H_2SO_4 , the anodic dissolution current density decreases with increasing Mo content on the alloy surface. Surface analysis by XPS showed that the surface is enriched with molybdenum in the Mo^{4+} chemical state. The current density in the passive state is similar for both the non-implanted and the implanted alloys. Surface analysis by XPS showed that the passive film has a bilayer structure (inner oxide and outer hydroxide) and that the hydroxide layer present on the surface of the passive film is markedly enriched with molybdenum in the Mo^{6+} chemical state. The XPS measurements indicate that the presence of molybdenum favors the formation of chromium hydroxide at the expense of chromium oxide. A significant enrichment of the alloyed (Cr,Ni) and implanted (Mo) elements was also observed in the metallic phase under the passive film. The possible mechanisms of the effect of molybdenum on the corrosion resistance of stainless steels are discussed in the light of the obtained surface analytical results.

Key terms : passivity, stainless steel, molybdenum, ion implantation, XPS.

Introduction

Molybdenum is known for its beneficial effect on the corrosion resistance of stainless steels. Several surface analysis studies have been carried out to understand the exact role of this element in the passivation and corrosion mechanisms of Fe-Cr-Ni alloys (1-5). The relatively low concentration of molybdenum in these alloys makes the molybdenum XPS signal difficult to analyse in a quantitative manner and thus the results remain somewhat

ambiguous. To overcome this difficulty, a pure polycrystalline austenitic stainless steel has been implanted with molybdenum ions. This technique allowed us to obtain significant molybdenum concentrations in the alloy and thus to enhance the effects of Mo. The molybdenum-implanted stainless steels used in this study have already been characterized in a previous work (6) using XPS and RBS. In this work, electrochemical measurements have been carried out in 0.5M H₂SO₄ and surface analyses by XPS have been done after polarization in the active and in the passive regions in order to relate the electrochemical behaviour with the chemical composition of the surface films.

Experimental Procedure and Reference Data for Quantitative Analysis

The implanted alloy is a 304 type austenitic stainless steel supplied by UGINE (F). The alloy composition is given in Table 1. Discs of 10 mm diameter were prepared by spark machining. After mechanical polishing, finished with 0.5 µm diamond paste, the samples were implanted with molybdenum at UNIREC (F). The implantation conditions are reported in Table 2. RBS measurements have been performed in the Van de Graff accelerator of the Groupe de Physique des Solides - Université Paris VII.

XPS studies have been performed with a VG ESCALAB MARK II spectrometer using the Mg Kα X-ray source (hν = 1253.6 eV). The pass energy was 20 eV for the high resolution spectra of Fe 2p_{3/2}, Cr 2p_{3/2}, Ni 2p_{3/2}, Mo 3d, O 1s, C 1s and S 2p and 50 eV for the survey spectra. The X-ray power was 300 Watts. The references for the reported binding energies are: Au 4f_{7/2} at 83.8 eV and Cu 2p_{3/2} at 932.7 eV. Angle-resolved measurements were performed at take-off angles θ = 45° and θ = 90° (angle of the sample surface with the direction of the analyser). Depth profiles were obtained by sputtering the surface with argon ions. Two ion guns were used. The sputtering conditions for the preparation of the samples before passivation were 4kV, pAr = 10⁻⁶ mbar and a current density of 12 µA cm⁻² using a VG AG21 ion gun mounted in the preparation chamber attached to the spectrometer. A VG AG60 ion gun mounted in the analysis chamber was used for sputter depth profiling of the passive films, under the following conditions: 2.5 - 3 kV, pAr = 10⁻⁵ mbar and a current density of 1 µA cm⁻². Prior to the electrochemical measurements, the samples were cleaned by ion sputtering in the preparation chamber of the spectrometer as described above and analysed by XPS. They were then transferred without exposure to air, using a special transfer vessel, into a glove box under inert gas where the electrochemical experiments were carried out. The electrochemical cell was composed of a saturated sulfate reference electrode, a Pt counter electrode and a working electrode. A PAR model 273 potentiostat interfaced to an IBM PC computer was used. The electrolyte was 0.5M H₂SO₄ prepared with ultra-pure water and pure sulphuric acid. After electrochemical treatments, the samples were extracted from the solution under potential, rinsed in ultra-pure water, dried in nitrogen gas and then transferred back to the spectrometer without exposure to air. Angle-resolved XPS analysis coupled with sputter depth profiling were then carried out. The experimental procedure is summarized in Figure 1.

The data processing of the high resolution spectra of Fe2p, Cr2p, Ni2p, Mo3d, O1s and S2p allowed us to identify the elements and their valence states in the passive films. The data processing is based on reference data acquired with reference materials. Oxides of the pure metals have been prepared in the preparation chamber of the spectrometer and analysed in order to characterize the different oxidation states of the alloyed elements. The parameters derived from a previous work (6), from this work and from literature data (2,7) were used for curve fitting of the XPS spectra. After background subtraction (iterative Shirley method), the spectra are fitted with Gaussian-Lorentzian curves using the reference parameters. The experimental photoelectron yield ratios were obtained from the measured intensities (peak area in counts eV s⁻¹) for the pure metals (ion-etched) and the oxides prepared in the preparation chamber of the XPS spectrometer. The values of the attenuation lengths of the electrons in the metals and in the oxides were calculated with the Seah and Dench formula (8).

The molybdenum chemistry is very complex and several studies have been performed by XPS to identify the various

oxides which could be found in passive films (7,9-11). In this work, we have synthesized and characterized MoO_2 and MoO_3 and studied the influence of sputtering on the oxidation state of the molybdenum oxides. A pure molybdenum single crystal ((111) face) was mounted on a heatable sample holder and cleaned by ion sputtering prior to oxidation. MoO_2 was prepared using the following oxidation conditions: $p(\text{O}_2)=10^{-6}$ mbar, $T=600^\circ\text{C}$, $t=60$ min. MoO_3 was prepared on the single crystal surface under the following conditions: $p(\text{O}_2)=1$ bar, $T=600^\circ\text{C}$, $t=5$ min. The spectra are shown in Figure 2. The spectra of Figure 2b were analysed with two doublets assigned to the species $\text{Mo}^{4+}(\text{ox})$ and $\text{Mo}^{4+}(\text{hyd})$ (ox=oxide and hyd=hydroxide), according to the corresponding O1s signals (O^{2-} and OH^-). It is well known that ion bombardment has a reducing effect on oxides (12). Ion sputtering of the oxides prepared in this work (MoO_2 and MoO_3) confirmed that the composition of the sputtered oxides is markedly modified. It is thus necessary to take such effects into consideration when studying Mo-containing passive films. The Mo 3d spectra of the passivated ion implanted alloy could all be fitted with the above chemical states, thus other Mo oxides which have been detected in other works (Mo_2O_7 , Mo_2O_9) (10) were not considered here.

The quantification procedure used in this work is summarized in Figure 3. From angle-resolved analyses coupled with depth profiling it is possible to conceive a qualitative model of the analysed film. From this model the equations relating the unknown concentrations and thicknesses and the theoretical XPS intensity ratios can be expressed. It is then possible to search for the set of values which give the best agreement between theoretical and measured XPS intensities. These calculations have been computerized. For each analysed film, it is thus possible to propose a model and calculate the corresponding concentrations of the detected compounds and the thicknesses of the layers constituting the model, as well as the enrichment of alloying elements under the passive film.

Results

Characterization of the implanted alloy.

XPS and RBS spectroscopies were used to characterize the alloy after Mo implantation. The XPS sputtering depth profile is shown in Figure 4. The molybdenum concentration was calculated using the equation [1], based on the hypothesis that selective sputtering can be neglected:

$$D_{\text{Mo}} = \left(1 + \frac{I_{\text{Fe}}^0 \lambda_{\text{Mo}}^{\text{all}} Y_{\text{Mo}}}{I_{\text{Mo}}^0 \lambda_{\text{Fe}}^{\text{all}} Y_{\text{Fe}}} + \frac{I_{\text{Cr}}^0 \lambda_{\text{Mo}}^{\text{all}} Y_{\text{Mo}}}{I_{\text{Mo}}^0 \lambda_{\text{Cr}}^{\text{all}} Y_{\text{Cr}}} + \frac{I_{\text{Ni}}^0 \lambda_{\text{Mo}}^{\text{all}} Y_{\text{Mo}}}{I_{\text{Mo}}^0 \lambda_{\text{Ni}}^{\text{all}} Y_{\text{Ni}}} \right)^{-1} \quad [1]$$

where D_{Mo} is the molybdenum concentration (at.%), λ_{M} is the attenuation length of the electrons emitted by the element M in the alloy, Y_{M} is the experimental electronic yield of the element M and I_{M} is the XPS intensity of the element M (peak area in counts eV s^{-1} after background subtraction using a non-linear Shirley method).

The molybdenum concentration at the beginning of the profile is ~ 4 at% Mo. This is due to the simultaneous sputtering occurring during the implantation of Mo. Then the concentration increases up to 9-10 at%. Comparing the position of the maximum in the profile with the RBS results enabled us to convert the sputtering time into a depth scale. In a previous work (6) the concentration at the maximum of the profile was derived from the RBS analysis, using TRIM 89 and RUMP programs. A value of 6-7 at% was obtained and the depth corresponding to the maximum in the implantation profile was found to be 210 Å below the surface. A more accurate RUMP simulation performed in the present work showed that the concentration at the maximum of the profile is ~ 8 at% and the maximum is at ~ 150 Å below the surface. The comparison of the XPS and RBS data revealed a small difference. The XPS profile is asymmetric and exhibits a tail at increasing depth. This may be due to a small enrichment of Mo during ion sputtering due to the different sputter yields of Mo with respect to Fe, Cr and Ni. The Mo concentration finally slowly

approaches the Mo concentration of the non-implanted alloy. The Mo concentration is significantly higher than the Mo concentration of the non-implanted alloy within a depth of ~ 600-700 Å. A $\gamma \rightarrow \alpha$ phase transformation induced by the implantation of molybdenum has been observed by TEM (13) on samples prepared under identical conditions. Knowing the implantation profiles, samples with well-defined surface concentrations of molybdenum were prepared, prior to the electrochemical measurements, by argon ion-etching the implanted alloy for a fixed time, and the surface was analysed to determine the molybdenum concentration at the surface.

Electrochemical behaviour.

Potentiodynamic experiments. Potentiodynamic curves have been recorded for the non-implanted 304 stainless steel and for the implanted alloys with different initial surface concentrations of molybdenum (from 3 to 9.5 at %).

After transfer of the sample from the spectrometer to the electrochemical glove box, the corrosion potential was checked during 1 min. before the beginning of the experiment. The electrochemical potential scans (1 mV/s) were carried out from -140 to +1260 mV/SHE. The i-E plots are reported in Figure 5 and the main electrochemical data are summarized in Table 3. It is observed in Figure 5a that the corrosion potential is shifted towards higher potentials when molybdenum is present on the initial surface. The activation peak disappears for the Mo-implanted alloy. Similar effects have already been observed for molybdenum-containing Fe-Cr-Ni alloys (1-6). In the 100-500 mV/SHE potential region, an oxidation or dissolution process occurs for the Mo-containing stainless steel. The extent of this feature depends on the initial surface concentration of molybdenum as shown by Figure 5b. The high potential region of passivity is similar for both the non-implanted and the implanted alloys with however a slightly higher residual current density for the implanted alloys. These results indicate that the implantation of Mo has no beneficial effect on the protective character of the passive film in 0.5 M H_2SO_4 .

Surface Analysis Results.

For the study of the passive films, the potential was stepped to +740 mV/SHE (which is in the passive region for all analysed samples) and the samples were polarized for 60 min. Surface analyses were also performed after polarization at active potentials which were in the range -80 to -30 mV/SHE depending on the i-E curve of the particular alloy. For the XPS analysis, the sample was removed from the cell under potential, rinsed in ultra-pure water, dried in nitrogen and transferred to the spectrometer without exposure to ambient air.

Influence of the implantation of molybdenum on the composition of the passive film formed on the 304 stainless steel. The XPS spectra obtained for the passivated non-implanted alloy and for the implanted alloys are shown in Figures 6 and 7, respectively. Similar chemical species are found in the films on both the non-implanted and the implanted alloys. Oxidized iron is found in the passive film though in smaller quantities than chromium oxide. No significant signal from nickel oxide is found after passivation, in agreement with other works (1-3,5,6): the weak Ni^{met} signal observed in the Ni 2p_{3/2} region is emitted by Ni in the alloy. The Cr 2p_{3/2} region indicates a marked enrichment of this element in the passive films for the implanted as well as for the non-implanted alloys. As regards the chemical states, oxidized chromium is found to be mainly in the +3 oxidation state. The chromium signal was resolved into chromium oxide $Cr^{3+(ox)}$ (Cr_2O_3 type, binding energy: 576.6 eV) and chromium hydroxide $Cr^{3+(hyd)}$ ($Cr(OH)_3$ type, binding energy: 577.2 eV). The comparison of the XPS spectra of Cr 2p for the non-implanted alloy and the Mo-implanted alloy reveals that the relative amount of Cr hydroxides with respect to Cr oxides is higher for the Mo-implanted alloy. Oxidized molybdenum is detected in the analysed passive film for the Mo-implanted alloys. The molybdenum signal has been resolved (Figure 7b) into the metallic form (Mo-implanted in the alloy) and three oxide states: $Mo^{4+(ox)}$ (MoO_3 type), $Mo^{4+(hyd)}$ ($Mo(OH)_2$ type) and $Mo^{6+(ox)}$ (MoO_3 type). The curve fitting of the molybdenum spectrum shows

that molybdenum is mainly present in the passive film in the form of $\text{Mo}^{6+}(\text{ox})$. A small amount of $\text{Mo}^{4+}(\text{ox})$ is also detected. The oxygen signal clearly reveals the presence of the oxide (O^{2-}) and hydroxide (OH^-) forms. A third peak is present at higher binding energy, corresponding to oxygen in H_2O and SO_4^{2-} .

The angle-dependent XPS (AD-XPS) experiments, which constitute a non-destructive method, provide reliable information on the in-depth localization of chemical species and allow us to validate or invalidate a multilayer model. The AD-XPS measurements are shown in Figure 7 for the implanted alloy. The $\text{Cr}^{3+}(\text{hyd})/\text{Cr}^{3+}(\text{ox})$ ratio is enhanced in the angular analysis at the low take-off angle (45°). This reveals the layered structure of the passive film: the chromium hydroxide is found to be in the outer part of the passive film (enhanced signal at 45°) whereas chromium oxide is in the inner part. The O 1s signal which has a OH^- component partly related to $\text{Cr}^{3+}(\text{hyd})$ shows the same tendency. Sputtering depth profiles have been recorded and are shown in Figure 8 for the non-implanted alloy and for the implanted alloy with an initial surface concentration of 8 at.% Mo. Chromium hydroxide appears to be located in the outer part of the passive film, which confirms the findings of the AD-XPS measurements. The increasing signals of the oxide states of iron and chromium oxides with sputtering indicate that the inner layer is composed of oxides of these elements, with an enrichment of chromium oxide near the film/alloy interface. The sharp decrease of the Mo^{6+} signal observed after the first ion sputtering indicates that Mo^{6+} is located in the outer part of the passive film. The total signal from oxidized molybdenum ($\text{Mo}^{4+} + \text{Mo}^{6+}$ in Figure 8) decreases rapidly during ion sputtering which also supports the preceding conclusion, even if some reduction of Mo^{6+} may be caused by sputtering. Depth profiling measurements thus confirm the bilayer structure of the passive film, and they show that Mo^{6+} is in the outer part of the film on the passivated implanted alloy.

In conclusion of this part, the bilayer structure of the film and the chromium enrichment are observed on both the non-implanted and the implanted alloys. However, the ratio of $\text{Cr}^{3+}(\text{hyd})/\text{Cr}^{3+}(\text{ox})$ is enhanced on the implanted alloy. Molybdenum is detected in the passive film of the implanted alloy in the form of Mo^{6+} and is essentially localized in the outer part of the film.

Comparison of the surface films formed on the molybdenum implanted 304 stainless steel in the active and the passive states. XPS spectra obtained after polarization of the molybdenum-implanted alloy in the active region (-30 mV/SHE) for an initial concentration of ~ 7 at.% Mo are shown in Fig. 9. As described above, no passivation peak was observed for the implanted alloys. We thus define here the active domain as the potential region situated just above the corrosion potential (-60 mV/SHE), and below the potential region in which an oxidation process is observed for the implanted alloys (100 - 500 mV/SHE). The detected chemical states of chromium are similar to those detected after passivation: the Cr 2p signal shows that $\text{Cr}^{3+}(\text{ox})$ and $\text{Cr}^{3+}(\text{hyd})$ are the main components. The presence of $\text{Cr}^{3+}(\text{ox})$ may be due to oxidation of the samples during transfer, but also to the fact that chromium is passive at such potentials. The Ni 2p signal shows traces of Ni hydroxide, which were not observed in the passive state. The major difference between the surface composition in the active state and in the passive state is observed in the Mo signal reported in Fig. 9b, which reveals that in the active state the molybdenum is essentially in the form of $\text{Mo}^{4+}(\text{ox})$. Angle-dependent XPS analyses have been carried out to obtain further information on the in-depth distribution of the different species. The angle-dependent analyses for the Cr 2p $_{3/2}$, Mo 3d $_{5/2}$, 3/2 and O 1s are also shown in Fig. 9. As expected, the signals of the oxidized elements are enhanced with respect to those of the metals at low take-off angle. In sharp contrast with what was observed for the passive films, the $\text{Cr}^{3+}(\text{hyd})/\text{Cr}^{3+}(\text{ox})$ ratio does not vary in the same way. This result is confirmed by the O^{2-} and OH^- contributions in the O 1s signal which are not affected by the take-off angle. This clearly proves that there is no bilayer structure at this potential. The surface film is a single layer containing the various species.

Models of the surface films and quantitative surface analysis. On the basis of the results reported above, the proposed models for the analysed films are shown in Figure 10. The method for determining the thicknesses and concentrations has been reported previously (6).

On both the non-implanted and implanted alloys (Figures 10a and 10b, respectively) the passive films have a bilayer structure with an outer hydroxide layer and an inner oxide layer. In both cases, the oxide layer is enriched in chromium oxide near the metal-film interface. On the implanted alloy, it is noticed that the outer chromium hydroxide layer is thicker than on the non-implanted alloy. Molybdenum is localized in the outer part of the hydroxide layer. The amount of Mo cations in the hydroxide layer is high (43%), but with respect to the entire passive film it is only 7%.

The alloy is enriched, underneath the passive film, in the alloyed and implanted elements Cr, Ni and Mo. This phenomenon is associated with the preferential dissolution of Fe.

The model proposed for the films formed in the active region on the implanted alloy is shown in Figure 10c. On the basis of the angle-resolved XPS the existence of a bilayer structure can be ruled out. The surface film formed at this potential is constituted of a single layer with different species: chromium oxide and hydroxide are found, as well as iron and molybdenum oxides. This surface film is thinner than the passive film formed at higher potential. The oxidation state of the molybdenum cations on the surface is essentially +4. The molybdenum cations are found in larger quantity than in the passive film and are distributed in the entire film. It is to be noted that the Fe concentration calculated for the modified layers of the alloy under the film formed in the active potential region is higher than after passivation. This shows that further selective dissolution of iron takes place during the formation of the passive film.

Discussion

Ion implantation can be used to prepare materials on which the effects on passivation and resistance to corrosion of elements such as molybdenum (6,14) or nitrogen (15) can be investigated.

The electrochemical study of the alloys with implanted molybdenum shows that the presence of Mo in the alloy lowers the dissolution rate in the active region.

In the active domain, the angle-dependent analyses (as well as the ion sputtering depth profiles) show that the surface film has not a layered structure but consists of different oxidized species, mixed in a single layer. The surface analyses performed after polarization in the active region revealed the presence of Fe^{2+} and Cr^{3+} . On the surface of the Mo-implanted alloy, molybdenum is found to be in the +4 oxidation state, $\text{Mo}^{4+(\text{ox})}$, which may be produced by the following reaction: $\text{Mo} + 2 \text{H}_2\text{O} \rightarrow \text{MoO}_2 + 4 \text{H}^+ + 4 \text{e}^-$. The $\text{Mo}^{4+(\text{hyd})}$ XPS signal recorded for the film formed in the active region may be due to the hydroxylation of MoO_2 .

In the passive state, the films formed on all samples have a bilayer structure, with an outer layer of hydroxide and an inner layer of oxide. The passivation process of these alloys is characterized by a single layer-to-bilayer transition. The passive film is enriched in oxidized chromium. The valence states observed for chromium are $\text{Cr}^{3+(\text{ox})}$ and $\text{Cr}^{3+(\text{hyd})}$. The $\text{Cr}^{3+(\text{hyd})}/\text{Cr}^{3+(\text{ox})}$ ratio is enhanced on Mo-implanted samples with respect to the passive films formed on the non-implanted 304 stainless steel. This finding does not support the view that molybdenum would favor the formation of chromium oxide (3). Chromium is not found in the +6 oxidation state. Chromium has been found in the +6 oxidation state when an iron-chromium alloy was polarized in the transpassive region (16). Our analysis of the XPS spectra is based on reference spectra and reference data obtained on synthesized compounds. Based on that work the resolution of the Cr 2p_{3/2} region does not show the presence of $\text{Cr}^{6+(\text{ox})}$, which is consistent with the fact that the samples have not been polarized in the transpassive region. In the passive film, the implanted Mo is found in the +6 oxidation

state. This supports the view that the oxidation process found in the [100,500] mV/SHE is associated with the transition $\text{Mo}^{4+} \rightarrow \text{Mo}^{6+}$.

The binding energies of the XPS signals of $\text{Mo}^{6+(\text{ox})}$ in MoO_4^{2-} and in MoO_3 are very close. As proposed in other papers (3), the following reaction may produce MoO_4^{2-} : $\text{MoO}(\text{OH})_2 + 4 \text{OH}^- \rightarrow \text{MoO}_4^{2-} + 3 \text{H}_2\text{O} + 2 \text{e}^-$. The low pH (0.3) of the solution is expected to favour the condensation of MoO_4^{2-} anions into polyanions such as $\text{Mo}_2\text{O}_7^{4-}$. Such big molecules are not likely to be incorporated in the passive film and, if they exist, would rather be on the surface of the passive film. However, the O 1s XPS signal should then display a spectrum with a much higher O^{2-} peak, which is not observed. As regards MoO_3 it is difficult to conceive that it could be mixed with the hydroxide layer. We propose that Mo^{6+} cations are incorporated in the chromium hydroxide top layer, and that they enhance the hydroxylation of the surface, as shown schematically in Fig. 11. It is to be noted that our results show that the presence of Mo^{6+} in the passive film has no beneficial effect in sulphuric acid.

The observed enrichment under the passive film of the alloyed (Cr, Ni) and implanted (Mo) elements is caused by the preferential dissolution of Fe. This phenomenon has already been observed for Mo-containing austenitic stainless steels (2). The composition of the metallic side of the passive film/alloy interface is important for the repassivation behaviour of the alloy, a crucial aspect in resistance to pitting.

A new finding of this work is the accumulation of molybdenum in the +4 valence state on the alloy surface during the pre-passivation stage and the $\text{Mo}^{4+} \rightarrow \text{Mo}^{6+}$ transition taking place during passivation. A fraction of the Mo^{6+} formed during this reaction remains in the passive film and part of it is dissolved.

There are direct implications of the above results on the effects of molybdenum on resistance to pitting in chloride solutions. The incorporation of Mo^{6+} ions in the outer hydroxide could modify the initial stage of the interactions between Cl^- ions and the passive film. One effect (with beneficial consequences on pit initiation) could be the trapping of Cl^- ions caused by the presence of strongly charged cations. No Mo^{6+} ions are found in the inner oxide, so that the implanted molybdenum probably has no effect on the properties of the oxide layer itself. Molybdenum is enriched under the passive film, which will diminish the dissolution rate in the case of passive film breakdown. It is also suggested that the observed accumulation of Mo^{4+} prior to passivation and the existence of a $\text{Mo}^{4+} \rightarrow \text{Mo}^{6+}$ transition leading to partial release of Mo^{6+} during passivation may have a significant effect on the repassivation kinetics of the Mo-implanted material in the presence of Cl^- . These ideas are now being tested by investigating by electrochemistry and XPS the behaviour of the Mo-implanted alloy in Cl^- -containing solution.

Conclusions

Molybdenum-implanted austenitic stainless steels have been studied by electrochemistry and XPS. Prior to the electrochemical experiments, the implantation profile has been characterized by RBS and XPS and surfaces with well-defined Mo concentrations have been prepared by ion sputtering the implanted alloy in the preparation chamber of the spectrometer. The effects of the implanted molybdenum on the electrochemical behaviour of the alloy in 0.5M H_2SO_4 have been investigated. The surface films have been analysed by angle-dependent XPS and by sputter depth profiling. The major conclusions are the following:

(i) The implanted molybdenum strongly modifies the electrochemical behaviour of the alloy. The dissolution rate is lowered by the implanted molybdenum: the active peak observed on the non implanted alloy is suppressed; a new anodic feature appears in the [100,500] mV/SHE potential region. The residual current density is slightly higher than for the non-implanted alloy, showing that the implanted Mo has no beneficial effect on passivity in chloride-free acid solution.

ii) At low anodic potential, molybdenum is found to be enriched on the surface in the +4 valence state. The passivation process of the implanted alloy is characterized by a Mo^{4+} to Mo^{6+} transition, with both Mo^{6+} partial dissolution and

incorporation in the film, accompanied by further selective dissolution of iron.

(iii) The passive film has a bilayer structure and the outer hydroxide layer is enhanced on the implanted alloy.

(iv) A marked enrichment of the alloyed (Cr, Ni) and implanted (Mo) elements is observed in the alloy near the alloy/passive film interface, due to the preferential dissolution of Fe.

Acknowledgements

This work was sponsored by Centre National de la Recherche Scientifique (CNRS, Groupement Scientifique Corrosion) and IRSID-Unieux.

References

1. I.Olefjord, *Mat. Science and Engineering*, 42 (1980): p. 161
2. I.Olefjord, B.Brox and U. Jelvestam, *J.Electrochem. Soc.*, 132 (1985): p. 2854
3. C.R.Clayton and Y.C.Lu, *J.Electrochem. Soc.*, 133 (1986): p. 2465
4. C.Cohen, D.Schmaus, A.Elbiache and P.Marcus, *Corrosion Science*, 31 (1990): p. 207
5. J.E.Castle and J.H.Qiu, *Corrosion Science*, 30 (1990): p. 429
6. E.De Vito and P.Marcus, *Surf.Interface Anal.*, 19 (1992): p.409
7. B.Brox and I.Olefjord, *Surf.Interface Anal.*, 13 (1988): p. 3
8. M.P.Seah and W.A.Dench, *Surf.Interface Anal.*, 1 (1979): p. 2
9. B.Brox, Wu Yi-Hua and I.Olefjord, *J.Electrochem. Soc.*, 135 (1988): p. 2184
10. Y.C.Lu and C.R.Clayton, *Corrosion Science*, 29 (1989): p. 927
11. M.Urgen, U.Stolz and R.Kirchheim, *Corrosion Science*, 30 (1990): p. 377
12. K.S.Kim, W.E.Baitinger, J.W.Amy and N.Winograd, *J.Electron Spectrosc.Relat.Phenom.*, 5 (1974): p. 351
13. L. Beaunier, to be published
14. M. B. Ives, U. G. Akano, Y. C. Lu, Guo Ruijin and S. C. Srivastava, *Corrosion Science*, 31 (1990): p. 367
15. P.Marcus and M.E.Bussel, *Applied Surf. Sci.*, 59 (1992): p. 7
16. J.A.Bardwell, A.J.Davenport, H.S.Isaacs, G.I.Sproule, B.MacDougall and M.J. Graham, *J. Electrochem. Soc.*, 139 (1992): p. 371

Table 1 : Chemical analysis of the austenitic stainless steel before implantation.

| Element | Fe | Cr | Ni | Mn | Si | Cu | Mo | C | N | P | S |
|----------------------|-------|-------|------|------|------|------|------|------|------|------|--------|
| Concentration (wt.%) | 72.01 | 17.38 | 8.28 | 1.43 | 0.49 | 0.15 | 0.14 | 0.05 | 0.04 | 0.03 | 0.0025 |

Table 2 : Ion implantation conditions

| Implanted ion | Dose | Energy | Residual pressure | Temperature |
|-----------------|---|---------|-----------------------|-------------|
| Mo ⁺ | 2.5 10 ¹⁶ atcm ⁻² | 100 keV | 10 ⁻⁵ Torr | Room temp. |

Table 3 : Electrochemical data for the different studied materials

| Sample | Corrosion potential (mV/SHE) | Passivation potential (mV/SHE)* | Current density max (μA/cm ²)** | Residual current density (μA/cm ²)*** |
|--------------------|------------------------------|---------------------------------|---|---|
| 304 SS | - 110 | 0 | 19 | 4 |
| Mo-impl.(3at%Mo) | - 60 | - | - | 7 |
| Mo-impl.(7at%Mo) | - 60 | - | - | 8 |
| Mo-impl.(9.5at%Mo) | - 60 | - | - | 7 |

* : potential measured at the maximum of the activation peak. ** : current density measured at the maximum of the activation peak. *** : minimum measured current density in the passive state.

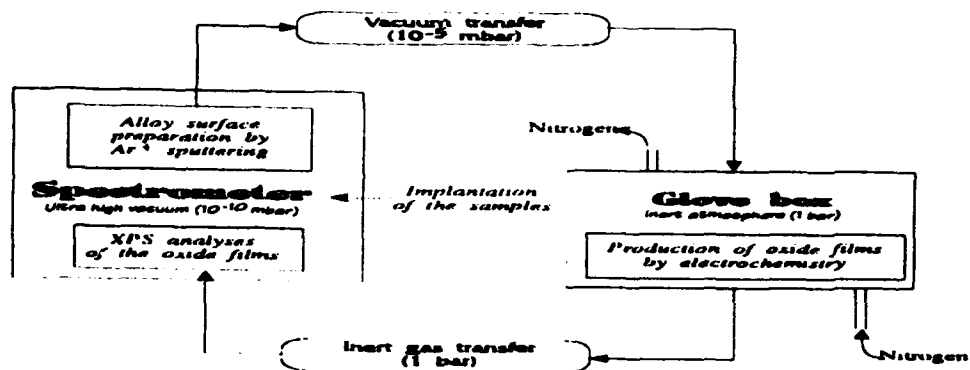


Figure 1 - Experimental procedure for the coupled XPS and electrochemical studies of the molybdenum-implanted stainless steels.

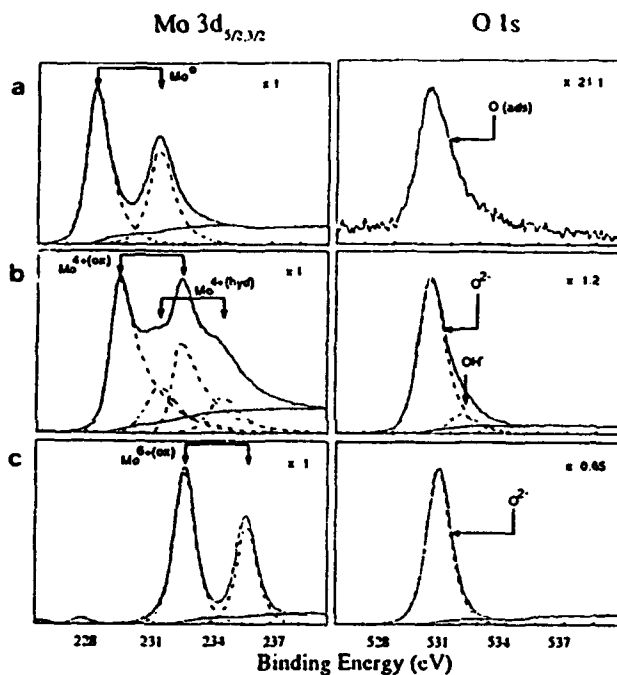


Figure 2 - Reference XPS spectra for molybdenum and molybdenum oxides (a) pure molybdenum (ion-etched) (b) MoO_2 and (c) MoO_3 .

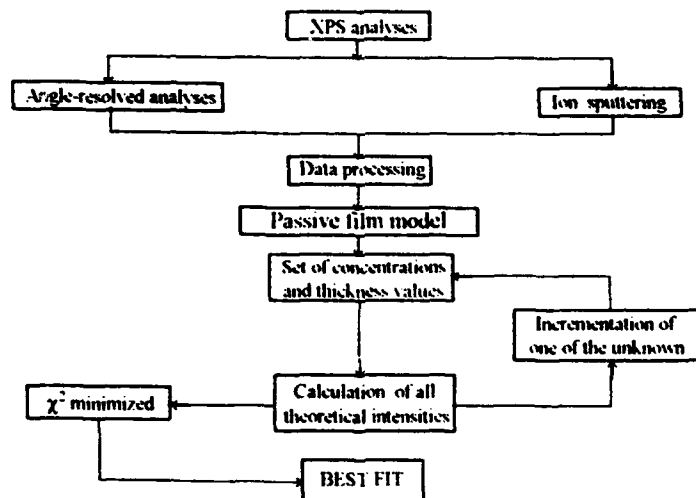


Figure 3 - Procedure for quantitative XPS analysis of passive films.

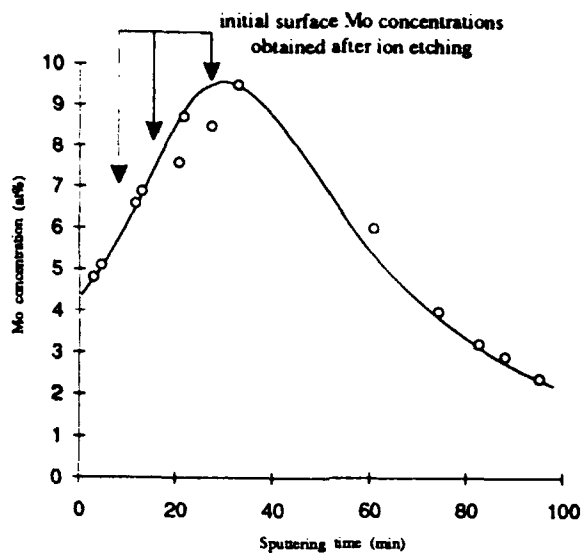


Figure 4 - XPS depth profile of molybdenum in the implanted austenitic stainless steel.

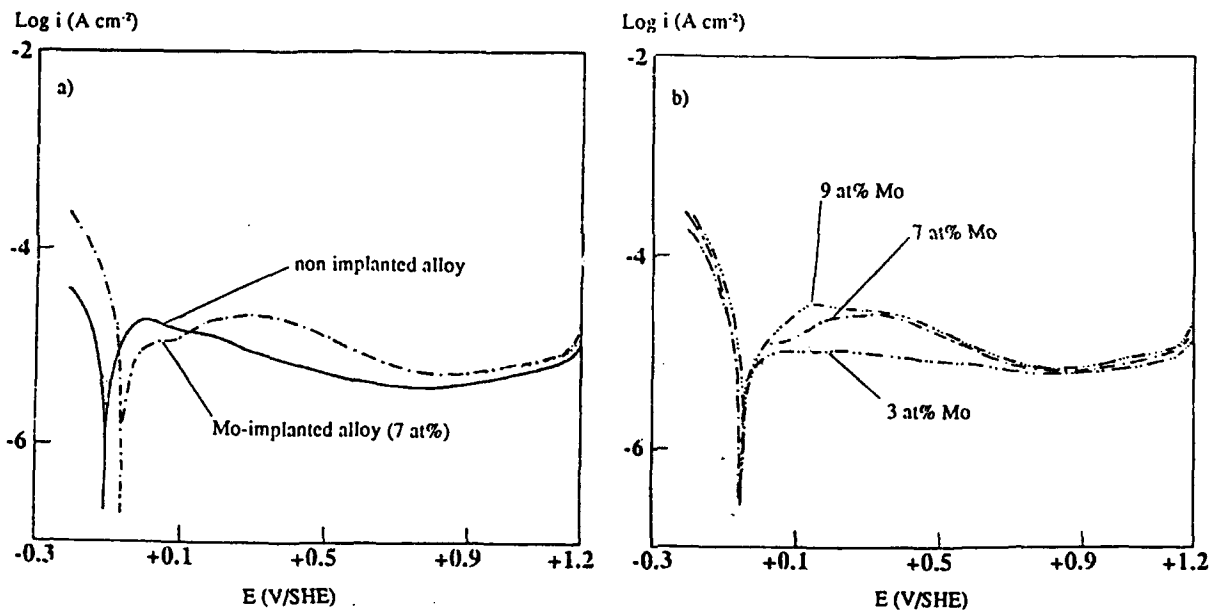


Figure 5 - Potentiodynamic curves : a) comparison between the non-implanted alloy and the Mo-implanted alloy and b) influence of increasing Mo concentration for the Mo-implanted alloys (0.5 M H_2SO_4 , 1 mV sec⁻¹).

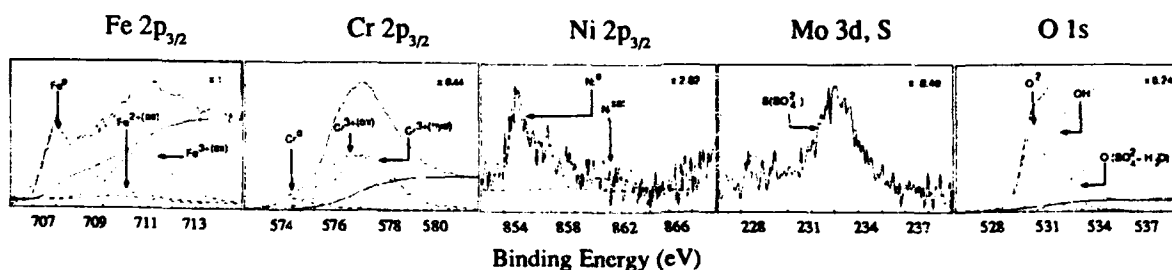


Figure 6 - XPS spectra of Fe $2p_{3/2}$, Cr $2p_{3/2}$, Ni $2p_{3/2}$, [Mo3d, S 2s] and O1s after passivation of the non-implanted alloy (0.5 M H_2SO_4 , 740 mV/SHE, 60 min).

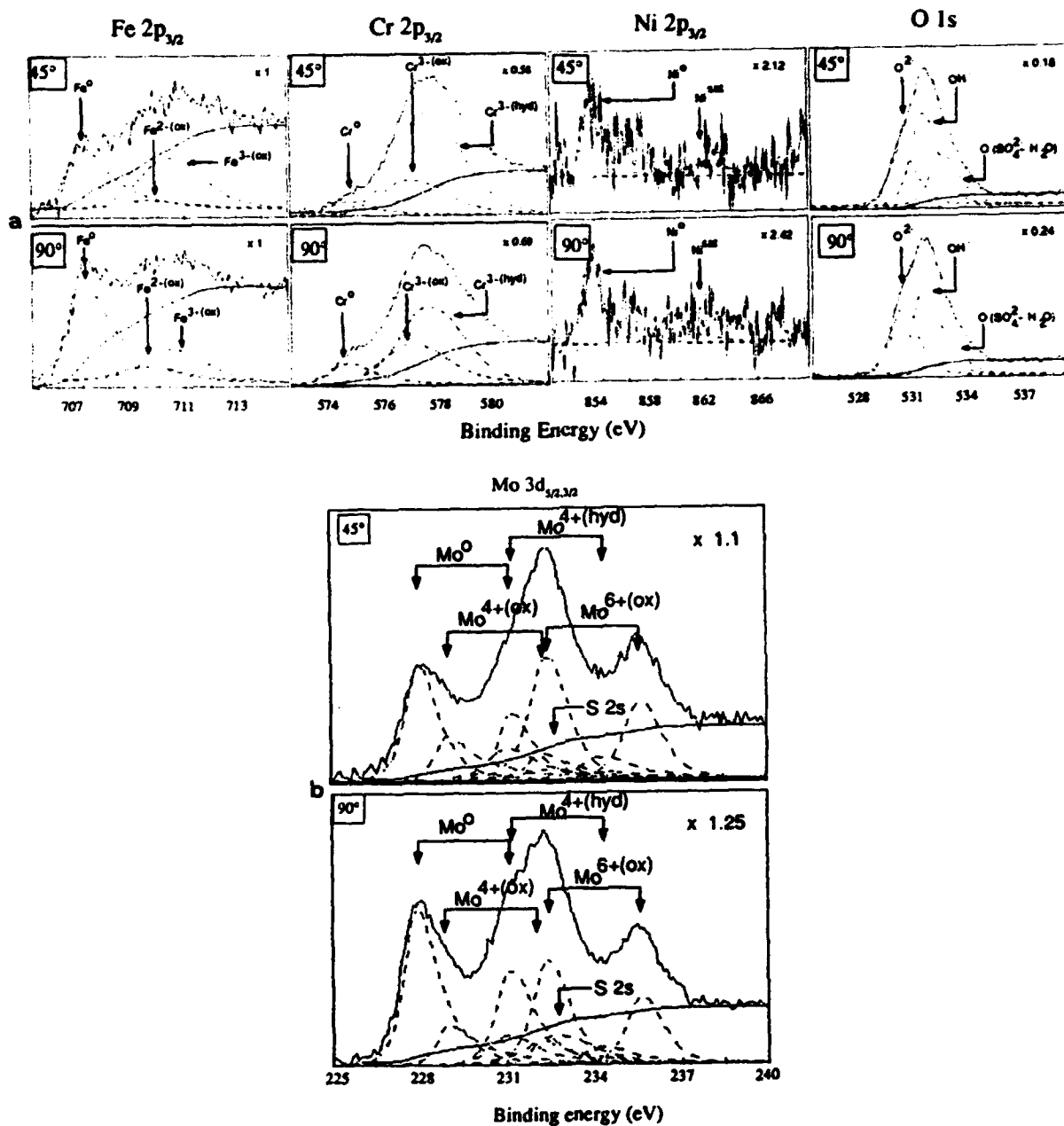


Figure 7 - Angle-dependent XPS spectra of a) Fe 2p_{3/2}, Cr 2p_{3/2}, Ni 2p_{3/2} and O 1s and b) Mo 3d, after passivation of the Mo-implanted alloy. Take-off angles: 45° and 90°.

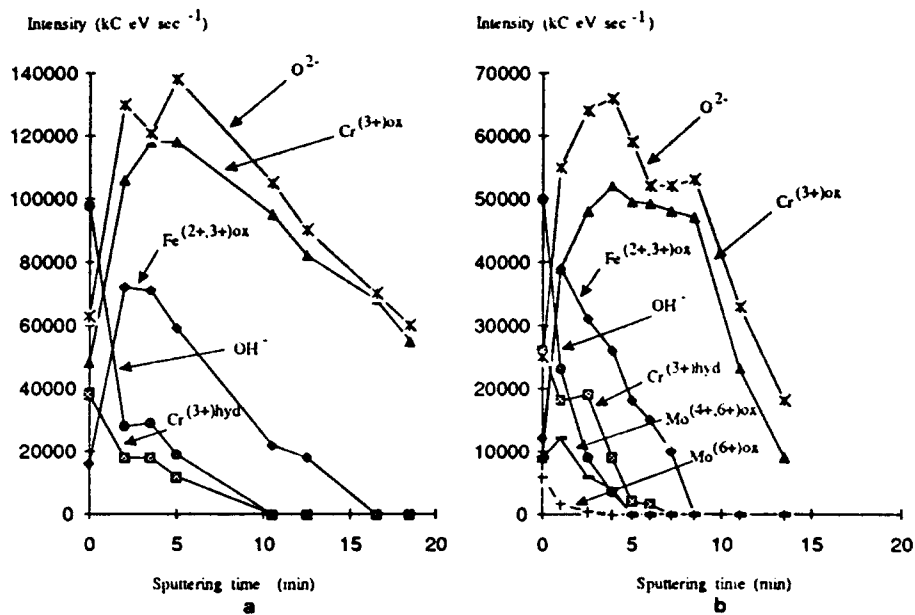


Figure 8 - XPS depth profiles of a) the non-implanted alloy and b) the implanted alloy (with 8 at%Mo) after passivation.

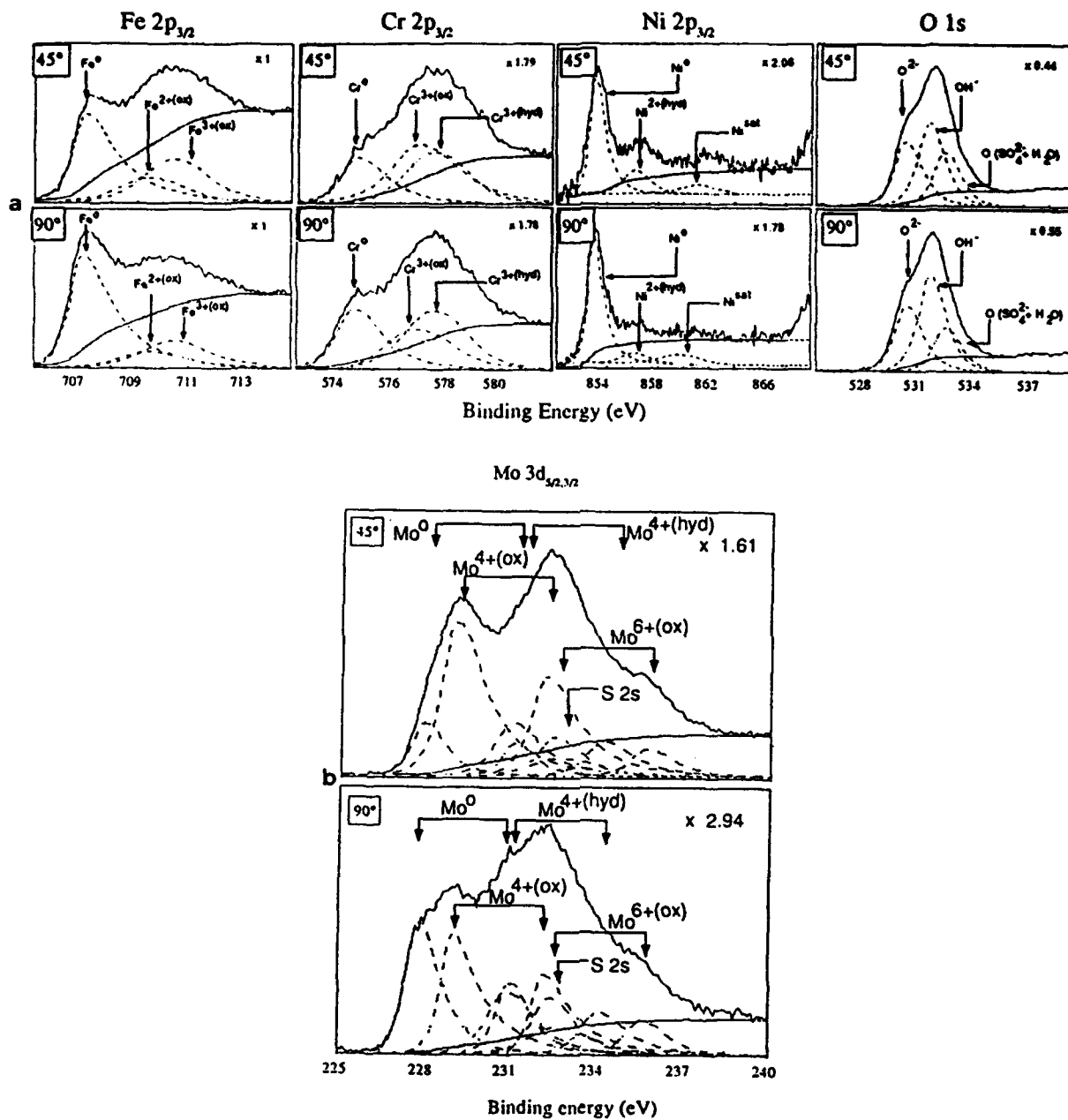


Figure 9 - Angle-dependent XPS spectra (take-off angles: 45° and 90°) of a) Fe 2p_{3/2}, Cr 2p_{3/2}, Ni 2p_{3/2}, O 1s and b) Mo 3d, after polarization of the Mo-implanted alloy at -30 mV/SHE (initial surface concentration of Mo:7 at%).

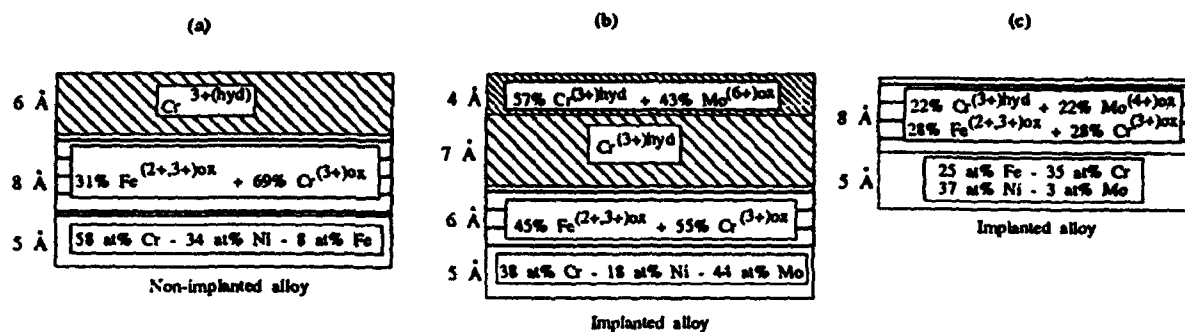


Figure 10 - Models of the surface films with the calculated compositions and thicknesses for a) the passivated non-implanted alloy, b) the passivated implanted alloy and c) the implanted alloy polarized in the active region.

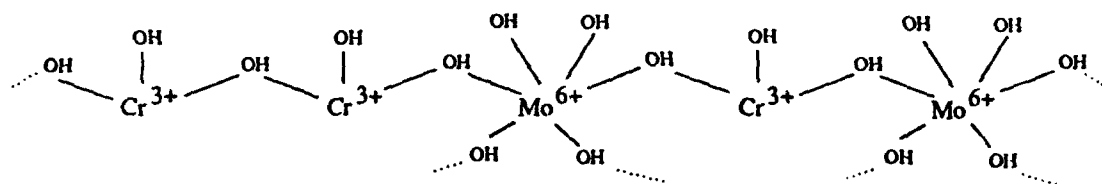


Figure 11 - Schematic view of the incorporation of the Mo^{6+} in the outer layer of the passive film formed on the molybdenum implanted stainless steels.

Comparative Analysis by AES and XPS of Passive Films on Fe-25Cr-X Model Alloys Formed in Chloride and in Sulfate Solution

C. Hubschmid, H.J. Mathieu, D. Landolt

Laboratoire de métallurgie chimique
Département des matériaux,
Ecole polytechnique fédérale de Lausanne (EPFL)
MX-C Ecublens
1015 Lausanne / Switzerland

Abstract

The influence of ternary alloying elements on the composition of passive films and on the pitting corrosion resistance of iron-chromium alloys was investigated with model alloys of the type Fe-25Cr-X (X = 6 at% of Mo, V, Si). Passive films formed in sulfate solution in the presence or absence of chloride were characterized by XPS and AES.

All ternary alloying elements increased the pitting potential compared with the corresponding binary alloy. Films formed in chloride containing sulfate solution contained both electrolyte anions. On the other hand, if films were first formed in sulfate then exposed to chloride the latter ion was not found in the passive films, independently of the ternary alloying element present.

Introduction

It is well known that certain alloying elements added to iron-chromium or iron-chromium-nickel alloys improve their resistance to pitting corrosion [1-17]. Molybdenum is the best known such alloying element but tungsten, silicon and vanadium have also been reported to have a beneficial effect [1,3,5,7,10,17]. In principle, the ternary alloying elements can influence the pitting behavior in different ways: by stabilizing the passive film towards breakdown, by favoring repassivation of formed pit nuclei, by slowing pit growth or by neutralizing the deleterious effect of non metallic impurities, notably sulfur. The present paper deals with the influence of ternary alloying elements on the composition and the stability of passive films.

Surface analysis methods, in particular XPS and AES have been used for a number of years for the study of passive films on metals and alloys. It has been found that molybdenum is incorporated into the passive film of ferritic and austenitic stainless steels [7,8,10]. The extent of molybdenum incorporation in Fe-Cr alloys depends on the chromium content and on applied potential [8]. In order to compare the behavior of different ternary elements it is therefore important to keep these two parameters constant. In addition, because the sensitivity of XPS and AES for these elements is relatively low it is advisable to use alloys of high ternary alloying element content. In the present study results are presented which were obtained with high purity ferritic model alloys of the type Fe-25Cr-X where X is Mo, V, Si, Nb added in a quantity of 6 at%. The cation ratio and the anion concentration were determined at different emission angles for passive films formed in the presence and absence of chloride.

Experimental

The chemical composition of the alloys is given in Table 1. They were furnished by Materials Research, Toulouse, France in the form of 30 mm long rods of 40 mm diameter. They were used in the as received condition without further heat treatment. Metallographic analysis revealed that the alloys containing Mo, V, or Si, respectively,

were single phase, and had an equiaxed grain structure. The Fe-Cr-Nb alloy, on the other hand, had a dendritic two-phase structure. Its behavior has been discussed elsewhere in detail [18].

Table 1: Composition of Fe-25Cr-X alloys

| Alloy | Fe %w | Cr %w | X %w | Fe %at | Cr %at | X %at |
|--------------|----------|----------|---------|-----------|-----------|----------|
| Fe-23Cr | 76.6 | 23.1 | - | 75.5 | 24.5 | - |
| Fe-25Cr-6V | 69.2 | 24.8 | 6.0 | 67.6 | 26.0 | 6.4 |
| Fe-25Cr-11Nb | 63.9 | 24.5 | 11.5 | 65.8 | 27.1 | 7.1 |
| Fe-25Cr-11Mo | 63.9 | 25.1 | 11.0 | 65.7 | 27.7 | 6.6 |
| Fe-25Cr-3Si | 72.0 | 25.11 | 2.8 | 68.8 | 25.8 | 5.4 |
| Fe-31Cr | 71.4 | 28.6 | - | 69.9 | 30.1 | - |

Electrochemical experiments were performed at 25°C in deaerated solutions using a rotating disk electrode at a constant rotation rate of 3000 rpm. A platinum counter electrode and a mercury sulfate reference electrode were used together with a Schlumberger 1286 potentiostat. For polarization measurements not involving surface analysis the 0.1 cm² disk electrodes were imbedded in epoxy. For experiments involving surface analysis a meniscus was formed allowing the rotating disk to be used without insulation. The disk electrodes were polished mechanically with 600 finish abrasive paper.

Film formation was carried out by anodic polarization at a constant potential of 0.5 V (she) for 60 minutes. Two types of electrolytes were used. Electrolyte A is a solution of 0.1 M H₂SO₄ + 0.4 M Na₂SO₄. Electrolyte B is a sulfate solution containing chloride of the composition 0.1 M H₂SO₄ + 0.4 M Na₂SO₄ + 0.12 M NaCl. In some experiments films were formed in solution A for 60 minutes, then chloride was added in such an amount that the composition corresponded to that of solution B, and the samples were exposed for an additional 30 minutes. This type of procedure will be called solution A⁺. After film formation or film exposure, respectively, the electrodes were removed from the electrolyte under the applied potential. They were rinsed, dried and then introduced into the UHV system for analysis.

Surface analysis was performed with a Perkin Elmer 5500 ESCA system including a hemispherical analyzer with Omnifocus lens and a fast entry lock. An Al K_α X-ray source was employed for XPS. Analysis was carried out at three emission angles: 20±4°, 45±4° and 65±4° with respect to the surface normal. Data acquisition and evaluation of XPS spectra were performed with Perkin Elmer software (version 3.0 D) and elemental area sensitivity factors from the Perkin Elmer data base (Table 2). The background was subtracted using the Shirley method and peak fitting was carried out using asymmetric Gauss-Lorentz functions described elsewhere in detail [19].

A simple model was used for the interpretation of XPS data. It assumes the presence of a surface contamination layer one to two monolayers thick, containing essentially hydroxide species, water and carbon. The actual passive oxide film lies underneath. The composition of the metallic substrate is uniform within the escape depth of the analyzed photoelectrons, but its composition may differ from that of the bulk alloy. For the calculation of the electron escape depth as a function of emission angle the mean free path values shown in table 2, calculated after Seah and Dench [20] were employed. All XPS data reported in this paper are the average of two independent experiments.

Table 2 XPS parameters

| Peak | Energy window | Sensitivity factor | Free mean path |
|--|---------------|--------------------|----------------|
| Fe 2p _{3/2} , 2p _{1/2} | 700-740 | 1.97 | 1.63 |
| Cr 2p _{3/2} , 2p _{1/2} | 570-600 | 1.58 | 1.77 |
| V 2p _{3/2} , 2p _{1/2} | 505-530 | 1.41 | 1.82 |
| Mo 3d _{5/2} , 3d _{3/2} | 220-242 | 2.01 | 2.07 |
| Si 2p | 95-115 | 0.34 | 2.18 |
| Cl 2p | 193-210 | 0.89 | 2.1 |
| O 1s | 525-540 | 0.71 | 1.81 |
| C 1s | 275-290 | 0.30 | 2.03 |
| S 2p | 158-174 | 0.67 | 2.12 |

Results

Polarization behavior

Potentiodynamic polarization curves were measured with different alloys in 0.1 M HCl + 0.9M NaCl at 25°. It followed from these data that the alloying elements Mo, V and Si improved the pitting resistance [21]. Indeed, the ternary alloys did not exhibit a pitting potential under the conditions of the experiments. Increasing the chromium content of the alloys had a similar effect. Polarization experiments in 2 M HCl at 50°C indicated that under these conditions the Fe-Cr-Mo alloy were most, the Fe-31Cr and Fe-Cr-V alloys least resistant towards pitting. In the solution B employed for surface analysis measurements none of the alloys exhibited a pitting potential during potentiodynamic polarization. All films were formed in the passive potential range at a constant potential of 0.50 V(she). Under these conditions the current-time behavior on a log-log plot exhibited a linear decrease [19]. No significant difference in the current-time behavior was observed between solutions A and B.

Film thickness

The thickness of the passive films formed on different alloys was estimated from AES profiles by taking the 50% value of the oxygen amplitude. The sputter rate was calibrated with Ta₂O₅ films and multiplied by 0.8 [22]. Results shown in Fig.1 suggest that the observed thickness is not significantly affected by the alloying elements added. Differences in film thickness between solutions A and B are within the error limits.

Cation fraction

Fig. 2 summarizes the XPS results for the cation fraction of Mo, Si and V in the passive films of the respective alloys, formed in the electrolytes A and B, respectively. The data were obtained at three emission angles with respect to the surface normal (20°, 45°, 65°). The figure indicates that under the conditions of the experiment all three elements are incorporated into the film. The V fraction corresponds approximately to that of the alloy (broken line), while that of Mo and Si is higher. The data are in qualitative agreement with AES measurements of Goetz et al [10]. It must be mentioned, however, that the absolute values of the cation ratios depend on the value of the sensitivity factors used, the precision of which may be limited. The observed variations of the cation ratio with emission angle are probably within the error limits of such measurements. No systematic differences between films formed in solutions A and B, respectively, are observed.

Fig.3 shows the relative chromium content of the films. Compared with the alloy (broken lines) all films are strongly enriched in chromium. The highest chromium content is observed for the films formed on Fe-31Cr (Fe-Cr-Cr in the figure), but the difference with respect to the Fe-25Cr is small. The data for binary alloys are in qualitative agreement with those of Asami [23], although the absolute values are slightly lower. Compared with the binary alloys, films formed on Fe-Cr-Mo and on Fe-Cr-Si alloys contain rather less chromium. The beneficial effect of ternary alloying elements for

corrosion resistance, therefore, can not be explained by a mechanism which postulates that they stimulate chromium segregation in the passive film. For Fe-Cr-Mo a consistently higher Cr signal is observed at large emission angle, i.e. when the relative contribution of the outer surface layers of the film is maximum. On the other hand, no systematic effect of emission angle is observed for the other alloys.

The relative iron content of the passive films determined by angle resolved XPS is shown in Fig.4. No attempt was made to quantitatively resolve Fe^{2+} and Fe^{3+} states. The iron content of the passive films formed on Fe-Cr and on Fe-Cr-Mo is of comparable magnitude. On Fe-Cr-Mo the iron oxide appears to be located preferentially in the inner part of the films, while on the other alloys no systematic trends are observed. Because the shape of the $Fe2p_{3/2}, 2p_{1/2}$ peak is relatively complex the peak fitting is subject to more uncertainty than for other elements. The observed iron oxide contents of films formed on Fe-Cr-Si, Fe-Cr-V and Fe-Cr-Cr respectively are comparable. This suggests that the beneficial action of Mo, V, and Si for pitting is not due a decreased iron content of the passive film.

Incorporation of electrolyte anions

Both, AES profiles and XPS measurements indicated that sulfate and chloride are incorporated in the passive films during film growth. According to the data of Fig.5 sulfate is present at a concentration of 2- 4 at%. Generally, although not in all cases, the sulfate signal is most pronounced at high emission angles, indicating that sulfate is located mostly in the outer part of the film. AES measurements reported elsewhere [21] confirm this observation. They also showed that the sulfate was indeed located in the film rather than at the surface. No systematic difference between solutions A and B is observed with respect to sulfate content of the passive films. Chloride is found in the films formed in solution B (Fig.6). The apparent chloride concentration is 0.8-1.6 %, independent of emission angle. Because of the low signal intensity the spectra for chloride were quite noisy [19]. This masks possible differences due to a variation of emission angle. AES profiles indicate that chloride is located within the outer part of the passive film [21].

Additional experiments were performed by first forming the films in solution A for 60 minutes, then adding chloride in an amount that the resulting electrolyte composition corresponded to that of solution B. After 30 minutes exposure, the films were removed from the electrolyte in the usual manner and analyzed by XPS. For all alloys no chloride was detected in the films prepared in this manner. This confirms previous observations with Fe-Cr [24] which indicated that chloride ions are incorporated in passive films only during growth, but not into films already formed.

Two phase alloys

A dendritic Fe-Cr-Nb alloy was investigated by scanning Auger microscopy (SAM). It was found that the dendritic phase was enriched with chromium, while essentially all of the niobium was located in the interdendritic eutectic. The passive film reflected the phase composition underneath, i.e. the film covering the electrode surface was not of homogenous composition. In spite of this fact the pitting resistance of the alloy was better than that of the comparable Fe-Cr binary alloy. This indicates that on one hand niobium improved the pitting resistance of the interdendritic eutectic. On the other hand, phase segregation led to chromium enrichment of the dendritic phase and improved its pitting corrosion resistance. The described results have been presented in detail elsewhere [18].

Conclusions

The present study of passive films formed on Fe-Cr-X alloys leads to the following conclusions:

The ternary elements Mo, V and Si do not affect the apparent thickness of passive films formed in the presence of sulfate and of chloride.

The ternary alloy elements Mo, V and Si are incorporated into the passive film.

Chloride ions are incorporated into films grown in chloride environments, but not into films grown in sulfate and subsequently exposed to chloride. The amount of chloride found in the films is not significantly affected by the ternary alloying elements Mo, V and Si.

Angle resolved XPS under present conditions provided only limited information on the depth distribution of different film constituents.

Acknowledgment

This work was financially supported by Fonds national suisse Bern, Switzerland

References

- 1) N.D. Tomashov, G.P. Chernova, O.N. Marcova, Corrosion NACE 20 (1964): p.166
- 2) K. Sugimoto, Y. Sawada, Corr. Sci. 17 (1977): p.425
- 3) E.A. Lyszlovs, Corrosion NACE 22 (1966): p.297
- 4) J.N. Wanklin, Corr. Sci. 21 (1981): p.211
- 5) R. Goetz, C. Boband, D. Landolt, Proc. 8th Internatl. Congress on Metallic Corrosion (ICC), Dechema Frankfurt 1981, p.247
- 6) I. Olefjord, B.O. Elfstrom, Corrosion NACE 38 (1982): p.46
- 7) N. Bui, A. Ihrzo, F. Dabosi, Y. Limousin-Maire, Passivity of Metals and Semiconductors, M. Froment editor, Elsevier Amsterdam 1983, p.599
- 8) H. Fischmeister, U. Roll, Fresenius Z. Anal. Chem. 319 (1984): p.639
- 9) R.Goetz, D. Landolt, Electrochim. Acta 29 (1984): p 667
- 10) R.Goetz, J. Laurent, D. Landolt, Corr. Sci. 25 (1985): p. 1115
- 11) I. Olefjord, B. Brox, U.Jelvestam, J. Electrochem. Soc. 132 (1985): p. 2854
- 11) R.C. Clayton, Y.C. Lu, J. Electrochem. Soc.133 (1986): p.2465
- 12) K. Masamura, T. Nishimura, Corr. Engr. 37 (1988): p.613
- 13) R.D. Davies, F.P.A. Robinson, Corrosion NACE 45 (1989): p.336
- 14) E. Wallis, Werkst. Korrosion 41 (1990):p.155
- 15) J. Chen, K. Wu, Corr. Sci. 30 (1990): p.53
- 16) H.C. Brookes, J.W. Bayles, F.J. Graham, J. Appl. Electrochem. 20 (1990): p. 223
- 17) S. Mischler, A. Vogel, H.J. Mathieu, D. Landolt, Corr. Sci. 32 (1991): p.925
- 18) C. Hubschmid, H.J. Mathieu, D. Landolt, Surf. Interface. Anal., in press
- 19) C. Hubschmid, Ph.D. thesis EPFL, No 1125, Lausanne 1993
- 20) M.P. Seah, W.A. Dench, Surf. Interf. Anal. 1 (1979): p.2
- 21) C. Hubschmid, H.J. Mathieu, D. Landolt, Proc. Congr. Modification of Passive Films, Paris 1993 to be published
- 22) R.L. Tapping, R.D. Davidson, T.E. Jackman, Surf. Interf. Anal. 7 (1985): p.105
- 23) K. Asami, K. Hashimoto, S. Shimodaira, Corr. Sci. 18 (1978): p.151
- 24) C. Hubschmid, D. Landolt, J.Electrochem. Soc. in press

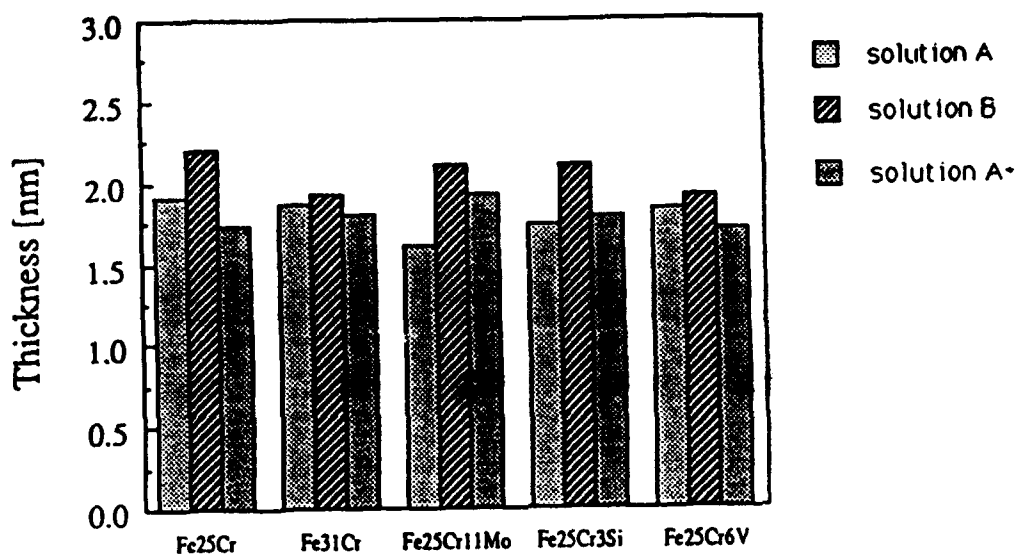


Fig.1 Apparent film thickness determined from AES depth profiles

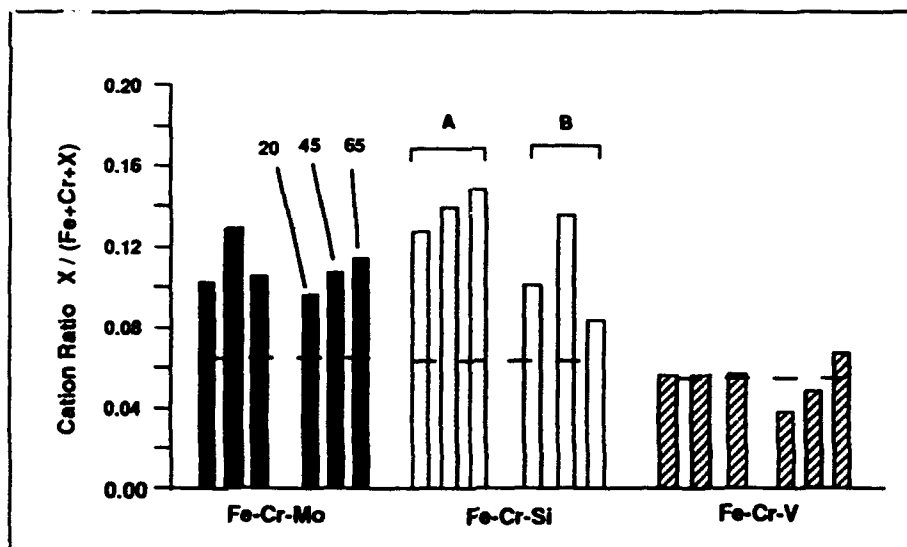


Fig.2 Cation ratio $X/Fe+Cr+X$ determined by XPS at three emission angles: 20°, 45°, 65° with respect to surface normal. X = Mo, Si, V. Passive films were formed in solutions A and B respectively.

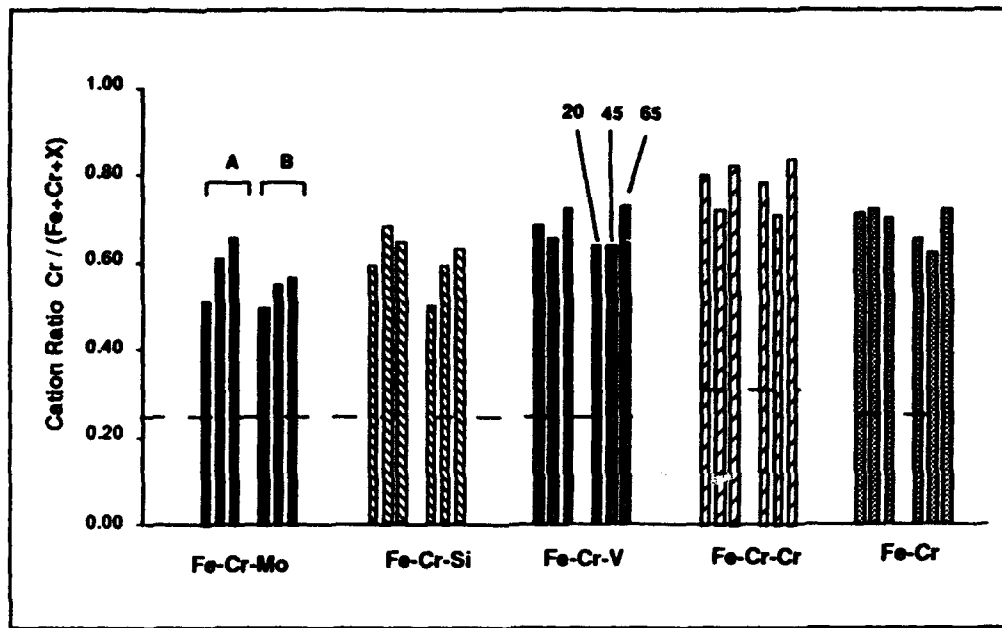


Fig.3 Cation ratio $Cr/Fe+Cr+X$ determined by XPS at three emission angles: 20° , 45° , 65° with respect to surface normal. X = Mo, Si, V. Passive films were formed in solutions A and B respectively.

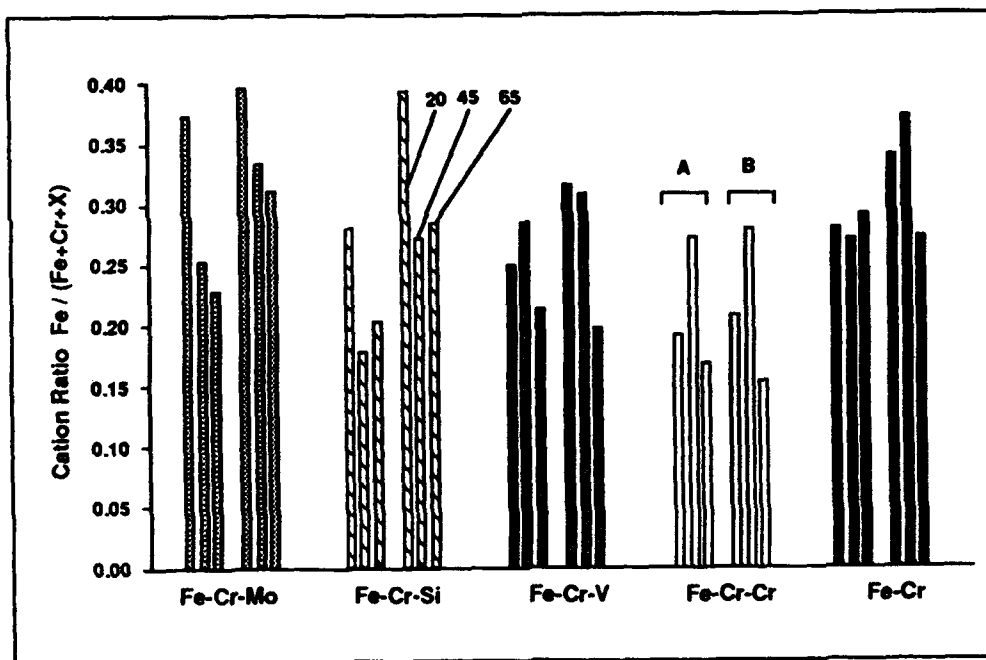


Fig.4 Cation ratio $Fe/Fe+Cr+X$ determined by XPS at three emission angles: 20° , 45° , 65° with respect to surface normal. X = Mo, Si, V. Passive films were formed in solutions A and B respectively.

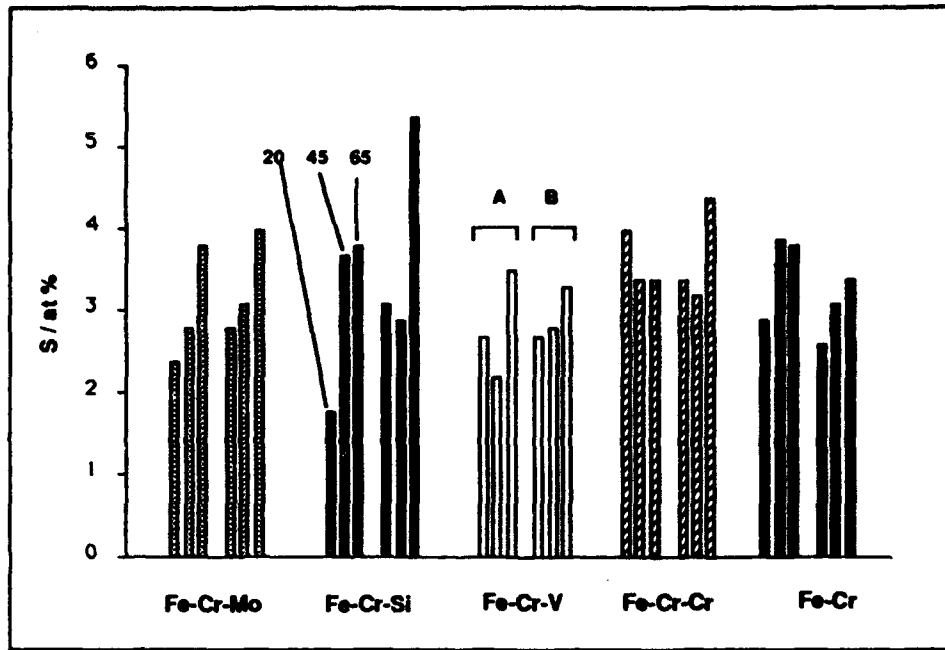


Fig.5 Sulfate concentration (at%) determined by XPS at three emission angles: 20°, 45°, 65° with respect to surface normal. Passive films were formed in solutions A and B respectively.

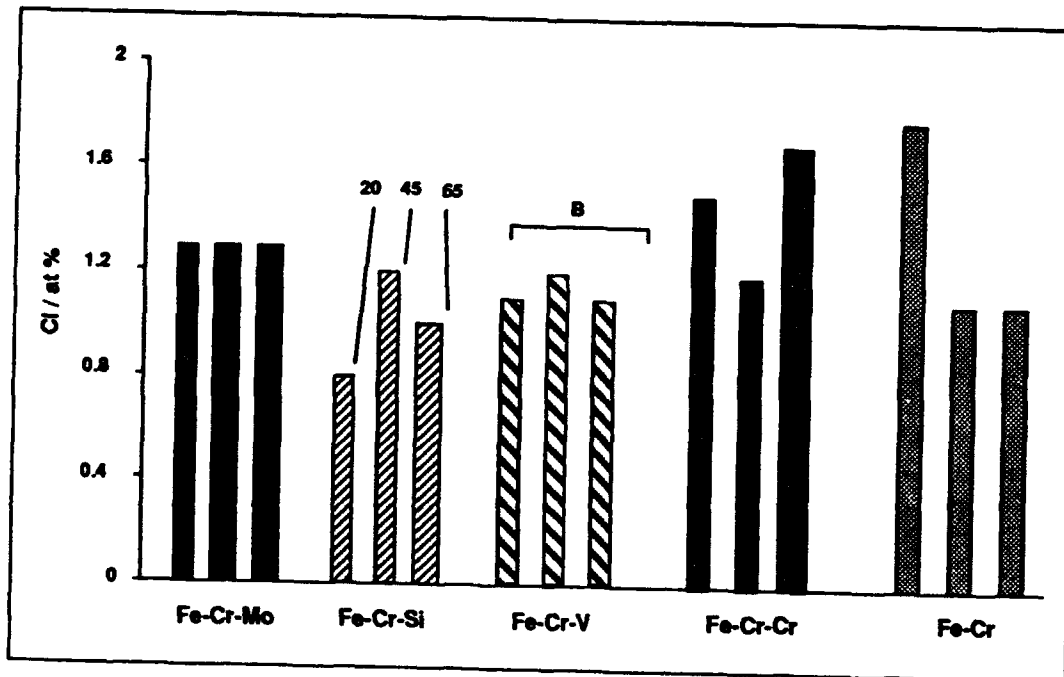


Fig.6 Chloride concentration (at%) determined by XPS at three emission angles: 20°, 45°, 65° with respect to surface normal on passive films formed in solution B.

In Situ Studies of Passive Film Chemistry using X-ray Absorption Spectroscopy

Alison J. Davenport
Brookhaven National Laboratory
Upton NY 11973, USA

Jennifer A. Bardwell
Institute for Microstructural Studies
National Research Council
Ottawa, Canada K1A 0R6

Hugh S. Isaacs
Brookhaven National Laboratory
Upton NY 11973, USA

Barry MacDougall
Institute for Environmental Chemistry
National Research Council
Ottawa, Canada K1A 0R6

Abstract

The passive film on sputter-deposited thin film Fe and Fe-26Cr electrodes has been examined using *in situ* X-ray Absorption Near Edge Spectroscopy (XANES). During the x-ray spectroscopic measurements, samples were maintained under potentiostatic control in pH 8.4 borate buffer. The passive film on both Fe and Fe-26Cr is formed from the metal without any detectable losses due to dissolution. Cathodic reduction leads to a loss of Fe from the film in both cases, but substantially less Fe is lost in the case of Fe-26Cr. Transpassive dissolution of Cr from Fe-26Cr only occurred on the second potential cycle after the film had been enriched in Cr due to the reductive dissolution of Fe. Simultaneous collection of both the Fe and Cr x-ray absorption edges provides quantitative information on the relative amounts of material lost during passivation and reduction.

Introduction

The chemistry of passive films formed on pure metals and alloys in aqueous electrolytes is the subject of much experimental investigation. Surface analytical work has been carried out using *e.g.* Auger, X-ray Photoelectron Spectroscopy (XPS) and Secondary Ion Mass Spectroscopy (SIMS), leading to a greater understanding of the composition of passive films. However, these measurements must be made *ex situ* in UHV and it has been demonstrated¹ that the passive film on Fe-Cr alloys is not stable when removed from an aqueous environment for *ex situ* examination. Thus, an *in situ* technique is to be preferred, particularly if it can yield detailed information about the composition and valence states of elements in the film. These requirements are met by *in situ* X-ray Absorption Spectroscopy²⁻⁴. In the present work, X-ray Absorption Near Edge Structure (XANES) has been used to study the passive films on Fe and Fe-26Cr.

Experimental

The experimental setup for *in situ* XANES measurements has been described previously³ and is shown in Figure 1. The design of the cell ensured good potential control of the sample at all times. Potentials

are quoted with respect to a saturated mercurous sulfate reference electrode ($\sim 0.4\text{V(SCE)}$). The electrolyte was a pH 8.4 borate buffer. The solution was deaerated throughout the experiments by bubbling with nitrogen which also ensured that all dissolution products were removed from the vicinity of the electrode. The samples consisted of a $6\mu\text{m}$ Mylar film onto which $\sim 100\text{\AA}$ of Nb or Ta were sputtered to provide electrical contact. 20 or 40\AA of the alloy under investigation (Fe or Fe-26Cr) was then deposited on top of the conducting layer. Measurements were made at Beamline X19A at the National Synchrotron Light Source. Data were collected in fluorescence geometry using a 13-element solid state detector (Canberra).

A set of absorption edges of standard compounds of known valency were measured in transmission geometry. The compounds were ground finely and sealed in adhesive Kapton tape. Absorption edges of metallic chromium and iron were collected from thin metal foils, also measured in transmission

Results and Discussion

A series edges of Cr and Fe standard compounds is shown in Figures 2 and 3 respectively. In general the absorption edge moves to higher energy as the oxidation state of the metal increases. The spectra of Fe and Cr both show relatively flat features after the edge, where the spectra for Fe_3O_4 , Fe_2O_3 and Cr_2O_3 show a sharp peak. The 6-valent Cr shows a distinctive pre-edge peak. These characteristics can be used to easily visualize the changes in oxidation state in a sample containing a particular element in more than one valence state.

Figure 4 shows a series of spectra collected at the iron *K* edge from a 40\AA film of iron polarized cyclically in a borate buffer. It should be noted that the edges are not normalized so changes in the edge height represent quantitative changes in the amount of iron present. The initial curve was collected after cathodic reduction of the air-formed oxide film at -1.5V . The edge position and flat top to the edge is characteristic of metallic iron. On stepping the potential to -0.4V and then to $+0.4\text{V}$, the edge position shifts to higher energies and the top of the edge begins to sharpen into a peak (both are characteristic of oxides). The height of the edge at the right hand side of the figure does not change indicating that in the solution used (a borate buffer), oxidation of iron proceeds by a solid state reaction without any detectable dissolution. Reduction of the passive film on stepping the potential back to -1.5V results in a spectrum identical in shape to the first one, but the drop in the edge height indicates the dissolution of a significant amount of iron. Spectra from the next cycle show that this process is repeatable a second time. Subsequent cycles do not show such clear behavior, probably due to a loss of integrity of the very thin film. The loss of material during reduction suggests that the 3-valent oxide is reduced to the soluble 2-valent state which dissolved away leaving a bare metal surface. If this reductive dissolution process were 100% efficient, then it should be possible to reconstruct the XANES signal originating from the oxide alone by subtracting curve (d) from curve (c). The result of this subtraction is shown as (l). Its shape is characteristic of 3-valent iron oxides (2) but the negative deviation in the curve around 7120 eV indicates that Fe in the metallic state has been gained upon cathodic reduction. Approximate fitting of this curve indicates that the ratio of reductive dissolution to solid state reduction is in the region of 2:1.

The total amount of metal lost in each potential cycle is listed in Table 1. It is calculated on the following basis: it is assumed that the height of the Fe *K* edge for the as-deposited sample (which has a very thin air-formed oxide film), not shown, corresponds to 40\AA of iron. If, for example, the edge height drops by 20%, this corresponds to a loss of iron equivalent to 8\AA of metal. From Table 1, it appears that each potential cycle for pure iron involves the loss of approximately 7\AA .

A similar set of experiments was carried out for thin films of Fe-26Cr. One of the advantages of using

a multi-element solid state detector is that different detector elements can be used to collect fluorescence data from different chemical elements. Thus iron and chromium *K* edges can be collected by scanning over both edges in a single spectrum whilst different detector elements collect Fe K_{α} and Cr K_{α} fluorescent photons. Figure 5(a) shows details of the Fe edge in a polarization experiment on Fe-26Cr.

The results are qualitatively similar to those found for pure iron: metallic Fe present at -1.5V undergoes oxidation at -0.4V and +0.4V without any loss of material, then undergoes significant dissolution as the sample is reduced back to -1.5V. This behavior is repeated on a second potential cycle (not shown). However, the amount of iron lost in each cycle is $\sim 2\text{\AA}$, considerably less than the $\sim 7\text{\AA}$ lost in the case of pure iron.

The chromium *K* edge, measured during the same two potential cycles, is shown in Figure 5(b). Whilst the data are noisy due to the low concentration of chromium and the diminished number of detector elements used, it is clear that the data fall into two bands. All the spectra are roughly similar in shape, but there is a significant loss of chromium indicated by a drop in the edge height during the second potential cycle when the potential is raised into the transpassive region (increased from -0.4V to +0.4V). Concurrent monitoring of the iron and chromium edges demonstrates the interplay between the two elements in the film: on the first potential cycle, both elements are oxidized into the film. However, chromium is not present in the film in a sufficient concentration for significant transpassive dissolution to take place. During reduction of the oxide at the end of the first potential cycle, iron is lost by reductive dissolution leading to enrichment of chromium in the passive film. On the second potential cycle, the chromium is now no longer protected by the iron and is present in a sufficient concentration for transpassive dissolution to occur. This model is consistent with similar work carried out on AlCr alloys⁵. In the presence of a protective alumina layer, chromium is trapped in the film but if the alumina dissolves, then transpassive dissolution of chromium can take place.

Cyclic voltammograms of the thin film Fe and Fe-26Cr electrodes were similar to those for bulk electrodes (after the second cycle in the case of Fe-26Cr) indicating that the electrochemistry is not affected by the thinness of the sample.

In situ x-ray absorption spectroscopy is thus a powerful technique for studying alloy passivation. In addition to providing *in situ* valency information, the approach allows sensitive measurement of the quantity of material lost from the alloy through dissolution or passivation. In principle, it is possible to determine which components of an alloy undergo selective dissolution, which are enriched in the passive film, and which are enriched under the film in the metallic state.

Conclusions

1. Formation of the passive film on both iron and Fe-26Cr proceeds without any metal dissolution.
2. Cathodic reduction of the passive film on iron leads to the loss of the equivalent of $\sim 7\text{\AA}$ of metal in dissolution. The ratio of reductive dissolution to solid state reduction is approximately in the region of 2:1.
3. Cathodic reduction of the passive film on Fe-26Cr leads to the loss of only $\sim 2\text{\AA}$ of iron.
4. Transpassive dissolution of chromium from Fe-26Cr can only take place on the second potential cycle once iron in the film has undergone reductive dissolution leading to enrichment of chromium in the passive film.
5. *In situ* x-ray absorption spectroscopy of passive films on thin film electrodes is an excellent technique for obtaining quantitative data on valency and dissolution during alloy passivation.

Acknowledgement

This work was performed in part under the auspices of the U.S. Department of Energy, Division of Materials Sciences, Office of Basic Energy Science under Contract No. DE-AC02-76CH00016. Measurements were carried out at Beamline X19A at the National Synchrotron Light Source with help from Lars Furenlid. The authors would like to acknowledge the assistance of M. J. Graham and G. I. Sproule.

References

1. J. A. Bardwell, G. I. Sproule, D. F. Mitchell, B. MacDougall and M. J. Graham, *J. Chem. Soc. Farad. Trans.* **87**, 1011 (1991).
2. M. Kerkar, J. Robinson and A. J. Forty, *Farad. Discuss. Chem. Soc.* **89**, 31 (1990).
3. A. J. Davenport, H. S. Isaacs, G. S. Frankel, A. G. Schrott, C. V. Jahnes and M. A. Russak, *J. Electrochem. Soc.* **138**, 337 (1991).
4. J. A. Bardwell, G. I. Sproule, B. MacDougall, M. J. Graham, A. J. Davenport and H. S. Isaacs, *J. Electrochem. Soc.* **139**, 371 (1992).
5. A. J. Davenport, H. S. Isaacs, G. S. Frankel, A. Schrott, C. V. Jahnes, and M. A. Russak, *submitted to J. Electrochem. Soc.*

Table 1. Amount of metal lost during potential cycling measured from the edge height and converted into an equivalent thickness of pure metal.

| edge measured | sample | sample thickness /Å | cycle | metal lost /Å ±1 |
|---------------|---------|------------------------|-------|------------------------|
| Fe | Fe | 40 | 1 | 8 |
| | | | 2 | 6 |
| | | | 3 | 2 |
| | Fe | 20 | 1 | 7 |
| | | | 2 | 2 |
| | Fe-26Cr | 40 | 1 | 2 |
| | | | 2 | 2 |
| | Fe-26Cr | 20 | 1 | 1 |
| | | | 2 | 3 |
| | Cr | Fe-26Cr | 40 | 1 |
| 2 | | | | 2 |
| Fe-26Cr | | 20 | 1 | 0 |
| | | | 2 | >3 [†] |
| Fe-26Cr | | 40 | 1* | 3 |
| | | | 2 | 2 |

*Sample was "activated" by stepping to +0.8V and back down to -1.5V.

†Sample sat in the transpassive region for several hours due to problems with the synchrotron.

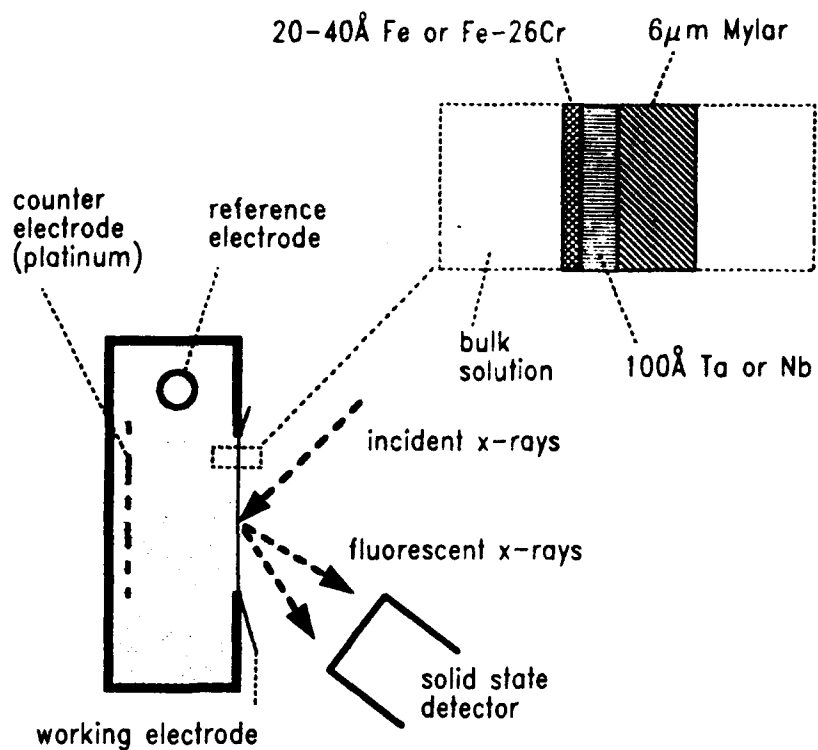


Figure 1. Experimental setup for *in situ* XANES measurements

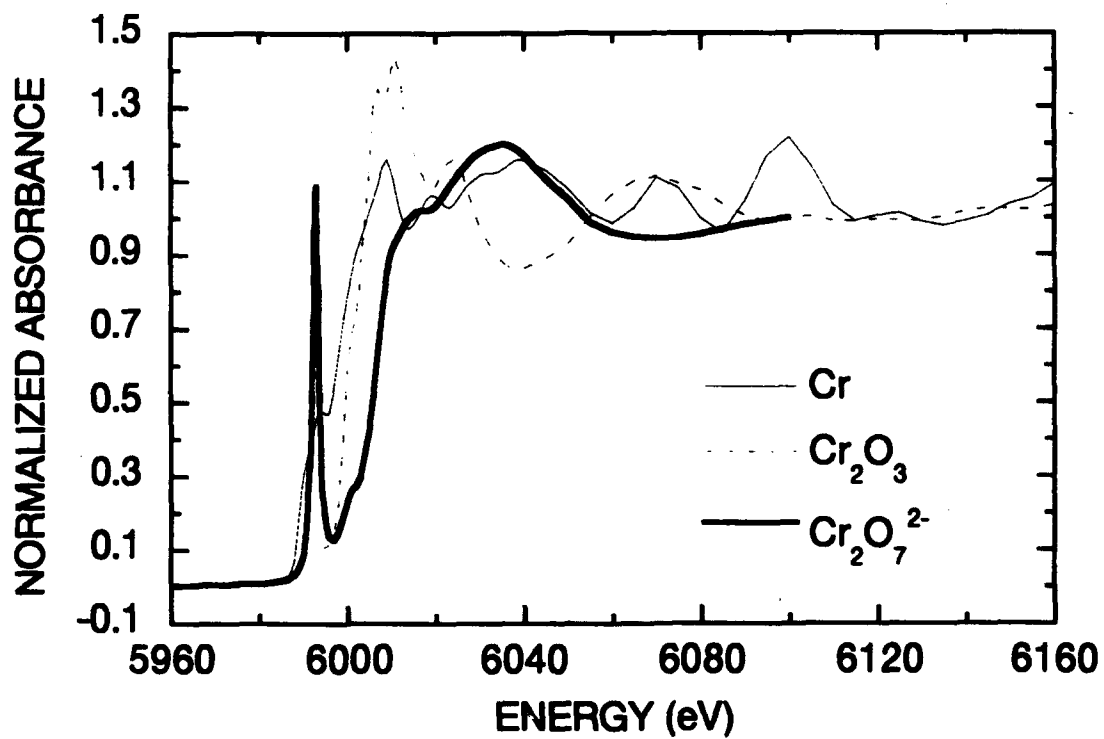


Figure 2. Cr K edges of standard compounds measured in transmission.

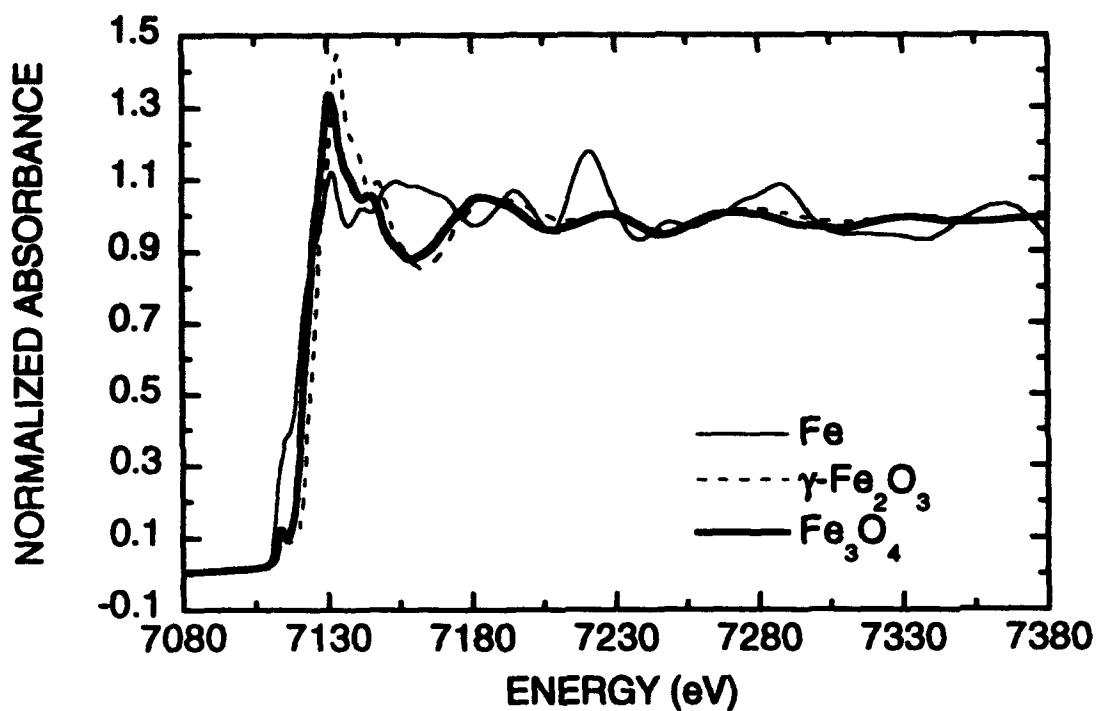


Figure 3. Fe K edges of standard compounds measured in transmission.

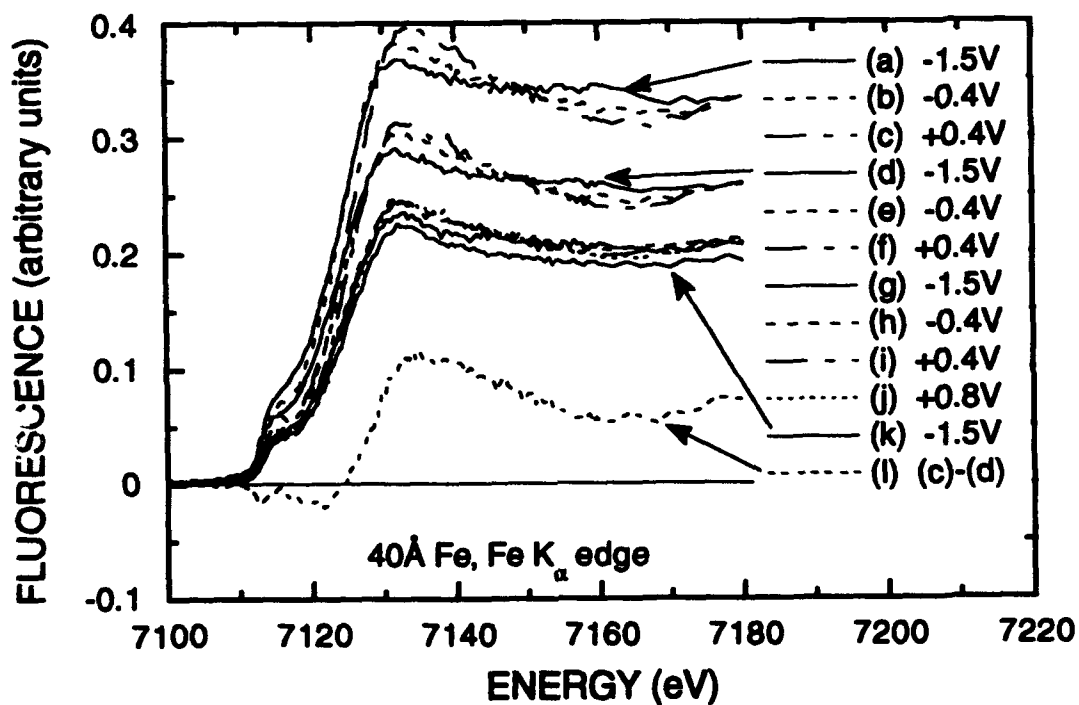


Figure 4. Fe K edge of 40Å of Fe on 100Å of Ta. The spectra were recorded on stepping the potential in the sequence indicated. Curve (l) is the difference between (c) and (d).

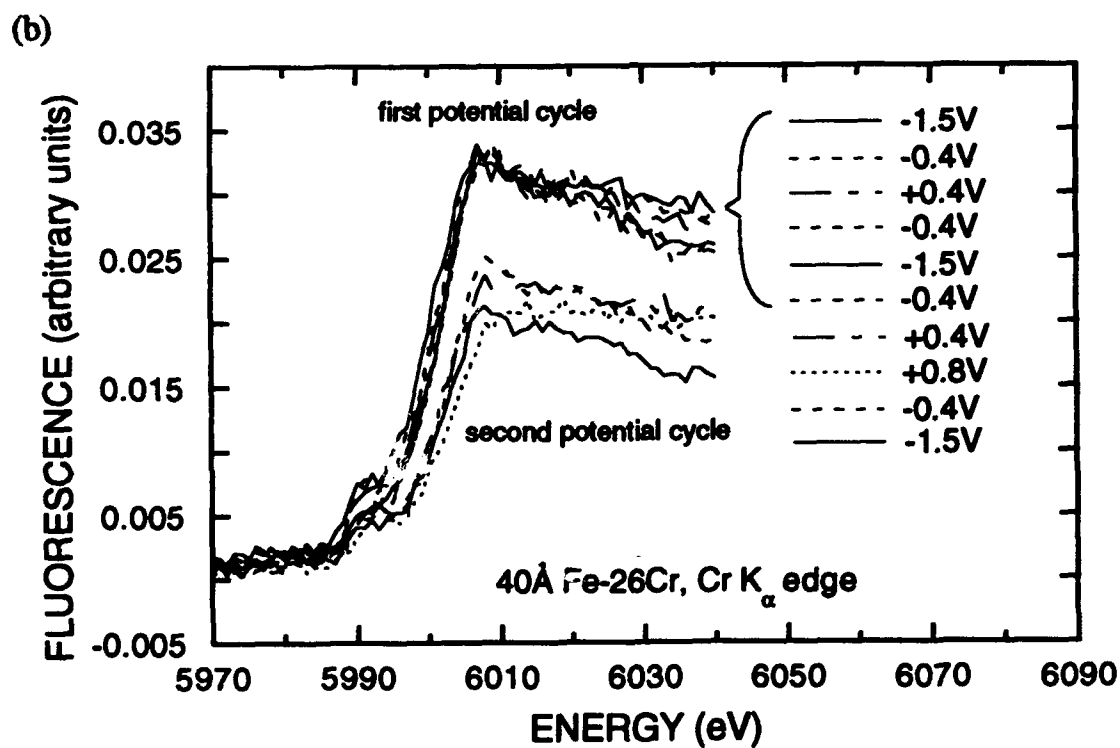
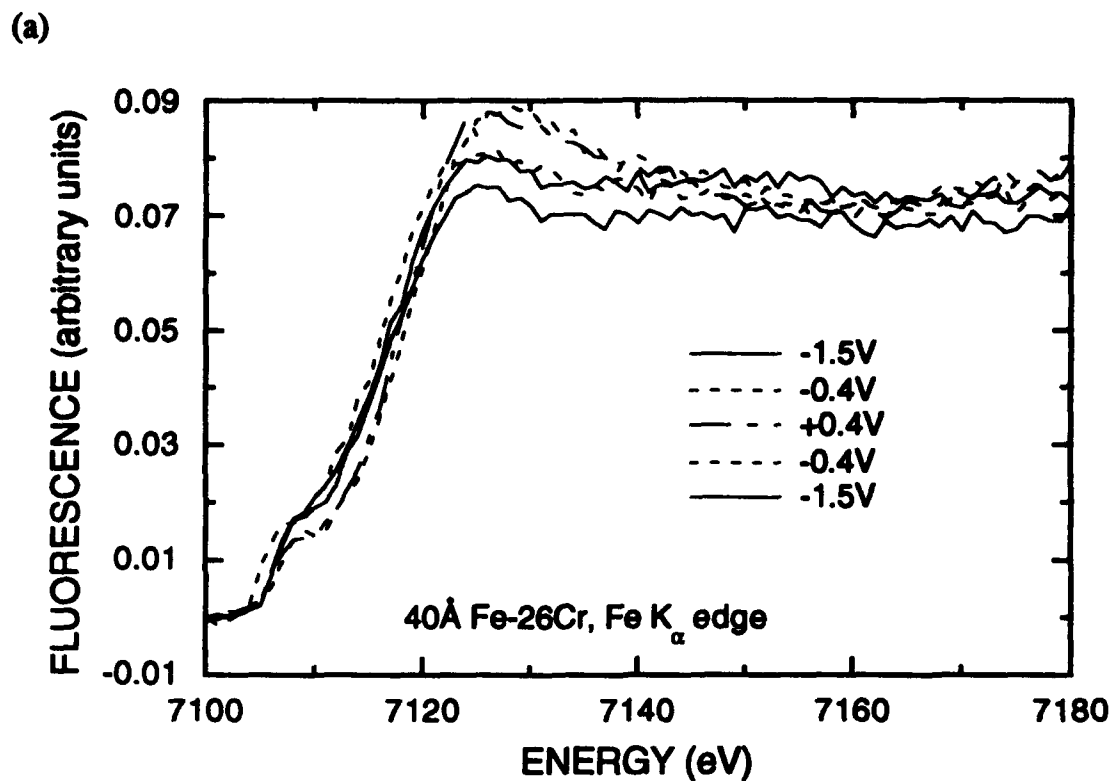


Figure 5. 40Å of Fe-26Cr stepped through two oxidation/reduction cycles with the potential sequence indicated: (a) Fe K edge (only the first potential cycle is shown); (b) Cr K edge.

Laser-Spot Imaging of Passive Films on Stainless Steels

P. Schmuki

Institute of Materials Chemistry and Corrosion
Swiss Federal Institute of Technology
ETH-Hönggerberg, CH-8093 Zürich, Switzerland

H. Böhl

Institute of Materials Chemistry and Corrosion
Swiss Federal Institute of Technology
ETH-Hönggerberg, CH-8093 Zürich, Switzerland

Abstract

The local photoelectrochemical properties of passivated surfaces of AISI 304 stainless steel were investigated by a laser spot scanning (LSS) technique which allows the resolution of the photocurrent response in a μm range. It was found that local variations in the photocurrent in several respects reflect the pitting corrosion behaviour of the investigated material.

At sites where an increased photocurrent is measured often a subsequent pit growth can be observed in an aggressive environment. On smooth sample surfaces high local photocurrents are mainly associated with inclusions present in the bulk of the commercial steel. With increasing surface roughness not only much larger variations in the photoresponse occur but also a much higher number of metastable pitting events can be detected. A statistical analysis of the results indicates that the distribution of the photocurrents and the pit initiation activity are strongly related. Therefore laser-spot imaging of passive films on stainless steels can be used to detect the distribution of potential pitting sites.

The laser-spot scanning technique can not only be employed as a surface characterization tool, but it can further be used to cause surface modifications. An example of passive film modification by the focussed laser light is presented which led to an improved corrosion resistance of the passive film. It could be shown that the improved corrosion resistance in acidic solutions after laser-spot mapping of the surface is probably due to a laser-induced oxide growth.

Key terms: photoelectrochemistry, laser-spot images, photocurrent, electronic properties, semiconductor, stainless steel, passive film, pitting corrosion

Introduction

Photoelectrochemistry has been successfully applied as an in-situ technique for the characterization of passive films. Generally it probes the opto-electronic properties of the surface film which is of great importance for the corrosion behaviour of materials. It

has been shown that the photoresponse is sensitive to the structural properties and the chemical composition of the film.

Recent photoelectrochemical investigations indicated that passive films on various stainless steels behave like an n-type semiconductor with a highly defective nature [1-12]. In several respects it was possible to evaluate concepts which relate the corrosion behaviour of the materials - particularly their resistance against pitting corrosion - with results obtained from photoelectrochemical measurements.

Most of the recent work in this field has been carried out by experimental arrangements in which the measured photocurrent characterizes an average behaviour of samples with a large area (typically some mm²). Since the breakdown of passivity in an aggressive environment - e.g. in Cl⁻-containing solutions - takes place at "weak" sites of the surface, knowledge of the local variation of the photoresponse can be of great significance for the understanding of the initiation mechanism of pitting corrosion.

Therefore in the past few years several investigators used focussed LASER beams to reveal differences in the photoactivity depending on the particular surface location [12-24]. In the present study a laser-spot scanning technique (LSS) has been used to create photocurrent maps of passivated stainless steel surfaces. A special aim of this work is to show correlations between inhomogeneities in the local photoelectrochemical behaviour of stainless steels and their susceptibility to pitting corrosion.

Experimental

The photoelectrochemical and electrochemical investigations were carried out on foils of an AISI 304 stainless steel (C: 0.048, Cr: 18.1, Ni: 8.6, Mn: 1.3, S: 0.004). Except where otherwise denoted the samples were mechanically polished with grit 4000 SiC emery paper and diamond paste (1 μm) and rinsed with distilled water and ethanol. All solutions were prepared from reagent grade chemicals and distilled water. The solutions were deaerated with N₂ prior to and during the measurements.

The experimental set-up for the measurement of local photocurrents is represented in Fig. 1. The samples which were embedded in three-component acrylic resin (Triofix, Struers) were placed 2.00 mm from the glass-window (Suprasil II) of the electrochemical cell. A platinum gauze as a counter electrode and the Haber-Luggin capillar of a saturated calomel electrode (SCE) were mounted into the cell in order to allow potentiostatic control (Jaissle 1002 T-NC) of the sample.

Photocurrents were generated by focussing the chopped (f = 30 Hz) light of a HeCd-LASER (λ = 325 nm, P = 4mW, Omnichrome) onto the working electrode at a fixed potential. This UV-type LASER was chosen, since passive films on stainless steels show generally considerable absorption only at λ < 400nm.

In all experiments the lock-in technique was applied to separate the photocurrents from the passive currents. For this the current output of the potentiostat was connected to the signal channel of the lock-in amplifier (EG&G 5210) and the trigger signal of the chopper (EG&G 9479) was fed to the reference input of the lock-in amplifier.

To obtain a surface map of the local photocurrents the cell was mounted on a xyz-stage (Newport 462XYZ) controlled via an interface card (Newport PMC300) by an IBM-PC.

The diameter of the LASER-spot could be measured by replacing the sample by a sharp blade and moving it out of the LASER beam in front of an optical power meter (Newport 835). In a dl/dx -plot, where l represents the light intensity and x the position, a Gaussian-type of curve was obtained. The half-width of this curve was defined as size of the LASER-spot.

Potentiodynamic polarization curves were registered with Schlumberger Solartron ECI 1286 controlled by a microcomputer using a traditional 3-electrode set-up and a sweep rate of 1mV/5s.

Results and Discussion

A. Detection of potential pitting sites

In Fig. 2a the local photocurrent distribution and in Fig.2b corresponding photocurrent contour map of a Laser-scanning experiment of the 304 stainless steel passivated for 20 min at 300 mV SCE in 0.05M H_2SO_4 and subsequently measured at -450 mV SCE are shown. After the scanning experiment NaCl solution was added to the electrolyte to establish a chloride concentration of 0.5M and a polarization curve (Fig. 3) was recorded - with a stable pitting process occurring at 120 mV SCE. The polarization curve was stopped at 300 mV SCE and the sample surface was examined microscopically. In Fig. 2c the same surface region is shown where previously the photocurrent mapping was performed. By comparing Fig. 2b and Fig. 2c it is obvious that pits were formed at surface locations which exhibit an enlarged photocurrent.

In order to evaluate possible reasons for a local increase of the photocurrents further photoelectrochemical investigations were carried out combined with a metallographic examination of the sample. Fig. 4 shows the photocurrent map (4a) of the 304 steel passivated at 300 mV SCE in 1M Na_2SO_4 solution for 1 h and the corresponding photograph (4b) of the same surface area. It is very clearly evident that the distribution of inclusions on the steel surface coincides with the distribution of high local photocurrents. It has to be mentioned that in this experiment a surface region has been examined which was particularly rich in inclusions - typically a significantly lower density of inclusions and hence much lower variations of the photocurrent were observed.

Combining the above findings it can be concluded that local photoelectrochemistry can be used to detect sites of inclusions in the bulk material. These sites represent a

"weak" spot of the steel surface at which - in an aggressive environment - the occurrence of pitting corrosion is favoured

These results are in good agreement with literature in which it has been shown that several types of inclusions or precipitates in the bulk material may act as initiation sites for pitting corrosion [25,26].

B. Effect of surface pre-treatment on laser-scans and pit initiation

Fig. 5a-c show the local resolution of the photocurrent response for an AISI 304 in 1M Na₂SO₄ at 300 mV SCE pretreated to a different surface finish. It is clearly to be seen that the sample with the roughest surface (SiC 320) shows the strongest variations in the photoresponse followed by SiC 1000 and the polished sample, at which only weak inhomogeneities in the photoresponse occur.

In order to gain statistically relevant information about the distribution of these inhomogeneities, 4 to 6 images with the same resolution at different locations were acquired for 2-3 samples for each surface pretreatment. In Fig. 6 the results of these runs are compiled in a probability plot.

It is obvious that most of the results belong to one normal distribution which does not differ strongly for the three treatments. This distribution can be attributed to either the experimental noise or irregularities associated with the investigated material.

The deviations from the straight behaviour at the high end of the plot are unlikely to be due to "noise" and are of a distinct nature for the different treatments. By applying a simple separation method after Preston [27], it was possible to subtract the "noise" distribution from the data sets. The remaining data-points were summed in order to obtain a measure of the overall effect of each treatment. In Fig. 7 this integrated "excess" photocurrent is given as a function of the surface treatments.

In Fig. 8 the number of metastable pitting events occurring during 24h of passivation in a 0.1M NaCl solution is shown as a function of the surface treatment. The smoother the surface, the less transients can be detected. It can be seen that on a very smooth surface the pitting rate can be reduced by a factor of 10. A comparison of this result with Fig. 7 shows a very similar behaviour in both plots.

Until now the origin of the effect of the surface pre-treatment on the local distribution of the photocurrents and on the localized corrosion susceptibility has not been conclusively clarified.

Preliminary results obtained by scanning tunneling microscopy and spectroscopy indicate that passive films formed on rough electrode surfaces show strong local variations in their electronic properties [28]. Particularly in the valleys of the grinding traces a significantly lower band-gap energy of the films was determined from tunneling spectra [28]. Hence such local differences could explain the variations in the magnitude of the photocurrents. It has been shown [10] that low band-gap energies and high photocurrents are often combined with a passive film structure, which is less resistant against pitting corrosion. Hence it could be concluded that sites

of high photocurrent indicate the presence of a weak spot in the passive film which exhibits a reduced resistance against metastable pitting.

At present it is not possible to completely exclude that above findings in the photocurrent measurements are associated with multiple reflections of the laser beam at particularly uneven surface sites and on the other hand that pit initiation is favoured at these sites.

C. Passive film modification by the focussed laser beam

Fig.9 shows a photograph of a 304 stainless steel surface passivated for 20 min at 300 mV SCE in a 0.05M H₂SO₄ solution twice laser-scanned at -450 mV SCE at the same location and exposed to the acidic solution for 3 days at -450 mV SCE. The value of -450 mV SCE for the potential corresponds approximately to the open-circuit potential of this sample when actively corroding. From the photograph it can be seen that the steel suffered from a uniform corrosion attack except of a square of 450 x 450 μm in the center of the sample. This square is located where the sample was exposed to focussed laser light during the laser scans.

To evaluate possible reasons for the improved corrosion resistance of the irradiated area the effect of the increased local temperature has to be considered since relatively high local energy-densities can occur in focussed laser beam experiments . In order to estimate the temperature increase ΔT in the laser affected zone and by assuming a Gaussian temperature distribution the following equation (1) can be used [29]:

$$\Delta T(t) = \frac{A \cdot P \cdot r}{2K \sqrt{\pi/2}} \arctan \sqrt{\frac{8 K t}{\rho c r^2}} \quad (1)$$

with $A = e^{-\alpha_\lambda d}$ and $P' = P/r^2\pi$

where

- α_λ : absorption coefficient of respective wavelength
- d: thickness of the absorption layer
- P: Power of the incident light
- r: radius of the laser spot
- c: specific heat
- K: thermal conductivity
- ρ : density

In equation (1) the arctan-term only contributes in a neglectible manner for $t > 10^{-3}$ s (and ρ and c within a reasonable range) since thermal equilibrium is established very rapidly.

For the experiment this means that changes in the chopper frequency (within physical limits) do not significantly influence the increase of temperature (i.e. ΔT is the same as if a continuous radiation was used).

Employing reasonable values for the parameters $\alpha_{\lambda}(\text{Fe}_2\text{O}_3) \approx 2 \cdot 10^7 \text{ m}^{-1}$ at 325 nm [30-32]; $d = 3 \text{ nm}$; $K = 40 \text{ W/mK}$ (average for steels [33]) and from the experiment $P = 3 \text{ mW}$; $r = 5 \text{ }\mu\text{m}$; an increase of the temperature $\Delta T = 2.8 \text{ K}$ results. According to eq. (1) ΔT varies directly proportional to P , r and K and therefore changes in the local temperature for other parameters can easily be calculated.

From the estimation of $\Delta T = 2.8 \text{ K}$ it can be concluded that the improved corrosion resistance is probably not due to processes associated with an increased local temperature. More likely is a laser-induced oxide growth which can occur either by direct participation of photogenerated electrons or holes in the mechanism or indirectly by a changed potential distribution in the illuminated oxide [34].

Conclusions

1. Laser-spot imaging of passive films can be used as a tool for detecting potential pit nucleation sites. On smooth surfaces high local photocurrents are often associated with inclusions present in the bulk of the commercial steels and these sites are particularly susceptible to pitting corrosion.
2. Mechanical surface pre-treatment influences the distribution of the photocurrents. With increasing surface roughness larger variations in the photoresponse occur. Further, a much higher number of metastable pitting events can be detected by increasing surface roughness. It could be shown that the distribution of the photocurrents and the pit initiation activity are strongly related.
3. Scanning of a passive surface with a laser-spot can induce a modification of the passive film which can lead to an improved corrosion resistance of the material. This beneficial effect is probably due to a laser-induced oxide growth.

Acknowledgements

The authors are pleased to acknowledge the Schweizerischer Nationalfonds zur Förderung der wissenschaftlichen Forschung for supporting this research within its national programme Nr. 24 (Chemie und Physik an Grenzflächen). Thank is also expressed to Boillat S.A. for partly financing the experimental equipment.

References

1. U. Stimming, *Electrochimica Acta*, 31 (1986): p. 415
2. A. Di Paola, F. Di Quarto, C. Sunseri, *Corr. Sci.*, 26 (1986): p. 935
3. C. Sunseri, S. Piazza, F. Di Quarto, *J. Electrochem. Soc.*, 134 (1987): p. 2193
4. T.D. Burleigh, R.M. Latanision, *J. Electrochem. Soc.*, 134 (1987): p. 135
5. A. M. P. Simoes, M. G. S. Ferreira, B. Rondot, M. da Cunha Belo, *J. Electrochem. Soc.*, 137 (1990): p. 82

6. A. Di Paola, D. Shukla, U. Stimming, *Electrochim. Acta*, 36 (1991): p. 345
7. D. Gorse, B. Rondot, M. da Cunha Belo, *Corr. Sci.*, 30 (1990): p. 23
8. A. M. P. Simoes, M. G. S. Ferreira, G. Lorang, M. da Cunha Belo, *Electrochim. Acta*, 36 (1991): p. 315
9. P. Schmuki, H. Böhni, *Werkstoffe und Korrosion*, 42 (1991): p. 203
10. P. Schmuki, H. Böhni, *J. Electrochem. Soc.*, 139 (1992): p. 1908
11. P. Schmuki, Ph. D. Thesis Nr. 9763, ETH-Zürich, Switzerland (1992)
12. P. Schmuki, H. Böhni, *Oxide Films on Metals and Alloys*, Proc.-Vol. 92-22, (Pennington, NJ: The Electrochemical Society, 1992): p. 326
13. M. A. Butler, *J. Electrochem. Soc.*, 130 (1983): p. 2358
14. M. A. Butler, *J. Electrochem. Soc.*, 131 (1984): p. 2185
15. D. Shukla, T. Wines, U. Stimming, *J. Electrochem. Soc.*, 134 (1987): p. 2086
16. D. Shukla, U. Stimming, *Werkstoffe und Korrosion*, 40 (1989): p. 43
17. K. Azumi, *Corr. Eng.*, 37 (1988): p. 335
18. M.R. Kozlowski, P.S. Tyler, W.H. Smyrl, R.T. Atanasoski, *Surf. Sci.*, 194 (1988): p. 505
19. M.R. Kozlowski, W.H. Smyrl, L. Atanasoska, R.T. Atanasoski, *Electrochim. Acta*, 34 (1989): p. 1763
20. K. Leitner, J.W. Schulze, *Ber. Bunsenges. Phys. Chem.*, 92 (1988): p. 181
21. G. Vercruysse, W. Rigole, W.P. Gomes, *Solar Energy Mater.*, 12 (1985): p. 157
22. R. Peat, A.M. Riley, D.E. Williams, L.M. Peter, *J. Electrochem. Soc.*, 136 (1989): p. 3352
23. R. Peat, A.R. Kucernak, D.E. Williams, L.M. Peter, *Semicond. Sci. Technol.*, 5 (1990): p. 914
24. A.R. Kucernak, R. Peat, D.E. Williams, *J. Electrochem. Soc.* 138, 1645 (1991)
25. Z. Szklarska-Smialowska, *Pitting Corrosion of Metals*, NACE, Houston (1986)
26. J. Stewart, D.E. Williams, *Corr. Sci.*, 33 (1992): p. 457
27. E. J. Preston, *Biometrika*, 40 (1953): p. 440
28. S. Virtanen, A. Schreyer, H. Böhni, to be published in *Proc. of 12th International Corrosion Congress*, Houston, TX (1993)
29. H.S. Carslav, J.C. Jaeger, *Conduction of Heat in Solids*, New York, Oxford United Press (1959)
30. D.C. Lewis, W. D. Westwood, *Can. J. Phys.*, 42 (1964): p. 2367
31. C.T. Chen, B.D. Cahan, *J. Electrochem. Soc.*, 129 (1982): p. 17
32. L.M. Abrantes, L.M. Peter, *J. Electroanal. Chem.*, 150 (1983): p. 593
33. H. Kuchling, *Taschenbuch der Physik*, Verlag Harri Deutsch, Thun und Frankfurt a. Main (1981)
34. H. Gerischer, *Corr. Sci.*, 29 (1989): p. 257

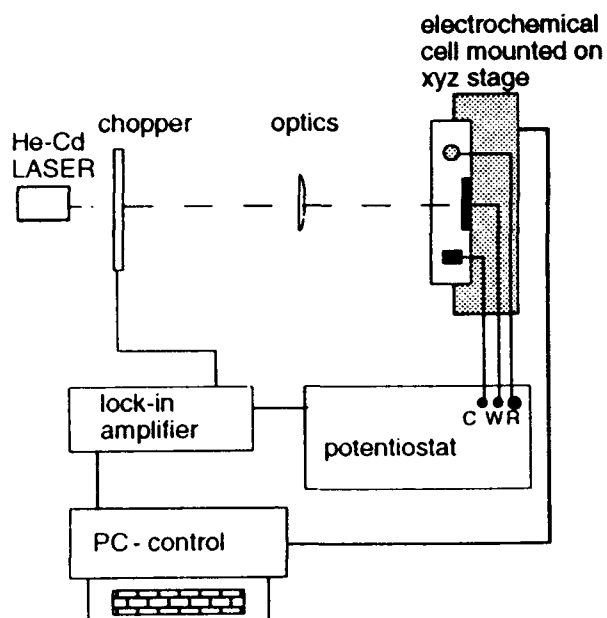


Fig. 1: Experimental set-up for Laser-spot scanning measurements

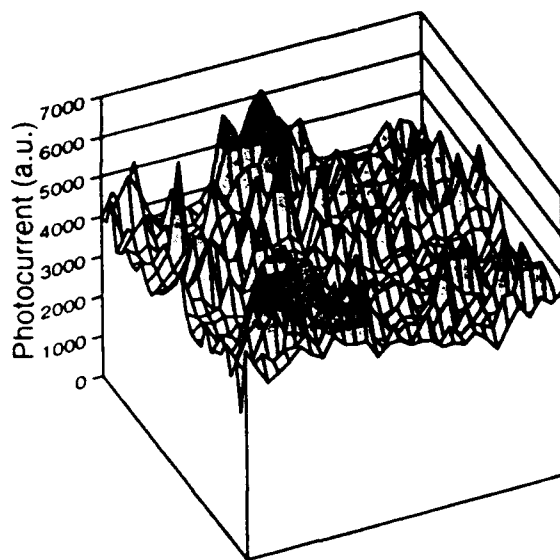


Fig. 2a): LSS image of an AISI 304 stainless steel surface at $-450 \text{ mV}_{\text{SCE}}$ in $0.05\text{M H}_2\text{SO}_4$
spot size = $10 \mu\text{m}$, step size = $15 \mu\text{m}$
image size = $450 \times 450 \mu\text{m}$

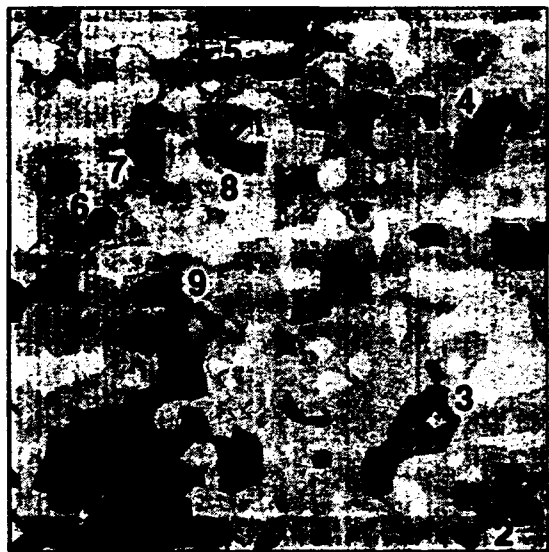


Fig. 2b): Contour-map of the local photocurrent (Replot of Fig. 2a)- Dark dots correspond to high photocurrents

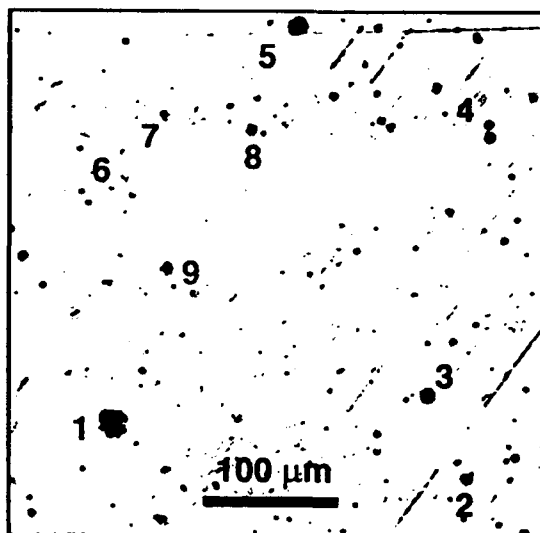


Fig. 2c): Photograph of the same surface region as in Fig. 2b) after recording the polarization curve from Fig. 3 and hence causing pitting attack

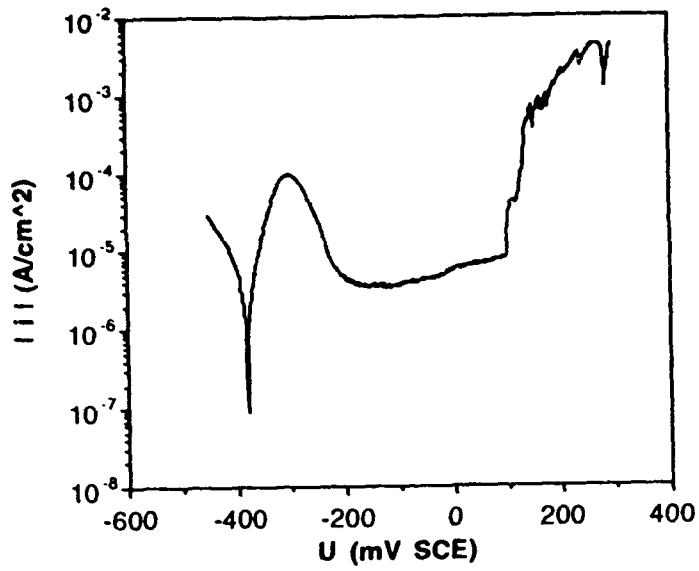
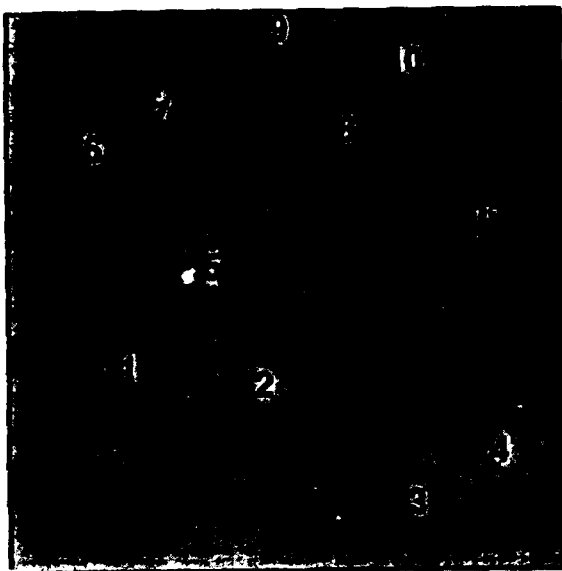
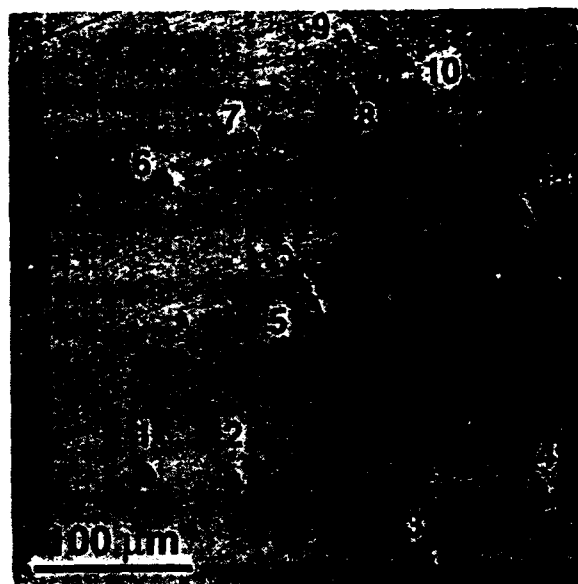


Fig. 3: Polarization curve of AISI 304 in 0.05M H₂SO₄ + 0.5M NaCl

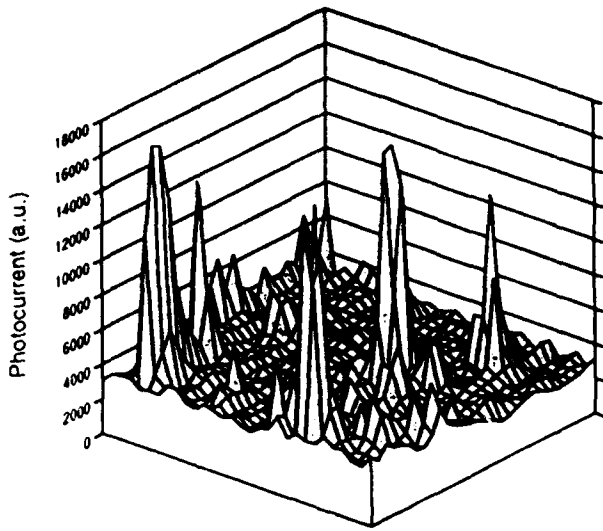


a)

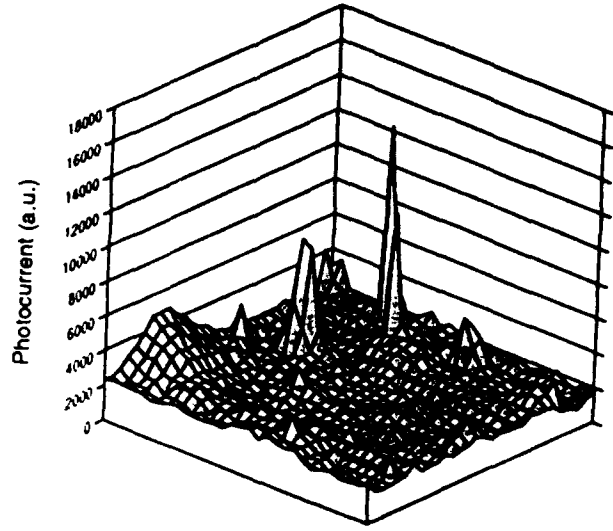


b)

Fig. 4: Contour map of the local photocurrent (a) and photograph (b) of AISI 304 passivated at 300 mV_{SCE} in 1M Na₂SO₄



a)

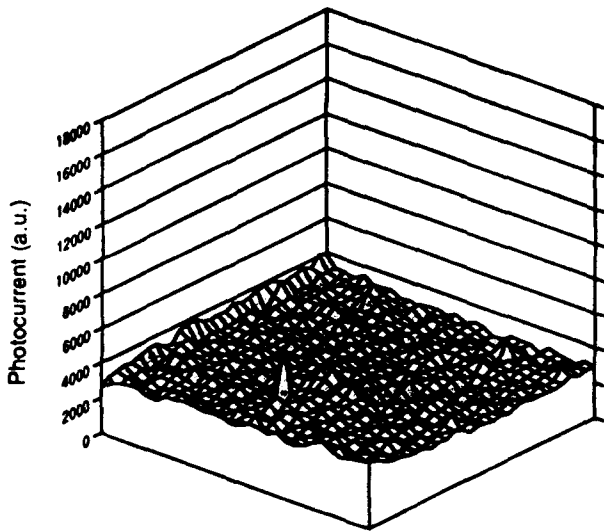


b)

Fig. 5: Typical LSS images obtained for different surface pre-treatments of AISI 304 passivated in 1M Na₂SO₄ at 300 mV SCE

a) SiC 320, b) SiC 1000 , c) polished 1 μm

spot size = 8 μm, step size = 15 μm, image size = 450 x 450 μm



5c)

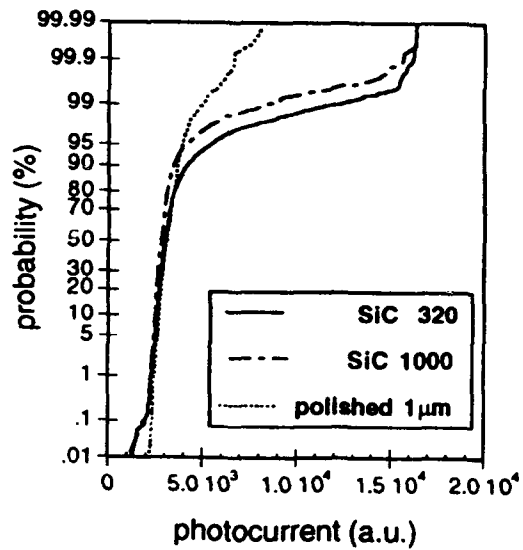


Fig. 6: Probability distribution of local photocurrents for three different surface treatments

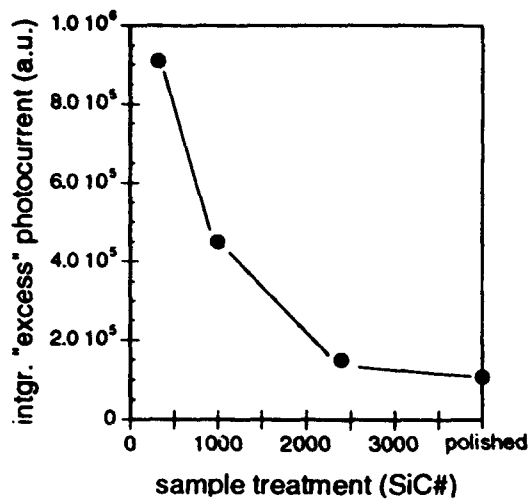


Fig. 7: Dependence of integrated "excess" photocurrent - evaluated from LSS-images - on different surface treatments

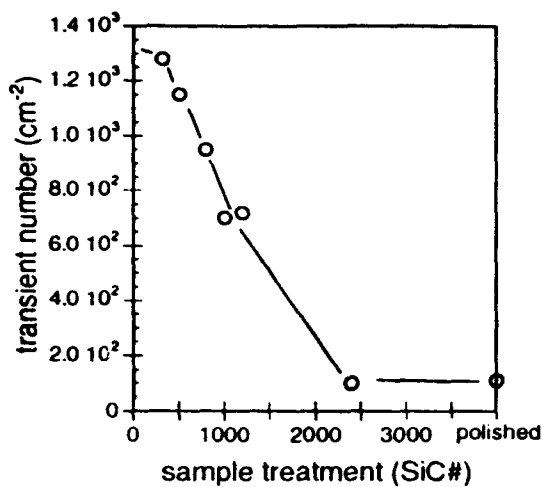


Fig. 8: Number of metastable pitting events - measured as current transients occurring at AISI 304 steel during 24h of passivation in 0.1M NaCl solution at 220 mV as a function of different surface treatments

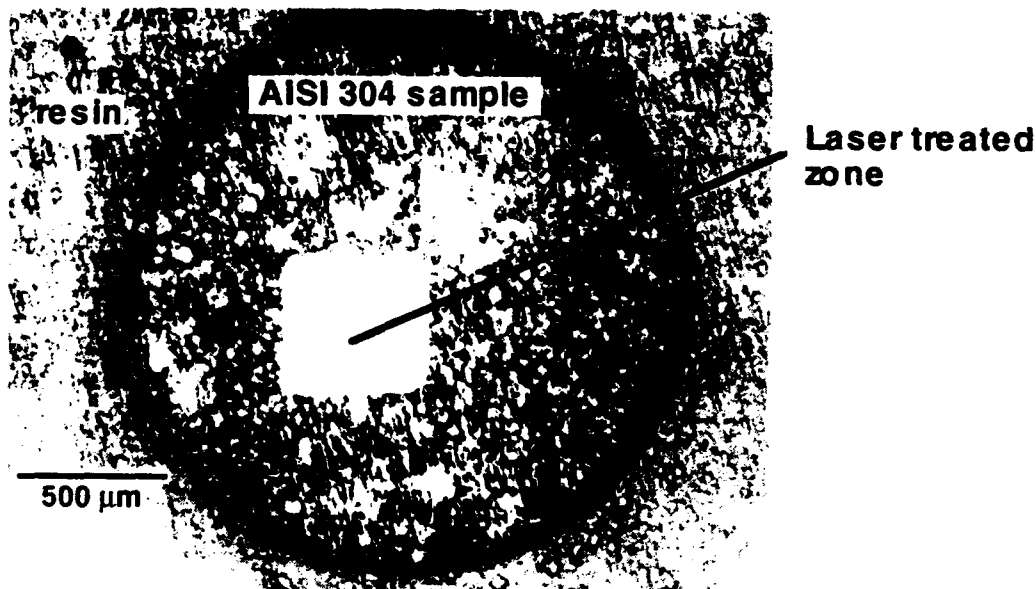


Fig. 9.: Effect of Laser-scanning on the corrosion resistance of AISI 304

Effect of Rinsing on Analytical Results for Passivity of Amorphous Iron-Chromium-Metalloid Alloys

K. Hashimoto, S. Kato, B. M. Im, E. Akiyama, H. Habazaki, A. Kawashima and K. Asami

Institute for Materials Research,
Tohoku University,
Sendai, 980 Japan

Abstract

Electrochemical and XPS studies of the passivation behavior of amorphous Fe-Cr-Mo-13P-7C alloys in deaerated stagnant 1 M HCl and in agitated 9 M H₂SO₄ open to air revealed that the difference in periods of preliminary air-exposure of the specimen polished in cyclohexane affects the passivation behavior. It was also found that whether washing and drying after passivation was done without air exposure or during air exposure affects largely the analytical results of the passive film.

Key terms: Amorphous alloys, XPS analysis, passivity

Introduction

Amorphous chromium-containing metal-metalloid alloys are well known to have extremely high corrosion resistance in chloride-containing strong acids¹. In particular, the addition of molybdenum to amorphous Fe-Cr alloys containing phosphorus is quite effective in improving the corrosion resistance and hence some amorphous Fe-Cr-Mo-P-C alloys passivate spontaneously even in 12 M HCl². Beneficial effects of molybdenum and phosphorus in enhancing the corrosion resistance of amorphous chromium-containing alloys are not well understood. Electrodeposited³⁻⁵ and melt-spun⁵⁻⁸ amorphous Ni-P alloys possess higher corrosion resistance than nickel metal in acidic solutions, although the amorphous Ni-P alloys are not passive in acidic solutions. Diegle *et al.*⁹ performed XPS analysis of the surface films without exposure of the specimens after polarization and observed elemental phosphorus on the Ni-P alloy surface. Some of the present authors¹⁰ proposed from the kinetic and XPS data that the preferential dissolution of nickel occurred from the amorphous Ni-P alloy with a consequent formation of an elemental phosphorus surface layer acting as the diffusion barrier for nickel dissolution. The formation of the elemental phosphorus layer on amorphous alloys containing both chromium and phosphorus in strong acids gives rise not only to a decrease in the anodic dissolution current but also to enhancement of cathodic oxygen and hydrogen reduction^{11,12}. This leads to

ennoblement of the open circuit potential to the passive region of chromium and to the formation of a passive chromium oxyhydroxide film. Nevertheless, it is quite difficult to identify the elemental phosphorus layer by *ex situ* analysis of the surface after corrosion, because of air oxidation of the elemental phosphorus layer.

On the other hand, the role of molybdenum in enhancing the corrosion resistance of chromium-bearing alloys is widely investigated. It has been revealed from XPS and electrochemical studies^{13,14} that molybdenum is passive, forming Mo^{4+} oxide film in the active region of chromium-bearing alloys, and a decrease of the anodic dissolution current with a consequent enhancement of passivation based on the formation of a passive hydrated chromium oxyhydroxide film. However, rinsing and drying the specimen in air after immersion or polarization of the alloys in that potential region give the analytical result of a high ratio of $\text{Mo}^{6+}/\text{Mo}^{4+}$ in the surface films because of oxidation of Mo^{4+} in the films to Mo^{6+} by air exposure¹⁴.

In this manner, the analytical results of the surface is often affected by post-treatment conditions such as rinsing and drying. On the other hand, the corrosion behavior itself is affected by pre-treatment of alloys before corrosion experiments. The present work reports interesting results obtained as a result of pre- and post-treatments of alloy specimens where the roles of chromium, molybdenum and phosphorus in enhancing the corrosion resistance have been studied.

Experimental Procedures

Fe-Cr-Mo-13at%P-7at%C alloy ingots were prepared by high frequency induction melting of laboratory-made iron phosphide and iron carbide, and commercial molybdenum, chromium and iron under an argon atmosphere. From these ingots amorphous alloy ribbons of about 1 mm in width and 20-30 mm in thickness were prepared by the rotating wheel method. Prior to electrochemical measurements and surface analysis, the amorphous alloy ribbons were polished in cyclohexane with silicon carbide paper up to No.1000, degreased in acetone and dried in air. The electrochemical measurements and surface analysis were performed on specimens immediately after drying and after standing in air for 24-40 h.

Electrochemical measurements for amorphous Fe-8Cr-Mo-13P-7C alloys were carried out in deaerated 1 M HCl solution at 30°C. The solution was deaerated previously by bubbling oxygen-free nitrogen and was introduced into an electrolytic cell without air exposure. Before the cell was filled with the electrolyte the specimen was installed in the cell and the cell was purged with oxygen-free nitrogen. Polarization of the specimen was started when the potentiostatically polarized specimen was immersed instantaneously in the solution or was wet by the solution due to elevation of the solution level. The

polarization potential chosen was -0.1 V(SCE) which is close to the lowest potential for passivation of chromium in order to detect the beneficial effect of molybdenum. Polarization was completed by the removal of the electrolyte, and the specimen was rinsed with oxygen-free water without exposure to air. The specimen was sealed in nitrogen in the upper part of the cell which was separated from the main part of the cell. The sealed upper part of the cell with the specimen was transferred into a glove box and was opened for drying the specimen in an argon atmosphere and for mounting the specimen on the specimen holder for XPS analysis. The specimen holder was installed into a transfer vessel of the X-ray photoelectron spectrometer in the glove box, and then the specimen was installed in the spectrometer without air exposure. After X-ray photoelectron spectra were measured the specimen was exposed to air for 1 h and the X-ray photoelectron spectra were measured once again for the air-exposed specimen. XPS analysis was also performed for the specimen rinsed with water in air and dried in air after polarization in the deaerated solution.

Another corrosion test was conducted for amorphous Fe-8Cr-13P-7C alloy specimens in 9 M H_2SO_4 . Since, even when the solution was open to air, prolonged immersion induced slight corrosion for spontaneously passive ribbon-shaped specimen due to an insufficient oxygen supply to the specimen surface, the solution in a kjerdahl flask open to air was agitated by mechanical shaking. After the corrosion test for prescribed time intervals, the kjerdahl flask was purged with oxygen-free nitrogen and the specimen was washed with deaerated water several times by decantation in oxygen-free nitrogen. The sealed kjerdahl flask with the specimen was transferred into the glove box in which the specimen was dried in argon and mounted on the specimen holder for XPS analysis. After the corrosion test some specimens for XPS analysis were rinsed with water in air and dried in air.

X-ray photoelectron spectra were mostly measured by a SHIMADZU ESCA-850 electron spectrometer with Mg K_{α} excitation. For some specimens rinsed in air a SSI SSX-100 electron spectrometer with Al K_{α} excitation was used. The composition and thickness of the surface film and the composition of the underlying alloy surface just below the surface film were quantitatively determined from the integrated intensities of spectral peaks¹⁵. Photo-ionization cross sections used were summarized elsewhere¹⁶.

Results and Discussion

Effects of Pre-Treatment

Figure 1 shows potentiodynamic polarization curves of amorphous Fe-8Cr-Mo-13P-7C alloys measured in deaerated 1 M HCl at 30°C. An increase in molybdenum content decreases the current density in both the active and passive regions, and decreases the cathodic current density. Because the decrease in anodic current density is larger than the decrease in cathodic current density, the

addition of 6 at% molybdenum results in spontaneous passivation. Figure 2¹⁷ shows the change in concentration of chromic ion in the passive films formed on amorphous alloys. The specimens were exposed to air for more than 24 h after polishing in cyclohexane before polarization, and were rinsed with water in air. Chromic ions in the surface film formed on the Fe-8Cr-13P-7C alloy at -0.1 V(SCE) increase with polarization time. By contrast, the passive film formed on the Fe-8Cr-7Mo-13P-7C alloy is quite stable, and hence no appreciable change occurs in the film composition during prolonged polarization. The concentration of chromic ions in the air-formed oxide films on both the alloys is almost the same as that of chromium in the bulk alloys. However, this is the case for the specimens exposed to air for prolonged time after polishing in cyclohexane.

Figure 3 shows the cationic fraction of chromium in the air-formed surface films and passive films on the amorphous Fe-8Cr-13P-7C alloy specimens. Chromic ions are concentrated in the air-formed film just after polishing in cyclohexane. The concentration of chromium in the underlying alloy surface for the specimen just after polishing in cyclohexane was almost the same as that in the bulk alloy. Accordingly, the enrichment of chromic ion in the air-formed film just after polishing in cyclohexane seems to be due to selective dissolution of iron in cyclohexane. The exposure of the specimen to air for 40 h after polishing resulted in film thickening and a decrease in the film chromium content due to preferential oxidation of iron. Hence the ratio of chromium to iron in the film after prolonged air exposure becomes almost the same as that in the bulk alloy. On the other hand, when the specimen just after polishing in cyclohexane and drying was polarized for 1 h at -0.1 V(SCE) in deaerated 1 M HCl, chromic ions are concentrated to about 57% in the passive film being accompanied by preferential dissolution of iron. This chromium concentration in the film is almost the same as that in the film formed on the specimen by polarization for 5 h shown in Figure 2, the specimen being exposed to air for a long time before polarization for 5 h. When the specimen exposed to air for 40 h after polishing in cyclohexane was polarized for 1 h at -0.1 V(SCE) in deaerated 1 M HCl, chromium enrichment in the film also occurs but the concentration of chromic ions in the film is lower than that in the film on the specimen polarized immediately after polishing. It can, therefore, be said that the gradual increase in chromic ion concentration in the film on the amorphous Fe-8Cr-13P-7C alloy specimen with time shown in Figure 2 occurred because polarization was done after prolonged air-exposure, but when the specimen was polarized immediately after polishing in cyclohexane the chromic ion concentration in the film reached the maximum value by polarization within 1 h. This means that the ageing of the air-formed oxide film through prolonged air-exposure prevents rapid dissolution of alloy constituents unnecessary for passivation during polarization in 1 M HCl and hence prevents rapid enrichment of chromic ions in the passive film.

Figure 4 shows the change in current density of amorphous Fe-8Cr-Mo-13P-7C alloys polarized at -0.1 V(SCE) in 1 M HCl. After an initial current increase due to breakdown of the air-formed films the anodic current density reaches a maximum value and then decreases sharply, because breakdown of the air-formed film is immediately followed by passive film formation. Increasing alloy molybdenum content decreases the amount of charge passed for the onset of passivation.

Figure 5 shows the ionic fractions in the films formed on the amorphous Fe-8Cr-13P-7C and Fe-8Cr-6Mo-13P-7C alloys polarized in 1 M HCl just after polishing in cyclohexane. Polarization in the passive region results in chromium enrichment in the films on both alloys. The maximum concentration of chromium in the films on the Fe-8Cr-13P-7C and Fe-8Cr-6Mo-13P-7C alloys is attained after polarization for about 300 and 120 s, respectively. The maximum concentration of chromic ions is almost the same on both alloys. It can, therefore, be said that the molybdenum addition enhances passivation through prevention of dissolution of chromic ions in the air-formed film. As can be seen from a comparison of Figures 2 and 5, the reproducibility of analytical data for the specimens just after polishing is not high. This is attributable to a scatter in the degree of ageing of the air-formed oxide films before polarization. However, the ageing of the air-formed film somewhat increases the stability of the film, and slows down the preferential dissolution of unnecessary elements from the alloy surface. Accordingly, prolonged polarization is required for the formation of stable passive films enriched in chromic ions when the specimens are previously exposed to air for a long period of time after polishing.

Effects of Post-Treatments

Figure 6 shows Fe 2*p* spectra of the specimens after polarization for 5 h. Because of prolonged polarization, passivity seems well established. The Fe 2*p* spectrum (a) for the specimen without air exposure shows a sharp Fe 2*p* peak for the metallic state of iron but the oxidized signal is very weak. However, air exposure of the same specimen for 1 h after XPS measurements resulted in oxidation of iron showing the Fe 2*p*_{3/2} peak of oxidized iron at about 710 eV (b). When the specimen was washed with water in air and dried in air, the strong Fe 2*p*_{3/2} peak of oxidized iron appears (c). The oxide components of Mo 3*d* spectra for these specimens are shown in Figure 7. The spectrum for the specimen without air exposure consists mostly of that for Mo⁴⁺. Air exposure of the same specimen for 1 h after XPS measurements resulted in the formation of Mo⁶⁺ due to oxidation of Mo⁴⁺ showing the Mo 3*d*_{3/2} peak of oxidized molybdenum at about 236 eV. When the specimen was washed with water in air and dried in air, the intensity of the Mo⁶⁺ 3*d*_{3/2} peak appears clearly.

Figure 8 shows schematically ionic fractions in the films. Polarization was carried out for the specimens immediately after polishing in cyclohexane. When the specimen whose X-ray photoelectron spectra were measured without

air exposure after polarization was exposed to air for 1 h, preferential oxidation of iron occurs with a consequent film thickening of about 10%. This indicates that the passive film formed by prolonged polarization for 5 h at a low potential in the passive region is not completely stable after being dried without air exposure. On the other hand, when the specimen polarized for 5 h was rinsed with water in air and dried in air, the film with a higher concentration of iron and a lower concentration of phosphorus in comparison with the two films mentioned above was formed without film thickening. Accordingly, phosphorus was dissolved during rinsing and iron was oxidized. Consequently, the passive film formed by prolonged polarization for 5 h at a low potential in the passive region is not completely stable when the specimen is washed before being dried in an inert atmosphere.

When passivation occurs in more aggressive solutions than 1 M HCl the passive film becomes more stable. When the amorphous Fe-8Cr-13P-7C alloy was immersed in agitated 9 M H₂SO₄ open to air, corrosive dissolution of the alloy occurred in the initial period of immersion, and the alloy became stable after immersion for 30 min. Figure 9 shows the change in the open circuit potential during immersion in agitated 9 M H₂SO₄ open to air. The open circuit potential is in the active region just after immersion but increases gradually with time. The open circuit potential is raised to the passive region of chromium after immersion for 30 min and continues to increase. As shown in Figure 10, analytical results for cationic fractions in the surface films formed in this very aggressive solution is not affected by a difference in post-treatments. A comparison of Figures 9 and 10 clearly reveals that the open circuit potential rises to the passive region of chromium before the chromium enrichment occurs in the film after breakdown of the air-formed film. This fact clearly indicates that the ennoblement of the open circuit potential to the passive region of chromium is not attributable to the formation of a chromium-enriched passive film. As shown later this fact results from the formation of an elemental phosphorus layer during initial active dissolution of the alloy. The formation of the elemental phosphorus layer enhances the cathodic reduction of oxygen, decreases the anodic dissolution current and hence enhances the formation of a passive chromium oxyhydroxide film.

Figure 11 shows P 2p spectra for the amorphous Fe-8Cr-13P-7C alloy specimens immersed in agitated 9 M H₂SO₄ open to air after being washed with deaerated water in oxygen-free nitrogen and dried in argon and after being washed with water in air and dried in air. It is clear that washing in air and drying in air induce oxidation of phosphorus. As shown in Figure 10, whether washing and drying was done without air exposure or during air exposure did not affect the ratio of chromium to iron in the film. Consequently, the elemental phosphorus layer existed on the passive film during immersion and was oxidized during rinsing and drying in air. In this manner, when passivation occurs in very aggressive solution due to ennoblement of the open circuit potential by the

protective action of the cathodically active elemental phosphorus layer, the difference in post-treatment of the specimen does not affect the analytical result for the ratio of chromium to iron in the passive film.

Conclusions

Electrochemical and XPS studies of the passivation behavior of amorphous Fe-Cr-Mo-13P-7C alloys in deaerated stagnant 1 M HCl and in agitated 9 M H₂SO₄ open to air led to the following results.

1. When XPS analysis was performed just after the specimen was polished in cyclohexane, chromium was enriched in the air-formed oxide film but air exposure of the specimen polished in cyclohexane led to preferential oxidation of iron with a consequent formation of a film in which the ratio of chromium to iron was almost the same as that in the bulk alloy.
2. The formation of a chromium-enriched stable passive film on the specimen exposed to air for a longer period of time requires prolonged polarization in comparison with the specimen polarized just after polishing in cyclohexane.
3. After XPS analysis was made without air exposure for the specimen polarized in deaerated 1 M HCl at -0.1 V(SCE) for 5 h, air exposure for 1 h gave rise to about a 10% increase in the film thickness due to preferential air oxidation of iron.
4. When the specimen was washed with water in air after polarization in deaerated 1 M HCl at -0.1 V(SCE) for 5 h, phosphorus was dissolved, and subsequent drying in air resulted in preferential oxidation of iron.
5. When the Fe-8Cr-13P-7C alloy specimen was immersed in agitated 9 M H₂SO₄ open to air, the specimen surface was initially covered with a cathodically active protective elemental phosphorus layer, which enhanced the formation of a chromium-enriched passive film due to ennoblement of the open-circuit potential.
6. When the Fe-8Cr-13P-7C alloy specimen immersed in agitated 9 M H₂SO₄ open to air was rinsed with water in air and dried in air, oxidation of the elemental phosphorus layer on the passive film occurred. Whether washing and drying was done during air exposure or without air exposure did not affect the ratio of chromium to iron in the passive film below the elemental phosphorus layer.

References

1. M. Naka, K. Hashimoto and T. Masumoto, *J. Japan. Inst. Metals*, **38**, 835 (1974).
2. K. Hashimoto, K. Kobayashi, K. Asami and T. Masumoto, Proc. 8th Int. Cong. Metallic Corrosion, DECHEMA, Frankfurt/Main (1981) Vol.I. p.70.
3. A. Brenner, D. E. Couch and E. K. Williams, *J. Res. Natl. Bur. Standards*,

- 44, 109 (1950).
4. K. Masui, H. Yamada and Y. Hisamatsu, *J. Met. Finish. Soc. Japan*, **32**, 410 (1981).
 5. A. Kawashima, Y.-P. Lu, H. Habazaki, K. Asami and K. Hashimoto, *Corros. Engng. (Boshoku Gijutsu)* **38**, 593 (1989).
 6. P. V. Nagarkar, P. C. Searson and R. M. Latanision, *Corrosion, Electrochemistry and Catalysis of Metallic Glasses*, R. B. Diegle and K. Hashimoto, Eds., p.118. The Electrochemical Society, Princeton (1988).
 7. R. B. Diegle, N. R. Sorensen and G. C. Nelson, *J. Electrochem Soc.* **133**, 1769 (1986).
 8. R. B. Diegle, C. R. Clayton, Y. Lu and N. R. Sorensen, *J. Electrochem Soc.* **134**, 138 (1987).
 9. R. B. Diegle, N. R. Sorensen, C. R. Clayton, M. A. Helfand and Y. C. Yu, *J. Electrochem Soc.* **135**, 1085 (1988).
 10. H. Habazaki, S.-Q. Ding, A. Kawashima, K. Asami, A. Inoue, K. Hashimoto and T. Masumoto, *Corros. Sci.* **29**, 1319 (1989).
 11. B.-P. Zhang, H. Habazaki, A. Kawashima, K. Asami and K. Hashimoto, *Corros. Sci.* **33**, 1519 (1992).
 12. B.-P. Zhang, H. Habazaki, A. Kawashima, K. Asami and K. Hashimoto, *Corros. Sci.* **34**, (1993).
 13. K. Hashimoto, K. Asami and K. Teramoto, *Corros. Sci.* **19**, 3 (1979).
 14. K. Asami, M. Naka, K. Hashimoto and T. Masumoto, *J. Electrochem Soc.* **127**, 2130 (1980).
 15. K. Asami, K. Hashimoto and S. Shimodaira, *Corros. Sci.* **17**, 713 (1977).
 16. K. Hashimoto and K. Asami, *Corros. Engng. (Boshoku Gijutsu)* **26**, 375 (1977).
 17. H. Habazaki, A. Kawashima, K. Asami and K. Hashimoto, *Mater. Sci. Engng.* **A134**, 1033 (1991).

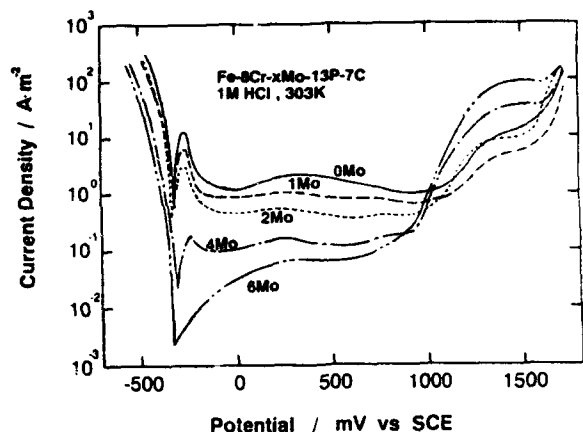


Figure 1. Potentiodynamic polarization curves of amorphous Fe-8Cr-Mo-13P-7C alloys measured with a potential sweep rate of 50 mV/min in deaerated 1 M HCl at 30°C.

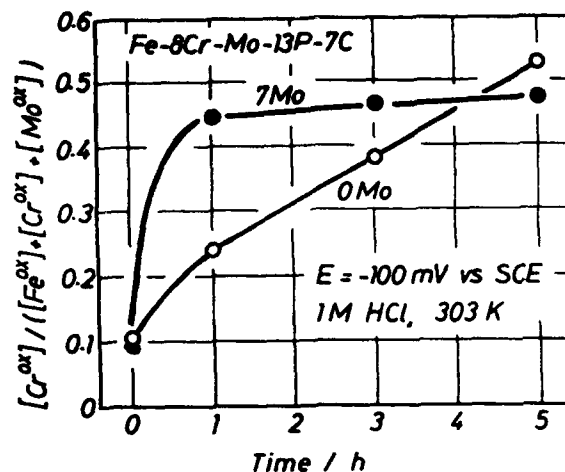


Figure 2. Change in cationic fraction of chromium in the surface films formed on the amorphous Fe-8Cr-13P-7C and Fe-8Cr-7Mo-13P-7C alloys at -0.1 V(SCE) in deaerated 1 M HCl as a function of polarization time¹⁷.

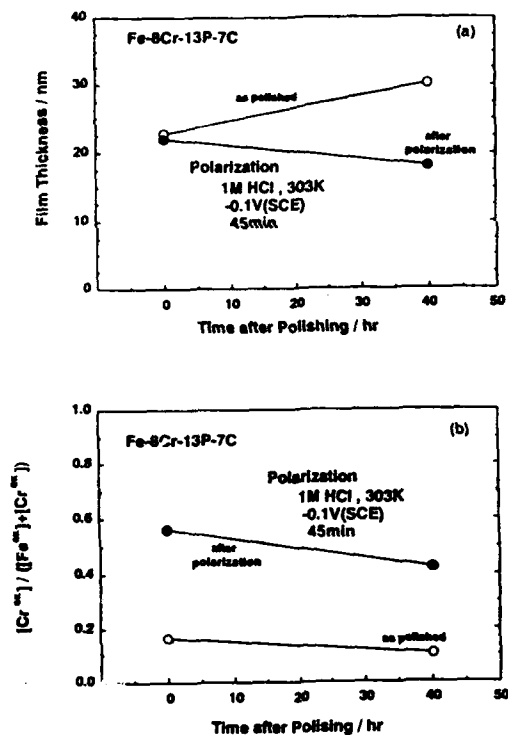


Figure 3. Thickness of the surface film (a) and cationic fraction of chromium in the film (b) formed on the amorphous Fe-8Cr-13P-7C alloy. Specimens were those just after polishing in cyclohexane and drying (○ at 0 h), polarized for 1 h at -0.1 V(SCE) in deaerated 1 M HCl just after polishing in cyclohexane and drying (● at 0 h), exposed to air for 40 h after polishing in cyclohexane (○ at 40 h), and polarized for 1 h at -0.1 V(SCE) in deaerated 1 M HCl after exposure to air for 40 h after polishing in cyclohexane (● at 40 h).

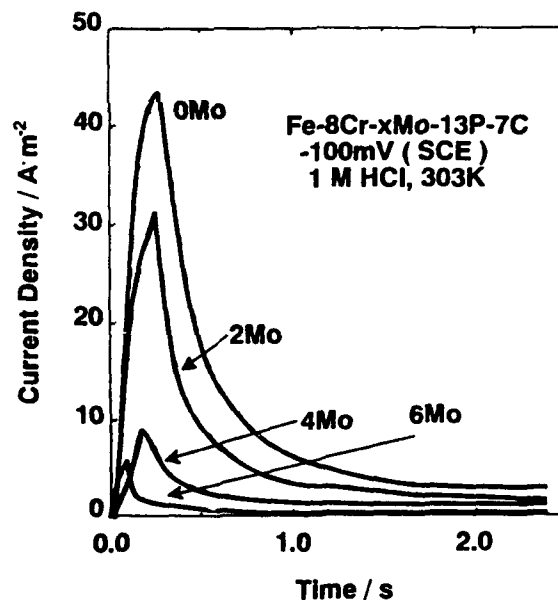


Figure 4. Initial change in current density for amorphous Fe-8Cr-Mo-13P-7C alloys as a function of time of polarization. Specimens were polarized at -0.1 V(SCE) in deaerated 1 M HCl just after polishing in cyclohexane.

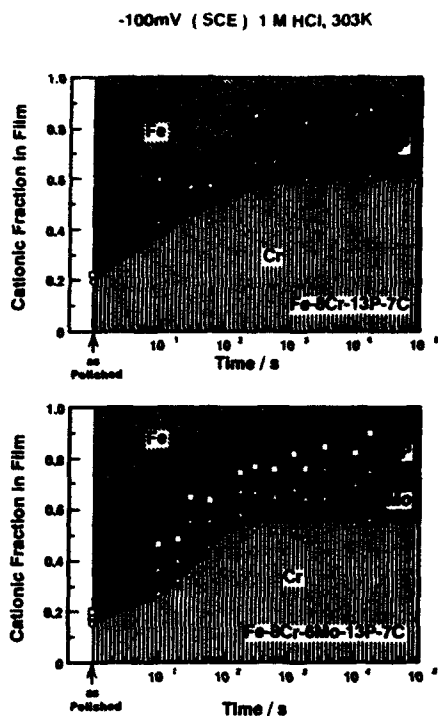


Figure 5. Ionic fractions in the film formed on the amorphous Fe-8Cr-Mo-13P-7C alloys as a function of time of polarization. Specimens were polarized at -0.1 V(SCE) in deaerated 1 M HCl just after polishing in cyclohexane and drying.

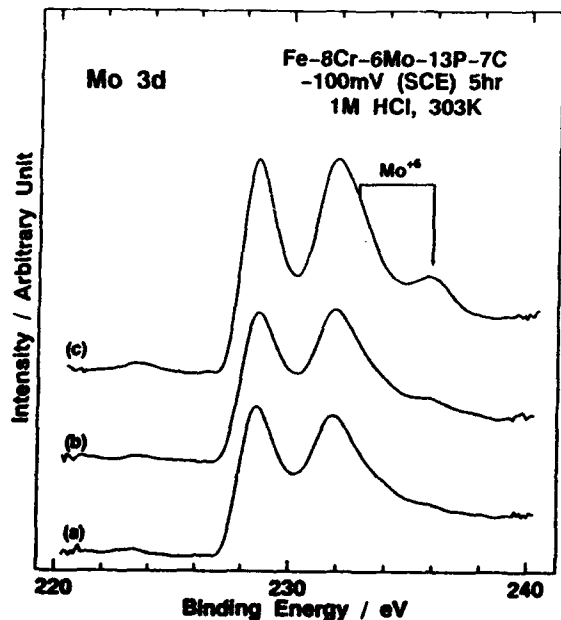


Figure 7. Mo 3d spectra of the amorphous Fe-8Cr-6Mo-13P-7C alloy specimens after polarization for 5 h at -0.1 V(SCE) in 1 M HCl. The spectra for the metallic state in the underlying alloy were subtracted from the observed spectra. After polarization specimens were (a) : washed with deaerated water in oxygen-free nitrogen and dried in argon. (b) : exposed to air for 1 h after XPS measurements of the specimen (a). (c) : washed with water in air and dried in air.

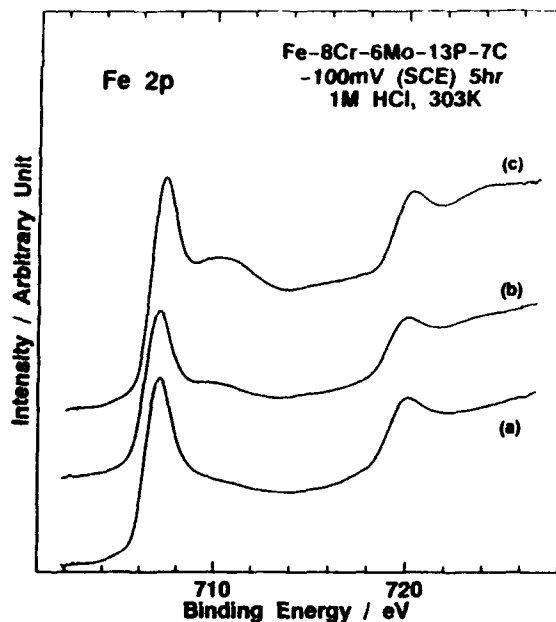


Figure 6. Fe 2p spectra of the amorphous Fe-8Cr-6Mo-13P-7C alloy specimens after polarization for 5 h at -0.1 V(SCE) in 1 M HCl. After polarization specimens were (a) : washed with deaerated water in oxygen-free nitrogen and dried in argon. (b) : exposed to air for 1 h after XPS measurements of the specimen (a). (c) : washed with water in air and dried in air

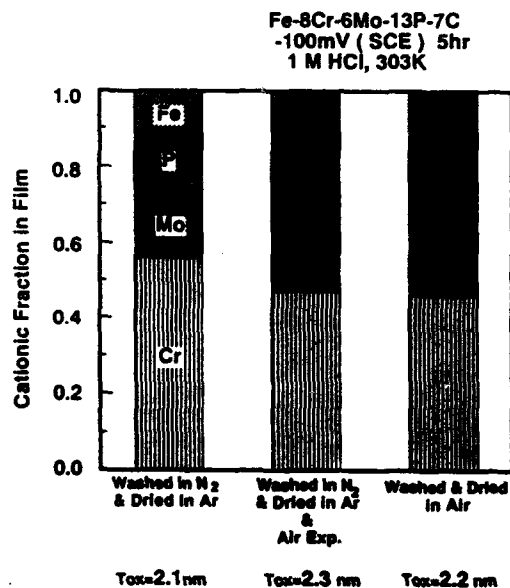


Figure 8. Cationic fractions estimated by XPS analysis for the surface films on the amorphous Fe-8Cr-6Mo-13P-7C alloy specimens after polarization for 5 h at -0.1 V(SCE) in 1 M HCl. The XPS analysis was conducted after the polarized specimen was washed with deaerated water in oxygen-free nitrogen and dried in argon, after being exposed to air for 1 h after XPS measurements of the above specimen, and for the specimen washed with water in air after polarization and dried in air.

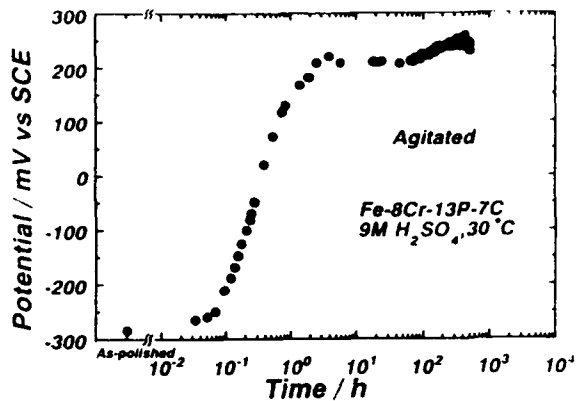


Figure 9. Change in the open circuit potential of the amorphous Fe-8Cr-13P-7C alloy immersed in agitated 9 M H₂SO₄ open to air as a function of time of immersion.

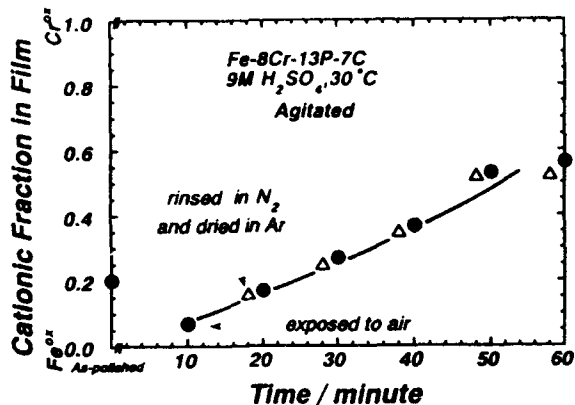


Figure 10. Cationic fractions in the surface film on the amorphous Fe-8Cr-13P-7C alloy immersed in agitated 9 M H₂SO₄ open to air. The XPS analysis was conducted after the immersed specimen was washed with deaerated water in oxygen-free nitrogen and dried in argon (open triangle) and after the immersed specimen was washed with water in air and dried in air (solid circle).

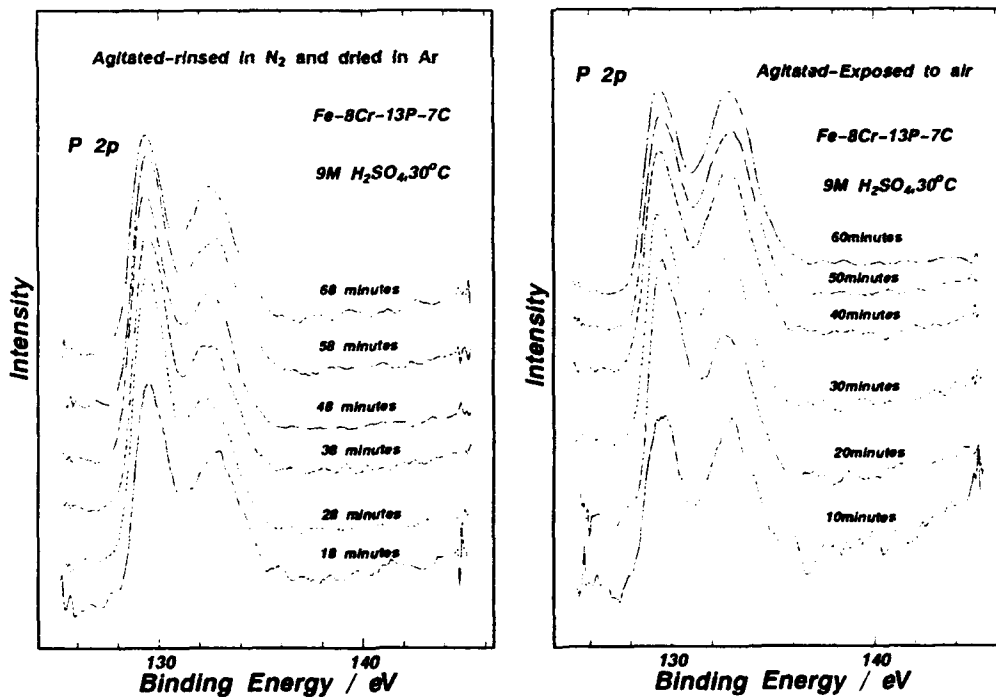


Figure 11. P 2p spectra for the amorphous Fe-8Cr-13P-7C alloy immersed for various periods of time in agitated 9 M H₂SO₄ open to air. The XPS analysis was conducted after the immersed specimen was washed with deaerated water in oxygen-free nitrogen and dried in argon (a) and after the immersed specimen was washed with water in air and dried in air (b).

Surface Analytical and Electrochemical Examination of Passive Layers on Cu/Ni Alloys

Peter Druska⁽¹⁾
Heinrich-Heine-Universität Düsseldorf
D-4 000 Düsseldorf 1, Germany

Hans-Henning Strehblow
Heinrich-Heine-Universität Düsseldorf
D-4 000 Düsseldorf 1, Germany

Abstract

The electrochemical formation of passive layers on Cu₂₀Ni and Cu₅₀Ni in 1 M NaOH has been examined with surface analytical methods like XPS, UPS and ISS. First a Ni(OH)₂ layer is formed. The rapidly growing Ni(OH)₂ leads to an accumulation of Cu at the metal surface which causes the formation of an oxide layer underneath consisting mainly of CuO. At more positive potentials NiO enters the oxide sublayer. Cu₂O appears to a minor extent at the metal/oxide interface during the initial stages of CuO formation and is no longer detected when CuO grows to a larger thickness at sufficiently positive potentials. In the potential range of the beginning transpassive behaviour the top Ni(OH)₂ layer is oxidized to NiOOH at its surface. The NiOOH formation leads to the incorporation of Cu(OH)₂ in the hydroxide overlayer. This transpassive oxidation causes a shift of the work function to larger values as determined by UPS and to the same shift to smaller binding energies of all XPS signals of oxide constituents similar to previous observations for pure Ni and its alloys. The passive layer on Cu/Ni alloys reflects the properties of both metal components.

Key Words: Passivity, Cu/Ni Alloys, XPS, UPS, ISS

Introduction

Cu/Ni alloys are materials which are highly resistant to corrosion in aggressive aqueous electrolytes at normal and elevated temperatures. These alloys are used for heat exchangers and for parts exposed to sea water as e.g. in the ship building industry because of their resistance to localized corrosion. Therefore various publications deal with their corrosion properties in sea water or NaCl-containing electrolytes ¹⁻⁵ and at elevated temperatures ⁶. These alloys are also widely used as catalysts for hydrogenation and dehydrogenation ^{7,8}. Although technologically very important, very little is known about the protecting passive layers and the films which form in the transpassive range. Therefore a systematic investigation of the chemical composition and structure of these layers has been started. In this paper results of films formed in 1 M NaOH are presented.

(1) Part of the PhD thesis of P. Druska

Fig. 1 depicts the potentiodynamic polarization curves in 1 M NaOH of both alloys for a better understanding of the surface analytical examinations. They show the main characteristics of pure Ni with an anodic peak at $E = -0.5$ V indicating the passivation of the alloys and a peak at $E = +0.7$ V characteristic for the transpassive behaviour of Ni.

Experimental

Specimen preparation. The surface analytical studies were performed with an Escalab 200 X (Fisons/VG Instruments) consisting of 3 vacuum chambers, the analyser, the preparation chamber and the fast entry lock. A fourth chamber was flanged to the lock where the electrochemical preparation was performed in a small vessel of ca. 2 cm² content. All electrolytes were Ar purged and could be introduced via appropriate feedthroughs. The electrochemical chamber could be filled with purified Ar and evacuated. Thus a specimen preparation and transfer without any air contact could be realized. The performance was routinely checked with standard procedures as the exposure of pure metals like Fe, without major oxide formation. Appropriate electrical feedthroughs and an electrolytical contact to a reference electrode form the potentiostatic circuit. A detailed description of the UHV system and its performance is given in detail elsewhere^{9,10}.

The Cu/Ni alloys were melted from 99.99% pure metals, mechanically treated and heat-treated to obtain void-free single phase materials. Circular specimen with a sharp edge were cut from the material. They were fixed to the specimen stub of the spectrometer with a 3 mm wide adherent cylindrical support with a thread. The circular front plane was polished with diamond spray with a 1 μ m final grading and cleaned ultrasonically in ethanol. Any further treatment occurred within the closed system without any air contact. The surface was first sputtered with Argon (AG21, VG Instruments, 4 keV, 20 μ A, 5 min) and then introduced into the electrolyte at open circuit potential. Then the selected electrode potential was applied for the passivation time of choice. For short time passivation transients of $t < 10$ s the specimen was introduced at $E = -0.96$ V for 10 min and finally pulsed to the potential in the passive range. For long-term passivations a previous reduction was not necessary and led to the same results which was carefully controlled. After passivation the surface was rinsed 4 times with pure water. Remaining adherent water was blown off with a jet of argon. The subsequent transfer to the UHV of the analyser chamber occurred within ca 5 min.

A potentiostat (Elektroniklabor W. Schiller) equipped with a function generator and pulse generators (Tektronix 26G) was used. All electrolytes were prepared with analytically pure substances and with deionized water (Millipore water purification system). Hg/HgO/1 N NaOH, $E = 0.14$ V served as a reference electrode. All potentials are given relative to the standard hydrogen electrode (SHE).

Surface Analysis. The XPS measurements were performed with a constant pass energy of 20 eV. The X ray source was run with the non-monochromatized Al K α radiation (1486.6 eV) with an input power of 300 W. The spectrometer was

calibrated routinely with the appropriate XPS lines of Au, Ag and Cu as given in ref. 11.

UPS measurements were performed with the He-I-line ($E = 21.22$ eV) of a UV source (UVS 10/35, Leybold Heraeus) with a discharge current of 90 mA, a pass energy of 3 eV and a negative specimen bias of 10 V.

For ISS measurements a scannable ion source (EX 05, VG instruments) was used with a Ne beam of 3 keV primary energy. For sputtering a larger window of 0.75 cm² with an ion current of 300 nA was used equivalent to 0.0624 nm/min. For ISS analysis 30 nA and 0.15 cm² equivalent to 0.0312 nm/min were applied. The two different windows prevented the crater effect during depth profiling. The sputter effect during the ISS measurement period was included in the evaluations. Sputter rates are given relative to that of Ta₂O₅ with 0.104 nm/min formed by anodic oxidation of Ta according to the procedure of ref 12. The size of the sputter windows was controlled by the colour changes of anodized Ta specimen after prolonged sputtering.

Standards. The XPS spectra were evaluated on the basis of well-characterized standards. The preparation of Ni standards as Ni_{met}, NiO, Ni(OH)₂, and NiOOH has been described in detail elsewhere^{13,14}. Comparison with the standard spectra prepared from Ni/Cu alloys with the same methods did not show any appreciable differences. Similar results are obtained for Cu. Therefore the standards for the pure metals and the pure compounds could be used for the evaluations instead of those from the alloys. Pure Cu was obtained by 10 min Ar sputtering. Cu(I)oxide was obtained by external electrochemical reduction of an alkaline CuO₂²⁻ solution in 5 M NaOH¹⁵. A 5 min cathodic reduction in 1 M NaOH at $E = -0.235$ V and its transfer into the UHV within the closed system removes traces of Cu(II)oxide formed during sample transfer through air. A CuO standard was obtained by 5 min heating of Cu at 800 °C in air and the immediate transfer into the UHV. Cu(OH)₂ was prepared by precipitation from a 0.1 M CuSO₄ solution added slowly to 5 M NaOH. The light blue precipitate was filtered, washed with pure water and transferred immediately into the UHV to avoid its transformation into black CuO. The dry light blue Cu(OH)₂ powder is stable for several days even in air. Cu compounds may be reduced during X ray radiation¹⁶. Prolonged radiation of several hours may lead finally even to Cu metal. The correction of the Cu(II)hydroxide signal from amounts of Cu₂O formed during XPS studies may be performed with the help of the Cu₂O standard spectra. For CuO this procedure was not necessary because the amount of Cu₂O formed during ca 20 min X ray radiation was negligible for both the standard and the passivated specimen. For the Cu(OH)₂ standard the correction was necessary as may be seen in Fig. 2b. Apparently the hydroxide is less stable to decomposition even in this regard. New Cu(OH)₂ surfaces may be obtained rather simply by removal of some changed material at the surface with tape. The OH⁻, and O²⁻ signals were taken from the corresponding oxide and hydroxide standards. Fig. 2 depicts the XPS spectra of the different standards which are the basis for further evaluations. After background correction according to Shirley¹⁷, the standard spectra are described with Gauss/ Lorenzians with a tail function to take care of the

asymmetry of the XPS signals. Fig 2 shows this deconvolution for the different species. Reference 14 gives the mathematical description and the related parameters. An appropriate program MFIT¹⁸ developed in our group permits the handling of the standard spectra and the processing of the data of passive layers including a least square fit routine.

For the evaluation of the contribution of Cu species the Cu XPS signals requires some special treatment. In the presence of Cu(II) the background correction according to Shirley is too large because of the presence of the pronounced shake up satellite. To avoid erroneous results a linear background correction was performed in this special case. Furthermore Cu metal and Cu(I) species cannot be distinguished by the Cu2P_{3/2} signal because of a negligibly small chemical shift. For this purpose the X-ray induced Cu L3MM Auger signal was used. This signal has been used previously for quantitative determination of Cu₂O on Cu¹⁹. It is relatively complicated and the description of each pure Cu standard needs 4 peaks with related requirements to the MFIT program (Fig.2). The contribution of the Cu(II) species to the Auger signal was estimated on the basis of the Cu2P_{3/2} signal. Its Auger peak is relatively broad and thus less characteristic and may lead to a larger error.

Data Evaluation. Any XPS signal of an actual passivated specimen surface was deconvoluted into the contributions of the different species on the basis of the standard spectra. For this purpose the characteristic data of the standard signals, especially the relative sizes of the peaks were kept constant and the their total size was varied to meet the actual signal with a least square fit routine of the MFIT program. The integrated intensity of the partial peaks of the components was used for further evaluation. Fig 3 gives an example of this procedure for the signals which are relevant to this study.

A similar evaluation was applied to the ISS spectra. The width of the signal is determined by the isotopic composition of the probe gas Ne as well as the target atoms. Thus the signal of pure standards was composed of simple Gaussians with a minor Lorentzian contribution for each isotopic combination. The peak parameters of the standards were kept constant, especially their relative heights, and the total height was adjusted to meet the spectrum of an actual specimen. Fig. 4 shows the deconvolution of the ISS signals for Cu and Ni and Fig. 5 depicts characteristic signals of a sputter depth profile of a passive layer indicating the variation of the composition by the related change of the peak areas. The sputter depth in nm refers again to the calibration with passivated Ta according to ref. 12.

Results and Discussion

Model of Layer Structure. Usually the passive layer has not a simple structure. At least a duplex film is discussed in the literature for different reasons. Strong support of this model is given by surface analytical methods. Besides other groups we have studied with XPS and partially with ISS passive layers of a large number of pure metals^{20,21}, as Fe^{9,22}, Cr²³, Ni¹³, Cu²⁴ and their binary alloys Fe/Ni^{13,25,26}, Fe/Cr^{9,21,27}, Cr/Ni²⁸, Al/Cu²⁹. The evaluation of the XPS data is

performed on the basis of a duplex or multilayer model. Any model has to be justified by appropriate measurements. Therefore we have performed angular dependent XPS measurements. Fig.6 presents a sequence of the intensity ratios of the different species depending on the take off angle Θ measured relative to the surface normal. All intensity ratios are normalized for $\Theta = 0$ deg. The curves correspond to the appropriate relations for the intensity ratios ¹⁴. Similar evaluations were performed in our group for passive layers on Cr/Ni alloys ²⁸. The upward bending in Fig. 6 shows clearly that the species whose intensity appears in the numerator is located outside. The close fit of the experimental values to the calculation proves the existence of a multilayer structure and a negligible influence of the possible surface roughness which usually leads to a flattening of presentations of the type of Fig 6. On the basis of this examination one comes to the conclusion of Fig. 7 for the layer structure. The inner oxide is covered by an outer hydroxide. The lower valent species are in the inner part of each sublayer. This leads to a further subdivision of both the oxide and the hydroxide. The higher valent species appear only at sufficiently positive potentials within the film. The contribution of the different sublayers to the total film thickness depending on the electrode potential are given in the upper part of Figs. 8 a,b for both alloys Cu20Ni and Cu50Ni.

On the basis of this model a quantitative evaluation of the XPS results is performed similar to the procedures and equations described previously ^{14,25,28}. The intensity ratios for this model, contain attenuation factors of overlayers and self attenuation factors for each sublayer. There exists a sufficient number of equations for the intensity ratios and the trivial equations for the weight fractions of the oxide and metal surface to get a solution for each of the unknowns, i.e. the thicknesses of the sublayers and their composition. The evaluation involves the values of Scofield ³⁰ for the photoionisation cross sections σ with an appropriate correction according to Reilman et al ³¹. The sensitivities for the Cu $2P_{3/2}$ signal may be related empirically to those of the X-ray induced Cu L3MM Auger signal with well known standards, so that the data evaluation may involve also the Auger line for a quantitative evaluation. One obtains the thicknesses and the compositions of the complicated multilayer structures.

Potential Dependence of Layer Composition. Apparently hydroxide is the major part of the surface layer at negative potentials and oxide at more positive potentials. The Cu_2O contribution is found in an intermediate potential range of $E = -0.1$ to 0.7 V whereas NiOOH forms at $E > 0.5$ V. The composition of the partial layers changes in a characteristic way with potential (Fig. 8 a, b). The metal surface is enriched in Cu with increasing potential i.e. with the growth of the passive layer. This result reflects the enrichment of the layer with the more reactive Ni leaving Cu metal behind. At lower potentials the developing inner oxide contains mainly Cu oxide. NiO enters only for $E > 0$ V. In contrast the hydroxide overlayer containing mainly $Ni(OH)_2$ and $Cu(OH)_2$ begins only for $E > 0.5$ V. According to these results the alloy forms first a $Ni(OH)_2$ layer. The related increase of the Cu-content at the metal surface causes the formation of mainly CuO at sufficiently positive potentials. Only in the potential range of $E = -0.1$ to 0.7 V a thin film of Cu_2O is formed directly at the metal surface. When

approaching the transpassive range, oxide and hydroxide reach a plateau value in thickness. The disappearance of Cu_2O i.e. its oxidation to CuO accompanies the oxidation of $\text{Ni}(\text{OH})_2$ to NiOOH at ca 0.5 to 0.8 V. The potentials have to be sufficiently positive to get the higher valent species. At $E > 0.5$ V $\text{Cu}(\text{OH})_2$ also enters the hydroxide layer.

The oxidation process of $\text{Ni}(\text{OH})_2$ to NiOOH in the vicinity of the transpassive behaviour may be followed by the chemical shift of all XPS signals of oxide components to smaller binding energies. A related observation is the increase of the work function by 0.5 eV as obtained from UPS spectra (Fig.9) which results in an appropriate shift of the secondary-cut-off of the photoelectrons. The interpretation is similar to for the case of pure Ni and Ni alloys^{13,14,25}. According to a simple semiconductor model of the passive layer the increasing band bending leads finally to a crossing of the valence band with the Fermi level. This introduces a large number of positive holes which act as a dopant leading finally to a decrease of the Fermi level. As the binding energies and the work function are given relative to the Fermi level this leads to a shift of both quantities by the same amount but with opposite sign. The formation of NiOOH in the transpassive potential range is an alternative picture to the accumulation of positive holes or of acceptor levels. Fig 9 c depicts the increase of the work function by 0.5 eV as obtained from the UPS-spectra of Fig. 9 a. A negative bias ensures the total acceptance of the secondary electrons. The energy difference ΔE between the secondary-cut-off and the Fermi edge yields the work function $e\Phi$ according to the relation $\Delta E = h\nu - e\Phi$ (Fig. 9b).

The ISS depth profile of passivated specimens matches nicely the XPS results obtained by evaluation on the basis of the bilayer structure. ISS cannot distinguish between the valence states of the atoms. Therefore a further subdivision of the oxide and hydroxide is not possible. Fig. 10 shows the profiles for three passivation potentials of Cu_{20}Ni together with the related XPS results. With Ne as the probe gas one cannot get backscattering of the lighter oxygen. Thus one cannot measure the O-content and only the cationic fractions X_{Cu} of Cu are shown. At $E = -0.16$ V a large $\text{Ni}(\text{OH})_2$ layer covers a very small oxide with high Cu content (Fig.8a). In agreement one obtains a large thickness with a very small Cu content with both analytical methods. The very thin Cu-oxide layer underneath is indicated only by a shoulder in the X_{Cu} profile. Sputter artifacts like ion mixing may reduce the depth resolution. The bulk level with $X_{\text{Cu}} = 0.8$ is reached at the expected depth. The relatively large scatter of the data of the metal surface is due to the small ISS signals. This is a consequence of the relatively large neutralization probability of the noble gas ions at a backscattering metal surface relative to an oxide surface with insulating or semiconducting properties. At $E = 0.44$ V, well within the passive range one detects clearly both layers with the ISS depth profile. The Cu content is still low in the hydroxide part in agreement with the XPS results. A larger content immediately at the surface might reflect some adsorption of $\text{Cu}(\text{II})$ species which may be dissolved in the first moment of the passivation transient. Its true nature remains however still uncertain. It is detected also for passivations in the transpassive range. The composition of the oxide part agrees extremely well with the XPS data (Fig. 10b). The layer model also agrees with the partial thicknesses

obtained by both methods. Fig. 10c with a passivation at $E = 0.89$ V refers to a potential within the transpassive region. In this situation the oxide layer is thicker than the hydroxide and an appreciable Cu content has entered the hydroxide part whereas Ni is incorporated within the oxide part thus reducing its Cu content to $X_{\text{Cu}} = 0.6$. In conclusion, ISS depth profiles reflect qualitatively and quantitatively the evaluation of the XPS results and thus further justify the bilayer structure. XPS however yields additional information for further subdivision into a total of 4 partial layers.

Time Dependence of Layer Composition. The results of time-dependent investigations are very close to those in the potential domain. It is a general observation that lower valent species appear first and will be oxidized later as has been shown for the case of passive Fe and Fe/Cr alloys^{9,22}. Fig 11 gives an example for Cu20Ni at two characteristic potentials, i.e. in the passive and in the transpassive range. The total thickness increases linearly with the logarithm of time indicating the presence of a barrier type of film. The hydroxide layer forms first and is already present within 1 ms. It takes about 10 to 100 ms to form the first oxide. Cu(I)- and Cu(II)-oxide are observed simultaneously within the oxide layer at $E = 0.44$ V (Fig.11a). At $E = 0.89$ V Cu(I)-oxide appears only for a short time to a very low level and is oxidized completely to Cu(II) (Fig.11b). Ni enters the oxide within ca. 0.1 s at both potentials. At 0.44 V the hydroxide consists of $\text{Ni}(\text{OH})_2$. At $E = 0.89$ V $\text{Cu}(\text{OH})_2$ enters within 0.1 to 1 s (Fig.11b) and reaches within 10 s the level of $\text{Ni}(\text{OH})_2$. Very characteristic is the formation of $\text{Ni}(\text{OH})_2$ within the first 0.1 s and its disappearance within ca 100 s. Simultaneously the NiOOH-containing film is formed which incorporates large amounts of $\text{Cu}(\text{OH})_2$ up to an equal content of both hydroxides. At $E = 0.44$ V no NiOOH is formed. The metal surface accumulates Cu which is a consequence of a preferential incorporation of Ni into the passive layer. The results for Cu50Ni are similar. The lower Cu content prevents its incorporation into the hydroxide layer and Ni^{2+} is transferred into the oxide part. In the transpassive range $\text{Ni}(\text{OH})_2$ forms within 1 ms to its maximum thickness and is continuously oxidized to NiOOH at shorter times due to the higher Ni content.

Reduction of the Passive Layer. The reduction of the layers at decreasing potentials reverses the oxide formation with electrode potential (Fig. 12). NiOOH is reduced to $\text{Ni}(\text{OH})_2$ in the range of $E = 0.9$ to 0.3 V. Cu_2O appears below 0.6 V and at $E = -0.7$ V most of the oxide has disappeared. The polarization curves of Fig 1 show a reduction peak in the range of $E = 0.8$ to 0.5 V where the NiOOH to $\text{Ni}(\text{OH})_2$ transition occurs. The reduction of Cu-oxides and the related disappearance of the oxide layer coincides with the cathodic currents at $E < 0.4$ V. The lack of a pronounced reduction peak agrees with the larger potential range where this reaction occurs.

Conclusion

Oxide formation in 1 M NaOH on Cu/Ni alloys reflects the specific properties of both elements. At negative potentials or short times of passivation $\text{Ni}(\text{OH})_2$ is formed first. This process leads to an increase of Cu at the metal surface, which

causes finally the formation of an oxide layer consisting mainly of Cu-oxides. This in turn permits the incorporation of NiO into the already existing inner oxide layer. However, the depletion of Ni at the metal surface remains independent of the potential and time for the later stages of oxidation. Cu forms first Cu_2O . At sufficiently long times and positive potentials of passivation Cu_2O is oxidized completely to $\text{CuO}/\text{Cu}(\text{OH})_2$. This behaviour is different from pure Cu where a duplex $\text{Cu}_2\text{O}/\text{CuO}, \text{Cu}(\text{OH})_2$ structure is observed up to the potentials of the start of transpassive behaviour. $\text{Ni}(\text{OH})_2$ is oxidized to NiOOH as has been found for pure Ni and other Ni alloys. This oxidation is facilitated with increasing Ni content within the alloy. Also $\text{Cu}(\text{OH})_2$ is incorporated in the hydroxide overlayer. For $E > 0.8 \text{ V}$ and Cu_{20}Ni 2/3 of $\text{Ni}(\text{OH})_2$ is oxidized whereas for Cu_{50}Ni the total amount has been changed to NiOOH . The oxide reduction occurs with an opposite sequence similar to its formation. The changes with potential are similar to those with time.

This investigation shows that the electrochemical processes during oxide formation and reduction may be studied with surface analysis. The related changes may be followed qualitatively and quantitatively by combining electrochemical and surface analytical methods. Thus the application of both disciplines give us a much better insight into the structure and the chemical properties and reactivity of passive layers. Not many systems have been studied in detail with a well-characterized electrochemical specimen preparation with a systematic variation of the different parameters. We think that investigations of a similar kind should be performed with other binary and later with more complex alloys to learn not only about the stationary composition of surface films but also about their changes, their formation kinetics and their reactivity. This will help to improve the interpretation of electrochemical studies.

Acknowledgement: The support of this work by the Deutsche Forschungsgemeinschaft Project Str 200/5 is gratefully acknowledged.

References.

1. D.E. Dobb, J.P. Storvick, G.K. Pagenkopf, *Corr. Sci.* 26, 525 (1986)
2. F.P. Ijsseling, L.J.P. Drolenga, B.H. Kolster, *Br. Corr. J.* 17, 162 (1982)
3. D.D. MacDonald, B.C. Syrett, S.S Wing, *Corrosion* 34, 289 (1978)
4. K.D. Eford, *Corrosion* 31, 77 (1975)
5. H.P. Dhar, R.E. White, G. Burnell, L.R. Cornwell, R.B. Griffin, R. Darby, *Corrosion* 41, 317 (1985)
6. N.S. McIntyre, T.E. Rummery, M.G. Cook, D. Owen, *J. Electrochem.Soc.* 123, 1164 (1976)
7. J.H. Long, J.C.W. Frazer, E. Ott, *J. Am. Chem. Soc.* 56, 1101 (1934)
8. J.H. Sinfelt, J.L. Carter, D.J.C. Yates, *J. Catal.* 24, 283 (1972)

9. S. Haupt, C. Calinski, U. Collisi, H.-W. Hoppe, H.D. Speckmann, H.-H. Strehblow, *Surf. Interf. Anal.* 9, 357 (1986)
10. S. Haupt, U. Collisi, H.D. Speckmann, H.-H. Strehblow, *J. Electroanal. Chem.* 194, 179 (1987)
11. M.T. Anthony, M.P. Seah, *Surf. Interf. Anal.* 6, 95 (1984)
12. M. Seah, *Community Bureau of References No.* 261 (1983)
13. H.-W. Hoppe, H.-H. Strehblow, *Surf. Interf. Anal.* 14, 121 (1989)
14. H.-W. Hoppe, H.-H. Strehblow, *Corr. Sci.* 31, 167 (1990)
15. U. Collisi, H.-H. Strehblow, *J. Electroanal. Chem.* 284, 385 (1990)
16. J.C. Klein, C.P. Li, D.M. Hercules, J.F. Black, *Appl. Spectroscopy*, 38, 729 (1984)
17. D.A. Shirley, *Phys. Rev. B* 5, 4709 (1972)
18. J. M. Abels, H.-H. Strehblow, to be published
19. H. D. Speckmann, S. Haupt, H.-H. Strehblow, *Surf. Interf. Anal.* 11, 148 (1988)
20. H.-H. Strehblow, *Surf. Interf. Anal.* 12, 363 (1988)
21. S. Haupt, H.-H. Strehblow, *Corr. Sci.* 29, 163 (1989)
22. S. Haupt, H.-H. Strehblow, *Langmuir* 3, 873 (1987)
23. S. Haupt, H.-H. Strehblow, *J. Electroanal. Chem.* 228, 365 (1987)
24. H.-H. Strehblow, H.D. Speckmann, *Werkst. Korr.* 35, 512 (1984)
25. H.-W. Hoppe, H.-H. Strehblow, *Surf. Interf. Anal.* 16, 271 (1990)
26. A. Rossi, C. Calinski, H.-W. Hoppe, H.-H. Strehblow, *Surf. Interf. Anal.* 18, 269 (1992)
27. C. Calinski, H.-H. Strehblow, *J. Electrochem. Soc.* 136, 1328 (1989)
28. T. Jabs, P. Borthen, H.-H. Strehblow, *Proceedings of Symposium on Oxide Films on Metals and Alloys, Electrochem. Soc., Meeting Toronto, Canada, Oct. 92*
29. H.-H. Strehblow, D.L. Malm, *Corr. Sci.* 19, 469 (1979)
30. J. H. Scofield, *J. Electron Spec.* 8, 83 (1976)
31. R. F. Reilman, A. Msesane, S.T. Manson, *J. Electron Spec.* 8, 389 (1976)

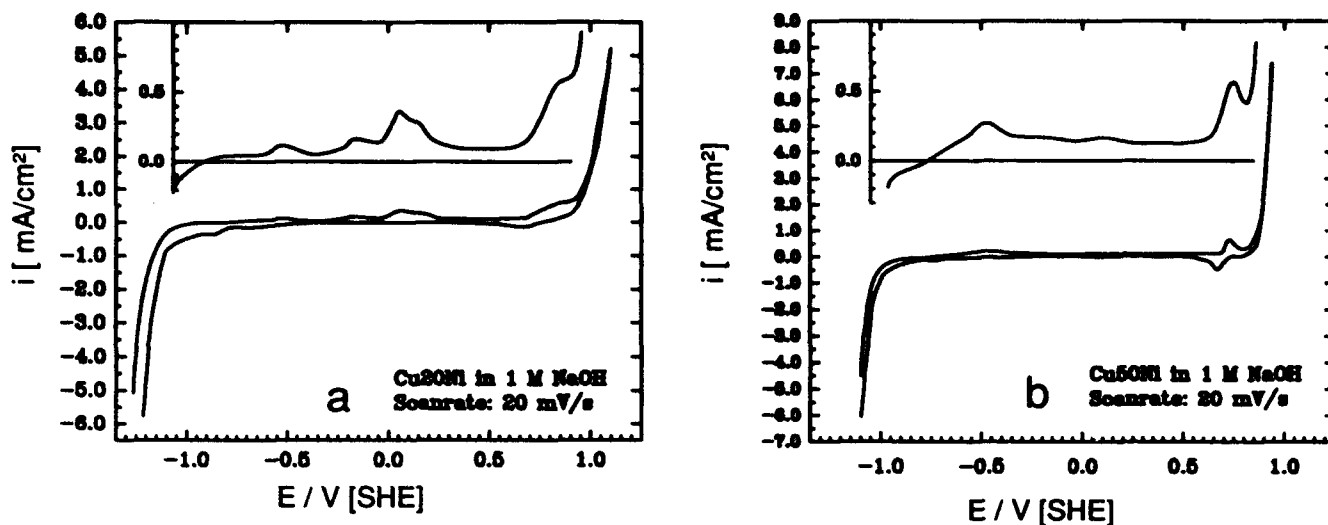


Fig. 1: Potentiodynamic polarization curves of (a) Cu20Ni; (b) Cu50Ni in 1 M NaOH

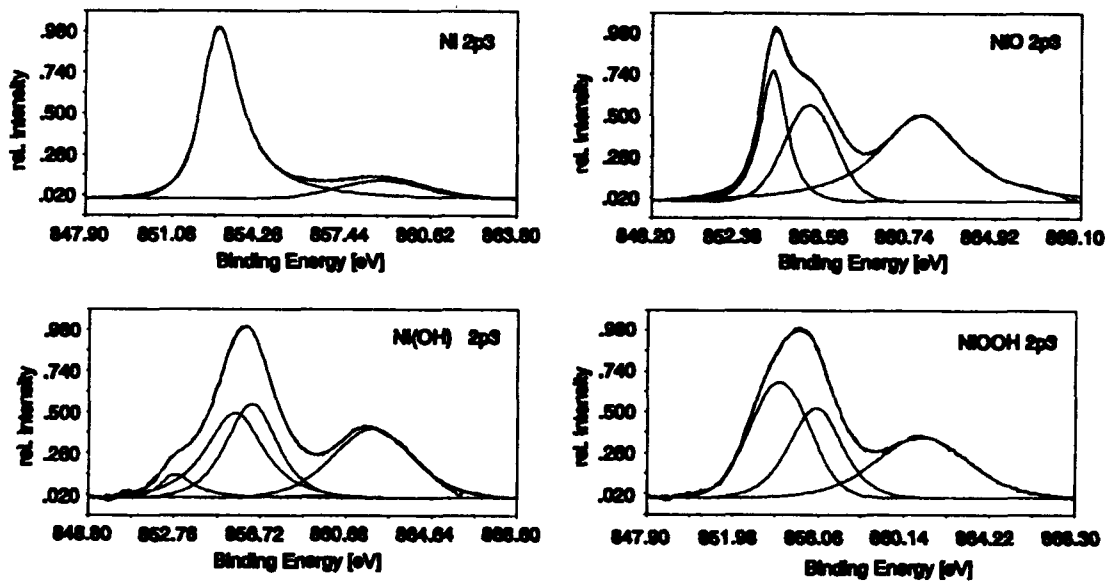


Fig. 2a: Peak deconvolution of the Ni 2p_{3/2} XPS signal of nickel and the nickel oxide/hydroxides

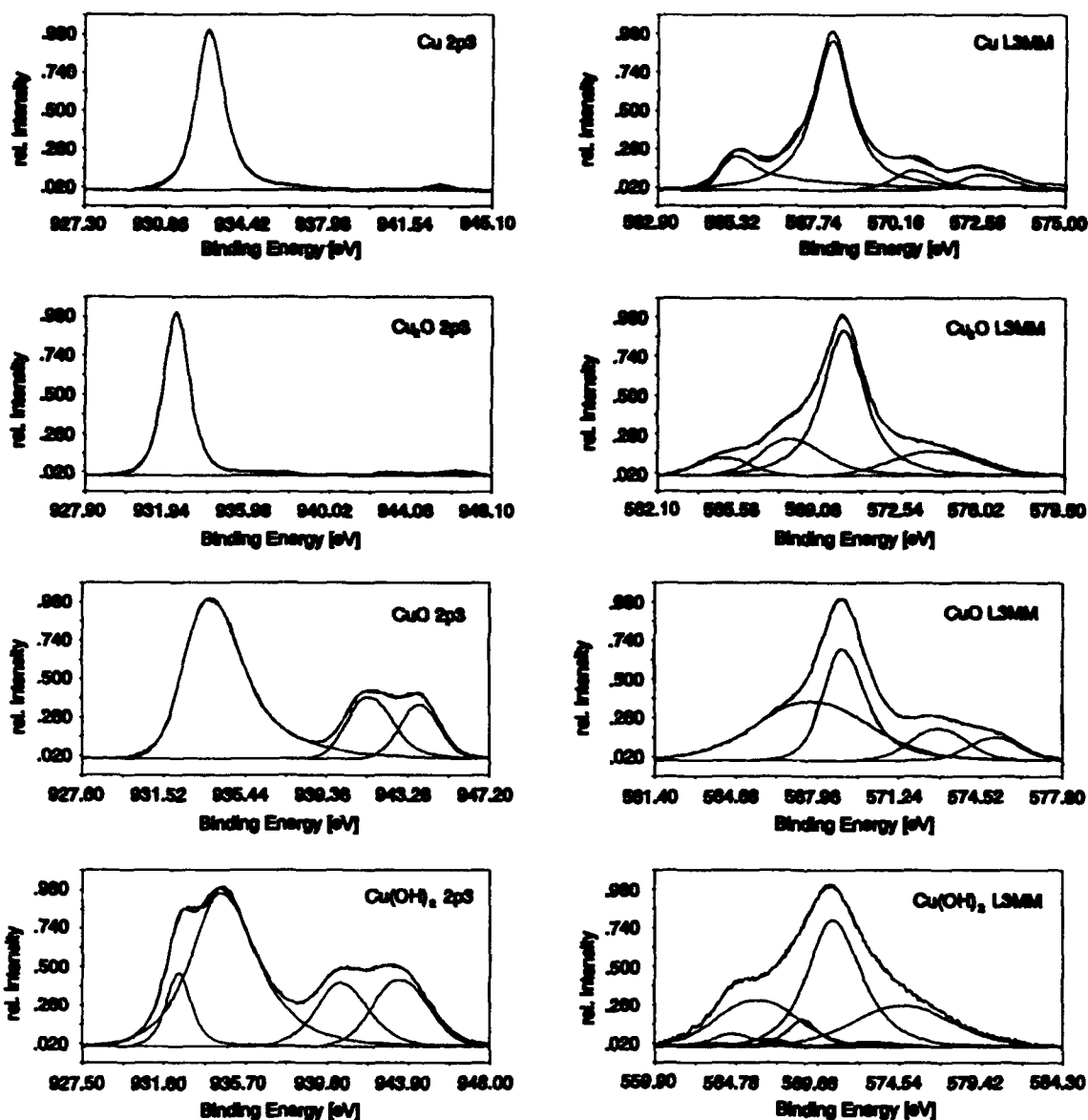


Fig. 2b: Peak deconvolution of the Cu 2p_{3/2} XPS signal and the x-ray induced Cu L3MM signal of copper and the copper oxide/hydroxides

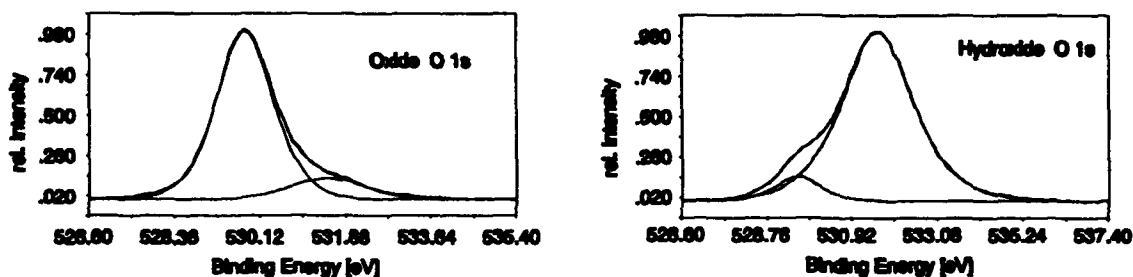


Fig. 2c: Peak deconvolution of the O 1s XPS signal of oxide and hydroxide

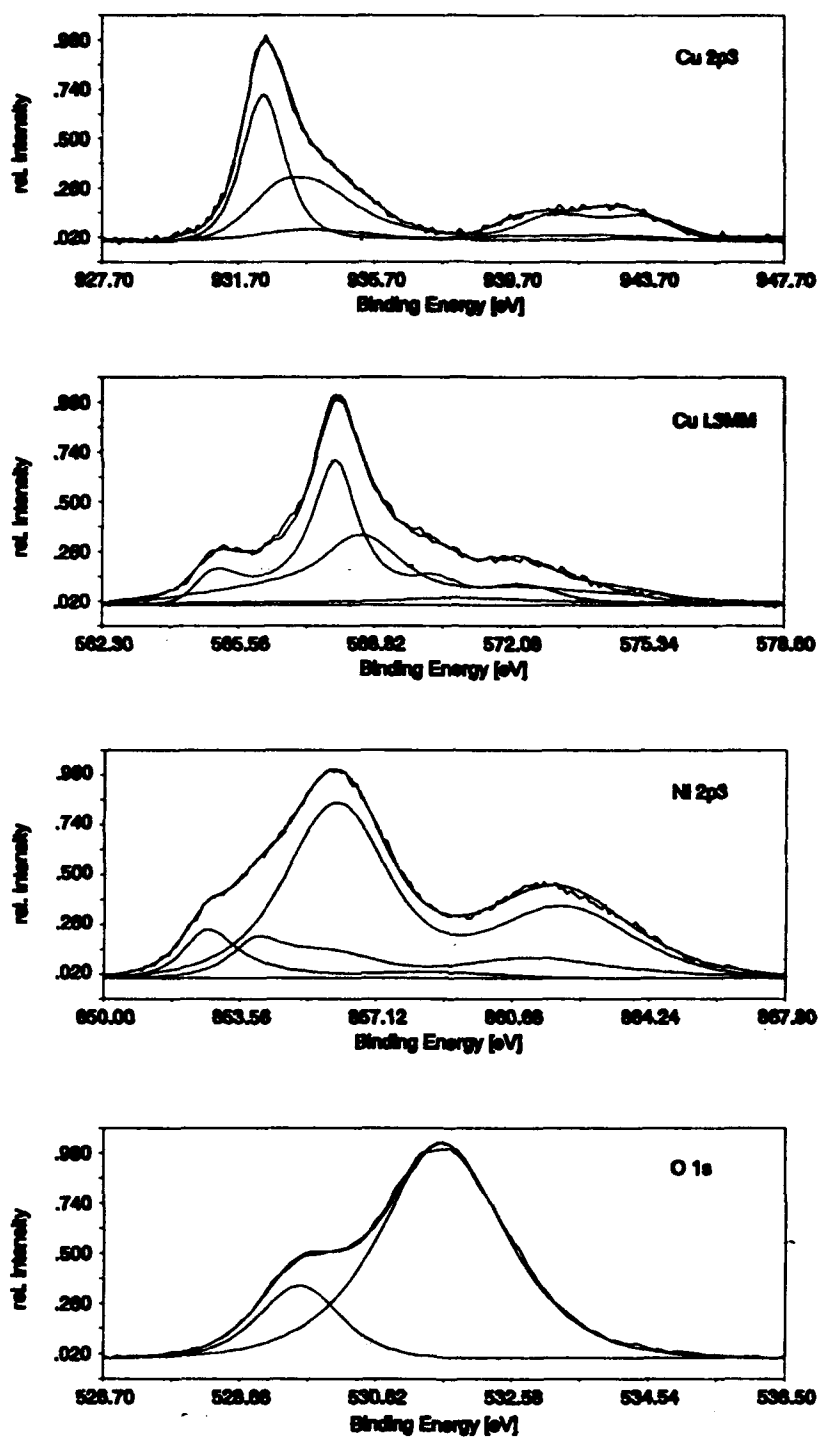


Fig. 3: XPS signals of Cu₂₀Ni passivated in 1 M NaOH for 300 s at 0.54 V [SHE] and the deconvolution with standards depicted in Fig. 2

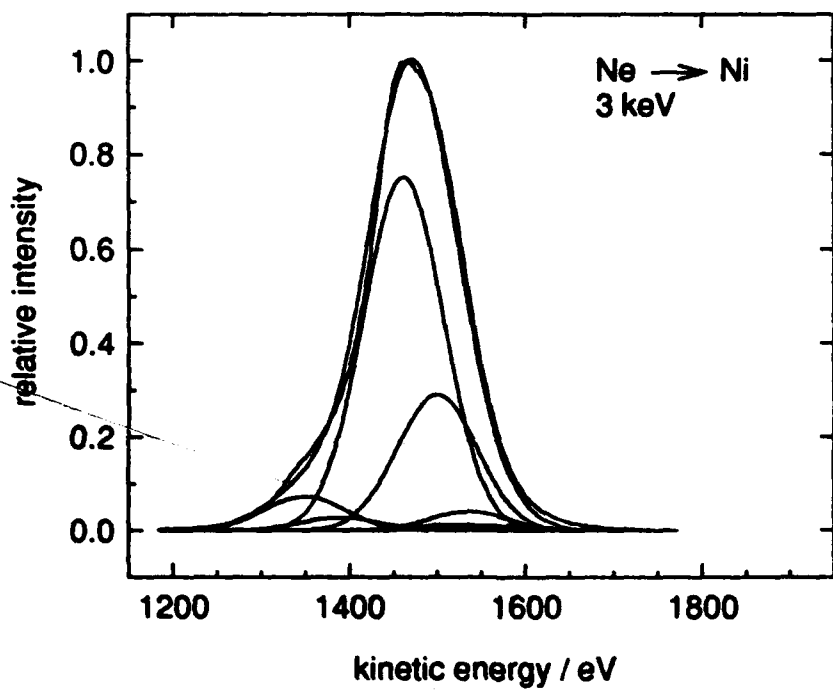
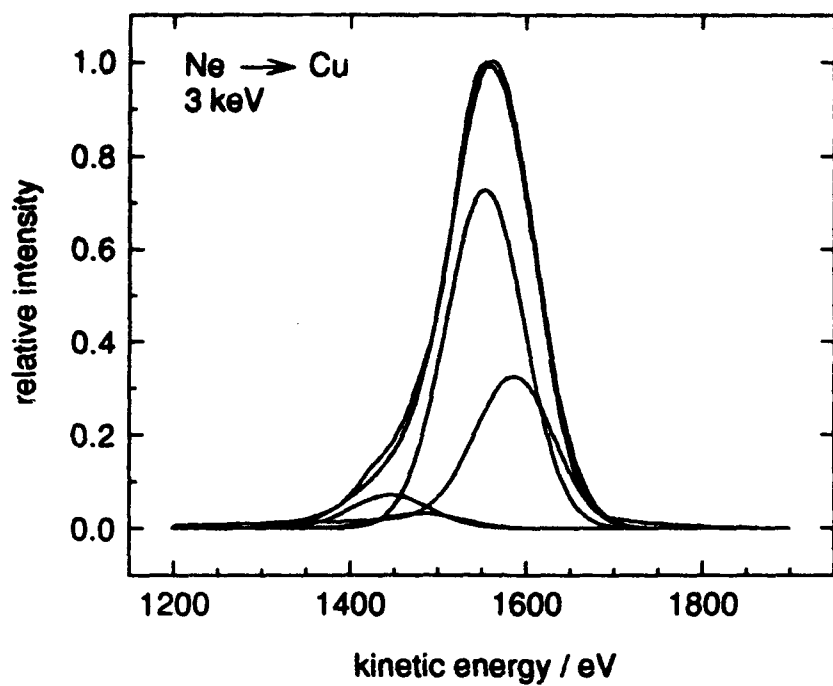


Fig. 4: ISS standard signals of pure copper and nickel and the deconvolution with different isotopic combinations

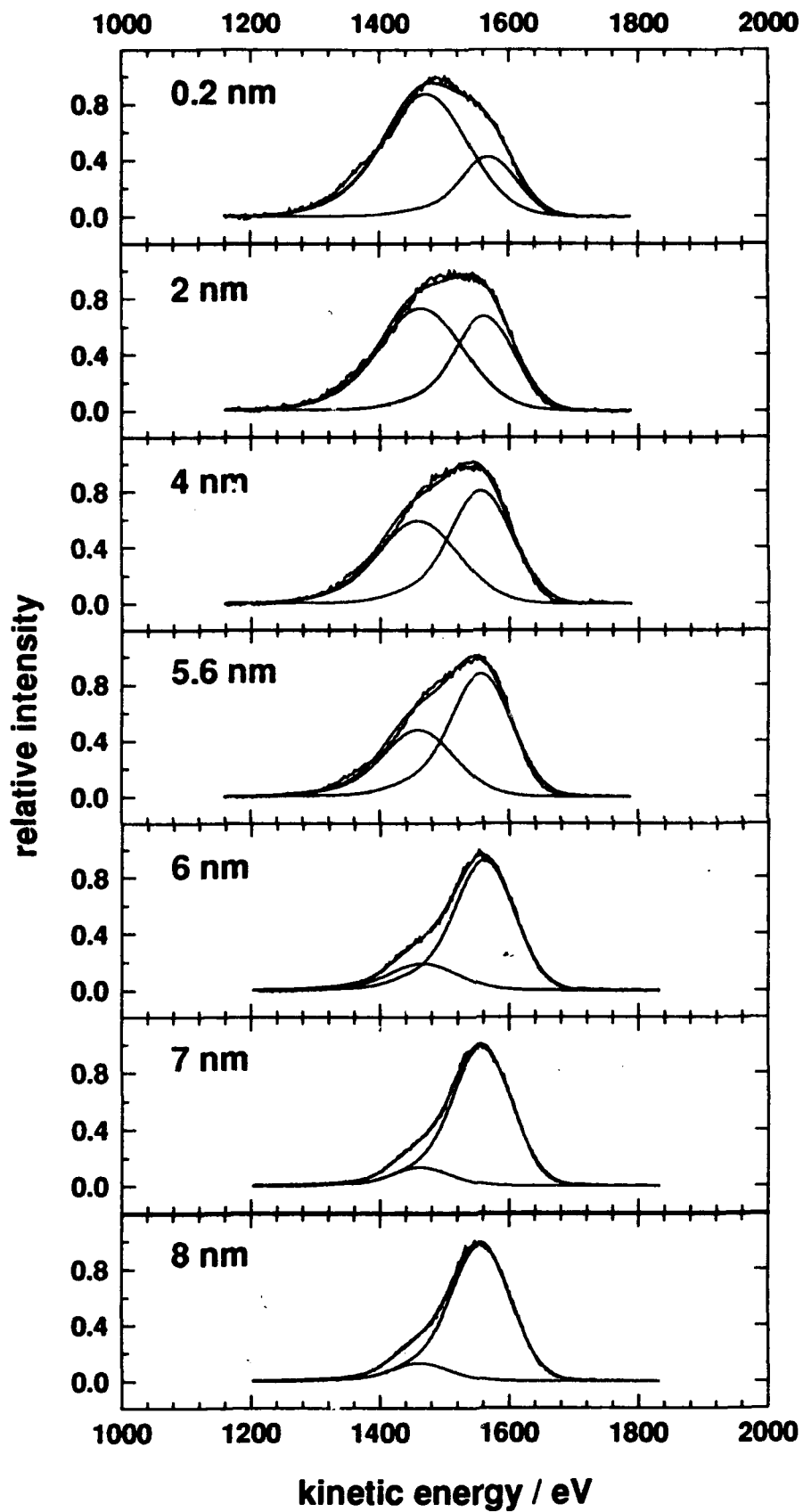


Fig. 5: ISS signals of Cu₂₀Ni passivated in 1 M NaOH for 300 s at 0.89 V [SHE] after seven characteristic sputter times of the depth profile depicted in fig. 10

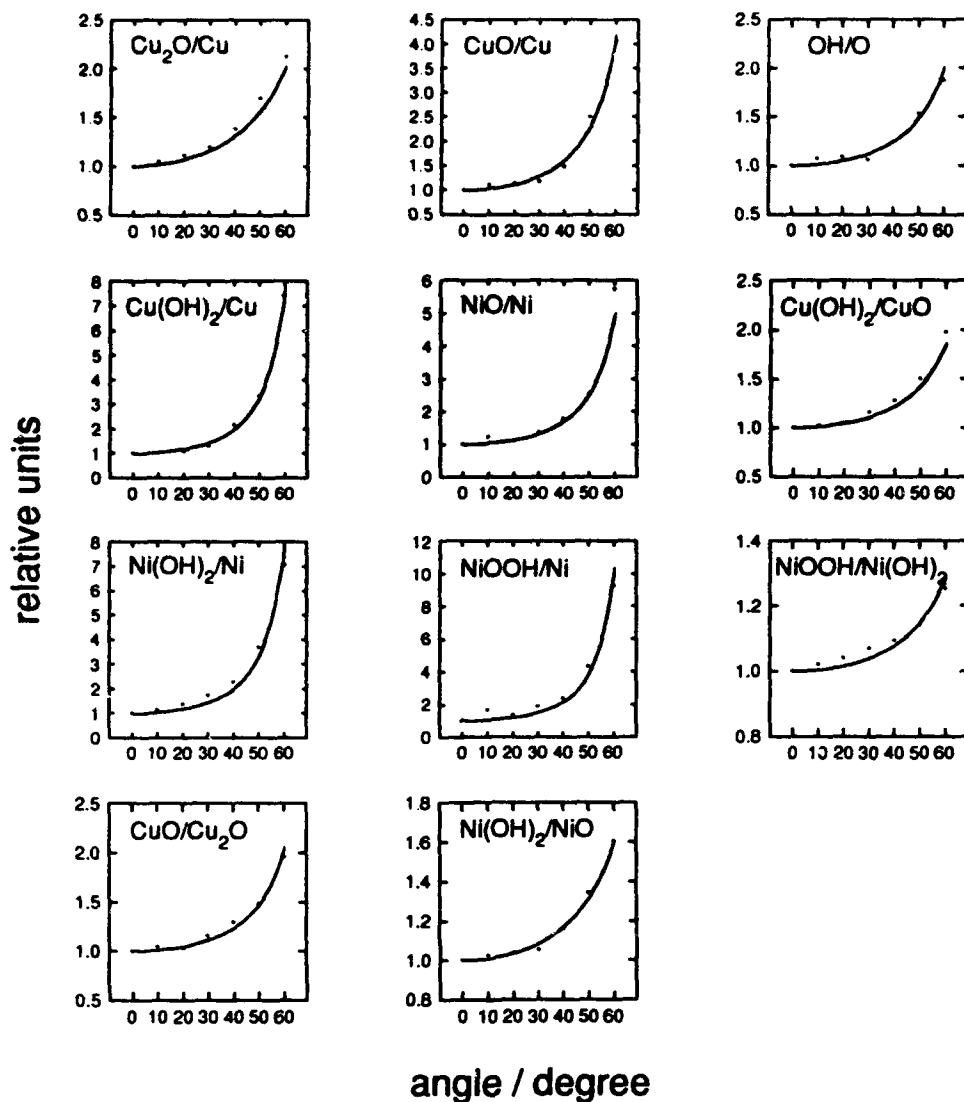


Fig. 6: Measured (•) and calculated (—) angle resolved XPS signal intensities of Cu20Ni in 1 M NaOH for 300 s at 0.89 V [SHE]

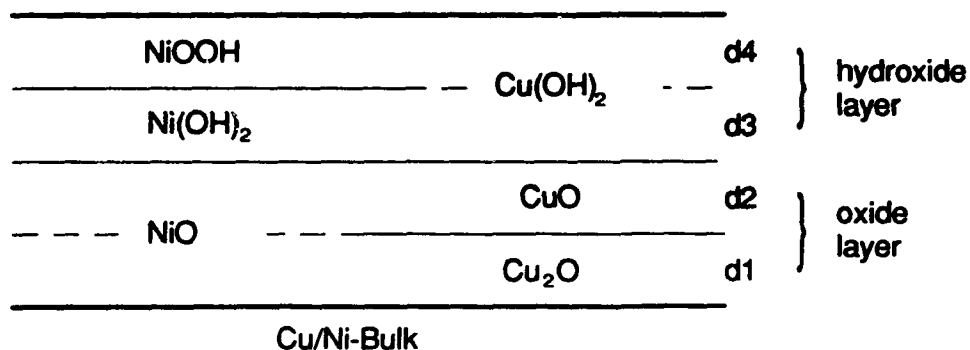


Fig. 7: Passive layer model of Cu/Ni alloys in 1 M NaOH

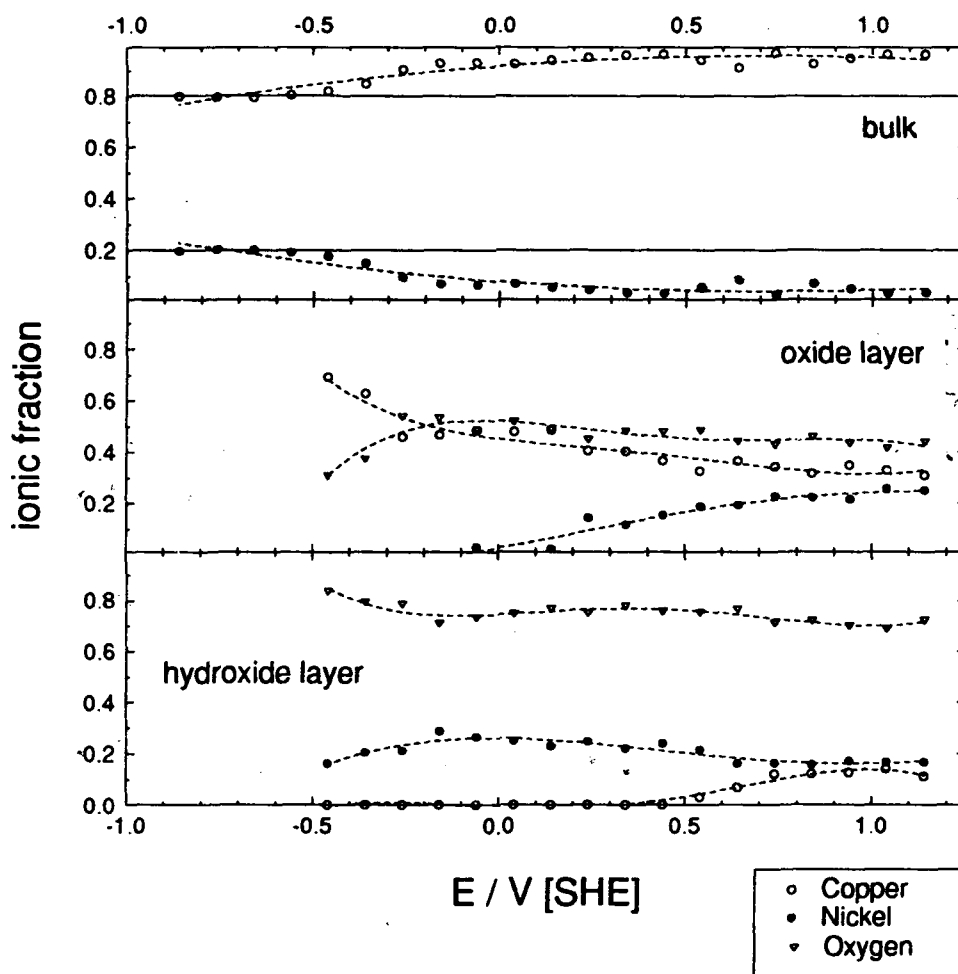
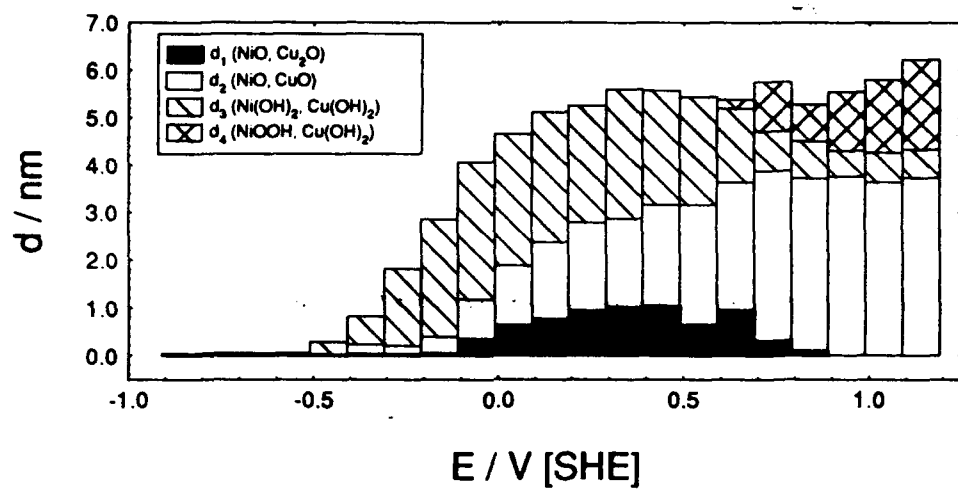


Fig. 8a: Thickness and composition of Cu₂₀Ni in 1 M NaOH for 300 s at different potentials

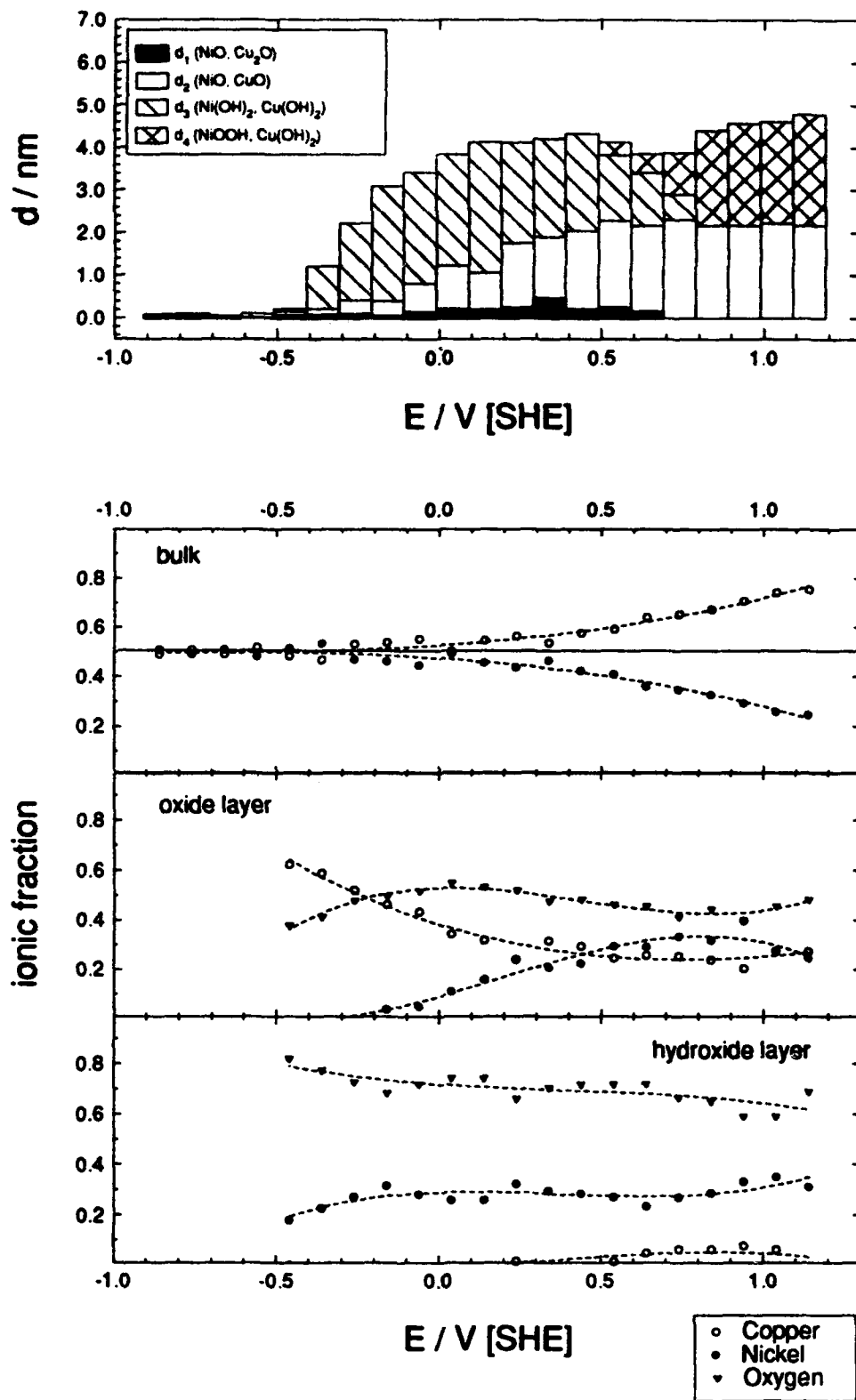


Fig. 8b: Thickness and composition of Cu50Ni in 1 M NaOH for 300 s at different potentials

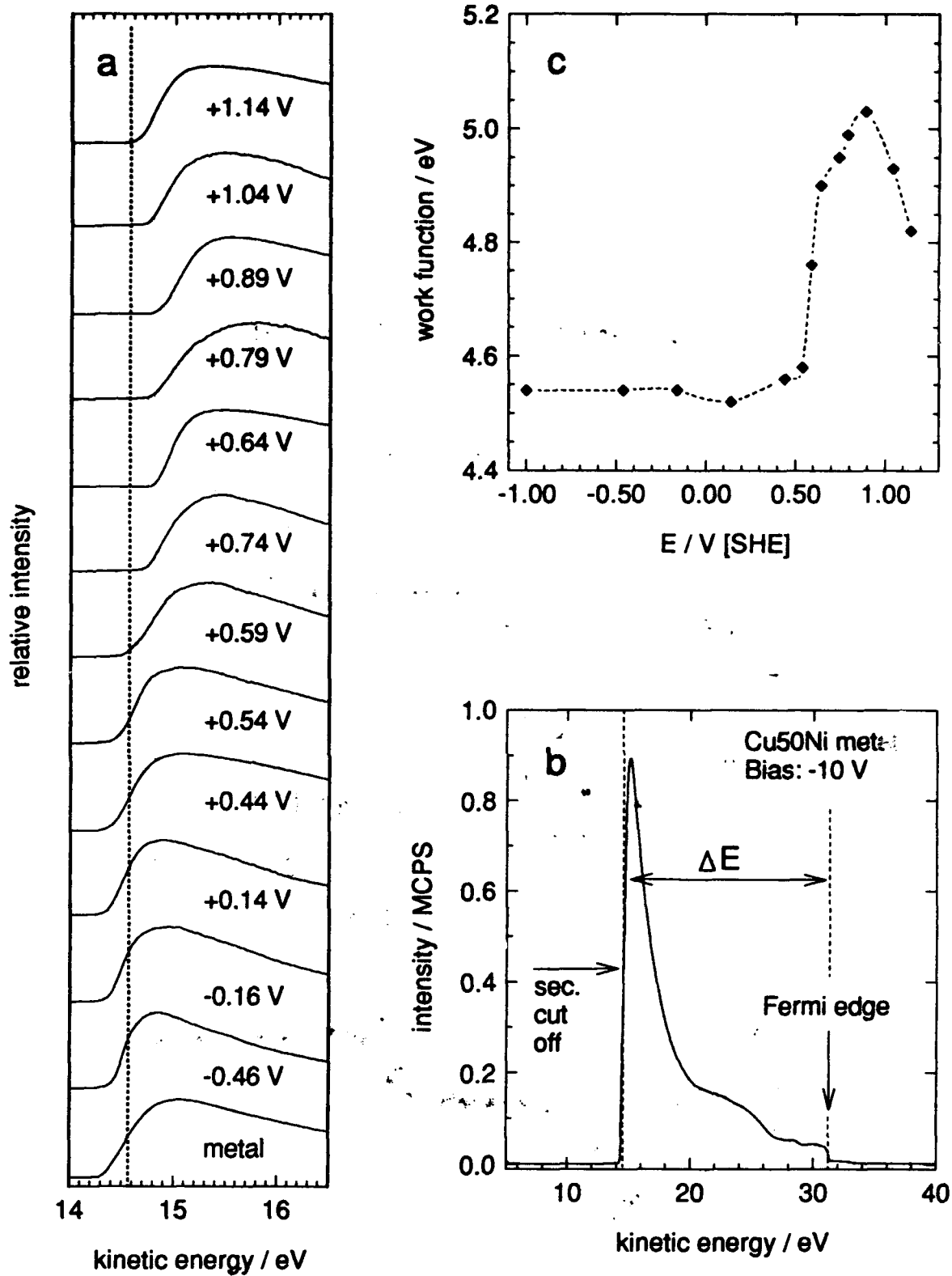


Fig. 9: UP spectra of Cu₅₀Ni; (a) secondary cut off of Cu₅₀Ni polarized at different potentials in 1 M NaOH for 300s; (b) sputtered alloy with Fermi edge, ΔE and sec. cut off; (c) change of the work function deduced from the width ΔE of the UP spectrum vs. the passivation potential E

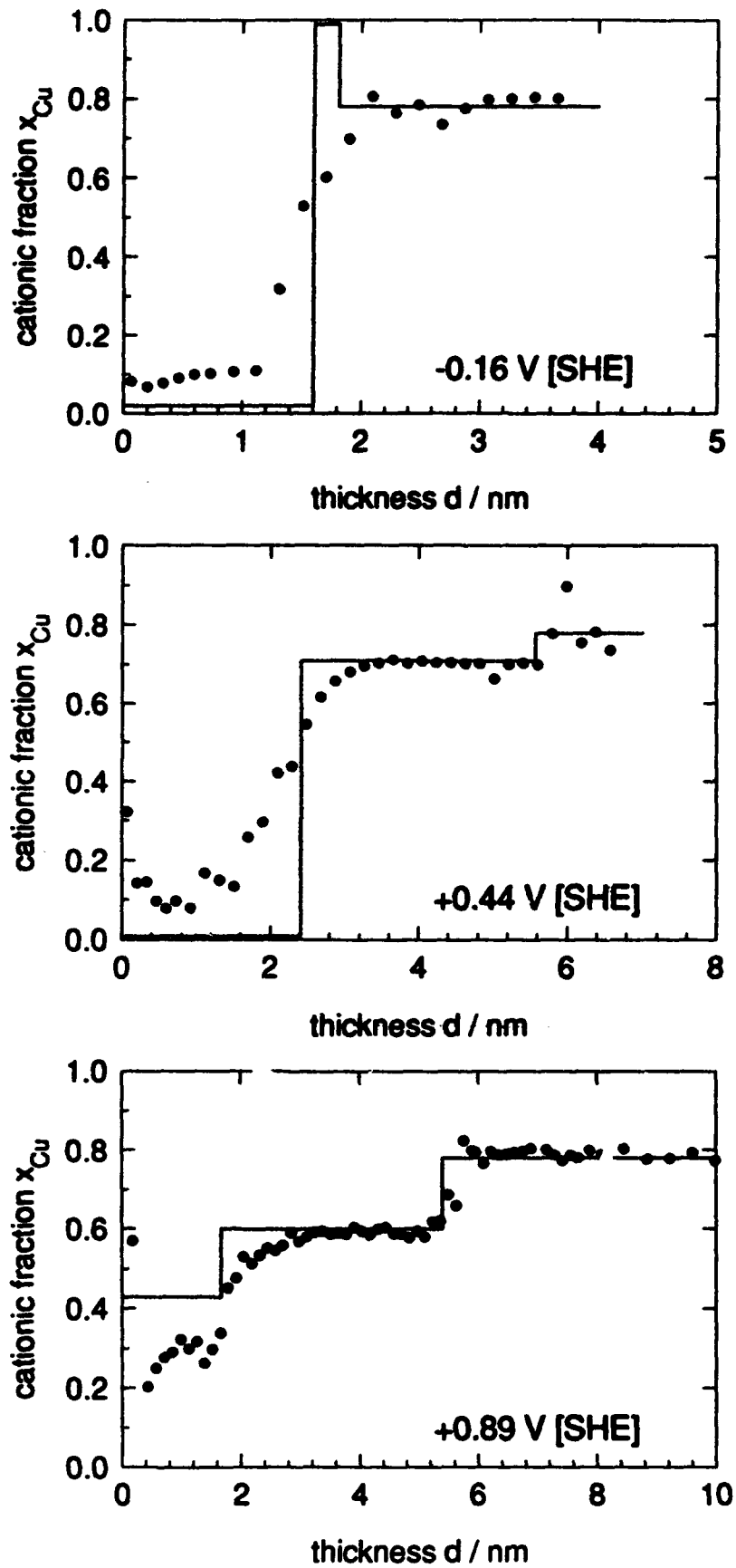


Fig. 10: ISS (•) and XPS (—) depth profile of Cu₂₀Ni in 1 M NaOH for 300 s at three potentials

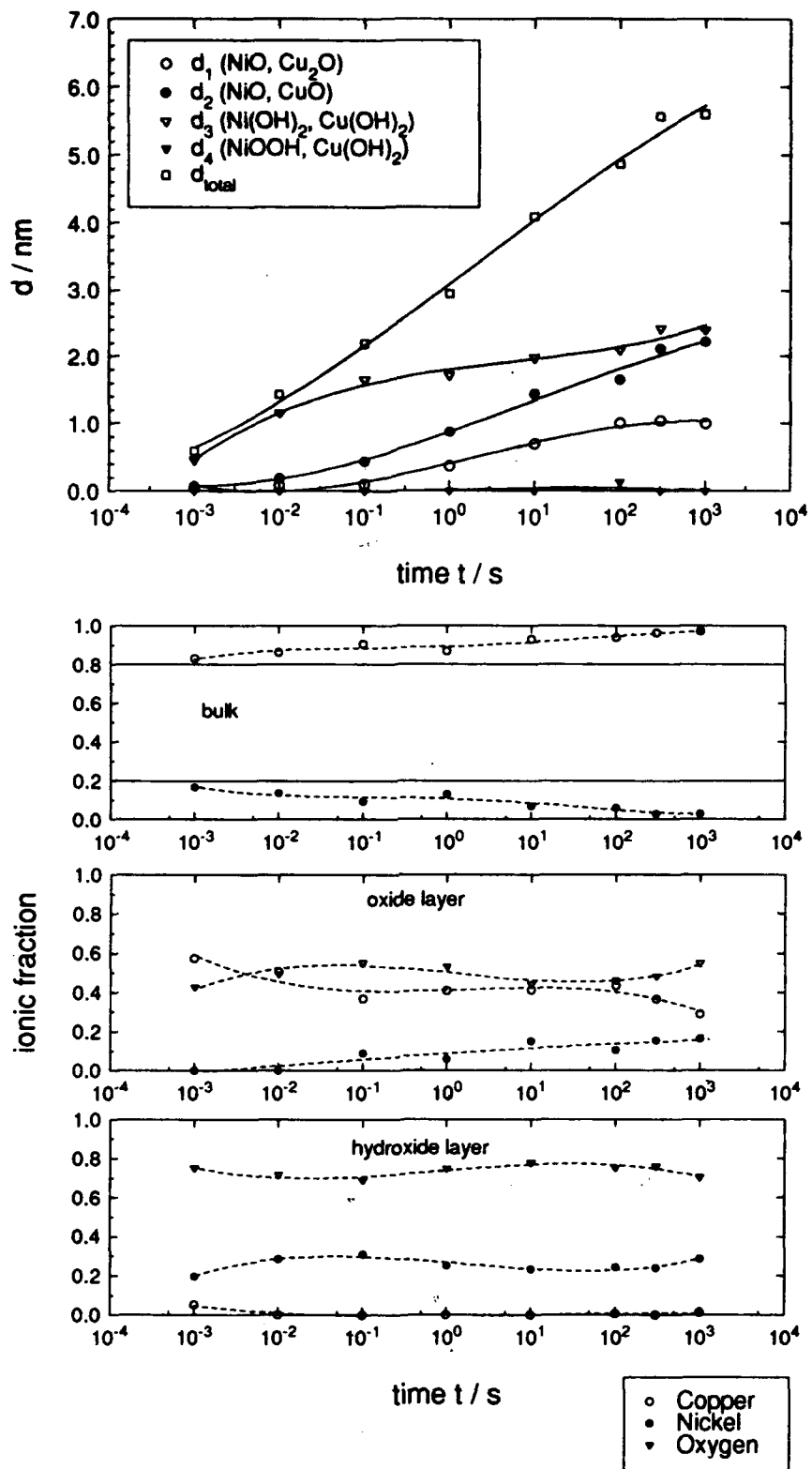


Fig. 11a: Time dependence of the thickness and composition of the passive layer of Cu₂₀Ni in 1 M NaOH for 300 s at 0.44 V [SHE].

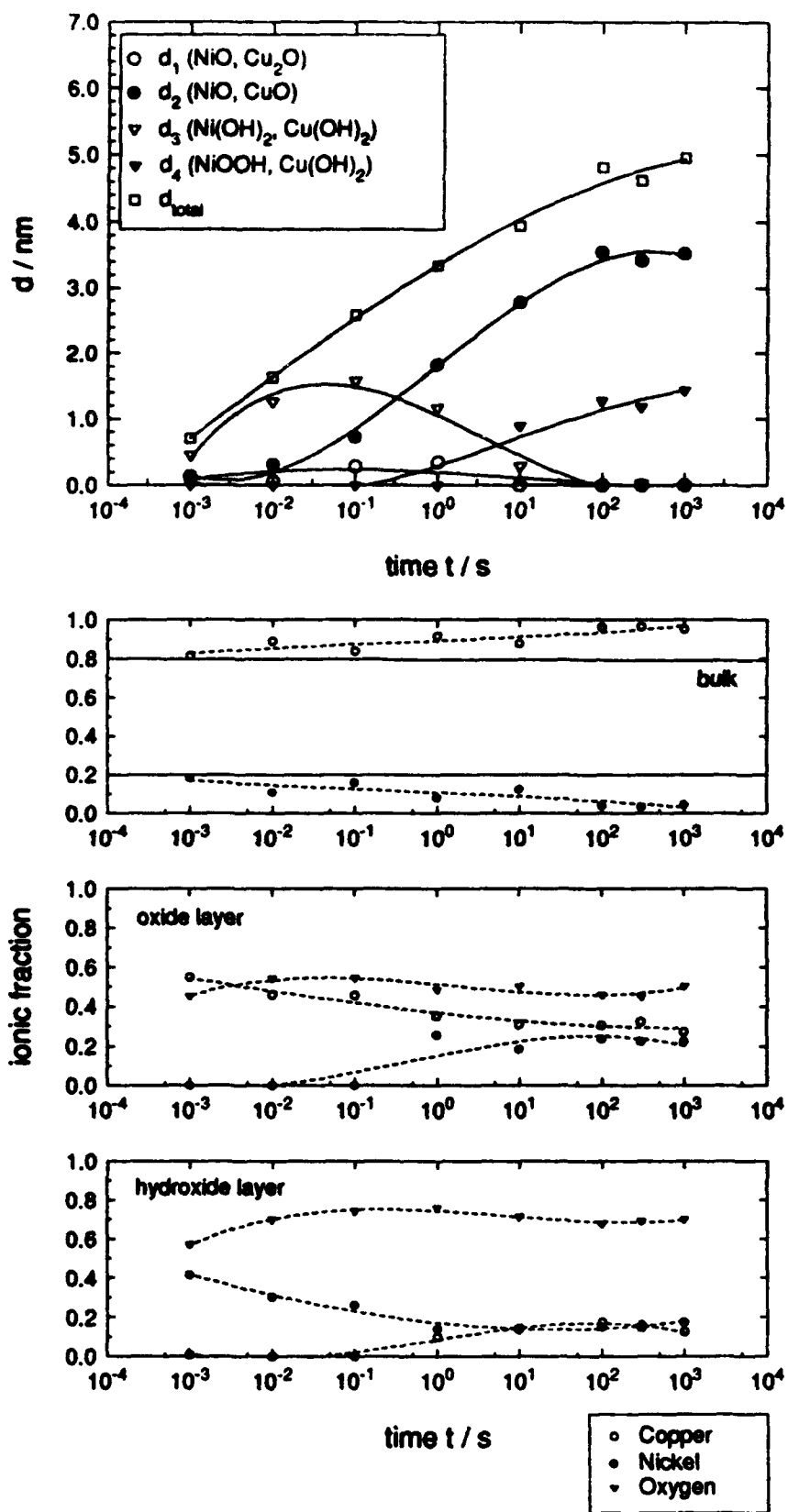


Fig. 11b: Time dependence of the thickness and composition of the passive layer of Cu₂₀Ni in 1 M NaOH for 300 s at 0.89 V [SHE].

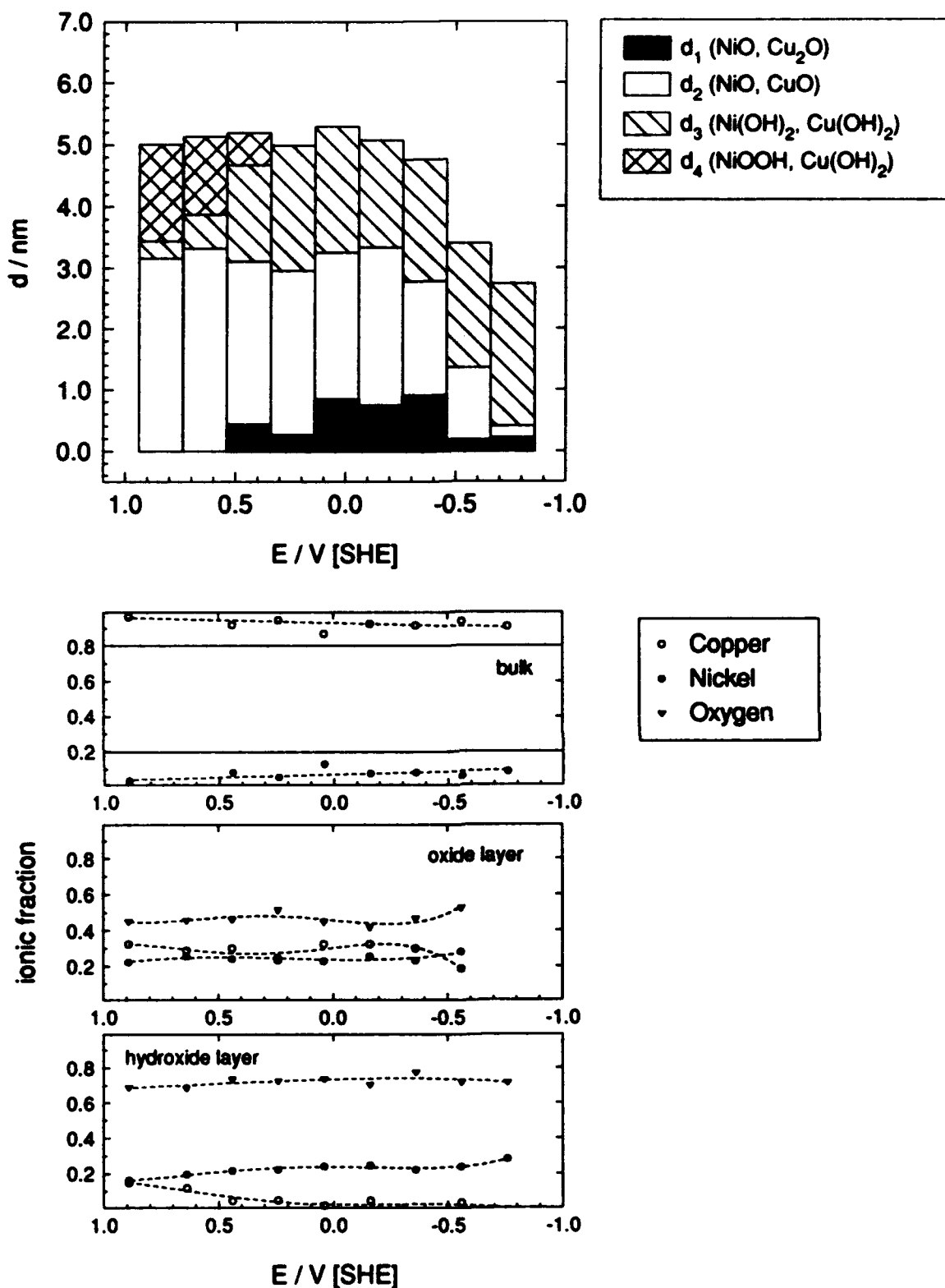


Fig. 12: Thickness and composition of Cu₂₀Ni in 1 M NaOH for 300 s at 0.89 V [SHE] and the gradual reduction down to -0.76 V [SHE]

Laser Raman and X-ray Scattering Studies of Corrosion Films on Metals

Carlos A. Melendres
Argonne National Laboratory
Materials Science and Chemical
Technology Divisions
Argonne, IL 60439, USA

Abstract

Optical spectroscopic and X-ray scattering techniques, coupled with electrochemical methods, are among the most useful in probing the structure of corrosion films on metals in-situ in aqueous environments. Laser Raman spectroscopy has been employed in our Laboratory for a number of years to investigate the composition of surface films on metals like iron, nickel, chromium, and stainless steel. We illustrate our work by presenting some results of studies of the composition of the passive film on nickel, using surface enhanced Raman scattering (SERS) with an electrodeposited silver overlayer. We find that both oxide and hydroxide species are present on the surface of Ni in the passive region. We also demonstrate the utility of specular X-ray reflection in providing complementary information on the physical structure of passivated metal surfaces. The thickness of the corrosion films formed, the density of surface layers, and the development of surface and interface roughness on Cu electrodes have been quantitatively monitored in-situ as a function of potential for the first time.

I. Laser Raman Spectroscopy of Surface Films on Metals

A technique that is employed in our laboratory to probe the structure of electrode surfaces in-situ is Raman spectroscopy, in particular, normal, resonance enhanced, or surface enhanced Raman spectroscopy (SERS). Significant information on the composition of corrosion films on metals has been obtained by this technique.¹⁾ The structure of adsorbed layers has also been extensively studied, mainly by SERS.²⁾ We have recently reviewed the former application and refer the interested reader to this work¹⁾ and the references quoted therein for details of the technique and applications. We will briefly illustrate here the general principles involved by describing results which we have recently obtained on the composition of the passive films on Ni in aqueous solutions.

A. Experimental

A schematic diagram of the experimental setup is shown in Fig. 1. This setup includes a special spectroelectrochemical cell consisting of three separate compartments to house the electrodes. The metal to be studied is made the working electrode and is positioned very close (~1 mm) to the quartz optical window of the cell. The laser beam is directed at about 30° with respect to the window (and electrode surface), and the scattered light is collected and analyzed using a SPEX Industries model 1403 double monochromator. Detection is made using a photomultiplier tube with pulse counting electronics.

High purity Ni foils (0.318-cm wide x 0.254-mm thick) were polished with 600 grit emery paper and then cleaned thoroughly with acetone and high purity water. Raman spectroscopic and electrochemical measurements were carried out as a function of solution pH and applied electrical potential. Because of the thinness of the passive film on Ni (< 20 Å) and its low Raman scattering

crosssection, it was necessary to use the technique of surface enhancement. This was done by electrodeposition of a silver overlayer on the Ni surface by a procedure that has been described previously.³⁾ Scanning electron microscopic study of the deposited silver shows an average particle size on the order of 500 to 1000 Å with only partial coverage of the Ni surface.⁴⁾

B. Results and Discussion

Fig. 2 shows the current-potential behavior of Ni in 0.1 M NaOH solution (pH 12) and the effect of the Ag overlayer on the electrochemical behavior. The anodic dissolution behavior with or without the Ag overlayer is essentially the same; the higher cathodic current at about -0.4 V with the Ag overlayer is due to the catalytic activity of Ag towards the reduction of dissolved O₂. The anodic peak (1) at -0.25 V and the cathodic one (2) at -0.2 V are due to the anodic oxidation and reduction of the Ag, respectively. Peaks I and II are due to oxidation of nickel leading to the formation of surface films, which were identified by SERS as discussed below.

Fig. 3 shows in-situ SER spectra of the surface film on Ni as a function of potential. Following the electrodeposition of silver and precleaning of the electrode at -1.3 V for 15 minutes, we obtained an in-situ spectrum of the surface on holding the potential at -1.0 V for 1 hour (Fig. 3a). The absence of a discernible Raman band indicates that initially the surface is relatively free of oxide or hydroxide films at this potential. On increasing the potential to -0.8 V (in the so-called prepассив region, Fig. 2), a band at about 450 cm⁻¹ starts to appear, indicating the formation of a surface film. This band is assigned to the Ni-OH vibration of Ni(OH)₂, in accordance with the work of DeSilvestro et al.⁵⁾, who have extensively studied the SER spectra of Ni(OH)₂ prepared by cathodic deposition on a roughened gold electrode. Further confirmation of the correctness of this assignment is the observation of the OH stretching vibration of Ni(OH)₂ at about 3630 cm⁻¹, as shown in Fig. 4a to 4c.

On scanning the potential further and holding at -0.4 V, we obtained the in-situ spectrum shown in Fig. 3c. A new band is evident at about 512 cm⁻¹, along with the old one at 456 cm⁻¹. We assign this new band to NiO by comparison with the spectrum of a standard sample of NiO.⁴⁾ Increasing the potential to 0 V resulted only in an increase in intensity of the two bands (Fig. 3d), presumably due to an increase in the thickness of the corresponding surface films with potential. A corresponding increase in intensity of the OH vibration is also observed (Figs. 4a to 4c).

On reversing the potential scan and holding at -0.9 V, we observed a considerable reduction in the intensity of the bands at 450 and 510 cm⁻¹ (Fig. 3e). The bands, however, do not completely disappear even after 2 hours, suggesting slow kinetics or some irreversibility in the reduction of the surface film.

Similar results are obtained in 0.15 M NaCl solution, for which the current-potential relation is shown in Fig. 5. The same two peaks (I and II) are observed as in 0.1 M NaOH. In contrast, however, breakdown of the passive film appears to occur at about 0.2 V in the presence of chloride. The in-situ Raman spectrum obtained upon potentiostating at -0.75 V is shown in Fig. 6a. The band at 450 cm⁻¹ assigned to Ni(OH)₂ is again clearly evident. On increasing the potential to -0.4 V, new bands appear at 215 and 510 cm⁻¹ (Fig. 6b). The former is assigned to Cl⁻ adsorbed on the Ag overlayer, which is commonly observed in SERS studies in chloride solutions⁶⁾. It is interesting to note once again how the appearance of the 510 cm⁻¹ band due to NiO correlates with the occurrence of wave II in the voltammogram. Spectra obtained in the

region of the OH vibration once more show a band at about 3640 cm^{-1} at potentials where the 450 cm^{-1} band is also observed.

Essentially the same spectroscopic results were obtained for Ni in acidified 0.15 M NaCl solution (pH 2.7), although the intensities of the 450 and 510 cm^{-1} bands are considerably lower, due presumably to the thinness of the film.

The principal results that emanate from this work are:

- 1) The observation of the presence of both $\text{Ni}(\text{OH})_2$ and NiO in the surface film(s) on nickel in the passive potential region for all the solution studied from pH 2.7 to 12.
- 2) The correlation between the formation of $\text{Ni}(\text{OH})_2$ with the first anodic wave (I) and that of NiO with the second wave (II) in the current-potential curve.

There has been no consensus on the composition of the passive film on nickel despite over fifty years of research investigations. Some workers^{7,8)} claim that the film is $\text{Ni}(\text{OH})_2$, while others believe that it is NiO .^{9,10)} Our results show unequivocally that both species are present in the surface film on Ni in the passive potential region. We also showed that $\text{Ni}(\text{OH})_2$ and NiO are formed separately, consistent with thermodynamic calculations,⁴⁾ and contrary to suggestions that NiO is produced by dehydration⁷⁾ of $\text{Ni}(\text{OH})_2$.

II. Specular X-ray Reflection from Electrode Surfaces

The advent of high intensity synchrotron radiation sources has recently led to a renaissance in the use of X-ray techniques for the study of surface and interface phenomena. X-ray reflectivity (XRR) measurements appear to have great potential for the in-situ characterization of the electrode/solution interface but this potential has not been generally appreciated. In spite of the early demonstration of the utility of the technique for investigation of surfaces in ambient air by Kiessig,¹¹⁾ its extension to the study of the solid/liquid interface under potential control has been limited. To our knowledge, Bosio et al.^{12,13)} appear to have carried out the first reflectivity measurements on an electrode in-situ; however, they were mainly interested in EXAFS information on the surface oxide on Ni and obtained this at grazing angle of incidence by a technique they called REFLEXAFS. Ocko et al.¹⁴⁾, more recently, studied the reconstruction of the Au(001) surface as a function of electrode potential using X-ray reflectivity and diffraction techniques. They showed that at -0.4 V (vs Ag/AgCl reference, in 0.01 M HClO_4 solution), the gold surface exhibits a hexagonal reconstructed layer with a mass density 21% greater than the underlying bulk layers. The reconstruction disappears above 0.5 V but is reversible when the potential is held again below -0.3 V . We have recently used X-ray reflectivity measurements to study the changes in the surface structure of a copper electrode as a function of applied potential in borate solution.¹⁵⁾ We present here briefly some of the results that demonstrate the utility of the technique for in-situ surface and interface characterization.

A. Experimental

An experimental setup for in-situ reflectivity measurements from electrode surfaces is shown schematically in Fig. 7. X-rays from a synchrotron or a rotating anode X-ray generator are monochromatized, collimated, and focused onto the electrode surface near the critical angle. The angle of incidence (θ) is scanned using a spectrometer that also serves to support and align the sample. The specularly reflected X-rays, with intensity I_R , are detected using a NaI scintillation

detector. This signal is used along with the monitored intensity of the incident beam, I_0 , to obtain the normalized reflectivity, I_R/I_0 .

The copper electrode consisted of ~ 250 Å film that was vacuum evaporated onto a polished Si(111) substrate; the active electrode area was ~ 0.32 -cm wide x 3.65-cm long. The electrode was mounted in an X-ray/electrochemical cell fitted with 0.025-mm-thick Teflon (FEP) windows. Details of this cell have been published.¹⁶⁾ The 1.48 Å X-rays used suffered a 95% decrease in intensity in traversing a solution path length of ~ 0.32 cm. The X-ray reflectivity was

measured in-situ as a function of $Q (= \frac{4\pi\sin\theta}{\lambda})$, the momentum transfer vector, and also at different potentials in borate buffer solution (pH 8.4).

B. Results and Discussion

The electrochemical behavior of copper in borate solution is shown in Fig. 8. Peaks I and II in the current-potential curve indicate the oxidation of the surface to form Cu(I) and Cu(II) oxides; subsequent reduction of the surface films occurs during the reverse scan of the potential (peaks III and IV).

Fig. 9 shows the reflectivity of the electrode measured while under potential control at four different points (i.e., A, B, C, and D in Fig. 8) in the current-potential curve. The reflectivity curves indicate the condition of the electrode surface at open circuit (A, -0.12 V), upon reduction of the surface film (B, -0.8 V), on anodic oxidation to form the surface oxides (C, $+0.4$ V), and on subsequent cathodic reduction at -0.8 V (D).

Several theoretical treatments of X-ray scattering from surface and multilayer films have appeared in the literature.^{17,18,19)} To obtain physical parameters from the experimentally measured reflectograms, application is made of Fresnel's laws of reflection for treatment of the data. In our analysis, we employed a kinematic approximation with conformally rough interfaces. This means that in our system, consisting of copper with a copper oxide film in contact with the solution, the roughness of the copper oxide/solution interface is correlated with that of the copper/copper oxide interface. In this case, the reflectivity, with appropriate corrections, has been derived by You,²⁰⁾ as:

$$\begin{aligned} \frac{I_R}{I_0} = & A^2 + B^2 \exp[-Q_{sol} \sigma_1] + C^2 \exp[-Q_{sol} \sigma_2] \\ & + 2AB \cos(Q_{sol} d_1) \exp[-Q_{sol}(\sigma_1 + \sigma_c)] \\ & + 2AC \cos[Q_{sol}(d_1 + \Delta d)] \exp[-Q_{sol}(\sigma_2 + \sigma_c)] \\ & + 2BC \cos(Q_{sol} \Delta d) \exp[-Q_{sol}(\sigma_1 + \sigma_2)] \end{aligned}$$

where:

$$A = \left(\frac{Q_{\text{Si}} - Q_{\text{Cu}}}{Q_{\text{Si}} + Q_{\text{Cu}}} \right) \left(\frac{4Q_{\text{sol}}Q_{\text{Cu}}}{(Q_{\text{sol}} + Q_{\text{Cu}})^2} \right)$$

σ_1 = rms roughness of the Cu/Cu₂O interface

σ_2 = rms roughness of the Cu₂O/solution interface

$$B = \left(\frac{Q_{\text{Cu}} - Q_{\text{Cu}_2\text{O}}}{Q_{\text{Cu}} + Q_{\text{Cu}_2\text{O}}} \right)$$

σ_c = correlated roughness of oxide film

d_1 = thickness of the copper film

$$C = \left(\frac{Q_{\text{Cu}_2\text{O}} - Q_{\text{sol}}}{Q_{\text{Cu}_2\text{O}} + Q_{\text{sol}}} \right)$$

Δd = thickness of the Cu₂O film

Also,

$Q_n = (Q^2 - 4.285 \times 10^{-4} \rho_n)^{1/2}$, for $n = \text{Cu}, \text{Si}, \text{Cu}_2\text{O}$, and the solution (sol), where ρ_n = the density of n .

Moreover, our data appear to be better fitted by assuming a Lorentzian distribution function instead of the Gaussian function commonly employed by others.¹⁸⁾ A nonlinear least squares fitting procedure using the foregoing equations allowed the film thickness d , density ρ , and σ parameters to be obtained from the experimental data. Taking the density of pure copper to be 8.92 g/cm³ and that of the copper oxide film to be 5.5 g/cm³ the parameters given in Table I are derived.²⁰⁾ The initial thickness of the copper film on silicon was 285 Å. This changes with potential due to the formation and reduction of the surface oxide (here taken as Cu₂O). The correlated roughness varies also with potential but the interface roughnesses seem relatively unaffected. The important point to emphasize here is that we are now beginning to obtain atomistic information on the physical structure of metals in solution environments in-situ under the influence of an applied potential; some of this information is not obtainable by any other means. One can expect application of the XRR technique to other interesting problems in corrosion science and technology in the near future.

III. Acknowledgment

The work on X-ray reflectivity was carried out in collaboration with H. You, Z. Nagy, V. A. Maroni, and W. Yun, all of Argonne National Laboratory. M. Pankuch carried out most of the laser Raman scattering measurements. The author gratefully acknowledges the contribution of these colleagues. Support for these research projects was provided by the Division of Materials Sciences, Office of Basic Energy Sciences, U.S. Department of Energy.

IV. References

- 1) C. A. Melendres, in Electrochemical and Optical Techniques for the Study and Monitoring of Metallic Corrosion, M. G. S. Ferreira and C. A. Melendres (editors), Kluwer Academic Publishers, Dordrecht (1992), p. 355.
- 2) R. K. Chang and T. E. Furtak (editors), Surface Enhanced Raman Scattering, Plenum Press, NY (1982).
- 3) C. A. Melendres, J. Acho, and R. L. Knight, *J. Electrochem. Soc.* **138**, 877 (1991); J. Gui and T. M. Devine, *ibid.*, **138**, 1376 (1991).
- 4) C. A. Melendres and M. Pankuch, *J. Electroanal. Chem.* **333**, 103 (1992).
- 5) J. Desilvestro, D. A. Corrigan, and M. J. Weaver, *J. Electrochem. Soc.* **135**, 885 (1988).
- 6) R. K. Chang and B. L. Laube, in CRC Critical Rev. Solid State Materials Sci. **12**, (1984).
- 7) W. Paik and Z. Szklarska-Smialowska, *Surface Science* **96**, 401 (1980).
- 8) B. Beden and A. Bewick, *Electrochimica Acta* **33**, 1965 (1988).
- 9) W. Visscher and E. Barendrecht, *Surface Science* **135**, 191 (1976).
- 10) B. MacDougall and M. Cohen, *J. Electrochem. Soc.* **123**, 191 (1976).
- 11) H. Kiessig, *Ann. Phys.* **10**, 714 (1931).
- 12) L. Bosio, R. Cortes, A. Defrain, M. Froment, and A. M. Lebrun, in Passivity of Metals and Semiconductors, M. Froment (editor), Elsevier, Amsterdam (1983), p. 131.
- 13) L. Bosio, R. Cortes, A. Defrain, and M. Froment, *J. Electroanal. Chem.* **180**, 265 (1984).
- 14) B. M. Ocko, J. Wang, A. Davenport, and H. Isaacs, *Phys. Rev. Lett.* **65**, 1466 (1990).
- 15) C. A. Melendres, H. You, V. A. Maroni, Z. Nagy, and W. Yun, *J. Electroanal. Chem.* **297**, 549 (1991).
- 16) Z. Nagy, H. You, R. Yonco, C. A. Melendres, W. Yun and V. A. Maroni, *Electrochim. Acta* **36**, 209 (1991).
- 17) L. G. Parratt, *Phys. Rev.* **95**, 359 (1954).
- 18) R. Cowley and T. W. Ryan, *J. Phys. D: App. Phys.* **20**, 61 (1987).
- 19) S. K. Sinha, E. B. Sirota, and S. Garoff, *Phys. Rev. B.* **38**, 2297 (1988).
- 20) H. You, C. A. Melendres, Z. Nagy, V. A. Maroni, W. Yun and R. M. Yonco, *Phys. Rev. B.* **45**, 11288 (1992).

TABLE I. Parameters derived from least squares fit to experimental data

| E/V | $d_{Cu}/\text{\AA}$ | $d_{Cu_2O}/\text{\AA}$ | $\sigma_c/\text{\AA}$ | $\sigma_{Cu_2O/Cu}/\text{\AA}$ | $\sigma_{Cu_2O/sol}/\text{\AA}$ |
|-------|---------------------|------------------------|-----------------------|--------------------------------|---------------------------------|
| -0.12 | 273 | 12 | 16 | 4.6 | 4.4 |
| -0.8 | 285 | (0) | 11 | 3.3 | 4.6 |
| +0.4 | 250 | 35 | 25 | 5.6 | 4.4 |
| -0.8 | 276 | (9) | 12 | 5.3 | 4.6 |

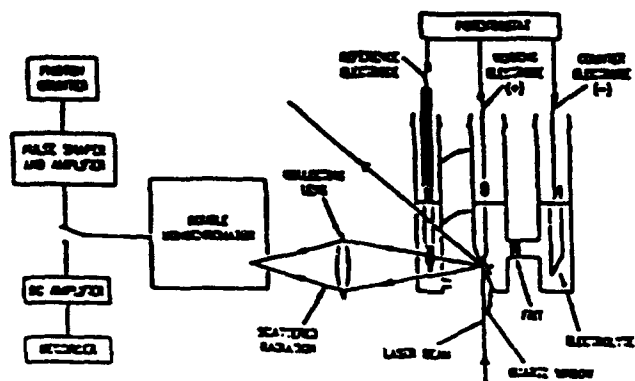


Fig. 1. Experimental set-up for laser Raman spectroelectrochemical studies.

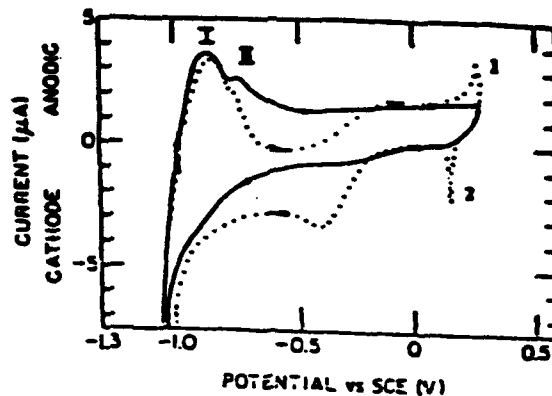


Fig. 2. Cyclic Voltammogram of Ni in 0.1 M NaOH solution. Scan rate = 5 mV/sec
 — without Ag overlayer
 ... with Ag overlayer

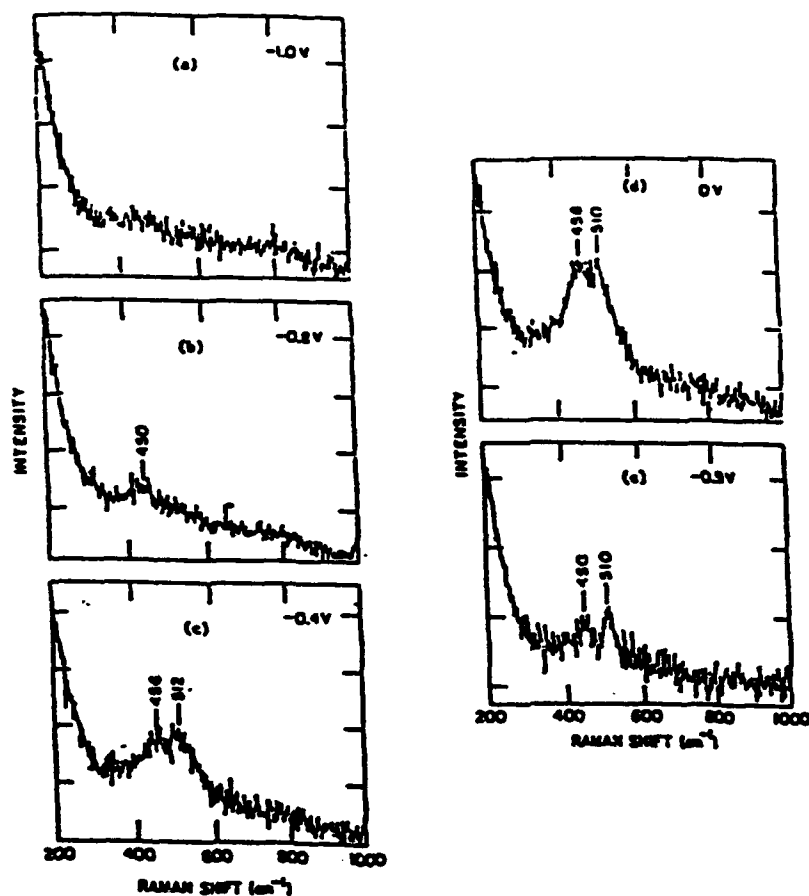


Fig. 3. Laser Raman Spectra of Nickel in 0.1 M NaOH Solution at Various Potentials. Ar⁺ Laser, 514.5 nm line, P~100 mW.

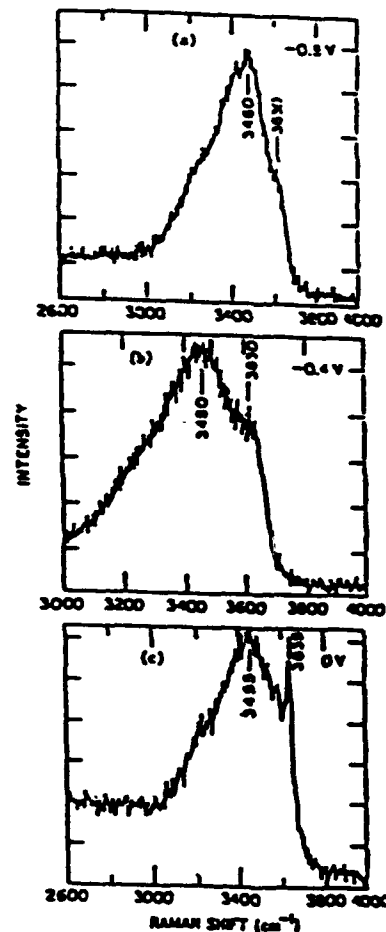


Fig. 4. Laser Raman Spectra of Ni in the OH Stretching Region.

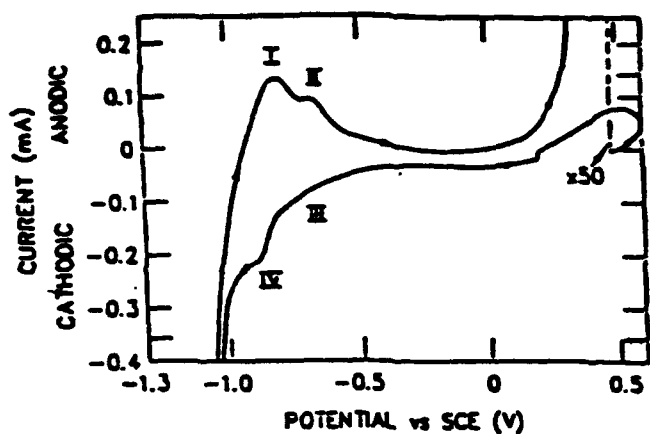


Fig. 5. Cyclic voltammogram of nickel in 0.15 M NaCl solution (pH 8.5). Scan rate = 10mV/sec.

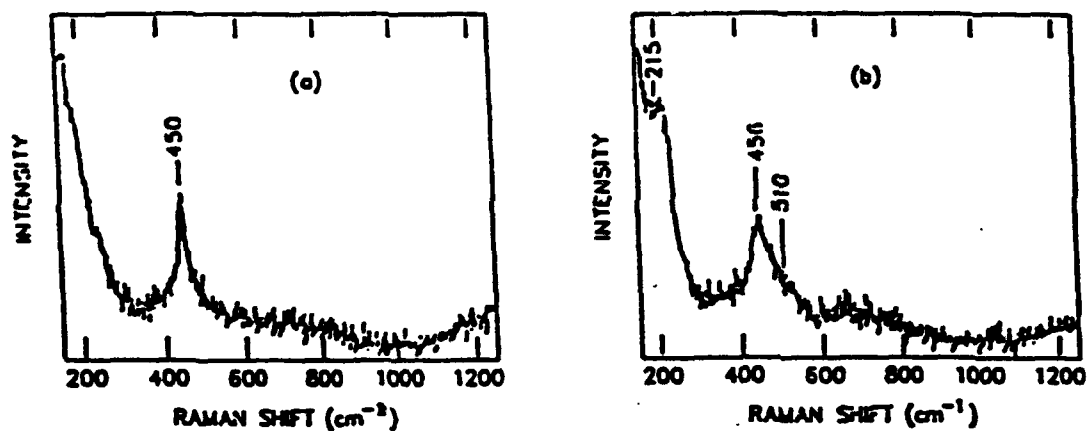


Fig. 6. Surface enhanced Raman spectrum of corrosion film on nickel in 0.15 M NaCl at various potentials. a) $E = -0.75$ V, b) $E = -0.40$ V. Ar⁺ laser, 514.5 nm line, 100 mW.

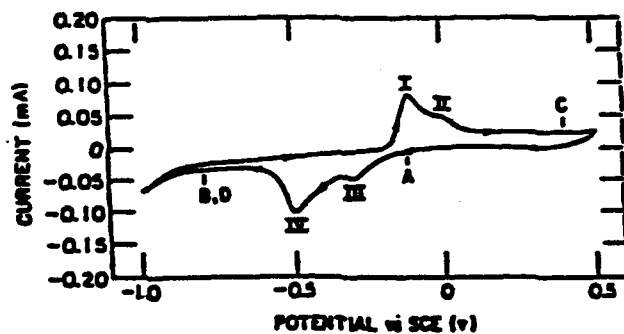


Fig. 8. Cyclic voltammogram of Cu-on-Si electrode in borate buffer solution (pH 8.4), Scan rate = 10 mV/sec.

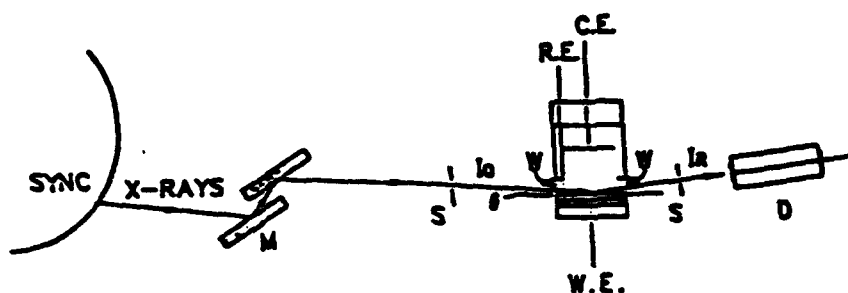


Fig. 7. Schematic of Set-up for In Situ X-ray Reflectivity Measurements

SYNC = Synchrotron source.

M = Si(111) double crystal monochromator.

S = Slit.

W = Teflon window

R. E. = Reference electrode.

C. E. = Counter electrode.

W. E. = Working electrode.

D = Scintillation detector.

I_0 , I_R = Incident and reflected X-ray beams, respectively.

θ = Angle of incidence.

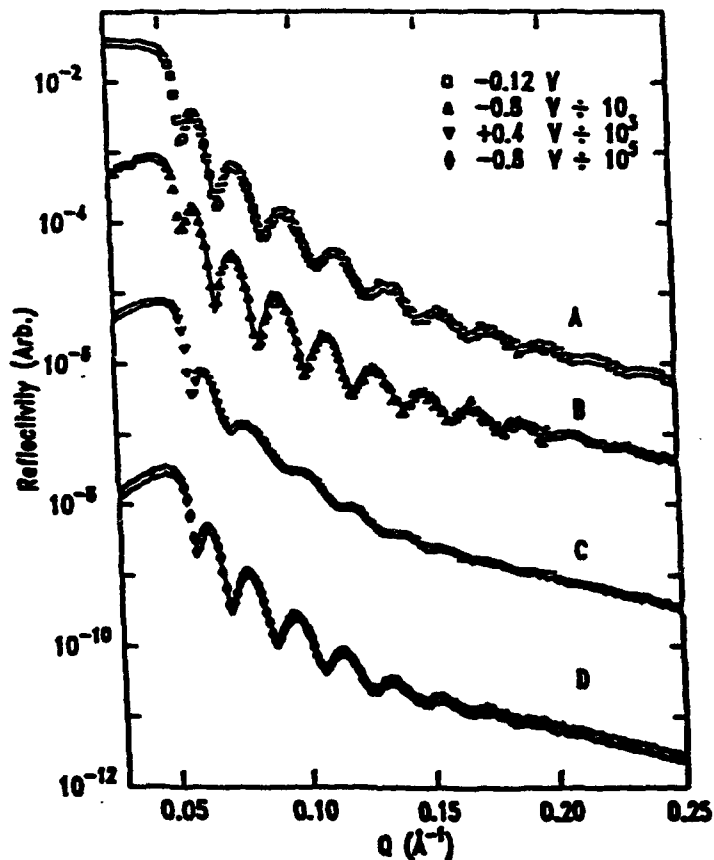


Fig. 9. Reflectivity of Cu-on-Si electrode at various potentials in borate buffer solution (pH 8.4). A, B, C, D correspond to potentials indicated in cyclic voltammogram of Fig. 8

Studies by Scanning Auger Microscopy of Electrochemical Corrosion: Serendipity and the SAM

J E Castle
Department of Materials Science and Engineering
University of Surrey
Guildford GU2 5XH England

Abstract

At any site of localised corrosion there will be microscopic separation of anodic and cathodic flows of current through the surface. The current flow will in turn set up concentration gradients within the electrolyte adjacent to the metal which in some cases leaves a tell-tale sign in the surface composition. At the macroscopic level this is seen as the 'cathodic chalk' deposited from marine environments on cathodic protection systems, or as staining by the ionic effluent from small pits. Over a period of many years we have sought these tell-tales by scanning Auger electron microscopy and now use them with some confidence to reveal the location and degree of separation of anodic and cathodic sites. In this paper the work is reviewed, giving examples from localised attack within crevices, at inclusions, and in metal matrix composites. Attempts have been made, by both calculation and by comparison with whole electrodes at controlled electropotentials, to relate the observed surface composition to the local electrode potential at the site of attack. Progress in this work will be described.

Key terms: Auger Electron Spectroscopy; Pitting Corrosion; Electrochemistry

Introduction

Auger spectroscopy is surface sensitive but is not particularly sensitive to chemical state. It is therefore of value in discovering foreign elements at the surface and of pinpointing their location. The question which is posed in this paper is whether we have to leave any positive outcome to serendipity (Defined in the Oxford English Dictionary as "The faculty of making happy and unexpected discoveries by accident") or whether the investigator can play a more purposeful role.

The starting point of course is that the presence, or otherwise, of particular elements on a surface does not establish a causal relationship with corrosion. We need to go further and associate the ions with either (a) a current flow through that part of the surface or (b) a particular electropotential on that surface. Either a current flow or a potential difference might then be used to infer electrochemical activity and hence establish that sites of damage were active at the time of removal from the electrolyte. Such observations would be then of great use in both field and laboratory investigations.

Some of the circumstances which lead to ions being segregated within the surface layer are as follows:

1. Changes in potential, causing redox reactions and deposition.

2. Changes in local ion concentration, exceeding the solubility product and leading to deposition.
3. Changes in pH, a special case of 2 interacting also with 1.
4. Electromigration or potential dependent adsorption
5. Ion-exchange giving a local indication of the ion concentrations in the electrolyte.
6. Specific ions found at flaws in the protective film, although the underlying reason for such an observation is likely to be found in points 1 to 5 above.

Some of these effects will provide the route by which observation of chemical changes at the surface can be coupled into classic interpretations such as the predictions of the Pourbaix diagram. In some cases the tell-tail signs of ion concentrations will arise through chance; in other cases ions might be added to the electrolyte as markers for particular types of electrochemical activity. This paper will it is hoped guide the interpretation of the former cases and assist in the choice of ions in the latter case.

Current Flux

Anodic Sites.

Deposition of ions as a result of a current flux arises by virtue of the concentration gradient established at the surface. Material will be deposited as long as the solubility product of a sparingly soluble species is exceeded. The classic example of this would be the deposition of a chloride as a salt-layer at the base of a pit. Such chloride deposits are readily observed by Auger spectroscopy and have been shown as SAM maps by Daud¹ and by Baker² among many others (Figures 1 & 2). In the former case the pits were found within artificial crevices formed from 316 grade stainless steel and in the latter on freely exposed surfaces after times as short as 10 seconds. Deposition of the salt in this case depends on the concentration of metal ions which in turn depends on the anodic current flowing through the exposed surface within the pit. There have been attempts to describe the change in pH within pits by quantitative models^{3,4} but these do not give an estimate of the critical current for salt deposition.

The problem of predicting the current for salt precipitation as a function of the chloride ion content of the electrolyte is made difficult by several factors: the flow of chloride ions towards the anode; the fact that the system is a highly concentrated occluded cell; and because of the drying out of any solution entrapped in the pit. It is thus not possible for the spectroscopist to probe the concentration of metal ions within the pit by varying the concentration of chloride ions in the electrolyte: the link between this and the concentration in the pit is too indirect. Moreover the chloride ion is active in the corrosion process itself and thus is not suitable as an inert marker.

Field Searching.

The observation of chloride, however, is a valid indicator that an active pit has been found and Baker⁵ used this as the basis of a routine for searching large fields of view for chemical anomalies. Such anomalies often represent the first evidence of pit initiation or of pits in the metastable phase of development, Figure 3. In his method the field of view is increased until any possible cluster of chloride ions, or other significant ions,

would occupy no more than a single pixel. The intensity of the given element in each pixel in a map is then fitted to a normal distribution, such as that shown in Figure 3a. Such a distribution is essentially the result of 15600 separate analyses (for a 125 x 125 map). Most of these analyses conform precisely to the normal distribution which represents the noise in the acquisition. The search routine considers only the high intensity tail. From the main body of the distribution it is possible to predict the intensity at which there is a probability of finding no more than a single pixel. Any pixels with an intensity greater than this value outlie the normal distribution and are likely to contain a concentration of the element which is statistically significant. The position of these pixels is returned by the search routine in various ways. That shown in Figure 3b highlights their position on the SEM micrograph of the surface. It is then easy to examine these reference positions at high magnification, as in Figure 3c. The results shown in figure 3 are based on searches for small sulphur-containing inclusions. There was a good record for the finding of inclusions, by this method, within what would otherwise be a very sparse field.

Cathodic Sites.

In contrast to the problems at the anode, there are real possibilities for probing the current at the cathode. The situation at this electrode is better because it is not normally hidden in an occluded cell. Both of the common cathode reactions create a change in local pH value and this can be searched for by use of a cation which has a sparingly soluble hydroxide. The potential problem of stirring by evolution of hydrogen gas is eliminated if we consider only the case of oxygenated solutions at near neutral pH values. The local pH will rise until the rate of generation of hydroxyl ions is equal to their escape by diffusion or by reaction with hydrogen ions. This equilibrium is reached rapidly⁶ and we can then write:

$$i/A = (F/\delta)\{D_{OH}\Delta[OH] - D_{H^+}\Delta[H]\} \quad (1)$$

Addition of eg. magnesium ions to the electrolyte will, at a critical concentration, cause the precipitation of $Mg(OH)_2$ which is readily detected by SAM. The delineation of cathodes by this method has been shown by Daud¹. The determination of the current density through the cathode is possible by solution of the equation derived from (1) using the solubility product of the relevant hydroxide and the ionic product of water:

$$i/A = (F/\delta)\{D_{OH}\{((k_{sp}/[Mg])^{1/2} - k_w/[H]) + D_{H^+}\{[H] - k_w([Mg]/k_{sp})^{1/2}\}\} \quad (2)$$

Castle⁶ has shown that, for near neutral electrolytes, only the first term of this is important and the result is almost independent of the bulk pH value over a range from pH6 to pH8.

The model represented by the equation above is simply Fickian diffusion over a planar geometry. In fact the hydroxyl ions diffuse out from the centre of a hemisphere but the adoption of this more suitable geometry seems unlikely to change the critical current for precipitation of the hydroxide. Figure 4a shows how the critical current density varies with the concentration of magnesium and the diffusion distance over which the pH varies. The diffusion coefficients of hydrogen and hydroxyl ions were taken as 0.93 and $0.52 \times 10^{-8} m^2 s^{-1}$ respectively; the solubility product for magnesium hydroxide was taken as 5×10^{-11} and the pH value for the curves shown in Figure 4a was taken to be 6.0.

Figure 4b shows the influence of pH value, the curves being calculated for a diffusion distance of 10 μm . The pH value, over the range 5.5 to 8.5, has much less influence than either the concentration of magnesium or the diffusion distance. It is this latter which is most difficult to estimate. In SAM maps of anode/cathode distribution, eg, as shown by Ke^9 (Figure 6), the annular cathode around the anode has a radius of about $2r$, where r is the radius of the central anode. The scale is thus somewhere in the range 1 μm to 40 μm and the curves provided straddle this range.

An illustration of the use of the curves is given in Figure 5, together with a scatter diagram for correlation. This shows an iron-aluminium intermetallic compound in a aluminium alloy 6061/silicon carbide MMC (metal matrix composite) which had been exposed in 0.1M MgCl_2 solution at pH7.

The correlation of magnesium and the iron intermetallic is revealed readily by use of the scatter diagram produced using software developed by Yan in this laboratory. A scatter diagram examines pairs of maps for correlations or anticorrelations. The pairs can be mixed as elements, as mode (X-ray, Auger electron, or secondary electron) and the analysis yields the position of particular surface phases, regions of interdiffusion, or even enables different thicknesses to be distinguished as shown in Figure 7. Scatter diagrams are thus invaluable for making informed searches of corroded surfaces. In this case, the strong correlation between Mg and Fe confirms the cathodic nature of the inclusions. No deposition occurred on the silicon carbide indicating that these lacked strong electrochemical activity. However scatter diagrams can yield the composition of any surface phases and are often as informative as the maps themselves.

In further studies, precipitation of magnesium hydroxide was found to occur in a solution of 1M sodium chloride containing magnesium ions at a concentration of 0.01M but not at 0.001M. This indicates that the current density through this cathodic particle reached at least $1.2\text{mA}/\text{cm}^2$. It is interesting to note that in this field of view there were several smaller intermetallics which had not picked up magnesium - showing the important influence of the diffusion distance; as shown in Figure 4 these would have required a significantly greater current density.

Curves similar to those in Figure 4 can be drawn for any cation which will precipitate at high pH and which does not interfere with the corrosion reaction: in our original work on plane electrodes we used cadmium ions also. There is thus ample scope for the SAM microscopist to undertake searches for active electrochemical systems using the method of cathode decoration. The sharp rise in current needed to sustain precipitation at pH values below 5 shows that the method is only suited to near-neutral conditions. Methods for the decoration of electrodes in the acidic conditions to which stainless steels are often exposed will therefore need to be based on different ions.

In recent work on pitting corrosion Baker⁷ has found evidence (serendipity again!) that anions too respond to the abrupt change in pH around the anode. In this case semi-permeable membranes of the type found in 'chemical gardens' appear to be formed by precipitation of silicates as the pH drops, Figure 6. Many other anions may be influenced by pH changes in the same manner and an indication of these is given in his paper. Whilst ions such as silicate and aluminate might be suitable markers, one

potential problem is that the formation of membranes is likely to give additional stability to metastable pits and thus have an influence on the course of corrosion.

Local Potential

Potential-Sensitive Deposition.

The precipitation reactions referred to above do not consume electrons and are not therefore sensitive to the electropotential of the surface. Other reactions, including some well known as providing marker action, are sensitive to potential. Typical of these is the reduction of copper ions to copper metal at the cathode. This reaction has been used in the past to decorate, and thus reveal, the presence of cracking in scales formed at high temperature⁸. In this paper it was shown that cathodic reduction of iron oxide would also accompany deposition of copper - a solution of nickel sulphamate has some advantages in this respect. Clearly, as in the case of searching for cathodic current with cation probes, there is also the possibility of searching for cathodic potentials with the cations of the electrochemical series. So far this does not seem to have been done in a purposeful manner. The important point is that the ions chosen should not themselves be part of the metal system, nor should they stimulate corrosion in any way.

Hydrogen ions will be involved in many possible reactions and the technique for decoration must then be related to the relevant part of the Pourbaix diagram for the compounds, concentrations and pH values involved. Figure 7 is a combination of an X-ray map for sulphur, showing the position of the central inclusion, and an Auger map, showing the annular cathode decorated with sulphur produced by hydrolysis of the inclusion. Once again this image is produced from information contained within a scatter diagram. Here the X-ray and Auger maps for sulphur are anticorrelated, the pixels high in X-ray intensity show the position of the inclusion whilst those high in Auger electron intensity show the surface deposit resulting from the corrosive attack. Ke⁹ proposed that the annulus of sulphur results from decoration of the cathode by reduction of partly oxidised sulphur. In keeping with the Pourbaix diagram she showed that deposition was marked at a bulk pH value of 5 but did not occur at pH9.

Transport of Corrosion Products.

Quite often transport of the corroding species itself is observed in a way which can be distinguished. In the course of the corrosion of steel around a sulphide inclusion, iron is deposited as a cap above the inclusion. The material is an oxide or oxyhydroxide and presumably marks the pH change between the anodic side wall exposed by corrosion of the inclusion and that of the bulk medium. The formation of such a cap can be seen in Figure 8. This work is also due to Ke. A transport which is more difficult to interpret is found in the corrosion of silicon carbide fibre-reinforced aluminium¹⁰. Exposure of the cross-section of this material to sodium chloride solution results in the deposition of aluminium oxide on the pure carbon core to the silicon carbide which is exposed. Aluminium solubility is a maximum at about pH5 and thus the deposition could result from either acidic or basic excursion of the electrolyte composition at the carbon, Figure 9.

SAM and XPS

The electrochemical separation of precipitation and other reactions which is observed in the SAM results from a lateral movement of ions across the surface whilst, on whole electrodes held at a single electropotential, the principal movement of ions is

perpendicular to the surface. This will give rise to a layer-like structure showing, in this, many of the pH sensitive precipitates which are separated laterally in the SAM maps. The surfaces and interfaces, if they can be separated, are best examined by XPS. With care, important correlations can be made between the two, enabling the chemistry around a pit to be linked to the similar chemistry at known potentials on whole electrodes. Daud has done this for the case of pits in 316 stainless steel, as has been reported in a previous review¹¹.

Conclusions

There is scope for the use of markers for electrochemical activity in SAM studies. There is most to gain from the use of cations of the alkaline earth metals to determine the local variation of pH value since an estimate can then be made of the current flow through that region of the surface. However the surface potentials can also be estimated by use of easily reduced cations, or by comparison of the surface chemistry with that observed on whole electrodes held at a uniform, known potential.

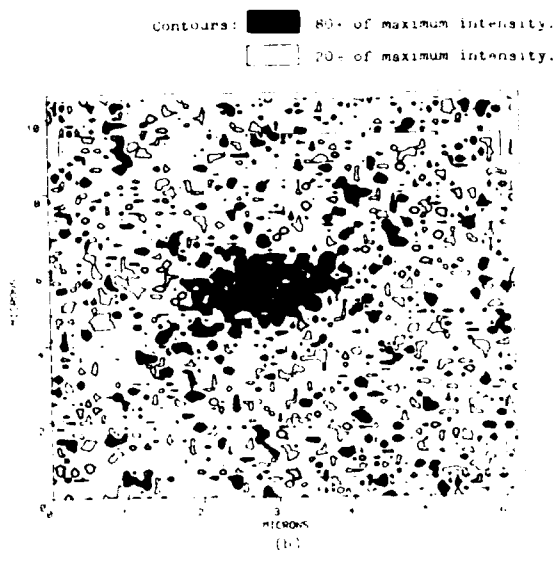
Semi-automatic searching of fields of view for significant chemical features can be undertaken by use of the intensity histogram or, preferably, by use of scatter diagrams.

Acknowledgements

It is a pleasure to acknowledge Li Sun for the provision of Figure 5 and Figure 9 in advance of publication, and M Baker for the provision of Figures 3 and 6.

References

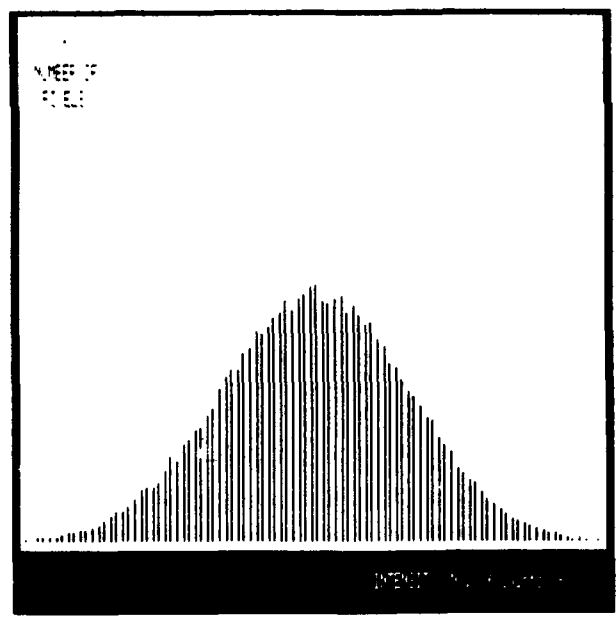
1. R. Daud, PhD Thesis, University of Surrey: (1982).
2. M. A. Baker and J. E. Castle, 11th Int. Corr. Cong. Florence. Associazione Italiana di Metallurgia (1990): pp5.1-5.15.
3. J. R. Galvele, *J. Electrochem.Soc.* **123**, (1976): pp464-474
4. R. C. Newman, *Corrosion Science*, **25**, (1985): pp341-350
5. M. A. Baker and J. E. Castle, *Inst. Phys. Conf. Sers. No.93 vol.1*, Chapter 5, (1988): pp269-270.
6. J. E. Castle and R. Tanner Tremaine, *Surf. & Interface. Anal*, **1**, (1979): pp49-52.
7. M. A. Baker and J. E. Castle, *Corrosion Science*, **33**, (1992): pp1295-1312.
8. R. Walker and S. A. Richardson, *Corrosion Science*, **20**, (1980): pp341-349.
9. J. E. Castle and R. Ke, *Corrosion Science*, **30**, (1990): pp409-428.
10. Li Sun, PhD Report, University of Surrey: (1993).
11. J. E. Castle, *Surface and Interface Analysis*, **9**, (1986): pp345-356.



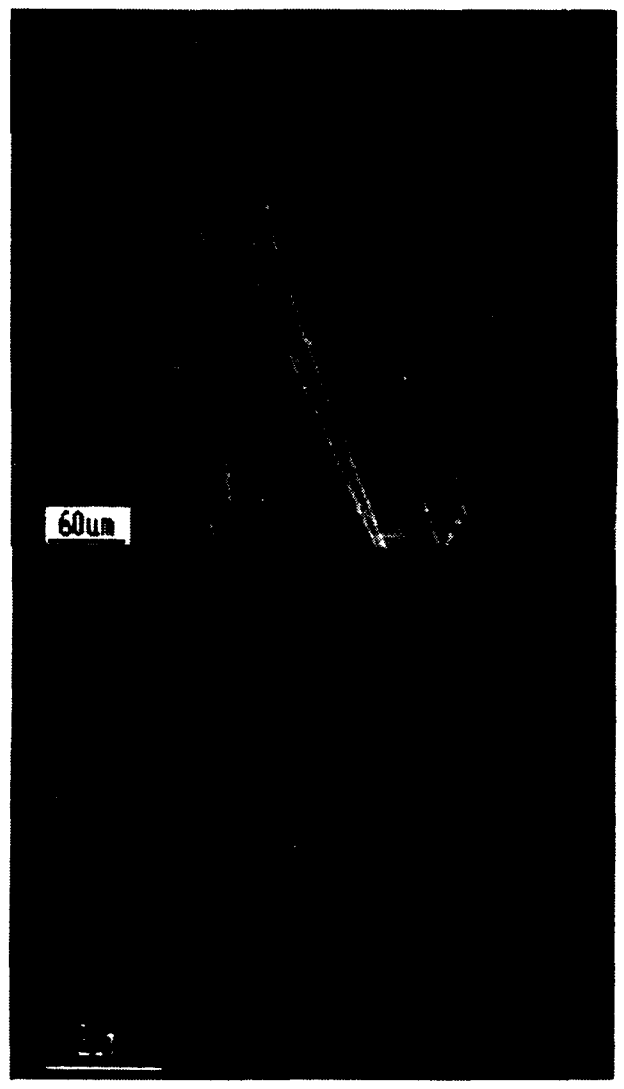
1. Map showing the chloride ions concentrated at the base of a small open pit in 316 stainless steel. The surface was exposed in an artificial crevice to 3.4% MgCl₂ solution.



2. SAM micrograph showing chloride ions clustered beneath the oxide cover on a metastable pit after an exposure to an electrolyte containing: 0.5M NaCl + 0.5M H₂SO₄ + 0.08% H₂O₂



3. Sequence showing the identification of high sulphur pixels in low magnification SAMs: The intensity histogram (top left) is examined at the high intensity tail for outliers. The position of these is indicated on the low magnification SEM (top right) and used to guide the high magnification SAM to the correct location (Side).



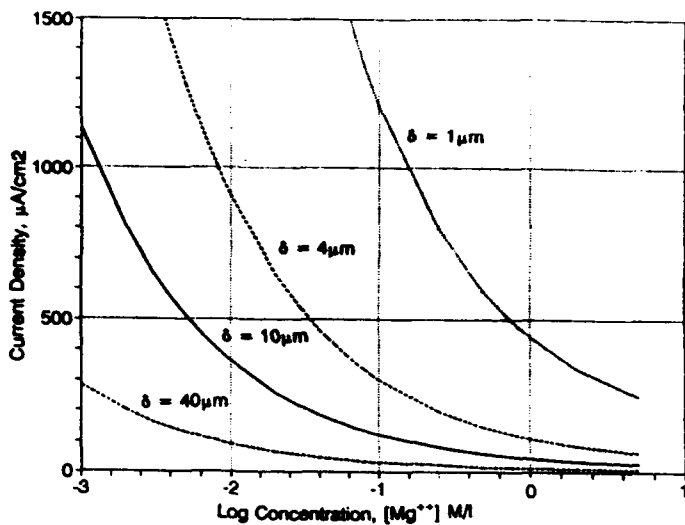


Figure 4a. The critical current density required at a cathode for the precipitation of magnesium hydroxide: the influence of magnesium concentration.

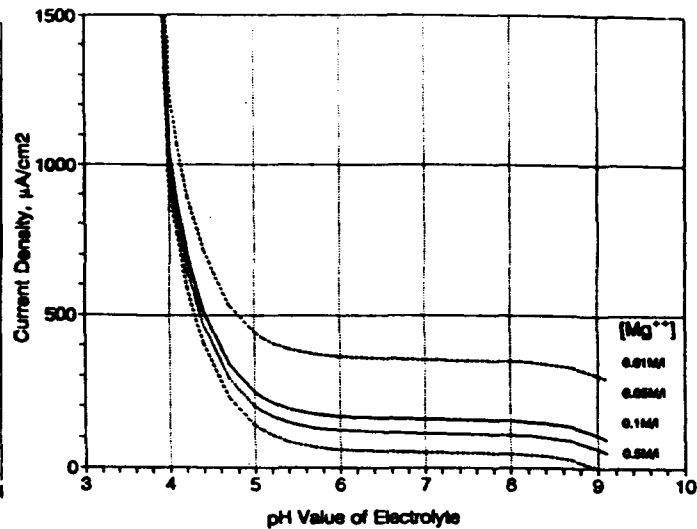


Figure 4b. The critical current density required at a cathode for the precipitation of magnesium hydroxide: the influence of pH.

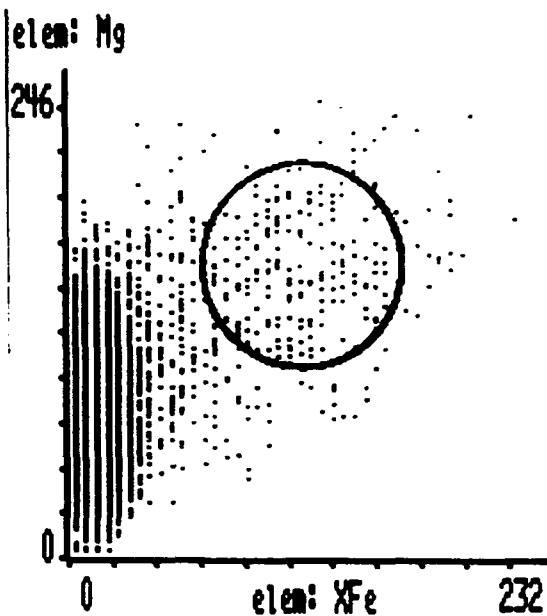


Figure 5a. The corrosion of an aluminium alloy/silicon carbide MMC. A scatter diagram showing correlated pixels which are high in both magnesium and iron. Those pixels identified within the circle are used to construct the map in figure 5b.

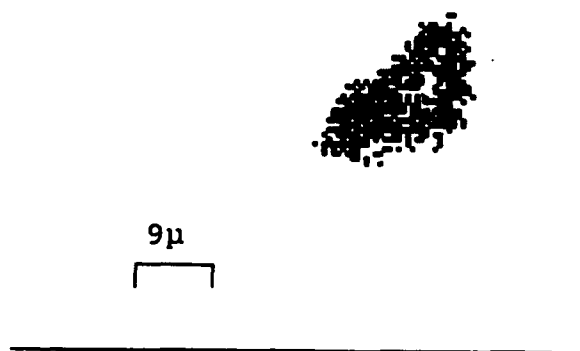


Figure 5b. Corrosion of aluminium alloy/silicon carbide MMC. A SAM showing the location of magnesium hydroxide, derived from the electrolyte, at an intermetallic particle in the alloy, which is identified by the presence of iron.

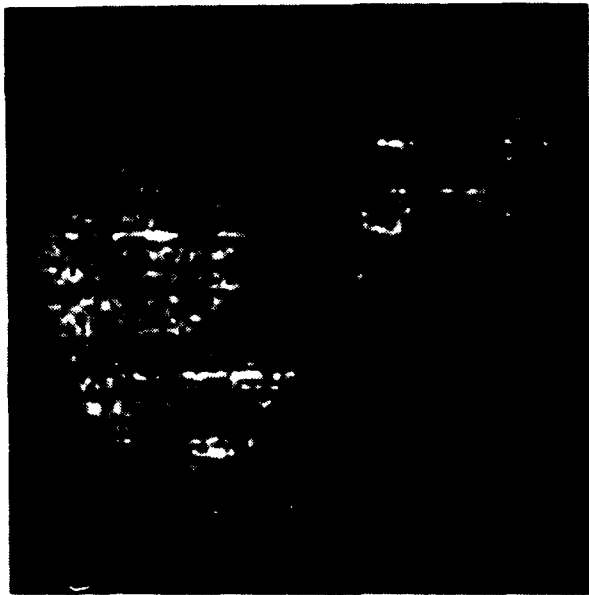


Figure 6. Corrosion of Iron-Chromium alloy. Silica, probably derived from a small oxide inclusion located between the two 'wings' has deposited as a membrane associated with an acidic effluent from the growing pit.

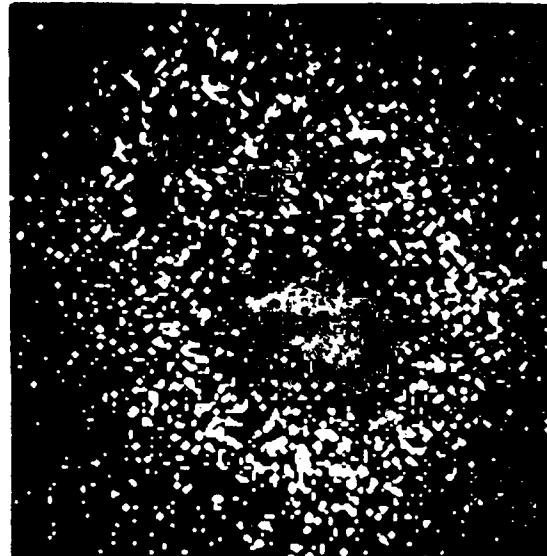


Figure 7. The initial stages of corrosive attack at a manganese sulphide inclusion in sodium chloride solution. This combination X-ray and Auger electron map shows the location of the central inclusion and the position of the surrounding anode which is decorated with electrodeposited sulphur.

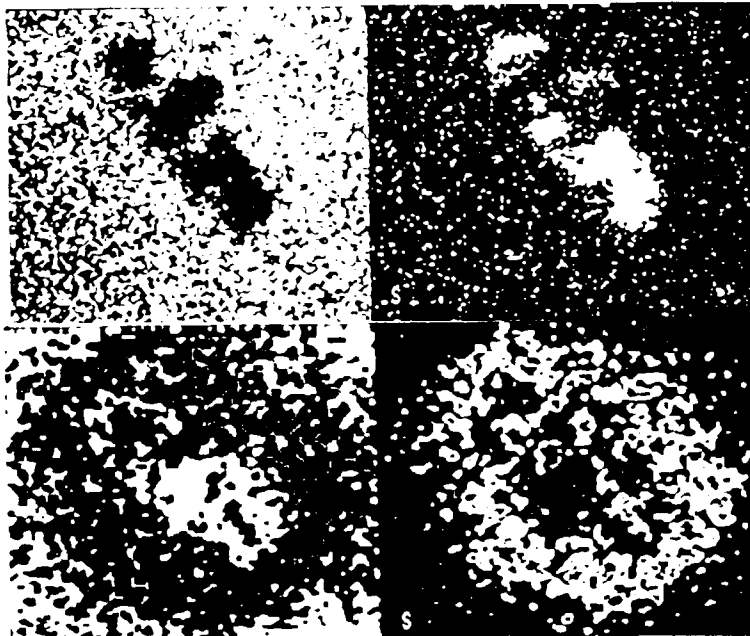


Figure 8. Corrosion of Stainless Steel. Iron is absent from the site of the manganese sulphide inclusion prior to corrosion (top left) but deposits as a cap to the inclusion during a 35min. exposure to sodium chloride solution (bottom left). During this time sulphur, hydrolysed from the inclusion (top right), is electrodeposited at the cathode.



Figure 9. Corrosion of silicon carbide fibre/aluminium alloy MMC. Transport of aluminium corrosion product to the exposed graphite core of the fibre.

Alloy Oxidation: Who is in Control as Studied by XPS

David L. Cocke
Gill Chair of Analytical Chemistry
Lamar University
Beaumont, TX 77710

Abstract

Metal alloys show a rich and complex surface chemistry in both thermal and anodic oxidation. By comparing the thermal oxidation of titanium-aluminum and titanium-copper alloys ($\text{Ti}_{36}\text{Cu}_{64}$ and $\text{Ti}_{36}\text{Al}_{64}$), we have been able to delineate those factors which are most important to the oxide formation process. XPS has been shown to provide valuable input to determining "who" is in control. This is clearly shown to be the potential and its accompanying electric field that develops or is applied during thermal or anodic oxidation, respectively.

Key terms: thermal oxidation, anodic oxidation, alloys, TiAl, TiCu,

Introduction

Alloy corrosion is today a major research and engineering challenge¹⁻³. Metal alloys show a rich and complex surface chemistry in both thermal and anodic oxidation. Today however there remains much to learn about alloy oxidation in both regimes. The interaction of individual crystalline metals with oxygen has been the subject of many studies⁴⁻⁹ and there is substantial understanding of both thin film and thick film oxidation. In recent years X-ray photoelectron spectroscopy, XPS, has played a substantial part in developing this understanding. The interaction of oxygen with alloys and amorphous metals has been less extensively studied than the individual crystalline metals^{10,11}. Low and medium temperature thermal oxidation processes have some strong commonalities with electrochemical oxidation processes as the recent works by Ritchie and co-workers^{12,13} has emphasized. A typical metal oxide system can be described in terms of four regions (see Figure 1): (A) the metal or alloy bulk. (B) a thin amorphous oxide layer at the metal/oxide interface, (C) a uniform crystalline oxide layer and (D) a thin outer layer where the metal is in its highest oxidation state. The study of the thermal oxidation of metals and alloys has been extensively studied in our laboratory by XPS and this work will be summarized and related to both electrochemical and thermal models.

Surface Reactivity

Surface reactivity involves the mutual interactions between the metal surface and the reactants and is linked to the electronic and geometric structure of surfaces and their defect structure. We have been studying the reactivity of oxygen with metals in the amorphous state, since they are structurally and chemically homogeneous while the crystalline state has grain boundaries, precipitates, segregates, and dislocations. Hashimoto¹⁴ concluded that for surface reactivity studies the amorphous state provides a good contrast to the crystalline state. Insight into the nature of the chemical interactions that are responsible for the unusual surface properties of amorphous metals will further our fundamental understanding of the influence of surface defects on gas-solid reactions^{15,16}. In addition to providing valuable information on the fundamentals of alloy oxidation, passivation, anodization and corrosion, the results are very pertinent to oxidative changes affecting heterogeneous catalysis by alloys where better understanding is coming from concurrent study of the crystalline¹⁷⁻²⁴ and the amorphous state²⁵⁻²⁷. Oxidative surface reactivity of metals and alloys can be divided into two very related areas of thermal and electrochemical processes. These areas will be introduced and shown to be quite similar in their theoretical interpretation.

Thermal Reactions. We have shown in our surface studies (see Table 1) of post chemisorptive oxidation of Cu-Mn²⁸, Ag-Mn²⁹, Ni-Zr¹⁸⁻²⁰, Ni-Ti²¹, Ni-Hf²², Ti-Cu^{24,27} and Ti-Al^{24,30} that the parameters that control alloy oxidation can be delineated and that selective oxidation of the components combined with ion movement are the key components of the surface layer growth and subsequent structure. In general, oxidation can be discussed in terms of the modified Cabrera and Mott model⁸:

$$\Delta\Phi = -\Delta G^\circ_f/2e + (kT/2e)\ln[4e^2N_s(a_{O_2})^{1/2}x/kT\epsilon\epsilon_0]$$

where $-\Delta G^\circ_f$ is the free energy of formation of oxygen anions at the surface (approximated by the free energy of formation of the oxide per oxygen atom), plus a term related to the temperature, T ; the total number of surface O^{2-} ions in unit area of surface, N_s ; the oxygen activity, a_{O_2} ; the film thickness, x ; the electronic charge, e ; the relative electron permittivity (the dielectric constant), ϵ ; and the electron permittivity in vacuum, ϵ_0 .

Electrochemical Oxidation. Electrochemical oxidation is complicated by the presence of water, ions and the reaction which supplies oxide ions: $OH^- = H^+ + O^{2-}$. However the exact mechanism of O^{2-} formation in thermal oxidation is not known, even though this reaction is probably the key reaction driving the oxidation process through the electric fields it produces. This can involve O^{2-} or other surface species, either charged (O^- , O_2^-) or uncharged (O_2 , O). The progress in understanding metal oxidation is illustrated by the recent series of papers of D'Alkaine and co-workers³¹⁻³³ on the electrochemical oxidation of niobium. These authors consider two of the three interfaces, illustrated in Figure 1, as well as the bulk of the oxide layer in their models. There has been some very important progress in understanding the anodic oxidation of alloys³⁴. Here selective oxidation, dissolution and interdiffusion are being considered. Seo and Sato³⁵ discuss surface enrichment and its effect on passivation. Heusler³⁶ and Kirchheim³⁷ have considered the phenomenological description of these processes. The advances in electrochemical oxidation of alloys is illustrated with the recent work of Marcus and Grimal³⁸ on the nature and composition of the passive film on Ni-Cr-Fe alloys. Here determination of the physical nature of the passive layer (bilayer structure, composition, chemical states of the elements, distribution of the species in the film, and film thickness) and the importance of hydroxides, selective dissolution of Ni and Fe and surface enrichment of chromium to the dissolution and passivation phenomena have allowed the passivation mechanisms to be divided in three steps: (1) enrichment of chromium at the alloy surface by selective dissolution and adsorption of hydroxyl ions, (2) growth of Cr_2O_3 islands within an hydroxide layer and (3) formation of a thin, continuous and compact chromium oxide layer covered with hydroxide. Characterization work of this nature is allowing continued progress in the development of models and theory of electrochemical oxidation.

Theory and Models

The thermodynamic driving force for the oxidation reaction can be considered as the change in the standard free energy resulting from the formation of the oxide from the reactants and is negative for all metals. In electrochemical processes, much of the work has considered the applied voltage to be used for the electric field inside the film, thus ignoring the contributions of the metal/oxide and the oxide/solution interfaces. In general, the hopping-motion model has been used or modified to account for some anomalous effects³⁹⁻⁴². In addition, an ionic motion model based on a non-simultaneous place exchange, as proposed by Fromhold⁴³ has been considered⁴⁴. The phenomenological equation relating the field strength and the current density for this modified model is the same as that for the hopping-motion model. If the

metal/oxide/solution system is considered, three kinds of overpotential⁴⁵ should be accounted for by the equation for the potential, E:

$$E = \eta_{m/f} + \eta_f + \eta_{f/s} + E_0$$

where E_0 is a constant that depends on the reference electrode and the junction potentials and $\eta_{m/f}$, η_f and $\eta_{f/s}$ are the metal/oxide, oxide film and oxide/solution interface overpotentials, respectively. D'Alkaine and co-workers³¹⁻³³ showed the importance of the electric field as the sole driving force for the anodic oxidation (see Figure 2).

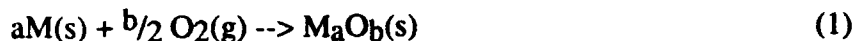
The mechanism for thermal oxide formation may be divided into two parts. The first step is the formation of a continuous oxide and involves the adsorption and dissociation of oxygen, metal/oxygen place exchange, possible oxygen absorption, and oxide nucleation. The second step is continued oxide growth or thickening, which involves the transport of anions and/or cations across the initially formed continuous oxide film.

The initial stage of the reaction of a clean metal surface with gaseous oxygen is the adsorption of oxygen on the metal surface. This adsorption, which appears to be dissociative with essentially zero activation energy⁴⁶, results in a decrease in the surface free energy and is exothermic. Oxygen is highly electronegative and has a large affinity for electrons (2-3 kcal/mole) - great enough to overcome the work function of the metal surface. Therefore, electrons from the surface metal atoms are transferred to the adsorbed gas "atoms" or molecules' vacant energy levels which lie below the Fermi level of the metal. The resulting bond is believed to be largely ionic; however, in cases where the unpaired d electrons of transition metals are involved, the bond may also be partially covalent. The chemisorbed oxygen produces a dipole layer with the positively charge end directed toward the metal surface.

Two possible locations have been postulated for the chemisorbed oxygen on the metal surface. One possibility involves little or no rearrangement of the surface metal atoms. The second possibility involves reconstruction of the metal surface such that the surface layer consists of both metal and oxygen atoms. The latter occurs by a place exchange mechanism first proposed by Lanyon and Trapnell⁴⁷. During place exchange, an interchange of adsorbed oxygen atoms and the surface metal atoms takes place assisted by the heat of chemisorption. The product of place exchange is a 'suboxide' in which an oxygen-metal bonds exist, but not in the three dimensions of a true oxide. The oxygen atoms in this subsurface layer may diffuse further into the bulk metal, or react with neighboring atoms to undergo nucleation (both of these processes may occur simultaneously). The formation of subsurface layers of oxygen/suboxides' and true oxides occurs via surface or internal nucleation for many metals⁹. The dissolution of oxygen into the metal surface region may also occur. Oxygen entering the metal lattice via reconstruction may be considered to form a solid solution. Transition metals, particularly those in Groups IVA (Ti, Zr, Hf) and VA (V, Nb, Ta), interstitially dissolve considerable amounts of oxygen. The dissolved oxygen in these metals is presumed to be located in octahedral positions. Bouillon concluded that oxygen dissolution and formation of surface oxide are competing reactions and the precipitation of oxide nuclei occurs as a result of supersaturation of the surface metal region⁴⁸. Mitchell and Lawless⁴⁹ proposed that the formation of oxide nuclei removes considerable amounts of oxygen from solution and that oxygen subsequently adsorbed reacts more easily with existing nuclei than going into solution. Bénard⁵⁰ has suggested that diffusion of surface oxygen to growing nuclei can result in zones of oxygen depletion surrounding the oxide nuclei in which no additional nuclei can form.

Following the formation of the oxide nuclei, lateral growth of the nuclei occurs. The nuclei will proceed to grow laterally across the surface until a continuous oxide film forms. The rate limiting process in this stage of oxide growth may be the adsorption, surface diffusion or capture of oxygen. The initial step in the oxidation reaction after the formation of a continuous oxide overlayer continues to be the adsorption of oxygen on the surface. Some oxides are semiconductors or become so at high temperatures and oxygen has a large electron affinity;

therefore, a transfer of electrons from the oxide to the adsorbate will most likely occur. Thus, the adsorbed oxygen species are expected to be negative ions such as O^- , O^{2-} , or O_2^- on oxides thinner than the tunneling length of electrons. The chemical reaction between a metal and gaseous oxygen can be written as



and can be divided into the nine steps depicted in Table 2 (after Bailey and Ritchie¹²):

Table 2
Nine Electrochemical Steps in the Overall Reaction*

| Step No. (s) | Step | Stoichiometric No. (v_s) |
|-----------------|---|---------------------------------|
| 7 | $M \rightarrow (M^{z+} M) + z_+e_M$ | a |
| 1 | $e_M \rightarrow e_O$ | az_+ |
| 2 | $(M^{z+} M) + \Delta_O \rightarrow (M^{z+} \Delta)_O$ | a |
| 3 | $e_O \rightarrow e_L$ | az_+ |
| 4 | $(M^{z+} \Delta)_O + \Delta_L \rightarrow (M^{z+} \Delta)_L + \Delta_O$ | a |
| 8 | $O_2(g) + S \rightarrow (O_2 S)$ | $b/2$ |
| 5 | $4e_L + (O_2 S) + S \rightarrow 2(O^{2-} S)$ | $b/2$ |
| 6 | $(M^{z+} \Delta)_L + S' \rightarrow (M^{z+} S') + \Delta_L$ | a |
| 9 | $a(M^{z+} S') + b(O^{2-} S) \rightarrow M_aO_b + aS' + bS$ | 1 |

*M represents a metal atom that reacts with O_2 in the ratio $a:b/2$ to form the oxide M_aO_b ; $(M^{z+}|M)$ represents a metal cation of charge z^+e situated within the metal at the metal-oxide interface; depending on the context, e represents either the magnitude of the electronic charge or an electron; $(M^{z+}|\Delta)$ represents a cation on an interstitial site Δ within the oxide; $(M^{z+}|S')$ represents a cation at a surface site S' on the oxide-oxygen surface; $(O_2|S)$ and $(O^{2-}|S)$ represent an oxygen molecule and an oxide ion, respectively, adsorbed at a site S on the oxide-oxygen surface; and the subscripts M, O, and L indicate the metal at the metal-oxide interface and the oxide at the metal-oxide ($x=0$) and the oxide-oxygen ($x=L$) interfaces, respectively. The stoichiometric number for steps s (i.e., the number of times that step s must occur for the formation of one molecule of M_aO_b) is given by v_s .

Steps 7-9 are those chemical steps where no charge transfer occurs. Steps 1-6 are the electrochemical steps, involving the transfer of electrons or interstitial cations across either an interface or the oxide layer. Following the treatment of Bailey and Ritchie¹² the importance of the reactions will be illustrated.

The cell potential, E_{cell} , for the above reaction in terms of the Gibbs free energy and ΔG_s , the free energy change for step s , $\Delta G_m = \sum v_s \Delta G_s$, ($s=1-9$) is

$$E_{cell} = -\Delta G_m/ne \quad (2)$$

$$\Delta G_s = (\sum_j v_j \mu'_j)_s \quad (3)$$

where n = total number of electrons transferred, j is the various reactants and products of step s , and v_j 's are the stoichiometric coefficients of the reactants ($v_j < 0$) and products ($v_j > 0$) and μ_j are the corresponding electrochemical potentials.

Step 1 ($e_M \rightarrow e_O$) is used to illustrate the analysis of the electrochemical steps 1-6, for:

$$\Delta G_1 = (\sum_j v_j \mu_j)_1 = \mu'(e)_O - \mu'(e)_M \quad (4)$$

where $\mu'(e)_O$ and $\mu'(e)_M$ are the electrochemical potentials for the electron in the oxide and metal, respectively. In terms of the chemical potentials, μ_j and electrostatic potentials, ϕ_j :

$$(\sum_j v_j \mu_j)_1 = [\mu(e)_O - \mu(e)_M] - e(\Delta\phi_1) \quad (5)$$

where $\Delta\phi_1 = \phi_O - \phi_M$. If step 1 occurs rapidly as compared to the overall reaction rate, it will be in virtual current equilibrium and $\Delta G_1 \approx 0$. The equilibrium potential, $V_{1(eq)}$, for step 1 is defined as:

$$V_{1(eq)} = [\mu(e)_O - \mu(e)_M]/e = \Delta G_1/e + \Delta\phi_1 \quad (6)$$

when step 1 is rapid, $\Delta G_1 \approx 0$, then $\Delta\phi_1 \approx V_{1(eq)}$. The above equation can be rewritten as:

$$\Delta G_1 = (\sum_j v_j \mu_j)_1 = -e(\Delta\phi_1 - V_{1(eq)}) = -e\eta_{t1} \quad (7)$$

where $(\Delta\phi_1 - V_{1(eq)})$ is the electrostatic potential difference across the metal-oxide interface for a reacting system minus the hypothetical potential difference that would exist if the system were in virtual current equilibrium. The expression $(\Delta\phi_1 - V_{1(eq)})$ can be viewed as the charge-transfer overpotential³⁶, for step 1, η_{t1} or η_{ts} for step s . Treating steps 1-6 similarly gives:

$$V_{s(eq)} = -(\sum_j v_j \mu_j)_s / z_s e \quad (8)$$

$$\Delta G_s = -z_s e \eta_{ts} \quad (9)$$

For steps 1 and 2, $\Delta\phi_s = \Delta\phi_{MO}$, the potential difference across the metal-oxide interface, for steps 3 and 4, $\Delta\phi_s = \Delta\phi_{OF}$, the potential difference across the oxide film, and for steps 5 and 6, $\Delta\phi_s = \Delta\phi_{OG}$, the potential difference across the oxide-gas interface. The concept of a charge-transfer overpotential has been applied to the transfer of electrons and interstitial cations across the metal/oxide interface, through the oxide film and across the oxide/gas interface. For those steps in virtual current equilibrium, ΔG_s and $\eta_{ts} \approx 0$.

The summation for ΔG_s can be divided into two parts - one part for $s = 1$ to 6 and the other for $s = 7$ to 9. Substituting $\Delta G_s = -z_s e \eta_{ts}$ gives

$$\Delta G_m = \sum_{s=1}^{s=6} v_s z_s e \eta_{ts} + \sum_{s=7}^{s=9} v_s \Delta G_s \quad (10)$$

where the value of $v_s z_s$ equals $\pm n$ and the positive sign applies to those steps that involve cation transport, for which $\eta_{ts} < 0$. For those steps that involve electron transport, $v_s z_s$ equals $\pm n$ and $\eta_{ts} > 0$. For $s=1-6$ $v_s z_s e \eta_{ts} = -ne|\eta_{ts}|$ and:

$$E_{\text{cell}} = -\Delta G_m / ne = \sum_{s=1}^{s=6} |\eta_{ts}| - \left(\frac{1}{ne} \right) \sum_{s=7}^{s=9} v_s \Delta G_s \quad (11)$$

This equation, according to Bailey and Ritchie¹², is the fundamental equation in corrosion. Considering the oxygen reduction reaction, the cathodic reaction, step 5 times 1/2 and the metal oxidation or anodic reaction, step 7, Eq. 11 becomes:

$$E_{\text{cell}} = |\eta_{15/2}| - (a) \Delta G_7 / 2e \quad (12)$$

where the anodic reaction and other reactions in Table 2 are considered to be in virtual equilibrium and $\Delta G_7 = 0$. Thus $E_{\text{cell}} = |\eta_{15/2}|$. Using $\eta_{15/2} = (1/2e)[\Delta G_{5/2} - \Delta G^\circ_{5/2}]$ for the cathodic reaction, equation (12) can now be written as:

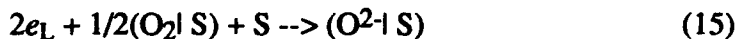
$$E_{\text{cell}} = (1/2e)[\Delta G_{5/2} - \Delta G^\circ_{5/2}] = -\Delta G^\circ_{5/2} / 2e + (kT/2e) \ln(1/K_{5/2}) \quad (13)$$

where $K_{5/2} = \{ [a_{(O^{2-})}] / [a_{(e)}]^2 [a_{(O_2)}]^{1/2} \}$. Equation 13 is the Nernst equation for gas phase oxidation. Using $E_{\text{cell}} = -\Delta G_s / ne = [\Delta \phi_s - V_{s(\text{eq})}]$ the Nernst equation can now be written in terms of "equilibrium potentials" that Bailey and Ritchie¹³ have used before:

$$V_{5/2(\text{eq})} = V^*_{5/2(\text{eq})} + (kT/2e) \ln(K) \quad (14)$$

where $V^*_{5/2(\text{eq})}$ is the equilibrium potential.

For thermal oxidation, Atkinson⁸, as Grimley⁵¹ did earlier, assumes that the adsorbed layer of ions is in equilibrium with the gas and provides the surface charge and the voltage, $\Delta \phi$, across the film. This electron transfer and adsorption reaction, one half of step 5 in Table 2 is:



Assuming equilibrium, gives the equilibrium constant as

$$K_{5/2} = a(O^{2-}) / a(O_2)^{1/2} a(e)^2 = \exp(-\Delta G_{5/2} / kT) \quad (16)$$

Where $\Delta G_{5/2}$ is the standard free-energy change when the surface coverage of excess O^{2-} ions is low, $a(O^{2-}) = n_0 / N_s$; where n_0 is the number of excess O^{2-} ions, N_s is the total number of O^{2-} ions/unit area of the surface, $a(e)$ is the activity of an electron with respect to the Fermi energy of the metal and is equal to $\exp(-e\Delta \phi / kT)$. Substituting gives:

$$K_{5/2} = n_0 / N_s a(O_2)^{1/2} [\exp(-e\Delta \phi / kT)]^2 = \exp(-\Delta G_{5/2} / kT) \quad (17)$$

$$n_0 = N_s a(O_2)^{1/2} \exp[-(\Delta G_{5/2} + 2e\Delta \phi) / kT] \quad (18)$$

Treating the film and the surface charges as a simple capacitor ($n_0 = \epsilon\epsilon_0\Delta\phi/2eX$) allows the surface excess of oxygen ions to be calculated and solving for $\Delta\phi$ gives the following:

$$2e\Delta\phi/kT + \ln[2e\Delta\phi/kT] = -\Delta G_{5/2}/kT + \ln[4e^2N_{sa}(O_2)^{1/2}X/kT\epsilon\epsilon_0] \quad (19)$$

$$\Delta\phi = -\Delta G_{5/2}/2e + [kT/2e]\ln[4e^2N_{sa}(O_2)^{1/2}X/kT\epsilon\epsilon_0] \quad (20)$$

where $e\Delta\phi/kT \gg 1$ allows the $\ln[2e\Delta\phi/kT]$ to be neglected. $\Delta\phi$ is strongly dependent on the free energy change of the reaction and on temperature T , but is only weakly dependent on $a(O_2)$ and thickness X . Equations 20 and 13 are identical when the dielectric properties of the oxide layer and the above definitions for $a(e)$ and $a(O^{2-})$ are considered for the latter.

The rate-controlling process is the injection of a defect into the oxide at either interface 1 or 3. An example is shown in Figure 3 for a cation conductor such as cuprous oxide⁵². Lattice imperfections, as shown, are important in the motion of ionic carriers.

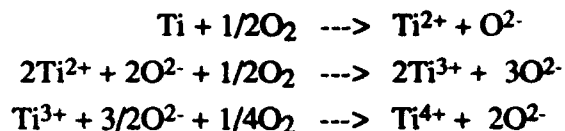
An Alloy Example: Ti-Al and Ti-Cu Alloys

In the present work, we have selected Ti-Cu and Ti-Al alloys for discussion, because each represents an extreme in the differences in ΔG°_f , or $(-\Delta G^\circ_f)$, of the elemental oxides, as illustrated by Table 3.

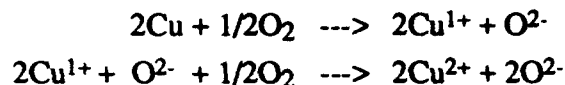
Table 3
Free Energies of Formation of the Oxides per Mole of Oxygen

| Oxide | $-\Delta G^\circ_f$ (KJ/mole oxygen) |
|--------------------------------|--------------------------------------|
| Al ₂ O ₃ | 527.5 |
| Cu ₂ O | 146.0 |
| CuO | 129.7 |
| TiO | 495.0 |
| Ti ₂ O ₃ | 478.1 |
| TiO ₂ | 444.8 |

The Ti-Cu and Ti-Al alloys were made in the co-condensation chamber attached to the XPS/UPS analysis system as depicted in Figure 4. After deposition the samples were analyzed and exposed to oxidizing environments in the separate reaction chamber. The alloys have been given identical oxidation treatments in controlled atmospheres in order to obtain insight into what controls alloy oxidation. In order to document the surface reactivity of the selected alloys, X-ray photoelectron spectroscopy (XPS) has been utilized since this technique is very powerful not only in determining the elemental composition of the near-surface region at the gas-solid interface, but also in providing the chemical nature or oxidation state of the elements comprising the analyzed region (few to 50 Å's). Using the techniques and equipment described elsewhere²⁴, surface reactivity studies were conducted on co-condensed Ti₃₆Cu₆₄ and Ti₃₆Al₆₄ alloys. Changes in the Ti(2p), Cu(2p), Al(2p), O(1s), C(1s), Cu Auger, and Ti Auger regions were monitored as the samples were subjected to a series of vacuum anneals and thermal oxidation treatments. The latter will be emphasized here and their XPS spectra are shown in Figure 5. Al has not been observed to oxidize stepwise and goes rapidly to Al³⁺. Ti and Cu have been observed to oxidize stepwise. Ti oxidizes as:



Cu oxidizes as:



The rate of oxidation of the various components are predicted to be in the following order: $\text{Al}^{3+} > \text{Ti}^{2+} > \text{Ti}^{3+} > \text{Ti}^{4+} > \text{Cu}^{1+} > \text{Cu}^{2+}$ by examining Table 3.

Ti₃₆Cu₆₄ Alloy: The X-ray photoelectron spectra presented in Figures 5a and 5b show the Ti(2p) and Cu(2p) regions, respectively, for the oxidized Ti₃₆Cu₆₄ alloy sample. Since it is not possible to unambiguously distinguish metallic Cu from Cu₂O in the 2p region, we have examined the kinetic energy values for the Cu L₃VV region. Ti is almost exclusively Ti(0) (small asymmetry indicates very small amount of Ti²⁺) in the as-deposited state. The copper is metallic copper, Cu(0). Titanium undergoes stepwise oxidation with TiO, Ti₂O₃, and TiO₂ initially present at the surface at 100°C. It may be recalled from Table 3, that the -ΔG^o_f value of TiO is larger than that for Ti³⁺ and Ti⁴⁺ and much larger than that for either copper(I) or copper(II) oxide, hence the observed oxidation states of the alloy components are not unexpected. As the temperature is increased, the titanium continues to oxidize until 500°C, at which point the oxide is exclusively TiO₂. In both vacuum-annealing and thermal oxidation treatments, it is observed that the copper is almost completely overgrown by titanium oxides. However, unlike the vacuum-anneal experiments, as the temperature is increased to 600°C in the thermal oxidation studies, there is a dramatic reappearance of the Cu(2p) signal. Evidently, the combination of high temperature and high oxygen partial pressure is necessary to drive the oxidation and subsequent migration of copper species back to the surface. A closer examination of the Cu L₃VV region reveals that the surface copper that is incorporated in the oxide overlayer is in the form of Cu¹⁺. This observed phenomenon could have significant catalytic applications since Cu¹⁺ species have been postulated to be active catalytic centers for processes such as methanol synthesis⁵², although this issue is still controversial⁵³. The monovalent copper species that is formed at 600°C in oxidizing atmospheres could be present as either copper(I) oxide or as copper(I) titanate. It is not possible to discriminate between these two species by solely comparing their respective Cu(2p) or Cu L₃VV regions. However, we did detect a 0.5 eV shift to lower binding energy in the Ti⁴⁺ peak as the temperature was increased from 500°C to 600°C. This shift may correspond to the rearrangement of the Ti⁴⁺ ions from the TiO₂ phase to the TiO₃²⁻ form. Similar shifts have been observed by Munuera and co-workers⁵⁴ for NiTiO₃ crystals. Further studies are underway to confirm the existence of the titanate phase.

Ti₃₆Al₆₄ Alloy: The as-deposited Ti₃₆Al₆₄ alloys were examined by XPS and the resulting Ti(2p) and Al(2p) regions are presented in Figures 5c and 5d, respectively. In this alloy system, the Ti on the surface is metallic Ti(0) in nature. Al, on the other hand, is partially oxidized, as inferred from the Al(0) peak at 71.2 eV and the Al(3+) (Al₂O₃) peak at 73.8 eV. The minimal amount of oxygen present in the residual gas is scavenged by aluminum, thereby resulting in an Al-rich (ca. 75% of total metal content) overlayer of passive alumina. The enhanced aluminum surface concentration and the presence of a thin Al₂O₃ layer at the surface can be attributed to the slightly larger -ΔG^o_f for Al₂O₃ over that of the lower valence titanium oxides (see Table 3).

In a recent study of aluminum oxidation by Raman spectroscopy⁵⁵, the transformation from an amorphous to a more structurally ordered γ-Al₂O₃ is shown to be accompanied by an

increase in octahedral coordination of Al^{3+} ions. This change in coordination number (from four in a tetrahedral site to six in an octahedral site) causes a change in the electronic environment of the Al^{3+} cation. It has been demonstrated that XPS can be utilized to differentiate between amorphous and crystalline alumina^{56,57}. The passive Al_2O_3 layer that forms initially on the Ti-Al alloy was shown to be amorphous in nature, as manifested by the Al(2p) binding energy at 73.8 eV. Al(2p) binding energy values for crystalline aluminum oxide in the literature range from 74.3 to 74.7 eV^{58,59}. Vacuum-anneal results also showed the general trend to be (a) as the temperature increases, there is an increase in the oxidation state of titanium at the surface, and (b) oxidation of surface aluminum continues until finally at 600°C, primarily Al_2O_3 species are observed. Vacuum annealing produced a slight increase in the Al surface concentration with a greater rate of change above 300°C, a temperature that corresponds with the transformation of the alumina from the amorphous to the crystalline state. According to Fehlner and Mott⁶⁰, structural reorganization of oxide films is not a surprising phenomenon, and the crystallization of an amorphous oxide overlayer can be aided by high fields, strain due to lattice mismatch between the oxide and underlying metal and the presence of impurities (particularly water). In contrast to the Ti-Cu alloy, decomposition of the Ti^{3+} oxide through oxygen absorption into the bulk is not as significant in $\text{Ti}_{36}\text{Al}_{64}$ as it is in $\text{Ti}_{36}\text{Cu}_{64}$ due to a lower solubility of the oxygen in the TiAl alloy or by the inclusion of the Ti^{3+} oxide in the Al_2O_3 overlayer which is known to be very stable. Results from oxidation of the $\text{Ti}_{36}\text{Al}_{64}$ alloys are presented in Figure 5c and 5d. As the temperature was increased to 100°C during the thermal oxidation treatments, the $\text{Ti}_{36}\text{Al}_{64}$ alloy showed slight enhancement in aluminum at the surface as a result of aluminum oxide formation. As shown by Figure 5d, there is the appearance of a shoulder on the high binding energy side of the Al (2p) peak (73.8 eV), possibly indicating the formation of the crystalline Al_2O_3 at this low temperature. The formation of the crystalline oxide occurs 200 degrees earlier than in the vacuum anneals. In the higher oxygen pressure, an increased electric field is expected to develop across the oxide film and a greater lattice strain could result from the more rapid oxidation of the aluminum as compared to the vacuum-anneal treatments. Either, or both, of these factors could contribute to the crystallization of the oxide at the lower temperatures. At 300°C, the oxidation of Al is nearly complete, this corresponds to (a) the onset of titanium enrichment in the surface region, and (b) the continued oxidation of titanium and the lower valence titanium oxides to TiO_2 by 500°C. Note that this enrichment of titanium occurs only in the presence of increased oxygen pressure and higher temperatures on the Ti-Al alloy. This is expected from a comparison of the $-\Delta G^\circ_f$ for the formation of Al_2O_3 with that of the $-\Delta G^\circ_f$ for the oxides of titanium. Titanium undergoes stepwise oxidation forming (a) TiO at 100°C, (b) TiO, Ti_2O_3 , and TiO_2 from 200-400°C, and (c) continued oxidation to TiO_2 by 600°C. This is in agreement with the work of Carley and co-workers^{61,62}, which showed that on pure titanium as the oxygen surface concentration increases, increasing amounts of TiO_2 are formed relative to the lower oxides of titanium.

Conclusions

Although alloy oxidation has a rich and complex chemistry in both thermal and anodic oxidation, XPS has been shown to provide valuable input into determining "who" is in control. This is clearly shown to be the potential and its accompanying electric field that either develops or is applied during thermal or anodic oxidation, respectively. Low and medium temperature thermal oxidation processes show strong commonalities with electrochemical oxidation processes as derived by Ritchie and co-workers^{12,13} and is correlated in this work with the treatment on thermal oxidation of metals by Atkinson⁸.

Comparing the thermal oxidation of titanium-aluminum and titanium-copper alloys ($\text{Ti}_{36}\text{Cu}_{64}$ and $\text{Ti}_{36}\text{Al}_{64}$), see Figure 6, delineates the important aspects of the oxide formation process and in both thermal oxidation and thermal oxide decomposition (during the vacuum anneals). The Cabrera-Mott treatment of thin film growth predicts that the driving force of metal

oxidation and the ensuing ionic mobility through the oxide is a function of not only the $-\Delta G^{\circ}_f$, but also the temperature and oxygen activity. By comparing Ti-Cu and Ti-Al, the importance of the differences in the $-\Delta G^{\circ}_f$ of the alloy components is better understood. Figure 6 shows the overlayer composition of the two alloys at various temperatures during the oxidation experiments. Initially, both alloys form a thin ($\ll 50\text{\AA}$) oxide overlayer that follows the Cabrera-Mott theory if the $-\Delta G^{\circ}_f$ data in Table 3 is considered. We have observed that titanium (Ti to TiO to Ti_2O_3 to TiO_2) and copper (Cu to Cu_2O to CuO) oxidizes in a stepwise fashion, which the Cabrera-Mott model (using the $-\Delta G^{\circ}_f$ data) predicts. Aluminum does not form any stable intermediate oxides; it rapidly forms an Al_2O_3 overlayer on the alloys at low temperatures and low oxygen activity as predicted by the second term of the Cabrera-Mott equation.

Our results lead us to the following conclusions: (a) the component with the larger $-\Delta G_f$ is shown to preferentially oxidize and segregate to the surface, (b) the magnitude of the change in the $M/(\text{Ti} + M)$ ratios is related to the difference in the $-\Delta G_f$ of the alloy component oxides, and (c) the reappearance of the component with the smaller $-\Delta G_f$ is related to oxygen pressure as well as temperature and is not solely due to thermal diffusion. However, the Cabrera-Mott model does not take into account the absorption of oxygen into the bulk which was found to be an important factor in the vacuum anneal treatments for $\text{Ti}_{36}\text{Cu}_{64}$ alloys at higher temperatures. The Cabrera-Mott model does appear to explain most all the nuances of alloy oxidation, if as the critical developments shown in this paper indicate, the $-\Delta G_f$ is considered on a per oxygen mole or atom basis. It provides a qualitative guideline for predicting alloy oxidation behavior. Bulk alloy composition affects the degree to which titanium participates in the formation of the oxide overlayer and the oxidation state of the titanium in the oxide overlayer. Additionally, the alloy composition affects oxide overlayer formation and the decomposition of the higher titanium oxides at high temperatures in vacuum.

Acknowledgments

The author is grateful for the financial support of the Robert A. Welch Foundation, Houston TX, and the National Science Foundation Grant DMR-89-03135. Special thanks go to Tom Hess and Don Mencer who did much of the experimental work on which this concept paper is based.

References

1. D. L. Cocke, in *NACE Corrosion 89*, (Houston, TX: National Association of Corrosion Engineers, 1989): p. 1.
2. D. L. Cocke and J. H. Block, *Werkstoffe und Korrosion*, 38, 668 (1987): p. 668
3. Z. Szklarska-Smialowska, *Pitting Corrosion of Metals*, (Houston, TX: National Association of Corrosion Engineers, 1986).
4. P. Kofstad, *High Temperature Oxidation of Metals*, (New York: John Wiley, 1966).
5. K. Hauffe, *Oxidation of Metals* (New York: Plenum Press, 1965).
6. W. W. Smeltzer and D. J. Young, *Prog. Solid State Chem.*, 10 (1975): p. 17.
7. F. P. Fehlner, *Low-Temperature Oxidation: The Role of Vitreous Oxides*, (New York: John Wiley, 1986).
8. A. Atkinson, *Rev. Mod. Phys.*, 57 (1985): p. 437.
9. K. R. Lawless, *Rep. Prog. Phys.*, 37 (1974): p. 231 .
10. G. R. Wallwork, *Rep. Prog. Phys.*, 39 (1976): p. 401.
11. G. C. Wood and F. H. Stott, *Mat. Sci. Technol.*, 3 (1987): p. 519.
12. J. M. Bailey and I. M. Ritchie, *Oxid. Met.*, 30 (1988): p. 405
13. J. M. Bailey and I. M. Ritchie, *Oxid. Met.*, 30 (1988): p. 419
14. K. Hashimoto, in *Fifth International Conference on Rapidly Quenched Metals*, edited by S. Steeb and H. W. Warlimont (Amsterdam: Elsevier Science Publishers, 1985): p. 1449.
15. D. L. Cocke, *J. Metals*, Feb. (1986): p. 70.
16. C. H. Yoon and D. L. Cocke, *J. Noncrystalline Solids*, 79 (1986): p. 217.
17. W. E. Brower, Jr., M. S. Matyjaszczyk, T. L. Pettit and G. V. Smith, *Nature*, 301 (1983): p. 497.
18. D. L. Cocke, M. S. Owens and R. B. Wright, *Appl. Surf. Sci.*, 31 (1988): p. 341.
19. D. L. Cocke and M. S. Owens, *Appl. Surf. Sci.*, 31 (1988): p. 471.
20. D. L. Cocke, G. Liang, M. Owens, D. E. Halverson and D. G. Naugle, *Mater. Sci. Eng.*, 99 (1988): p. 497.
21. D. L. Cocke, M. S. Owens and R. B. Wright, *Langmuir*, 4 (1988): p. 1311.
22. D. L. Cocke and M. S. Owens, *J. Colloid and Interf. Sci.*, 19 (1989): p. 166.

23. D. L. Cocks, W. E. Daulat, M. S. Owens and R. B. Wright, *Solid State Ionics*, 32/33 (1989): p. 930.
24. D. L. Cocks, T. R. Hess, T. Mebrahtu, D. E. Mencer, Jr., and D. G. Naugle, *Solid State Ionics*, 43 (1990): p. 119.
25. D. L. Cocks, D. E. Mencer, Jr. and D. G. Naugle, in *Industry-University Advanced Materials Conference*, (The Metallurgical Society Golden, 1987): p. 365.
26. D. L. Cocks, D. E. Mencer, Jr., D. G. Naugle and C. Tsai, *Materials Chem. and Phys.*, 18 (1987): p. 71.
27. T. Mebrahtu, T. R. Hess, D. E. Mencer, Jr., K. G. Balke, D. G. Naugle and D. L. Cocks, *Mater. Sci. Eng.*, A134 (1991): p. 1041.
28. C. Yoon and D. L. Cocks, *Appl. Surf. Sci.*, 31 (1988): p. 118.
29. D. E. Mencer, Jr., D. L. Cocks and C. Yoon, *Surface and Interfacial Analysis*, 17 (1991): p. 31.
30. D. E. Mencer, Jr., T. R. Hess, T. Mebrahtu, D. L. Cocks and D. G. Naugle, *J. Vacuum Sci. Tech.*, A9 (1991): p. 1610.
31. C. V. D'Alkaine, L. M. M. de Souza and F. C. Nart, *Corr. Sci.*, 34 (1993): p. 109.
32. C. V. D'Alkaine, L. M. M. de Souza and F. C. Nart, *Corr. Sci.*, 34 (1993): p. 117.
33. C. V. D'Alkaine, L. M. M. de Souza and F. C. Nart, *Corr. Sci.*, 34 (1993): p. 129.
34. M. Janik-Czachor and J. Banas, *Corr. Sci.*, 30 (1990): p. 735.
35. M. Seo and N. Sato, *Langmuir*, 3 (1987): p. 917.
36. K. E. Heusler and D. Huerta, *J. Electrochem. Soc.*, 135 (1988).
37. R. Kirchheim, B. Heine, H. Fischmeister, S. Hoffmann, H. Knotte and U. Stolz, *Corr. Sci.*, 29 (1989): p. 899.
38. P. Marcus and J. M. Grimal, *Corr. Sci.*, 33 (1992): p. 805.
39. L. Young, *Trans. Faraday Soc.*, 52 (1956): p. 506.
40. G. B. Adams, Jr. and T. Kao, *J. Electrochem. Soc.*, 107 (1966): p. 640.
41. L. Young and F. G. R. Zobel, *J. Electrochem. Soc.*, 113 (1967): p. 277.
42. L. Young, *Anodic Oxide Films*, (New York: Academic Press, 1961).
43. A. T. Fromhold, Jr., *J. Electrochem. Soc.*, 127 (1980): p. 411.
44. J. Perriere and J. Siejka, *J. Electrochem. Soc.*, 230 (1983): p. 1260.
45. K. J. Vetter, *Electrochemical Kinetics: Theoretical and Experimental Aspects*, (New York: Academic Press Inc., 1967).

46. G. Erlich, in *Trans. 8th Vacuum Symp. and 2nd Int. Congress*, (New York: Pergamon Press, 1962): p. 126.
47. M. A. H. Lanyon and B. M. W. Trapnell, *Proc. Roy. Soc.*, A227 (1955): p. 387.
48. F. Bouillon, G. van der Schrick and C. Kaaeckenbeeck-van der Schrick, *Acta. Met.*, 10 (1962): p. 649.
49. D. F. Mitchell and K. R. Lawless, *J. Paint Tech.*, 39 (1966): p. 575.
50. J. Bénard, F. Grönlund, J. Oudar and M. Duret, *Z. Elektrochem.*, 63 (1959): p. 799.
51. T. B. Grimley, in *Chemistry of the Solid State*, edited by W. E. Garner (London: Butterworths, 1955): p. 336
52. G. R. Sheffer and T. S. King, *J. Catal.*, 115 (1989): p. 376.
52. S. K. Chawla, B. I. Rickett, N. Sankarraman and J. H. Payer, *Corr. Sci.*, 33 (1992): p. 1617.
53. G. C. Chinchén and K. C. Waugh, *J. Catal.*, 97 (1986): p. 280.
54. G. Munuera, A. R. González-Elipé and J. P. Espinós, *Surface Sci.*, 211/212 (1989): p. 1113.
55. P. V. Thomas, V. Ramakrishnan and V. K. Vaidyan, *Thin Solid Films*, 170 (1989): p. 35.
56. D. L. Cocke, E. D. Johnson and R. P. Merrill, *Catal. Rev.-Sci. Eng.*, 26 (1984): p. 163.
57. D. E. Halverson and D. L. Cocke, *J. Vac. Sci. Technol.*, A7 (1989): p. 40.
58. B. Strohmeier, *Appl. Surface Sci.*, 40 (1989): p. 249.
59. B. Strohmeier, *J. Vac. Sci. Technol.*, A7 (1989): p. 3238.
60. F. P. Fehlner and N. F. Mott, *Oxid. Met.*, 2 (1970): p. 59.
61. A. F. Carley, P. R. Chalker, J. C. Riviere, and M. W. Roberts, *J. Chem. Soc., Faraday Trans. I*, 83 (1987): p. 351.
62. C. T. Au, A. F. Carley, and M. W. Roberts, *Phil. Trans. R. Soc. Lond.*, A318 (1986): p. 61.

Table 1: Summary of Our Alloy Studies to Date

| Alloy | Interest | Discoveries |
|--------------|--|---|
| Cu-Mn | Model for Hopcalite Oxidation Catalyst | a. Cu ₂ O oxide decomposition due to absorption of oxygen in bulk discovered and interpreted b. Application of Cabrera-Mott (C-M) model suspected |
| Ag-Mn | Model Oxidation Catalyst | a: C-M model found to apply b. Ag oxides only at higher O ₂ P |
| Ni-Zr | Hydrogenation Catalyst Precursor | a. ZrO ₂ instability due to oxygen absorption in bulk found b. Found carbide formation Reaction c. C-M model confirmed d. High catalytic activity |
| Ni-Nb | Hydrogenation Catalyst Precursor | a. C-M model applies b. Ni less dispersed on Nb ₂ O ₅ after reduction than in Ni/ZrO ₂ |
| Ni-Zr-Al | Hydrogenation Catalyst Precursor | a. Al ₂ O ₃ segregation dominates b. Al ₂ O ₃ acts as a catalyst poison |
| Ti-Al | Structural Material & Catalyst Substrate Precursor | a. Co-condensed amorphous 15<Ti<60 At % stability range b. Bulk composition strongly affects oxidation properties c. Phase change control of surface oxidation |
| Ti-Cu | Methanol Synthesis Catalyst Precursor | a. TiO ₂ and Ti ₂ O ₃ instability found b. Carbide formation c. Obeys C-M model |
| Ti-Cu-Al | Methanol Synthesis Catalyst Precursor | Plasma control of surface composition and structure |
| Ti-Ni | Hydrogenation Catalyst Precursor | a. Obeys C-M Model b. Hydride formation importance |
| Ti-Ru-Si | Hydrogenation Catalyst and Electrocatalyst Precursor | A-C Transition at 526 °C |

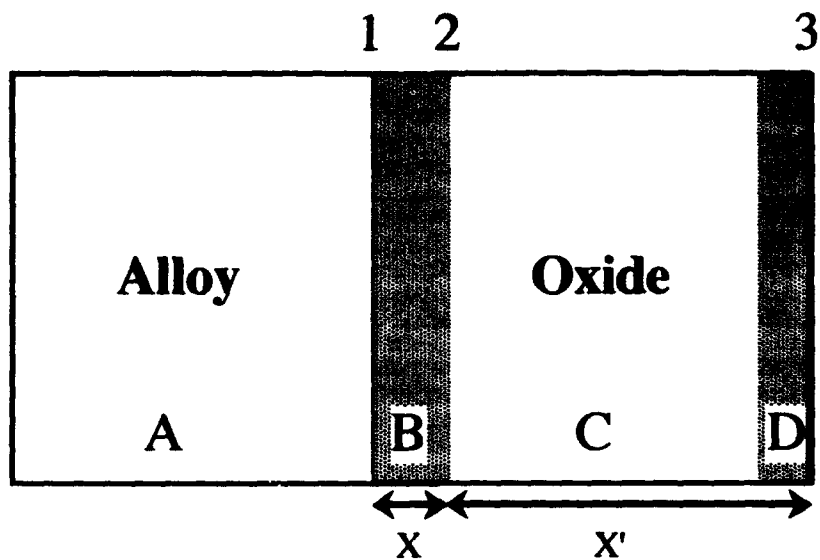


Figure 1: Schematic diagram of a typical metal oxide system, where (A) is the metal or alloy bulk. (B) is a thin amorphous oxide layer at the metal/oxide interface, (C) is a uniform crystalline oxide layer, (D) is a thin outer layer where the metal is in its highest oxidation state, (1) is the metal/amorphous oxide interface, (2) is the amorphous oxide/crystalline oxide interface and (3) is the oxide/gas interface.

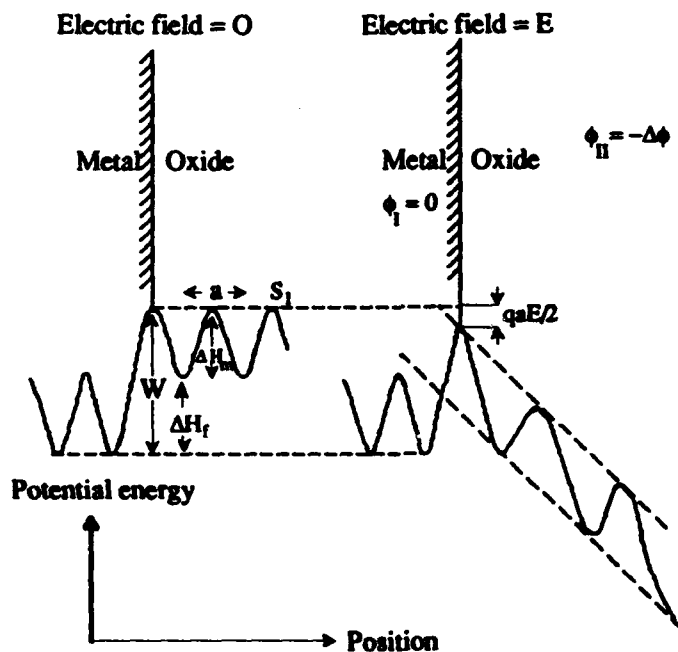


Figure 2: Schematic diagram of effect of electric field on the potential energy of a metal ion at the metal/oxide interface. The electric field may be generated by the formation of oxygen anions at the oxide gas interface (i.e. thermal oxidation) or by an applied electric field. It is this electric field that drives the diffusion of ions across the oxide. (Figure adapted from Atkinson⁸)

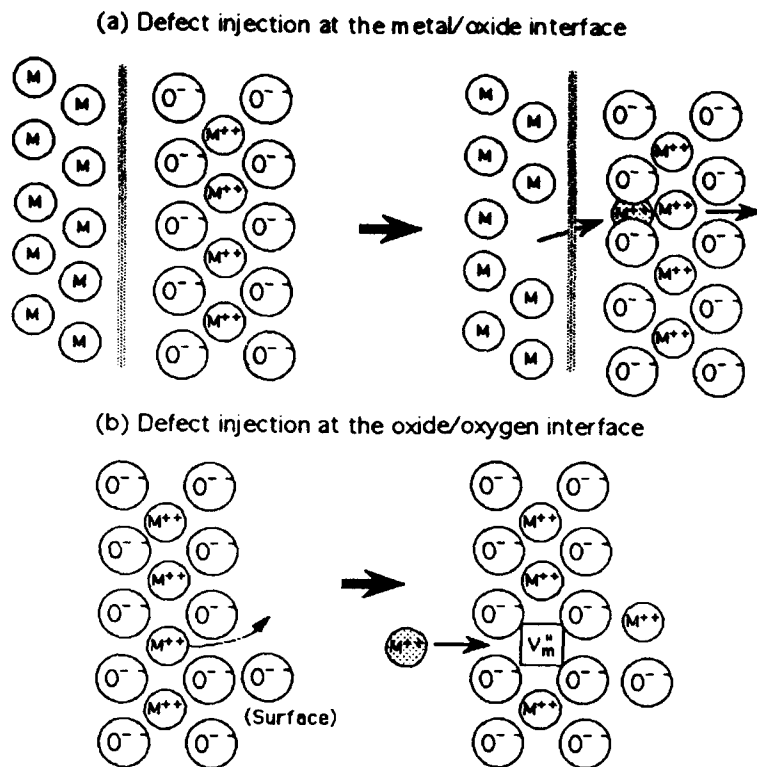


Figure 3: Schematic diagram of the injection of a defect site at (a) the metal/oxide interface and (b) the oxide/oxygen interface. According to the Cabrera-Mott model, the injection of the defect at one of the film interfaces is the rate-controlling step.

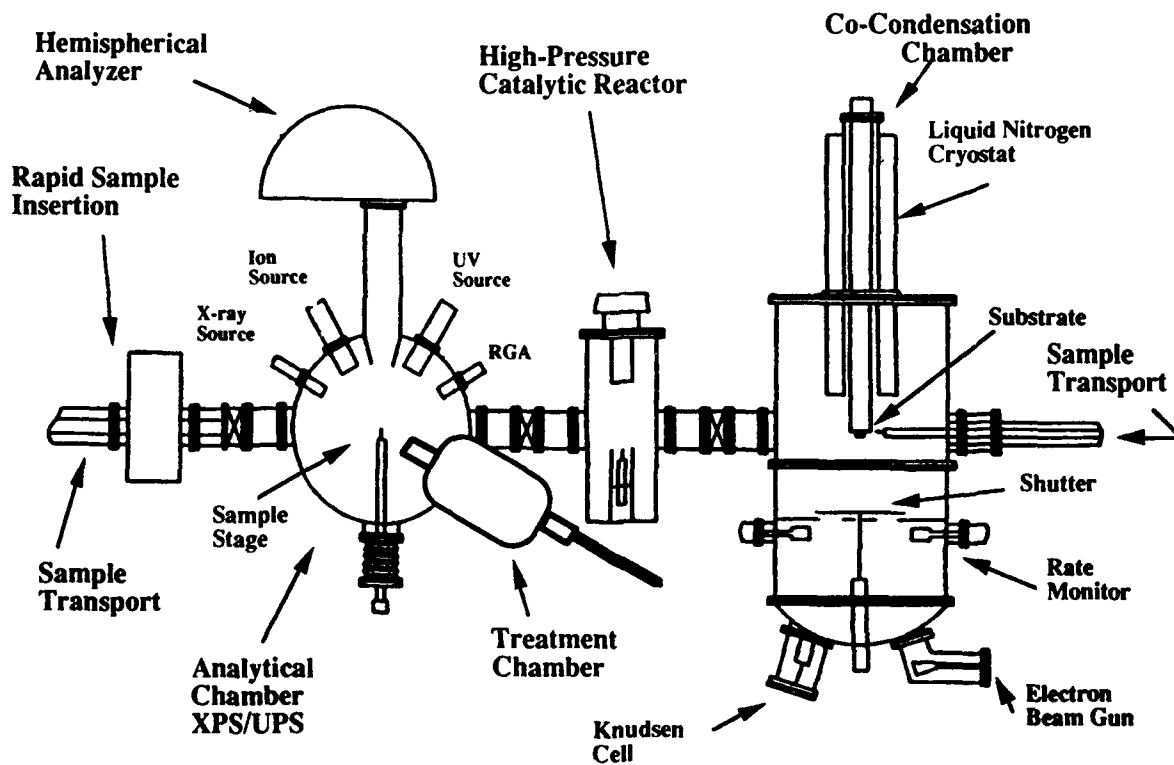


Figure 4: Alloy co-condensation and surface characterization system.

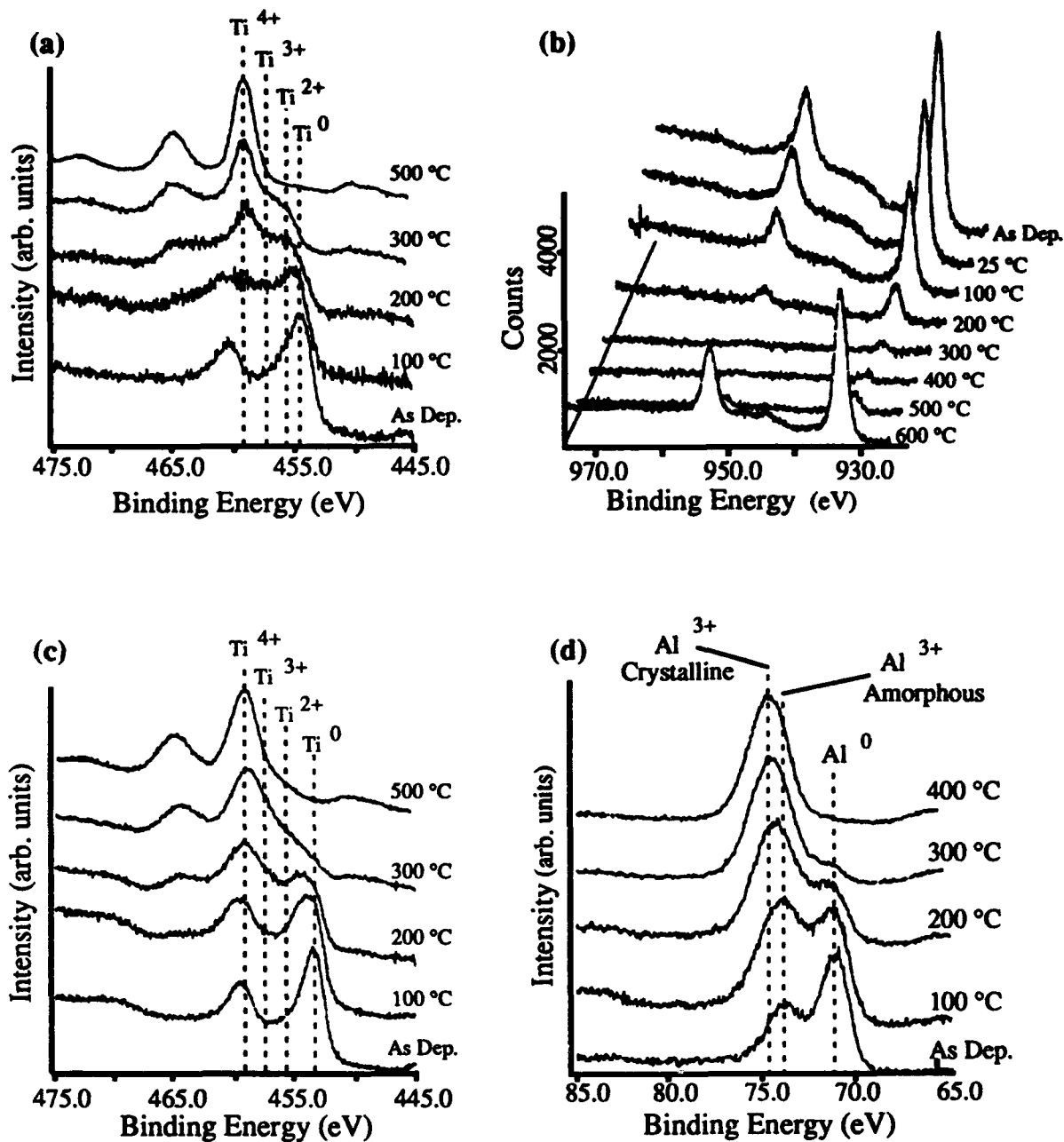


Figure 5: (a) Selected Ti(2p) XPS spectra of $Ti_{36}Cu_{64}$ after co-deposition and oxidation at successively higher temperatures. (b) Selected Cu(2p) XPS spectra of $Ti_{36}Cu_{64}$ after co-deposition and oxidation at successively higher temperatures. (c) Selected Ti(2p) XPS spectra of $Ti_{36}Al_{64}$ after co-deposition and oxidation at successively higher temperatures. (d) Selected Al(2p) XPS spectra of $Ti_{36}Al_{64}$ after co-deposition and oxidation at successively higher temperatures.

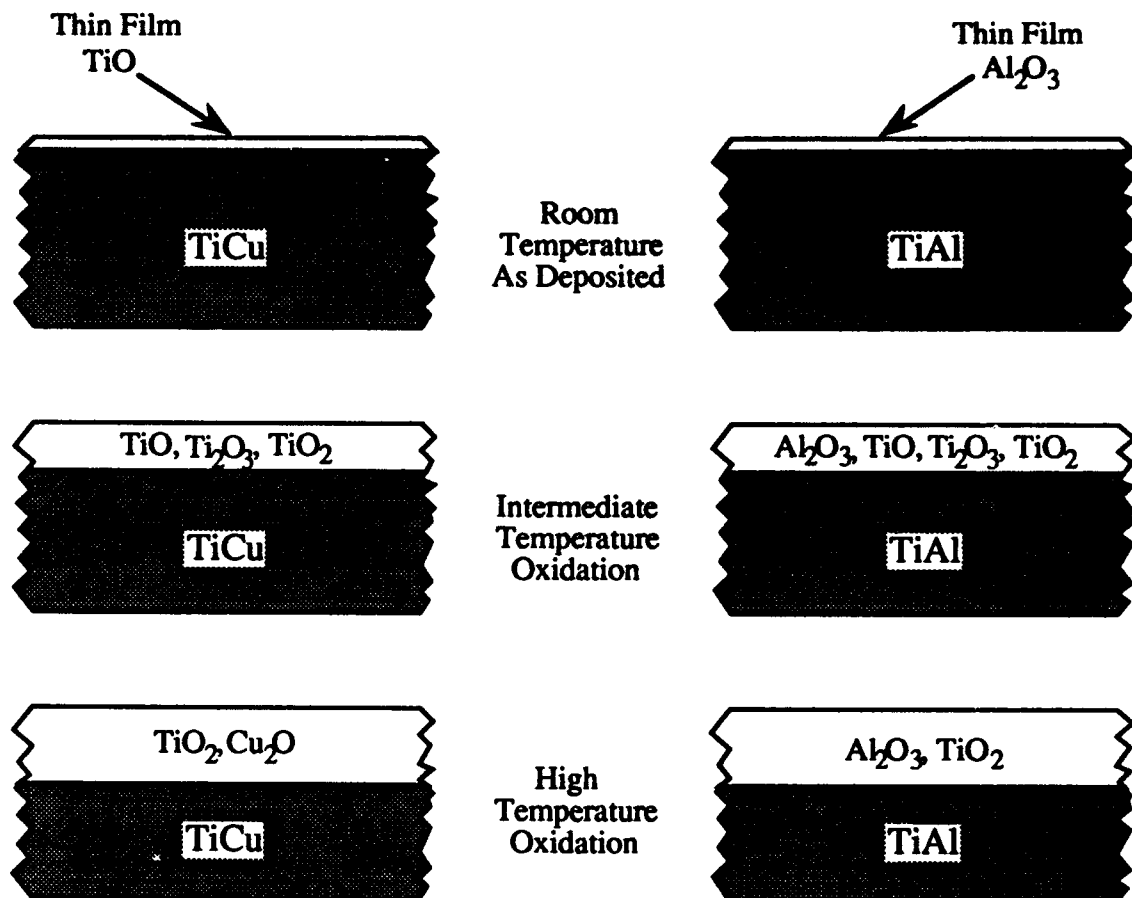


Figure 6: Representation of the proposed oxide overlayer compositions for Ti₃₆Cu₆₄ and Ti₃₆Al₆₄ alloys after the thermal oxidation treatments.

**Identification of the Chemistry of Corrosion Films Induced
on W-Ni-Fe Alloys by Immersion in Aqueous NaCl Using XPS**

A. N. Mansour
Naval Surface Warfare Center
10901 New Hampshire Avenue
Silver Spring, MD 20903-5000

K. L. Vasanth
Naval Surface Warfare Center
10901 New Hampshire Avenue
Silver Spring, MD 20903-5000

Abstract

Tungsten alloys referred to as "superalloys" because of their high density and strength are prepared by liquid phase sintering in which tungsten particles are dissolved in a liquid solution of Ni-Fe, Ni-Cu, or Ni-Co. Despite their importance, the corrosion characteristics of these alloys are not yet fully understood. In this investigation, the chemistry of corrosion films on two W-Ni-Fe superalloys with differing composition have been investigated using X-ray photoelectron spectroscopy (XPS). XPS is a surface analytical technique which provides elemental and chemical analysis of the near surface region. The chemistry of corrosion products on two W-Ni-Fe alloys with composition 98.5 W, 0.9 Ni, 0.6 Fe and 94.8 W, 3.4 Ni, 1.9 Fe by weight percent, hereafter referred to as alloys K1 and S1 respectively, were investigated. The corrosion films were induced by immersing these alloys in 3.5 wt% NaCl solution at ambient laboratory temperature and pressure for 4 hours, 2, 10, and 17 days.

The K1 alloy exhibited uniform corrosion while the S1 alloy exhibited non-uniform corrosion reminiscent of localized corrosion. The surface of the S1 alloy showed black colored regions consisting mainly of tungsten products and brown colored areas consisting of significantly greater concentrations of Fe and Ni compared to those of the black colored regions. Analysis of the XPS data indicates that the chemical and structural nature of Fe in the corrosion products of both alloys is similar to that of Fe in Fe_3O_4 , a highly oxygen deficient Fe_2O_3 , in which Fe is present in the Fe^{2+} and Fe^{3+} charge states. The chemistry of nickel in the corroded alloys, on the other hand, is similar to that of Ni in $Ni(OH)_2$. Tungsten is the component of the alloy which is least affected by corrosion induced due to immersion in 3.5 wt% NaCl solution due to the formation of a surface film coating which consisted of WO_2 and WO_3 . However, the coating thickness of the S1 alloy was greater than that of the K1 alloy indicating higher corrosion immunity for tungsten particles of the S1 alloy. This coating was also present on the surface of the control samples (no immersion) of both alloys.

Key terms: W-Ni-Fe superalloys, chemistry of corrosion films, Fe_3O_4 , $Ni(OH)_2$, WO_2 , WO_3 , sodium chloride, passivation, and X-ray photoelectron spectroscopy (XPS).

Introduction

Tungsten alloys referred to as "superalloys" because of their high density and strength are important engineering materials for numerous military and industrial applications.¹ In military applications, they are used as the armor piercing core of medium to large caliber kinetic energy ammunition and as preformed fragments in various anti-craft and anti-missile warheads. Industrial applications, on the other hand, include counter balances, gyroscope rotors, and radiation shields. These alloys are prepared by liquid phase sintering in which tungsten particles are dissolved in a liquid solution of Ni-Fe, Ni-Cu, or Ni-Co.² The outcome of this process is a two phase structure consisting of tungsten particles cemented together with an alloy containing a solid solution of W-Ni-Fe, W-Ni-Cu, or W-Ni-Co. The W in the solid solution is present in very small quantities compared to Fe, Ni, Cu, or Co.

The corrosion characteristics of tungsten alloys with various alloying elements have been studied by several authors. Andrew et al.³ reported that a W-3.5 wt% Ni-2.5 wt% Co alloy readily corrodes when exposed to air saturated with water vapor. Koger⁴ observed that the corrosion rate for a W-3.5 wt% Ni-1.5 wt% Fe alloy increased with increase in pH. Vasanth et al.⁵ and Vasanth and Dacres⁶ reported on the polarization resistance measurements and pitting studies for five W-Ni-Fe alloys immersed in 3.5 wt% sodium chloride (NaCl) solution. Based on immersion studies of these five alloys in natural sea water, they reported a corrosion rate of less than 2 mils per year. Furthermore, Mansour and Vasanth⁷ reported on the chemistry of corrosion products of two W-Ni-Fe (also used in the present investigation) induced by immersion in 3.5 wt% NaCl solution using X-ray absorption fine structure (XAFS) spectroscopy. In that investigation, a highly disordered form of Fe₂O₃ was revealed as the major component of the corrosion products. While XAFS revealed some oxidized Ni and W were also present, it failed to specifically identify their chemistries because the Ni and W films were too thin to be detected by XAFS spectroscopy despite the fact that the W XAFS data were measured in the electron yield mode which, to a certain degree, is surface sensitive. Thus, despite all of these research efforts, the chemical nature of corrosion products is not yet fully understood.

The aim of the present investigation is to determine the effect of alloy composition on corrosion and examine the chemistry of Fe, Ni, and W in the corrosion products of two W-Ni-Fe alloys with differing composition using x-ray photoelectron spectroscopy (XPS). XPS is a surface analytical technique which provides elemental and chemical analysis of the near surface region. Corrosion products were induced by immersing the samples in 3.5 wt% NaCl solution.

Experiment

Two W-Ni-Fe alloys with bulk compositions of 98.5 W, 0.9 Ni, 0.6 Fe and 94.8 W, 3.4 Ni, 1.9 Fe by wt%, hereafter, referred to as alloys K1 and S1 respectively, were used in this investigation. In terms of atomic percents, these concentrations are 95.4 W, 2.7 Ni, and 1.9 Fe for the K1 alloy and 84.9 W, 9.5 Ni, and 5.6 Fe for the S1 alloy. Detailed analysis of the micro-structure and composition of these alloys as determined by scanning electron microscopy and energy dispersive X-ray analysis was presented previously.^{5,6} These two alloys were

selected because they represent the distinct corrosion trends observed among five different alloys previously examined for their corrosion properties.^{5,6} Based on continuous immersion tests in natural sea water, the corrosion rate for the S1 alloy is roughly half as much as that of the K1 alloy. Furthermore, alloy K1 showed uniform corrosion while the S1 alloy corroded preferentially in certain selected areas.

For the present experiment, samples in disc form roughly 1.2 cm in diameter and 0.4 cm thick were cut from the alloy material using a diamond disc saw. The specimens were wet polished with 320A, 400A, and 600A silicon carbide paper, rinsed with distilled H₂O, acetone degreased, and air dried. The corrosion was then induced by immersing the samples in a glass beaker containing 3.5 wt% NaCl solution (which mimics sea water) at ambient laboratory temperature and pressure for 4 hours, 2, 10, and 17 days. After removal from the solution, the samples were thoroughly rinsed in distilled H₂O.

XPS data were collected using a Perkin-Elmer/Physical Electronics Division photoelectron spectrometer (model 5400) under computer control. All spectra were obtained with non-monochromatized Mg x-rays ($h\nu=1253.6$ eV). The anode operated at 15 KV drawing a current of 27 mA. During the XPS measurements, the analysis chamber pressure was kept in the range of $(1-3)\times 10^{-8}$ Torr. The XPS data were collected from an analysis area of 1mm x 3mm except for the data from the S1 alloy immersed in the solution for 17 days where an analysis area of 1mm x 1mm was employed.

For binding energy and quantitative composition analysis, the photoelectron peaks were fit with a combined Gaussian-Lorentzian line shape. Binding energies were referenced to adventitious carbon (C 1s at 285.0 eV). The atomic concentrations of the various elements were calculated from peak areas after correcting for the photoionization cross section using Scofield values⁸ and the energy dependence of the photoelectron mean free path.

Results and Discussion

A comparison of the XPS survey spectra for control and corroded K1 and S1 alloys are shown in Figures 1 and 2, respectively. The data for the corroded K1 and S1 alloys are shown after immersion in 3.5 wt% NaCl for 2 days and 17 days, respectively. Visual inspection of the spectra indicates a composition consisting mainly of C, O, Si, Fe, Ni and W. As can be seen from the spectra of the control samples, Ni and Fe 2p photoelectron lines are just barely visible due to the low concentrations of Ni and Fe relative to that of W. The Fe and Ni 2p lines are clearly visible in the spectra of the corroded samples indicating an increase in the concentrations of both Ni and Fe relative to those of the control samples. The presence of silicon which is not part of the original composition of the alloy is a product of our sample polishing procedure described in the above section. Silicon is not bonding to any of the alloy components and can be completely removed with extended periods of sample wash and rinsing in distilled H₂O.

For quantitative composition analysis and chemical state identification higher resolution (relative to survey scans) XPS multiplexes of the C 1s, O 1s, Si 2p, Fe 2p, Ni 2p, and W 4f

photoelectron lines were measured. The surface compositions, as determined from these XPS multiplexes for the K1 and S1 alloys as a function of immersion time in 3.5 wt% NaCl solution, are listed in Table I. Carbon is usually present on most surfaces as a contaminant with the major component in the form of adventitious hydrocarbon. The other components in the form of carbon singly bonded to oxygen, carbonyl, carboxyl, or CO_3^{2-} are present only in small quantities. Silicon in the corroded samples is also present in small quantities in the form of a carbide or an oxide. The carbon and silicon are believed to be irrelevant to the corrosion process. Hence, the carbon and silicon concentrations have been excluded from Table I.

Typical spectra of the Fe and Ni 2p photoelectron lines of both alloys after immersion in 0.35 wt% NaCl solution are shown in Figures 3 and 4, respectively. The Fe 2p spectra for the corroded K1 alloy for all immersions (2, 10, and 17 days) and that of the corroded S1 alloy immersed in the solution for 17 days are very similar indicating the presence of a single Fe chemistry. Comparing the Fe 2p spectra for the corroded samples with those of structurally well defined samples of $\alpha\text{-Fe}_2\text{O}_3$, $\gamma\text{-Fe}_2\text{O}_3$, $\gamma\text{-FeOOH}$, and Fe_3O_4 published by many researchers⁹⁻¹³ shows that the binding energy and shake-up structure most closely resemble those of Fe_3O_4 . In an earlier investigation using X-ray Absorption Fine Structure (XAFS) Spectroscopy, it was reported that the atomic structure and chemistry of Fe after immersion in 3.5 wt% NaCl for 17 days is similar to that of a disordered form of Fe_2O_3 .⁷ Considering the fact that Fe_3O_4 is an oxygen deficient form of Fe_2O_3 in which 11% of the oxygen sites are vacant, then both XPS and XAFS results are in agreement with each other. Thus, Fe in the corrosion products of both alloys assumes the oxidation states of both Fe^{2+} and Fe^{3+} in proportions which depend on the degree of oxygen deficiency. The only exception, is the spectra of the corroded S1 samples after the 4 hour and 2 day immersions in the solution where small quantities of Fe in the form of metallic Fe and FeO was also present in addition to Fe_3O_4 .

The Spectra of the Ni 2p photoelectron line shown in Figure 4 for the corroded K1 and S1 alloys after immersion in the solution for 2 and 17 days, respectively, resemble very closely that of Ni(OH)_2 published by McIntyre and Cook.¹⁴ The Ni 2p spectra of the corroded K1 alloy are virtually identical for all immersions of 2, 10, and 17 days in the solution. The presence of only a single component indicates that the Ni(OH)_2 is thick enough ($> 100 \text{ \AA}$) to mask the underlying metallic signal. The presence of a thin upper surface coating of Ni_2O_3 , as suggested by Barr¹³ can not be ruled out due to the proximity of the binding energies for Ni(OH)_2 and Ni_2O_3 . However, under the corrosion conditions of this investigation Ni_2O_3 is very unlikely to form. The spectra of the corroded S1 alloy for both the 4 hour and 2 day immersions showed the presence of nickel in the form of NiO in addition to Ni(OH)_2 . In all cases the Ni(OH)_2 chemistry was the dominant one. The formation of a surface film of Ni(OH)_2 on metallic Ni in KOH and chloride solutions (pH 2.7 to 12) in the passive potential region was also observed using the technique of surface-enhanced Raman Spectroscopy.¹⁵

Spectra of the W 4f photoelectron line for control and corroded alloys are shown in Figures 5 and 6. Peak synthesis of these spectra using standard non-linear least square fitting procedures reveals that a minimum of 6 components are required to satisfactorily fit the data. Two components for each single chemistry due to the spin-orbit splitting of the 4f line with an energy

splitting approximately 2.1 eV are required. Comparing with reference data,¹⁶ three different chemistries, namely metallic tungsten, tungsten dioxide (WO₂), and tungsten trioxide (WO₃), were identified to be present in both the control and corroded samples of both alloys and the data are summarized in Table II. These results are interpreted in terms of metallic tungsten particles with WO₂ and WO₃ coatings rather than in terms of the presence of three separate phases. It is observed that the metallic W content of the K1 alloy is significantly larger than that of the S1 alloy indicating an oxide coating for the S1 alloy significantly thicker than that of the K1 alloy. For the corroded K1 alloy, it is observed that the mole percent for W metallic component decreases with immersion time with a corresponding increase in the mole percents of WO₂ indicating an increase in the WO₂ coating thickness with increase in immersion time at least up to 10 days. The thickness of the WO₃ for the K1 alloy appears to remain approximately constant with immersion time. The mole percents of various tungsten chemistries for the S1 alloy immersed in the solution for up to 2 days remains the same as those of the control sample. However, after immersing the S1 alloy in the solution for 17 days, the tungsten metallic content decreases with a corresponding increase in the WO₃ content indicating the growth of the WO₃ coating. Note that after 17 days immersion in the solution the chemistry of tungsten is similar in both alloys. The observed tungsten chemistries are similar to those observed by Shaw et al.¹⁷ for passivation on W-Al alloys induced by anodization in 0.1 KCl solution. Thus, the enhanced passivity of the W-Ni-Fe alloys can be attributed to the formation of the WO₂ and WO₃ coatings which makes the alloys less susceptible to attack by the NaCl solution.

Iron is known to be unstable in the presence of water and a large number of aqueous non-oxidizing solutions.¹⁸ Both tungsten alloys (K1 and S1) considered in the present investigation contain Fe and Ni as alloying elements and were studied in 3.5 wt% NaCl solution (a pH of roughly 6.3). Under these conditions iron has a tendency to form Fe²⁺ and Fe³⁺ which will finally lead to the formation of Fe₂O₃ and Fe₃O₄. A careful analysis of the Pourbaix diagram for Fe and water shows that for pH values below 9.5 and greater than 12.5 the potential will lie inside the corrosion domains, which means that iron may corrode with the evolution of hydrogen. Though the test samples and solution were kept exposed to ambient laboratory environment in our investigation, the oxygen level below pH of 8 will be insufficient to bring about the passivation of iron. This agrees with the fact that some of the corrosion products from the sample fell off from the surface and collected as insoluble residue in the bottom of the glass beaker. The open circuit potential for these alloys in 3.5 wt% solution⁵ also falls within the range of active corrosion as shown by the Pourbaix diagram.

With regard to nickel, the Pourbaix diagram suggests¹⁹ that it should be resistant to corrosion in neutral or alkaline solution free from oxidizing agents, slightly corrodible in acid solutions free from oxidizing agents, and very corrodible in acid or very alkaline solutions containing oxidizing agents. Neutral or slightly alkaline oxidizing solutions should produce an oxide surface layer on nickel. At the conditions of the present investigation, a 3.5 wt% NaCl solution with pH equal to 6.3 is slightly acidic and one should expect a slight corrosion of nickel. Based on the XPS results of this investigation, we show that nickel corrodes through the formation of Ni(OH)₂. Ni(OH)₂ is a thermodynamically stable substance in the presence of water in neutral or slightly alkaline solutions free from oxidizing or reducing agents. However, it dissolves in

acid solutions with the formation of Ni^{2+} . The fact that our present XPS study proved more useful for studying corrosion products of nickel than our previous XAFS study⁷ is probably due to the solubility of $\text{Ni}(\text{OH})_2$. The solubility of the corroding product, $\text{Ni}(\text{OH})_2$, in acid solutions results in the formation of a thin surface layer which is more amenable to surface analytical techniques such as XPS rather than bulk analytical techniques such as XAFS.

According to the potential-pH equilibrium diagram for the tungsten-water system by Pourbaix²⁰, in the presence of non-complexing acid solutions, tungsten tends to be covered with WO_2 or a higher oxide. Clearly, our results show the formation of both WO_2 and WO_3 , as expected leading to the great corrosion resistance of tungsten.

Conclusions

Based on XPS analysis of corrosion products for W-Ni-Fe superalloys induced by immersion in 3.5 wt% NaCl solution the following conclusions are made: (i) the chemistry of Fe is similar to that of Fe in Fe_3O_4 (an oxygen deficient form of Fe_2O_3), (ii) the chemistry of Ni is similar to that of Ni in $\text{Ni}(\text{OH})_2$, (iii) W is the component of the alloy which is more immune to corrosion due the formation of passive films of WO_2 and WO_3 , (iv) the lower corrosion rate for the S1 alloy relative to that of the K1 alloy is probably due to an already existing WO_2 and WO_3 coatings which are thicker on the surface of the S1 alloy, and (v) localized corrosion is more apparent on the surface of the S1 alloy and is probably due to non-uniform distribution of the tungsten particles in the S1 alloy relative to those in the K1 alloy.

Acknowledgements

This work was supported by NAVSEA.

References

1. P. N. Jones, "The Use of Tungsten in Armament Related Products," in Proceedings of the Second International Tungsten Symposium, (San Francisco, CA, 1982), p. 81.
2. D. J. Jones and P. Munnery, Powder Metallurgy, 10 20 (1967): p. 156.
3. J. F. Andrew, M. T. Baker, and H. T. Heron, "Corrosion and Protection of Sintered Tungsten Alloy Ammunition Components," in Proceedings of the Second Charlottesville Conference on High Density KE Penetrator materials, (1980).
4. J. W. Koger, "Corrosion of Tungsten-3.5 Nickel-1.5 Iron and its Constituent Phases in Aqueous Chloride Solutions," Corrosion/75, paper no. 42 (Toronto, Canada: National Association of Corrosion Engineers, 1975).
5. K. L. Vasanth, R. Conrad, and C. M. Dacres, "Pitting Behavior of Tungsten Alloys in 3.5% NaCl Solution," in Proceedings of the 11th International Corrosion Congress, (Florence, Italy, 1990), vol. 5, p. 5.223.
6. K. L. Vasanth and C. M. Dacres, "Corrosion of Tungsten Alloys in Marine Environments," in Proceedings of the 1987 Tri-Service Conference on Corrosion, W-PAFB, OH, AFWAL-TR-87-4139, Vol. II, 1987, p. 165.

7. A. N. Mansour and K. L. Vasanth, "XAFS Studies of Corrosion Products on W-Ni-Fe Alloys" in Proceedings of the Symposium on X-Ray Methods in Corrosion and Interfacial Electrochemistry, (Phoenix, AZ, 1991), published by the Electrochemical Society, The 180th Meeting of the Electrochemical Society, Vol. 92-1, p. 272.
8. J. H. Scofield, *J. Electron Spectrosc.*, 8 (1976): p. 129.
9. H. Konno and M. Nagayama, *Passivity of Metals: Proceedings of the Fourth International Symposium on Passivity*, (Princeton, NJ: Electrochemical Society, 1978), editors: R. B. Frankenthal and J. Kruger, p. 585.
10. N. S. McIntyre and D. G. Zetaruk, *Analytical Chemistry*, 49 11 (1977): p. 1521.
11. G. C. Allen, M. T. Curtis, A. J. Hooper, and P. M. Tucker, *J.C. S. Dalton*, (1974): p. 1525.
12. K. Asami and K. Hashimoto, *Corros. Sci.*, 17 7 (1977): p. 559.
13. T. L. Barr, *J. Phys. Chem.*, 82 16 (1978): p. 1801.
14. N. S. McIntyre and M. G. Cook, *Analytical Chemistry*, 47 13 (1975): p. 2208.
15. C. A. Melendres and M. Pankuch, *J. Electroanal. Chem.*, 333 (1992): p. 103.
16. C. D. Wagner and D. M. Bickham, *NIST Standard Reference Database 20, NIST X-Ray Photoelectron Spectroscopy Database, Version 1.0*, (Gaithersburg, MD: NIST, 1989).
17. B. A. Shaw, G. D. Davis, T. L. Fritz, B. J. Rees, and W. C. Moshier, *J. Electrochem. Soc.*, 138 11 (1991): p. 3288.
18. M. Pourbaix, *Atlas of Electrochemical Equilibria in Aqueous Solutions*, (Houston, TX, National Association of Corrosion Engineers, 1974), p. 307.
19. M. Pourbaix, *ibid*, p. 330.
20. M. Pourbaix, *ibid*, p. 280.

Table I. Summary of XPS atomic percents for the K1 and S1 alloys as a function of immersion time in 3.5 wt% NaCl solution. The carbon and silicon concentrations were excluded due to their irrelevance to the corrosion process. Those of oxygen includes, in part, the oxygen signal bonding to carbon.

| Sample | Immersion Time | Atomic percent of | | | |
|----------|--|-------------------|------------|-------------|--------------|
| | | Oxygen | Iron | Nickel | Tungsten |
| Alloy K1 | 0 (control) | 54.3 | 0.7 | 0.9 | 44.1 |
| | 2 days | 56.1 | 4.3 | 4.6 | 35.0 |
| | 10 days | 65.1 | 2.9 | 4.2 | 27.9 |
| | 17 days | 58.2 | 2.7 | 2.6 | 36.5 |
| Alloy S1 | 0 (control) | 53.1 | 0.6 | 1.8 | 44.4 |
| | 4 hours | 43.4 | 1.1 | 1.9 | 53.7 |
| | 2 days | 46.3 | 1.5 | 2.5 | 49.7 |
| | 17 days (black areas) (brown areas) | 66.0 66.6 | 1.2 8.9 | 1.6 10.0 | 31.2 14.6 |

Table II. Summary of various tungsten chemistries for the K1 and S1 alloys as a function of immersion time in 3.5 wt% NaCl solution.

| Sample | Immersion Time | Mole Percent of | | |
|-----------|--|-----------------|-----------------|-----------------|
| | | W | WO ₂ | WO ₃ |
| Alloy K 1 | 0 (control) | 67 | 17 | 16 |
| | 2 days | 26 | 35 | 39 |
| | 10 days | 10 | 49 | 41 |
| | 17 days | 33 | 19 | 48 |
| Alloy S1 | 0 (control) | 41 | 32 | 27 |
| | 4 hours | 46 | 35 | 19 |
| | 2 days | 41 | 37 | 22 |
| | 17 days (black areas) (brown areas) | 24 19 | 31 22 | 45 60 |

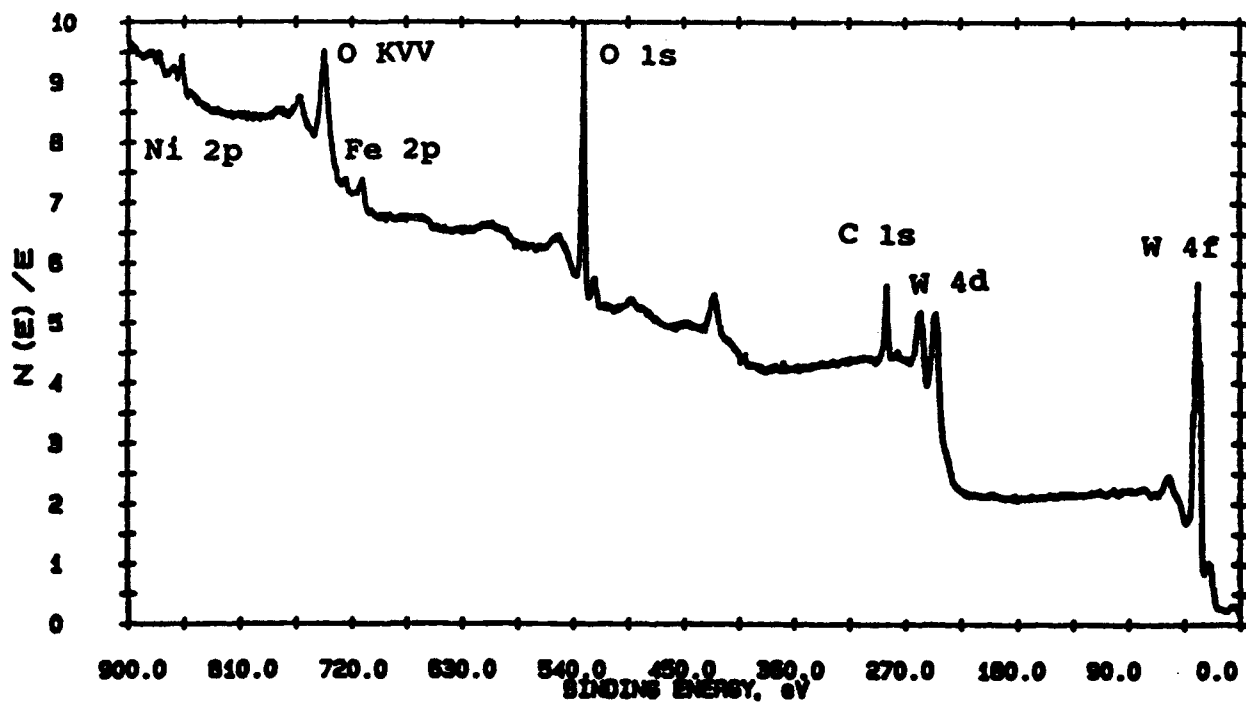
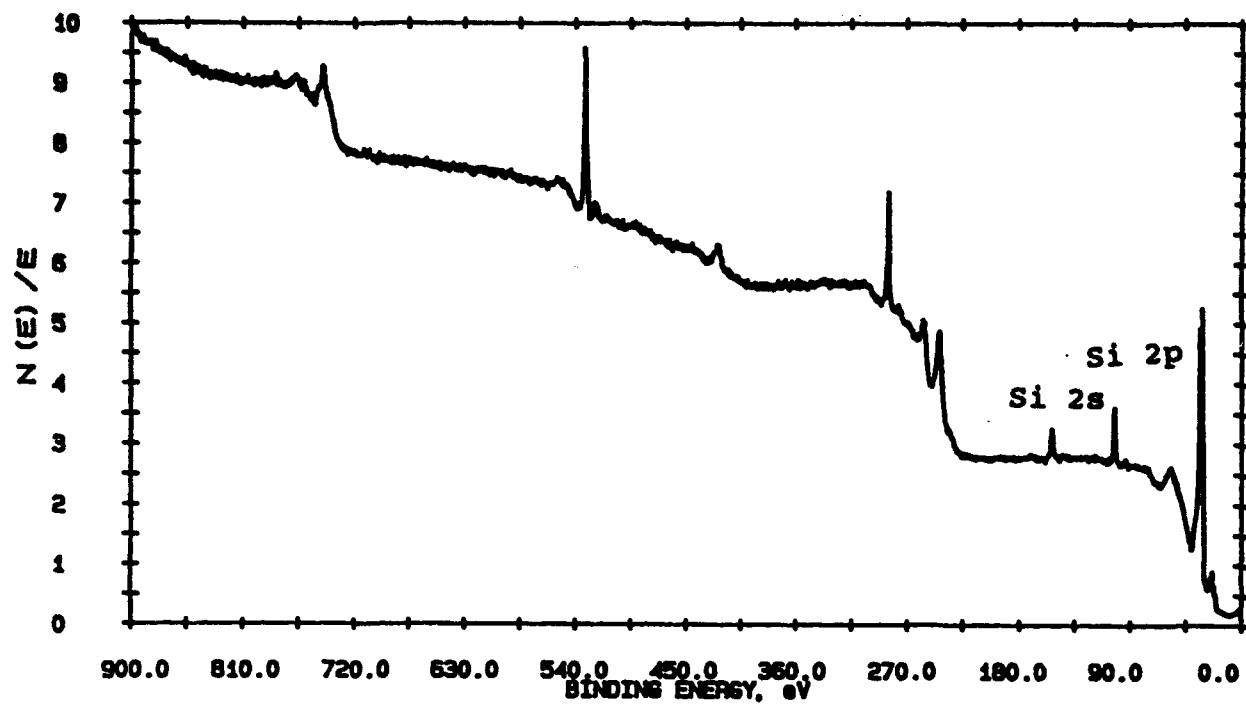


Figure 1 XPS survey spectra for K1 alloy: control (top) and after immersion in 3.5 wt% NaCl solution for 2 days (bottom).

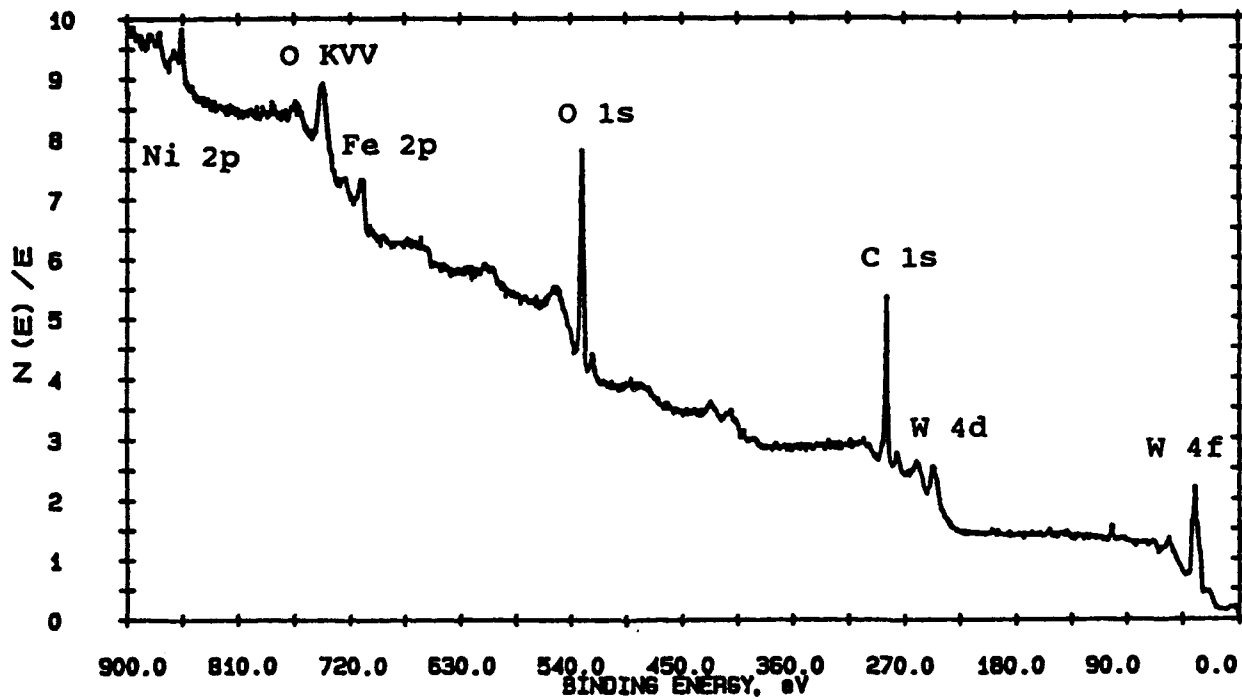
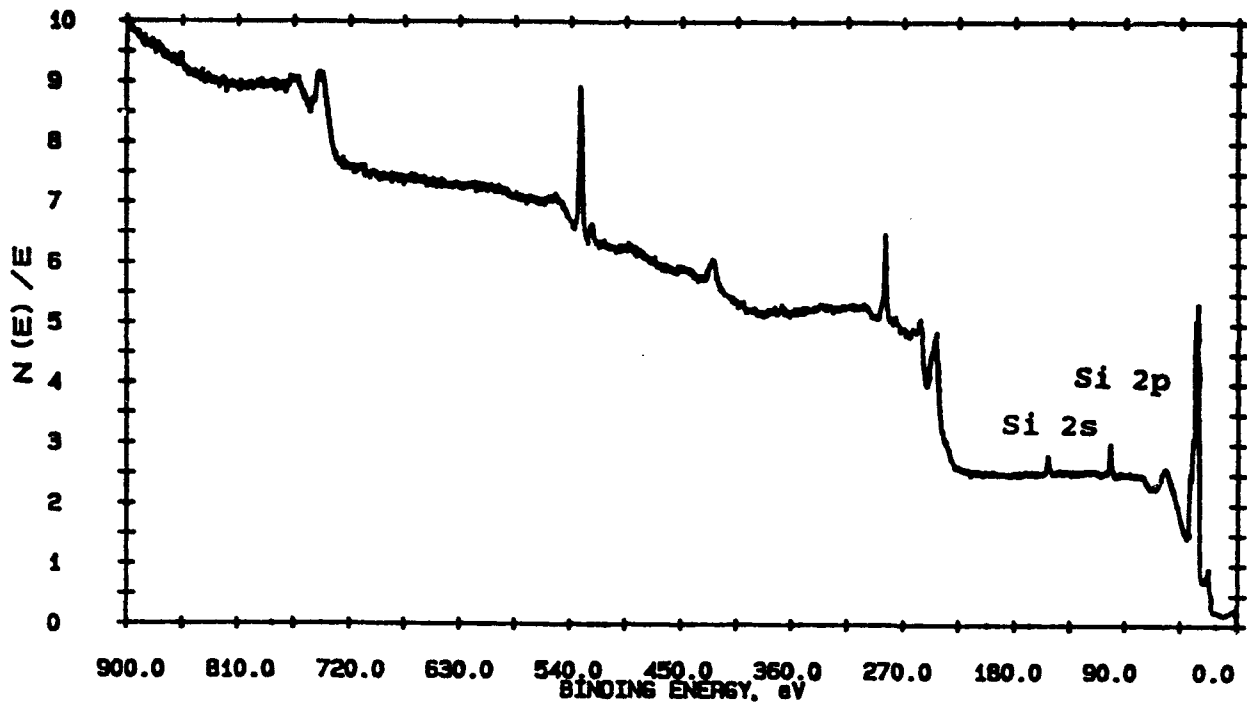


Figure 2 XPS survey spectra for Si alloy: control (top) and after immersion in 3.5 wt% NaCl solution for 17 days (bottom).

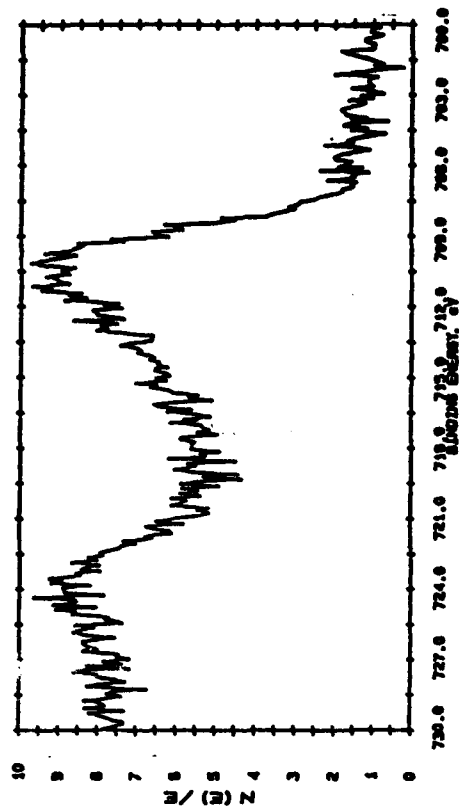


Figure 3 Fe 2p XPS spectra for the K1 alloy (left) and the S1 alloy (right) after immersion in 3.5 wt% NaCl solution for 2 and 17 days, respectively.

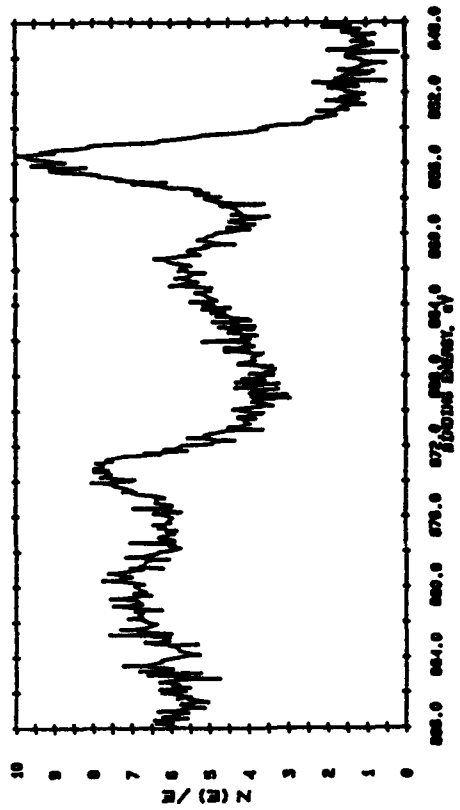


Figure 4 Ni 2p XPS spectra for the K1 alloy (left) and the S1 alloy (right) after immersion in 3.5 wt% NaCl solution for 2 and 17 days, respectively.

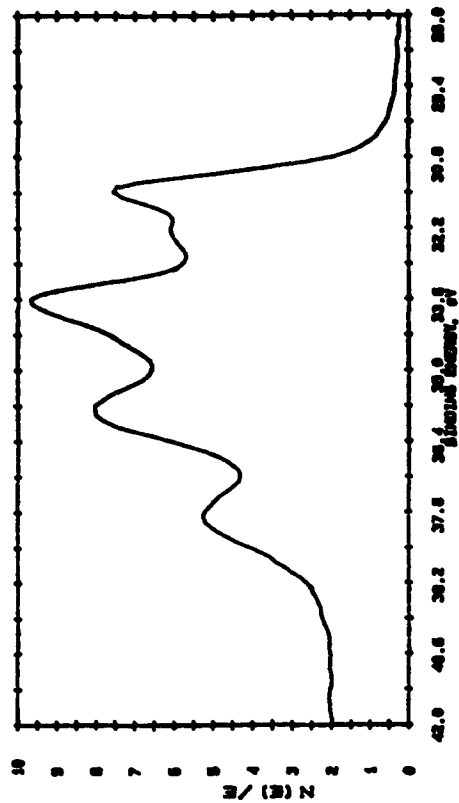


Figure 5 W 4f XPS spectra for the K1 alloy: control (left) and after immersion in 3.5 wt% NaCl solution for 2 days (right).

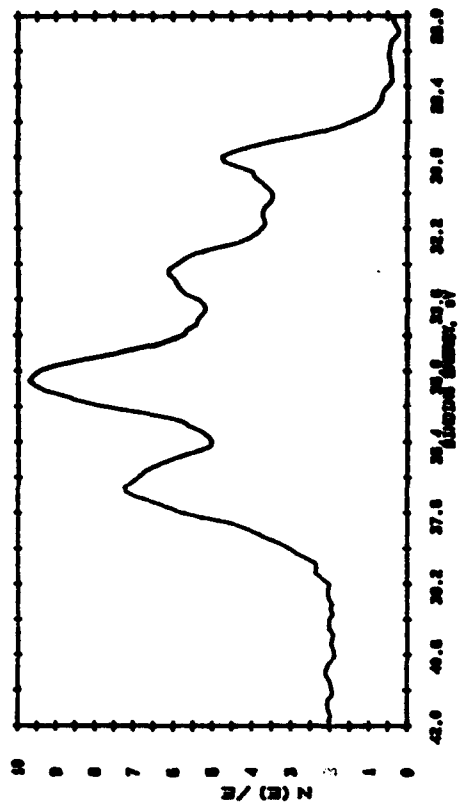


Figure 6 W 4f XPS spectra for the S1 alloy: control (left) and after immersion in 3.5 wt% NaCl solution for 17 days (right).

The Effect of Surface Conditions on the Localized Corrosion of a Candidate High-Level Nuclear Waste Container Material

D.S. Dunn
Center for Nuclear Waste Regulatory Analyses
Southwest Research Institute
6220 Culebra Road
San Antonio, TX 78228-0510

N. Sridhar
Center for Nuclear Waste Regulatory Analyses
Southwest Research Institute
6220 Culebra Road
San Antonio, TX 78228-0510

G.A. Cragnolino
Center for Nuclear Waste Regulatory Analyses
Southwest Research Institute
6220 Culebra Road
San Antonio, TX 78228-0510

Abstract

The effect of surface conditions on the localized corrosion of alloy 825, in simulated groundwater containing chloride, was investigated. It was found that the corrosion, breakdown, and repassivation potentials for mill-finished surfaces were more active than for polished surfaces. This was related to the depletion of chromium in the initial surface layers. Thermal oxidation in a dry environment at temperatures up to 300°C did not change the breakdown and repassivation potentials in a wet environment. The corrosion potential was also found to increase with temperature and to a lesser extent with thermal exposure time. The repassivation potential was observed to be independent of the charge density for deep pits. In aerated solutions containing H₂O₂, the repassivation potential was approximately equal to or slightly less than the corrosion potential.

Key terms: Pitting, surface effects, repassivation, alloy 825, nuclear waste

Introduction

The high-level nuclear waste packages intended for geological disposal are required by the U. S. Nuclear Regulatory Commission (USNRC) to contain radionuclides for at least 300 to 1000 years. In order to minimize the possibility of corrosion related failures under the unsaturated conditions prevailing at the proposed repository site at Yucca Mountain, it has been proposed that a high thermal loading of the repository be used to create a dry-out area in the geologic surroundings adjacent to the containers. However, several studies have indicated that remote condensation of evaporated groundwater and backflow to containers through fractures is plausible [1-3]. It has also been demonstrated that the concentration of anions in groundwater increases with the number of evaporation cycles [4]. Therefore, a conservative estimation of container lifetimes should assume at least some degree of container wetting with aqueous solutions containing varying amounts of aggressive anions.

Previous studies have proposed the use of the repassivation potential as a lower bound parameter in predicting the service life of nuclear waste containers [5-10]. In the case of pitting corrosion, the repassivation potential was first proposed by Pourbaix et. al. [11], as the potential below which all existing pits cease to grow, and above which existing pits grow without the formation of new pits. Investigations by Sridhar and Cragolino [5] indicated that the repassivation potential, E_{rp} , was not as strongly dependent as the breakdown or pitting potential, E_p , on the concentration of chloride. It has also been shown that E_{rp} decreases with pit depth for very shallow pits but was independent of pit depth for deep pits [7]. With the exception of pit depth, the effect of surface conditions on E_{rp} has only received limited attention in previous publications. Sydberger [12] found that various surface preparations, such as different grit finishes and types of pickling operations, had a marked effect on the initiation of pitting and crevice corrosion of austenitic and ferritic stainless steels. These results were attributed to the efficacy of the different surface preparations in removing sulfide inclusions. It has also been demonstrated that the chromium depleted surface layers, which were found to be present on some stainless steels and nickel based alloys, were responsible for an increased susceptibility to crevice corrosion in both ferric chloride and sea water [13,14].

The objective of this investigation was to determine the relationship between surface conditions and the corrosion properties of alloy 825. Since, in a repository setting, the waste containers are expected to be at temperatures as high as 250°C for long periods of time (> 100 years), the effects of thermal oxidation on the breakdown and repassivation potentials was studied. The corrosion potential was also measured under several possible simulated repository conditions. The detrimental effects of the chromium-depleted, mill-finished surface on the performance of the material were also examined.

Experimental Procedures

All experiments were conducted on alloy 825 received in the form of 12.5 mm plate with a mill-finished surface. The bulk and surface compositions of the material are given in Table 1. Cylindrical specimens 6.35 mm diameter were machined transverse to the rolling direction. Short specimens, 19.05 mm long, were used for cyclic potentiodynamic polarization tests. Longer specimens, 48.65 mm long, were used in potential staircase repassivation potential tests. The specimens were polished to a 600 grit finish using wet SiC paper, cleaned in an ultrasonic bath containing detergent, rinsed in high purity water, degreased with acetone, and dried. Experiments with chromium-depleted surfaces were conducted using specimens measuring 12.5 mm × 12.7 mm × 17.8 mm. This geometry incorporated two 12.7 mm × 17.8 mm mill-finished surfaces. The four remaining surfaces, which were measured to be of bulk composition, were polished to either a 60 or 600 grit finish. These specimens were cleaned ultrasonically in detergent.

rinsed in high purity water, cleaned ultrasonically in acetone, and dried. The weights of all specimens were then recorded. Specimens undergoing thermal oxidation were placed in forced air convection ovens at 100°C or 300°C for periods of 1, 10, and 30 days. Upon removal, the specimens were allowed to cool to room temperature and reweighed. Corrosion testing was carried out by first connecting the specimens to an ASTM G-5 [15] specimen holder and then partially immersing them to prevent crevice corrosion at the gasket-specimen interface. Test solutions representative of groundwater at Yucca Mountain, with a higher chloride concentration to simulate the effect of evaporation cycles, were prepared using analytical grade reagents and high purity water. The solutions consisted of 500-10000 ppm Cl^- , 85 ppm HCO_3^- , 20 ppm SO_4^{2-} , 10 ppm NO_3^- , and 2 ppm F^- , all as sodium salts. All tests were done at $95 \pm 2^\circ\text{C}$. Solutions were deaerated with high purity nitrogen or argon. Measurements of the corrosion potential, E_{corr} , were also conducted in aerated solutions with and without the addition of 5 mmol H_2O_2 . Aeration was achieved by bubbling a high purity 79:21 mixture of N_2 and O_2 so as not to introduce CO_2 into the solution.

Repassivation tests were conducted in an ASTM G-31 type one-liter reaction kettle (approximately 900 ml solution) with a fritted glass bubbler, a platinum counter electrode, and a luggin probe with a porous silica tip. A saturated calomel electrode was used as the reference electrode in all experiments. Details of the experimental setup have been published elsewhere [7]. Specimens were tested in deaerated solutions containing 500, 1000 and 10000 ppm Cl^- . Pits were initiated in the 500 and 1000 ppm Cl^- solutions at 600 mV_{SCE}. After initiation, the pits were grown at 500 mV_{SCE} in the 500 ppm Cl^- solution and 400 mV_{SCE} in 1000 ppm Cl^- solutions. For the 10000 ppm solution, the pits were initiated at 400 mV_{SCE} and grown at 200 mV_{SCE}. When a predetermined charge density was reached, the potential was reduced at 5 mV/sec. The potential at which the current density remained below 50 $\mu\text{A}/\text{cm}^2$ was determined to be the repassivation potential. Cyclic potentiodynamic polarization (CPP) experiments were conducted in an ASTM G-5 type five-neck flask equipped with a calibrated thermometer, and a platinum counter electrode. A luggin probe with a porous silica tip was filled with 0.5 M NaCl to provide electrical contact to a remote saturated calomel reference electrode maintained at room temperature. Argon was bubbled at approximately one atmosphere pressure for a minimum of one hour prior to the start and throughout the duration of the test. Electrochemical measurements were made with an EG&G PARC Model #173 potentiostat equipped with a Model #276 current converter and an IEEE-488 interface. The potentiostat was controlled with a 386 computer using PARC M342C software. The data was converted to an ASCII format and analyzed at the end of the experiment.

After testing, specimens were ultrasonically cleaned in a mixture of 4 ml 2-butyne-1,4-diol (35% aq. solution), 3 ml concentrated HCl, and 50 ml high purity water to remove the attached corrosion products [16]. Previous tests on control samples confirmed that this cleaning procedure does not result in measurable corrosion of the substrate. The specimens were then reweighed and examined using a 70x stereoscope. Selected specimens were examined using a scanning electron microscope (SEM) for areal pit density, pit depth and composition using energy dispersive spectrometry (EDS).

Results

Representative multiple CPP scans for the mill-finished surfaces are displayed in Figure 1. These are CPP scans conducted on a single specimen successively with fresh solution being used after each scan. Very low E_p and E_m values were obtained in the initial scans of chromium depleted surfaces but only uniform corrosion was observed. Subsequent scans, however, exhibited large hysteresis, indicating the presence of localized corrosion. The passive current density tended to decrease with successive scans while E_p and E_m increased. Examination of the specimens using a 70x stereoscope revealed that the mill-

finished surfaces pitted after 3 or 4 scans. The pits were randomly distributed on the immersed portions of the mill-finished surfaces and no evidence of preferential pitting at the solution vapor interface was observed. On the other hand, the adjacent surfaces, having the bulk composition through grinding to either a 60 or 600 grit finish, did not show any evidence of pitting. For the as-received and thermally treated mill-finished surfaces, E_p was found to increase with cumulative charge density, contrary to previous results obtained for polished specimens [7]. Analysis of these specimens using EDS revealed that the chromium content at the surface increases with the amount of charge passed. In Figure 2, the results of the CPP tests in terms of E_p and E_{np} are plotted as a function of the chromium content measured on non-pitted regions at the conclusion of successive scans. This figure was generated using the results of both mill-finished surfaces having less than the bulk concentration of chromium and polished specimens having 22.10 percent chromium. It is evident from this plot that E_p and E_{np} are strongly dependent on the concentration of chromium at the surface. It must also be noted that the molybdenum content of the surface is lower than that of the bulk as indicated in Table 1. Below a surface chromium concentration of 17 percent, uniform corrosion predominated. Localized corrosion occurred at surface chromium concentrations higher than 17 percent and pitting of the chromium depleted surfaces was initiated at potentials as low as 220 mV_{SCE}. The E_{np} of these surfaces, following the initiation of pitting, was found to be much more active than that of the bulk material.

Visual observation of the thermally treated specimens revealed that all specimens treated at 300°C appeared to have a gold color oxide film. The mill-finished specimens treated at this temperature had a much darker colored film than polished specimens. Specimens treated at 100°C did not have this appearance. No weight change (± 0.00015 g) was measured at the conclusion of thermal treatment in the range of times and temperatures investigated.

The results in Table 2, obtained using CPP, indicate that E_p and E_{np} are neither functions of temperature nor length of thermal oxidation in the ranges studied. It may also be seen that the passive current density decreases whereas E_{corr} increases with the temperature of thermal exposure. During post-test examination, pits were noted on all of the specimens.

Results obtained using the decreasing potential staircase technique are shown in Figure 3. As previous reports have indicated, E_p is initially a strong function of charge density [18,19]. In 1000 ppm Cl⁻ solutions, beyond approximately 100 coulombs/cm², E_p is virtually independent of charge density. This result was apparent for both as-polished and thermally oxidized specimens. The effect of chloride concentration is also indicated in this figure. Specimens tested in more concentrated chloride solutions had lower E_p values. In comparison to the CPP results, which used a slower scan rate, the E_p values measured by this technique were more active. The observation that E_p decreases with scan rate has been previously documented [7].

Examination of the pitted specimens revealed that the pits were uniformly distributed over the surface. Excellent correlation ($R^2=0.99$) was found between weight loss and charge density indicating that the charge passed went to either pit initiation or pit growth. This relationship was experimentally determined to be

$$\text{Weight Loss} = 2.59 \times 10^{-4} \text{ g/coulomb} \quad (1)$$

This compares well to the theoretical weight loss of 2.64×10^{-4} g/coulomb assuming that the dissolution of iron, chromium and nickel occurs as Fe²⁺, Cr³⁺, and Ni²⁺, respectively in the same ratio as they are present in the alloy. The weight loss contributed by the dissolution of the other alloying additions was

assumed to be insignificant. The relationship between areal pit density and charge density, plotted in Figure 4, was found to be

$$\text{Percent area pits } (A) = 0.34 (Q)^{0.56} \quad (2)$$

where Q is the charge density in coulombs/cm². The scatter in the data ($R^2=0.87$) reflects both the difficulty of the measurements, especially on cylindrical specimens, and the fact that not all of the charge density went to the formation of new pits. Estimation of the maximum pit depth was done by cross-sectioning the specimens. The relationship between the amount of charge passed and the pit depth is given by

$$\text{Depth, } d \text{ (mm)} = 0.11 (Q)^{0.42} \quad (3)$$

The exponent in this equation is significantly different than 0.33 expected for hemispherical shaped pits, although most of the pits observed were found to be hemispherical. However, deep pits appeared to be formed by the initiation and growth of new pits in the bottom of existing ones. This resulted in some pits having a more cylindrical shape which would increase the exponent in equation 3. Inaccurate depth measurements may also be due to the difficulty in sectioning pits in the deepest location. An additional source of error, particularly at low charge densities, is that an increasingly large fraction of the charge density went towards pit initiation and not necessarily existing pit growth.

Open circuit potential measurements (E_{oc}) carried out on thermally treated specimens in a range of solutions are shown in Figure 5. The results show that E_{oc} increased as a result of aeration and 5 mmol H₂O₂ added to simulate the effect of radiolysis. Specimens treated at 300°C had E_{oc} values in the range of 100 to 400 mV more noble than the specimens treated at 100°C. For specimens treated at the lower temperature, the time of exposure was also important. The difference in E_{oc} of polished specimens treated at 100°C for 1 and 30 days was 200 mV. Specimens with a mill-finished surface were characterized by more active corrosion potentials. The effect of thermal oxidation temperature is also not as pronounced. At the conclusion of the rest potential measurements in aerated solutions containing H₂O₂, reddish-brown corrosion products were observed on some of the mill-finished surfaces. Examination of these surfaces, however, did not reveal any pits. For both bulk and mill-finished specimens whether thermally aged or not, E_{oc} in aerated solutions containing H₂O₂ was very near or slightly greater than E_p in deaerated solutions.

Discussion

The mill-finished surfaces were found to have E_p values that increased with charge density. Observation of the curves generated by CPP during initial scans reveals that the breakdown and repassivation behavior of the chromium-depleted surfaces differs considerably from that of the bulk material. The increase in E_p and E_r during successive scans was found to be related to the amount of chromium on the surface of the alloy. This result can be likened to the previous investigation by Wilde and Williams [17] who demonstrated that the E_p of stainless steels increases with the concentration of chromium. The fact that several scans were needed to form pits indicates that uniform corrosion initially occurs on the chromium-depleted surface. After the initial surface layers are removed, the surface composition has a higher concentration of chromium and becomes more corrosion resistant. Pitting of the surface can then occur at potentials more noble than E_p for the initial surface layer but much more active than E_p for the bulk material. The results obtained here suggest that surface compositions containing approximately 17 percent chromium are susceptible to pitting. The E_p for the pitted chromium-depleted surface was also more

active compared to the bulk material. However, the pits formed were shallow, resulting in a low cumulative charge density ($< 7 \text{ C/cm}^2$). The chromium-depleted layer on some nickel based alloys has been measured to be up to $12 \mu\text{m}$ deep [13]. Deeper pits, penetrating through the initial chromium-depleted surface layer, would be expected to have E_p values similar to those of the bulk material. Hence, the E_p value of bulk specimens can still be used to predict long-term performance of the proposed container material.

Decreasing potential staircase tests indicated that E_p is a function of charge density for shallow pits. Combining the results displayed in Figures 3 and 4, it can be calculated that for pits deeper than 0.7 mm , E_p is independent of pit depth. Similar results have previously been reported [17,18].

The passive films formed by thermal oxidation did not yield higher breakdown potentials or alter E_p in the range of chloride concentrations tested. Both as-polished and thermally oxidized specimens were found to have E_p which were dependent on scan rate and charge density. This is not surprising since even very shallow pits would be expected to easily penetrate the oxide films.

Thermal exposure had a marked effect on E_{corr} of the polished specimens. As the temperature of thermal oxidation increased, the value of E_{corr} was observed to shift to a more noble potential. This effect can be attributed to an improvement in the protective properties of the passive film. Similarly, a decrease in the passive current density from $1.4 \mu\text{A/cm}^2$ for the as-polished surface to values between 0.04 and $0.1 \mu\text{A/cm}^2$ for specimens exposed to 300°C was observed. Specimens exposed to 100°C had passive current densities that decreased with exposure time. These observations suggest that prior exposure to a hot dry environment may result in either a growth of the passive film or a change in the electronic properties of the film.

The corrosion potential was observed to increase by aeration of the solutions. An additional increase was observed in aerated solutions when H_2O_2 was added to simulate the effects of radiolysis. E_{corr} in these solutions was in the range of the repassivation potentials for the material in a deaerated 1000 ppm Cl^- solution. This result points out the possible inability of the material to repassivate following the initiation of localized corrosion in such an environment. The mill-finished surfaces consistently had lower E_{corr} values than their bulk composition counterparts. In addition, thermal oxidation had less of an effect on the value of E_{corr} for the chromium-depleted surfaces. The differences observed are most likely caused by a different type of oxide film being formed on the mill-finished surface as a result of the different surface composition. Since the mill-finished surface is deficient in chromium, nickel, and molybdenum, which are the most significant alloying elements that determine the localized corrosion resistance, the passive films formed on this surface can be expected to have inferior protective properties compared to the bulk material. E_{corr} for these surfaces treated under similar conditions appeared to vary considerably from sample to sample. The passive current density of the mill-finished surfaces, while highly variable, was $2.2 \mu\text{A/cm}^2$, 50 percent greater than that of the polished specimens.

Conclusions

This investigation on the surface effects of alloy 825 has shown that in the ranges tested, the length and temperature of thermal exposure in a dry environment had no effect on the breakdown potential, E_p , or the repassivation potential, E_p , in a wet environment. This was true for both bulk composition and mill-finished specimens. Thermal oxidation, however, shifted the corrosion potential, E_{corr} , to a more noble value in correspondence with a reduced passive current density. The mill-finished surfaces were observed to have E_p and E_p values that were dependent on the chromium content of the surface layers. Multiple

cyclic potentiodynamic polarization tests showed that after some initial uniform corrosion of the surface layers, pitting of the chromium depleted regions was initiated at $220 \text{ mV}_{\text{SCR}}$, when the chromium content of the depleted layer reached about 17 percent. In solutions containing H_2O_2 , E_{corr} was, in some cases, more noble than E_p . From the results of this study, it is evident that while the E_p is a useful parameter in predicting long-term performance, the localized corrosion behavior of this proposed container material is compromised by the presence of a chromium-deficient, mill-finished surface. Additional investigations into the detrimental effects of chromium-depleted surfaces on other proposed high-level nuclear waste container materials are warranted.

Acknowledgments

The assistance of Steve Griffin in conducting the experiments is acknowledged. This paper was prepared to document work performed by the Center for Nuclear Waste Regulatory Analyses (CNWRA) for the U.S. Nuclear Regulatory Commission under Contract No. NRC-02-88-005. The activities reported here were performed on behalf of the NRC Office of Nuclear Regulatory Research, Division of Regulatory Applications, Dr. M.B. McNeil, Project Officer. The paper is an independent product of the CNWRA and does not necessarily reflect the views or regulatory position of the NRC.

References

1. W. C. Patrick. "Spent Fuel Test - Climax: An Evaluation of the Technical Feasibility of Geologic Storage of Spent Nuclear Fuel in Granite." Final Report, UCRL-53702, Lawrence Livermore National Laboratory, Livermore, CA, March 30, 1986.
2. A. L. Ramirez, ed. "Prototype Engineered Barrier System Field Test (PEBSFT) Final Report," UCRL-ID-106159, Lawrence Livermore National Laboratory, Livermore CA, August 1991.
3. R. M. Zimmerman, R. L. Schuch, D. S. Mason, M. L. Wilson, M. E. Hall, M. P. Board, R. P. Bellman, and M. P. Blanford. "Final Report: G-Tunnel Heated Block Experiment." SAND84-2620, Sandia National Laboratories, Albuquerque, NM, May 1986.
4. J. A. Beavers, N. G. Thompson, and C. L. Durr. "Pitting, Galvanic and Long-Term Corrosion Studies on Candidate Container Alloys for the Tuff Repository." NUREG/CR-5709. Cortest Columbus Technologies, Inc., Columbus, OH, January 1992.
5. N. Sridhar, G. A. Cragnolino, and D. Dunn, "Experimental Investigations of Localized Corrosion of High Level Waste Container Materials", CNWRA 93-004, Center for Nuclear Waste Regulatory Analyses, San Antonio, TX, February 1993.
6. N. Sridhar, G. A. Cragnolino, J. C. Walton, and D. Dunn, "Prediction of Crevice Corrosion using Modeling and Experimental Techniques." Application of Accelerated Corrosion Tests to Service Life Prediction of Materials, ASTM STP 1194, G. Cragnolino and N. Sridhar, Ed., American Society for Testing and Materials, Philadelphia, PA, in press.
7. N. Sridhar, and G. A. Cragnolino, "Long-term life prediction of localized corrosion of Fe-Ni-Cr-Mo high-level nuclear waste container materials." Corrosion/93. Paper No.93-197. National Association of Corrosion Engineers (NACE), Houston, TX, 1993.

8. S. Tsujikawa, and Y. Hisamatsu, "Repassivation potential as a crevice corrosion characteristic for austenitic and ferritic stainless steels", *Improvement of Corrosion Resistance of Structural Materials in Aggressive Media*, Ya. M. Kolotykin, Ed., Nauka Publishers, Moscow, Russia, p. 119, 1984.
9. S. Tsujikawa, and Y. Kojima, "Repassivation method to predict long term integrity of low alloy titanium for nuclear waste package", *Scientific Basis for Nuclear Waste Management XIV, Materials Research Society Symposium Proceedings*, T. A. Abrajano and L. H. Johnson Eds., Materials Research Society (MRS), Pittsburgh, PA, Vol. 212, p. 261, 1990.
10. G. Nakayama, H. Wakamatsu, and A. Masatsune, "Effects of chloride, bromide and thiosulfate ions on the critical conditions for crevice corrosion of several stainless alloys as a material for geological disposal package for nuclear wastes", *Scientific Basis for Nuclear Waste Management XVI, MRS Symposium Proceedings*, C. G. Interrante and R. T. Pabalan Eds., Materials Research Society, Pittsburgh, PA, Vol. 294. 1992, (in press).
11. M. Pourbaix, L. Klimzack-Mathieu, C. Martens, J. Meunier, C. Vanlengenhaghe, L.D. Munch, J. Laureys, L. Nellmans, and M. Warzee. *Corros. Sci.* Vol. 3, p. 236, 1963.
12. T. Sydberger. *Werkst. Korros.* Vol. 32, p. 119, 1981.
13. J. S. Grubb, "Pickling and Surface Chromium-Depletion of Corrosion-Resistant Alloys". *Proceedings of the International Conference on Stainless Steels*. The Iron and Steel Institute of Japan, p. 944, 1991.
14. M. A. Streicher, *Mater. Perf.*, Vol. 22, No. 5, p. 37, 1983
15. *Annual book of ASTM Standards, Section 3, Vol. 03.02*, American Society for Testing and Materials, Philadelphia Pa, 1992.
16. D. Tromans, and L. Frederik, *Corrosion*. Vol. 40, p. 633, 1984.
17. B. E. Wilde and E. Williams, *J. Electrochem. Soc.* Vol. 118, No. 7, p. 1057, 1971.
18. H. Yashiro and K. Tanno, *Corros. Sci.* Vol. 31, p. 485, 1990.
19. T. Nakayama and K. Sasa, *Corros.*, Vol. 32, No. 7, p. 283, 1976.

Table 1. Bulk and surface composition in weight percent of alloy 825.

| Analysis | Fe | Ni | Cr | Ti | Cu | Mo | Si | Al | C |
|--------------------|------|------|------|-----|-----|-----|-----|-----|------|
| Bulk (Vendor) | 30.4 | 41.1 | 22.1 | 0.8 | 1.8 | 3.2 | 0.5 | 0.1 | — |
| Bulk (EDS) | 30.4 | 41.1 | 22.1 | 0.8 | 1.8 | 3.2 | 0.2 | 0.1 | — |
| Mill Surface (EDS) | 43.4 | 35.3 | 15.7 | 0.4 | 1.6 | 2.1 | 0.9 | 0.5 | 0.01 |

Table 2. Results of cyclic potentiodynamic polarization tests on as received and thermally aged specimens of alloy 825.

| Specimen treatment | Corrosion potential, E_{corr} , mV_{SCE} | Passive current density, $\mu A/cm^2$ | Breakdown potential, E_p , mV_{SCE} | Repassivation potential, E_{rp} , mV_{SCE} |
|--------------------|--|---------------------------------------|---|--|
| As-polished (bulk) | -595 | 1.42 | 692 | 158 |
| 100°C, 1 day | -534 | 1.25 | 684 | 115 |
| 100°C, 10 days | -400 | 1.00 | 683 | 166 |
| 100°C, 30 days | -339 | 0.92 | 706 | 137 |
| 300°C, 1 day | -158 | 0.04 | 693 | 156 |
| 300°C, 10 days | -151 | 0.10 | 705 | 156 |
| 300°C, 30 days | -96 | 0.06 | 678 | 141 |

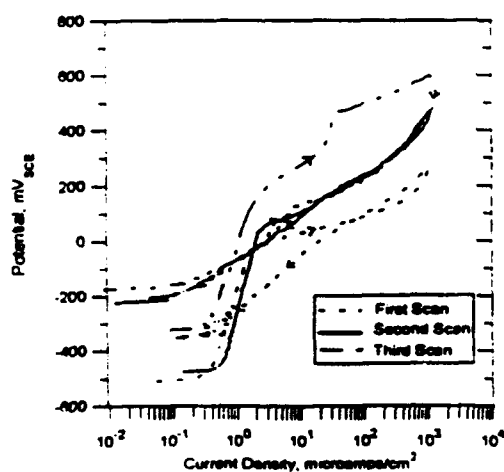


Figure 1. Successive cyclic potentiodynamic polarization scans for mill finished alloy 825 in deaerated 1000 ppm Cl⁻ at 95°C. Scan rate = 0.17 mV/sec. Fresh solution was used for each scan.

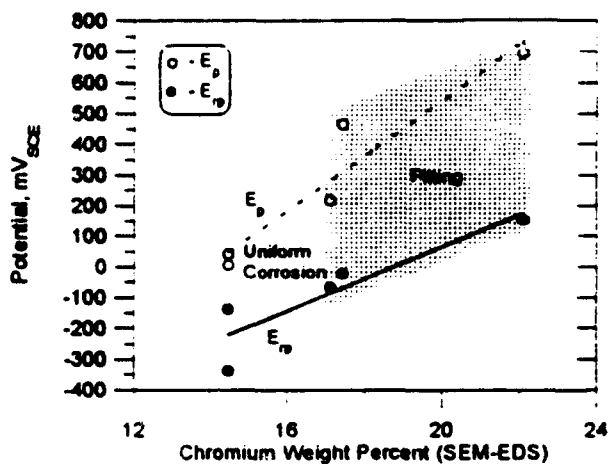


Figure 2. Breakdown and repassivation potential in deaerated 1000 ppm Cl⁻ solution at 95°C vs. weight chromium measured by SEM-EDS on corroded and cleaned specimens. Scan rate = 0.17 mV/sec.

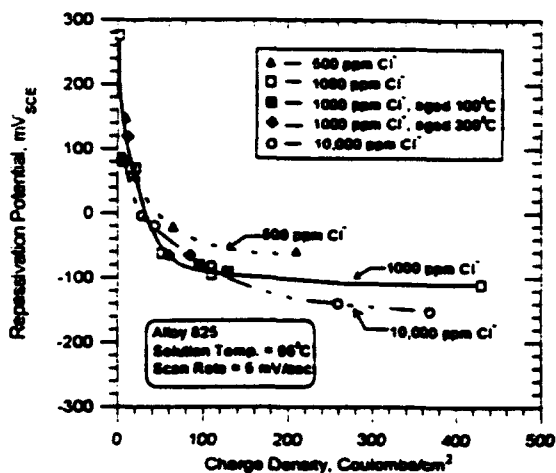


Figure 3. Repassivation potential of polished and thermally oxidized specimens in deaerated 1000 ppm Cl⁻ solution at 95°C as a function of charge density at various chloride concentrations. Scan rate = 5 mV/sec.

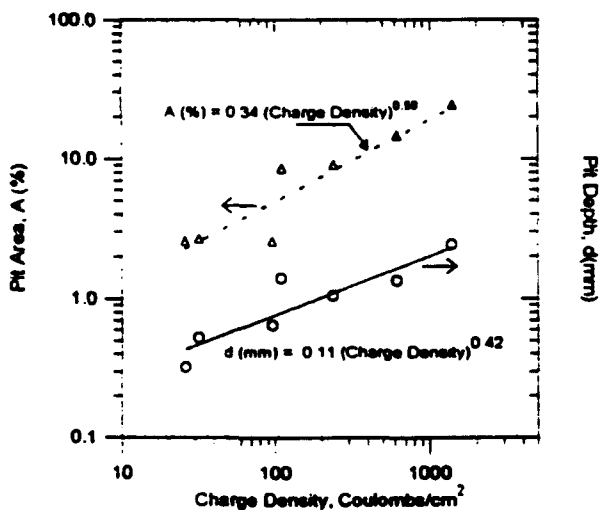


Figure 4. Pit areal density and pit depth as functions of charge density.

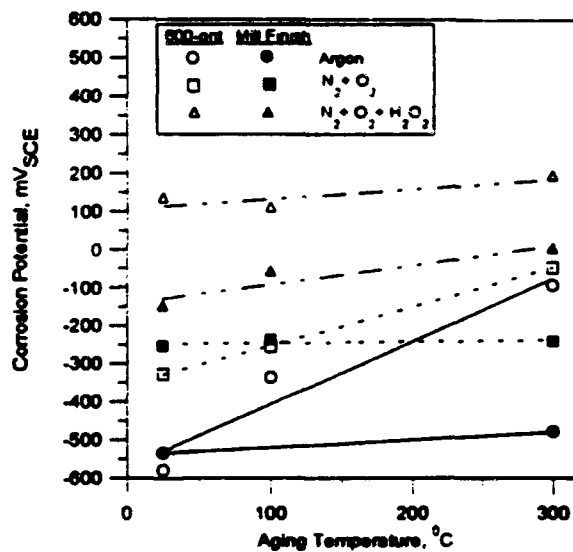


Figure 5. Corrosion potential of alloy 825 in deaerated 1000 ppm Cl⁻ solution at 95°C after thermal oxidation for 30 days at various temperatures.

The Influence of Long-Term Low Temperature Aging on the Performance of Candidate High-Nickel Alloys for the Nuclear Waste Repository

F. G. Hodge
Haynes International, Inc.
1020 West Park Avenue
Kokomo, Indiana

H. S. Ahluwalia
Haynes International, Inc.
1020 West Park Avenue
Kokomo, Indiana

Abstract

The phase stability of candidate alloys under repository-relevant conditions is a critical issue that will have an impact on the long-term mechanical and corrosion properties of the metal barrier. For waste packages with the highest thermal outputs, the surface temperature of the containers will rise to a peak temperature of about 250°C. After 100 years the temperature will drop to about 150°C and will continue dropping slowly.

This paper discusses the metallurgical phase stability in terms of precipitation and ordering behavior of Ni-Cr-Mo-W alloys after long term aging at temperatures below 550°C. In addition, the effect of low temperature aging on the mechanical and corrosion properties is presented. Charpy impact testing and tensile testing have been used to evaluate the effect of aging on mechanical properties. The corrosion resistance has been assessed using standard ASTM G28A and B test methods.

Key terms: Nickel base alloys, aging, corrosion, impact strength, nuclear waste canisters, phase stability

Introduction

The current proposed design for the containment of spent nuclear fuel includes a metallic outer canister¹ which provides structural support and acts as a corrosion barrier against the local groundwater. Early research identified a variety of materials as candidates for the canister including 316L stainless steel and alloy 825.²⁻⁵ Concerns were expressed that the original short list of materials did not include any material that would completely resist the potential conditions so the program was expanded to survey other materials. A recent review of the extensive selection analyses suggested three materials, alloy 825, alloy C-4 and titanium grade 12, which were recommended for the Advanced Conceptual Design of the Yucca Mountain Program.⁶ Corrosion testing done earlier has shown that in a chloride solution that would simulate a concentrated J-13 wellwater, alloy 825 exhibits considerable pitting and crevice attack⁷ while C-22 alloy is free from attack. J-13 wellwater is accepted as being representative of the nominal groundwater in the vicinity of Yucca Mountain. Corrosion resistance of the canister material is therefore an important factor in material selection.

After placement in the storage facility, it is anticipated that the temperature of the canister surface will increase to 250-260°C for several years.⁸ The temperature will then begin a slow decline towards ambient; however, concern exists that this long-term thermal cycle will produce metallurgical changes in the alloy which will alter the corrosion resistance. Most commercial nickel base alloys are in a metastable condition having been quenched to room temperature from an annealing temperature. It is therefore necessary to estimate, by aging at elevated temperatures, the potential kinetics of the formation of any deleterious second phases. Since the kinetics are anticipated to be very slow at the expected canister temperature, slightly elevated temperatures have been used to demonstrate the stability of three alloy C-type alloys. In addition to corrosion resistance, the effect of aging on the mechanical properties was also examined.

Experimental Procedure

The alloys used in this program were HASTELLOY® alloys C-4 (N06455), C-276 (N10276), and C-22 (N06022). The nominal compositions are shown in Table 1. Production hot rolled and annealed 12 mm plates were aged at temperatures of 260, 340, 425, 482, 500, 538, and 593°C in an air atmosphere muffle furnace. A variety of production heats were used and not all heats were exposed at all temperatures.

Following exposure at the desired temperature, samples were prepared for corrosion testing in both the ASTM G-28A and G-28B environments. These environments are accelerated quality control tests used to evaluate the effect of microstructure on corrosion performance. The origin of these two tests was in the work of Streicher⁹ and Manning¹⁰ to find environments that would highlight the presence of an inappropriate microstructure with a significant increase in corrosion rate.

The mechanical properties were determined by measuring the room temperature tensile strength and hardness. The potential loss in toughness was measured by determining the Charpy impact strength. Metallographical examination by optical and transmission electron microscopy to correlate structure with properties completed the evaluation.

Results and Discussion

The mechanical properties as determined from the aged samples for alloys C-276, C-4, and C-22 are presented in Tables 2, 3, and 4 respectively. In an effort to better see the effect of time and temperature, the yield strength data for alloy C-276 have been normalized and presented in Figure 1. Data for 425°C and 538°C at 4000, 8000, and 16000 hours were obtained from an earlier investigation.¹¹ Note that the yield strength is virtually unaffected until the aging at 425°C exceeded 20,000 hours. Even though the yield at 38,000 hours is 1.5 times the annealed yield, the material still exhibited a reduction in area of 64% and the impact strength is 79% of the annealed condition. The sample aged at 482°C for 38,000 hours has doubled its yield strength, however, the material still exhibits 54% reduction in area. The impact strength has reduced to 126 joules, however, this does not constitute a brittle material.

Figure 2 contains the plot of the yield data for alloy C-4. Again it is observed that the properties do not begin to change at 425°C until the time exceeds 20,000 hours. After

46,000 hours the yield ratio is 1.3 but the reduction in area is still 60% and the impact strength is 73% of the annealed condition. Even the sample aged for 38,000 hours at 482°C, which has doubled in strength, still has 58% reduction in area. The impact strength has reduced to 122 joules, but that still is a usable material.

For alloy C-22 no data exist for aging times beyond 20,000 hours or for temperatures above 425°C. Within the scope of this investigation, no measurable change in properties has occurred.

The corrosion rates as determined in both the ASTM G-28A and G-28B solutions are shown in Table 5. The G-28A solution is an oxidizing, chloride free, environment that was developed to be a measure of microstructure for alloy C-276. All three alloys in the annealed condition exhibit uniform attack unless the microstructure is heavily sensitized. The rate in this test is dependent on the chromium/molybdenum ratio, therefore alloy C-22 has consistently lower values. In comparing the corrosion data with the plot of yield strength in Figure 1, the corrosion rate for alloy C-276 increased by 25% after 38,000 hours at 425°C, and this corresponds with a change in the yield strength for alloy C-4, however, the increase in yield strength (Figure 2) after 46,000 hours at 425°C is not accompanied by a corresponding increase in corrosion rate. Even after aging for 38,000 hours at 482°C, the corrosion rate shows only a small increase while the yield strength is doubled.

The G-28B solution is a highly oxidizing high chloride media that was developed to be even more sensitive to the presence of second phases in the grain boundaries of alloy C-276. This test has become the standard quality control test for alloy C-22 and is replacing the G-28A solution as the standard for alloy C-276. Because the critical pitting temperature for alloy C-4 in the G-28B solution is only 90°C, the attack on alloy C-4 is severe in the boiling (105°C) environment regardless of microstructural condition. The high rates make it impossible to detect small changes in rate. For alloys C-22 and C-276, no changes in rate are noted for aging times up to 20,000 hours at 425°C, although the rates for C-22 alloy are consistently lower than those for alloy C-276. In the case of alloy C-276 aged for 38,000 hours at 482°C, the corrosion rate is virtually unaffected even though the yield strength has doubled. Only aging at 538°C produces significant increases in the corrosion rates for alloy C-276. This difference in performance is related to the phases present in the microstructure.

To understand what changes are occurring in the microstructure to produce the observed changes in mechanical property and corrosion resistance and how these might alter the behavior of samples aged at lower temperatures, requires an understanding of the physical metallurgy of these alloys.

All three alloys fall in the gamma phase solid solution region of the Ni-Cr-Mo phase diagram at 1200°C, however, at lower temperatures three metallurgical reactions are possible to varying degrees.¹² A mu-phase based on the Fe₃Mo₂ structure has been identified¹³ in alloy C-276 that begins to precipitate on grain boundaries at about 1075°C. Only 6 minutes at 900°C are required to precipitate enough mu-phase to significantly alter the corrosion rates. The reaction rate decreases with time so that approximately 1000 hours at 650°C are required before precipitates are observed. Alloy C-4 was developed to be mu-phase free by

controlling the Nv of the alloy to a value which was observed experimentally to delay precipitation for 1000 hours at 900°C.¹⁴ Because the tungsten was eliminated to gain the phase stability desired, the localized corrosion resistance was decreased. When alloy C-22 was developed, the composition was balanced in an attempt to improve the localized corrosion resistance beyond that of alloy C-276 without the thermal stability problem.¹⁵ In all three alloys, the kinetics of mu-phase precipitation are slow, and the data suggest that at temperatures below 600°C, it should not be present in the microstructure.

The carbon content required for these alloys to be completely free from carbide precipitation is unknown. The carbon levels are typically less than 0.010 weight percent but M_6C carbides can still precipitate in all three alloys. Curves showing the precipitation of carbides in alloy C-276 were also developed during the mu-phase study.¹³ When the Nv controlled alloy C-4 was developed, it was found that increasing the total stability also slowed the kinetics of carbide precipitation.¹⁴ It is believed that this situation exists because the composition of the mu-phase and carbides are identical except for the fact that carbon is present in one.¹⁶ The curve showing the precipitation of carbides as a function of temperature versus time in alloy C-276 was observed to lay parallel to the mu-phase curve but approximately one order of magnitude shorter in time at temperatures below 700°C. Extrapolation of this curve would suggest that grain boundary carbide precipitation would only be present when the temperatures are above about 500°C.

The third metallurgical reaction is the formation of a long range ordered compound based on the formula A_2B . This reaction has been studied extensively in the binary Ni-Cr system by Klein.¹⁷ The first identification of this phase in a commercial alloy was in connection with a reactor made from alloy C-276 which had been operated at approximately 500°C for 2 years.¹⁸ The presence of the phase was identified by using transmission electron microscopy and selected area diffraction. The composition was assumed to be $Ni_2(Cr,Mo)$. Experiments were performed to show that aging for 1000 hours at 500°C produced an increase in the yield strength with little or no loss in ductility or impact strength in alloy C-276.¹⁹ The A_2B reaction is considered as a second order phase transformation. If one compares the specific heat versus temperature curve a discontinuity occurs in the vicinity of 600°C which indicates that the ordering reaction is proceeding. This same discontinuity exists for all three alloys, indicating that the same reaction occurs in all three alloys.

The microstructures of alloys C-4, C-276, and C-22 after aging for 20,000 hours at 425°C are presented in Figure 3. The photomicrographs at 500X show that the alloys are basically single phase with no precipitates in the grain boundaries. Some scattered second phases are present but these are primary phases produced from solidification segregation in the ingot and they do not participate in the low temperature precipitations. A transmission electron micrograph for the alloy C-22 sample (Figure 4) shows that only the face centered cubic structured matrix is present.

Examination of the structure of alloy C-4 aged for 45,896 hours at 425°C (Figure 5) indicates that the A_2B long range ordering has begun. For alloy C-276 after 37,896 hours at the same temperature (Figure 6) only the matrix phase is present. This would suggest that the phase boundary for A_2B probably would be crossed somewhere between these two times. When

the temperature of aging was increased to 482°C (Figure 7), alloy C-276 has a well developed A_2B structure for the same aging time of 37,896 hours. Increasing the temperature and time produced still further changes. When alloy C-276 was aged 53,880 hours at 538°C a grain boundary phase was present (Figure 8a). Transmission microscopy identified this phase as M_6C (Figure 8b) and also indicated that the A_2B structure is present. The presence of the grain boundary carbide phase in the structure coincides with the rapid increase in corrosion rate (Table 5) and the large drop in impact strength (Table 2). A diagram was constructed (Figure 9) showing the phases identified for all samples. It is obvious that the increase in strength experienced by those samples aged at temperatures above 425°C or longer than 35,000 hours is due to the precipitation of the A_2B phase. This phase is also responsible for the slight increases in corrosion rate experienced by these same samples. In addition to A_2B , the two samples aged at 538°C also contained M_6C carbides. These samples suffered the most significant loss in corrosion resistance and impact strength.

Assuming that the A_2B boundary as drawn on the phase stability diagram (Figure 7) is correct, it would predict that it would take 100 years to cross this boundary at approximately 380°C. Since the maximum temperature in the metal canister is expected to be 260°C, the time required to develop the ordered structure would be about 400,000 years assuming that the boundary can be extrapolated for 3 more decades on the time axis. The canister is only expected to be at the maximum temperature for 10-15 years before it begins to decay. The data presented here definitely suggest that no measurable change would occur in these alloys during this time period.

Conclusions

The examination of a series of long term aged alloy C-type compositions has shown that

- 1) Development of the ordered A_2B phase in these alloys would not be expected at the maximum expected canister temperature for times in excess of 100 years.
- 2) The presence of the ordered structure does not appreciably reduce the corrosion resistance or the impact strength of the alloys even if it does form.
- 3) The corrosion resistance of alloy C-22 is the best of the three alloys which should make it the leading candidate for the canister material.

® HASTELLOY is a registered trademark of Haynes International, Inc.

References

1. W. C. O'Neal et al, "*Preclosure Analysis of Conceptual Waste package Designs for a Nuclear Waste Repository in Tuff*," Report UCRL-53595, Lawrence Livermore National Laboratory November 1, 1984.
2. R. D. McCright, et al, "*Progress Report on the Results of Testing Advanced Conceptual Design Metal Barrier materials Under Relevant Environmental Conditions for a Tuff Repository*," UCID-21044 Lawrence Livermore National Laboratory, Livermore, CA 1987
3. J. A. Beavers, N. G. Thompson, W. V. Harper; "*Potentiodynamic Polarization Studies of Candidate Container Materials in Simulated Tuff Repository Environments*," Materials Research Society Symposium Proceedings, Vol. 176, p 533, 1990.
4. G. Cvagnolino, N. Sridhar; "*A Review of Localized Corrosion of High-Level Nuclear Waste Container materials-1*," NRC Contract No. NRC-02-88-005, CNWRA Report No. 910004, Southwest Research Institute, April 1991.
5. R. D. McCright, "*An Annotated History of Container Candidate Material Selection*," UCID-21472, Lawrence Livermore National Laboratory, 1988.
6. R. D. McCright, et al; "*Candidate Container Materials for Yucca Mountain Waste Package Designs*," Proceedings of Nuclear Waste Packaging Focus '91, American Nuclear Society, LaGrange Park, IL, 1991, page 125.
7. S. J. Lukezich and H. S. Ahluwalia; "*The Corrosion Performance of Candidate High Nickel Alloys in Simulated Nuclear Waste Repository Environments*," IBID, page 170.
8. R. Skaggs, et al; "*Thermal and Metallurgical Considerations of a Novel Design for the Nuclear Waste Container*," IBID p. 153.
9. M. A. Streicher, Corrosion, 32 No. 3 p. 79 (1963).
10. P. E. Manning, "*An Improved Intergranular Corrosion Test for HASTELLOY alloy C-276*," ASTM STP 866, American Society for Testing and Materials, Philadelphia. 1985 p. 437-454.
11. S. J. Matthews, "*Thermal Stability of Solid Solution Strengthened High Performance Alloys*," R&D Reports 8979 and 9265, Haynes International Inc., Kokomo, Indiana.
12. M. J. Cieslak, et al; Metallurgical Transactions A, Vol. 17A, November 1986, p. 2035.
13. F. G. Hodge; Corrosion Vol. 29, No. 10, 1973, p. 375.
14. R. W. Kirchner and F. G. Hodge, Werkstoffe und Korrosion, Vol. 24, No. 12 (1973) p. 137.

15. P. E. Manning and J. D. Schöbel, *Werkstoffe and Korrosion*, Vol. 37 No. 3 (1986) p. 1042.
16. H. J. Goldschmidt, *Interstitial Alloys*, Plenus Press, New, NY, 1967.
17. H. J. Klein, C. R. Brooks, E. E. Stansbury, *Physica Status SOLIDI*, Vol. 38, No. 2, Apr 1970, p. 831-836.
18. J. D. Frenck, F. G. Hodge, and H. J. Klein; *High Temperature Exposure Effects on Corrosion Properties of a Nickel-Chromium-Molybdenum Alloy*, presented at Corrosion '74 Chicago, IL, March 1974, National Association of Corrosion Engineers, Houston, TX 1974.
19. S. J. Matthews, H. J. Klein, and F. G. Hodge, U.S. Patent 4,129,464.

TABLE 1

Nominal Alloy Compositions

| Element | Alloy Composition (wt.%) | | |
|---------|--------------------------|-------------|------------|
| | Alloy C-4 | Alloy C-276 | Alloy C-22 |
| Ni | 65 | 57 | 56 |
| Co | 2.0* | 2.5* | 2.5* |
| Cr | 16 | 16 | 22 |
| Mo | 16 | 16 | 13 |
| Fe | 3* | 5 | 3 |
| W | - | 4 | 3 |
| C | 0.01* | 0.01* | 0.01* |
| Si | 0.08* | 0.08* | 0.08* |
| Mn | 1* | 1* | 0.5* |
| P | .020* | .020* | 0.020* |
| S | .004* | .004* | .004* |
| Ti | 0.7* | - | - |
| V | - | 0.35* | 0.35* |
| | | * Maximum | |

TABLE 2
Mechanical Properties Alloy C-276

| Alloy Condition | Rockwell Hardness | Yield Strength MPa | % Reduction in Area | Impact Strength Joules ^(b) |
|--------------------|-------------------|--------------------|---------------------|---------------------------------------|
| Heat 7-3868 | | | | |
| annealed | B89 | 358 | 74 | 358 |
| 10,000 hrs @ 260°C | B90 | 345 | 72 | 358 |
| 20,000 hrs @ 260°C | B93 | 352 | 74 | 358 |
| 10,000 hrs @ 340°C | B92 | 400 | 65 | 352 |
| 20,000 hrs @ 340°C | B93 | 407 | 66 | 358 |
| 10,000 hrs @ 425°C | B93 | 345 | 68 | 358 |
| 20,000 hrs @ 425°C | B89 | 345 | 68 | 358 |
| Heat 4-3962 | | | | |
| annealed | B93 | 352 | 78 | 358 |
| 37,896 hrs @ 425°C | C22 | 545 | 64 | 284 |
| 37,896 hrs @ 482°C | C32 | 731 | 54 | 126 |
| Heat 0-3179 | | | | |
| annealed | 453 | 358 | 78 | - |
| 4,000 hrs @ 425°C | A55 | 358 | 80 | - |
| 8,000 hrs @ 425°C | A55 | 365 | 79 | - |
| 16,000 hrs @ 425°C | A53 | 386 | 76 | - |
| 4,000 hrs @ 538°C | A67 | 737 | 51 | - |
| 8,000 hrs @ 538°C | A67 | 772 | 21 | - |
| 53,880 hrs @ 538°C | C28 | 786 | 18 | 2 |

TABLE 3
Mechanical Properties Alloy C-4^(a)

| Alloy Condition | Rockwell Hardness | Yield Strength MPa | % Reduction in Area | Impact Strength Joules ^(b) |
|--------------------|-------------------|--------------------|---------------------|---------------------------------------|
| Heat 8-0942 | | | | |
| annealed | B90 | 379 | 73 | 358 |
| 10,000 hrs @ 260°C | B90 | 345 | 73 | 307 |
| 20,000 hrs @ 260°C | B90 | 352 | 70 | 358 |
| 10,000 hrs @ 340°C | B90 | 352 | 71 | 336 |
| 20,000 hrs @ 340°C | B91 | 352 | 71 | 358 |
| 10,000 hrs @ 425°C | B91 | 372 | 68 | 338 |
| 20,000 hrs @ 425°C | B93 | 393 | 66 | 358 |
| Heat 5-0826 | | | | |
| annealed | B92 | 345 | 73 | 358 |
| 37,896 hrs @ 425°C | B95 | 379 | 69 | 292 |
| 37,896 hrs @ 482°C | C30 | 703 | 58 | 122 |
| Heat 2-7141 | | | | |
| annealed | B92 | 379 | 73 | 323 |
| 1,000 hrs @ 425°C | B92 | 410 | 65 | - |
| 4,000 hrs @ 425°C | B92 | 393 | 70 | - |
| 8,000 hrs @ 425°C | B91 | 412 | 63 | - |
| 16,000 hrs @ 425°C | B92 | 420 | 69 | 274 |
| 45,896 hrs @ 425°C | C20 | 483 | 60 | 237 |
| 1,000 hrs @ 538°C | A68 | 786 | 51 | - |
| 4,000 hrs @ 538°C | A67 | 779 | 51 | - |
| 8,000 hrs @ 538°C | A68 | 800 | 47 | - |
| 16,000 hrs @ 538°C | - | 772 | 42 | 28 |
| 45,896 hrs @ 538°C | C35 | 779 | 41 | 26 |

(a) each value represents the average of 2 samples
(b) capacity of testing machine 358 joules

TABLE 4
Mechanical Properties Alloy C-22

| Alloy Condition | Rockwell Hardness | Yield Strength MPa | % Reduction in Area | Impact Strength Joules ^(b) |
|--------------------|-------------------|--------------------|---------------------|---------------------------------------|
| Heat 7-3173 | | | | |
| annealed | B90 | 365 | 83 | 358 |
| 10,000 hrs @ 260°C | B90 | 345 | 83 | 358 |
| 20,000 hrs @ 260°C | B90 | 365 | 82 | 358 |
| 10,000 hrs @ 340°C | B89 | 386 | 82 | 358 |
| 20,000 hrs @ 340°C | B93 | 379 | 82 | 358 |
| 10,000 hrs @ 425°C | B93 | 365 | 81 | 358 |
| 20,000 hrs @ 425°C | B93 | 379 | 81 | 358 |

TABLE 5

Corrosion Rates (mm/y^r)^(a)

| Alloy Condition | ASTM G-28A ^(b) | | | ASTM G-28B ^(c) | | |
|--------------------|---------------------------|-------------|-----------|---------------------------|-------------|-----------|
| | Alloy C-22 | Alloy C-276 | Alloy C-4 | Alloy C-22 | Alloy C-276 | Alloy C-4 |
| Annealed | 0.84 | 4.3 | 3.2 | 0.13 | 0.9 | 56 |
| 10,000 hrs @ 260°C | 0.86 | 4.5 | 3.3 | 0.18 | 0.9 | 86 |
| 20,000 hrs @ 260°C | 0.91 | 4.4 | 3.4 | 0.15 | 0.9 | 72 |
| 10,000 hrs @ 340°C | 0.91 | 4.8 | 3.3 | 0.20 | 0.8 | 79 |
| 20,000 hrs @ 340°C | 0.91 | 5.0 | 3.4 | 0.15 | 0.9 | 71 |
| 10,000 hrs @ 425°C | 0.84 | 4.3 | 3.4 | 0.15 | 0.8 | 71 |
| 20,000 hrs @ 425°C | 0.91 | 4.3 | 3.4 | 0.18 | 0.9 | 85 |
| 37,896 hrs @ 425°C | - | 5.4 | 3.1 | - | 1.0 | 40 |
| 45,896 hrs @ 425°C | - | - | 3.1 | - | - | - |
| 37,896 hrs @ 482°C | - | 5.9 | 3.6 | - | 1.0 | 46 |
| 45,896 hrs @ 538°C | - | - | 10.2 | - | - | 55 |
| 53,880 hrs @ 538°C | - | 102 | - | - | 84 | - |

(a) each value represents the average of 2 samples
 (b) boiling 24 hour test in 50% H₂SO₄ + 42 g/l Fe₂(SO₄)₃
 (c) boiling 24 hour test in 23% H₂SO₄ + 1.2% HCl + 1% FeCl₃ + 1% CuCl₂

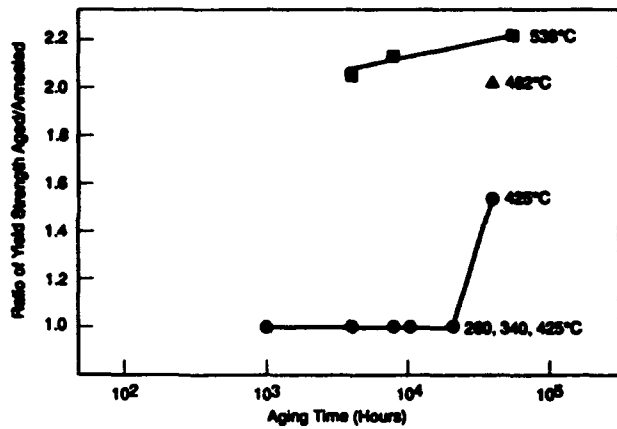


Figure 1: Effect of aging on yield properties of alloy C-276.

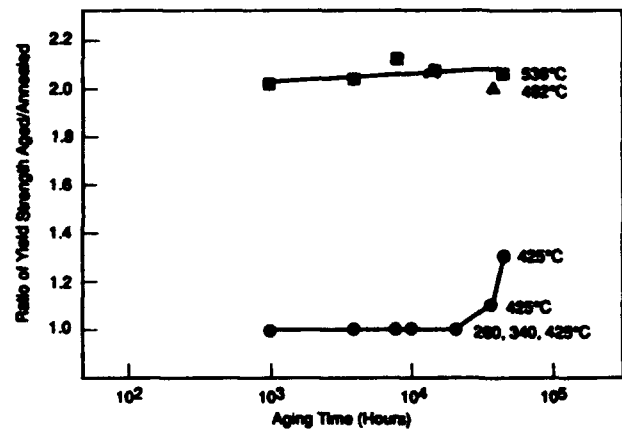
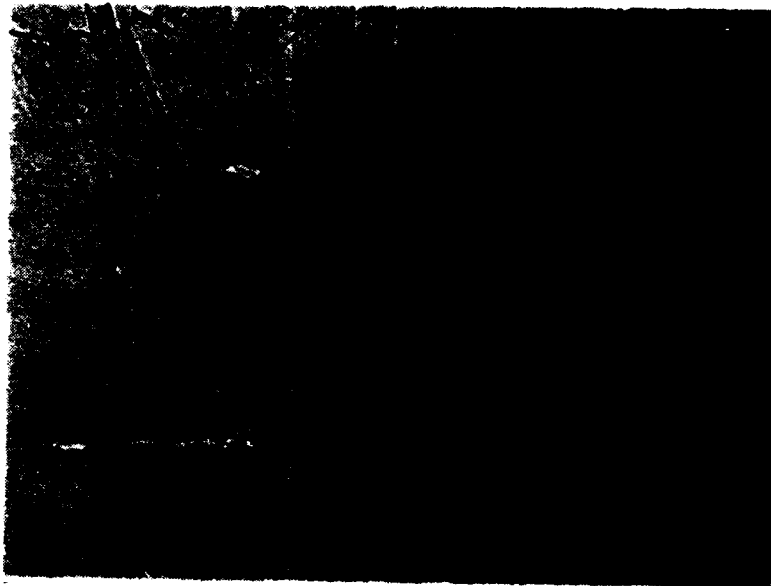


Figure 2: Effect of aging on yield properties of alloy C-4.



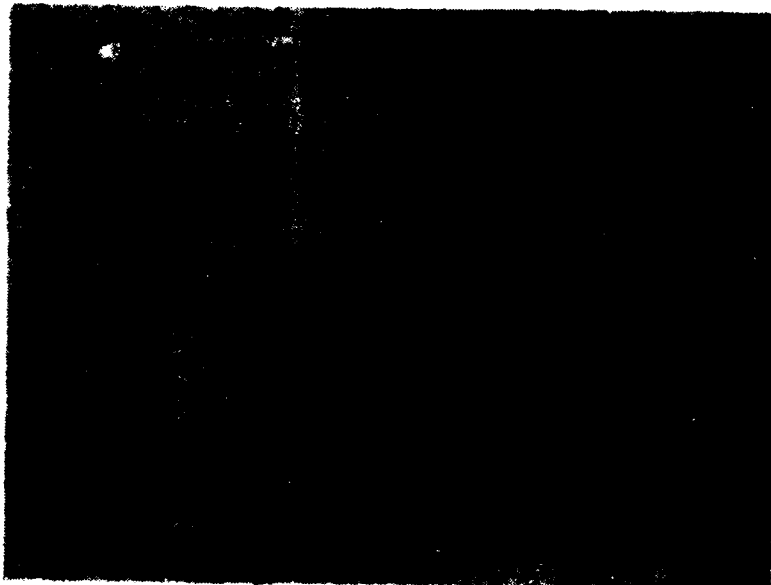
alloy C-4
Heat 8-0942

Magnification 500X



alloy C-276
Heat 7-3868

Magnification 500X



alloy C-22
Heat 7-3173

Magnification 500X

Figure 3: Microstructures of alloys aged at 425°C for 20,000 hours

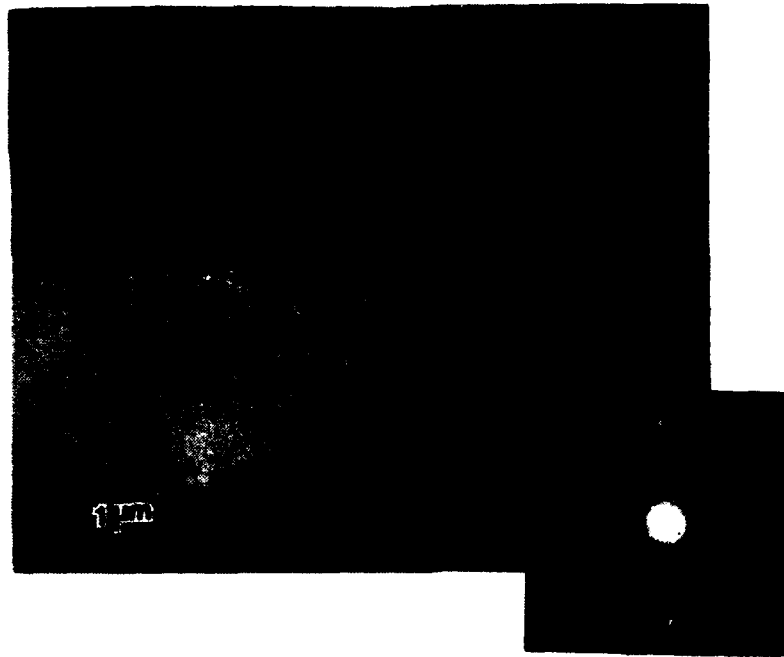


Figure 4: Alloy C-22 aged 20,000 hours at 425°C with [100] matrix pattern



Figure 5: Alloy C-4 aged 45,896 hours at 425°C with [100] matrix showing weak A_2B superlattice spots

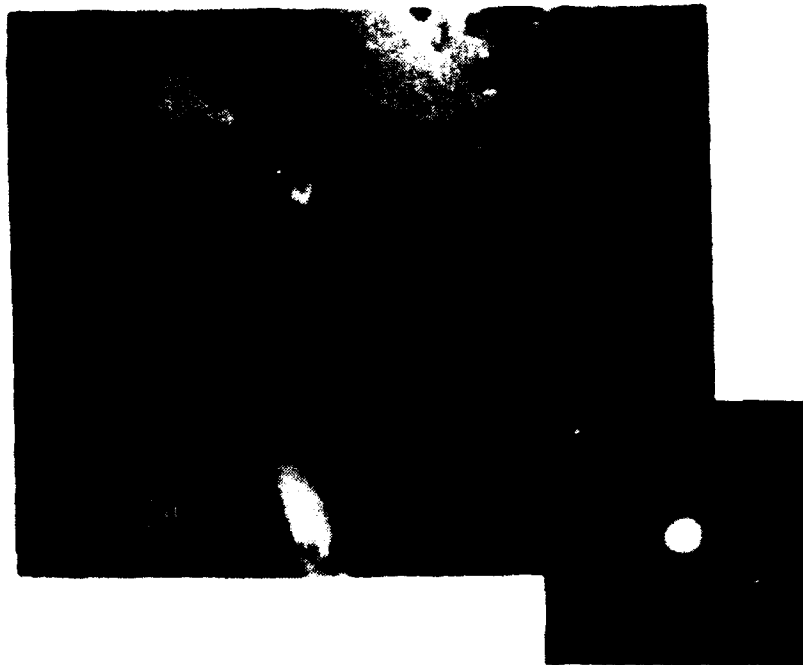
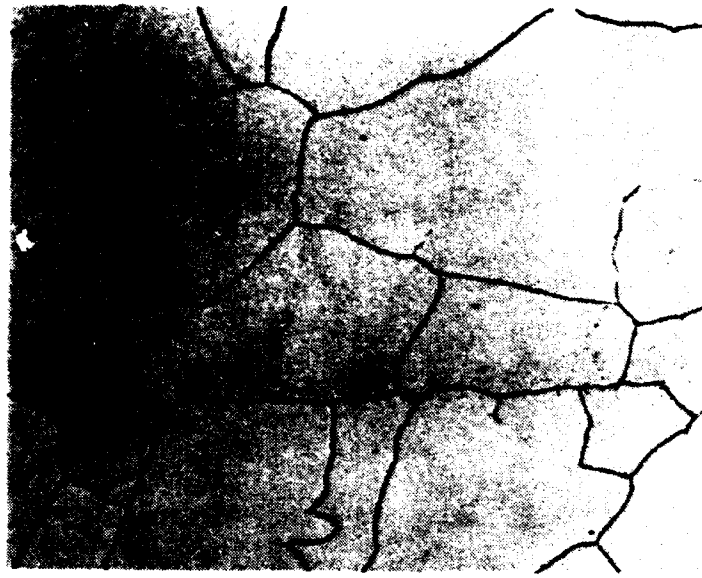


Figure 6: Alloy C-276 aged 37,896 hours at 425°C with [100] matrix pattern



Figure 7: Alloy C-276 aged 37,896 hours at 482°C with [100] matrix showing well developed A₂B superlattice spots



(a) 500X



(b)

Figure 8: Alloy C-276 aged 53,880 hours at 538°C

- (a) Shows presence of grain boundary phase
- (b) [100] matrix pattern shows A_2B phase present in grains and [110] matrix pattern identifies grain boundary phase as M_6C

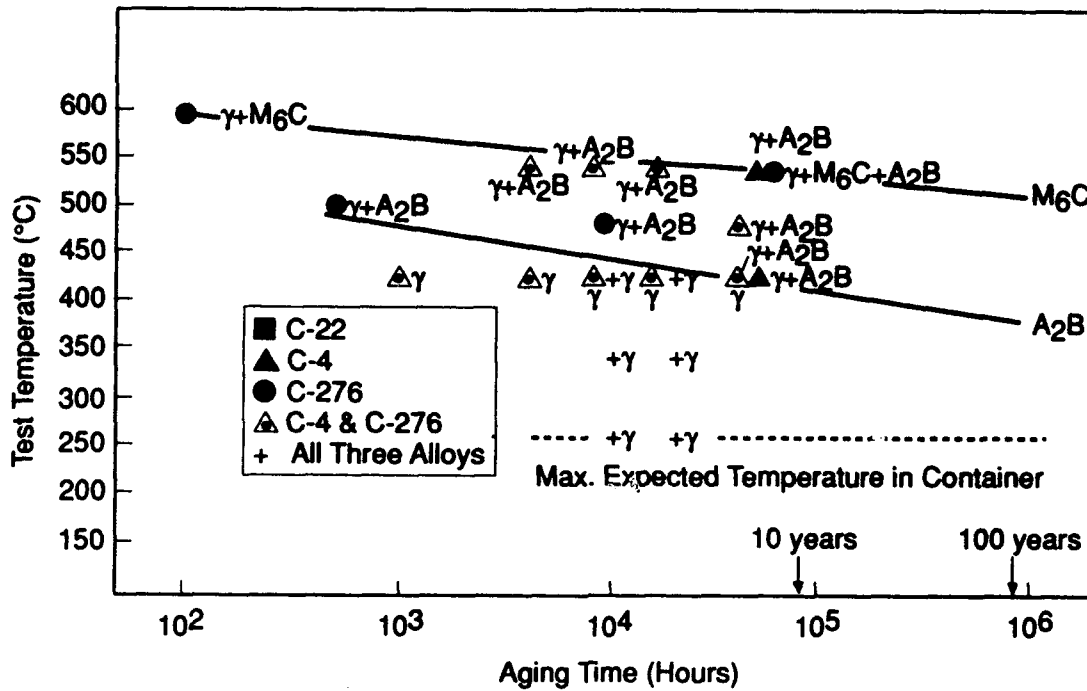


Figure 9: Phase Stability Diagram for Alloys

List Of Negative Numbers

Figure 3: 67154
67156
67158

Figure 4: 10331 (BF)
10330 (DP)

Figure 5: 10297 (BF)
10299 (DP)

Figure 6: 10309 (BF)
10311 (DP)

Figure 7: 10318 (BF)
10313 (DP)

Figure 8: 67170
10319 (BF)
10320 (DP-A₂B)
10326 (DP-M₆C)

**ON-LINE MONITORING OF CORROSION IN FIELD
PIPE GATHERING SYSTEMS**

K. Lawson*, A. N. Rothwell*, L. Fronczek⁺ and C. Langer⁺

* CAPCIS MARCH Ltd
Bainbridge House
Granby Row
Manchester
M1 2PW
United Kingdom

+

Southern California Gas Company
555 West Fifth Street
Los Angeles
California CA 90013-1011
United States of America

ABSTRACT

This paper describes the use of real-time on-line electrochemical corrosion monitoring to characterise the corrosion behaviour in a wet gas withdrawal system. The corrosion activity was found to vary enormously with gas extraction rates with some conditions resulting in periods of high corrosion being identifiable. The corrosion attack was not continuous and several mitigating factors were examined in order to determine the most effective in terms of minimising corrosion attack.

INTRODUCTION

This paper discusses the results obtained during a period of continuous on-line real-time corrosion monitoring at one of the gas storage facilities operated by Southern California Gas. The gas storage facility investigated consists of a number of gas storage wells which are connected into a common withdrawal header system. Whilst the injection gas is supplied dry, upon withdrawal the gas is produced 'wet' with approximately 9000-13000 ppm chloride and 0.8-1.2% CO₂; the produced fluids are normally found to comprise 50:50 oil:brine with ambient temperatures ranging from 60-100°C and line pressures of up to 700 psig. In solution chemical terms, the relatively high concentration of chloride and the presence of CO₂ imply that the produced fluids are, potentially, highly corrosive. It was suspected, however, that variations in the operation of this gas storage field could generate service environments which would promote corrosion and others which would limit it. This investigation, therefore, was concerned with characterising the natural corrosion behaviour during normal plant operations with a view to determining whether part (or parts) of the process caused enhanced corrosion attack.

Previous experience at Southern California Gas had shown that corrosion attack was found to occur predominately at bottom dead centre at low points in the withdrawal line. Regular inspection had indicated that corrosion attack was not being alleviated to the degree anticipated, even though inhibitors were being injected both at the well head and gathering line, and despite rigorous drainage of the produced fluids from low points twice a day.

METHODOLOGY

In the majority of cases the use of a single corrosion monitoring technique will not satisfactorily detect all corrosion conditions, therefore multiplexing a number of powerful and complementary monitoring techniques provides a useful investigative tool for determining the factors that lead to corrosion and the resulting morphology of attack [1].

The CML portable multi-system 'MUSYC' corrosion monitor was utilised during this work. This system incorporates the simultaneous logging of the coupling (or ZRA) current, electrochemical potential noise (EPN), electrochemical current noise (ECN), and linear polarisation resistance (LPRM). Whilst LPRM is useful for determining overall corrosion rates, the electrochemical noise

techniques are particularly sensitive in regimes where localised corrosion activity is the predominant mode of attack, eg. pitting corrosion [1].

Sensor probes used during this work were inserted through industry standard 2-inch high pressure fitting. The sensors were located at bottom dead centre of the withdrawal line at low points. Several sensors were installed in the withdrawal line, however, for the purpose of this paper, we shall only consider the results obtained from two, these being located at manual drains 2 and 6.

SOLUTION CHEMISTRY

The chemistry of the CO₂-water system is complex [2] and shall therefore be treated very briefly here. Field data had shown that CO₂ partial pressures were of the order of 5.6 to 8.4 psig (based upon a line pressure of 700 psig) and that the solution pH ranged from pH 6 to pH 8. Calculations were performed using the known chemical equilibria for this system in order to determine the solution pH as a function of pCO₂. When this was done it was found that the solution pH should be of the order of pH 4.6 to pH 4.2 respectively, based upon the above CO₂ partial pressures, therefore it can be concluded that in this system the pH is not controlled by the CO₂ partial pressure. Other calculations were run which show that pH's at the metal surface are markedly higher than those in the bulk solution (Figure 1). This reflects the very poor buffering ability of this system, in kinetic terms, and shows that carbonate film formation may be possible even though the bulk chemistry implies that it may not be favourable.

RESULTS

Prior to the commencement of corrosion monitoring, all inhibitor injection was stopped. This allowed the system to be characterised in terms of 'base-line' behaviour. Typical responses from the CML 'MUSYC' instrument at manual drain 2 during this base-lining period, Figure 2, and approximately 24 hours after inhibitor injection commenced, Figure 3, illustrate some very interesting and characteristic features:

- (i) Pronounced step-like changes in the signal responses were found to occur at certain times during plant operation (Figure 2). The "step" exhibited in Figure 2 represents an increase in corrosion rate (at 2:20pm, January 10, 1992) from approximately 0.3 mpy to 218 mpy (corrosion rates being calculated by using the LPRM data and applying the Stern-Geary

equation). ZRA currents also increased markedly from approximately $0.56\mu\text{A}$ to $287\mu\text{A}$, consistent with enhanced corrosion attack.

- (ii) Corrosion rates were found to be very high even when inhibitor injection had been implemented 24 hours earlier. Figure 3 shows an almost constant corrosion rate of approximately 232 mpy despite inhibitor injection to 25ppm.
- (iii) The electrochemical noise signals in both Figures 2 and 3, and indeed throughout, were found to be consistent with general corrosion attack.

Pronounced step-like changes in corrosion activity were not only peculiar to the "base-lining" period of the investigation where all inhibitor injection was stopped. Rapid, step-like increases in corrosion activity were also found to occur even when inhibitor injection had been implemented, as shown by the signal responses in Figure 4. This behaviour was all the more surprising particularly in view of the fact that for the period coinciding with that in Figure 4, the inhibitor rate had increased to 160 ppm.

The corrosion activity at manual drain 6 was found to be very similar to that observed at manual drain 2, in that characteristic step-like changes in the signal responses were also in evidence, again despite inhibitor dosing (Figure 5). However, the lower limiting corrosion rate tends to be much higher at manual drain 6 than that observed at manual drain 2 (compare the lower limiting corrosion rate in Figure 5 (approximately 8 mpy) with those in Figures 2 and 4 (approximately 0.3 mpy)).

Longer term trends in the corrosion behaviour at both locations were ascertained by combining numerous data files together (each data file representing a logging period of eight hours), converting the electrochemical signals into corrosion rates and plotting these in real-time, typically to cover a period of three days. Figures 6 and 7 correspond to two such corrosion rate-time plots for manual drain 2 and manual drain 6 respectively. From these data one can highlight the following points:

- (i) The range of corrosion rates measured was found to be enormous (0.2 to 250 mpy), however, of greater significance is the fact that the corrosion rate could change almost instantaneously.

- (ii) As previously mentioned, the lower limiting corrosion rate at manual drain 6 was typically found to be greater than that at manual drain 2 (with reference to Figures 6 and 7, these ranged from about 0.2-0.3 mpy for manual drain 2 and 4-9 mpy for manual drain 6)
- (iii) At certain periods the corrosion rate was found to be highly variable, however by comparison with the pronounced "steps", these changes were found to occur over considerably shorter time intervals, varying in an almost oscillatory fashion.
- (iv) In all cases transient changes in the corrosion rate were observed despite dosing the system with inhibitors.

DISCUSSION

The results obtained during this monitoring project are only explicable when one refers to the relevant process parameters for the periods coincident with the changes in the corrosion rate. When these comparisons were made it was found that the corrosion rate at either manual drain 2 or manual drain 6 was a function of the withdrawal status of gas wells upstream. This is demonstrated when one refers to the annotations made in Figures 6 and 7, which represent wells either being switched over to withdrawal or shut-in. It is also clear from the process information that no single gas well was responsible for causing enhanced corrosion at either location.

It is postulated that the observed corrosion behaviour is a function of the local gas velocity. This is assumed because the local gas velocities would increase dramatically once more and more wells upstream are switched over to withdrawal, and vice versa when shut-in. At low local gas velocities the produced fluids could settle out, whilst at high velocities the probability of fluid drop-out would be very small. The "step-like" way in which the corrosion rate was found to change would appear, therefore, to reflect the tendency for fluid drop-out as the local gas velocity changes.

The extremely variable nature of the corrosion rate at certain periods was very probably due to small "slugs" of fluid being forced through the line at intermediate gas velocities where the "wetting" and "drying" cycles would be rapid. Once the local velocity becomes low enough, the "slugging" effect would stop and the corrosion rate would become constant and high. This

concur with the behaviour exhibited in Figure 6, where initially the corrosion rate was highly variable until well 22 directly upstream was shut-in, and the "slugging" effect ceased.

One can ascertain the degree of corrosion attack by comparing the cumulative metal loss (calculated from Faraday's law) for both manual drains 2 and 6; these were calculated in mils and subsequently plotted with respect to real-time for the period studied (Figures 8 and 9). From these data it becomes obvious that the metal loss at manual drain 6 was approximately twice as great as that at manual drain 2. Moreover, the majority of the corrosion damage was sustained over relatively short time scales, as evidenced for example in the case of manual drain 6, where approximately 83% of the total cumulative metal loss was sustained within a period of only 15 days (15% of the measurement period), Figure 10.

Manual drain blow-down, which simply involved the rigorous drainage of the accumulated fluids, was a method that was initially thought to be useful for controlling corrosion. Monitoring at both manual drains 2 and 6 showed conclusively that this operation made no significant impact in terms of reducing the corrosion rate, since it was likely that once the fluids had been drained off, they were rapidly replenished from wells upstream.

The inhibitor packages employed were found to be relatively ineffective in controlling the corrosion of the pipeline system even when dosage rates were recorded of up to 400 ppm. The relationship between inhibitor dosage and corrosion rate can be seen in Figure 11.

CONCLUSIONS

1. The corrosion attack observed at both manual drains 2 and 6 was undoubtedly due to fluid drop out. The corrosion attack was not constant, and was found to vary with the withdrawal status of gas wells upstream.
2. Manual drain blow-down operations did not make any significant impact in terms of controlling corrosion.
3. The corrosion inhibitors used during this investigation were found to be relatively ineffective in terms of reducing the corrosion rate, even when dose rates were increased to very high levels. It is likely that corrosion control by inhibitors could still be achieved,

however, one cannot over-emphasise too strongly, the importance of inhibitor chemistry in terms of its "in-service" performance. Whilst it is undoubtedly true that initial laboratory tests would be a useful inhibitor "screening" process, actual field performance can only be established through plant monitoring.

4. Cumulative metal loss calculations have shown that the majority of corrosion damage had been sustained within very short periods of time. Identifying these periods of enhanced corrosion attack, and their causes, allowing the operator to implement suitable measures to control it, thus extending the useful lifetime of the pipeline.

REFERENCES

1. Eden, D. A., Rothwell, A. N., "Electrochemical noise data: analysis, interpretation and presentation, NACE Corrosion '92, Nashville, Tennessee, April 1992.
2. Turgoose, S., Cottis, R. A., Lawson, K., "Modelling of electrode processes and surface chemistry in carbon dioxide containing solutions", Proceedings of Computer Modelling for Corrosion, Nov. 1990, ASTM, in press.

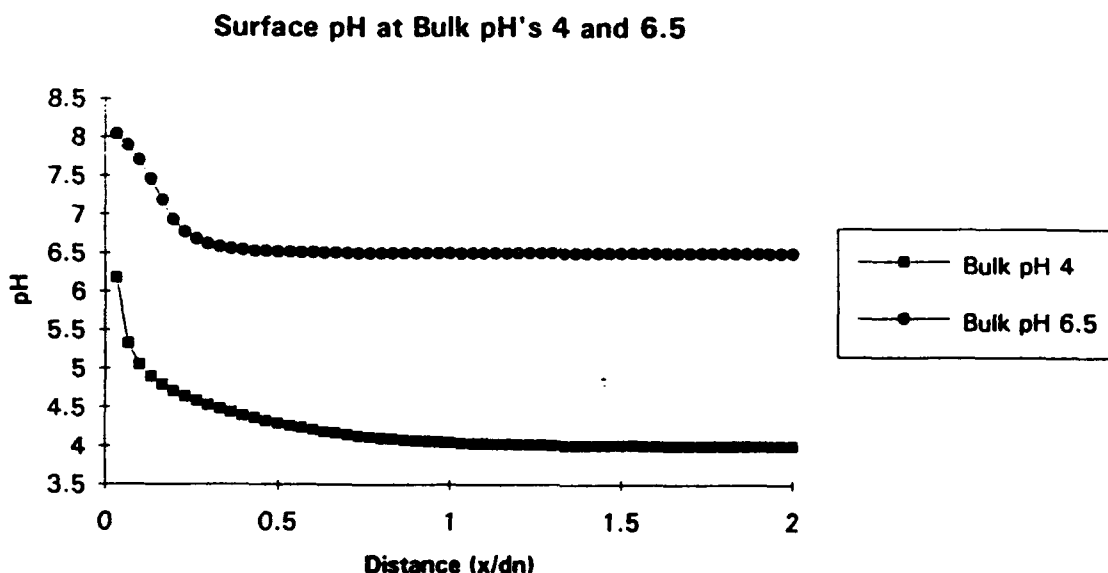


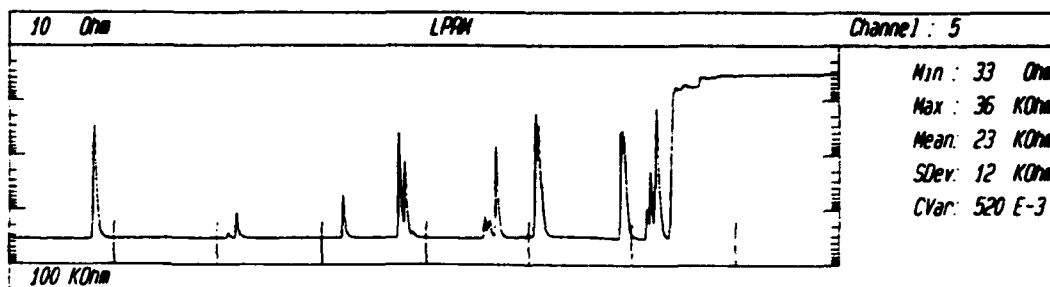
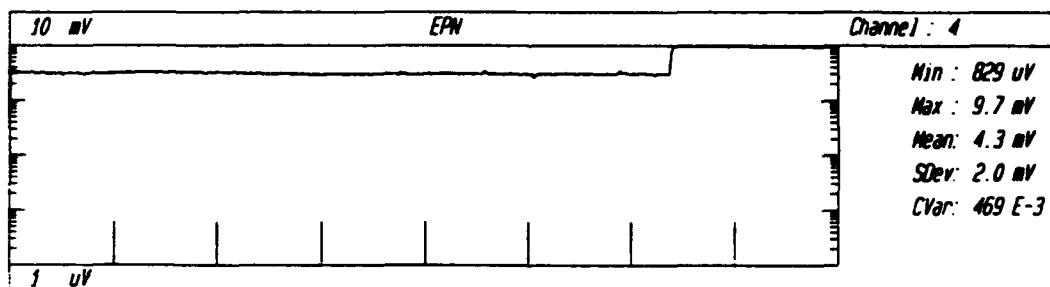
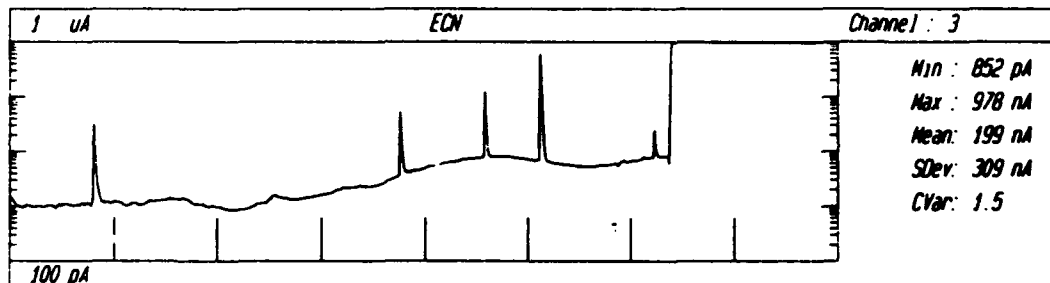
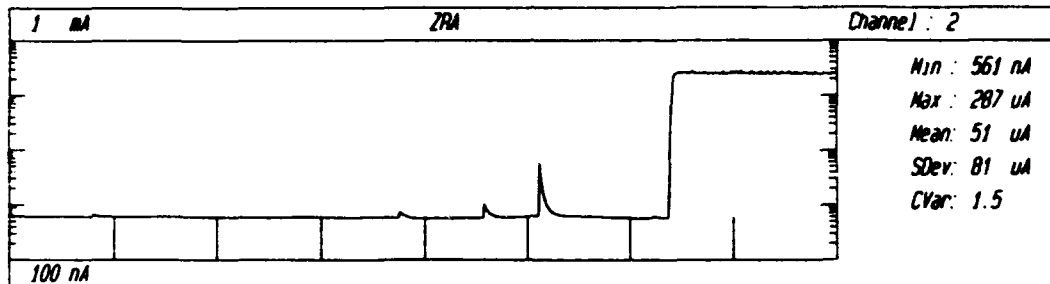
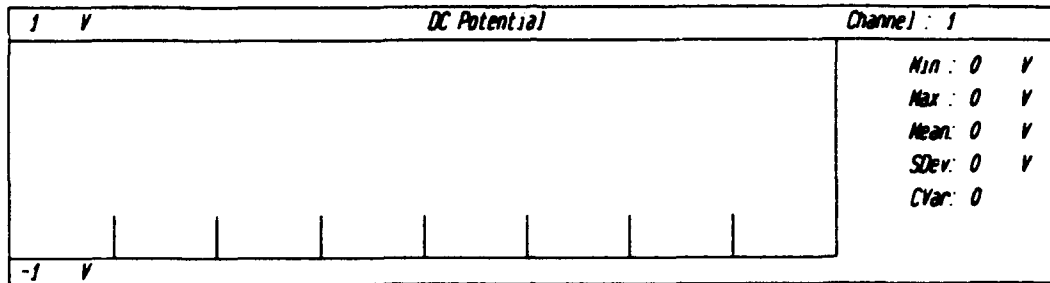
Figure 1: Illustrating the change in pH as the metal surface is approached. The parameter dn is the Nernst diffusion layer thickness for protons and x is a finite subdivision of dn . pH's were calculated using the phase equilibria for this system

MINNIE v3.20

CAPCIS MARCH 1990

CAPCIS MARCH Ltd

Tag : CM. File started at 23.05 on 10 January 1992



File : 92A10W05.D2A
Time Span : 7 hrs 58 mins 59 secs

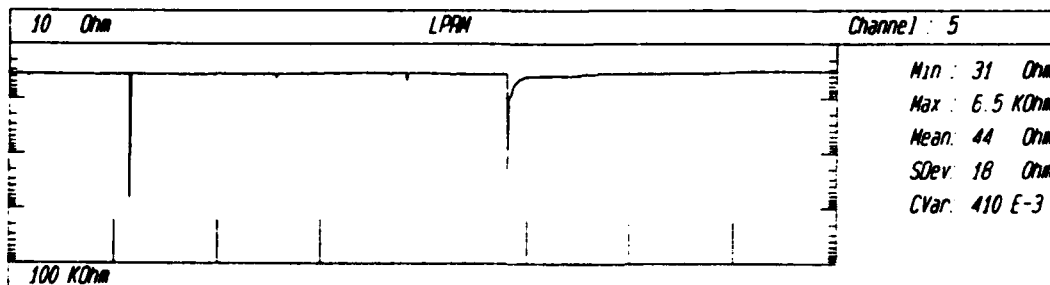
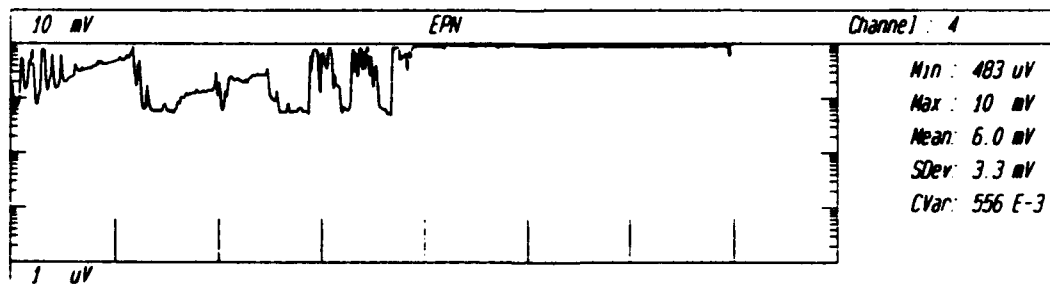
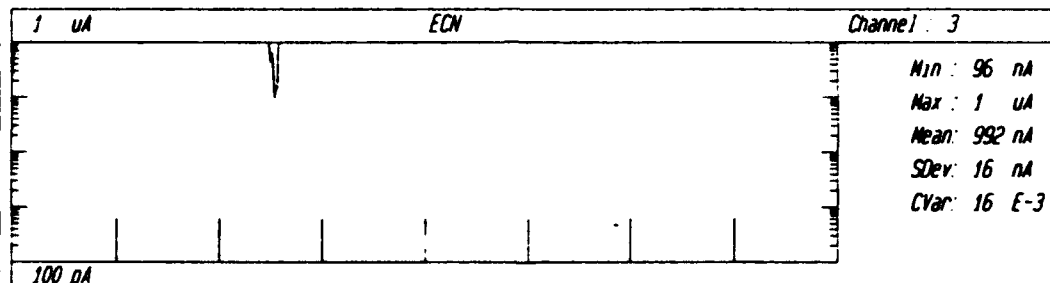
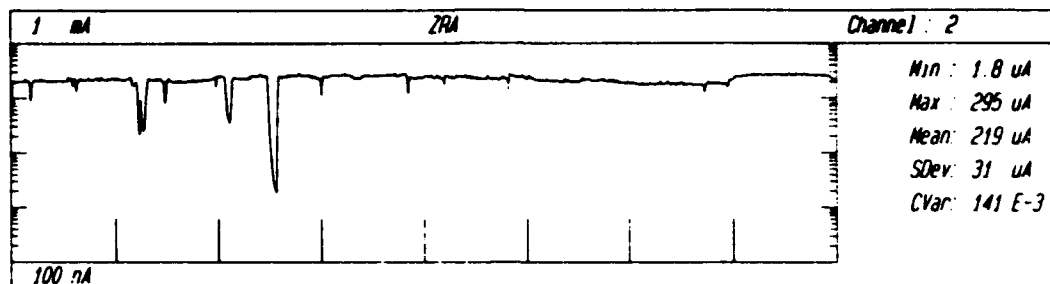
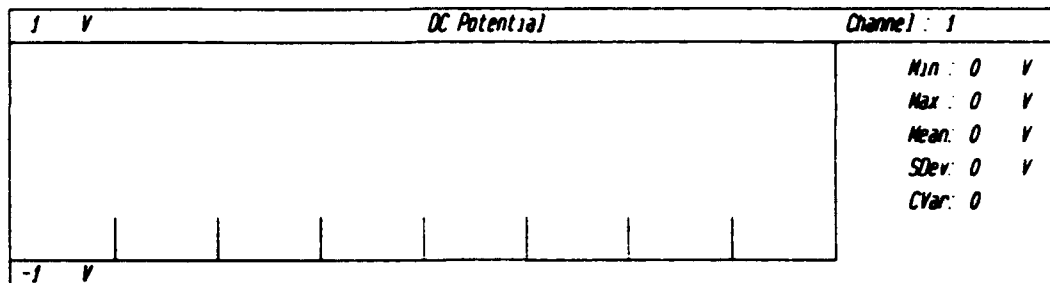
Figure 2

MINNIE v3.20

CAPCIS MARCH 1990

CAPCIS MARCH Ltd

Tag : CM. File started at 2.07 on 15 January 1992



File : 92A15807.D2A
Time Span : 7 hrs 58 mins 59 secs

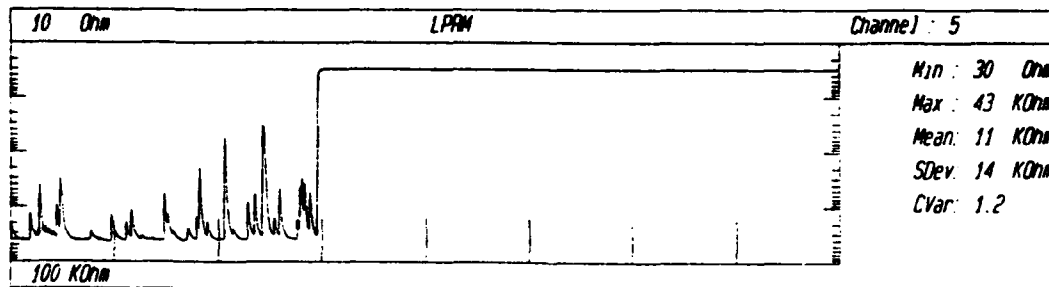
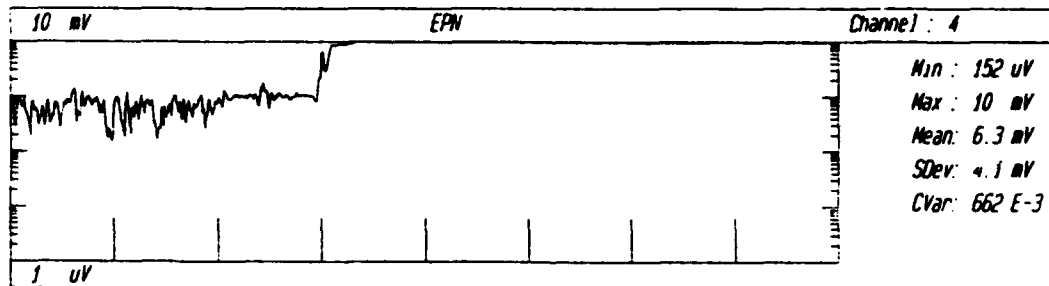
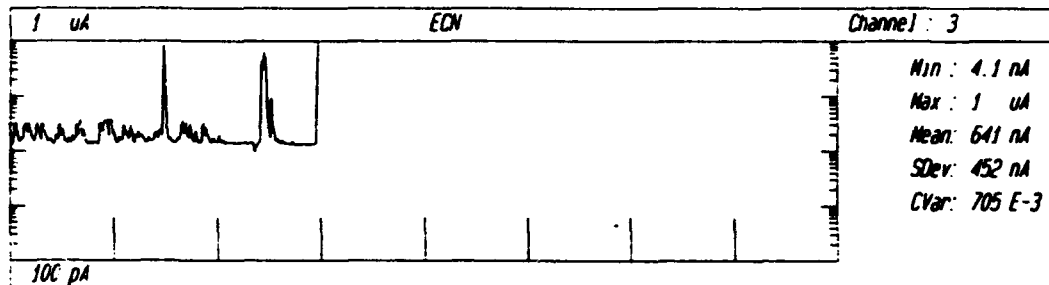
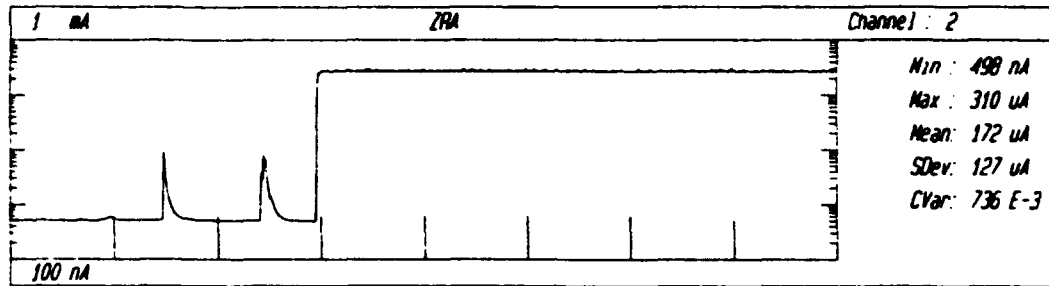
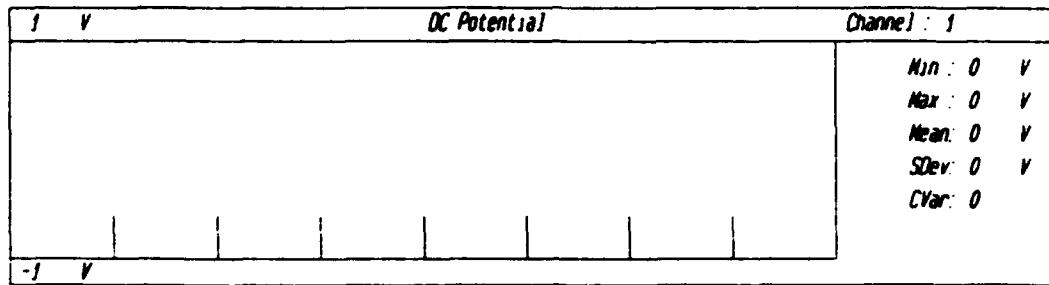
Figure 3

MINNIE v3.20

CAPCIS MARCH 1990

CAPCIS MARCH Ltd

Tag : CM. File started at 20.46 on 29 January 1992



File : 92A29T46.D2A
Time Span : 7 hrs 58 mins 59 secs

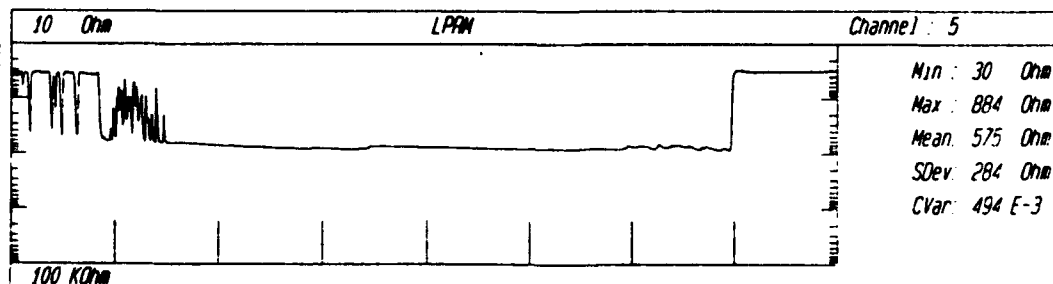
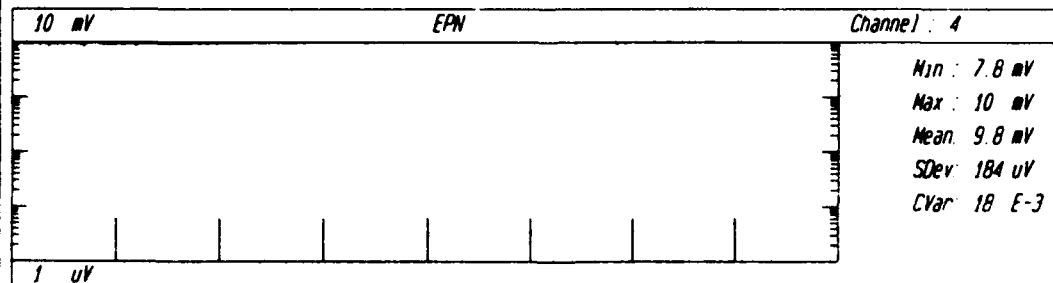
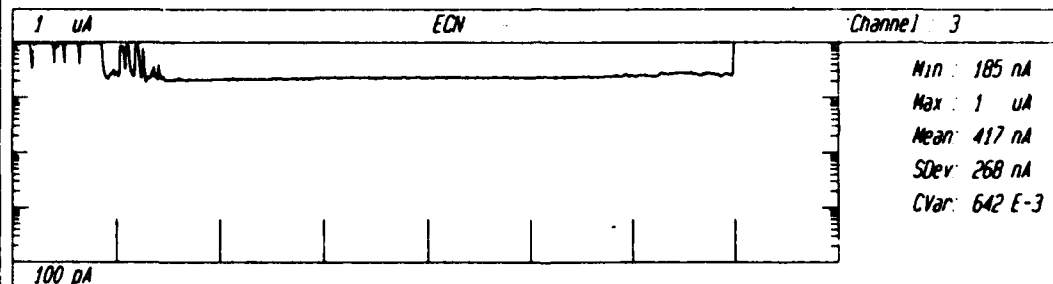
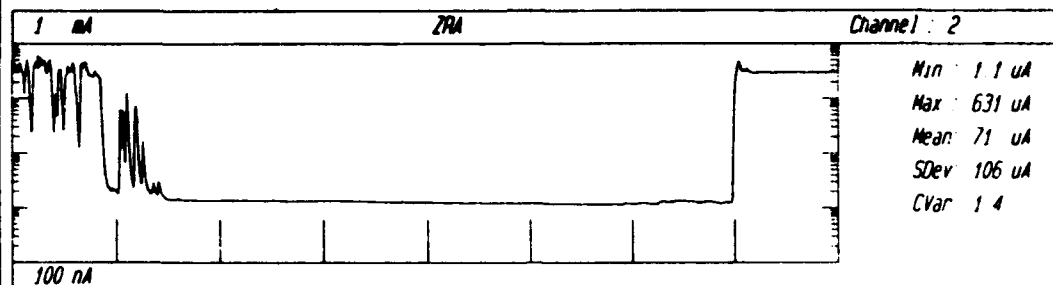
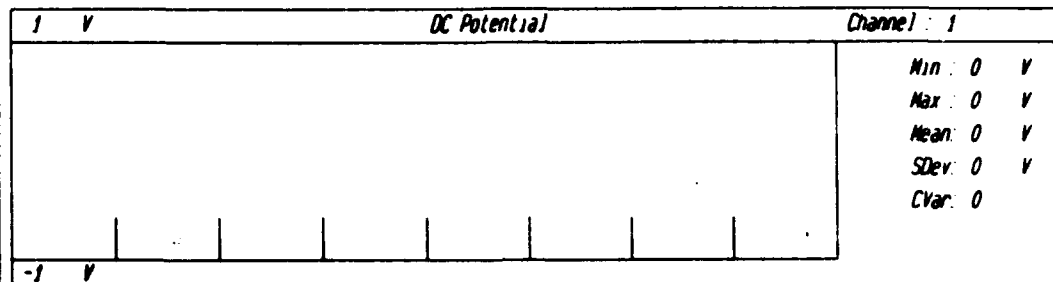
Figure 4

MINNIE v3.20

CAPCIS MARCH 1990

CAPCIS MARCH Ltd

Tag : CM. File started at 7.05 on 17 January 1992



File : 92A17G05.D6A
Time Span : 7 hrs 58 mins 59 secs

Figure 5

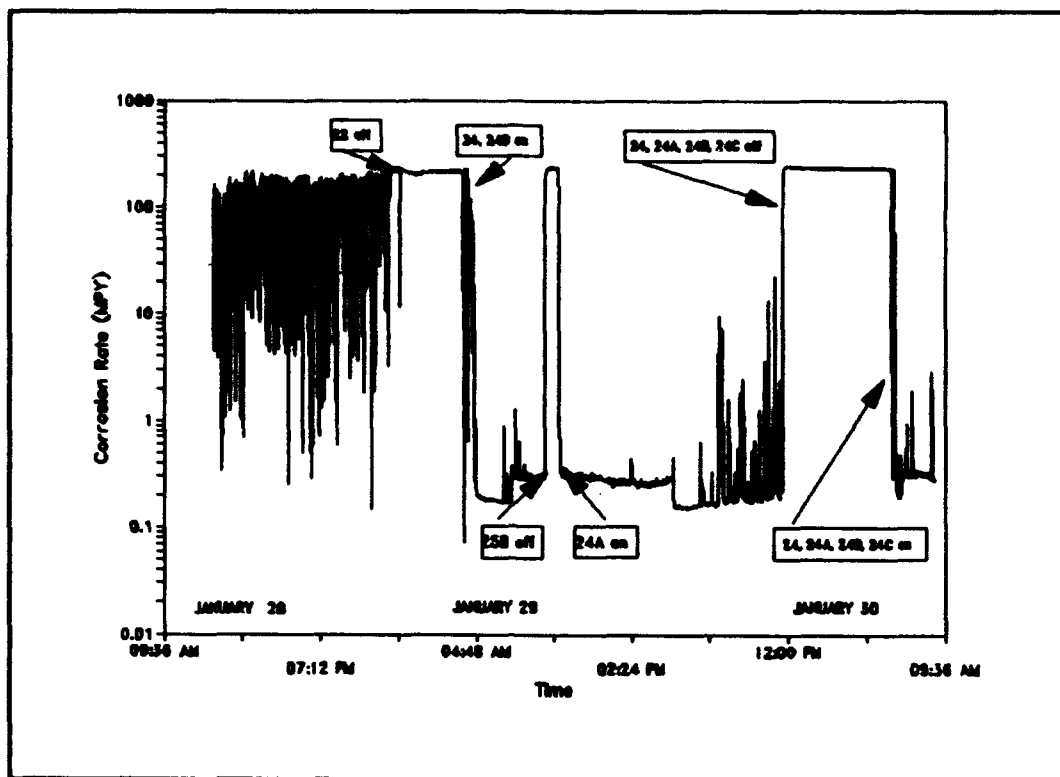


Figure 6: Instantaneous Corrosion Rates, Manual Drain 2.

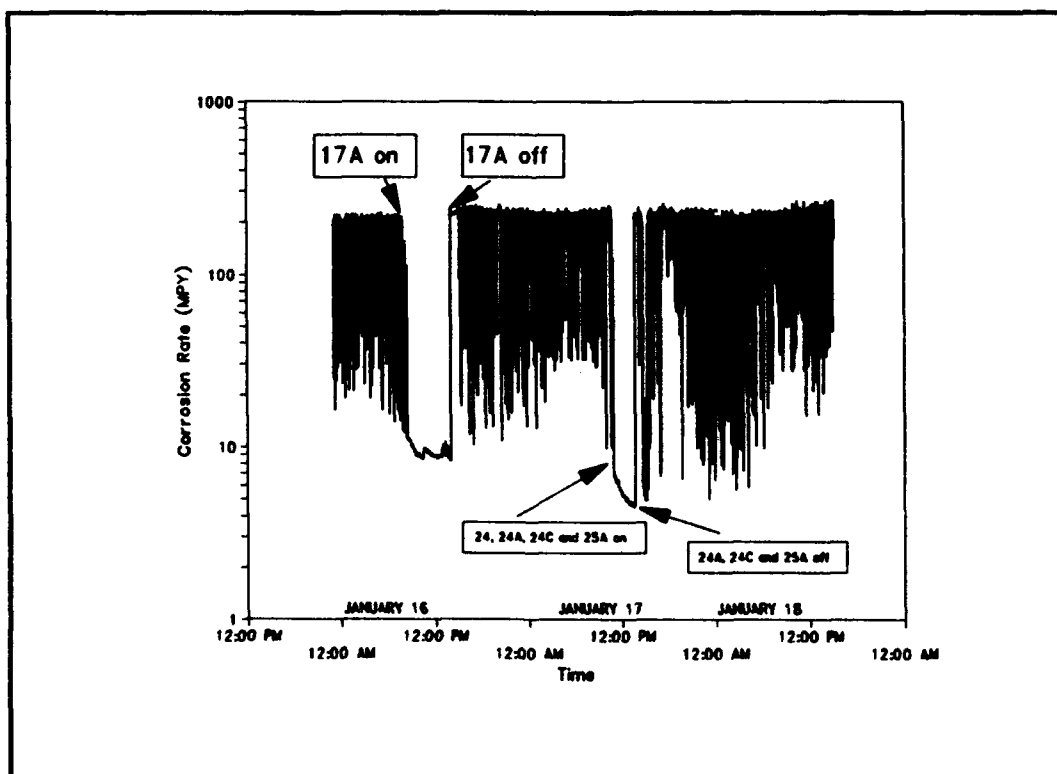


Figure 7: As Figure 6, But Manual Drain 6.

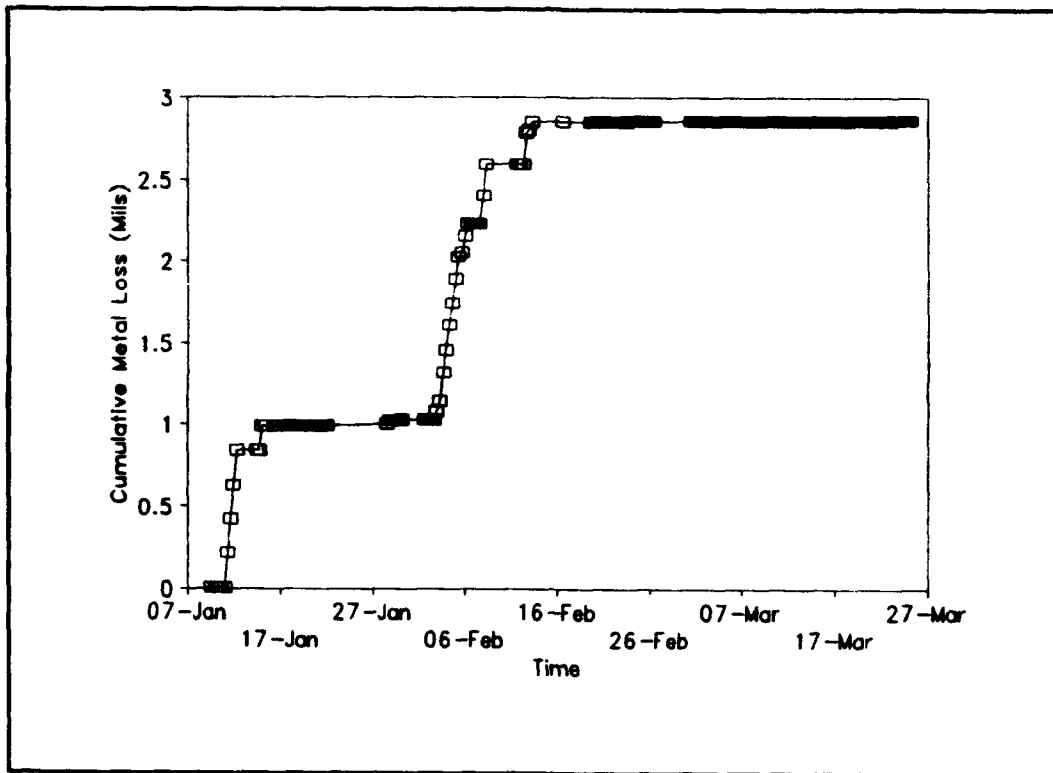


Figure 8: Cumulative Metal Loss For Manual Drain 2

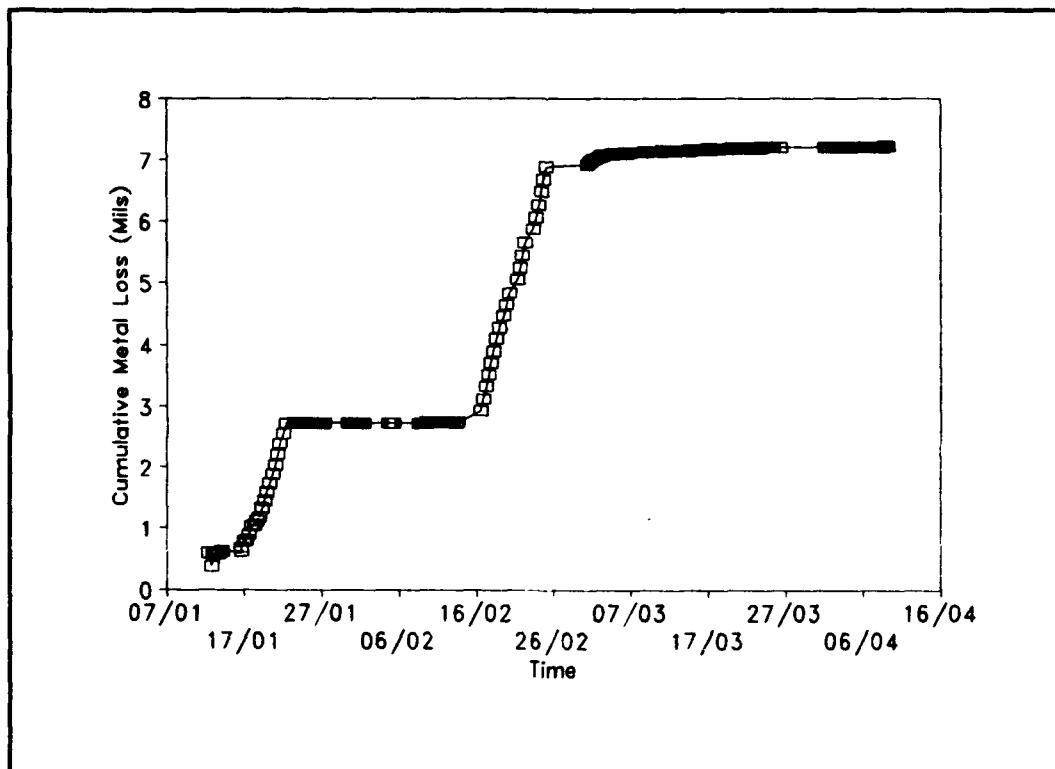


Figure 9: Cumulative Metal Loss For Manual Drain 6

Mean and Cumulative Corrosion Rates In Manual Drain 2.

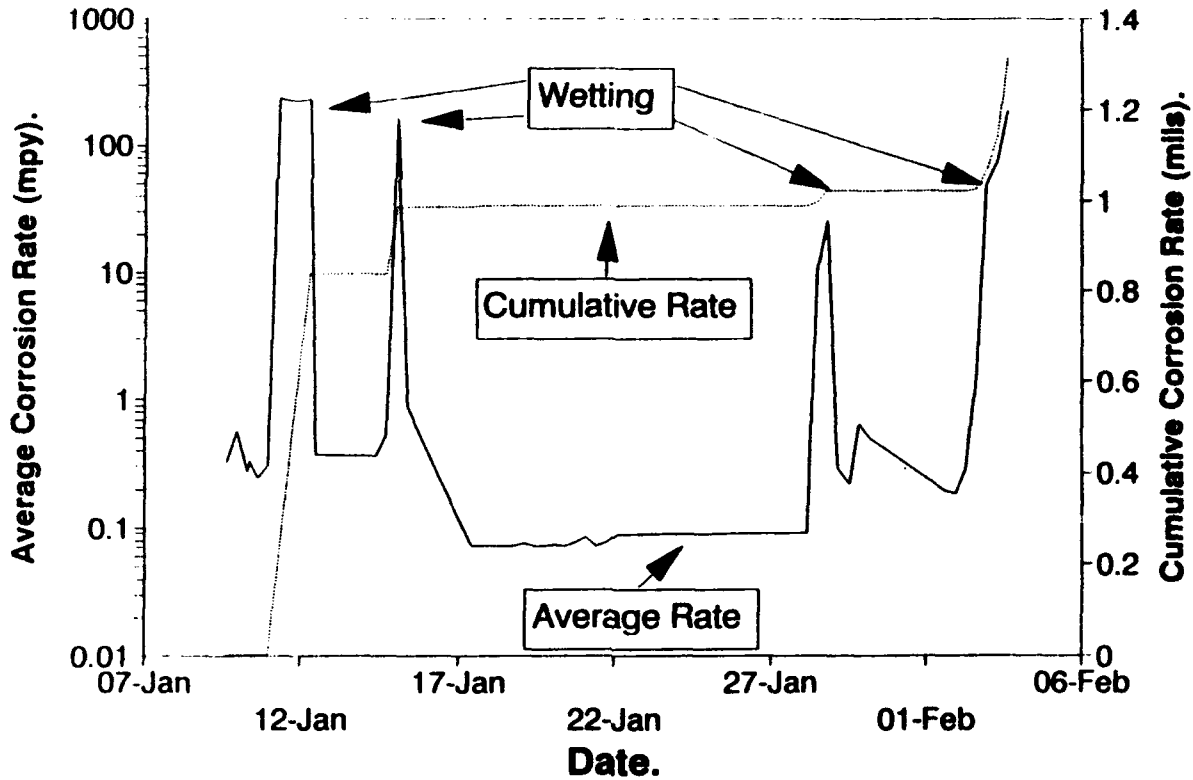


Figure 10. Mean and Cumulative Rates, Manual Drain 2.

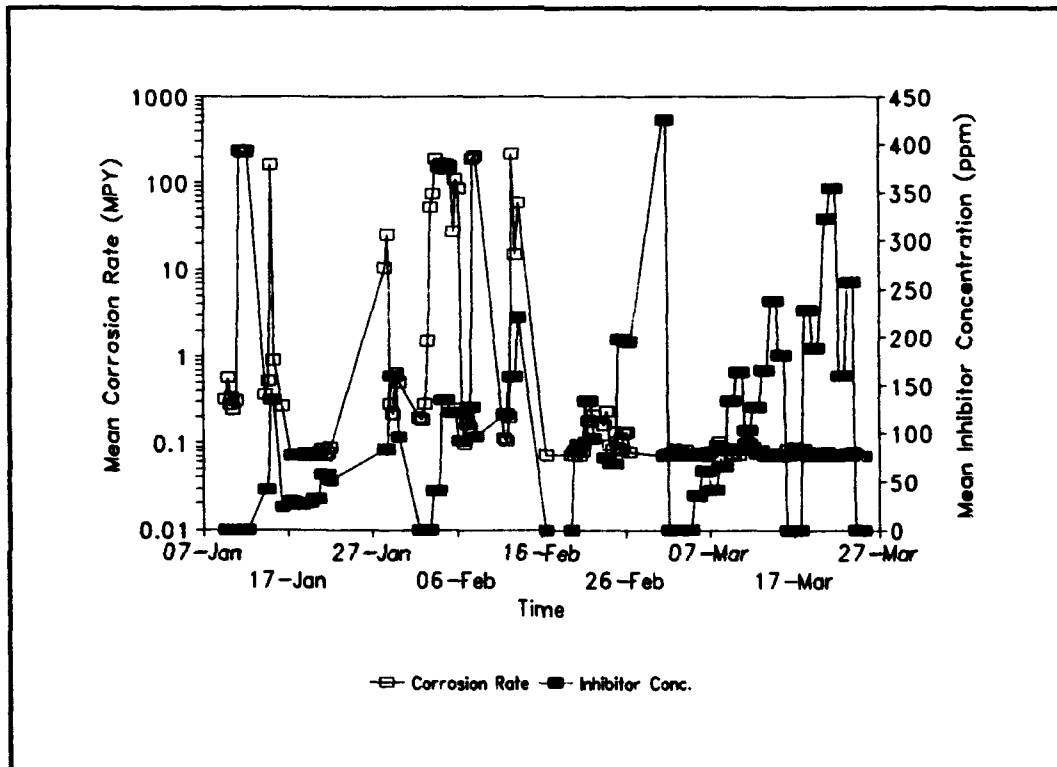


Figure 11: Average Corrosion Rate With Inhibitor Injection

Corrosion Potential Monitoring and Its Simulation in BWR Conditions

Masanori Sakai
Hitachi Research Laboratory
Hitachi, Ltd.
3-1-1, Saiwai-cho, Hitachi-shi
Ibaraki-ken
317 Japan

Noriyuki Ohnaka
Hitachi Research Laboratory
Hitachi, Ltd.
3-1-1, Saiwai-cho, Hitachi-shi
Ibaraki-ken
317 Japan

Katsumi Ohsumi
Hitachi Works
Hitachi Ltd.
3-1-1, Saiwai-cho, Hitachi-shi
Ibaraki-ken
317 Japan

Abstract

A simulation algorithm of corrosion potentials for BWR plant materials has been demonstrated. Cathodic and anodic electrochemical kinetic equations have been derived by analyzing kinetic models involving water radiolysis products of oxygen, hydrogen peroxide, and hydrogen. Corrosion rates of type 304 stainless steel with respect to corrosion potentials are formulated by numerical analysis as well. An electrochemical mixed potential theorem is applied to compute corrosion potentials. Flow rate effects of coolants on corrosion potentials of plant structural materials are expressed as a function of diffusion layer thickness. A fundamental technique and a theory to simulate corrosion potentials have been developed. Corrosion potentials in BWR conditions can be simulated by these results.

Key terms: corrosion potential, ECP, stress corrosion cracking, water chemistry, BWR

Introduction

Corrosion potential monitoring of structural materials is of great interest as a means for stress corrosion cracking(SCC) mitigation. In BWR plants, ECP(electrochemical potential) is accepted as synonymous to corrosion potential¹). An ECP threshold for SCC has been considered as a criterion for water chemistry control. The hydrogen injection technique which reduces ECP by reducing concentrations of oxygen and hydrogen peroxide in BWR coolants has been one of practical approaches for water chemistry control. ECP measurements by ECP sensors, e.g., silver/silver chloride, are essential monitoring techniques for this hydrogen injection effects on SCC mitigation. Since the emplacement of an ECP sensor into plant components has been mainly restricted by plant structures, especially for reactor core regions, ECP simulation becomes a significant method to evaluate ECP at locations of infeasible ECP measurements.

Macdonald demonstrated simulated ECP data of practical BWR plants under hydrogen injection conditions(1). ECP evaluations have been discussed from various view points of electrochemistry, flow velocity of coolant, and water radiolysis(2-5).

However, quantitative kinetic expressions presented earlier in the papers to evaluate ECP did not properly take into account the processes occurring in BWR conditions(1-5). They were, therefore, unable to explain kinetics even for the case of oxygen alone. No electrochemical kinetics relating to BWR water environments has been demonstrated yet. Elucidation of electrochemical kinetics of water radiolysis products and structural materials means obtaining a benchmark for ECP simulations. In BWR conditions, oxygen and hydrogen peroxide are oxidants for structural materials. Hydrogen and steels that are oxidized by the above species are reductants. Electrochemical kinetics of oxygen and hydrogen peroxide have closely related mechanisms(6-9). Moreover, oxygen and hydrogen peroxide kinetics under BWR conditions are different from those proposed for ambient temperature conditions(6-9). A primary difference is that hydrogen peroxide is not only an intermediate for oxygen reduction but it is initially present in the core regions(1, 4).

Here, analytical model for cathodic and anodic reaction mechanisms under BWR conditions are demonstrated and kinetic equations for ECP simulations are derived.

Kinetics for Corrosion Potential(ECP) Simulation

The ECP is calculated by employing mixed potential theorem and solving an equation with unknown electrode potential for which a cathodic and

1) In this paper, it is also convenient to express corrosion potential as ECP, even though correct definitions of these terms may be different.

an anodic charge transfer rates are equal to each other(1,10). In this section, cathodic and anodic charge transfer rates are elucidated.

Cathodic Kinetic Model & Equations

Figure 1 shows the kinetic model of cathodic reactions for BWR environments. A chemical decomposition of hydrogen peroxide is assumed in Eq.[1](11).



k_4 and k_5 appearing in Figure 1 are chemical decomposition rate constants at steel surfaces and in BWR coolants, respectively. Hydrogen peroxide is also decomposed by the electrochemical process designated in terms of the heterogeneous rate constants k_2' and k_3 . Oxygen reduction takes place two consecutive charge transfer reactions which may occur simultaneously and parallel to another charge transfer reaction designated by the heterogeneous rate constant k_1 (9,12). The consecutive charge transfer mechanism involving hydrogen peroxide as intermediate is the most possible since the steels are covered with thick passive films in BWR conditions(12). α_j is the cathodic transient coefficient for each charge transfer step for $j=1,2$ or 3 . E_0 , E_{10} , and E_{20} are the standard electrode potentials for each transfer step. Thus, k_1 , k_2 , k_2' , and k_3 are expressed as $k_{10} \exp\{-4\alpha_1 F(E-E_{10})/RT\} [\text{H}^+]^4$, $k_{20} \exp\{-2\alpha_2 F(E-E_{20})/RT\} [\text{H}^+]^2$, $k_{20}' \exp\{2(1-\alpha)F(E-E_{20})/RT\}$, and $k_{30} \exp\{-2\alpha_3 F(E-E_{30})/RT\} [\text{H}^+]^2$, respectively. $k_{10} [\text{H}^+]^4$, $k_{20} [\text{H}^+]^2$, k_{20}' , and $k_{30} [\text{H}^+]^2$ are the rate constants with units of cm/s. F , R , and T have their usual significance. E is the so-called electrode potential. From Figure 1, linear diffusion processes of oxygen and hydrogen peroxide near vicinities of steels are expressed by Eqs.[2-3].

$$\partial C_A(x,t)/\partial t = D_A [\partial^2 C_A(x,t)/\partial x^2] + (k_5/2) C_B(x,t) \quad [2]$$

$$\partial C_B(x,t)/\partial t = D_B [\partial^2 C_B(x,t)/\partial x^2] - k_5 C_B(x,t) \quad [3]$$

where A is oxygen, B the hydrogen peroxide, C_j the concentration for $j=A$ or B, and D_j the diffusion coefficient for $j=A$ or B. Mass balances for A and B at steel surfaces($x=0$) are expressed by Eqs.[4-5].

$$D_A[\partial C_A(x,t)/\partial x]_{x=0} = (k_1+k_2)C_{AS} - (k_2+k_4/2)C_{BS} \quad [4]$$

$$D_B[\partial C_B(x,t)/\partial x]_{x=0} = (k_2+k_3+k_4)C_{BS} - k_2C_{AS} \quad [5]$$

where C_j s is the surface concentration for $j=A$ or B . Under steady-state conditions, Eqs.[6-8] are expressed as

$$\partial C_A(x,t)/\partial t = \partial C_B(x,t)/\partial t = 0 \quad [6]$$

$$x \geq \delta_A \text{ for } C_A(x) = C_A^*, \quad x \geq \delta_B \text{ for } C_B(x) = C_B^* \quad [7]$$

$$x=0 \text{ for } C_A=C_{AS}, \quad x=0 \text{ for } C_B=C_{BS} \quad [8]$$

where δ_j is the diffusion layer thickness for $j=A$ or B and C_j^* the bulk concentration for $j=A$ or B . From Figure 1, an overall charge transfer rate, i_1 , is expressed by Eq.[9].

$$i_1 = 2F [(2k_1+k_2) C_{AS} + (k_3 - k_2) C_{BS}] \quad [9]$$

After combining Eqs.[2-8], simultaneous equations with two unknowns of C_{AS} and C_{BS} can be solved analytically. Thus, the overall charge transfer rate, i_1 , is expressed by the following Eq.[10], after substituting the determined two unknowns into Eq.[9].

$$i_1 = 2F (\zeta_1 \Xi_1 + \zeta_2 \Xi_2) \quad [10]$$

$$\text{with } \zeta_1 = 2k_1 + k_2, \quad \zeta_2 = k_3 - k_2 \quad [11]$$

$$\Xi_1 = (\Lambda_1 \Phi_2 + \Lambda_2 \Phi_1) / [\zeta_3 \Phi_2 + \Phi_1 k_2 \exp\{-(2\alpha_2 F/RT)(E-E_{20})\}] [H^+]^2 \quad [12]$$

$$\Xi_2 = [\zeta_3 \Lambda_2 - \Lambda_1 k_2 \exp\{-(2\alpha_2 F/RT)(E-E_{20})\}] [H^+]^2 / [\zeta_3 \Phi_2 + \Phi_1 k_2 \exp\{-(2\alpha_2 F/RT)(E-E_{20})\}] [H^+]^2 \quad [13]$$

$$\zeta_3 = k_1 + k_2 + D_A / \delta_A \quad [14]$$

$$\Lambda_1 = C_A^* D_A / \delta_A - (C_B^* D_B / 2\delta_A) \{ \exp(-\lambda_2) + \exp(\lambda_2) + 2\lambda_2 \} / \{ \exp(-\lambda_1) - \exp(\lambda_1) \} \quad [15]$$

$$\Lambda_2 = 2D_B C_B^* \sqrt{(k_5/D_B)} [1 / \{ \exp(-\lambda_1) - \exp(\lambda_1) \}] \quad [16]$$

$$\Phi_1 = [(D_B / 2\delta_A) \{ \exp(-\lambda_1) \{ \exp(\lambda_2) - \lambda_2 \} - \exp(\lambda_1) \{ \exp(-\lambda_2) + \lambda_2 \} \} / \{ \exp(-\lambda_1) - \exp(\lambda_1) \}] + k_2' + k_4 / 2 - D_B / 2\delta_A \quad [17]$$

$$\Phi_2 = [D_B \sqrt{(k_5/D_B)} \{ \exp(-\lambda_1) + \exp(\lambda_1) \} / \{ \exp(-\lambda_1) - \exp(\lambda_1) \}] - k_2' - k_3 - k_4 \quad [18]$$

$$\lambda_1 = \delta_B \sqrt{(k_5/D_B)}, \quad \lambda_2 = \delta_A \sqrt{(k_5/D_B)} \quad [19]$$

Equation [10] expresses the overall charge transfer rates of the cathodic reactions appearing in Figure 1.

Anodic Kinetic Models & Equations

In this study, anodic reactions of hydrogen and structural materials are assumed to have independent kinetics from each other.

Hydrogen kinetic Model and Equations. Figure 2 shows the kinetic model of hydrogen oxidation on steels. An ad-atom of hydrogen is assumed to be an intermediate for two consecutive processes of one electron charge transfer. k_{h1} , k_{h2} , k_{h3} , and k_{h4} are expressed as $k_{h10} \exp\{\beta_1 F(E-E_{h10})/RT\}$, $k_{h10} \exp\{-(1-\beta_1)F(E-E_{h10})/RT\}$, $k_{h20} \exp\{\beta_2 F(E-E_{h20})/RT\}$, and $k_{h20} \exp\{-(1-\beta_2)F(E-E_{h20})/RT\}$, respectively. k_{h10} and k_{h20} are the standard rate constants, β_1 and β_2 the anodic transient coefficients, E_{h10} and E_{h20} the standard electrode potentials for each

step of the two consecutive charge transfer reactions. K_w is the dissociation constant of water, which is calculated at 561K to be $2.5 \times 10^{-18} \text{ (mol/cm}^3\text{)}^2$ (13).

H^+ (H_3O^+), OH^- , and water are assumed to be in equilibrium, as usual in charge transfer reactions.

From Figure 2, an overall charge transfer rate, i_2 , is expressed by Eq.[20]:

$$i_2 = F [k_{h1} C_{CS} + (k_{h3} - k_{h2}) C_{DS} - k_{h4} C_{ES}] \quad [20]$$

where C_{CS} , C_{DS} , and C_{ES} are the steel surface concentrations of hydrogen, the intermediate, and proton, respectively. Mathematics to solve for the surface concentrations of C_{CS} , C_{DS} , and C_{ES} in Eq.[20] are analogous to those in Eq.[2-8] without the chemical reactions. Thus, equations [21-24] for C_{CS} , C_{DS} , and C_{ES} are obtained as

$$C_{CS} = \frac{(D_C C_C^* / \delta_C)(k_{h2} + k_{h3} + D_D / \delta_D)(k_{h4} + D_E / \delta_E) + k_{h2} k_{h4} (1.58 \times 10^{-9} D_E / \delta_E) - k_{h3} k_{h4} D_C C_C^* / \delta_C}{\Theta} \quad [21]$$

$$C_{DS} = \frac{(1.58 \times 10^{-9} D_E / \delta_E) k_{h4} (k_{h1} + D_C / \delta_C) + k_{h1} (D_C C_C^* / \delta_C)(k_{h4} + D_E / \delta_E)}{\Theta} \quad [22]$$

$$C_{ES} = \frac{(1.58 \times 10^{-9} D_E / \delta_E)(k_{h1} + D_C / \delta_C)(k_{h2} + k_{h3} + D_D / \delta_D) + k_{h1} k_{h3} D_C C_C^* / \delta_C - (1.58 \times 10^{-9} D_E / \delta_E) k_{h1} k_{h2}}{\Theta} + 1.58 \times 10^{-9} \quad [23]$$

$$\Theta = \frac{(k_{h1} + D_C / \delta_C)(k_{h2} + k_{h3} + D_D / \delta_D)(k_{h4} + D_E / \delta_E) - k_{h3} k_{h4} (k_{h1} + D_C / \delta_C) - k_{h1} k_{h2} (k_{h4} + D_E / \delta_E)}{\Theta} \quad [24]$$

in which subscripts C, D, and E designate hydrogen, the intermediate, and proton, respectively. D_j , C_j^* , and δ_j are the diffusion coefficient, the bulk concentration, and the diffusion layer thickness, respectively, for $j=C, D, \text{ or } E$.

Formulation of Stainless Steel Corrosion Rate. Corrosion rates of stainless steel with respect to ECP are formulated by numerical analysis, employing the current-potential curve measured by Hirayama et al.(14). The authors measured the current-potential curve of type 304 stainless steel without supporting electrolytes at 563K in deoxygenated conditions, by employing a potentiostat equipped with an

IR compensation circuit(14). The current potential-curve showed slightly different shape from that measured with supporting electrolytes, e.g., sodium sulfate. Since coolants of BWR plants do not have ionic concentrations in conventional electrochemical measurements, electrochemical experiments are desired to be performed under simulated high temperature water conditions. Least square method is applied to the digitized data of the current-potential curve measured in pure water at 563K, and then corrosion rate, i_3 , of the type 304 stainless steel with respect to an electrode potential, E, which is equivalent to ECP, is expressed in polynomial form of Eq.[25]:

$$i_3 = 7.5973 + 68.052E + 305.08E^2 - 241.97E^3 - 3800.9E^4 - 2143.6E^5 \\ + 17770E^6 + 17681E^7 - 28244E^8 - 33621E^9 \text{ (}\mu\text{A/cm}^2\text{)} \quad [25]$$

where E is the electrode potential of the stainless steel. Figure 3 shows a current-potential curve expressed by Eq.[25]. The correlation coefficient, r, was 0.9996.

ECP Simulation

From Eqs.[10], [20], and [25], an overall charge transfer rate, i, involving both anodic and cathodic reactions is expressed by

$$i = i_1 - i_2 - i_3 \quad [26]$$

Employing a numerical calculation, we can compute the ECP by solving equation [26] for $i=0$ in which case the unknown electrode potential, E, is equal to ECP.

Flow Rate Effect on ECP

Holser et al. analyzed turbulent flow effects on diffusion limiting currents(15). On the basis of their findings and after some rearrangements of their equations, a diffusion layer thickness function of a flow rate of the coolant is expressed by Eq.[27]:

$$\delta_j = 12.64 v^{-0.70} D_j^{0.356} \nu^{0.344} d^{0.30} \text{ (cm)} \quad [27]$$

where δ_j is the diffusion layer thickness for species $j=A, B, C, D, \text{ or } E$, D_j the diffusion coefficient for species $j=A, B, C, D, \text{ or } E$, v the flow velocity(cm/s), ν the kinematic viscosity(cm^2/s), and d the pipe diameter(cm). δ_j for $j=A$ or B , appearing in Eq.[7], is represented by

Eq.[27]. Flow rate effects on ECP are predicted by diffusion layer thickness changes calculated by Eq.[27].

References

1. D.D.Macdonald, *Corrosion*, **48**, 3(1992) : p.194.
2. N.Ichikawa, Y.Hemmi, and J.Takagi, "Estimation on Corrosion Potential of Stainless Steel in BWR primary Circuit," (London, Water Chemistry of Nuclear Reactor Systems 6, British Nuclear Energy Society, 1992), p. 127.
3. C.C.Lin, F.R.Smith, N.Ichikawa, and M.Itow, *Corrosion*, **48**, 1(1992) : p.16.
4. C.P.Ruiz, C.C.Lin, and R.N.Robinson, "Model Calculations of Water Radiolysis and Electrochemical Potentials in BWR Primary Coolant II," (London, Water Chemistry of Nuclear Reactor Systems 6, British Nuclear Energy Society, 1992), p. 141.
5. D.D.Macdonald, H.Song, K.Makela, and K.Yoshida, *Corrosion*, **49**, 1 (1993) : p.8.
6. V.S.Bagotskii, V.Yu.Filinovskii, and N.A.Shumilova, *Elektrokhimiya*, **4**, 10(1969) : p.1247.
7. H.Behret, W.Clauberg, and G.Sandstede, *Helvetica*, **81**, 1(1977) : p.54.
8. H.S.Wroblowa and S.B.Qaderi, *J.Electroanal.Chem.*, **279**, (1990): P.231.
9. A.Damjanovic, M.A.Genshaw, and J.O'M.Bockris, *J.Electrochem.Soc.*, **114**, 5(1967) : p.466.
10. L.P.Hammett and A.E.Lorch, *J.Amer.Chem. Soc.*, **54**, (1932) : p.2128.
11. C.C.Lin, F.R.Smith, N.Ichikawa, T.Baba, and M.Itow, "Decomposition of Hydrogen Peroxide in Aqueous Solutions at Elevated Temperatures," (London, Water Chemistry of Nuclear Reactor Systems 5, British Nuclear Energy Society, 1989), p. 145.
12. J.Jovancicevic and J.O'M.Bockris, *J.Electrochemical.Soc.*, **133**, 9(1986) : p.1797.
13. W.L.Marshall and E.U.Frank, *Water and Steam, Their Properties and Current Industrial Applications*, (Edited by J.Starb and K. Scheffler, Pergamon Press), p.506.
14. H.Hirayama, Y.Yamashina, S.Nakamura, T.Kawakubo, and M.Hishida, *Japan Society of Corrosion Engineering(Boshoku Gijutsu)*, **34**, 2(1985) : p.86.
15. R.A.Holser, G.Prentice, R.B.Pond Jr., and R.Guanti, *Corrosion*, **46**, 9(1990) : p.764.

Twenty Years of Experience of Dezincification Resistant Brasses in Swedish Tap Water Systems

Mats Linder
Swedish Corrosion Institute
Roslagsvägen 101, Hus 25
104 05 Stockholm Sweden

Abstract

Brass came early in extensive use for valves and fittings in tap water systems in Sweden. The reasons were the comparatively low material cost, as well as the good properties concerning casting, forging, machining and corrosion resistance. With the increasing use of copper pipe systems, however, problems occurred with dezincification of ordinary brass in waters with low alkalinity, which are common in large parts of Sweden. In 1970 Swedish authorities issued regulations which required use of dezincification resistant brass in tap water systems. To receive approval the brasses had to be tested with respect to dezincification resistance. A test method was developed at the Swedish Corrosion Institute (SCI). The method was based on exposure of samples in 1% CuCl_2 solution at 75°C with a solution volume specific to the exposed brass area. The method was standardized in Sweden and later on adopted as International Standard ISO 6509. Approval criteria to be used in Sweden at laboratory testing were determined after a field test of a number of brasses in very aggressive water. It was appointed that the average and maximum dezincification depth must not exceed 200 μm and 400 μm respectively. It was suggested that a possible revision of the criteria could be made after some years of practical experience of approved brasses. For that reason samples were removed from buildings and examined 1978 after 4 years' service. It was then concluded by an expert committee that more stringent criteria were not needed.

During 1983–85 SCI investigated 211 samples from insurance cases of water leakage from tap water systems. No case of dezincification appeared in approved brass while 12 cases were found in ordinary brass. In February 1993 an inquiry was sent to 16 companies and organizations including users and producers of alloys and products of approved brasses. In all 16 answers it was declared that no damages due to dezincification of approved brasses were known and that more stringent approval criteria were not needed.

The development of alloys which has taken place, particularly in Sweden, has resulted in a large number of approved brasses for different methods of component production. This has given a variety in chemical composition and of the content of dezincification sensitive β -phase of the approved brasses. Some of the approved brasses got laboratory test results close to the approval limit, but these brasses have also been known for very good service behaviour.

Today more than 50 dezincification resistant brasses are approved in Sweden for use in tap water systems and many have been in use for about 20 years. The very good practical experience tells that there is no reason for more stringent approval limits, than those which have been used successfully in Sweden since it from the users point of view would not result in better quality.

Key terms: Dezincification, dealloying, brass, tap water, testing.

Introduction

Brass was early in extensive use as material for taps, valves and fittings in tap water systems in Sweden. The reasons for this were the comparatively low cost as well as the good properties concerning casting, forging, machining and corrosion resistance. With the increasing use of copper pipe systems, however, problems arose as damages caused by dezincification of ordinary brass occurred in areas with aggressive water. Aggressivity with respect to dezincification is due to a low ratio of alkalinity to chloride content of the water. This relationship has been shown by Turner¹, Figure 1. In Sweden and other Nordic countries the cause for the water aggressivity is mainly the low alkalinity which is prevailing in large areas.

Damages caused by dezincification comprised jamming valve stems, blockage due to voluminous corrosion products, loss of mechanical strength and water leakage. To counteract the dezincification problems the National Swedish Board of Physical Planning and Building in 1970 issued regulations² for use of dezincification resistant brass in tap water installations. Instead of standardization of alloys a type approval procedure was set up which permitted development of various alloys. To receive approval the brasses had to be tested with respect to dezincification resistance. The specified test appeared to be less reliable and therefore an improved method was developed at the Swedish Corrosion Institute (SCI). The method was based on 24 hours' exposure of samples to 1% CuCl₂ solution at 75°C with a solution volume specific to the exposed brass area³. After exposure the dezincification depth is determined by metallographic examination of cross sections of the samples. The method was standardized in Sweden and later on adopted as international standard and national standards in different countries. A detailed description of the test method is given in ISO 6509.

The acceptance criteria are, however, not specified in the ISO standard. This paper deals with the evaluation technique at laboratory testing, the establishing of acceptance criteria by tests under service conditions and practical experience gained when many approved brasses have been in use for about 20 years.

Evaluation at Laboratory Testing

The measurement of the dezincification depth after laboratory exposure according to ISO 6509 is carried out by metallographic examination of a section perpendicular to the exposed surface. At the development of the test method it was early found out that the maximum depth only would not give a sufficient measure of the susceptibility of the brass. If only the maximum dezincification was used for assessment it appeared that brasses with large difference in behaviour could get the same test result. This is visualized in Figure 2. An attack in a solitary streak of β -phase in the longitudinal direction of a rod will not be harmful e.g. in a valve stem while an average attack to the same depth might be detrimental due to decreased mechanical strength and to blockage by voluminous corrosion products. Hence it was concluded that the average dezincification depth should be determined in addition to the maximum.

For determination of the average the dezincification is measured in consecutive visual fields (preferably minimum 25) along the maximum possible length of the specimen. The measurement is made at a fixed scale in each visual field. The average is calculated from the individual measurements. Details of the measurement are shown in Figure

3. The technique with maximum and average dezincification depth for acceptance criteria has been used at the type approval testing in Sweden and the use of average depth has recently been adopted in the Australian Standard AS 2345-1992.

Acceptance Criteria

When the development of the test method had resulted in a proposal a joint investigation was carried out simultaneously at three different laboratories in 1973. Ten brasses known for different dezincification resistance were tested and concordant results were obtained at the 3 laboratories. The results were also in good agreement with the service experience of the tested alloys. Seven of these 10 alloys were in 1974 tested 1 year under service conditions in hot water systems at 60° and 90°C in hospitals in places with aggressive waters. The materials were exposed to tap water in copper tube rigs which were installed in hot water circulation lines in the buildings. The tested specimens had the shape of threaded rods with 8 mm diameter screwed into gun metal holders which were brazed to the copper tubes. The water exposed end of the rod had no thread and thus a narrow crevice was formed towards the gun metal holder. The results from the field test were, particularly for the most corrosive water in Gothenburg, in close agreement with the results from the accelerated tests³. The composition of the Gothenburg water at the time of the testing is shown in Table 1.

The results from these tests were used for establishment of acceptance criteria to be used at type approval testing. The acceptance limits were set rather liberally since they aimed at sorting out brasses with poor dezincification resistance and at approval of brasses with comparatively good resistance. Total immunity to dezincification was consequently not required. The acceptance criteria for approval in Sweden were that after laboratory testing with the developed method the average dezincification depth must not exceed 200 µm and in addition the maximum dezincification depth must not exceed 400 µm.

A long term field test of 5 brasses was carried out during 3.5 years, 1978-1981, by Gränges Metallverken⁴. The test was carried out in Gothenburg at the same site and under the conditions used by SCI 1974. In addition all brasses were laboratory tested according to ISO 6509. The test results supported the reliability of the test method and the acceptance criteria.

Service Experience of Approved Brasses

Buildings in Gothenburg

To evaluate the service performance of dezincification resistant brasses which were laboratory tested and approved according to the established criteria SCI in 1978 investigated valves and fittings which had been in use in copper tubes for about 4 years in hot water systems in buildings in Gothenburg⁵. This city was selected since the water at that time was known to be extremely corrosive with respect to dezincification. In total 133 components from valves and fittings were examined. Seventynine of these were made of approved brasses and 54 of ordinary, not approved brasses.

With guidance of an acceptable life-span of a tap water system a maximum corrosion attack less than 100 µm after 4 years in a very corrosive water was regarded as

tolerable. Using this limit only 15% of the samples of not approved brasses were satisfactory while the corresponding portion of the components made of approved brasses was 92%. Two of the 6 samples of approved brass with more than 100 μm corrosion attack had significant dezincification. One of these 2 had a localized attack of 200 μm depth which was judged as being of minor importance. The other had a 800 μm deep attack in a solitary streak of β -phase in the extrusion direction of a valve stem. This longitudinal attack was judged to be of little importance for the functioning of the stem. Two samples had other corrosion than dezincification namely intergranular attack and crevice corrosion respectively. Two chillcast valve-samples from the same foundry had severe localized corrosion attacks with interspersions of dezincification. The attacks had connection with pores in the material which seemed to have been formed at the casting.

With the experience from 4 years service in Gothenburg as a basis it was in 1980 concluded by an expert committee that there was no need for more stringent approval criteria.

Insurance Cases

During 1983 SCI started an investigation of insurance cases of corrosion in water systems in areas with corrosive water⁶. The aim of the investigation was to determine the frequency of different phenomena which result in damages by leaking water in buildings.

Insurance Companies sent in samples from 211 cases for investigation. In 199 of these cases the damages had other causes than dezincification and occurred mostly in other materials than brass. In the remaining 12 cases the damage was caused by dezincification of not approved ordinary brass in brazing solder and fittings. Consequently no case of dezincification appeared in components of approved brass.

Inquiries

Many of the dezincification resistant brasses which are approved in Sweden have been in use for about 20 years and some of them were used even before the regulations were issued. Informal inquiries during the years to users and producers have supported the impression of very good service performance of the approved brasses.

For completion a formal inquiry was in February 1993 sent to 16 companies and organizations including authorities, users and producers of alloys and products of approved brasses. In the inquiry it was asked whether any cases of dezincification of approved brasses were known and if so when and to what extent. Finally it was asked if the approval criteria were considered too hard, too mild or sufficient. In all 16 answers it was declared that damages due to dezincification of approved brass were not known. Fifteen of the answers expressed the opinion that the approval criteria are sufficient. In one answer it was stated that the criteria are sufficient to corrosive water but too hard for not corrosive water.

Approved Brasses

As a result of the development of alloys which has taken place, particularly in Sweden, more than 50 dezincification resistant brasses are approved at present for use in tap water systems. There are brasses for production of components by pressure die-casting, chill-casting, hot forging and machining from rod. Some brasses require a final heat-treatment others not. This development has given a variety in chemical composition and content of dezincification susceptible β -phase in the approved brasses.

An important matter regarding the suitability of the acceptance criteria is whether any approved alloys in reality have got attacks close to the upper limits at the laboratory test. That the latter has been the case is shown in Figures 3 and 4 presenting the number of brasses as a function of maximum and average attacks respectively at laboratory testing.

The nominal copper content of approved brasses covers a span between 61.5 and 66%. The fraction of brasses as a function of nominal Cu-content is shown in Figure 6. Brasses with the lowest Cu-content usually require heat-treatment as a final production step to decrease the β -phase content. Brasses with the highest Cu-content are usually alloyed with aluminium. Aluminium is favourable to the dezincification resistance but on the other hand it favours formation of β -phase. Aluminium containing alloys must therefore have a copper content high enough to keep the β -phase content on a suitable level. Other common minor alloying constituents are tin and silicon. All approved brasses are alloyed with either arsenic or antimony. Antimony is preferred in alloys for casting as it is easier than with As to keep it on a stable content in the melt. Arsenic is preferred in alloys for extrusion since Sb may contribute to brittleness during the process. All brasses are in addition alloyed with lead which is necessary for the machinability. The fraction of approved brasses as a function of nominal Pb-content is shown in Figure 7. The number of brasses intended for different production methods is shown in Table 2.

Discussion

The experience of dezincification resistant brasses in Sweden has shown that there is a most satisfactory agreement between results from laboratory testing according to ISO 6509 and the service performance of approved alloys after 20 years. During this period no case of damage due to dezincification of an approved brass has appeared in the consultancy service at SCI. Furthermore the different field tests and investigations of components from tap water systems which have been carried out as well as other experience including a recent inquiry have supported that the used comparatively liberal acceptance criteria are sufficient. This means that more stringent approval criteria which have been used in some other countries should not be needed since they from the users point of view would not result in better quality. The Swedish opinion is shared with the other Nordic countries. This fact was confirmed 1989 in the Nordic Product Rules NKB 12 and 13 for brass fittings and valves respectively.

As the alloying constituent (normally As or Sb) which is necessary for inhibiting dezincification of a brass (with Zn-content higher than ca 15%) only protects the α -phase the microstructure of a duplex $\alpha + \beta$ brass is determinant for its resistance. In this respect the distribution rather than the percentage of the susceptible β -phase is of great importance.

If the β -phase has formed a continuous network through the material the dezincification can proceed rapidly in a corrosive water. If on the other hand the β -phase is discontinuous the parts of it which are located at the metal surface and exposed to water from the beginning will corrode but this attack ceases when it reaches the inhibited α -phase. This fact is important and supports the standpoint that total immunity at laboratory testing is not required for approval. It seems that the laboratory method and the used approval criteria have sorted out brasses with too high grade of continuity in the β -phase distribution.

It also seems that the Swedish expert group made a good decision in 1980 when it concluded that more stringent approval criteria were not needed even though some localized dezincification was discovered in a small number of components after 4 years service in a very corrosive water.

Very good dezincification resistance can be obtained by minimizing the β -phase content by heat treatment at 500-550°C as a final production step. This additional procedure seems however not to be generally needed. More than 50% of the brasses which are approved in Sweden are not heat-treated but have in spite of that shown an inviolable service performance.

Lead pick up in the water from leaded copper alloys has attracted attention in different countries for some years. Some of this lead probably originates from corrosion of the metal and some from a film which is spread on interior surfaces at the machining of valves and fitting. The dezincification resistant brasses have an additional advantage in this connection since they have a rather low lead content compared with e.g. leaded gun metal in combination with the high corrosion resistance.

Conclusions

Results of long term field tests and service experience for 20 years justify the following conclusions:

- The Swedish regulations issued 1970 for approval of dezincification resistant brasses for tap water systems have been successful.
- The ISO standard 6509 is a reliable method for prediction of dezincification resistance of brasses.
- The evaluation at laboratory testing according to ISO 6509 should be based on both maximum and average dezincification depth.
- The acceptance limits used for approval in Sweden and the other Nordic countries at laboratory testing according to ISO 6509 have appeared to be sufficient. These limits are:

average dezincification $\leq 200 \mu\text{m}$
maximum dezincification $\leq 400 \mu\text{m}$

References

1. M.E.D. Turner, "The influence of water composition on the dezincification of duplex brass fittings", Proc. Soc. Water Treatment and Examination 10 (1961), p 162.
2. Regulations on water and sanitation installations, issued by National Swedish Board of Physical Planning and Building, Stockholm, Publ. No.34 (1970) (in Swedish).
3. M. Linder, E. Mattsson, "Test method for determination of dezincification resistance of brass used in pipe fittings", Proc. Eurocorr 77, London (1977), p 445-451.
4. R. Holm, R. Sundberg, E. Mattsson, Experience with brass components for water installations in Sweden. Internat. Symp. Corrosion of Copper & Copper Alloys in Buildings, Proceedings, Tokyo, Japan Copper Development Assoc. (1982), p 230-232.
5. S. Brennert, "Dezincification of brass in valves and fittings - service experiences." VVS 9 (1980), p 40-42 (in Swedish).
6. L. Dahl, E. Mattsson, "Corrosion in housing water systems - analysis of insurance cases", Swedish Corrosion Institute. Report 64 144 (1986) (in Swedish).

Table 1. Water composition at the test site at the time of the field tests.

| | |
|--------------------------------------|-------|
| pH | 8.5 |
| Conductivity, mS/m | 17 |
| Ca, mg/l | 18 |
| Total hardness, °dH | 2.3 |
| Fe/mg/l | 0.02 |
| Mn, mg/l | <0.05 |
| HCO ₃ ⁻ , mg/l | 15 |
| Cl ⁻ , mg/l | 13 |
| SO ₄ ²⁻ , mg/l | 30 |

Table 2. Number of approved brasses for different production methods, with and without final heat-treatment.

| Production method | Numbers of brasses | | |
|-----------------------------|--------------------|--------------|-------|
| | Not heat-treated | Heat-treated | Total |
| Pressure die-casting | 11 | 0 | 11 |
| Chill-casting | 9 | 1 | 10 |
| Hot forging | 4 | 10 | 14 |
| Machining from rod and tube | 2 | 13 | 15 |
| All | 26 | 24 | 50 |

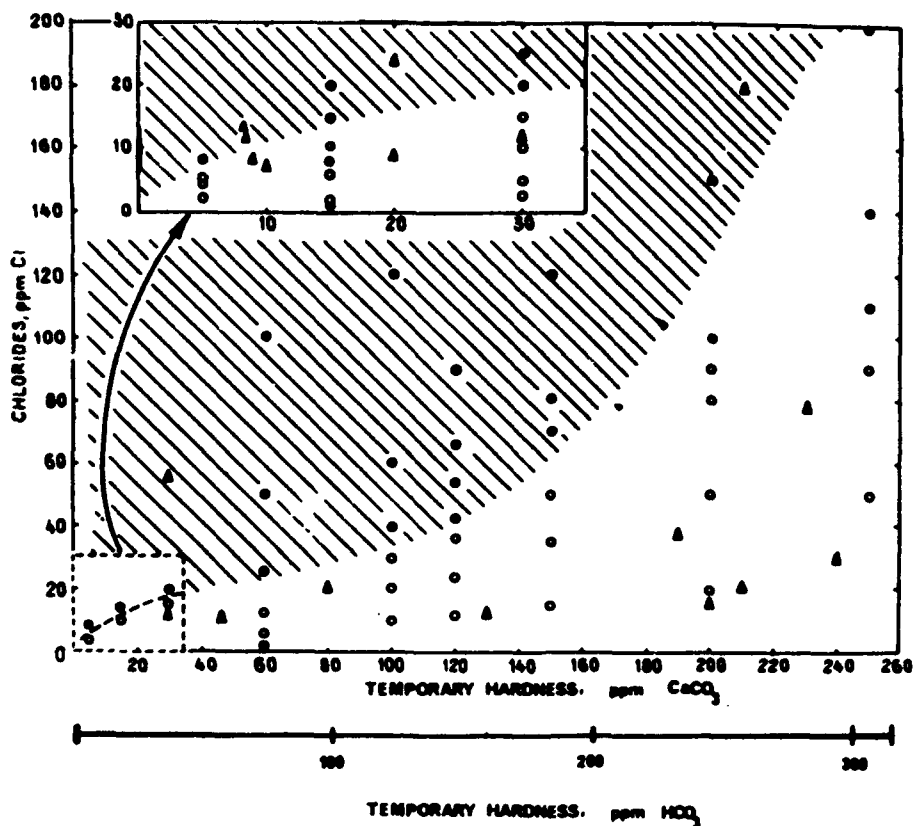


Figure 1. Influence of the content of Cl^- and HCO_3^- in water on dezincification of brass according to Turner¹.
The lined area represents corrosive water.

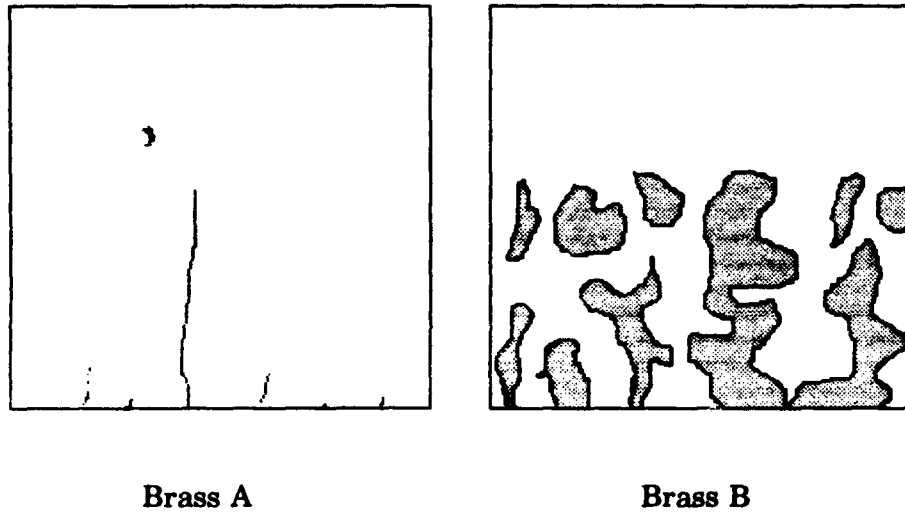


Figure 2. Cross-section through two brass pieces with different dezincification resistance. Dark areas represent attacks in β -phase starting at the bottom edge of the pieces. If only max. dezincification depth is used as criterion A and B are judged equally resistant.

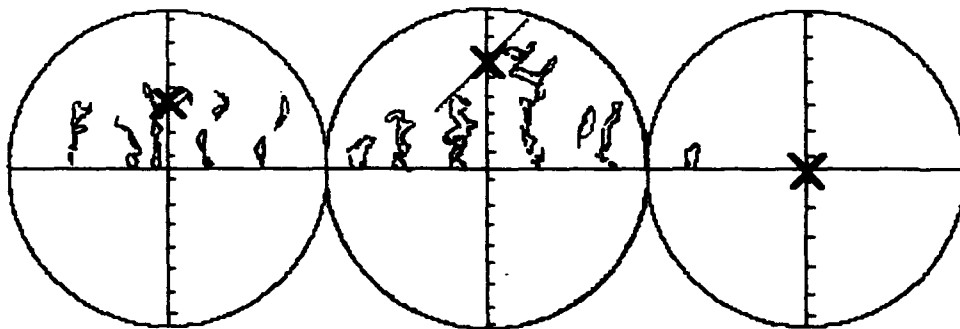


Figure 3. Illustration of three consecutive microscope visual fields along a cross-section of a tested brass-specimen. The attacks (dark areas) have started at the central horizontal line. Measurements for calculation of average dezincification depth are made at the crosses.

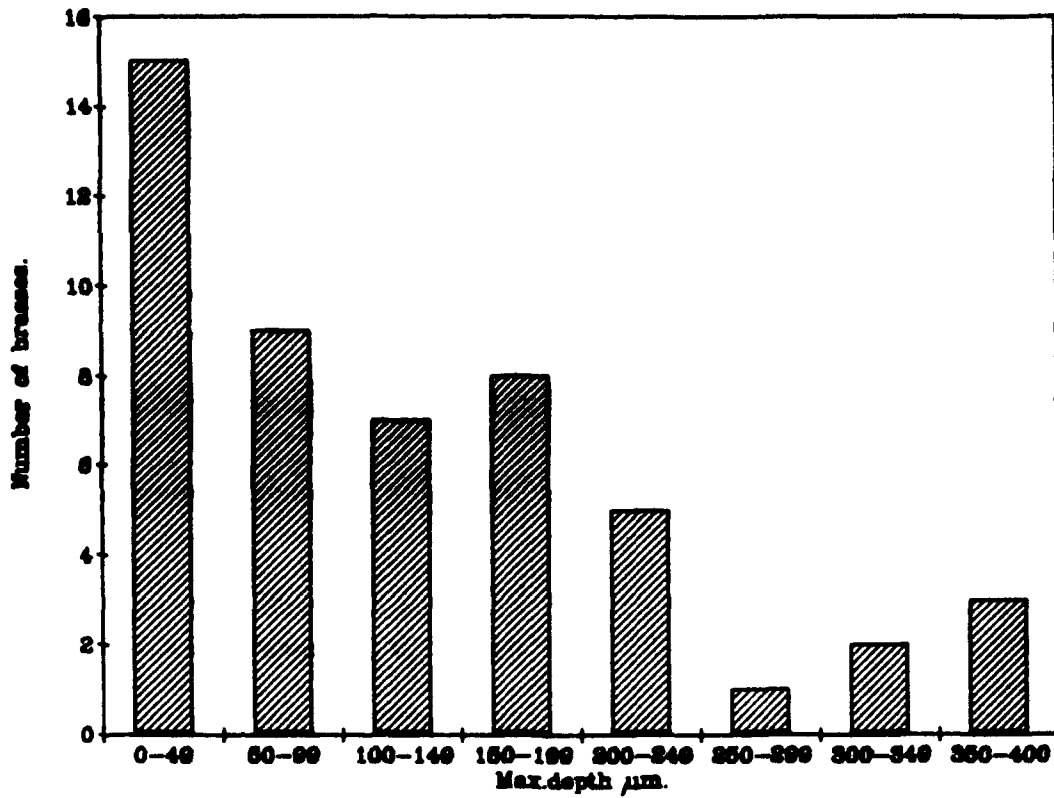


Figure 4. Number of approved brasses as a function of maximum dezincification depth at laboratory testing according to ISO 6509.

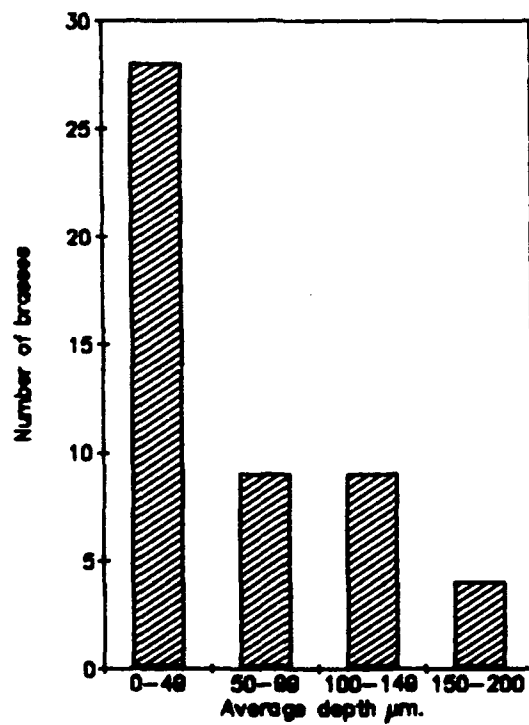


Figure 5. Number of approved brasses as a function of average dezincification depth at laboratory testing according to ISO 6509.

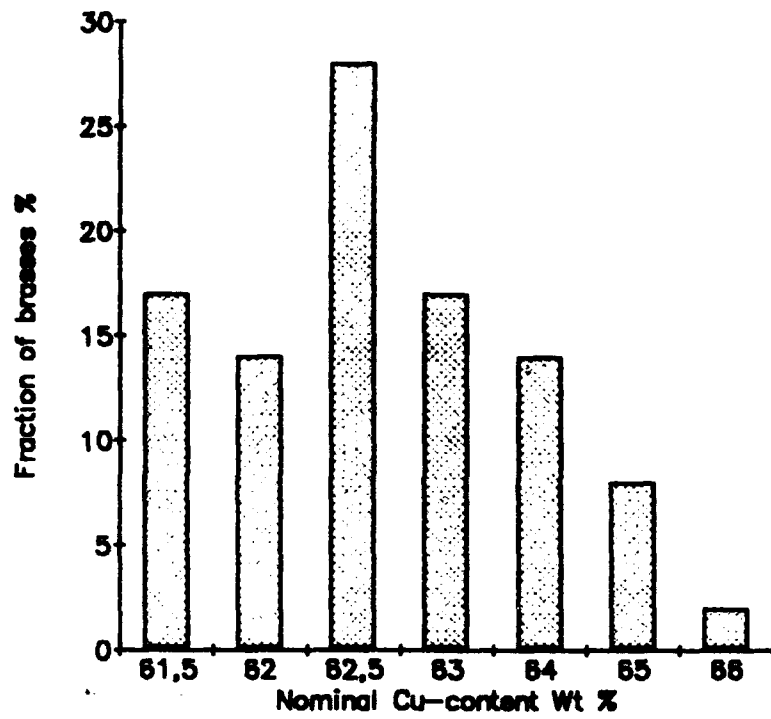


Figure 6. Fraction of approved brasses as a function of nominal copper content.

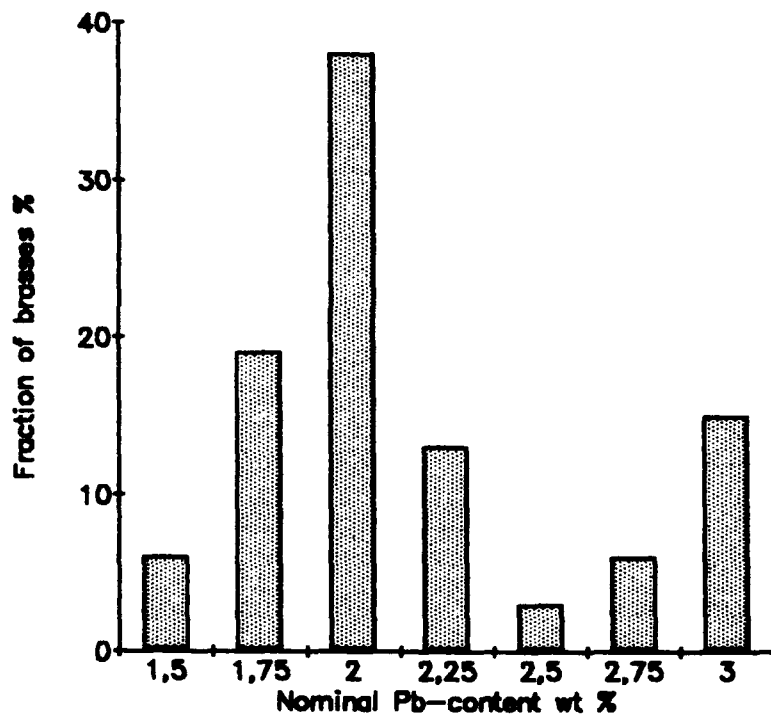


Figure 7. Fraction of approved brasses as a function of nominal lead content.

Corrosion Protection due to Deaeration Using a Hollow Fiber Membrane for Water Distribution Systems in Buildings

Tetsuo Fujii,
MIURA CO., LTD. Koraku Bld. 7F, 1-12-10 Shinbashi,
Minato-ku, Tokyo 105, Japan

Yasuo Ochi
MIURA CO., LTD. Horiecho 7
799-26 Matsuyama-shi, Japan

Yuji Ukena
MIURA CO., LTD. Horiecho 7
799-26 Matsuyama-shi, Japan

Yukinori Tobisaka
MIURA CO., LTD. Koraku Bld. 7F, 1-12-10 Shinbashi,
Minato-ku, Tokyo 105, Japan

Abstract

It has been well established that deaeration is an essential means for corrosion protection of water piping in power generating plants. However, the existing mechanical vacuum or steam injector systems are too expensive for treating large quantities of and once-through potable waters. Recently, a hollow fiber membrane made of polyolefin which can economically separate dissolved oxygen in water was developed. Compact deaeration equipment which can treat water of 1 to 12 m³/h as the standard specification was manufactured by using a module with a fine and thin hollow fiber membrane and a water-sealed vacuum pump. By passing through the deaeration system, water containing 8.2 ppm oxygen content was easily reduced to 0.5 ppm at 25 C under standard operating conditions. Deaerated water was continuously supplied to water piping in buildings and thereby 'red -water' problems were completely eliminated 2 to 3 weeks after installation. The existing rust became black in color due to the reduction of FeOOH to magnetite in the absence of dissolved oxygen. The deaeration system can also be applied to copper tubing in the hot water supply and is able to avoid localized corrosion such as pitting and erosion-corrosion.

Case studies of this deaeration system with a hollow fiber membrane are given for low-pressure boilers, cold and hot water distribution systems, and also closed cooling water systems in buildings.

Key terms: deaeration, hollow fiber membrane, water piping, red-water, buildings

1. Introduction

Corrosion occurring in water distribution systems of urban buildings has been a serious problem in the last few decades. Fresh water in Japan is corrosive to the metal piping systems because of the softness of the water. The Saturation Index(S.I.) of city waters in major cities generally ranges from -1.5 to -2.0. Therefore, these waters do not form a protective films of calcium carbonate scale inside the galvanized pipes. Raising the Saturation Index to a positive value is not an effective means for the water in Japan. For corrosion problems encountered in water piping, the Welfare Ministry of Japan conventionally allows the addition of 5 mg/l (SiO_2 or P_2O_5 equivalent) of sodium silicate or sodium polyphosphates as corrosion inhibitors. However, in soft water protection from corrosion is not expected from the addition of a small amount of these chemicals. It is well recognized that polyphosphate treatment is only effective as a sequestering action to prevent red-water problems rather than inhibiting corrosion. In recent years countermeasures due to physical means such as magnetic and electrostatic devices have been proposed instead of the addition of chemicals. But, the corrosion protection mechanism of these methods is not yet clarified and the reproducibility of the protection effect is unreliable.

Galvanized steel pipe has long been used for water supply systems in buildings and city water distribution. But, the corrosion resistance of galvanized steel pipe deteriorates due to an increase in the corrosiveness of polluted water. Today, plastic-lined steel pipe has usually been recommended for a water supply system. However, severe corrosion still occurs at the pipe joints. Copper tubing, which is the main plumbing material in hot-water supply systems, is also suffering failure from pitting and erosion-corrosion. Yet to date there have been no effective means to mitigate this damage.

On the contrary, deaeration has long been used as a reliable corrosion preventive measure in the fields of high-pressure boilers and nuclear power reactors. In the U.S., the first cold-water deaerator was installed in a building in 1924, which employed a high-vacuum mechanical deaerating apparatus and which reduced the DO to 1.4 ppm.¹⁾ However, existing deaeration methods using the mechanical vacuum or steam ejector processes are generally too expensive for preventing equipment corrosion in buildings.

Recently, a hollow fiber membrane which shows a high gas separation efficiency has been developed. Using this hollow fiber membrane, the deaeration apparatus was constructed and deaeration of cold-water was accomplished economically for the water supply systems in buildings. This deaeration method using a hollow fiber membrane should be a promising corrosion preventive process in the field of water treatment not only for steel but also for copper tubing systems.

2. Deaeration Equipment Using a Hollow Fiber Membrane

Figure 1 shows the schematic diagram for the gas separation mechanism for the system using a fine and thin, hollow fiber membrane. The hollow fiber membrane is made of polyolefin which is 0.2 mm in i.d. and 500mm in length. A module consists of several tens of thousand fibers which is encapsulated in a PVC case. The outer chamber of a bundle of fibers is evacuated by a water-sealing vacuum pump. Feedwater enters the deaeration module and the oxygen molecules are exhausted. The oxygen concentration in water decreases from 8.2 to 0.5 mg/l(25C) as it passes through the module under standard operating conditions.

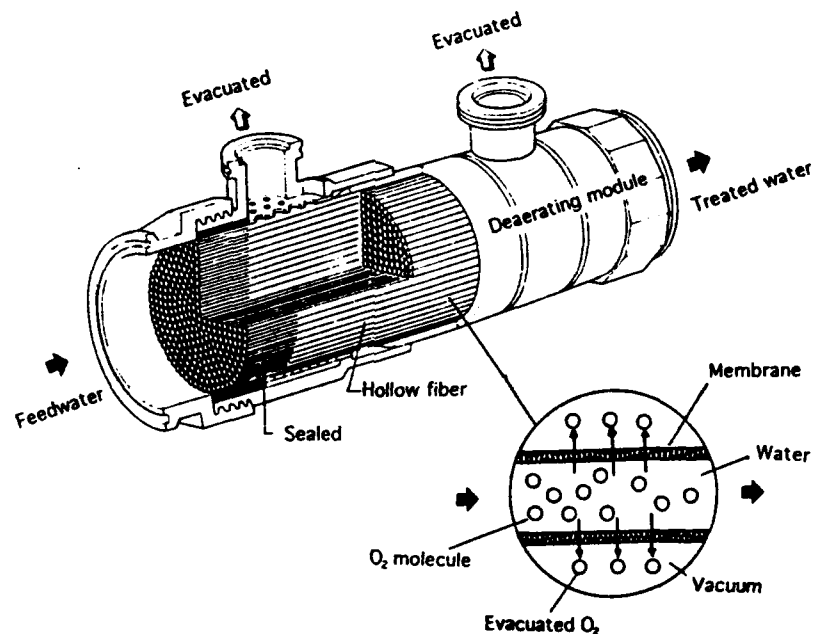


Fig. 1 Deaerating module and gas separation mechanism.

A deaeration module (165mm o.d. x 500mm length) has the capability to treat 1000 liters of water per hour.

Figure 2 shows the flow diagram of the deaerating system. The sealing water for the vacuum pump was recycled and cooled by heat exchange with feedwater. The feedwater was supplied to the deaerating module after the removal of solid substances.

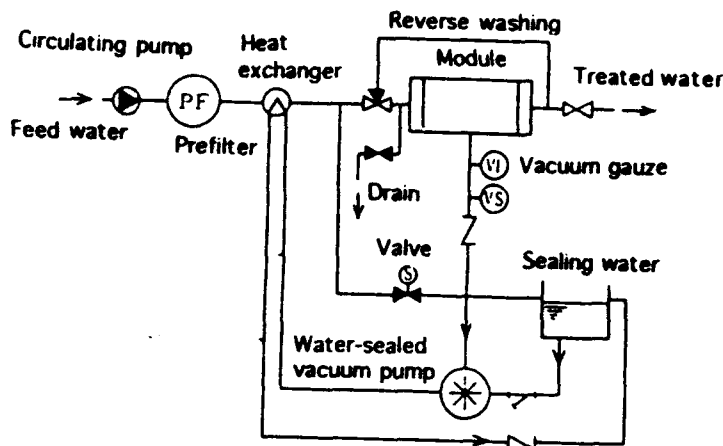


Fig. 2 Flow diagram of deaerating system

3. DO Concentration and Corrosion Rate for Mild Steel

The corrosion rate of mild steel in water is generally controlled by the diffusion rate of dissolved oxygen, although an abrupt decrease in the corrosion rate may occur at high water velocities because of the passivation phenomena. Figure 3 shows the relation between the corrosion rate of mild steel and the DO content in water.

In corrosion testing, mild steel specimens were exposed to city water of different DO levels at a water flow velocity of 0.1 m/s for 4 weeks. Generally the corrosion rate of mild steel is proportional to the DO content water and also increases with water temperature. From the figure we concluded that corrosion of the steel pipe can be virtually eliminated by lowering the DO level to 0.5 ppm. Thus the water supply piping may be expected to last at least three times as long under the deaerated condition.

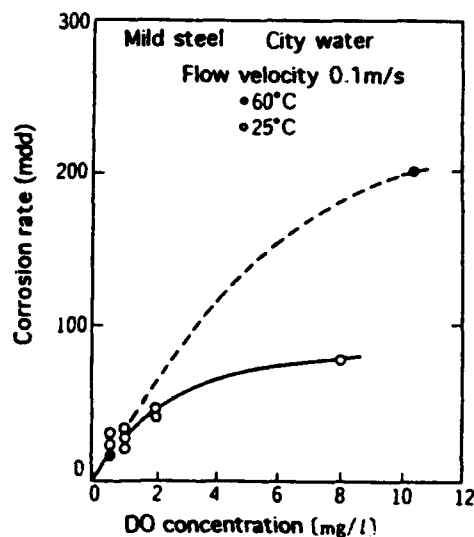


Fig.3 Relation between DO concentration and corrosion rate for mild steel in water

4. Installation of the Deaeration System in Buildings

The membrane type deaeration system can be installed either on a

elevated tank or on a receiving tank.

Figure 4 shows a schematic drawing of the installation of a membrane type deaeration system. Water from the elevated tank is treated by passing through the deaeration unit and supplied to the water supply main. Thus the DO content in water can be kept at levels less than 1.0 mg/l at the end water faucet. The choice of the best system is made by considering the highest peak-load of water usage.

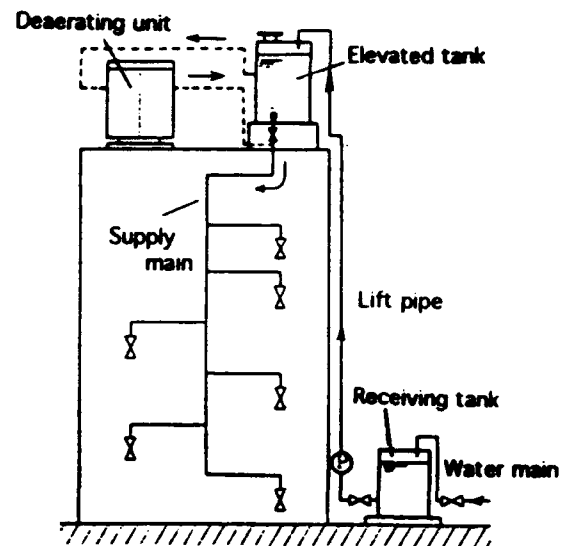


Fig. 4 Installation of deaerating unit in a building

Fortunately, residual chlorine legally required as a disinfectant is not removed by passing through the hollow fiber membrane, because most of the residual chlorine is dissolved in water as hypochlorite in an ionic state. The DO content of water can be easily recovered to some extent by the use of an air-bubble making faucet. Thus the corrosion of the inside surface of the steel pipe can virtually be eliminated, and accordingly, the red-water problems are also resolved.

In hot-water systems, deaerated water can be supplied to the water expansion tank and localized corrosion, such as pitting, erosion-corrosion and cuprosolvency encountered in copper tubing can be avoided. The pitting corrosion mechanism of copper tubing seems to be complicated. In the previous work²⁾ it was discussed that the formation of a particular passive film on copper is a prerequisite factor for the occurrence of pitting under the presence of dissolved oxygen and residual chlorine in hot water. Thus deaeration is an effective means for the prevention of pitting.

In the closed system dissolved oxygen is consumed by the corrosion reaction, but corrosion problems sometimes occur due to DO accompanied by replenished water. Therefore, in the closed cooling water system, water replenishment can be made through the deaeration unit, and water in the system is also partially extracted and returned to the loop after deaeration. Thus, in water that is nearly free of DO, corrosion of the water recirculating loop will be negligible.

5. Case Studies of Deaeration Corrosion Protection

A. Non Chemical Water Treatment in Low-pressure Boilers

In low-pressure boilers, deaeration is a very effective means for corrosion prevention. In the usual injection of chemicals such as hydrazine as a deoxygenating agent, feed-water pipes are sometimes susceptible to pitting corrosion at the entrance of the feed water pipe, because the reaction of the deoxygenating chemicals with DO is relatively slow at ordinary temperatures. In low-pressure boilers the pH of boiler water is commonly maintained at about 11.0 to 11.5 by alkali addition for scale control. However, without the addition of alkali, the pH is easily attained by the decomposition of bicarbonate ions sufficiently contained in boiler feed-water. Thus, combined with an automatic softening apparatus, non-chemical water treatment has successfully been accomplished in the low-pressure boiler.

B. Application to the Cold- and Hot-water Supply in a Hotel

Figure 5 shows changes in the total iron concentration in water with time. Water samples of 200ml were taken every 5 seconds after turning on a faucet. Within a year after construction red-water complaints were already reported. In this figure, comparatively high levels of total iron were detected, particularly in the hot-water system before installation.

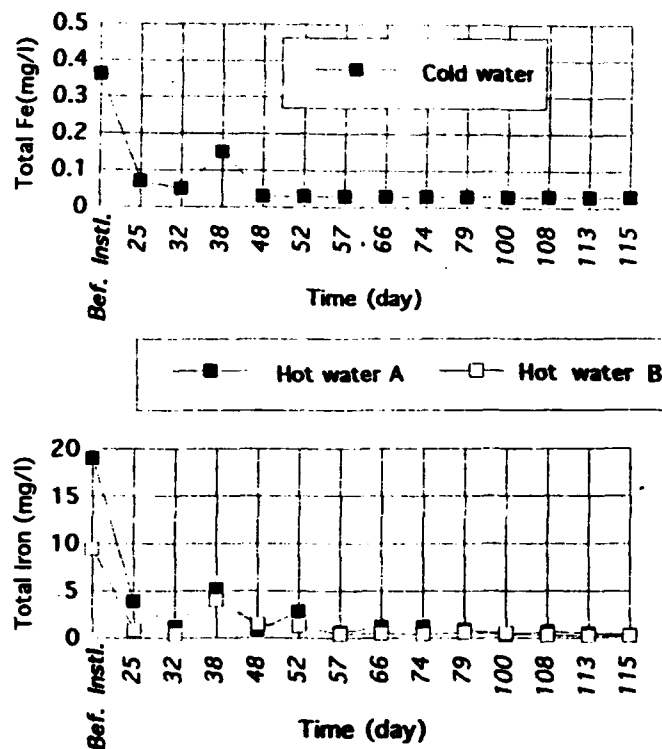
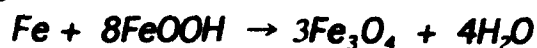


Fig. 5 Changes of total iron in waters with time.

The DO value dramatically decreased after installation of the deaeration unit and thereafter a low level of iron was maintained. Turbidity and color changed in the same manner as the iron

concentration. These results indicate that no more corrosion is occurring in the presence of the low level of DO. The existing FeOOH rust will be electrochemically reduced to magnetite after the total consumption of dissolved oxygen.



C. Red-water Problems in a Company Dormitory

This building has been used for 18 years since construction. Galvanized steel pipes have been used for both cold- and hot-water supply systems. A very high content of iron due to severe corrosion has been detected in the hot-water system. Figure 6 shows the change in iron content of water with time before and after installation of the deaeration equipment. Total iron is decreasing

gradually with time. This indicates that the existing rust was stabilized under the low DO content. In the cold-water system the total iron was lowered below the drinking water standard (0.3mg/l) shortly after installation. It is also demonstrated that deaeration is very effective, even with severe corrosion of the galvanized pipes in hot-water systems.

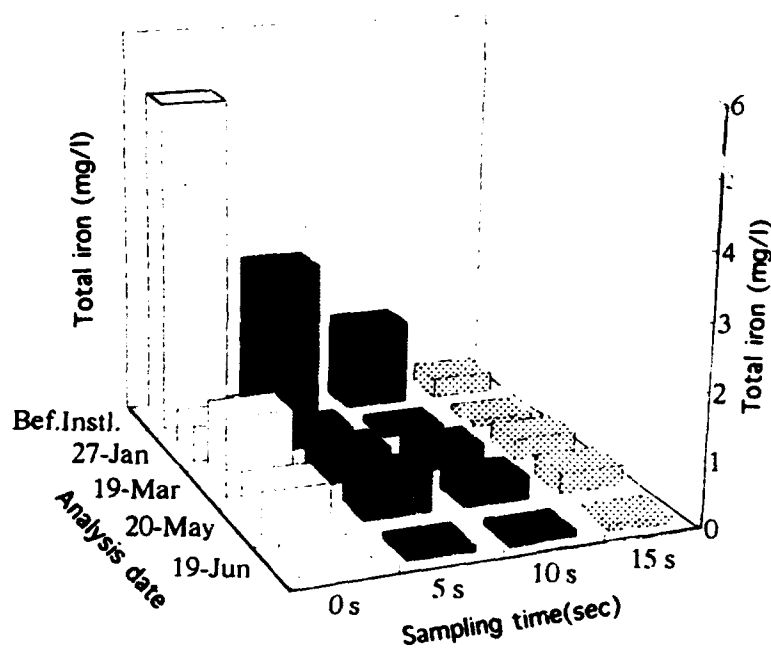


Fig. 6 Changes of total iron content before and after installation.

D. Application to Closed Systems

Deaeration equipment was applied to the closed system of air-conditioning water pipes in an intelligent building equipped with business computers, in which no interruption of cooling water service due to corrosion trouble is allowed. Galvanized steel pipes were used for the water recirculating system. A Fan-coil unit made of copper tubing was installed in the circuit. Mild steel specimens were exposed in the deaerated cooling water of the bypass line for 56 days. Table 1 shows the water quality and results of corrosion testing after 6 months of

Table 1 Water Quality and Corrosion Rate in Closed System

| | System A | System B | System C |
|--------------------------------------|----------|----------|----------|
| Water temperature(°C) | 28.7 | 30.7 | 11.8 |
| pH | 8.5 | 8.9 | 8.7 |
| DO(mg/l) | 0.3 | 0.35 | 0.34 |
| Conductivity (µS/cm) | 202 | 198 | 199 |
| M-Alkali.(mg/l CaCO ₃) | 59 | 60 | 54 |
| Chloride(mg/l) | 18 | 17 | 17 |
| Total Hard.(mg/l CaCO ₃) | 89 | 79 | 77 |
| Silica (mg/l) | 8 | 14 | 7 |
| Fe(mg/l) | 0.03 | 0.05 | 0.08 |
| Cu(mg/l) | 0.04 | 0.04 | 0.04 |
| Zn(mg/l) | 0.17 | 0.08 | 0.31 |
| Corrosion rate(mdd) ^a | 1.27 | 1.88 | 1.42 |

* Average corrosion rate of mild steel specimens (three pieces).
Testing period: 56 days in each loop.

installation. The average corrosion rates calculated from weight loss were 1.27 to 1.88 mdd. These are very low compared to 30 to 60 mdd obtained in the air-saturated waters. The total amount of iron and copper in the water was also very low in concentration. Although the copper content in water is low below 0.1 ppm, copper deposition was found on some specimens, which shows that the dissolved oxygen was almost completely expelled from the cooling water loop system. The zinc content came from the corrosion of galvanized steel pipe ranging from 0.08 to 0.31 mg/l, which means that the corrosion of the galvanized steel pipes is also very small.

6. Conclusion

In soft water corrosion protection measures to be taken are limited because of drinking use. Deaeration using a hollow fiber gas separation membrane was successfully applied as the corrosion protection of the cold- and hot-water supply systems in buildings. It was demonstrated that corrosion and red-water problems were virtually eliminated by reducing the DO content below 0.5 ppm in water. Deaeration without the addition of chemical agents should be reconsidered as a corrosion protective measure from the view point of environmental concerns.

[References]

1. F.N. Speller, Corrosion, Cause and Prevention, (McGraw-Hill, New York, 1951.), p.438.
2. T. Fujii, T. Kodama and H. Baba, Corrosion Science, 24, 10, (1984)p.901.

The Impact of Environmental Considerations on Corrosion Control Economics and Technology

Authored by:
Thomas M. Laronge
Thomas M. Laronge, Inc.
P.O. Box 4448
Vancouver, WA 98662-4448
USA

Abstract

Corrosion phenomena, namely the aggregate effects of one or more material degradation mechanisms, cost society large amounts of money. Large amounts of disposable money are the results of even larger amounts of human labor. These monies and these labors are unnecessary if corrosion control is successful. The economics of the control are favorable. There are also favorable economics to developing technology for corrosion control. However, many environmental activities and "Save the Earth Movements" work against the favorable economics for corrosion control. With the proper actions, the development of corrosion control technology and many of these pro-environment activities can be complimentary.

Corrosion

The purpose of this paper is not to define corrosion. This has been done by many sources, in many different ways and with many different resulting controversies. For purposes of this discussion, it does not matter whether corrosion is purely involving electron changes at the atomic level or not. What is important is strictly that corrosion results in the degradation of materials. The degradation of materials, in turn, results in the impairment of structural integrity of systems, introduction into the environment of unwanted materials in the form of corrosion products and advanced effects such as impairment of human safety. None of these results of corrosion are desirable in terms of the preservation of the world in which we live.

Losses such as those associated with corrosion are best measured in currency units. When this is done, the magnitude of the world's corrosion losses are estimated to be between many hundreds of millions of dollars and several billion dollars per year. Corrosion losses are not small items. They tend to be overlooked because their disastrous affects are spread out over long periods of time. Therefore, the immediacy of addressing a corrosion problem is often masked by other problems which elicit themselves as apparent emergencies. This is unfortunate, because corrosion, properly addressed on a continuing basis, can be stifled. The benefits are both short term and long term economically favorable.

Corrosion Control

Corrosion control basically falls into two different categories. The first category actually involves keeping corrosion from happening. We should properly call this corrosion prevention. Corrosion prevention is accomplished using materials which do not deteriorate at an accelerated rate in the environment in which they operate. Additionally, corrosion prevention can be accomplished by removing any one of the elements required to produce corrosion in a specific environment. For an example, if the cathode of a corrosion cell is removed from electrical contact with the anode, electron transfer cannot occur. If electron transfer cannot occur, the anode will not corrode in that cell. Corrosion may also be prevented by applying surface coatings, linings and other devices which isolate either the anode or the cathode of a corrosion cell from contact with an electrolyte. Similarly, hard coatings and linings may resist abrasion and erosion, thus preventing corrosion by these mechanisms.

A second type of corrosion control involves the slowing of the kinetics of the corrosion process. This is truly a rate control phenomenon. Most important among the rate control technologies is the use of corrosion inhibitors. Generally, corrosion inhibitors interfere with the reactions causing corrosion. The degree of interference translates directly to a percentage of corrosion inhibition. Often, the control can be effected by changes in inhibitor concentration or by other environmental considerations such as moisture content, oxygen content, acid content, temperature, pressure, etc.

Corrosion reaction retardants behave in such a way that they directly affect the rate of reaction. They need not decouple contact between or among the elements required to produce the corrosion.

Electrochemical corrosion control techniques such as anodic protection, cathodic protection, etc. are truly rate controlling corrosion reaction inhibitors. Electrochemical techniques are not corrosion preventing except when they operate perfectly. Needless to say, perfection and human experience do not coexist in the same world for any extended period of time.

Corrosion Control Deterrents

As has already been pointed out, corrosion costs the world tremendous amounts of money and labor. As such, effective corrosion control is economically favorable. This control is sufficiently economically favorable that research which results in effective corrosion control technology is also economically favorable. The reason for separating the costs of research from the costs of corrosion control is simply that the costs of research tend to be somewhat higher than the costs of the actual control. This rests in the sociology elements and not in the other technical elements associated with stalling or halting corrosion processes.

Unfortunately, society does not always perform in the most logical or beneficial fashions with respect to economics.

As world governments build structures in their own and in foreign lands, they tend to not provide for "sinking funds". The accountant allows for depreciation in value, but

the creator does not allow for the maintenance of value. This, is a deterrent to corrosion control.

Bridges rust, concrete cracks, glass flows and etches, plastics embrittle, etc. Stated differently, naturally occurring processes tend to promote material degradation. Mankind tends to be lax with setting up preventative maintenance funds. The reason probably lies in the fact that this would make politicians less effective in their jobs. The establishment of preventative maintenance funds would make the apparent costs of goods and services in a society higher at the outset. This is simply politically unattractive.

Unfortunately, economic analysis continues to show over and over that what appears to be socially unattractive may actually be highly beneficial. The problem lies in the apparent appearance of the short run costs versus the true long run costs. What appears to be expensive in the short run would actually be inexpensive in the long run. The taxpayer is forced to bite the bullet in the beginning and to pay the extra money for the corrosion control.

Alternatively, if corrosion control is properly packaged by politicians and sold to their constituency, all parties benefit. More real dollars are paid upfront. Less real dollars are paid long term. Normally corroding structures last longer and better serve their functions with improved safety.

A second deterrent to corrosion control is best termed "Acts of God". Weather changes, earth quakes, volcanoes, tidal upsets, "dry years", "wet years", all affect corrosion control in a somewhat adverse and/or unexpected fashion. Corrosion is typically designed for average conditions. The engineer often neglects odd events such as the aforementioned.

A new deterrent to corrosion control has sprung up in society as a result of mankind's efforts to save the environment. The latter involves the conflicts between conventional corrosion control technology and conventional environmental protection technology. For example, the use of hexavalent chromate as a corrosion inhibitor in carbon steel systems and in carbon steel and yellow metal systems containing water has historically been the most effective corrosion control technology available. From essentially 1990 forward, this technology is banned as a result of the various environmental movements. Chromates tend to be toxic to living organisms as well as being carcinogenic to many organisms. Because of these unwanted effects to living species, the environmentalist has won out over the corrosion control scientist. In briefest essence, the use of chromates to inhibit corrosion in open environments is banned.

Alternative corrosion control technologies do exist. However, substitute corrosion control technologies do not exist. Each of the corrosion control technologies which have been developed to replace the use of hexavalent chromate have proven to be either more expensive and/or somewhat less effective. It is for this reason that we choose to look at the different technologies as being chromate alternatives and not chromate substitutes.

The ban on chromates is not the only divorce between corrosion control technology and environmental protection technology. Many other corrosion inhibitors have unwanted environmental side effects. Even the use of chlorine as a microbiocide, macrobiocide and/or disinfectant in water systems is severely restricted by the environmentalist. In the future, other oxidizing type, broad spectrum biological control agents promise to be banned and/or severely restricted as a result of the efforts of the environmentalists.

Society pays a tremendous price when selecting among these alternative technologies. As with the case of hexavalent chromate salts, biocides which are alternative to chlorine and oxidizing by nature, are either less effective or more costly than is chlorine. This means that corrosion control for microbiologically influenced corrosion and other forms of corrosion which result from the proliferation of biological organisms are less effective due to environmental considerations.

Other potential corrosion control technologies are stifled by efforts related to the environmentalists. For example, the use of electrochemical protection promises to be severely regulated by consideration of the effects of the related electric fields and magnetic fields. Nondestructive inspection techniques and remote monitoring techniques involving x-ray technologies and radioactive isotopes will be severely regulated by environmental concerns. Corrosion inhibitors other than hexavalent chromate promise to be severely regulated. Many of the regulations are already promulgated or in the process of being promulgated. In general, heavy metal corrosion inhibitors promise to be restricted from discharge to air, water or ground. Monitoring costs associated with such materials increase the cost of corrosion control.

Industrial systems are being built with double walls, dikes, and other environmental protection barriers. A significant portion of the costs associated with these structures is a direct increase in the cost of corrosion control technology.

Another item which works against effective corrosion control is the cost of designing associated structures to be environmentally acceptable. Perhaps this refers to nothing more than the esthetics of blending into the environment. Nevertheless, there is an associated, positive incremental cost. This works directly against the promotion of corrosion control. This is highly undesirable in the long run.

The Marriage Of Corrosion Control and Environmental Technologies

For the overall well being of society, it is necessary that both the end products of the environmentalists and the end products of the corrosion control scientists be compatible. These technologies can be easily and effectively wed. In order to do this, the economist must dovetail the efforts of the corrosion control scientist with those of the environmental scientist.

When the latter is done properly, it becomes apparent the environment can be protected and corrosion can be minimized by prudent planning and acting in the beginning. Where continuing corrosion control technology must be applied to a system to protect the environment and the system, this is best done in the early stages of design. In fact, environmental research and corrosion control research can be

combined in a cost effective fashion. What is required is simply that the outcome of the research be compatible with the needs of both technologies. The cost of the research will not double as there will be synergies realized through the focus of the combined efforts.

Mankind will benefit dramatically from the realization of both corrosion control and environmental protection. People who make their career in the areas where environmental and corrosion control technology overlap will realize more interesting careers and more varied experiences. System operators will have the benefit of lower corrosion product inventories in their system coupled with more consistent operation. Finally, personnel safety and structural integrity of systems will be greatly heightened.